LEABHARLANN CHOLÁISTE NA TRÍONÓIDE, BAILE ÁTHA CLIATH | TRINITY COLLEGE LIBRARY DUBLIN
Ollscoil Átha Cliath | The University of Dublin

Terms and Conditions of Use of Digitised Theses from Trinity College Library Dublin

Copyright statement

All material supplied by Trinity College Library is protected by copyright (under the Copyright and Related Rights Act, 2000 as amended) and other relevant Intellectual Property Rights. By accessing and using a Digitised Thesis from Trinity College Library you acknowledge that all Intellectual Property Rights in any Works supplied are the sole and exclusive property of the copyright and/or other IPR holder. Specific copyright holders may not be explicitly identified. Use of materials from other sources within a thesis should not be construed as a claim over them.

A non-exclusive, non-transferable licence is hereby granted to those using or reproducing, in whole or in part, the material for valid purposes, providing the copyright owners are acknowledged using the normal conventions. Where specific permission to use material is required, this is identified and such permission must be sought from the copyright holder or agency cited.

Liability statement

By using a Digitised Thesis, I accept that Trinity College Dublin bears no legal responsibility for the accuracy, legality or comprehensiveness of materials contained within the thesis, and that Trinity College Dublin accepts no liability for indirect, consequential, or incidental, damages or losses arising from use of the thesis for whatever reason. Information located in a thesis may be subject to specific use constraints, details of which may not be explicitly described. It is the responsibility of potential and actual users to be aware of such constraints and to abide by them. By making use of material from a digitised thesis, you accept these copyright and disclaimer provisions. Where it is brought to the attention of Trinity College Library that there may be a breach of copyright or other restraint, it is the policy to withdraw or take down access to a thesis while the issue is being resolved.

Access Agreement

By using a Digitised Thesis from Trinity College Library you are bound by the following Terms & Conditions. Please read them carefully.

I have read and I understand the following statement: All material supplied via a Digitised Thesis from Trinity College Library is protected by copyright and other intellectual property rights, and duplication or sale of all or part of any of a thesis is not permitted, except that material may be duplicated by you for your research use or for educational purposes in electronic or print form providing the copyright owners are acknowledged using the normal conventions. You must obtain permission for any other use. Electronic or print copies may not be offered, whether for sale or otherwise to anyone. This copy has been supplied on the understanding that it is copyright material and that no quotation from the thesis may be published without proper acknowledgement.

SOLID-STATE CHARACTERISTICS OF PRE- AND POST-SPRAY DRIED ACTIVE PHARMACEUTICAL INGREDIENTS, SALTS AND CO-CRYSTALLINE FORMS

by
Krzysztof Jan Paluch, M.Sc. (Pharm.), M.P.S.I.

Being a thesis submitted for
the degree of
Doctor of Philosophy in Pharmaceutics

at
University of Dublin, Trinity College

Under the direction and supervision of
Anne Marie Healy, B.Sc. (Pharm.), Ph.D., M.P.S.I.

February 2011

TRINITY COLLEGE
2 5 SEP 2012
LIBRARY DUBLIN

Thesis 9644

Declaration

This thesis is submitted by the undersigned to the University of Dublin, Trinity College, for examination for the degree of Doctor of Philosophy.

I declare that this thesis has not been submitted as an exercise for a degree at this or any other university and it is entirely my own work. I agree to deposit this thesis in the University's open access institutional repository or allow the Library to do so on my behalf, subject to Irish Copyright Legislation and Trinity College Library conditions of use and acknowledgement.

I myself carried out all the practical work except where duly acknowledged.

This manuscript was completely written by me with the aid of editorial advice from Dr Anne Marie Healy, Dr Lidia Tajber and Prof. Owen I. Corrigan.

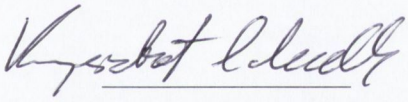

Krzysztof Jan Paluch

To Jaś

Table of Contents

Acknowledgements..... i

Presentations and Publications associated with this thesis..... iii

Abbreviations and symbols v

Summary..... xiii

Introduction

Origin and scope of the thesis..... 1

1. Chapter 1. Introduction

1.1. Preformulation..... 3

1.2. Characterisation of pharmaceutical solids..... 6

1.2.1 Physicochemical crystallography..... 6

1.2.1.1. Hirschfield surface..... 12

1.2.2. Thermal analysis..... 13

1.2.3. Dynamic vapour sorption analysis..... 16

1.2.4. Specific surface area analysis by BET..... 17

1.2.5. Particle size analysis..... 19

1.3. Solid state Properties of pharmaceutical materials..... 21

1.3.1. Crystals..... 22

1.3.1.1. Salts and co-crystals..... 23

1.3.1.2. Solvates (pseudopolymorphic forms)..... 24

1.3.2. Amorphous state..... 26

1.4. Physical processing of pharmaceutical solids..... 26

1.4.1. Spray drying..... 27

1.4.2. Preformulation in tablet formulation development..... 31

1.4.2.1 Orally disintegrating tablets (ODTs)..... 34

1.5. Active pharmaceutical ingredients used in current work..... 35

1.5.1. Chlorothiazide..... 35

1.5.2. Salbutamol..... 38

Experimental

2. Chapter 2. Materials and methods

2.1. Materials used in experiments 39

2.2 Methods 40

2.2.1. Production of active pharmaceutical ingredients..... 40

2.2.1.1. Chlorothiazide sodium and potassium..... 40

2.2.1.1.1. Crystallization studies of CTZ CTZNa and CTZK 40

2.2.1.1.2. Preparation of chlorothiazide salts for tableting (Chapter 7)..... 40

2.2.1.3. Salbutamol adipate and succinate..... 41

2.2.1.3.1. Crystallization studies of salbutamol adipate and succinate..... 41
2.2.2. Spray drying..... 42
2.2.2.1. Spray drying of chlorothiazide and CTZ salts..... 42
2.2.3. Preparation of powders for tableting..... 43
2.2.4. Tableting..... 44
2.2.4.1. Measurement and calculation of tablet geometry parameters..... 45
2.2.4.2. Hardness test, calculation of tensile strength (σ_t) of the tablet..... 45
2.2.4.3. Tablet porosity (ε_t)..... 45
2.2.5. Thermal methods..... 45
2.2.5.1. Differential scanning calorimetry (DSC)..... 45
2.2.5.2. Temperature modulated differential scanning calorimetry (MT-DSC StepScan™) 45
2.2.5.3. Thermogravimetric analysis (TGA)..... 46
2.2.6. Density measurement..... 46
2.2.6.1. Density measurement by helium pycnometry..... 46
2.2.7. X-ray crystallography..... 46
2.2.7.1. Powder X-ray diffraction (PXRD)..... 46
2.2.7.2. Single crystal X-ray diffraction (SC-XRD)..... 47
2.2.7.2.1. Chlorthiazide sodium and potassium..... 47
2.2.7.2.2. Salbutamol adipate and succinate..... 47
2.2.8. Elemental analysis..... 47
2.2.9. Nuclear magnetic resonance (^{1}HNMR, ^{13}CNMR)..... 48
2.2.10. Microscopy..... 48
2.2.10.1. Scanning electron microscopy (SEM)..... 48
2.2.11. Solid state Fourier transform infrared spectroscopy (FTIR)..... 48
2.2.12. Karl Fischer titrimetry- water assay..... 48
2.2.13. Ethanol and acetone assays 48
2.2.13.1. Gas chromatography – mass spectrometry (GC-MS)..... 48
2.2.14. Methanol and butyl acetate assay..... 49
2.2.14.1. Gas chromatography with flame ionisation detector GC-FID..... 49
2.2.15. Sodium and potassium assays..... 49
2.2.15.1. Inductively coupled plasma–mass spectrometry (ICP-MS)..... 49
2.2.16. High performance liquid chromatography (HPLC)..... 50
2.2.16.1. Decomposition of CTZ, CTZNa and CTZK..... 50
2.2.16.2. Detection of adipic and succinic acid in aqueous solution..... 50
2.2.17. Aldehyde detection..... 51
2.2.18. Particle size characterisation..... 51
2.2.18.1. Particle size characterisation by laser diffraction 51
2.2.19. Specific surface area analysis (T_{BET}) by Brunauer, Emmett, Teller (BET) isotherm 51

2.2.20. Solubility studies..... 51
2.2.20.1. Solubility studies of CTZ in water and organic solvents (acetone, ethanol)..... 51
2.2.20.2. Solubility of chlorothiazide, chlorothiazide sodium and potassium..... 52
2.2.20.3. Solubility of salbutamol, salbutamol adipate and salbutamol succinate 52
2.2.21. Intrinsic dissolution rate studies of salbutamol salts 53
2.2.22. Dissolution studies of tablets containing chlorothiazide and its salts..... 53
2.2.23. Water vapour sorption analysis of pharmaceutical solids..... 54
2.2.23.1. Dynamic vapour sorption (DVS)..... 54
2.2.23.2. Detection of critical relative humidity of recrystallisation of amorphous solids..... 54
2.2.24. Solid state stability studies..... 54
2.2.25. Statistical analysis..... 55
2.2.26. Data analysis..... 55

Results and discussion

3. Chapter 3. Preparation and solid state characterisation of chlorothiazide sodium intermolecular self assembly suprastructure

3.1. Introduction..... 57
3.2. Results and discussion..... 59
3.2.1. Crystal structure..... 59
3.2.2. NMR studies 63
3.2.3. Thermal analysis..... 65
3.2.4. Dynamic vapour sorption 66
3.2.5. Other physicochemical characteristics 69
3.3. Conclusions..... 71

4. Chapter 4. Preparation and characterisation of novel chlorothiazide potassium solid-state salt forms: intermolecular self assembly suprastructures

4.1. Introduction 73
4.2. Results and discussion..... 75
4.2.1. Physicochemical analysis..... 75
4.2.2. Crystal structure..... 84
4.2.3. Hirschfield surfaces..... 91
4.2.4. NMR studies 96
4.3. Conclusions 100

5. Chapter 5. Impact of spray drying variables: solvent, feed concentration, inlet temperature and drying mode, on the physicochemical and micromeritic characteristics of chlorothiazide

5.1. Introduction 101
5.2. Results and discussion..... 103

5.2.1. Solubility studies of CTZ..... 103

5.2.2. Spray drying of CTZ 105

5.2.2.1. Spray drying CTZ from acetone and acetone/water solutions..... 105

5.2.2.1.1. Impact of solvent composition and feed concentration..... 105

5.2.2.1.2. Impact of spray drying mode..... 111

5.2.2.2. Spray drying CTZ from ethanol and ethanol/water and water solutions..... 112

5.2.3. Crystallinity of spray dried CTZ..... 113

5.2.4. Investigations into the cause of the variable solid-state properties of spray dried CTZ..... 117

5.3. Conclusions..... 121

6. Chapter 6. Impact of spray drying variables on morphology of microparticles of chlorothiazide sodium and potassium salts

6.1. Introduction 123

6.2. Results and discussion 125

6.2.1. Spray drying 125

6.2.2. Morphology and micromeritic properties of spray dried CTZNa and CTZK 126

6.2.3. Effect of increasing feed concentration and spray dryer configuration on CTZNa and CTZK particle morphology 131

6.2.4. Physicochemical properties of spray dried samples 140

6.2.5. DVS studies of amorphous CTZNa and CTZK..... 147

6.2.6. Residual solvent content..... 149

6.3. Conclusions 151

7. Chapter 7. Assessment of compactibility performance of spray dried nanoporous microparticles of chlorothiazide, chlorothiazide sodium and potassium

7.1. Introduction..... 153

7.2. Results and discussion..... 155

7.2.1. Physicochemical characterisation of powders subjected to compaction..... 155

7.2.2. Geometrical characterisation of compressed tablets..... 161

7.2.3. Compression force versus force to tensile failure and tensile strength – Compactibility..... 163

7.2.4. Compression force versus tablet porosity- Compressibility..... 168

7.2.5. Compression force versus tablet specific surface area..... 172

7.2.6. Dissolution test results..... 182

7.3. Conclusions..... 189

8. Solid state characterisation of novel active pharmaceutical ingredients: co-crystal of a salbutamol hemiadipate salt with adipic acid (2:1:1) and salbutamol hemisuccinate salt

8.1. Introduction 191
8.2. Results and discussion..... 193
8.2.1. Single crystal X-ray analysis 193
8.2.2. Analysis of hydrogen bond network 193
8.2.3. Hirshfeld surfaces analysis..... 198
8.2.4. Results of PXRD analysis..... 200
8.2.5. NMR studies 201
8.2.6. Stoichiometry and elemental analysis..... 204
8.2.7. Thermal analysis..... 204
8.2.8. FT-IR analysis..... 205
8.2.9. Dynamic Vapour Sorption (DVS)..... 206
8.2.10. Solubility and dissolution studies..... 207
8.3. Conclusions 211
9. Chapter 9. General Discussion
9.1. Introduction..... 213
9.2. Characterisation and processing of chlorothiazide (CTZ)..... 213
9.3. Solid state studies..... 215
9.3.1. Solid state nature and physicochemical properties of chlorothiazide salts..... 215
9.3.2. Solid state nature and physicochemical properties of salbutamol adipate and salbutamol succinate..... 218
9.4. Processing of chlorothiazide salts, morphology studies..... 219
9.5. Tabletability of solid state forms of chlorothiazide..... 225
Main findings..... 235
Future work..... 237
References..... 239
Appendix I..... 255
Appendix II..... 267

Acknowledgements

I would like to thank to my supervisors Dr Anne Marie Healy, Dr Lidia Tajber and Professor Owen Corrigan.

Thank you for your guidance, for your ideas and never ending advice and help on my work.
Thank you for every meeting and every hour we spent discussing the results presented in this thesis.
It was a privilege for me to work under the supervision of such experienced researchers.

I would like to thank to Dr Thomas McCabe, Dr Simon Lawrence, Dr John Walsh, Dr John O'Brien and Dr Curtis Elcoate.
Thank you for your help and guidance, especially on single crystal X-ray analysis, nuclear magnetic resonance and spectroscopic analyses.

Thanks to the Center of Microscopic Analysis:
Neal Leddy, Leona Mulvey, Clodagh Dooley, Dr Heath Bagshaw and Colin Reid for technical support and advice on microscopic and mass spectroscopy analyses.

Thanks to Adam Coburn and Ann Connolly for performing elemental analysis.

Thanks to my colleague Bożena Adamczyk, you made Chapter 7 possible to happen and in the way I wanted. Thanks to Joanne Crean and Vincent Curtin for proof reading of this thesis.

Thanks to Patrick Quinlan, Ray Keaveny, Brian O'Reilly, Conan Murphy and Derek Coss for advice and technical support.

Finally thank to you all: Anita Umerska, Christine Grossjohann, Evelyn O'Shea, Maria Ines Amaro, Dr Orla Ni Ógáin, Arun Katheri, Dr Frederic Tewes, Dr Shadeed Gad, Stefano Bianco and Dr Vincent Caron, it was my pleasure to work among you.

Once again special thanks to Lidia for everything you taught me.

This work was founded by sources of
Irish Research Council for Science, Engineering and Technology
and
Solid State Pharmaceutical Cluster founded by Science Foundation Ireland.

Presentations and publications associated with the thesis

Articles:

Paluch, K.J., Tajber, L., McCabe, T., O'Brien, J.E., Corrigan, O.I., Healy, A.M., Preparation and characterisation of novel chlorothiazide potassium solid-state salt forms: intermolecular self assembly suprastructures *European Journal of Pharmaceutical Sciences, 2011, 42, 220–229.*

Paluch, K.J., Tajber, L., McCabe, T., O'Brien, J.E., Corrigan, O.I., Healy, A.M., Preparation and solid state characterisation of chlorothiazide sodium intermolecular self assembly suprastructure, *European Journal of Pharmaceutical Sciences, 2010, 41, 603–611.*

Paluch, K.J., Tajber, L., Zarys metod charakterystyki fizykochemicznej układów amorficznych produkowanych metodą suszenia rozpyłowego (Physicochemical methods of characterisation of amorphous materials produced by spray drying - an outline), *Farmacja Polska, 2009, 65(2), 93-99.*

Paluch, K.J., Tajber, L., Elcoate, C.J., Corrigan, O.I., Lawrence, S.E., Healy A.M., Solid state characterisation of novel active pharmaceutical ingredients: co-crystal of a salbutamol hemiadipate salt with adipic acid (2:1:1) and salbutamol hemisuccinate salt.
Journal of Pharmaceutical Sciences, Submitted on 27.12.2010.

Oral presentations:

Paluch, K.J., Tajber, L., McCabe, T., O'Brien, J.E., Corrigan, O.I., Healy, A.M., Intermolecular self-assemblies of chlorothiazide potassium solvates- physicochemical characterisation, *9th International Workshop on Crystal Growth of Organic Materials, Singapore, 2010*, 2010

Paluch K., Tajber L., Healy A.M., Corrigan O. , Impact of solvent variable on chlorothiazide and chlorothiazide sodium physico-chemical properties, processed by spray drying, *All Ireland Schools of Pharmacy 31st Research Seminar, Dublin, 2009*, 2009

Poster presentations:

Paluch, K.J., Tajber, L., Corrigan, O.I., Healy, A.M., Investigation of physicochemical interactions of spray dried composites comprising polymer and chlorothiazide, chlorothiazide sodium or chlorothiazide potassium, *APS Amorphous III proceedings, Nottingham, 2010*, 2010

Paluch, K.J., Tajber, L., McCabe, T., O'Brien, J.E., Corrigan, O.I., Healy, A.M., Salt or intermolecular self-assembly - physicochemical analysis of crystalline chlorothiazide and chlorothiazide sodium, *All Ireland Schools of Pharmacy 32nd Research Seminar, Belfast, 2010*, 2010

Paluch, K., Tajber, L., Corrigan, O.I., Healy, A.M., An investigation of the effect of spray drying from different solvents on the physicochemical properties of chlorothiazide and chlorothiazide sodium, *AAPS Annual Meeting and Exposition, 8-12 November, Los Angeles, 2009*, 2009, ppM1333

Paluch, K.J., Tajber, L., Corrigan, O.I., Healy, A.M., Solid state characterisation of novel active pharmaceutical ingredients: co-crystal of (R,S) salbutamol mono-adipate and (R,S) salbutamol hemisuccinate, *Solid State Pharmaceutical Cluster Meeting, Limerick, 2010*, 2010

Paluch K, Tajber L, Corrigan OI, Healy AM, An investigation of the effect of spray drying from different solvents on the physicochemical properties of chlorothiazide and chlorothiazide sodium, *IRCSET Symposium Innovation fuelling the Smart Society, Dublin, 2009*, 2009

Paluch, K., Tajber, L., Healy, A.M. and Corrigan, O.I., Comparison of the physico-chemical properties of spray dried chlorothiazide, chlorothiazide sodium and their PVP composite systems, *6th World Meeting on Pharmaceutics, Biopharmaceutics and Pharmaceutical Technology, Barcelona, Spain, 1-10, April, 2008*, 2008

Paluch, K., Tajber, L., Healy, A.M. and Corrigan, O.I., Solid-state characteristics of spray dried chlorothiazide, chlorothiazide-PVP composites, sodium chlorothiazide and sodium chlorothiazide-PVP composites, *All Ireland Schools of Pharmacy 30th Research Seminar, Cork, 2008*, 2008

Abbreviations and symbols

Symbol	Description
$[A^{2-}]$	concentration of the fully dissociated acid species (Eqn. 8.4)
$[HA^{-}]$	concentration of the monodissociated acid species (Eqn. 8.3)
$[S^{-}]$	concentration of monobasic salbutamol species (Eqn. 8.6)
$[SH^{+}]$	concentration of protonated salbutamol species (Eqn. 8.5)
°C	Celsius degree
µg	microgram
µl	microlitre
µm	micrometer
φ	equilibrium in the saturation pressure of adsorbate (Eqn. 1.6.)
$2r_1$	diameter of the tablet
A	slope, or surface area
Å	angstrom
a	axial length
AC	acetone
A_{cap}	surface area of the cap
A_{cl}	cylindrical part of the tablet
AD	additional, secondary drying
ANH	anhydrous
A_p	PXRD peak area (Eqn. 5.2)
API…(s)	active pharmaceutical ingredient(s)
A_t	surface area of the tablet
ATR	attenuated total reflectance
b	axial length
BA	butyl acetate
BET	Brunauer Emmett Teller (isotherm- analysis)
br	broad
c	axial length, or BET constant (Eqn. 1.7)
C_0	feed concentration (Eqn. 6.1)
C_b	bulk concentration
CCDC	Cambridge Crystallographic Data Centre

C_I	crystallinity index
CIF	crystallographic information file
CM	closed mode
cm	centimetre
COSY	correlation spectroscopy
CP	close packing
C_p	heat capacity
C_s	solubility
CTZ	chlorothiazide
CTZK	chlorothiazide potassium
CTZNa	chlorothiazide sodium
d(10)	equivalent diameter where 10% of the particles (by volume) of the powder has a smaller diameter
d(50)	equivalent diameter where 50% of the particles (by volume) of the powder has a smaller diameter
d(90)	equivalent diameter where 90% of the particles (by volume) of the powder has a smaller diameter
d[1,0]	number diameter mean
d[2,0]	number surface mean
d[3,0]	number volume mean, number weight mean, volume mean diameter (VMD)
d[3,2]	diameter of sphere of equivalent surface area, Sauter mean diameter (SMD)
d[4,3]	diameter of sphere of equivalent volume
D	diffusion coefficient
d	dublet
d_0	true density
d_e	external distance from atom to Hirshfeld surface
DH	dihydrate
D-H…A	donor-hydrogen…acceptor
d_{hkl}	interplanar distance between (hkl) planes
d_i	internal distance from atom to Hirshfeld surface
DMSO-D_6	deuterated dimethyl sulphoxide
d_{norm}	normalised distance from atom to Hirshfeld surface
dDPI	dry powder inhaler
DSC	dynamic scanning calorimetry
d_t	density of the tablet
DVS	dynamic vapour sorption

d_{XRD}	the crystallite size
E	the ratio of the solute surface concentration to the average solute concentration in a droplet (Eqn.5.4)
e^-	electron
E_1 or E_L	heat of adsorption (Eqn.1.7)
EtOH	ethanol
F	compression force
FID-GC	flame ionised detector gas chromatography
FTIR	Fourier transform –infrared spectroscopy
FWHM	full width at half-maximum
g	gram
GC-MS	gas chromatography mass spectrometry
GIT	gastro intestinal tract
GPa	gigaPascal
H	height of the tablet
h	hour or thickness of diffusion layer or Miller index
h_1	height of the spherical cap of the tablet
h_2	band thickness of the tablet
$H_2A_{solution}$	equilibrium solubility of the acid (Eqn. 8.1)
HF-DSC	heat flow DSC
HSQC	heteronuclear single quantum coherence
HPLC	high performance liquid chromatography
I	y- intercept
ICP-MS	inductively coupled plasma mass spectrometry
IDR	intrinsic dissolution rate
ISA	intermolecular self-assembly
J	Joule
k	constant (Eqn. 1.13) or Miller index
K	Kelvin degree
$K_{1/3}$	Hixson Crowell constant (Eqn. 1.17)
K_a	acid dissociation constant
$K_{a1,H2A}$	first dissociation constant for the acid (Eqn. 8.3)
$K_{a1,S}$	first dissociation constant for the drug (Eqn. 8.5)
$K_{a2,H2A}$	second dissociation constant for the acid (Eqn. 8.3)
$K_{a2,S}$	second dissociation constants for the drug (Eqn. 8.6)
k_B	Boltzmann constant
KF	Karl Fischer titrimetry
kN	kiloNewton

kPa	kiloPascal
K_{sp}	soluble product constant (Eqn. 8.2)
l	litre or Miller index
LD	laser diffraction
$\log P_O$	octanol/water partition coefficient
LP	loose packing
M	molar concentration
m	mass or multiplet
m_0	initial mass
mbar	milibar
MCS	Morphology Classification System
MeOH	methanol
mg	milligram
MH	monohydrate
min	minute
ml	millilitre
mm	millimetre
mN	miliNewton
MP(s)	microparticle(s)
mp	melting point
MPa	megaPascal
$MPa^{1/2}$	Hildebrand solubility parameters
MS	mass spectrometry
MT-DSC	modulated temperature DSC
mW	miliWatt
N/A	not applicable
n	number, quantity, amount
n_1	order of reflection
N_A	Avogadro's number
nL/h	norm litres per hour
nm	nanometre
NMR	nuclear magnetic resonance
NPMP…(s)	nanoporous microparticles
ODT….(s)	orally disintegrating tablet(s)
OM-B	open, blowing mode
OM-S	open, suction mode
P	fracture load (shear strength under compressive load), or gas pressure (Eqn. 1.5.)

p..... probability or crystal face

P_0..... atmospheric pressure (Eqn. 1.5.)

PC-DSC..... power compensated DSC

PDE..... permitted daily exposure

pH..... $pK_a+\log[A^-]/[salt]$

pK_a..... $-\log_{10}K_a$

pMDI...(s)..... pressurised metered dose inhaler(s)

PVP..... polyvinyl pyrrolidone

PXRD..... powder X-ray diffraction

Q..... quantity (Eqn. 1.13)

q..... crystal face

R..... ideal gas constant

r..... radius of the sphere of the cylindrical cap of the tablet or crystal face

r_0..... initial radius (Eqn. 1.16)

r_1..... radius of the tablet

R^2..... linear correlation coefficient

RC..... relative crystallinity

Ref..... reference (sample or material)

RH..... relative humidity

s..... second or singlet

S..... sample

S_0..... initial solution saturation (Eqn.5.4)

SA..... salbutamol (hemi)adipate co-crystal with adipic acid (2:1:1)

SB..... salbutamol (base)

$S_{cocrystal}$..... co-crystal solubility (Eqn. 8.7)

SC-XRD..... single crystal X-ray analysis

SD..... spray drying

SEM..... scanning electron microscopy

S-H_2A..... co-crystal/salt in the solid phase (Eqn. 8.1)

SS..... salbutamol sulphate

S_{salt}..... salt solubility (Eqn. 8.8)

SSDDS..... solid state drug delivery system

$S_{solution}$..... equilibrium solubility of the drug (Eqn. 8.1)

SSU.MeOH..... salbutamol hemisuccinate tertmethanolate

SSU..... salbutamol succinate

T..... temperature

t	time or triplet
T_{BET}	specific surface area by BET
Tg	glass transition (midpoint temperature)
TGA	thermogravimetric analysis
T_{LD}	specific surface area by laser diffraction
T_t	surface area of the tablet
UV	ultraviolet
v/v	volume/volume
v/w	volume/weight
V_{cap}	volume of the cap of the tablet
V_{cl}	volume of the cylindrical part of the tablet
V_t	volume of the tablet
W	water or Watt
XRD	X-ray diffraction
XX	distance, section
Z	symmetry axis
α	axial angle, or adsorption constant (Eqn.1.5.)
β	difference in the full width at half-maximum (Eqn. 5.1) or axial angle
γ	axial angle
Δ	change per unit (time or temperature)
δ_d	dispersion component
δ_h	H-bond component
δ_p	polarity component
δ_t	total solubility parameter
$\Delta\delta$	NMR peak shift
ε_t	tablet porosity
θ	diffraction angle, or fractional, monolayer coverage of the surface (Eqn.1.5.)
κ	solvent evaporation rate
λ	wavelength
ν(F1)	NMR peak position
Σ	a sum
σ_r	relative standard deviation
σ_t	tensile strength
τ_D	characteristic droplet drying time (Eqn.5.4)
τ_p	precipitation window (Eqn.5.4)
τ_{sat}	characteristic time to saturation (Eqn.5.4)

υ..... adsorbed gas volume (Eqn. 1.6.)

υ_m..... monolayer adsorbed gas quantity (Eqn. 1.6)

$\Phi(T_{BET})$..... estimated particle diameter calculated from T_{BET}

Φ_d..... diameter of a droplet (Eqn. 6.1)

Summary

Salt or co-crystal formation is one of the methods of altering the physicochemical properties of an active pharmaceutical ingredient (API). The drug characteristic can also be changed upon processing. This thesis focused on solid-state characteristics of pre- and post-spray dried APIs, salts and co-crystalline forms. Two model APIs were investigated, chlorothiazide (CTZ), as an example of poorly water soluble acidic API, and salbutamol (SB), as an example of an amphoteric molecule, which is sparingly soluble in water. CTZ and SB were chosen in order to investigate how the selection of co-formers alters the physicochemical properties of the solid state form of the new forms of the APIs. Sodium and potassium cations, as the co-formers, were selected for CTZ, while the properties of SB were altered with adipate and succinate anions.

The solid state forms were characterised using thermal methods such as differential scanning calorimetry (DSC), temperature modulated differential scanning calorimetry (MT-DSC StepScan™) and thermogravimetric analysis (TGA). Crystallographic studies comprised powder X-ray diffraction (PXRD) and single crystal X-ray diffraction (SC-XRD). Results of X-ray analyses were supported by elemental analysis, nuclear magnetic resonance (^{1}HNMR, ^{13}CNMR) and solid state Fourier transform infrared spectroscopy (FTIR). Water vapour sorption analysis was performed by dynamic vapour sorption (DVS). Solvent content was analysed by Karl Fischer titrimetry and gas chromatography. Sodium and potassium contents were analysed using inductively coupled plasma–mass spectrometry (ICP-MS). Micromeritic properties were characterised using scanning electron microscopy (SEM), particle size analysis by laser diffraction, specific surface area analysis (T_{BET}) by Brunauer, Emmett, Teller (BET) isotherm and true density measurements based on helium pycnometry. Solubility studies of the compounds were carried out and intrinsic dissolution rate studies of salbutamol salts and co-crystal performed. Selected new API forms were processed by spray drying and tableting. Characterisation of tablets involved measurement and calculation of tablet geometry parameters, hardness testing, calculation of tensile strength (σ_t), tablet porosity (ε_t) and dissolution studies. Solid state stability studies of CTZ salts post spray drying were carried out.

CTZ can form salts with sodium (CTZNa) and potassium (CTZK) counterions; these salts can present different solid state forms. CTZNa can be obtained as a dihydrate (CTZNa DH), anhydrous and amorphous form. CTZK can be obtained as a dihydrate, monohydrate, monohydrate hemiethanolate, anhydrous and amorphous form. CTZNa DH formed an intramolecular self-assembly (ISA) when crystallised from water or water/acetone (1:1 v/v) mixture. CTZ formed two different ISAs with potassium cations when crystallised from water and ethanol. Anhydrous CTZNa and CTZK had the following melting/decomposition points: ~289 °C and ~263 °C, respectively. The glass transition temperatures of CTZNa and CTZK were determined to be 192 °C and 160 °C, respectively. The solubilities of CTZNa DH and CTZK DH were determined to be ~80 mg/ml.

Spray drying of CTZ resulted in an amorphous form with Tg at 135 °C. Spray drying was an effective method of production of microparticles (MPs) and nanoporous microparticles

(NPMPs) of amorphous CTZNa and CTZK. The Morphology Classification System of spray dried particles (MCS) developed was a useful tool for characterisation of morphology of spray dried powders. NPMPs with specific surface areas of 70 m^2/g and 90 m^2/g for CTZNa and CTZK, respectively, and morphology types of V1BS (porous conglomerates of nanoparticles (V), spherical (1), crumpled (B) and with solid, non-hollow interior (S)) of MCS were obtained with satisfactory yields (~90-95%) by spray drying from 2% w/v feed and composed of methanol/butyl acetate (MeOH/BA) (3:7 v/v) mixture.

NPMPs of CTZNa and CTZK produced by spray drying had better compactibility and compressability in comparison to crystalline and non-porous spray dried (MPs) salts. NPMPs compacts maintained large specific surface area, at the same time presenting large tablet porosity and satisfactory tensile strength. CTZNa and CTZK NPMPs tablets presented very good dissolution performance presenting the shortest times for complete release of the API dose loaded.

For the first time it was reported that salbutamol can form a co-crystal. The involvement of adipic acid molecule in the formation of a co-crystal of a salt was reported for the first time. The salbutamol succinate tertmethanolate (SSU.MeOH) which was prepared was a rare example of the succinate constituting a solvated salt form. The intrinsic dissolution rate of salbutamol succinate (SSU- desolvated SSU.MeOH) was around 4-fold greater than that of salbutamol adipate (SA), consistent with the ~5-fold difference in aqueous solubility of salbutamol in SA and SSU.

Careful selection of co-former can allow for considerable alteration of the physicochemical properties of the API. While co-former selection is still largely an empirical process, the results presented in this thesis may ultimately contribute to an improved understanding and ability to predict the physicochemical properties of different API solid state forms.

Introduction

Origin and scope of the thesis

The physicochemical properties of an active pharmaceutical ingredient (API) are the key parameters defining its utility and processability. These can be modified deliberately or unintentionally as an effect of processing.

One of the most popular approaches to the modification of API properties is the formation of salts. Recent progress in physicochemical, crystallographic characterisation of organic compounds resulted in differentiation of co-crystallised materials (an API and co-former) between salts, co-crystals and compounds which may be considered to be a combination of both salt and co-crystal. Salts or co-crystals will usually present different physicochemical properties than the parent compound. Modifications may alter the aqueous solubility of the API and thereby its crystal structure or solid state form, melting point, solubility in organic solvent, bioavailability etc. From a regulatory point of view a new salt of an API molecule is considered to be a new chemical entity. It may benefit from additional or new intellectual property rights for an already existing API or its derivative. The choice of salt or co-crystal co-former remains predominantly empirical. The impact of co-former on the physicochemical properties of a co-crystallised form is poorly understood to date. A change in the solid state form of an API as an unexpected effect of processing or co-processing may result in a significant alteration of processability of the API. Changes may affect both: production process and pharmaceutical properties of final dosage form.

This work originates from the previous studies on thiazide diuretics (Corrigan et al., 1984), who reported atypical behaviour of chlorothiazide (CTZ) upon spray drying, which, in contrast to the other processed thiazides, resulted in a crystalline material. This different behaviour of CTZ warranted further investigations on the use of other process parameters of spray drying than those used by Corrigan et al. and their impact on the solid state forms of CTZ. Also, in the light of previous studies on salts of diclofenac (O'Connor and Corrigan, 2001) and the studies on the effect of environmental factors on dehydration of diclofenac dihydrate and theophylline monohydrate (Ledwidge and Corrigan, 1997) it was of interest to investigate the salt forming abilities of CTZ and characterise any successfully produced salt forms.

Previous studies of Healy et al. (2008) on excipient-free nanoporous microparticles (NPMPs) of bendroflumethiazide produced by spray drying from solutions, resulted in attempts to produce NPMPs of CTZ and its salt forms, since examples of crystalline NPMPs are scarce (unpublished data) and it was of interest to compare the process requirements for salt and non-salt APIs. Aerodynamic properties of NPMPs have already been studied and reported (Nolan et al., 2009, Nolan et al., 2011 and Ni Ógáin et al., 2011). However, other functional properties of NPMP materials, such as compactibility, remain unknown.

Studies of Corrigan et al. (2004, 2006a and 2006b) on co-processing salbutamol sulphate with lactose, polyethylene glycol and chitosan by spray drying led to an idea of producing

alternative co-crystalline forms of salbutamol in order to achieve a decreased intrinsic dissolution rate of salbutamol, thus avoiding co-processing with matrix formers.

It was hypothesised, that the selection of co-formers for each API; chlorothiazide and salbutamol, will result in an alteration of physicochemical properties of the new solid state form such as a glass transition (Tg) of amorphous forms or altered solubility, dissolution rate of the co-crystallised API. It is expected that observed changes may reflect physicochemical differences between selected co-formers.

The main objectives of this thesis were:

1. To investigate the impact of co-formers on the physicochemical properties of poorly soluble model APIs, chlorothiazide (an acidic molecule with high melting point) and salbutamol (an amphoteric molecule). Sodium and potassium, small, inorganic and monovalent cations were chosen as co-formers for CTZ, while two organic bivalent dicarboxylic anions, succinate and adipate, were selected as the co-formers for salbutamol.

2. To examine the solid-state changes and other physicochemical properties of CTZ, chlorothiazide sodium (CTZNa) and chlorothiazide potassium (CTZK) on spray drying through systematic studies involving the impact of feed composition, configuration of the spray drier and process parameters. The ability of these compounds to form NPMPs was also investigated.

3. To study the compaction properties of a range of pre- and post-processed CTZ, CTZNa and CTZK materials to elucidate the influence of the solid-state and micromeritic properties on API tabletability.

Chapter 1

Introduction

1.1. Preformulation

The detailed characterisation of the physicochemical properties of active pharmaceutical ingredients (APIs) is essential for the successful formulation of solid state drug delivery systems (SSDDS).

If the specification of the final dosage form is known, based on the detailed characterisation of the API in the preformulation stage of product development, the physicochemical properties of that API may be modified to meet formulation requirements. The preformulation stage, involving the comprehensive characterisation of the API, minimises unexpected formulation problems in later stages of drug form development as well as the costs and time necessary to deliver an optimised dosage form to subsequent stages of product development. As preformulation is one of the very first steps in product development, it is expected that it will deliver the correct physicochemical form of the API characterised by the desired biopharmaceutical and physicochemical properties.

An optimised API molecule should possess the following characteristics: expected dissolution rate at a given pH, good aqueous solubility, high melting or decomposition point, low hygroscopicity or other desired process requirements, examples of which are listed in table 1.1. In the case of the development of an API by spray drying, preformulation will be focused on determining, for example, melting and glass transition temperatures (Tg) and organic solvent solubility, but in the case where the final dosage form is a tablet, other properties, such as compactibility of the API, will be addressed. The direction and the scope of preformulation studies can also be determined by the desired delivery route. For example, particle size, morphology and specific surface area of the material is important for pulmonary delivery.

Preformulation is related to the lead optimisation phase (for example solid-state form optimisation), though it can also commence in the lead identification phase (selection of a chemical molecule for further product development), assuring identification of polymorphic or pseudopolymorphic forms of prenominated APIs (Gibson, 2001). Selected physicochemical properties of APIs intended to be formulated as SSDDS are listed in table 1.1.

Table 1.1. Selected characteristics of APIs and their preformulation implications

Properties of API	Preformulatory implications
Solubility (aqueous) - high, pH independent	Potentially high bioavailability
Organic solvents solubility	Improved processability
Intrinsic dissolution rate (IDR)	Faster or slower dissolution
Crystallinity	Better physical stability than that of amorphous forms
Polymorphic forms	Risk of solid state transformation
Amorphous form	Improved solubility, decreased physical stability, modified chemical stability
Solvation	Risk of desolvation upon processing
Melting point (mp)/Tg/decomposition point	High MP may imply low solubility, low Tg suggests risk of recrystallisation
Hygroscopicity	Impacts on the physicochemical stability and processability
Non-flammable, Non-explosive	Safety, processability
Organoleptic properties	Final dosage form selection

In the modern pharmaceutical industry the tablet form is a first choice SSDDS for systemic drug delivery. SSDDS are also accepted for pulmonary delivery of locally acting APIs.
Some physicochemical properties appear to be time dependant and require study over time, for example stability studies. Solid state transformations can occur under environmental conditions of storage, handling or material transportation. Compatibility studies may be desired to assess the effect of interactions between the API and one or more formulation excipients. To characterise properties of APIs, several analytical techniques can be applied. Selected techniques are listed in table 1.2.

Table 1.2. Selected analytical methods used in preformulation characterisation.

Analytical method	Result
Physical characterisation	
Nuclear magnetic resonance (^{1}H, ^{13}C NMR)	Molecular structure confirmation
Fourier transform infrared spectroscopy (FT-IR), Raman	Molecular structure confirmation
X-ray diffraction, single crystal X-ray analysis	Molecular structure determination, polymorphic screening, detection of amorphous phase
Differential scanning calorimetry (DSC) including temperature modulated DSC	Residual solvent content, solvate formation, Tg, MP detection, thermal recrystallisation, decomposition
Thermogravimetric analysis combined with DSC	Residual solvent content, solvate formation, sublimation, evaporation, decomposition
Helium pycnometry	True density
Dynamic vapour sorption (DVS)	Hygroscopicity, solvate formation, humidity of recrystallisation, surface area
Chemical characterisation	
Elemental analysis	%w/w content of selected atoms e.g. C, H, N
Spectroscopy	Purity
UV Spectrometry	Chemical content, purity
Chromatography	Chemical content, purity
Karl-Fischer titrimetry	Water content
Micromeritic characterisation	
Scanning electron microscopy (SEM)	Morphology, crystal habit
Laser diffraction	Particle size analysis by volume, particle size distribution
Surface area analysis by BET	Specific surface area

1.2. Characterisation of pharmaceutical solids

1.2.1 Physicochemical crystallography

X-ray diffraction analysis (XRD) is an analytical method, which allows the crystalline or amorphous nature of a solid material to be determined. The principle of the analysis is based on a Bragg law (Bragg, 1913), which states that X-ray waves scatter on the faces of crystalline materials. As a result, XRD generates a unique crystal peak pattern for each crystalline material present in a given crystal form (Hull, 1919). As a consequence, XRD allows (pseudo)polymorphic transformations to be monitored.

In preformulation, powder X-ray diffraction can be applied to monitoring of intentional or unexpected solid state transformations of API upon processing. Modern XRD equipment can be used to investigate crystal lattice changes with changing temperature, humidity or pressure factors, as well as detecting solvate or hydrate transformations.

Regular and repeating planes of atoms that form the crystal lattice define the three-dimensional structure of the crystalline materials. When a focused X-ray beam interacts with these planes of atoms, parts of the beam are transmitted, absorbed, refracted, scattered or diffracted. X-rays are diffracted by each sample differently, depending on the contents of the crystal lattice and the atomic arrangements.

In powder X-ray diffraction, X-rays are generated within a sealed tube that is under vacuum. Applied current heats a filament within the tube. The filament emits the electrons. A high voltage (15-60 kV) applied within the tube accelerates the electrons. The beam of electrons hits a copper target causing the production of X-rays. These X-rays are filtered, collimated and directed onto the sample. The detector collects the X-ray signals and converts them into a count rate.

All X-ray diffraction techniques are based on Bragg's law, which describes the diffraction of a monochromatic X-ray beam (fixed wavelength) impinging on a plane of points. Parallel incident rays strike the crystal planes at an angle q and diffraction is observed from the crystals only when the angle between the X-rays and the planes in the crystal fulfil the Bragg condition (Eqn. 1.1)

$$n_1\lambda = 2d_{hkl}\sin\theta \qquad \text{Eqn.1.1}$$

where: n_1 is an order of reflection, λ is a wavelength of incident X-ray beam (λ=1.542 Å for CuK_α radiation), d_{hkl} is interplanar distance between (hkl) lattice planes $(hkl)_n$ and $(hkl)_{n+1}$ and θ is a diffraction angle. The Bragg equation states that the product of the diffraction order (n) and the wavelength (λ) is equal to twice the product of the distance between the lattice planes (d_{hkl}) and the sine of the diffraction angle ($\sin\theta$). The diagram that leads to the Bragg equation is presented in Figure 1.1, where the XY distance is equal to $n\lambda$.

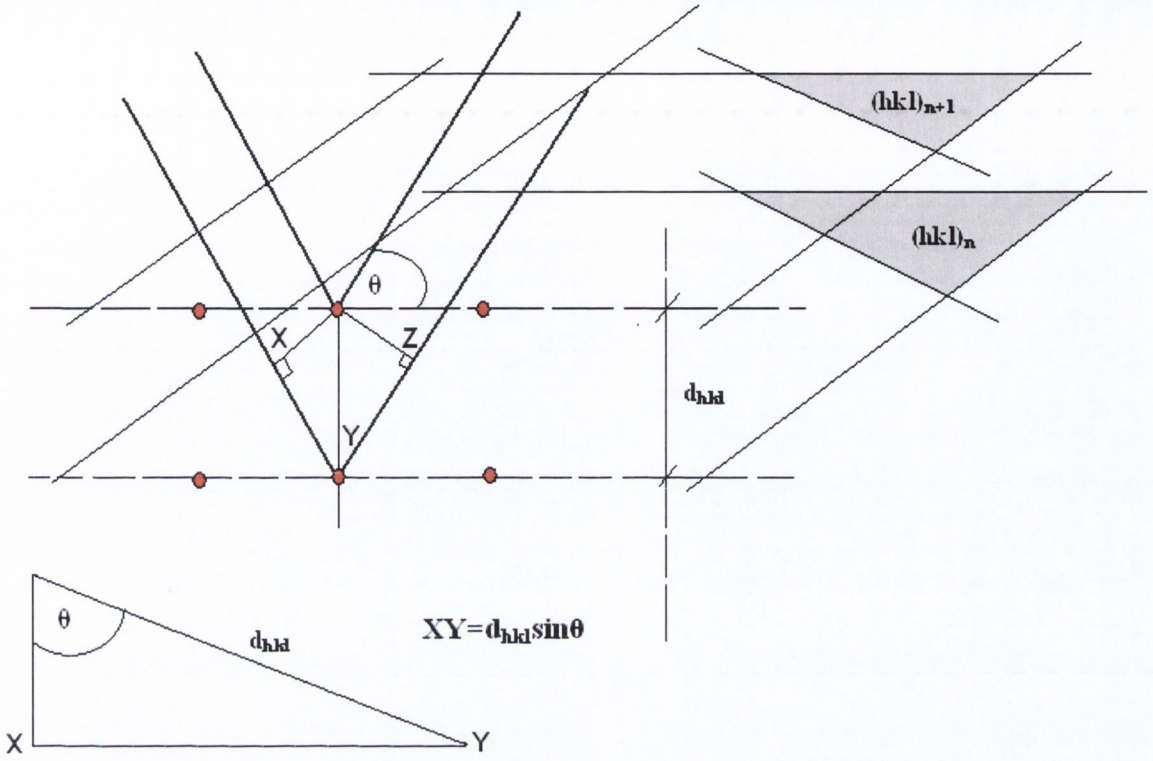

Figure 1.1. Schematic diagram of how the Bragg equation is derived from a crystal structure.

The description of a single crystal cell requires three crystal faces to be chosen which will be named coordinate planes (Fig. 1.2).

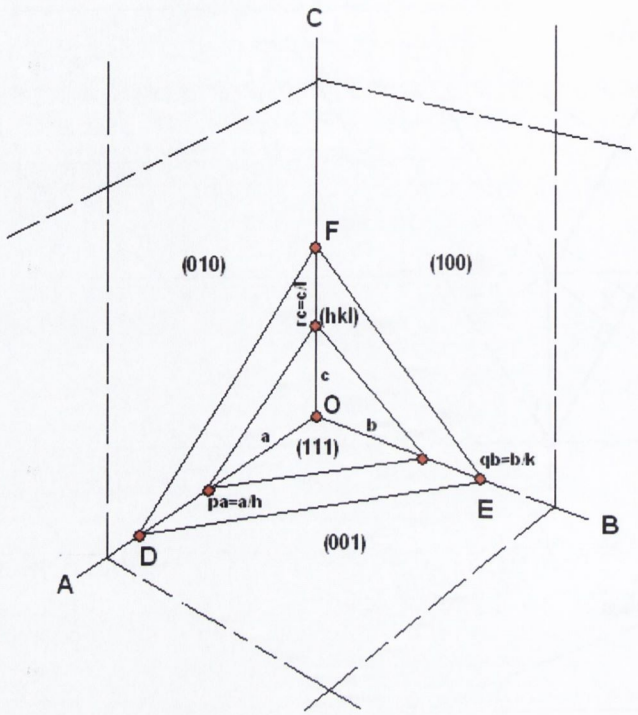

Figure 1.2. The three axial basis set planes, with parametral plane with symbols.

Intersections of coordinate planes will define coordinate axes (A, B and C). A fourth crystal face, named the unit face or parametral face, is placed at the distance from the coordinate centre (O). The intercepts of the unit face with coordinate axes form lengths: a, b and c, named axial lengths. All four determined faces are named fundamental faces. The positive axial directions (axial angles) are: α (between b and c), β (between a and c) and γ (between a and b). The a, b, c and α, β, γ are called direct crystal elements. The C axis is vertical. The A axis is placed in the sagittal plane (back to front direction, sloping towards the observer). The B axis is placed in the back to front direction, sloping right. The direction of any crystal face can be described in direct (Cartesian) set of three coordinate axes, by three parameters p, q and r. Parameters are the ratios of intercepts on the axes, expressed in axial length (Eqn. 1.2):

$$p = \frac{OD}{a};\ q = \frac{OE}{b};\ r = \frac{OF}{c} \qquad \text{Eqn. 1.2}$$

The inverse of these ratios are used as Miller indices (De Jong, 1959) (Eqn. 1.3):

$$h = \frac{1}{p} = \frac{a}{OD}; k = \frac{1}{q} = \frac{b}{OE}; l = \frac{1}{r} = \frac{c}{OF} \qquad \text{Eqn. 1.3.}$$

The direction of the face is indicated by the symbol (hkl) where the h:k:l ratio is constant. If the face is parallel to an axis, one of the symbol indices is zero. The coordinate plane symbols are: (100), (010), (001) and (111) for the unit plane. If the index of the plane symbol is negative, then the minus sign is placed above it. The direction of an edge is indicated by the symbol comprising the three coordinates (indices) of an arbitrary point on the edge (Fig. 1.3). The coordinates are expressed in axial lengths. The symbols of the axes are [100], [010] and [001], the unit edge symbol is [111] (De Jong, 1959).

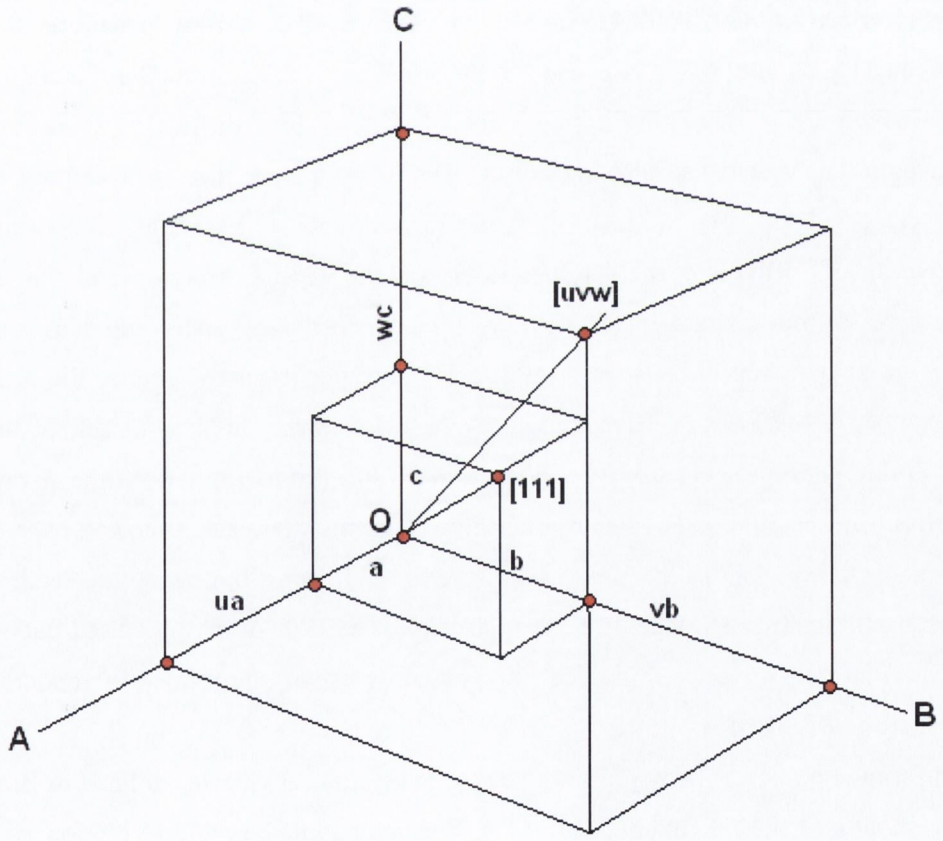

Figure 1.3. The direction [111] and [uvw] (arbitrary) in three-axial set (De Jong, 1959).

The result of a powder XRD measurement is a diffractogram. The information contained in a powder diffraction pattern can be summarised as: faces present (peak positions), face concentration (peak height), amorphous content (background) and crystallite size/strain (peak

widths). Powder diffraction is mainly used for "finger print identification" of solid materials. In powder or polycrystalline diffraction it is important to have a sample with a smooth flat surface. If possible, the sample is normally ground prior to analysis. The ideal sample is homogeneous and the crystallites are randomly distributed (random distribution of all possible h, k, l planes). The sample is pressed into a sample holder so as to present smooth and flat surface. Only crystallites having reflecting planes (h, k, l) parallel to the specimen surface contribute to the reflected intensities. If the sample is truly random, each possible reflection from a given set of h, k, l planes have an equal number of crystallites contributing to it. All possible reflections are recorded by exposing the sample to a range of glancing angles θ (for example 5°- 40° 2θ°).

An extreme case of non-random distribution of the crystallites is referred to as "preferred orientation". The intensities of peaks in a randomly oriented diffraction pattern and a preferred oriented diffraction pattern can be entirely different. Quantitative analysis depends on intensity ratios which are greatly distorted by preferred orientation. Several methods have been developed to overcome the problem of preferred orientation. For instance, transmission powder XRD is superior to reflective powder XRD as in the former the X-rays penetrate the sample and the detected signal is averaged over the various orientations of crystals (Blake et al., 2009).

In contrast, X-rays striking a single crystal will produce diffraction spots in a sphere, referred to as Ewald sphere, around the crystal. Definition of parameters describing the Ewald sphere is presented in (Figure 1.4). Each diffraction spot corresponds to a single (hkl). The distribution of diffraction spots is dependent on the crystal structure and the orientation of the crystal in the diffractometer. The relative intensity of spots provides information on the placement of atoms in a single crystal cell. Since the electrons scatter the X-ray beam, recorded points are the electrons densities in every point of the single unit cell of the crystal, expressed as the number of electrons per cubic unit in Angstroms [$e^-/Å^3$]. As the X-ray beam is diffracted from the whole crystal, electron density represents the result averaged over the whole crystal not a single unit cell, as the X-ray scan is performed over a finite time the electron density image is time-averaged. The image of electron density of each atom may be fused due to thermal vibration of an atom. To reduce this effect, X-ray scan is usually performed in vapours of liquid nitrogen (Blake et al., 2009).

The resolution of an X-ray scan is given by a minimum d value as defined in Bragg's law, which corresponds to the maximum value of θ. The maximum possible resolution is λ/2 when $\sin(\theta_{max})=1$ and for Mo K_α at θ_{max} 25° it is 0.84 Å and for Cu K_α radiation it is 0.77 Å (Blake et al., 2009).

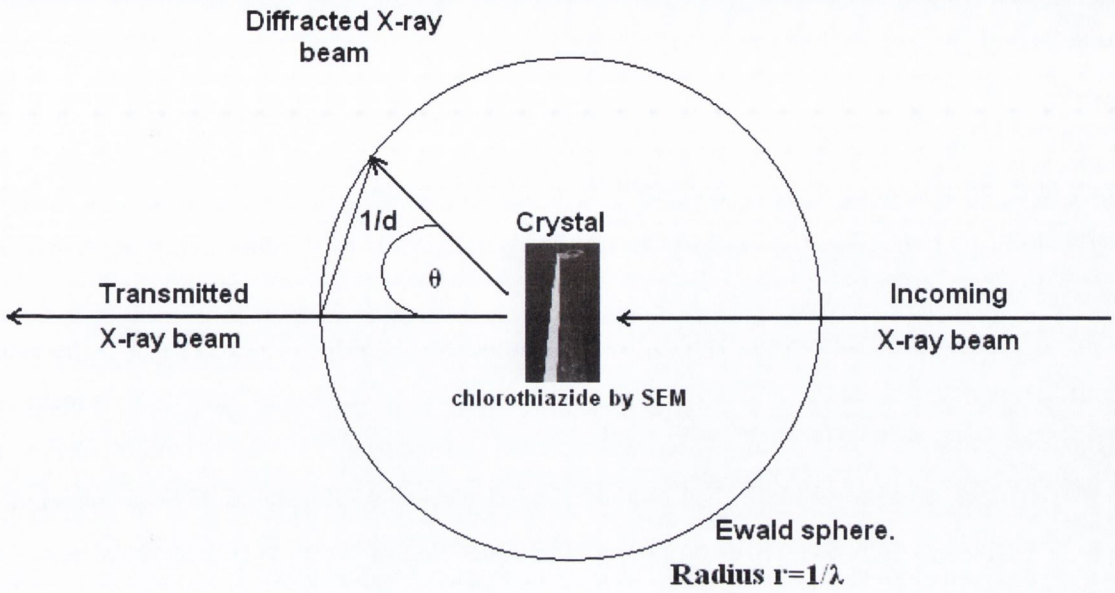

Figure 1.4. The Ewald sphere: definition of parameters. Adopted from Blake et al., (2009).

The single crystal sample is a perfect (all unit cells aligned in a perfect extended pattern) and refractive crystal with a cross section of about 0.3 mm. The single crystal X-ray diffractometer and associated computer package is used mainly to elucidate the molecular structure of novel compounds. The final result of the analysis is a crystallographic information file (CIF).

The specification of the CIF standard was published by Hall et al. (1991). The CIF format is used to archive crystallographic data, to transfer data between crystallographic programs or between laboratories, to provide supplementary paper data containing crystal structure determination, to deposit crystal structure in databases and to create standard printed tables.

1.2.2. Hirshfeld surface analysis

One of the analytical methods based on the examination of a single crystal X-ray data file is Hirshfeld surface analysis. Surface maps based on this approach are very valuable for analysing intermolecular interactions in the different crystal structures (McKinnon et al., 2007). Parameters describing the surface are d_i and d_e, where d_i corresponds to the distance between the surface and the atom placed the closest internally to the surface and d_e corresponds to the distance between the surface and the atom placed the closest externally to the surface. d_{norm} is the sum of d_i and d_e where each parameter is normalised to the van der Waals radius of the involved atom (Hirshfeld, 1977).

3-D images of surfaces of molecules are partially coloured and partially gray. The colour spectrum ranges from blue to white to red. If the surface is coloured blue, it means, that reciprocal interactions between two molecules placed internally and externally to the Hirshfeld surface are longer (weaker) in relative scale than van der Waals forces. White planes indicate interactions which are equal to van der Waals distance, while red surfaces represent interactions which are stronger (shorter) than van der Waals forces.

The 3-D surface surrounding the molecule can be depicted by a D-2 fingerprint plot where $d_e=f(d_i)$. Fingerprint plots bring additional information, apart from an analysis of how strong contacts are compared to van der Waals forces. The fingerprint plot depicts the percentage of the overall Hirshfeld surface covered by a particular type of bond. A red, strong interaction, or so called "hot-spot" can be crucial in the formation of a particular crystal structure, but will not cover a large percentage of the Hirshfeld surface, so the overall stabilising effect on the crystal structure of this bond can be weaker than a less intensive, blue interaction, which covers a larger percentage of the Hirshfeld surface.

1.2.3. Thermal analysis

Differential scanning calorimetry (DSC) is a physical method of investigation of heat transfer (flow) within a material (solid or liquid) relative to an applied temperature program (heating, cooling, isothermal analysis) in reference to the control sample (Höhne et al., 1996). With temperature change, the detector records the difference in heat output of the two heaters (for power compensated DSC) for sample and reference. The heat absorbed or released by the sample is plotted versus temperature. The heat flow is seen as units of heat (H) per a unit of time (t) - ΔH. The heating rate is temperature increase (T) per a unit of time (t) - ΔT. Heat capacity Cp can be therefore defined as equation 1.4.

$$C_p = \frac{\Delta H}{\Delta T} \qquad \text{Eqn. 1.4.}$$

Specific heat is an amount of work, in Joules [J], required to be done by heat flow to raise the temperature of 1 gram of material by 1 °C. From equation 1.4 it can be seen that key parameters that can affect heat flow (ΔH) in DSC are the heating rate (ΔT) and a change of specific heat capacity ΔC_p. The ΔC_p occurs because of the change of thermal resistance between the sample and the reference. As the reference (an empty sample holder) remains unaffected by the temperature and time change, the entire change is related to the change of thermal resistance of the sample material.

Resistance can be decreased, which is recorded as an endoenergetic event (energy is absorbed by the material) and ΔH increases during, for example, melting. Recrystallisation of an amorphous phase on heating results in an increase in thermal resistance of the material. Recrystallising material releases excess energy, which is recorded as an exoenergetic event.

Two types of DSC equipment can be distinguished: the heat flux DSC (HF-DSC) and the power compensation DSC (PC-DSC). HF-DSC has a common heater for sample and reference. The measured signal is a difference in temperature between the sample and reference upon controlled ΔT. Heat exchange between the furnace and sample takes place by heat conduction, radiation and convection. In contrast to HF-DSC, PC-DSCs have separate heaters and separate temperatures sensors for the sample and reference. The temperature control is more complex as it requires as small differences as possible between heating furnaces, sample and reference. The heat flow difference is measured as the difference in power required to be delivered to the heaters to keep the sample and reference at the same temperature. The PC-DSC can give more precise results of measurement, but are more sensitive to contamination and require more maintenance attention.

If the temperature programme employed in the DSC analysis is linear, this DSC method is often referred to as "standard". To facilitate non-routine applications of DSC, a few variants of DSC analysis are distinguished and available commercially from Perkin Elmer™ as Hyper

Scan™ DSC with Step Scan™ method (HS-DSC, SS-DSC method), Thermal Analysis Instruments™ as Temperature Modulated DSC and Mettler Toledo™ as TOPEM™ analysis.

HS-DSC allows for investigation of solid state transformations upon ΔT up to 500 °C/min. Helium is used to improve conductivity between the furnaces and sample. HS-DSC has higher ΔH sensitivity and better temperature resolution, which allows for example for the detection of Tgs undetectable on conventional scans or for better separation of solid state transformations (thermo-induced polymorphic forms). HS-DSC instruments with heating rates up to 200K/s are currently in use (Zhang et al., 2002).

SS-DSC and TM-DSC are modifications of conventional linear ΔT scans. In SS-DSC, the ΔT pattern is trapezoidal over time and linear ΔT are separated with isothermal periods. In TM-DSC the ΔT is sinusoidal and in TOPEM ΔT is stochastic (random). All these three methods allow for separation of transitions of first and second order and reversibility versus ΔT of thermal events. This allows, for example, the Tg from residual solvent evaporation events to be separated (McGregor et al., 2004).

Unfortunately, DSC does not record a mass change, thus an analysis complementary to DSC is thermogravimetric analysis (TGA). TG analyser is a precise microbalance, where the sample under dry gas flow (usually nitrogen or air) is introduced to a pre-programmed ΔT (Mackenzie, 1969). The mass loss events are recorded and plotted against ΔT or time. The pattern of mass loss differentiates the loss of surface bonded moisture, absorbed residual solvent and solvated forms. Sometimes TGA is able to separate the different degrees of solvation of the given material or evaporation of differently absorbed solvents, such as ethanol or water.

Due to the novel analytical approach combining analytical methods in modular systems, so-called hyphenated methods e.g. TGA Interface™, it is currently possible to evaluate both, the qualitative mass loss by TGA and identity of the removed compound using FTIR or MS-Evolved Gas Analysis.

TGA instruments can be divided into two general types: vertical and horizontal balances. Vertical balance instruments have a specimen pan hanging from the balance. It is necessary to calibrate these instruments in order to compensate for buoyancy effects due to the variation in the density of the purge gas with temperature as well as the type of gas. Vertical balance instruments generally do not have reference pan. Horizontal balance instruments normally have two pans. They are considered free from buoyancy effects, but require calibration to compensate for differential thermal expansion of balance arms. A method known as Hi-Res™ TG by TA Instruments™ is often employed to obtain greater accuracy in areas where the derivative curve peaks are indistinguishable (Robens and Unger, 2005). In this method, the temperature increase slows as weight loss increases. This is done so that the exact temperature at which a peak occurs can be more accurately identified. Selected thermal event detectable by thermal analysis and investigated in the preformulation stage of product development are listed in table 1.3.

Table 1.3. Thermal events detectable using DSC and/or TGA.

DSC			**TGA**
Event	ΔH [J/g]	Reversibility	Initial mass change (Δm_0)
Evaporation of adsorbed solvent/ moisture	Endoenergetic	No	Negative
Residual solvent evaporation	Endoenergetic		
Solvated solvent evaporation	Endoenergetic		
Sublimation	Endoenergetic		
Glass transition	Endoenergetic	Yes	N/A
Recrystallisation	Exoenergetic	No	
Solid-solid transformation	Exoenergetic	Yes	
Melting	Endoenergetic		
Solidification	Exoenergetic		
Evaporation	Endoenergetic		Negative
Condensation	Exoenergetic		N/A
Boiling	Endoenergetic	No	Positive/Negative
Thermal degradation	Exo/Endoenergetic		

1.2.4. Dynamic vapour sorption (DVS) analysis

DVS instrument in its principle is very similar to TGA instrumentation. It is a precise microbalance, which continuously records mass change of the sample over time. The sample is placed in a thermostatic chamber and exposed to vapours of solvents or to a flow of dry gas (nitrogen). Depending on the experiment, the sample can be exposed to a laminar flow of vapours of water imitating relative humidity conditions, or to vapours of organic solvents interacting with the tested material. The programmability of exposure of the material to a particular concentration of solvent/water vapour is very flexible. The sample can be exposed to constant conditions of relative humidity (RH) over a range of time (t) or until the mass change ($\Delta m/\Delta t$) of the sample reaches a certain value, considered as constant. The sample can be exposed to RH changes in pre-programmed steps e.g. 0-90-0% RH or over a certain time or until a constant $\Delta m/\Delta t$ is reached. At every time point the output is given as a percentage of the initial mass of the sample m_0 ($\%m/m_0$). Other possible method of analysis involves exposing the sample to ramp (linear change) conditions of changing RH over time.

To broaden the range of possible experiments, the modular design of modern DVS instrument allows for investigation of micromeritic changes of the materials (optical camera or microscope) or chemical transformations thanks to FT-IR or Raman attachments. If required, the sample can be pre-dried using an additional programmable heater.

In preformulation, DVS may be applied to the following (York, 1983 or Zografi and Kontny, 1995):

- Measurement of water sorption/desorption profiles of solid state materials,
- Analysis of surface sorption (adsorption) capability of the material,
- Analysis of capability of solvent to penetration/deposition in bulk material (absorption),
- Assessment of hygroscopicity of material,
- Identification of amorphous content of solid state material,
- Determination of critical humidity of recrystallisation,
- Determination of critical time of recrystallisation in given humidity,
- Assessment of critical humidity of solvate/hydrate formation or desolvation,
- Investigation of material surface transformation upon given RH,
- Determination of the rate of water uptake and water diffusion coefficients,
- Assessment of the difference in water vapour uptake between the sorption and desorption isotherms (hysteresis).

1.2.5. Specific surface area analysis

The specific surface area of a bulk material is a derived (micromeritic) property of the API. Specific surface area can determine the dissolution profile of the API. Intrinsic (fundamental such as melting point or chemical nature) and solid state properties of the API may impact on processability and can determine the surface area of the processed material.

To evaluate the surface area of a solid material, the theory of Stephen Brunauer, Paul Hugh Emmett and Edward Teller, known as BET theory, is applied (Brunauer et al., 1938). It explains the physical adsorption of gas molecules on a solid surface and gives rise to a technique for the measurement of the specific surface area of a material. The concept of the theory is an extension of the Langmuir equation (1916). This equation describes physical adsorption of molecules (gas) on a solid surface depending on gas pressure or concentration in isothermal conditions (Eqn. 1.5).

$$\theta = \frac{\alpha \cdot P}{1 + \alpha \cdot P} \quad \text{Eqn. 1.5.}$$

Where θ is a fractional, monolayer coverage of the surface and P is gas pressure or concentration. The α parameter is the adsorption constant which increases with an increase in the binding energy of adsorption and with a decrease in temperature.

BET theory expands the monolayer theory of Langmuir to multilayer adsorption with assumptions that gas molecules physically adsorb on a solid in layers infinitely and the Langmuir theory can be applied to each layer. The resulting BET equation 1.6 is expressed by:

$$\frac{1}{\upsilon[(P_0 / P) - 1]} = \frac{c-1}{\upsilon_m c}\left(\frac{P}{P_0}\right) + \frac{1}{\upsilon_m c} \quad \text{Eqn. 1.6.}$$

Where: $\varphi = \frac{P}{P_0}$ is the equilibrium in the saturation pressure of adsorbate at the temperature of adsorption, υ is the adsorbed gas volume, υ_m- is the monolayer adsorbed gas quantity, c is the BET constant, which is expressed by Eqn. 1.7.

$$c = \exp\left(\frac{E_1 - E_L}{RT}\right) \quad \text{Eqn. 1.7.}$$

Where: E_1 is the heat of adsorption for the first layer, and E_L is that for the second and higher layers and is equal to the heat of liquification. R is the ideal gas constant 8.314472 [J/mol K]. T is the absolute temperature (77 K for boiling nitrogen).

The linear relationship of equation 1.6 is maintained only in the range of $0.05 < P / P_0 < 0.35$ (Brunauer et al., 1938). The value of the slope A and the y-intercept I of the line are used to calculate the monolayer adsorbed gas quantity v_m (Eqn. 1.8) and the BET constant c (Eqn. 1.9) respectively:

$$\upsilon_m = \frac{1}{A+I} \quad \text{Eqn. 1.8.}$$

$$c = 1 + \frac{A}{I} \quad \text{Eqn. 1.9.}$$

The BET method is widely used in surface science for the calculation of surface areas of solids by physical adsorption of gas molecules. A total surface area $S_{BET,total}$ and a specific surface area S_{BET} are evaluated by the following equations 1.10 and 1.11.

$$S_{BET,total} = \frac{(\upsilon_m N_A s)}{V} \quad \text{Eqn. 1.10.}$$

$$S_{BET} = \frac{S_{total}}{a_1} \quad \text{Eqn. 1.11.}$$

Where N_A is Avogadro's number, the s is adsorption cross sectional area of the single, closely packed adsorbate (gas) molecule, V is the molar volume of adsorbent gas and the a_1 is the molar mass of adsorbed molecules.

BET analysis instruments usually carry out surface area analysis using nitrogen as adsorptive gas. Nitrogen cross-section is 0.162 nm^2. Adsorption is carried out at the low temperature of liquid nitrogen -196 °C to enhance adsorption, desorption is carried out at ambient conditions.

1.2.6. Particle size analysis

Particle size of the API can be a very important parameter when formulation of a multi-particulate delivery system is under consideration. It is particularly important in pulmonary delivery where the API is delivered as a dispersion of particles in dispersing gas or liquid. Particles below 5 μm can be distributed deep into the smaller airways and this penetration correlates well with good clinical response for local treatment (Malcolmson and Embleton, 1998). The particle fraction with aerodynamic diameter (d_A) in the 1-2 μm range is probably the most efficient for deposition into the capillary-rich alveolar airspaces. This is the target for the systemic delivery of drugs which are less efficient or less convenient when delivered by other routes. Submicron particles ($d_A < 0.5$ μm) can be exhaled, if they are not aggregated and/or if insufficient time is available for their migration to the lung walls (Chow et al., 2007).

Particle size can impact on powder flowability of the material (Teunou et al., 1999) subjected to dry compaction (Herting and Kleinebudde, 2007), agglomeration (Sherif et al., 2004), granulation or tableting (Maschke et al., 2008). It can impact on blending with other excipients.

Laser diffraction is one of the most widely used techniques for particle size analysis. In laser diffraction particle size analysis, a representative dispersion of particles passes through a broadened beam of laser light, which is scattered onto a Fourier lens (Kippax, 2005). The laser beam is broadened so it may interact with a large number of particles in the sample cell. The lens focuses the scattered light onto a detector array and, using an inversion algorithm, a particle size distribution is inferred from the collected diffracted light data. Laser diffraction particle size analysis relies on the fact that particles, passing through a laser beam, will scatter light at an angle that is directly related to their size. As particle size decreases, the observed scattering angle increases logarithmically.

The resolution of a laser diffraction particle size analyser can be defined as the ability of a system to differentiate between similarly sized particles and therefore measure the correct shape and true width of the particle size distribution (Allen, 1992), finding any 'tails' or 'shoulders'. Optimal size distribution results are achieved by covering a wide angular range with a sufficient number of detectors to ensure that important information from the scattered light is not lost or overlooked.

Modern laser diffraction instruments use Mie Theory as the basis of their size calculations. The Mie theory is built on Maxwells's electromagnetic field equations and is based on two important assumptions. The particle is assumed to be spherical and the result is based on volume of equivalent spherical particles. The result of analysis is given in diameter of spheres. This diameter is calculated from the measured volume of the particle and it is assumed that it is a diameter of sphere possessing equivalent volume to the measured particle. This assumption always needs to be taken into account when laser diffraction analysis results are analysed. Modern instruments measure the cloud of particles and require suspension or cloud to be diluted enough,

that scattered radiation is directly measured by the detector (single scattering) and not rescattered (multiple scattering).

Measurements can be performed in liquid suspension or in dry gas dispersion. The first method is considered as less preferable in analysis of materials which are not to be used in suspensions as the final drug form. The use of the liquid method requires concerning if measured particles do not dissolve in suspending liquid, if dispersion of mono-particulate suspension devoid agglomeration is formed (addition of a surfactant may be considered as helpful) and the lack of particle sedimentation is also required.

The dry method is not devoid of issues needing consideration. The measured dry powder is firstly pre-dispersed on a vibrating tray, then dispersed via coarse mesh with metal beads and is further mixed with dry air to gain the desired mono-particulate dispersion. The pressure of the dispersing gas may be adjusted in the range of 0.1 to 3.9 bar (Malvern Instruments, 1998). If particles are fragile, the dispersion pressure should be large enough to break small agglomerates and not too big to shatter particles.

Laser diffraction can generate the d[4,3] or equivalent volume mean. Table 1.4 presents selected parameters describing particle size (including other methods than laser diffraction) and particle size distribution.

Table 1.4. Selected parameters describing particle size and particle size distribution.

Parameter symbol	Description	
d(10)	The diameter from which 10% of populated particles is smaller	
d(50)	Median diameter from which 50% of populated particles is smaller	
d(90)	The diameter from which 90% of populated particles is smaller	
d[1,0]	Number diameter mean	$d[1,0] = \frac{\sum d}{n}$
d[2,0]	Number surface mean	$d[2,0] = \frac{\sum d^2}{n}$
d[3,0]	Number volume mean, number weight mean, volume mean diameter (VMD)	$d[3,0] = \frac{\sum d^3}{n}$
d[4,3]	Diameter of sphere of equivalent volume	$d[4,3] = \frac{\sum d^4}{\sum d^3}$
d[3,2]	Diameter of sphere of equivalent surface area, Sauter Mean Diameter (SMD)	$d[3,2] = \frac{\sum d^3}{\sum d^2}$
Mode	The most common value of the frequency distribution	
Span	$Span = \frac{d(90) - d(10)}{d(50)}$	

The particle size distribution (d(10), d(50), d(90)) and span inform how broad or narrow is particle size distribution. This information indicates the consistency of the bulk material in terms of size, confirms the quality (uniformity) of the production process (micronisation, milling, spray drying) and informs if particle size distribution is normal or skewed. Poly-modal particle size distribution is another measure (besides span) of un-uniformity of material bulk, and often is an undesired effect of a production process.

1.3. Solid state properties of pharmaceutical materials

There are two types of solid state materials: crystalline and amorphous. Both can be found in pharmaceutical solids.

1.3.1. Crystals

A crystal or crystalline solid is a solid material whose constituent atoms, molecules or ions are arranged in an orderly repeating pattern extending in all three spatial dimensions. The crystal structure of a material or the arrangement of atoms in a crystal structure can be described in terms of its unit cell (the unit cell is described in Section 1.2.1).

The crystal structure has a three dimensional shape. The space group of a crystal or crystallographic group is a mathematical description of the symmetry inherent in the structure. The word 'group' in the name comes from the mathematical notion of a group, which is used to build the set of space groups. A crystallite comprises multiplication of single crystal cells in all three dimensions along three cell axes, so a given plane of one single crystal cell is shared with a neighbouring unit. Crystallites can develop several crystal habits (needles, prisms, cubes etc.). Crystals can be made by the API and one or more other components that may be a solid, liquid or gas forming e.g. salts, co-crystals, solvates.

An API may form several crystal forms, termed polymorphs, having different pharmaceutical properties and varying in physical stability (metastable forms). Each polymorphic form can exhibit several crystal habits with different pharmaceutical properties.

Due to the complex nature of crystallographic studies of solids; geometric, structural, chemical and physical characterisation of crystals can be distinguished. Descriptions of these analyses are presented below (Table 1.5).

Table 1.5. Crystallographic characterisation in preformulation

Crystal characterisation	Description
Geometric	External shape of crystal, which can impact on, for example, the compaction properties of crystalline solids
Structural	Description and determination of the internal geometry of the structure
Chemical	Description and analysis of structural organisation of atoms, ions and bonds between molecules
Physical	Description of physical properties of crystal

1.3.1.1. Salts and co-crystals

In salts two or more solids or a solid and a liquid forming the crystal are attracted by ionic interactions. If attractions between two or more solids are based on weaker (H-bond) interactions, this form is termed a co-crystal.

Salt formation and co-crystal formation may be used to alter the physicochemical, biopharmaceutical and processing properties of a drug substance without modifying its core chemical structure. The salt approach is a simple, and usually the first choice, method of tuning properties of an API containing ionisable functional groups. The new salt has unique properties to overcome undesirable features of the parent drug (usually solubility profile). The formation of a salt from the parent drug rarely affects the pharmacology of the drug substance. Salts can differ greatly from the parent drug in physicochemical properties such as melting point, solubility, dissolution rate, hygroscopicity, chemical stability, crystal form and solution pH.

The most common examples of salts used in the pharmaceutical sector are hydrochloride salts of basic drugs and sodium salts of acidic drugs (Stahl and Wermuth, 2008). The salt formers (counterions) may be chosen from a few classes. The first class of salt formers have unrestricted use for that purpose because they are physiologically ubiquitous ions (e.g. Cl^-, Na^+, K^+) or because they occur as intermediate metabolites in biochemical pathways (e.g. trimetrexate, glucuronate). Nearly 90% of the reported pharmaceutical salts are formed with sodium, calcium, potassium, magnesium, meglumine or ammonia with more than 55% made with sodium cations (Stahl and Wermuth, 2008).

Most of the newly synthesised APIs are classified as poorly water soluble and furthermore, have no ionisable groups able to form salts. Those APIs may form co-crystals, if suitable co-formers are identified. Interactions weaker than ionic interactions play a role in their formation. Co-crystal formation, similarly the salt formation, may result in an improved solubility of the API (Shan and Zawrotko, 2008).

The possibility of using co-crystals in a similar manner to salts in order to alter the physicochemical properties of an API was presented in 2003 by Bailey et al., who described binary crystalline phases involving ibuprofen, flurbiporfen and aspirin. Since then, the possibility of co-crystal formation has been explored in order to improve the oral bioavailability of an API using glutaric acid (McNamara et al., 2006). In the same year Variankaval et al. (2006) reported nonstochiometric co-crystals of phosphodiesterase-IV inhibitor with L-tartaric acid. Zegarac et al. (2007) published co-crystalline forms of sildenafil with acetylsalicylic acid. This form had an improved aqueous solubility in comparison to the marketed citrate salt. Shan and Zaworotko (2008) reviewed the roles of co-crystals in pharmaceutical sciences highlighting the marketed co-crystal of fluoxetine hydrochloride (Prozac™). Dova et al. (2008) patented a co-crystal of tenofovir disoproxil with fumaric acid.

1.3.1.2. Solvates (pseudopolymorphic forms)

The most common way of producing crystals is to nucleate them from a solution by the formation of a supersaturated solution, in the metastable zone, followed by nucleation and precipitation of crystals. This means that molecules of the API are in direct contact with the solvent. If, at the nucleation stage, the enthalpy of a potential crystal lattice of the API with molecules of the solvent is lower than that of the crystal lattice of the API molecules on their own, a solvate will be formed.

A solvate it is a crystalline material of the API with incorporated molecules of a solvent. Molecules of the solvent can be bonded, coordinated by molecules of the API or they may be trapped in the interstitial space of the crystal lattice and held there by H-bond interactions with the API. Usually the ratio of the coordinated solvent to the API is constant and stoichiometric (Kim et al., 1990). The stoichiometry of the interstitial, channel solvates may vary (Stephenson and Diseroad, 2000).

If solvent molecules are water, hydrates are formed. Hydrate formation was observed for APIs such as theophylline, cefixime and caffeine. The interstitial, channel content of water molecules may vary depending on environmental conditions, raising physical stability issues. Pseudopolymorphic forms refer to the API crystallising in different conditions as different solvated crystal forms and should not be confused with polymorphism (McCrone, 1965, Halebliand and McCrone, 1969). Solvatomorphism was coined to describe the different crystal forms of a solvate (Brittain, 2009).

Pseudopolymorphic forms, as in the case for polymorphs, may exhibit different physical properties such as density, habit, stability, dissolution rate or bioavailability. The main properties affected are melting and sublimation temperatures, heat capacity, conductivity, volume, density, viscosity, crystal hardness, crystal shape, colour, refractive index, solubility, dissolution rate, stability, hygroscopicity and solid state reactions.

Processing during production, if the drug substance is a solvate or a hydrate and partially loses its structure, is another area of concern for the pharma industry. The formation of a hydrate has been observed during wet granulation, pelletisation or after storage of tablets or capsules. Examples where this occurs include theophylline (Jørgensen et al., 2004), caffeine (Howell et al., 1997), codeine phosphate (European Pharmacopia, 2010), nitrofurantoin (Tian et al., 2010) and oxytetracycline (Gans and Higuchi, 1957). Phase transformations, existing between the different phases, including the anhydrous or non-solvate form, vary with, for example, temperature, pressure, relative humidity and solvent. In many cases the solvent molecule(s) is an integral part of the crystal structure and desolvation leads to the collapse of the original structure of the crystal and the generation of a new crystal structure. At the other side of the scale are solvates in which the solvent is very loosely bound. In this case desolvation does not require extreme conditions and the process will not lead to the original structure (McCrone, 1965).

Solvate formation should not be overlooked in crystallisation processes. A solvate form may be crystallised and then transformed into a desolvated form on drying. The desolvate may be thermodynamically stable or metastable. If hydrate formation occurs only in water and if no transition of the anhydrous form to a hydrate occurs at high relative humidity levels, the anhydrous form will be preferred, but if the hydrate is formed at low humidities, the choice of the best form may be complicated. A great number of solvates have been reported, especially for steroids (Kuhnert-Brandstätter and Gasser, 1971) and antibiotics (Hickey et al., 2007). A range of solvated forms of chlorothiazide, such as chlorothiazide formic acid solvate (Johnston et al., 2007a), chlorothiazide N,N-dimethylacetamide disolvate (Johnston et al., 2007b), chlorothiazide DMSO solvate (Johnston et al., 2007c) and chlorothiazide-pyridine solvate (Johnston et al., 2008) have also been prepared and their crystal structures described.

Solvates and hydrates are best distinguished from polymorphs by the combination of DSC and TGA applied to the desolvatation process.

The possibility of solvate formation raises preformulation issues related to solvate physicochemical stability, risk of desolvation, impact of solvation on the API solubility etc., which should be addressed. The stable crystal form is expected to be robust under handling, storage and processing conditions (mechanical stress, thermal stress, humidity, time. The effect of polymorphism or pesudopolymorphism on bioavailability is the most important factor if the bioavailability is mediated via dissolution (Otsuka, 1993).

1.3.2. Amorphous state

In contrast to crystals, an amorphous substance is a material that does not exhibit any crystal lattice inherently e.g. polyvinyl pyrrolidone (PVP) or hydroxypropyl methylcellulose (HPMC) or a crystalline material devoided of the crystal lattice by mechanical activation or thermal induction. Accolate™ (zafirlukast), Ceftin™ (cefuroxime axetil), Accupril™ (quinapril hydrochloride), Rezulin™ (troglitazone) and Humulin L™ (insulin analogue), are examples of marketed dosage forms containing amorphous APIs.

Amorphous APIs have different physicochemical properties than the corresponding crystalline materials. They are thermodynamically unstable (higly energetic, disordered forms) and have the tendency to recrystallisation (Saleki-Gerhardt et al., 1994), since, according to the second law of thermodynamics, the matter will minimise enthalpy at equilibrium. The amorphous form may be unstable on storage; additionally it is usually more hygroscopic than the equivalent crystalline form. An amorphous material is characterised by a glass transition temperature (Tg), a critical thermal parameter of a comparable significance to a melting point of a crystalline substance. The glass transition temperature in this work is defined as the midpoint temperature of this thermal event, related to an increase in specific heat of the material. Physically, the glass transition temperature is a transformation of the amorphous material from a solid-brittle form to a so called, rubbery-plastic form. Tg, preceding thermal recrystallisation of the amorphous form, will always be lower than the melting point (MP) of the crystalline material.

The advantages of the amorphous state include increased solubility (Allesø et al., 2009) and dissolution rate. These, in consequence, may lead to an improved bioavailability of the API. It may also allow formulation of modulated release dosage form such as e.g. Lilly's Humulin L®, where the amorphous form is responsible for immediate release of insulin at the first stage and the crystalline form is responsible for the prolonged release. In the modern pharmaceutical industry, where often new APIs with strongly reduced solubility or bioavailability are produced, the advantages presented by the amorphous state may overcome associated disadvantages and prompt the design of new dosage forms (Carstensen et al., 1993, Sheth et al., 2005).

1.4. Physical processing of pharmaceutical solids

Examples of production processes which enable amorphous arrangement are: spray drying, spray freeze drying, atmospheric spray freeze drying, hot stage extrusion as well as precipitation by solvent evaporation, quench cooling or milling.

Spray freeze drying is a two stage process. It has not been developed as an industrial scale process, only the lab scale is available. It is based on atomisation of a solution containing the dissolved API and then freezing the droplets in liquid nitrogen. The second stage is long lasting lyophilisation. Due to the lyophilisation stage, the process is limited to only a few solvents e.g. water, butyl alcohol and solvents with low melting points (such as methanol, ethanol, acetone)

cannot be used. Similar limitations are characteristic of atmospheric spray freeze drying. Here the sample is frozen in extremely cold air with the cooling agent being liquid nitrogen.

Hot melt extrusion allows amorphous extrudates to be obtained which are intermediate products and require further technological processing like milling. Additionally, this process uses conditions of high and long lasting thermal stress. Therefore it is unsuitable for thermally labile API.

Production of amorphous solids by solvent evaporation can be employed for materials with weak crystal lattices, weak enough to be counteracted by molecular interactions with a suitable solvent. It is possible, on laboratory scale, to obtain amorphous forms of drugs at room temperature.

Quench cooling encompasses sample melting and quick solidification for example, in liquid nitrogen. This method allows for the production, on laboratory scale only, of samples which are thermally stable up to their melting points.

Formation of amorphous forms by milling is also possible but involves long milling periods and it is difficult to obtain a powder with homogenous physicochemical properties (Gupta et al., 2003).

1.4.1. Spray drying

Spray drying is a one-step manufacturing method for the production of microparticles. It is available as an industrial scale process, but small, lab-scale equipment also exists. It produces morphologically uniform microparticles with a narrow particle size distribution therefore it may be regarded as being superior to milling, which may require subsequent sieving of the powder.

A spray drying process can be divided into several steps. The first step encompasses solution delivery to the atomisation nozzle. This is provided by a peristaltic pump and silicon or solvent-resistant plastic tubes. The second step is solution atomisation. It can be done using a standard two- or a three-fluid nozzle, whereby one or two liquids are mixed with compressed gas. It is also possible to use an ultrasonic nozzle or a rotary atomiser. In the next step the dispersed droplets are dried by air, carbon dioxide or nitrogen. Dry particles are then separated from the gas stream in a cyclone and collected in a collecting vessel fitted underneath the cyclone. Exhaust gas is additionally filtered.

Solid materials can be obtained from solutions, suspensions and emulsions using spray drying. It is a flexible process where process parameters can easily be changed depending on the required properties of the resulting powder. For instance, a wide range of solvents or mixtures of solvents could be used. The limitation could be the flash point of the solvent. The process can also be carried out in an oxygen-free atmosphere in an open or closed mode. The latter involves entrapment of solvent vapours and recirculation of the drying gas. This allows for a wider design space to obtain the optimum particle morphology.

To summarise, some process variables are briefly listed and described in tables 1.6 and 1.7.

Table 1.6. Variables impacting on the spray drying process: factors related to the dried system.

Variables related to dried system		
	Variables	**Implications**
API and its properties before processing ⇩	Melting point, Tg, molecule parameters: polarization constant, presence of ionic or strongly polarised bonds, dipole moment, molecule size, enthalpy of molecule, hydrophilic/hydrophobic character, moisture stability, thermal stability. Enthalpy of crystal lattice. ⇨	Feed concentration range, ⇩ Solvent selection, ⇩ Inlet temperature
Solvent or solvents mixture ⇩	Boiling point(s), pH, density, viscosity, surface tension, heat capacity, heat of evaporation ⇨	Inlet temperature selection, ⇩ Outlet temperature ⇩ Particle morphology, Solid-state nature of processed material
API/solvent mixture properties ⇩	Boiling point(s), pH, density, viscosity, surface tension, feed temperature ⇨	Chemical stability of API in solution, Particle morphology
Type of feed	Solution, suspension, emulsion ⇨	Particle morphology
Saturation	Concentration of dissolved solid(s) ⇨	Particle size, Process of droplet drying
API properties after solvent evaporation	Degree of crystallinity, rheological properties of material, bulk and true density, compressibility, particle size, melting point, glass transition point. ⇨	Solvent residue ⇩ Process efficiency

Table 1.7. Variables of impacting on the spray drying process. Factors related to the spray dryer (Buchi B-290).

Variables related to Büchi B-290		
Parameter	**Variables**	**Implications**
Feed/gas delivery mode	Type of nozzle, relative placement of peristaltic pump in relation to nozzle on vertical plane	Uniformity of particle size, uniformity of content, particle morphology
Feed rate	The speed of delivery of feed to atomisation nozzle: 0-30 ml/min	Droplet and in consequence particle size
Gas type	Air, nitrogen, carbon dioxide	Outlet temperature
Gas pressure	5-8 bar	Particle size Drying conditions related to outlet filter pressure
Drying gas flow	200-800 l/h	Particle size, Production yield, Solvent evaporation efficiency
Spray gas flow	84-819 l/h at pressure drop 0.15-1.8 bar	Droplet size, Particle size
Actual gas volume flow	283-2293 l/h	Evaporation rate
Evaporating capacity	Max. 1l/h H_2O, higher for organic solvents	Solvent evaporation efficiency
Nozzle (two fluid) tip diameter	0.7 mm, 1.4 mm and 2 mm	Droplet size, Particle size
Nozzle (two fluid) cap diameter	1.4 mm, 1.5 mm	Droplet size, Particle size
Gas aspiration	20-35 l/h at 50-100% aspirator efficiency	Production yield
Drying mode: open/closed	Filter outlet pressure	Drying conditions, Solvent residue in dried powder
Cyclone: standard/ high efficiency		

The variables that may impact on the final product in spray drying can be divided into two groups: those related to the liquid feed components (Table 1.5) and those related to the drying unit (Table 1.6). The flexibility in design of a spray drying process can often be restricted due to equipment availability and limitations of the model to be used but this can be overcome, at least partially, by manipulating the liquid feed e.g. API concentration, solvent choice etc.

API and its properties define the type of solvent to be used. In addition to a pure solvent, a mixture of two or more solvents can also be used, which allows the morphology of the spray dried material to be altered (Healy et al., 2008, Nolan et al., 2009, Nolan et al., 2011, Ni Ógáin et al., 2011).

Although spray drying is considered as a process which is easy to control, it is demanding in its design of optimum performance. Each step of the spray drying process including:

- feed preparation and composition,
- delivery of liquid feed to atomizer,
- atomization,
- mixing of atomized droplets with drying gas,
- distribution of drying gas/droplets in the drying chamber,
- droplet drying,
- particle conveying,
- separation of powder from drying gas,
- powder discharge,

needs to be analysed and optimised, often with implications on spray dryer selection. Modern design of a spray drying process on an industrial scale is modular e.g. different atomisers can be used, secondary drying equipment can be attached etc.

Spray drying is a known method of producing of amorphous solids. In 1983 Corrigan et al., reported that spray drying was an effective method of producing amorphous hydroflumethiazide. Subsequently, a range of thiazide compounds was processed by spray drying and resulted in the production of amorphous forms of bendroflumethiazide, cyclopenthiazide, polythiazide and cyclothiazide. Exceptions were hydrochlorothiazide and chlorothiazide, which were obtained as crystalline forms Corrigan et al. (1984). In 1985 Corrigan et al., published studies on co-spray drying of indomethacin with polyvinylpyrrolidone (PVP), where PVP was used to stabilise the physically unstable amorphous form of indomethacin.

The production of crystalline products by spray drying is also possible (Di Martino et al., 2001). Spray drying may also alter the crystalline form of processed material resulting in a polymorphic transformation. Such transition was reported for phenobarbitone, which upon spray drying transformed from a crystalline form II to form III. The latter had a large specific surface area of 17 m^2/g and had an improved apparent solubility of about 25% in comparison to form II (Corrigan et al., 1983). Di Martino et al., 2001 reported polymorphic transformations

of spray dried acetazolamide, when investigated the impact of spray drying on compressibility of processed acetazolamide.

1.4.2. Preformulation in tablet formulation development

Tablets as solid state drug delivery systems (SSDDSs) are expected to be sufficiently robust to withstand packaging, shipping, storage and administration conditions, but to readily disintegrate or directly dissolve in the gastrointestinal tract (GIT) or even in the oral cavity if designed as orally disintegrating tablets (ODS). The role of the tablet as a drug form is firstly to deliver the API quantitatively to the site of absorption (absorption window) and secondly to expose the API to the dissolving medium within the expected period of time (from ultra rapid to modified release (prolonged, retarded)). Additionally, as with every drug form, tablets are expected to meet stability requirements.

The tablet performance, among several parameters, depends on the physicochemical properties of the API. Thus a comprehensive characterisation of the API is a key part of the formulation development. The characterisation of mechanical properties of the API is a part of preformulation.

Preformulation characterisation of powders intended for direct compression is focussed on simplifying manufacturing. The produced tablets should have a desired hardness with low friability, long shelf-life, desired time of disintegration and(or) dissolution. Physicochemical properties of powders intended for direct compression determine tablet stability and dissolution behaviour. If the API is the main component of the tablet, the ease of manufacture, hardness and friability can be controlled by the use of excipient only to a limited extend. In relation to tablet formulation, API properties can be divided into intrinsic physicochemical properties of the API that cannot to be changed without a chemical modification of the API and micromeritic properties which can be adjusted to meet the formulation needs (Table 1.8).

Table 1.8. Selected physicochemical and micromeritic properties of API impacting on the performance of tablets (Augsburger and Hoag, 2008).

Property	Classification	Performance implication
octanol/water partition coefficient ($logP_O$)	Molecular-chemical	Aqueous Solubility
pK_a	Molecular-chemical	pH solubility
melting point, Tg	Molecular-chemical	Hardness
Solid state form	Molecular-physical	Dissolution rate
Crystal habit	Molecular-physical	Hardness
Surface area	Micromeritic-physical	Dissolution rate
Particle size	Micromeritic-physical	Dissolution rate, Flowability
Particle shape	Micromeritic-physical	Flowability, Compactibility
Porosity	Micromeritic-physical	Dissolution rate, Compactibility, Hardness

Dissolution of the API from the tablet involves a number of steps. The tablet, when placed in a dissolution medium, is first wetted then the liquid starts to penetrate the tablet with two simultaneously ongoing processes: erosion (disintegration) and dissolution.

Several equations can be used to describe dissolution kinetics from pharmaceutical dosage forms (Costa and Lobo, 2001). Noyes-Whitney equation (Eqn. 1.13) assumes that the surface area of the dissolving material is constant and describes the dissolution rate ($\Delta Q/\Delta t$) is proportional to the difference between solubility (C_s) and the bulk concentration (C_b) of the dissolving substance.

$$\frac{\Delta Q}{\Delta t} = k(C_s - C_b) \qquad \text{Eqn. 1.13.}$$

Modifications of this equation by Nernst (1904) and Brunner (1904) (Eq. 1.14) showed that the proportionality constant k from equation 1.13 could be related to the diffusion layer h surrounding the dissolving particle, diffusion coefficient (D) of the dissolving material in the layer and the surface area of the particle (A).

$$\frac{\Delta Q}{\Delta t} = DA\frac{(C_s - C_b)}{h} \qquad \text{Eqn.1.14.}$$

Therefore the dissolution rate is determined by the diffusion rate through the layer as it is described by Nernst Brunner model (Qiu et al., 2009). When the bulk concentration of the drug is not higher than that present in a sink condition, which is commonly assumed to be no more than

10% of the drug solubility (Qiu et al., 2009), the concentration of the drug in the bulk medium parameter incorporated into Nernst-Brunner equation can be ignored. If the particle is large, the diffusion layer on the particle may be assumed to be planar, as the thickness of the diffusion layer is much smaller than the particle diameter.

Hixson and Crowell (1931) acknowledged that the regular area A of spherical particles of density d_0 and quantity $Q=d_0V$ is proportional to cubic root of its volume (V). In equation 1.15 Q is the initial amount of substance in the pharmaceutical dosage form, Q_t is the retained amount of the substance in the dosage form at time t (the amount undissolved) and $K_{1/3}$ is a constant incorporating the surface volume relation (Eqn. 1.15).

$$Q^{1/3} - Q_t^{1/3} = K_{1/3}t \qquad \text{Eqn. 1.15}$$

$K_{1/3}$ is further described by Eqn. 1.16 as:

$$K_{1/3} = \left(\frac{\Pi}{6d_0^{\,2}}\right)^{1/3} \frac{2DC_s}{h} \qquad \text{Eqn. 1.16.}$$

Where D is the diffusion layer and C_s is a solubility of the substance in the medium.
The complete dissolution time of the spherical particle is (Eqn. 1.17):

$$t = \frac{r_0 d_0 h}{DC_s} \qquad \text{Eqn. 1.17.}$$

The Hixson and Crowell model applies to the dosage forms, including tablets, where dissolution occurs in planes parallel to the drug surface, if the tablet dimensions diminish proportionally in the manner that the initial geometrical form remains constant all the time. This model was used previously to describe the release profile of the particles with decreasing surface of the drug particles during dissolution by Niebergall et al., (1963), Prista et al., 1995).

The parameter A in Eq. 1.13 relates to the micrometric characteristics of the API. It can be modified relatively easily using the following approaches: comminution (milling, micronisation, precipitation) or production of porous materials. The increase of porosity decreases the bulk density of the produced material (Nolan et al., 2009). Furthermore, an increase of surface area of the API is beneficial for its compactibility and as a consequence impacts on the tensile strength of the tablets produced (Westermarck et al., 1998).

Compactibility of an API powder involves consolidation of the powder bed under applied pressure, by porosity reduction and tablet formation mainly due to particle rearrangement, plastic deformation, brittle fraction, fusion or interlocking (Augsburger and Hoag, 2008). Compression of powder into tablets is directly related to the reduction of volume of the material.

Due to the importance of compactibility of pure materials or due to an impact of compactibility of pure material on compactibility of blend of powders (formulation), different aspects of compactibility of pure pharmaceutical compounds are often reported in the literature (Sun et al., 2001, Joiris et al., 1998). Several factors controlling powder compactibility have been

reported to date. These factors can be divided into three main groups: particle mechanics, particle dimensions and particle adhesiveness. The most common reported relationships include an increase of tablet strength following a decrease of particle size of the powder and greater tablet strength related to greater particle shape irregularity.

In a tablet, depending on the compactibility characteristic of each of ingredients, they may play a role of either a binder or a disintegrant, affecting the overall compactibility performance of the formulation.

1.4.2.1. Orally disintegrating tablets

Unfortunately, not every API can be presented as a conventional tablet or a hard capsule, because of poor solubility, insufficient absorption from the gastro-intestinal tract (GIT), a slow dissolution rate or because of poor patient compliance. Patients may refuse to swallow or may be unable to swallow a tablet or a capsule (geriatric, disabled patients or children). Often, the above issues can be solved by formulating the API as orally disintegrating tablets (ODTs).

ODTs can be taken with or without water. Therefore, a major benefit for people using ODT products is to take them for "as needed" conditions e.g. seasonal allergies, migraines or when travelling when they are not near a suitable water supply. Clinically, the fast onset of action is especially desired for e.g. migraines. Pregastric absorption can result in improved bioavailability and as a result of reduced dosage, improved clinical performance through a reduction of unwanted effects. For many children the ability of the tablet to "disappear" in the mouth results in greater compliance and a better acceptance, particularly if sweetening/flavouring agents are used. A change of delivery site, for tablets containing APIs which are poorly soluble in the low pH of the stomach (pH≈1-2), to the higher pH of the mouth and upper part of GIT (pH≈6.8-7) can result

in a better dissolution profile. Additionally, gastro-intestinal irritation may be avoided. Some APIs can absorb better in the mouth and upper GIT than in the other parts of gastrointestinal tract, for example because of first-pass effect is bypassed.

A good example of an API formulated as an ODT is hydrochlorothiazide, classified as class III (good solubility, poor permeability) of the biopharmaceutics classification system (BCS). Hydrochlorothiazide was found to have a better absorption profile when administered as ODTs, prepared by lyophilisation, than the reference formulation (Esidrex™) (Corveleyn and Remon, 1998). Pharmacopoeial guidelines restrict ODTs to disintegrate within 3 minutes, though the USP monograph for ondansetron ODTs says that the disintegration cannot be longer than 10 seconds.

Examples of APIs which are marketed as ODTs are loratadine (Alvert™), rizatriptan benzoate (Maxalt™), ondansetron (Zofran™), lansporazol (Zoton™ FastTab™), olanzapine (Zyprexa™ VeloTab™ vel Zydis™), sumatriptan (Imigran Radis™), ibuprofen (Nurofen

FastMelt™), aspirin (Fasprin™), methadone (Methadose™), donepezil (Aricept™) or aripiprazole (Abilify™). Patented ODTs formulations include: RediTabs, Zydis, SolTab, OraSolv, Flash Dose, DuraSolv, Wowtab, Maxalt-MLT, Fastmelt, VeloTab, FasTab. Table below (Table 1.9) presents a summary of marketed technologies of some ODT products.

Table 1.9. A summary of marketed technologies used to prepare ODTs:

Basis for technology	Company	Technology
Lyophilisation (freeze drying) process	Cardinal Health	Zydis™
	Janssen Pharmaceutica	Quicksolv™
	Pharmalyoc	Lyoc™
Cotton candy process	Biovail	FlashDose™
Compaction (tableting)	Cima Labs	OraSolv®/DuraSolv™
	Yamanouchi	WOWTAB™
	Ethypharm	Flashtab™
	SPI Pharma	Pharmburst™

Lyophilisation results in tablets that are fragile with a porous wafer appearance. A solution or emulsion containing all formulation ingredients is freeze dried directly in a blister-pack. Despite the fact that these tablets disperse very rapidly on the tongue, the method is limited to approximately 60 mg of water soluble API per tablet. Cotton candy method is based on the production of an amorphous, saccharide-based matrix formed during a shearfoam process. The porous matrix with large surface area and porosity is then cured and milled. Tablet compression technology may include direct compression or granulation methods and is based on conventional manufacturing tooling.

1.5. Active pharmaceutical ingredients used in current work

1.5.1. Chlorothiazide

The chemical name of chlorothiazide (CTZ) (Fig.1.X) is: 6-chloro-4H-1,2,4-benzothiadiazine-7-sulfonamide 1,1-dioxide (Connors et al.,1986). As presented on figure 1.X., dissolved CTZ exists in two tautomeric forms, the presence of which depends on the pH of the solution. As a weak acid CTZ undergoes dissociation in alkaline solutions; the pKa values of CTZ are: 6.8 and 9.4.

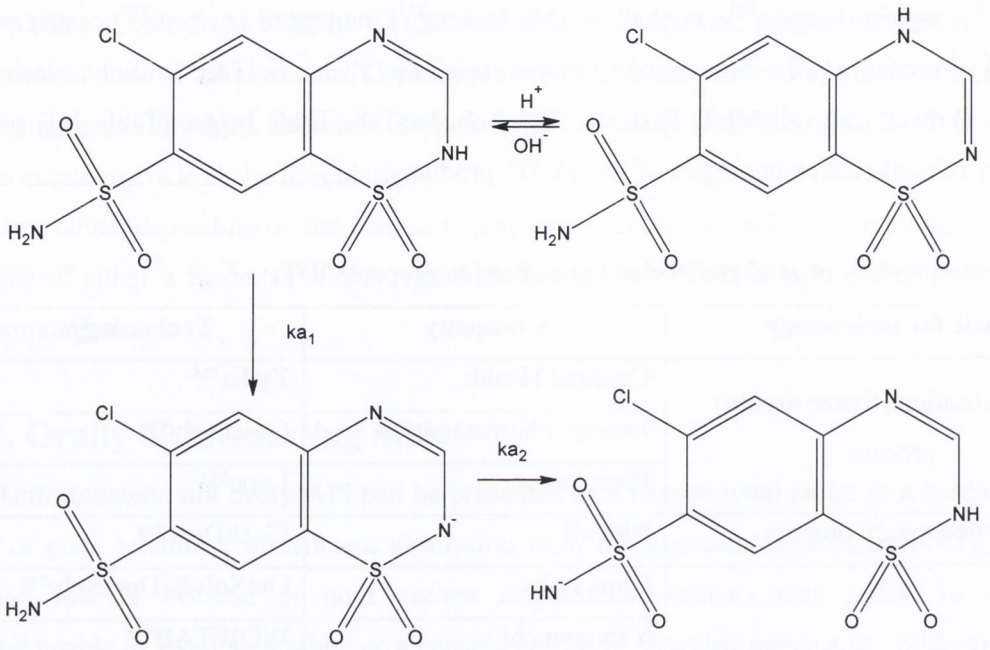

Figure 1.5. Tautomeric forms of chlorothiazide and dissociation products (Connors et al.,1986).

CTZ was designed by Merck (Beyer, 1977). A previously known molecule containing a sulphonamide group was sulphanilamide. Mann and Keilin (1940) reported that sulphanilamide works as a carbonic anhydrase inhibitor, causing alkalinisation of the patient's urine during chemotherapy. In 1942 Hober reported that alkalinisation of urine was related to increased sodium and bicarbonates excretion, while Schwartz (1949) indicated that the impact on chlorine ions excretion was not significant. Substitution of the aromatic amine group of sulphanilamide with a carboxylic group resulted in p-carboxybenze-sulphonamide (CBS) and improved secretion of sodium and chlorine ions. Beyer in 1954 reported that despite these compounds directly influencing the transport of cations, the diuretic effect seemed to be too weak to be utilised. The introduction of a second sulphoamoyl group into CBS at the meta position resulted in the formation of m-chloro-o,p-disulphonamide aminobenzene (CDSA), with significantly increased potency. Further exploration of disulphoamylobenzene analogues resulted in the discovery of the CTZ molecule.

The molecular formula of CTZ is $C_7H_6ClN_3O_4S_2$. It is a white, or practically white crystalline compound with a molecular weight of 295.73 amu. CTZ is very slightly soluble in water, poorly soluble in acetone, ethanol and methanol but readily soluble in aqueous alkali solutions (European Pharmacopia 2010).

Charnicki et al. (1956) and Connors et al. (1986) reported that as CTZ is stable in low pH (0 - 3.5) but in alkaline solutions the rate of degradation increases and CTZ undergoes hydrolysis (Fig. 1.X) to 4-amino-6-chloro-m-benzene disulphonamide.

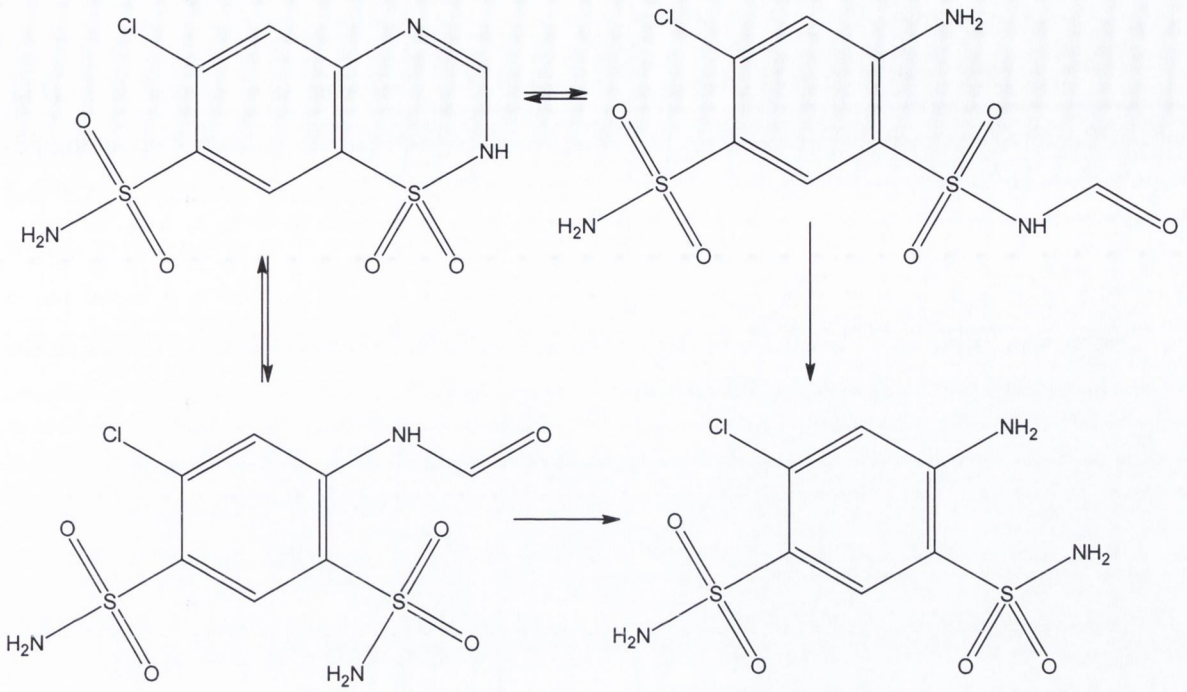

Figure 1.6. Possible products of degradation of chlorothiazide.

CTZ was chosen as a model compound in this work, due to its high melting point and very low aqueous solubility. It is a small molecule with polar moieties and a reported potential of salt formation (Charnicki et al., 1956), however no characteristics of salt forms of chlorothiazide have been published to date.

1.5.2. Salbutamol

The (R,S)-alpha1-[(tert-butylamino)methyl]-4-hydroxy-m-xylene-alpha,alpha'-diol (Fig. 1.X) is an active pharmaceutical ingredient (API) known as salbutamol (SB). It is a short acting β2-mimetic used as a bronchodilator. It is marketed as an equal racemic mixture in inhalers (liquid and powder), nebules, injections, syrups and tablets. Salbutamol was the first selective β_2-receptor agonist to be marketed in 1968. It was first sold by Allen & Hanburys under the brand name Ventolin. Enantimers (C17- R, S) differ in bioactivity. The R form is reported to be twice as active as the racemic mixture (Sjosward at all 2004).

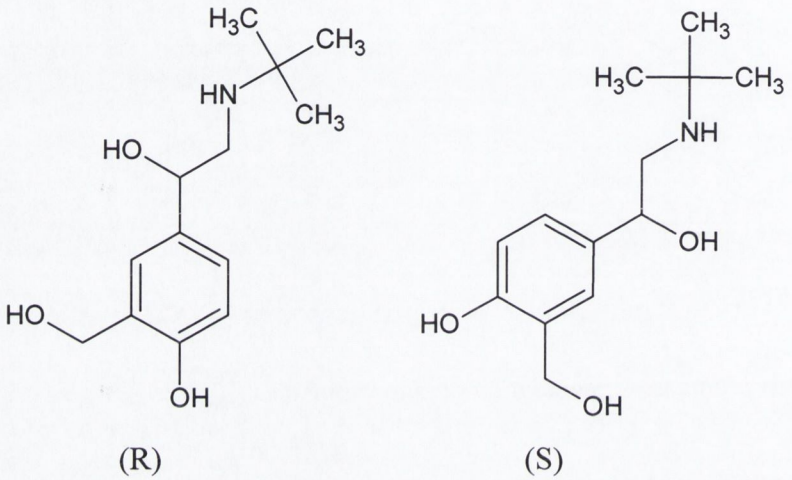

Figure 1.7. Chemical structure of (R,S)-salbutamol.

Salbutamol was reported to have amphoteric characteristics by Imboden and Imanidis (1999). The pKas of salbutamol are 9.1 and 10.4. The decomposition of salbutamol as salbutamol sulphate was studied in the pH range 1.9–8.8 at 65°C by Mälkki and Tammilehto (1990) and Mälkki-Laine et al. (1995). Depending on the pH of the solution, one to four major decomposition products were detected. The decomposition of salbutamol sulphate in aqueous solution followed first-order kinetics. The reaction rate increased with increasing initial drug concentration and elevated temperatures. The maximum stability of salbutamol in aqueous solution occurred at a pH of about 3.5 (Hakes et al. 1980). The degradation products of salbutamol formed in aqueous solution were identified and structurally elucidated (Mälkki-Laine and Bruins, 1994). Salbutamol can also undergo bimolecular reactions, which result in the formation of a range of dimers (Altria K.D., 1993).

The chemical instability of salbutamol in pharmaceutical formulations (pressurised metered dose inhalers), containing ethanol as cosolvent, has also been reported (Tzou et al., 1997).

Experimental

Chapter 2

Materials and method

2.1. Materials used in experiments

Material	Supplier Manufacturer
acetic acid	Riedel de Haën (Germany)
acetone (AC) (analytical grade)	Corcoran Chemicals (Ireland)
acetonitrile	Fischer Scientific (Ireland)
adipic acid (99%+ grade)	Sigma-Aldrich (Germany)
chlorothiazide (CTZ)	Sigma (Ireland)
deuterated dimethyl sulphoxide (DMSO-D_6)	Apollo Scientific Limited (UK)
Dipac™	Amstar Corp. U.S.A.
disodium hydrogen phosphate	Riedel de Haën (Germany)
ethanol (EtOH) (H_2O<0.1%)	Corcoran Chemicals (Ireland)
ethyl acetate	Lab Scan (Ireland)
formic acid (HPLC grade)	Sigma (Ireland)
Hydranal-Composite™	Riedel de Haën (Germany)
hydrochloric acid 32% (extra pure)	Riedel de Haën (Germany)
hydrogen peroxide 30%	Riedel de Haën (Germany)
magnesium stearate	Sigma Germany
methanol (MeOH) (HPLC grade)	Sigma (Ireland)
n-butyl acetate (BA)	Merck (Germany)
nitric acid 69% (Aristar)	BDH (UK)
n-propanol	Lab Scan (Ireland)
paraffin wax	BDH Laboratory Supplies Poole, England
phosphorus pentoxide desiccant	Fluka (Ireland)
potassium bromide (FT-IR grade)	Sigma (Ireland)
potassium hydroxide	Merck (Germany)
Purpald™ reagent	from Sigma (Ireland)
salbutamol base	CHEMOS GmbH Germany
sodium dihydrogen phosphate	Riedel de Haën (Germany)
sodium hydroxide	Riedel de Haën (Germany)
succinic acid (99%+ grade)	Sigma-Aldrich Chemical Company (USA)
water deionised (W)	Purite Prestige Analyst HP, Millipore Elix 3 (UK)

2.2. Methods

2.2.1. Production of active pharmaceutical ingredients

2.2.1.1. Chlorothiazide sodium and potassium

Chlorothiazide sodium (CTZNa) and chlorothiazide potassium (CTZK) were prepared by mixing of 1M NaOH or KOH aqueous solution with chlorothiazide powder (~1.2 M equivalence). The suspensions obtained were evaporated under forced air flow at 70 °C until dry, re-suspended at 70 °C in water, filtered through a 0.45 μm membrane filter and the filtrate was recrystallised by solvent evaporation at 70 °C, until dry. The 24 hours drying of powders in 70 °C resulted in white powder of CTZNa hereafter referred to as CTZNa anhydrous form while CTZK powder was referred to as monohydrate form I.

2.2.1.1.1. Crystallization studies of CTZ CTZNa and CTZK

The crystals subsequently used for single crystal X-ray and other analyses were prepared from solutions. The solutions of CTZ, CTZNa or CTZK were saturated for each solvent used. Saturation was obtained by introducing an excess of raw material into the appropriate solvent at ambient conditions by shaking for an hour on a WhirliMixer® (Fisons Scientific Equipment). 10 ml of the suspension obtained was filtered through a 0.22 μm membrane filter into a glass vial which was kept in a glove box (Clean Sphere CA 100, Safetech Limited) under constant nitrogen flow at room temperature (20-23 °C). The moisture content in this controlled environment was less than 1% relative humidity. The dry nitrogen flow and temperature control were maintained to provide reproducible conditions of solvent evaporation.

Compounds were crystallised by solvent evaporation. CTZ crystals were obtained by evaporation of acetone or ethanol. CTZNa crystals were obtained by evaporation of water or 1:1 acetone/water mixture or ethanol.

CTZK crystals were obtained by evaporation of water or 1:1 acetone/water mixture (both referred to as form II) or ethanol (referred to as form IV). A desolvated form IV was obtained by additional drying of crystals at 80 °C for 24 hours and this material is referred to as form V.

The anhydrous form III of CTZK was prepared by additional drying in the thermogravimetric analyser (TGA) using the following temperature programme: 25 °C-180 °C-25 °C with a heating/cooling rate of 10 °C/min.

2.2.1.1.2. Preparation of chlorothiazide salts for tableting (Chapter 7)

Chlorothiazide sodium (CTZNa DH) and potassium (CTZK DH) dihydrates were obtained by vacuum evaporation of the water from equimolar solutions of respective hydroxide and

chlorothiazide (Methods 2.2.1.1). Solutions were placed in a 250 ml round bottomed flask. The flask was attached to a Rotavapor R210 unit (Büchi) supplied with a heating bath B491 set to 50 °C. Rotation was set to level 4. Vacuum controller V850 was set to 42 mbar. Negative pressure was generated by the vacuum pump V700. Solid residues were recovered from the evaporation vessel and subsequently dried in a glove box (Clean Sphere CA 100 by Safetech Limited) under constant nitrogen flow at room temperature (20 °C-23 °C) for three hours. The moisture content in the environment was controlled and was less than 1% relative humidity.

Anhydrous CTZNa was obtained as previously described (Methods 2.2.1.1.).

CTZK anhydrous form III, alternatively to method described (Methods 2.2.1.1.1.), was prepared by spray drying of CTZKDH from water and secondary tray drying at 170 °C for 3 hours in an oven (Memert, Germany).

2.2.1.3. Salbutamol adipate and succinate

A stoichiometric mixture of salbutamol and adipic acid in a 1:1 molar ratio was dissolved in methanol at 0.05 g/ml concentration of solid at 25 °C. Methanol was evaporated under forced air flow at an evaporation rate 0.40 g/min (monitored using a balance every 5 min), whilst stirring. The white precipitate was filtered close to the end of methanol evaporation. The precipitate was dried for an hour under constant air flow at 25 °C. The dry powder was subjected to elemental analysis and was determined to be salbutamol mono adipate (SA). It was obtained with a 95% yield.

A stoichiometric mixture of salbutamol and succinic acid in a 2:1 molar ratio was dissolved in methanol at 0.05 g/ml concentration of solid at 25 °C. Methanol was evaporated under forced air flow at an evaporation rate of 0.40 g/min (monitored using a balance every 5 min), whilst stirring. After nucleation of the salt, the temperature was dropped to 20 °C and the evaporation rate of methanol was kept constant (0.40 g/min) until the concentration of solid in methanol reached 0.1 g/ml. The white precipitate was filtered and dried at 25 °C. Elemental analysis of the white crystalline powder determined it to be salbutamol hemi-succinate tetramethanolate (SSU.MeOH). It was obtained with a 80% yield. Further drying of the precipitate under constant air flow at 25 °C for 24 hr resulted in formation of the desolvated salbutamol hemi-succinate (SSU).

2.2.1.3.1. Crystallization studies of salbutamol adipate and succinate

Attempts were made to crystallize salbutamol with adipic acid and succinic acid by solvent evaporation from ethanol, methanol and water. The tested molar ratios of salbutamol to the acid were: 1:2, 1:1 and 2:1 for each solvent. It was observed that successful crystallization was achieved only for salbutamol mixed with adipic acid in the 1:1 molar ratio using methanol or water as the solvent and for salbutamol and succinic acid mixed in the 2:1 molar ratio using methanol

(details of the procedure are described below). Other combinations resulted, either in crystallization of one or two of the components separately or in the production of a glassy/amorphous material.

The crystals subsequently used for single crystal X-ray and other analyses were prepared from saturated solutions, which were obtained by introducing an excess of raw material into the appropriate solvent at ambient conditions and shaking for an hour on a WhirliMixer® (Fisons Scientific Equipment). 10 ml of the suspension obtained was filtered through a 0.22 μm membrane filter into a glass vial which was kept in a glove box (Clean Sphere CA 100, Safetech Limited) under constant nitrogen flow at room temperature (20-23 °C). The moisture content in this controlled environment was less than 1% relative humidity.

Dry nitrogen flow and temperature control were provided to maintain reproducible conditions of solvent evaporation. Crystallization of SA from methanol resulted each time in a very rapid nucleation of the crystals. Modification of the environmental conditions, including slowing down the evaporation rate of methanol and decreasing the temperature, did not retard the crystal growth. Very small crystals with crystal defects (inclusions) were not of sufficiently good quality to be analyzed by single crystal X-ray analysis. A change of the solvent to water resulted in slow crystal growth and good quality crystals of SA, with a PXRD pattern consistent with that obtained for crystals produced from methanol, hence the SA crystals obtained from water were later used for single crystal X-ray analysis.

2.2.2. Spray drying

2.2.2.1. Spray drying of chlorothiazide and CTZ salts

Spray drying was performed using a Büchi B-290 Mini Spray Dryer. An inert loop Büchi B-295 (for organic solvents) and additionally a dehumidifier Büchi B-296 (for water/organic solvent mixtures) were used for the closed mode operation. The spray dryer, depending on the sample, was used in a closed mode with recirculation of nitrogen as the drying and nozzle gas or as an open system with nitrogen (open, suction mode) or in a mixed mode where compressed nitrogen was used to atomise the solution but air was used as the drying gas (open, blowing mode). The drying gas in the open mode, in contrast to the closed mode, was not recirculated. The blowing open mode was employed as it resembles the typical gas flow layout used in larger scale equipment (Masters, 2002).

A standard atomization nozzle with a 1.5 mm cap and 0.7 mm tip was employed for all processing. The drying gas pressure of 6 bar at 4 cm gas flow (rotameter setting), equivalent to 473 norm litres per hour (nL/h) of gas flow in normal conditions (p=1013.25 mbar and T=273.15 K) (Büchi 93001 en.). The nozzle pressure drop was measured to be 0.41 bar. The pump speed was

set to 30% (9-10 ml/min) and the aspirator was operated at 100%. Other conditions varied depending on the system spray dried and are summarised in Tables 5.2, 6.1.

Additional, secondary drying (AD) was performed using the same temperature as that of the outlet spray drying temperature for 12 hours for samples #6.19 and #6.20 (with the samples exposed to AD later referred to as #6.19* and #6.20*). Batches of 20-30 g of the spray dried material were placed between two 0.032 mm aperture, 20 cm diameter sieves and placed in an incubator with forced air flow (Gallencamp Economy Incubator with fan). The environmental humidity in the laboratory was monitored using Testo^{TM} 175-H1 Logger humidity and temperature control system.

2.2.3. Preparation of powders for tableting

Dipac^{TM} and chlorothiazide raw material (CTZ) were used for tableting as supplied. Spray dried materials (produced as described in Section 2.2.2.1) were additionally tray dried in the oven (Memert, Germany) for 12 hours at 100 °C, until the mass loss by thermogravimetric analysis (TGA) was lower than 1% in the temperature range of 25-150 °C at heating rate of 10 °C/min.
The particle size of other materials was reduced using a mortar and pestle.

2.2.4. Tableting

Tablets (n=10) were compressed using an experimental, laboratory scale tablet press MTCM 1 from GlobePharma (USA) supplied with Enerpac (USA) single-acting general purpose cylinder oil press working in the range from 0-700 bar (max. 5 tons, 45 kN), Enerpac AC RC53 piston and standard concave 10 mm diameter punch and die tooling. The die was loaded manually with a known weight (Sartorius BP121S balance) of the powder (250 mg) and compressed in the range from 20 to 200 bars. Pressure was released immediately after reaching the desired compression force. Tablets were pushed out of the die using the upper punch. To lubricate the tablet press tooling die and upper punch were dusted using a paint brush with magnesium stearate.

In order to assess if materials do not undergo solid state transformation upon compression, samples of materials (250 mg) were subjected to compression in Perkin Elmer hydraulic press under 10 tons load for 1 minute. Formed discs (10 mm diameter) were subjected to PXRD analysis, then ground in an agate mortar and tested again using PXRD. None of the tested materials indicated a surface and/or bulk solid state change in comparison to the starting powder (data not shown).

2.2.4.1. Measurement and calculation of tablet geometry parameters

The height (H), diameter ($2r_1$) and the band thickness (h_2) of the tablets (Fig. 2.1.) were recorded (n=10) using an electronic outside micrometer IP 54 form RS (0-25 mm ±0.001 mm) equipped with ABS- anti crushing system.

This allowed for calculation of the surface area of the tablet (A_t) (Eqn. 2.1) (Ford et al., 1991).

$$A_t = 2\Pi r_1 h_2 + 2\Pi\left(r_1^2 + \frac{H - h_2}{2}\right) \qquad \text{Eqn. 2.1.}$$

Measured geometric parameters of the tablet allowed for calculation of the volume of the tablet (V_t) using equation 2.2 (Cobby et al., 1974).

$$V_t = \frac{\Pi\left(\frac{H - h_2}{2}\right)^3}{3 + r_1^2\left(h_2 + \frac{H - h_2}{2}\right)} \qquad \text{Eqn. 2.2.}$$

2.2.4.2. Hardness test, calculation of tensile strength (σ_t) of the tablet

A set of ten tablets, was subjected to radial hardness testing using Dr. Schleuniger, Pharmatron, Model 6D tablet tester. Fracture load (shear strength under compressive load) (P) [N] was recorded for each tablet (n=10). It was monitored if the tablet capped under applied force, or if the breakage of the tablet occurred otherwise than in vertical radial cross section.

Tensile strength of the materials (σ_t) was calculated using empirical model introduced by Pitt et al. in 1989 and expanded by Es-Saheb in 1996 for convex tablets (Eqn. 2.3).

$$\sigma_t = \frac{10P}{\Pi 4r_1^2} \cdot 1/\left(\frac{2.84H}{2r_1} - \frac{0.126H}{h_2} + \frac{3.15h_2}{2r_1} + 0.01 \right) \qquad \text{Eqn. 2.3.}$$

2.2.4.3. Tablet porosity (ε_t)

Tablet porosity was calculated as a function of true density of the compacted material (d_0) and density of the tablet calculated after compaction (d_t), equation 2.4.

$$\varepsilon_t = 100 - \frac{100 d_t}{d_0} \qquad \text{Eqn. 2.4.}$$

2.2.5. Thermal methods

2.2.5.1. Differential scanning calorimetry (DSC)

DSC experiments were performed in triplicate using a Mettler Toledo DSC 821^e (Switzerland) with a refrigerated cooling system LabPlant RP-100. Nitrogen was used as the purge gas. Aluminium sample holders were sealed with a lid and pierced to provide three vent holes. Sample volume was sufficient to provide proper contact between the powder and the bottom of the pan, and sample weight was ≥5 mg. DSC measurements were carried out at a heating/cooling rate of 10 °C/min (Tajber et al., 2005). The DSC system was controlled by Mettler Toledo STAR^e software (version 6.10) working on a Windows NT operating system. The unit was calibrated with indium and zinc standards.

2.2.5.2. Temperature modulated differential scanning calorimetry (MT-DSC StepScan™)

A PerkinElmer (USA), Diamond DSC unit with HyperDSC was implemented to detect glass transition temperatures of amorphous systems (Holubová et al., 2005). The unit was refrigerated using an ULSP B.V. 130 (Netherlands) cooling system and operated under a nitrogen flow of 40 ml/min. The gas flow was controlled using a PerkinElmer Thermal Analysis Gas Station (TAGS). Samples were heated at 5°C/min and 2 °C steps. Between each of the dynamic steps a 1

minute isothermal step was applied. The area algorithm was applied to calculate the specific heat of glass transition from the enthalpy flow. A baseline run was performed for each sample to minimise sample holder mass error. Samples were tested in 18 μL aluminium holders sealed with pierced lid to provide three vent holes. Sample volume was sufficient to provide proper contact between powder and a pan bottom, never less than 5 mg. The unit was calibrated with indium and zinc standards. Presented results are the average of triplicate analyses.

2.2.5.3. Thermogravimetric analysis (TGA)

TGA was performed using a Mettler TG 50 (Switzerland) module linked to a Mettler MT5 balance. Samples were placed into open aluminium pans (5-12 mg). A heating rate of 10 °C/min was implemented in all measurements (Tajber et al., 2005). Analysis was carried out in the furnace under nitrogen purge and monitored by Mettler Toledo STAR^e software (version 6.10) with a Windows NT operating system. Presented results are the average of triplicate analyses.

2.2.6. Density measurement

2.2.6.1. Density measurement by helium pycnometry

The true density was measured by AccuPyc 1330 Pycnometer MicromeriticsTM using helium (99.995% purity) to determine the volume of the sample. A 1 cm^3 sample holder was used. The instrument was calibrated immediately before performing the analysis at room temperature. Each sample was analysed in triplicate and averaged results are presented in this thesis.

All the samples unless stated otherwise, were dried for at least 12 hours prior to analysis using a vacuum oven (Gallencamp, UK) operated at 30 °C and -600 mbar pressure. Crystals of CTZNa dihydrate where dried in a glove box (Clean Sphere CA 100 by Safetech Limited) under constant nitrogen flow at room temperature (20-23 °C) for three hours. The moisture content in the environment was controlled and was less than 1% relative humidity.

2.2.7. X-ray crystallography

2.2.7.1. Powder X-ray diffraction (PXRD)

Powder XRD analysis was conducted using a Miniflex II Desktop X-ray diffractometer Rigaku with Ilaskris cooling unit. The tube output voltage used was 30 kV and tube output current was 15 mA. A Cu-tube with Ni-filter suppressing Kβ radiation was used. Measurements were taken from 5 to 40 on the 2 theta scale at a step size of 0.05° per second in each case (Tajber at al., 2009). Scans were performed at room temperature.

2.2.7.2. Single crystal X-ray diffraction (SC-XRD)

Cambridge Crystallographic Data Centre contains the supplementary crystallographic data for this thesis: CCDC 757605 (CTZNa dihydrate), CCDC 761198 (CTZK dihydrate), 761199 (CTZK monohydrate hemiethanolate), CCDC 801059 (SA) and 801060 (SSU.MeOH).
The data can be obtained free of charge from The Cambridge Crystallographic Data Centre via www.ccdc.cam.ac.uk/data_request/cif.

2.2.7.2.1. Chlorthiazide sodium and potassium

Single crystal XRD data was collected on a Rigaku Saturn 724 CCD diffractometer. Suitable crystals were selected and mounted using inert oil on a 0.30 mm quartz fibre tip and immediately placed on the goniometer head in a 150K nitrogen gas stream. Each data set was collected using Crystalclear-SM 1.4.0 software and 1680 diffraction images, of 0.5° per image, were recorded. Data integrations, reductions and corrections for absorption and polarization effects were all performed using Crystalclear-SM 1.4.0 software. Space group determinations, structure solutions and refinements were obtained using Crystalstructure ver. 3.8 and Bruker Shelxtl ver. 6.14 software. To evaluate the data, Mercury 2.2 software was used (Blessing, 1995).

2.2.7.2.2. Salbutamol adipate and succinate

X-ray diffraction measurements were made on a Bruker APEX II DUO diffractometer using graphite monochromatized MoK_α radiation (λ = 0.7107 Å) and an Oxford Cryosystems COBRA fitted with a N_2 generator. All calculations were made using the APEX2 software (APEX2 v2009.3-0, Bruker AXS, 2009; Sheldrick, 2008) and the diagrams prepared using Mercury (Macrae et al., 2008).

2.2.8. Elemental analysis

Elemental analysis was carried out using an Exeter Analytical CE440 CHN analyser. The molar amount of carbon as carbon dioxide, nitrogen, as nitrogen oxide and hydrogen as water, was determined by oxidation of the sample (n=3, around 10 mg) and the thermal conductivity analysis of obtained gases and water vapour.

2.2.9. Nuclear magnetic resonance (^{1}HNMR, ^{13}CNMR)

A Bruker Avance 400 NMR with 4-nucleus (^{1}H, ^{13}C, ^{31}P and ^{19}F) probe was used for NMR studies. Deuterated DMSO-D_6 was used to prepare the samples. Sample concentration was in the range 20-40 mg/ml. Spectrometer frequency was 400 MHz with an acquisition time of 2s. The number of scans was appropriate to gain good quality spectra. Standard Pulse Sequence supplied by Bruker was used for ^{1}H, ^{13}C and 2-dimensional experiments.
Appendix II contains supplementary NMR spectra.

2.2.10. Microscopy

2.2.10.1. Scanning electron microscopy (SEM)

SEM analysis was performed using a Hitachi S-3500N variable pressure scanning electron microscope, Tescan Mira Variable Pressure Field Emission Scanning Electron Microscope and Zeiss Supra Variable Pressure Field Emission Scanning Electron Microscope. The resolution was 3 nm at 30 kV, accelerating voltage was 5 kV and the detector was secondary electron. Samples were glued onto aluminium stubs and sputter-coated with gold under vacuum prior to analysis.

2.2.11. Solid state Fourier transform infrared spectroscopy (FTIR)

Infrared spectra were recorded in duplicate on a Nicolet Magna IR 560 E.S.P. spectrophotometer equipped with MCT/A detector, working under Omnic software version 4.1. A spectral range of 650-4000 cm^{-1}, resolution 2 cm^{-1} and accumulation of 64 scans were used in order to obtain good quality spectra. A KBr disk method was used with a 0.5-1% sample loading. KBr disks were prepared by direct compression under 8 bar pressure for 1 minute (Healy et al., 2008). The sample preparation did not affect the spectra as confirmed with an attenuated total reflectance (ATR) spectrometer (data not shown).

2.2.12. Karl Fischer titrimetry - water assay

0.5 g of CTZNa or CTZK sample (n=3) was dissolved in pre-titrated 50 ml of methanol. As Karl-Fischer reaction is not stoichiometric in alkaline solutions (Scholz, 1987), the pH was adjusted with 50 µl of 32% hydrochloric acid. Metrohm 841 Titrando was used for titration and the unit was calibrated with 20 µl of water. The results were averaged.

2.2.13. Ethanol and acetone assays

2.2.13.1. Gas chromatography – mass spectrometry (GC-MS)

A known weight of each sample (n=3) was placed in a headspace vial to which 1 ml of deionised water was added. The vials were sealed. The vials were then heated and agitated at 80 °C for 10 minutes in a headspace auto-sampler where the volatile organics in the samples

were driven into the headspace of the vial (the air above the sample). 1 ml of the headspace gas was then extracted by syringe from the vial and injected onto the GC-MS Varian Saturn 22700 column. The ethanol eluted at 8.1 min and acetone at 8.7 min. The column used for the analysis was a WCOT fused Silica 60m x 0.32 mm ID coating CP-SELECT 624 CB DF=1.8.

2.2.14. Methanol and butyl acetate assay

2.2.14.1. Gas chromatography with flame ionisation detector GC-FID

A GC-FID PerkinElmer Clarus 500 with auto sampler and Supelco SPB-GC column (60m x 0.25 mm x 0.5μm, 35% phenyl 65% dimethyl polysiloxane filling) were used to detect the residual content of methanol and butyl acetate (EU Pharmacopeia, 2010) in the spray dried CTZNa and CTZK. Helium at 8 psi pressure was used as a carrier gas. The oven temperature was 50 °C and the detector temperature was set to 325 °C. Both solvents were assayed based on individual calibration curves with internal standards included (ethyl acetate for butyl acetate and n-propanol for methanol). The injection volume was 1.0 μl and the retention times were the following: methanol: 3 min 57 s (±0.00 s), n-propanol: 4 min 34 s (±0.01 s), butyl acetate: 12 min 50 s (±0.01 s) and ethyl acetate: 5 min 00 s (±0.00 s). The total duration of the method was 20 min. Samples (n=3) were prepared by dissolving between 100 mg and 500 mg of the tested powder in 10 ml of water, depending on the expected residual solvent content. The solubility of butyl acetate and ethyl acetate in water was reported to be 0.7 g/100 ml and 8.3 g/100 ml (Flick, 1998), respectively, and was well above the expected concentrations of the solvents in water.

2.2.15. Sodium and potassium assays

2.2.15.1. Inductively coupled plasma–mass spectrometry (ICP-MS)

Known weights of the samples (n=3) were placed in separate digestion vessels. 7 ml of 69% HNO_3 and 1 ml of 30% H_2O_2 were then added to each sample. The vessels were sealed and placed in a microwave digester where they were heated to 200 °C at 1000 W and held for 20 minutes at these conditions. The samples were then made up to a final volume of 50 ml with deionised water. This digest was then analysed by ICP-MS Varian 820, to measure the levels of sodium and potassium. Certified calibration standards were used to calibrate the ICP-MS and the samples were diluted where necessary to bring them into the range of the calibration curve.

2.2.16. High performance liquid chromatography (HPLC)

2.2.16.1. Decomposition of CTZ, CTZNa and CTZK

Decomposition of CTZ, CTZNa and CTZK was determined with a high performance liquid chromatography (HPLC) using a method modified from Ulvi and Keski-Hynnilä (1994). The HPLC system used was a Shimadzu HPLC Class VP series with a LC-10AT VP pump, SIL-10AD VP autosampler and SCL-10AVP system controller. The mobile phase was filtered through a 0.45 μm membrane filter (Gelman Supor-450, USA) The analytical column used was a Waters Spherisorb™ ODS2 column (250 mm length, internal diameter 4.6 mm, particle size 5 μm). UV detection was carried out at a wavelength of 260 nm and the injection volume was 10 μl. Separation of degradation products was carried out isocratically at ambient temperatures with a flow rate of 1 ml/min. The mobile phase consisted of 0.1M NaH_2PO_4 phosphate buffer/acetonitrile 10:1 (v/v) brought to pH 3.0±0.1 with phosphoric acid. Under these conditions the retention times of chlorothiazide (CTZ) was ~12. Samples were analysed in triplicate.

2.2.16.2. Detection of adipic and succinic acid in aqueous solution

The content of adipic and succinic acids in SA and SSU aliquots was determined with a high pressure liquid chromatography (HPLC). The HPLC system used was a Shimadzu HPLC Class VP series with a LC-10AT VP pump, autosampler SIL-10AD VP and SCL-10AVP system controller. The mobile phase was filtered through a 0.45 μm membrane filter (Gelman Supor-450, USA) before use. The HPLC method used for the analysis of the dicarboxylic acids was modified from Ziegler (1998) and Kordis-Krapez et al. (2001). The analytical column used was a LiChrosorb RP-10 column (250 mm length, internal diameter 4 mm, particle size 10 μm). UV detection was carried out at a wavelength of 210 nm and the injection volume was 20 μl.

Separation of adipic acid was carried out isocratically at ambient temperatures with a flow rate of 1 ml/min. The mobile phase consisted of methanol:phosphoric acid solution (pH 2.1) 20:80 (v/v).

Separation of succinic acid was carried out using a gradient method with a flow rate of 1 ml/min. The mobile phase consisted of two eluents: (A) phosphoric acid solution (pH 2.1) and (B) methanol:phosphoric acid solution (pH 2.1) 20:80 (v/v). The following gradient was used: a linear gradient from 0 to 50% B over 7 min, then a linear gradient from 50 to 100% B over 1 min and this composition was maintained for 7 min. Then again a linear gradient from 100 to 0% B over 10 min was applied and the final mobile phase composition was continued for a further 5 min. Under these conditions the retention times of adipic acid and succinic were 4.3 and 6.5 min, respectively.

2.2.17. Aldehyde detection

Purpald® (4-amino-3-hydrazino-5-mercapto-1,2,4-triazole) was used as a reagent for the selective detection of aldehydes (Quesenberry and Lee, 1996). 10 mg of powder was added to approximately 20 mg of Purpald® dissolved in 2 ml of 1M NaOH. The mixture was aerated and the colour noted after a few minutes. The change of colour from yellow to purple indicates the presence of aldehyde in the tested solution. The samples in duplicate were compared against a reference solution containing dissolved Purpald reagent and CTZNa anhydrous material (negative control).

2.2.18. Particle size characterisation

2.2.18.1. Particle size characterisation by laser diffraction

Measurements of particle size and particle size distributions were obtained using a laser diffraction particle sizer Mastersizer 2000 (Malvern Instruments, UK). Particles were dispersed using a Scirocco dry feeder instrument with 2 bar pressure. An obscuration rate of 0.5-6% was obtained under a vibration feed rate of 50%. Results reported are the average of three analyses.

2.2.19. Specific surface area analysis (T_{BET}) by Brunauer, Emmett, Teller (BET) isotherm

Samples (n=3) were dried prior to analysis under nitrogen flow at 50 °C for 12 hours using a Gemini SmartPrep (USA) drying station. To determine the bulk specific surface area a Micromeritics Gemini VI (USA) surface area analyzer was used. Compressed nitrogen was used as an adsorptive gas. Each measurement consisted of six steps, determining the amount of gas adsorbed at 6 relative pressure points in the range of 0.05 to 0.3 of relative pressure P/P_0 with equilibration time of 10 s. Free space was determined separately for each sample using helium gas. Saturation pressure P_0 was determined prior to the measurement of each sample.

2.2.20. Solubility studies

2.2.20.1. Solubility studies of CTZ in water and organic solvents (acetone, ethanol)

Solubility studies were carried out in a shaking water bath at 50 rpm, for 24 hours in 25 °C. Approximately a three-fold excess of CTZ was loaded into 10 ml glass vials and suspended in 5 ml of the solvent. Vials were sealed hermetically to prevent solvent evaporation. The suspensions were filtered through a 0.2 μm membrane filter after 24 hours of equilibration and 1 ml samples (n=3) of the filtered solutions were evaporated at 80 °C under forced air flow until dry. TGA analysis (at 10 °C/min heating rate) was used to confirm the samples contained no residual moisture/solvent traces. The mass loss upon drying varied in the range of 0.02 to 0.05%.

2.2.20.2. Solubility of chlorothiazide, chlorothiazide sodium and potassium

For CTZ salts, powdered CTZNa or CTZK dihydrate was added in excess (approximately three times the expected saturated concentration) directly to water at 37 °C, shaken at 100 cpm and analysed after 5 min and every 10 min until 30 min. The concentrations obtained at the final three time points were the same and were averaged to give the saturated stoichiometric solubility (Anderson and Flora, 1996). All alkali solutions of CTZNa were analysed within one hour, as within this time frame alkaline decomposition of the compound is insignificant (Charnicki et al., 1959).

For CTZ, excess of CTZ powder (approximately three times of the expected saturated concentration) was suspended in 10 ml of water in a 20 ml volumetric flask. The suspension of chlorothiazide was shaken at 70 cpm at 37 °C for 24 hours.

Suspensions were filtered through a 0.45 μm membrane filter. In the case of CTZNa or CTZK, the excess of material recovered after 30 minutes was analysed using DSC and PXRD. Analysis confirmed the residue of material to be CTZNa or CTZK dihydrate with no traces of pure CTZ precipitation (data not shown). The pH of the aqueous saturated solutions was measured using a Thermo Orion 420+ pH-meter.

The quantity of CTZ and CTZNa or CTZK dissolved in water was assayed by UV spectrophotometry at 292 nm (Shimadzu UV-1700 Pharmaspec). CTZ aliquots were diluted with 0.1M NaOH and water was used to dilute CTZNa or CTZK samples to obtain the appropriate concentration range.

2.2.20.3. Solubility of salbutamol, salbutamol adipate and salbutamol succinate

Powdered SA, SSU and SB were added in excess (approximately three times the expected saturated concentration of salbutamol) directly to 2 ml of water in an Eppendorf vial at 37 °C (Fadda et al., 2010). Additionally, the SA powder was suspended in a NaOH solution to investigate its solubility at a pH value other than that measured for the sample in pure water. The Eppendorfs were placed horizontally in a water bath and shaken at 100 cpm. Suspensions were filtered through a 0.22 μm membrane filter. The content of salbutamol in the saturated solutions was assayed by UV spectrophotometry at 276 nm (Shimadzu UV 1700 Pharmaspec). SB, SA and SSU aliquots were diluted with water to obtain the appropriate concentration range. Samples were withdrawn and analysed after 10, 11 and 12 hours and as equilibrium appeared to be reached after 10 hours, the values were averaged over these three time points. The content of adipic and succinic acids in SA and SSU aliquots was determined with a high pressure liquid chromatography (HPLC) (Methods 2.2.16.1.2.)

2.2.21. Intrinsic dissolution rate studies of salbutamol salts

Discs of SS, SSU and SA were prepared by compressing 300 mg of the given material in an IR hydraulic press (PerkinElmer, UK). The 13 mm diameter discs had a 1.33 cm^2 top surface area. The bottom and side surfaces of the discs were coated with paraffin wax and mounted in the centre of the bottom of a standard dissolution vessel (Healy and Corrigan, 1996). Each dissolution experiment was performed in triplicate, as long as the dissolving disc kept a visibly constant surface area.

Intrinsic dissolution studies were performed with a type 2 dissolution test apparatus (VanKel VK7000 dissolution test station) equipped with VK650 heater/circulator) (European Pharmacopoeia, 2010). The rotation speed of the paddle was set to 100 rpm. 900 ml of deionised, degassed water was used as the dissolution medium, equilibrated at 37 °C. To sample the dissolution medium a standard dissolution vessel was equipped with a medium recirculation system. The dissolution medium was constantly circulating using a LSMatec peristaltic pump fitted with a 10 μm filter through a 2 mm flow-through UV cuvette placed in a Cecil CE2020 UV-spectrophotometer set to 276 nm (Nocent et al., 2001). The rate of medium circulation was set to 25 ml/min and the pH of the aqueous medium was monitored using a Thermo Orion 420+ pH-meter.

2.2.22. Dissolution studies of tablets containing chlorothiazide and its salts

Dissolution studies were performed with a type 2 dissolution test apparatus (VanKel VK7000 dissolution test station) equipped with VK650 heater/circulator) (European Pharmacopoeia, 2010). The rotation speed of the paddle was set to 50 rpm. 900 ml of, degassed phosphate buffer pH 6.8 (European Pharmacopeia 2010) was used as the dissolution medium, equilibrated at 37 °C. To sample the dissolution medium a standard dissolution vessel was equipped with a medium recirculation system. The dissolution medium was constantly circulating using a LSMatec peristaltic pump fitted with a 10 μm filter through a 2 mm flow-through UV cuvette placed in a Cecil CE2020 UV-spectrophotometer set to 265 nm. The rate of medium circulation was set to 25 ml/min.

2.2.23. Water vapour sorption analysis of pharmaceutical solids

2.2.23.1. Dynamic vapour sorption (DVS)

Vapour sorption experiments were performed on a DVS Advantage-1 automated gravimetric vapour sorption analyzer (Surface Measurement Systems Ltd., London, UK). The DVS-1 measures the uptake and loss of water vapour gravimetrically with a mass resolution of ± 0.1 μg. The temperature was maintained constant at 25.0 ± 0.1 °C. A mass of around 10 mg of powder was loaded into a sample net basket and placed in the system. The samples were equilibrated at 0% of relative humidity (RH) until dry, reference mass was recorded. The samples were exposed to the following % of RH profile: 0 to 90% in 10% steps and the same for desorption. At each stage, the sample mass was equilibrated (dm/dt ≤ 0.002 mg/min for at least 10 min) before the change of relative humidity. An isotherm was calculated from the complete sorption and desorption profile. Amount of water was expressed as a percentage of the dehydrated chlorothiazide sodium (reference mass).

2.2.23.2. Detection of critical relative humidity of recrystallisation of amorphous solids

Vapour sorption experiments were performed on a DVS Advantage-1 automated gravimetric vapour sorption analyzer (Surface Measurement Systems Ltd., London, UK). The DVS-1 measures the uptake and loss of water vapour gravimetrically with a mass resolution of ± 0.1 μg. The temperature was maintained constant at 25.0 ± 0.1°C. A mass of around 10 mg of amorphous powder was loaded into a sample net basket and placed in the system. The samples were equilibrated at 0% of relative humidity (RH) until a dry, reference mass was recorded. The samples were exposed to the sorption programmes ranging from 0 to 90% RH at the following %RH rate changes: 2.5% RH per hour (2.5 ΔRH%/h), 5 ΔRH%/h, 7.5 ΔRH%/h and 10 ΔRH%/h). An isotherm was calculated from the complete sorption profile. Amount of sorbed water was expressed as a percentage of the dry mass. Recrystallisation of the material was indicated by the points of inflection. %RH of recrystallisation were then plotted versus ΔRH%/h and linearly extrapolated to 0 ΔRH%/h (Burnett et al., 2004).

2.2.24. Solid state stability studies

Amorphous, spray dried samples of CTZNa and CTZK were subjected to stability studies in desiccated conditions over phosphorus pentoxide at 25 °C (Gallencamp Economy Incubator with fan). Samples were characterised on a monthly basis using PXRD, DSC and HPLC assay.

2.2.25. Statistical analysis

Statistical analysis was carried out using Minitab™ statistical software, version 14 (Minitab Inc, USA). Two sample t-tests were used to compare the means (n=3 or more) and standard deviations of two independent samples. The test was carried out at a significance level of 0.05, with a p-value less than 0.05 taken as indicating that the observed difference between the means was statistically significant, i.e. rejecting the null hypothesis.

2.2.26. Data analysis

The following software was implemented to analyse the data: Omnic 4.1™ - FTIR spectra analysis with baseline auto correction, Chem Sketch™ freeware - to calculate theoretical element contributions for elemental analysis and theoretical element contributions for elemental analysis and partial polarizability volumes (Gad et al., 2008).TopSpin 2.1™ - to evaluate ^{1}HNMR and ^{13}CNMR results.

The crystallographic data was analysed in detail using Ortep-3 (Faruggia, 1997) and Platon (Spek, 2003) software whereas the program Crystal Explorer 2.1 (McKinnon et al., 2004) was used to visualise and analyse Hirshfeld surfaces of molecules (Hirshfeld, 1977). The enhancement factor of 100% was used in all fingerprint plots to improve visualisation of interactions.

Results and discussion

Chapter 3

Preparation and solid state characterisation of chlorothiazide sodium intermolecular self assembly suprastructure

3.1. Introduction

There is considerable interest in the impact of solid state physicochemical properties of drugs on their biopharmaceutical properties. Thus, for example, the fraction of a drug absorbed has been correlated with its solubility and with the inverse of the drug's melting point (Chu, Yalkowsky, 2009). Consequently, drug bioavailability may be improved by the preparation of lower melting point polymorphs, co-crystals, solvates of the drug (Stahly, 2007) or alternatively by preparing a more soluble salt form (Berge et al., 1977).

Chlorothiazide (CTZ), 6-chloro-4H-1,2,4-benzothiadiazine-7-sulfonamide 1,1-dioxide (Beyer, 1982), with a molecular formula $C_7H_6ClN_3O_4S_2$, is a thiazide diuretic which is administered orally in the crystalline form as tablets or as an oral suspension (Brunton et al., 1996). Chlorothiazide is classified in class IV of the Biopharmaceutics Drug Classification System (BCS) (Amidon et al., 1995 and Taub et al., 2002), indicative of its low solubility and low permeability. It is very slightly soluble in water, poorly soluble in acetone, ethanol and methanol but readily soluble in aqueous alkali solutions, which is as a result of its acidic properties, allowing salt formation (European Pharmacopoeia, 2010). CTZ has a particularly high melting point (~350 °C with degradation), one of the highest for a molecular crystalline drug administered to man and it exhibits incomplete absorption following oral administration (Chu, Yalkowsky, 2009). The bioavailability of CTZ, administrated to three healthy volunteers, was found to decrease from 33% to 6% as the dose increased from 0.21 to 1.75 g (Corrigan, O'Driscoll, 1980). Considering the drug's poor physicochemical profile, it is considered advantageous to prepare a more soluble form, which may have a lower melting point.

The first report of X-ray crystallographic studies on CTZ was published by Dupont and Dideberg in 1970, while the crystal structure of CTZ was first solved and presented by Shankland and co-workers (1997). The structure of CTZ was subsequently confirmed by the joint use of powder neutron diffraction and powder X-ray diffraction (synchrotron) techniques (Leech et al., 2008). A good overview of CTZ physicochemical properties is contained in the European Pharmacopoeia (2010). Furthermore, Oswald and co-workers recently described the formation of CTZ Form II, a new polymorph created by applying high pressure to the crystals of Form I, the only known polymorph of CTZ recrystallised at ambient conditions (Oswald et al., 2010). Unfortunately, CTZ Form II converts into the Form I at ambient pressure and any pharmaceutical advantages of CTZ Form II were not determined.

In contrast, there appears to be no published reports on the crystal structure and the solid state characteristics of a sodium salt form of chlorothiazide in spite of its wide use as an injectable (parenteral) form of the drug as an intravenous solution. The soluble injection, to be reconstituted before use, is described as 6-chloro-2H-1,2,4-benzothiadiazine-7-sulfonamide 1,1-dioxide monosodium salt, with a molecular weight of 317.71 amu (empirical formula $C_7H_5ClN_3NaO_4S_2$), a sterile lyophilized white powder containing mannitol as an inactive ingredient (Hankins et al.,

2001). This is available in the USA, marketed as Diuril Sodium®. The crystal and solid state profiles of this form of CTZ are unknown despite the apparent clinical and formulation benefits of the salt. Therefore the objective of this work was to prepare a crystalline sodium salt of chlorothiazide, determine its crystal structure and physicochemical properties and compare them to those of chlorothiazide with the aim of presenting comprehensive information on the solid state characteristics of the salt form.

3.2. Results and discussion

3.2.1. Crystal structure

Chlorothiazide sodium (CTZNa) crystallised from water, 1:1 water/acetone mixture and ethanol resulted in the same crystal and molecular structure, as determined by single crystal XRD studies. The Ortep view of CTZNa is presented in Figure 3.1. The crystal structure of CTZNa determined in this work is triclinic and the crystal space group type is P-1. A summary of the key crystallographic information for CTZNa is given in Table 3.1.

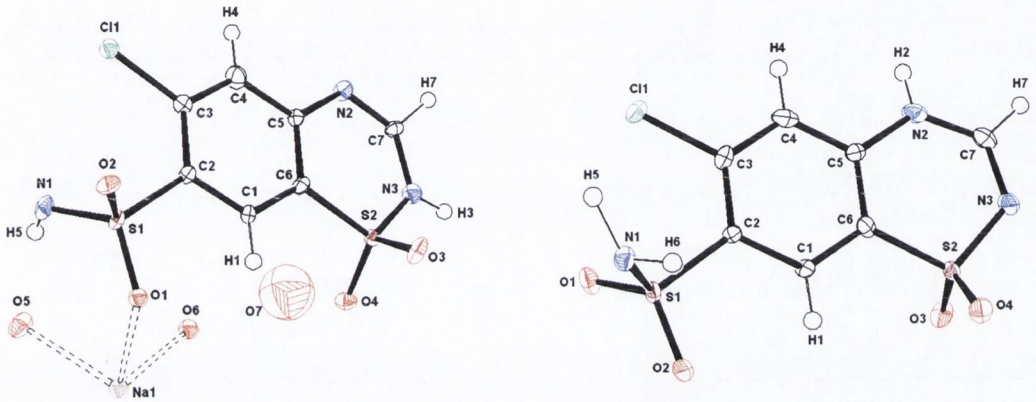

Fig. 3.1. Ortep diagram of: a) chlorothiazide sodium and b) chlorothiazide (with ellipsoids at 50% probability level).

In comparison to CTZNa, the crystal structure of CTZ is triclinic with the crystal space group type of P1 as presented by Shankland (1997) and Leech (2008). The CTZNa unit cell comprises two chlorothiazide molecules bonded together with sodium cations through water bridges. The coordinate centre consists of the following sequence: $(CTZ)_3 \cdot (H_2O) \cdot Na(H_2O)_2Na \cdot (H_2O) \cdot (CTZ)_3$ (Fig. 3.2). Additionally, some molecules of water O(7) were found on two opposite planes of the crystal cell; these are non-coordinated and most likely of an interstitial type, trapped in the void of the crystal cell.

The polymeric-like chains including sodium cations are built from distorted [Na(1)-O(6)] fragments forming a distorted octahedral unit stretching along the b-axis. Every asymmetric unit of the sodium linkage consists of two sodium cations each coordinating six oxygen atoms. Each of the sodium cations coordinates three molecules of chlorothiazide through a SO_2 group. Two CTZ molecules are bridged to each sodium(I) through an oxygen atom of the SO_2 group attached to the benzene ring. The third chlorothiazide molecule is bridged to the sodium cation through the oxygen of SO_2 belonging to the heterocyclic ring. The second SO_2 of this CTZ molecule attached to the benzene ring connects with a second layer of the polymeric structure (Fig. 3.2).

The distance between the two sodium cations sharing water molecules is 3.46Å (determined using the "measurement distance" tool in the Mercury software) and that between two sodium cations linked via the SO_2 group is significantly longer at 5.73Å.

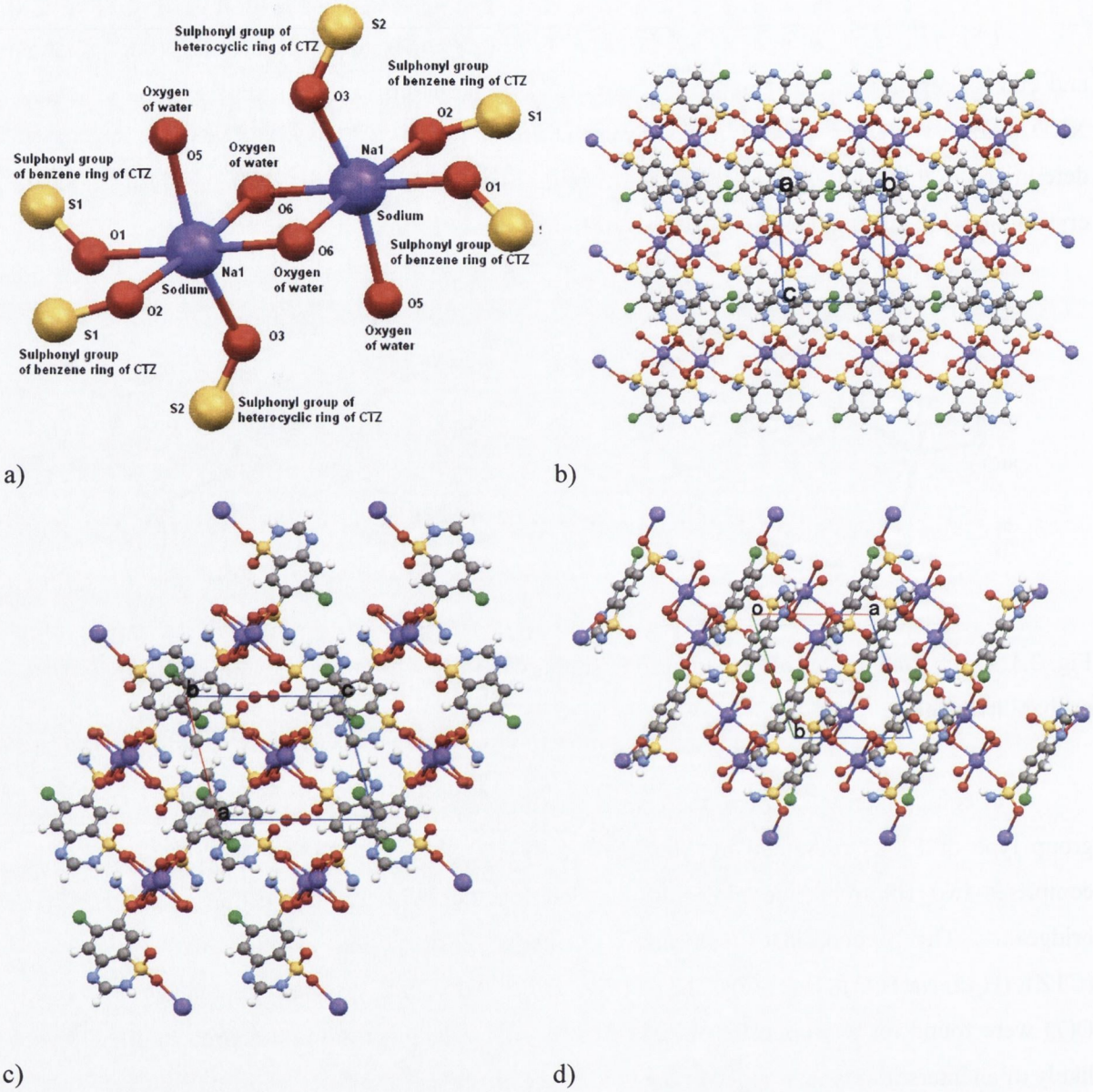

Fig. 3.2. Crystal structure of chlorothiazide sodium dihydrate: a) coordinates of the sodium cations, b) crystal cell structure packing along **a** axis, c) crystal cell structure packing along **b** axis, d) crystal cell structure packing along **c** axis. Atom colours: carbon: grey, nitrogen: blue hydrogen: white, oxygen: red, sulphur: yellow, chlorine: green, sodium: violet.

The parallelogram formed by the two sodium cations and two water molecules (Fig. 3.2) can be characterised by the bond lengths of 2.44Å and 2.34Å between Na(1) and O(6) and angles: [Na(1)-O(6)-Na(1)] of 92.7° and [O(6)-Na(1)-O(6)] of 87.3°. One of the two distances between the sodium cation and oxygen of SO_2 bonded to the benzene ring is 2.47Å and the other is 2.36Å,

which is the same as the distance formed between the same sodium cation and the heterocyclic SO_2 group.

Some of the bond distances are different for CTZNa compared to CTZ, reflecting the different neighbourhood around the chemical groups and their engagement in different types of bonds. A shortening of the [S(1)-N(1)] (1.613(5)Å in CTZ to 1.584(5)Å in CTZNa) bond is observed, consistent with the disappearance of H-bonds formed in CTZ by the primary sulphonamide group.

Table 3.1. Crystal data and structure refinements for chlorothiazide sodium.

Analysis parameters	**Chlorothiazide sodium dihydrate**	
Identification code	Shelxl	
Empirical formula	$C_{14}H_{10}Cl_2N_6Na_2O_{14}S_4$	
Formula weight	731.40	
Temperature	150K	
Wavelength	0.71073 Å	
Crystal system	Triclinic	
Space group	P-1	
Unit cell dimensions	$\alpha = 82.80(3)°$	a = 8.3567(17) Å
	$\beta = 73.93(3)°$	b = 9.0728(18) Å
	$\gamma = 70.31(3)°$	c = 9.6486(19) Å
Volume	661.4(2) Å3	
Z	1	
Density (calculated)	1.836 g/cm^3	
Absorption coefficient	0.674 mm^{-1}	
Crystal size	0.2 x 0.2 x 0.2 mm^3	
Reflections collected	4591	
Completeness to theta = 25.00°	96.1 %	
Goodness-of-fit on F^2	1.205	
Final R indices [I>2sigma(I)]	$R^1 = 0.0654$, $wR^2 = 0.1948$	
R indices (all data)	$R^1 = 0.0705$, $wR^2 = 0.2157$	

Shorter [N(2)-C(5)] (1.392(6)Å in CTZ to 1.380(5)Å in CTZNa) and [N(2)-C(7)] bonds (1.350(7)Å in CTZ to 1.327(5)Å in CTZNa) suggest significant changes in the heterocyclic ring associated with changes at N(2), probably due to proton migration. On the other hand an increase of the [S(2)-O(3)] distance 1.457(4)Å in CTZNa compared to CTZ 1.438(5)Å indicates involvement of the group in bonds forming the complex Na-O octahedral structure. The greatest lengthening of the bond is seen for [N(3)-C(7)] (1.291(6)Å in CTZ to 1.345(6)Å in CTZNa) and supports the hypothesis of proton relocation around the heterocyclic ring. Other major differences in torsion angles between CTZ and CTZNa involving the sulphonamide parts of the molecule were also noticed.

Shankland et al. (1997) determined the hydrogen bond distances in the crystal lattice between the molecules of CTZ and stated that they were typical for organic molecules with those functional groups and were as follows: [N(1)-H(5)...N(3)], [N(1)-H(6)...O(3)], [C(4)-H(4)...O(4)]

and [N(1)-H(6)...O(1)]. A more extensive network of hydrogen bonds in the CTZ crystal than previously reported has been determined in the present work and is compared to H-bonds present in CTZNa in Table 3.2. Hydrogen bonding between the C-H groups as proton donors and the oxygen of the sulphonyl groups is not observed in the crystal lattice of, for example, hydrochlorothiazide (Dupont and Dideberg, 1972). The rich H-bond network found in CTZ is consistent with the high stability of the crystal lattice. Only a few hydrogen bonds can be observed in CTZNa (Table 3.2) as a consequence of some of the groups being now engaged in Na-O interactions.

Table 3.2. Bond lengths [Å] and dihedral angles [°] for hydrogen bonding interactions in chlorothiazide and chlorothiazide sodium.

Bond type (D-H...A)	D-H [Å]	H..A [Å]	D...A [Å]	D-H...A [°]
Chlorothiazide				
N(2)-H(2)...O(3)[(a)]	0.86	2.57	2.887(6)	103
N(2)-H(2)...N(1)[(b)]	0.86	2.61	3.327(7)	142
N(1)-H(5)...N(3)[(c)]	1.13(6)	2.12(6)	3.132(7)	148(4)
N(1)-H(6)...O(1)[(d)]	0.91(6)	2.59(7)	2.917(6)	102(5)
N(1)-H(6)...O(3)[(e)]	0.91(6)	2.14(7)	3.015(6)	161(6)
C(1)-H(1)...O(2)	0.95	2.41	2.831(6)	106
C(4)-H(4)...O(4)[(f)]	0.95	2.26	3.152(7)	157
C(7)-H(7)...O [(g)]	0.95	2.43	3.369(6)	170
Chlorothiazide sodium dihydrate				
N(1)-H(5)...O(5)	0.65(7)	2.27(7)	2.913(6)	169(7)
N(3)-H(3)...N [(a)]	0.86	2.10	2.949(6)	169
C(1)-H(1)...O(1)	0.93	2.34	2.756(5)	107

Symmetry codes: (a) 1+x, -1+y, z.; (b) x, 1+y, -1+z; (c) -1+x, y, 1+z; (d) x, y, 1+z; (e) 1+x, y, z; (f) -1+x, 1+y, z; (g) 1+x, 1+y, -1+z.

A literature search was undertaken to compare the molecular structure of CTZNa with similar compounds. The work of Mizuno et al. (1969) describing sodium hexa- water coordinates of a xanthine sodium salt reported that the O-Na-O angles ranged from 84.5° to 97.0°. The angles reported here for CTZNa are about the same size, however, the pattern of Na-O bonds is far more complex than that in xanthine sodium as oxygen atoms participating belong not only to water, but also to the sulphonyl groups. The crystal structure of sulfadimidine sodium (SDMNa) was reported by Patel (1995). SDMNa was recrystallised from an aqueous solution at ambient temperature. The sodium cation of SDMNa coordinates a molecule of SDM directly through the oxygen of the sulphonyl group of SDM in a similar way as in CTZNa. Na(I) is able to coordinate one molecule of water, but it does not bridge to the other sodium cation through two molecules of water, as observed for CTZNa. The crystal structure of SDMNa has an interstitial oxygen atom (most likely of water) similar to data of CTZNa.

The type of sodium complex presented here is commonly referred to as a polymeric self-assembly (Whitesides et al., 1991). To the best of our knowledge, no similar structure with the same architecture of the hydrated cation-ligand complex in which the ligand is an active pharmaceutical ingredient has been published. Work on the crystal structure of pharmaceutical sodium salts including cromolyn, cefazolin and fenoprofen sodium hydrates (Stephenson, Diseroad, 2000) and naproxen sodium (Kim et al., 1990) reveals that those highly ordered and polymeric intermolecular hydrate structures of sodium salts of pharmaceutical substances are rather uncommon.

Stephenson and Diseroad (2000) stated that water molecules in cromolyn sodium and cefazolin sodium have the character of channel hydrate and ion-coordinated type. Based on SC-XRD, in CTZNa two of the water molecules are coordinated by the sodium cation, but a third one may be of an interstitial type. Figure 3.2, which presents the crystal structure of CTZNa, indicates that the orientation of CTZ molecules facilitates the formation of similar channels capable of holding water molecules. Additional evidence of very weak bonding of interstitial water was obtained by Ortep analysis of the single crystal X-ray data. There is less certainty associated with the placement of this particular oxygen compared to the water molecules which are bonded in the crystal structure. This means that even at low temperature conditions, as in single crystal X-ray analysis, this oxygen atom position tends to be unstable.

3.2.2. NMR studies

Recrystallised samples of CTZNa and CTZ were subjected to solution nuclear magnetic resonance (NMR) analysis. The structure of CTZ was reported previously by Jakobsen and Treppendahl (1979) and comparative studies were carried out for CTZNa to elucidate the differences between the two molecules.

^{1}HNMR analysis of CTZNa detected three CH groups (Table 3.3). The [N(1)-H(5)] (v7.42ppm) group was detected to be attached to the [O(1)-S(1)-O(2)] group. Peak integration of the former confirmed that this group in fact is ionised to NH- (with the integral of 0.96), consistent with results of the single crystal X-ray analysis, suggesting that only one proton is attached to N(1). It is hypothesised that this deprotonated sulphonamide group will neutralise the positive charge coming from the two sodium cations in its close neighbourhood (N-Na+ distances are approximately 3.6Å and 3.7Å). A similar phenomenon was described by Garcia-Raso and co-workers (2000) in Hg(sulfamide)$_2$ complexes where a deprotonated [SO_2NH^-] group interacted with the Hg cation.

Table 3.3. Results of ^{1}HNMR analysis of chlorothiazide sodium and chlorothiazide.

Peak	CTZNa DH	CTZ	Peak shift
	ν(F1) [ppm]	ν(F1) [ppm]	Δδ H
C(4)H(4)	8.19	7.54	+0.65
C(1)H(1)	7.34	8.29	-0.95
C(7)H(7)	7.22	8.12	-0.90
N(2)H(2)	-	12.62	-
$N(1)H_2(5,6)$	-	7.89	-
N(1)H(5)	7.43	-	-

Barbosa et al. (1998) reported values of pK1 and pK2 of chlorothiazide to be 6.7 and 9.5, respectively. The pK1 refers to deprotonation of the secondary sulphonamide group in the heterocyclic ring, while the pK2 relates to deprotonation of the primary sulphonamide group. The aqueous solution of CTZNa had a pH of 9.0±0.3 therefore it is likely that the primary sulphonamide group is deprotonated. No proton was detected by ^{1}HNMR in the heterocycle, which may perhaps indicate its delocalised nature.

^{13}CNMR (Table 3.4) analysis confirmed the presence of all seven carbons in the chlorothiazide molecule as it was reported before by Jakobsen and Treppendahl (1979). CH heteronuclear single quantum coherence (HSQC) analysis confirmed that two protons (ν8.19 ppm and ν7.34 ppm) are attached to the carbons of the benzene ring (ν125 ppm and ν126 ppm respectively) and one proton (ν7.2 ppm) is attached to the carbon (ν155 ppm) of the heterocyclic ring of CTZ.

Table 3.4. Results of ^{13}CNMR analysis of chlorothiazide sodium and chlorothiazide.

Peak	CTZNa DH	CTZ	Peak shift
	ν(F1) [ppm]	ν(F1) [ppm]	Δδ C
C(4)H(4)	124.8	120.3	+4.5
C(1)H(1)	126.5	125.0	+1.5
C(7)H(7)	155.5	148.6	+6.9
C(5)	150.9	138.9	+12.0
C(6)	134.5	137.8	-3.4
C(2)	122.6	134.4	-11.9
C(3)	131.3	120.2	+11.1

Numerous shifts are observed in ^{1}HNMR and ^{13}CNMR spectra of CTZ compared to CTZNa consistent with the changes in chemical structure determined by single X-ray diffraction (Table 3.3 and 3.4). Upfield shifts were noted for H(1) and H(7) in contrast to a downfield shift for H(4). A large downfield shift was observed by ^{13}CNMR for C(5) directly bonded to N(2) and the carbon C(3) to which the chlorine is attached (shifts of +12.0 and +11.1, respectively). The most affected signal, compared with CTZ, was that of the C(5) of the benzene ring and together with the upfield shift of H(7) bonded to C(7), this suggests a change in protonation

of N(2) and migration of H(2) to N(3). However, no signal from proton bonded to N(3) was detected to directly confirm this hypothesis (Table 3.3).

3.2.3. Thermal analysis

CTZNa obtained after synthesis (Methods 2.2.1.1.) was a white crystalline powder. The DSC scan presented an endotherm with an onset at 83.7 ± 0.5 °C possibly related to the loss of hydrated water (Figure 3.3). An onset of the melting/decomposition point of CTZNa was 289 ± 1 °C. This is lower that the melting/decomposition point of CTZ, which was determined to be 363.51 ± 2.00 °C. The first endotherm corresponds to a 10.4 ± 0.5% mass loss observed by TGA which, when converted to a molar ratio, indicates that 1 mol of chlorothiazide sodium contains two moles of water (theoretical calculated water content is 10.18%) (Fig. 3.3b). This result was confirmed by Karl-Fischer titration where the water content was estimated to be 9.8 ± 0.3%. Therefore, it can be said that this material was a dihydrate.

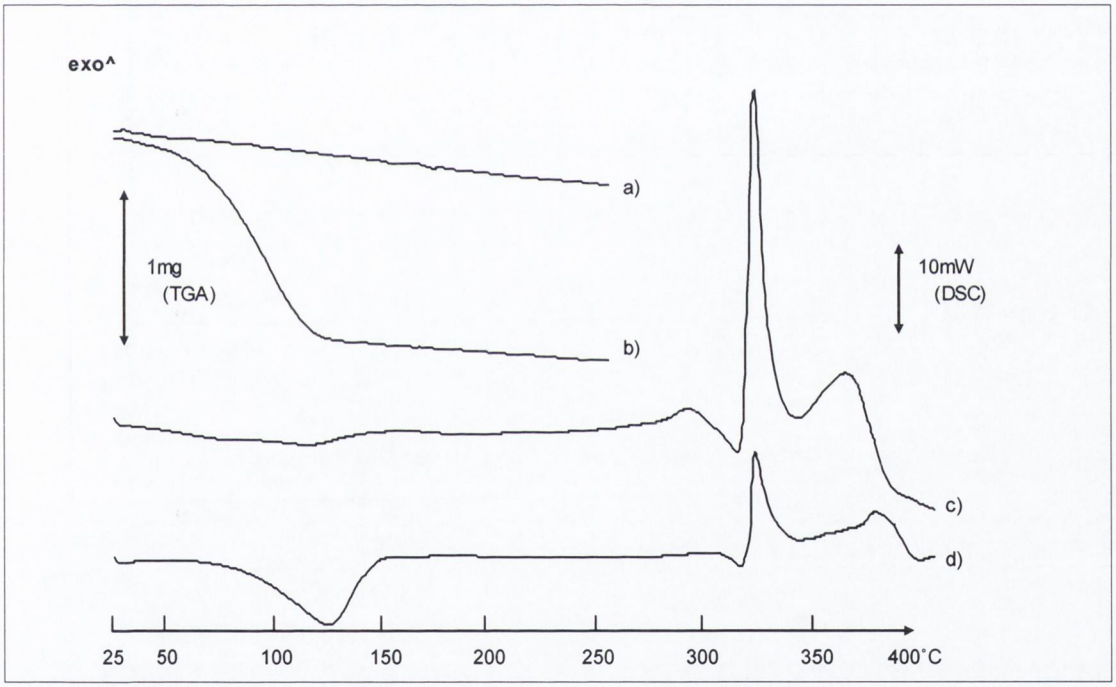

Fig. 3.3. Thermal analysis of anhydrous CTZNa: a) TGA, c) DSC and CTZNa dihydrate: b) TGA, d) DSC.

24 hours of drying (Methods 2.2.1.1) allowed the hydrated water to be removed and converted the dihydrate to a practically anhydrous state (Fig. 3.3a, c). The DSC/TGA analysis of anhydrous CTZNa gave different patterns to those of the dihydrate form. The DSC of anhydrous form presents an endotherm with an onset at 55 °C, related to just a 1.0 ± 0.2% mass loss. A similarly shaped TGA pattern to that of the hydrate was reported by Zhu et al. (1997) for water evaporation from nedocromil zinc hydrates.

3.2.4. Dynamic vapour sorption (DVS)

To investigate the hydration behaviour of chlorothiazide sodium under changing conditions of relative humidity (RH%) a dynamic vapour sorption (DVS) isothermal (25 °C) experiment was conducted (Fig. 3.4). To evaluate concurrent changes in the material PXRD (Fig. 3.5), DSC (Fig. 3.6) and TGA were also undertaken.

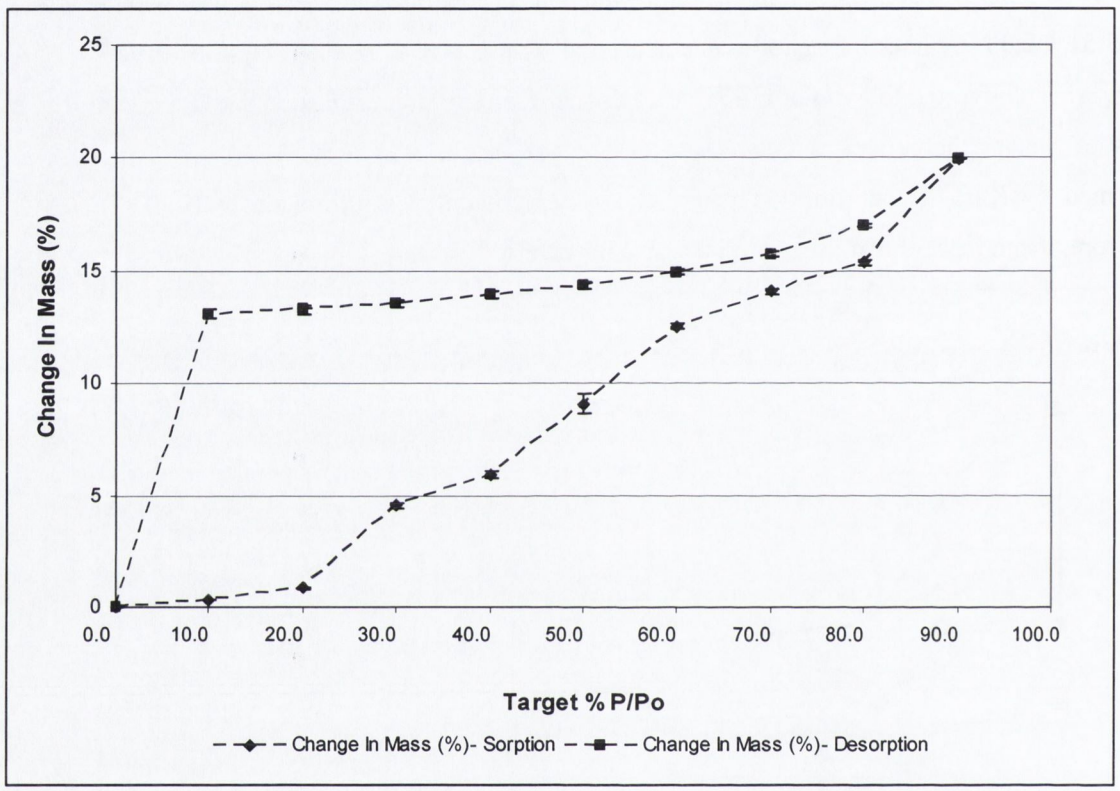

Fig. 3.4. Isothermal (25 °C) plots of sorption and desorption of water for CTZNa.

The starting material was dehydrated CTZNa, crystalline by PXRD (Fig. 3.5. g). Analysis after equilibration of the sample at 0% RH indicated a residual moisture content of about 2.6% mass loss by TGA This mass loss corresponded to a starting endotherm with onset at 30.4 °C, peaking at 54.8 °C on the DSC. Dehydrated CTZNa was stable during hydration (Fig. 3.4) in the range from 0 to 20% RH, where adsorbed moisture, most likely surface adsorbed, did not exceed 1% of the initial sample mass (m_0).

From 20% RH the sample started to gain water more rapidly in the range from 20-30% RH to reach a possible first mass equilibrium at 30-40% RH. The sample recovered from the DVS after equilibration at 30% RH had a residual water content of about 6.6% (by TGA), corresponding to an endotherm in the DSC (Fig. 3.6b) peaking at 77.2 °C. The m_0 increased by nearly 5% (by DVS), which corresponds to the theoretical percentage of water content calculated

for a chlorothiazide sodium monohydrate. The PXRD analysis (Fig. 3.5. f) shows significant differences in the intensity of Bragg peaks (at 16.64, 19.63 and 26.52 2θ) in comparison to the pattern of the dehydrated form, with the disappearance of some peaks, e.g. at 17.72 and 26.52 2θ. However, the overall powder diffractogram of this sample resembles that of anhydrous CTZNa. Attempts were made to produce CTZNa monohydrate, but were unsuccessful, indicating that if the monohydrate exists, it is very unstable and can only be observed to form in situ by DVS. It may also be a transient structure occurring upon hydration of the dehydrated CTZNa.

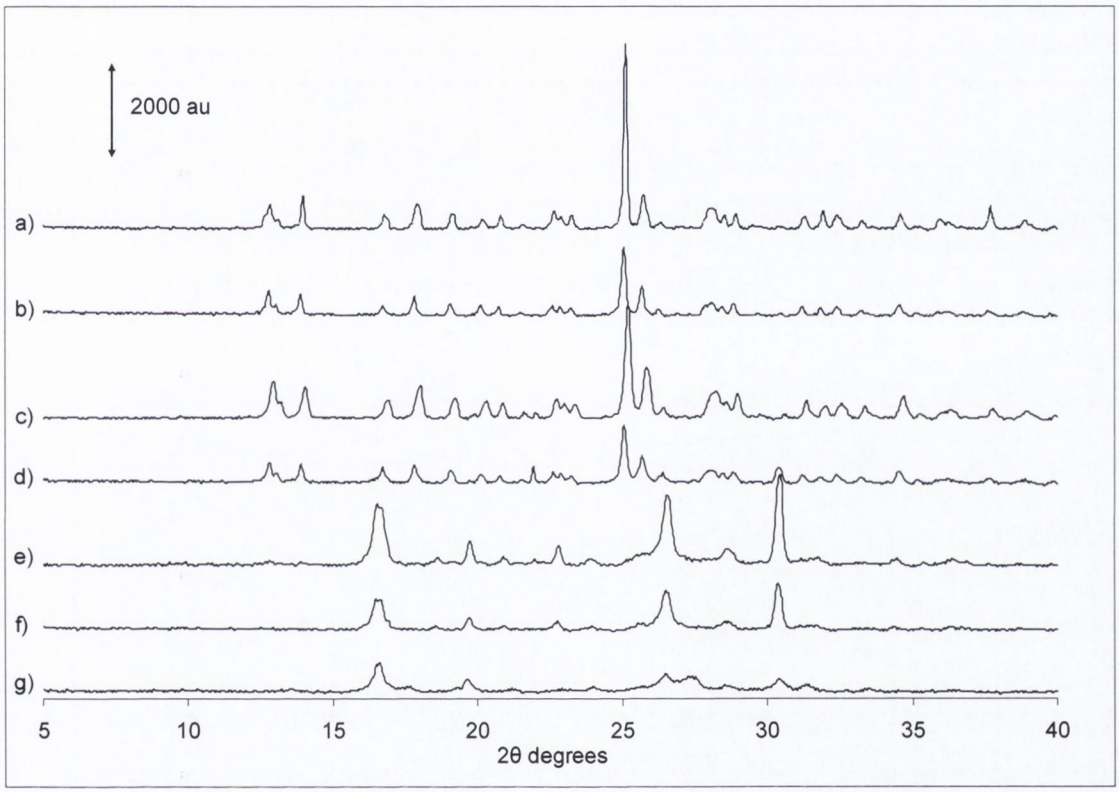

Fig. 3.5. Powder XRD patterns of: a) CTZNa dihydrate single crystal X-ray material, b) CTZNa dihydrate recovered from DVS after desorption at 10% RH, c) CTZNa dihydrate recovered from DVS after sorption at 90% RH, d) CTZNa dihydrate recovered from DVS after sorption at 60% RH e) CTZNa recovered from DVS after sorption at 40% RH, f) CTZNa recovered from DVS after sorption at 30% RH, g) CTZNa dehydrate recovered from DVS after equilibration of reference mass at 0% RH.

A second period of rapid water uptake occurred in the range from 40 to 60% of RH and was followed by a second mass equilibration in the range of 60-80% RH. The sample, equilibrated at 60% RH, had a TGA mass loss of 11.8%, corresponding to an endothermic DSC (Fig. 3.6c) event with a peak at 114.6 °C. The increase in mass by 12%, correlates with the theoretical 10% water content corresponding to CTZNa dihydrate. The PXRD analysis (Fig. 3.5. d) presents a different Bragg peak pattern in comparison to the dehydrate (Fig. 3.5.g)

and it is consistent with the PXRD pattern of the recrystallised CTZNa used for single crystal X-ray analysis (Fig. 3.5. a).

Further hydration of the material did not result in the production of other forms characterised by a different PXRD pattern than that of the dihydrate (Fig. 3.5. c). The sample finally equilibrated at 90% RH gaining 19% of the starting sample weight. This is well above the 10% of water content calculated for the dihydrate and could be attributed to surface adsorbed moisture and/or a channel/interstitial type hydrate, where water molecules can be placed in the interstitial spaces between the CTZNa molecules.

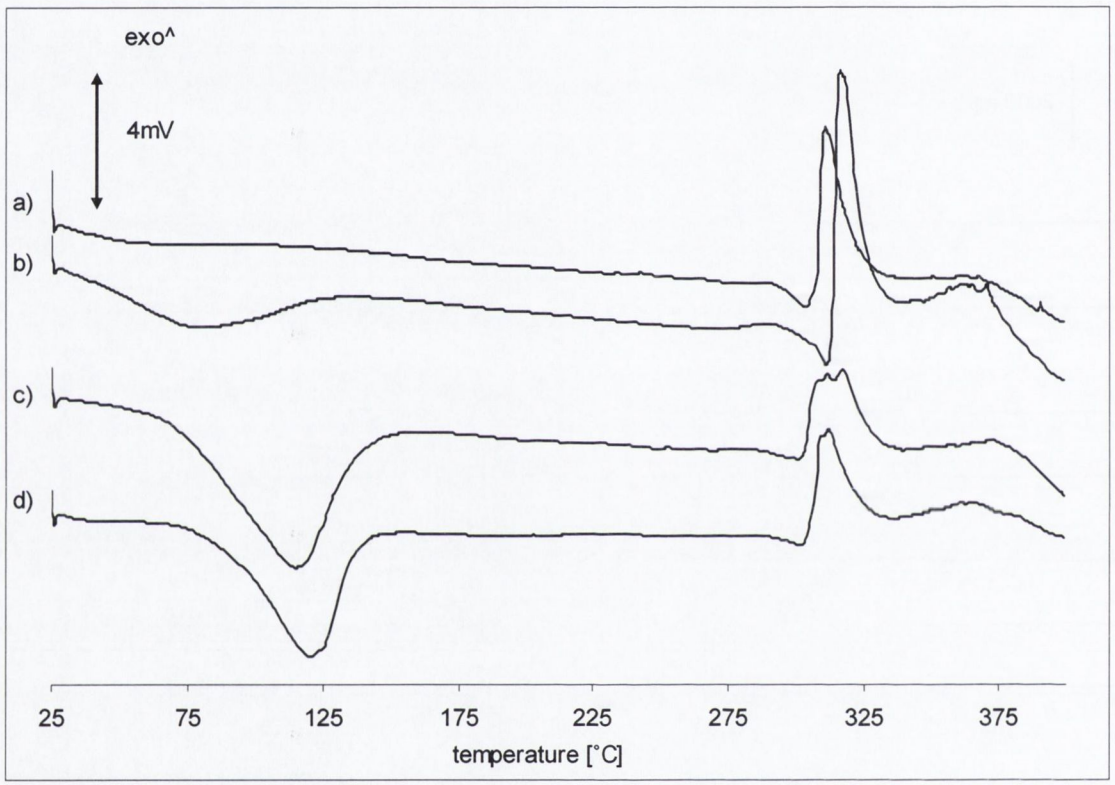

Fig. 3.6. DSC sans of chlorothiazide sodium samples recovered from DVS instrument after equilibration at: a) 0%RH, b) 30%RH, c) 60% RH and d) 90%RH

This type of structure was suggested by the single crystal XRD analysis and discussed in the sections related to crystal structure above, but was not subsequently confirmed by the thermal studies and Karl-Fischer titration. The discrepancy can be related to different environmental conditions (relative moisture, temperature) of the techniques used. However, it is certain that at high RH% at least the dihydrate, as indicated by PXRD, is formed. A variable level of hydration, due to the interstitial/channel space was previously reported for cromolyn sodium, which is believed to be able to accommodate up to nine water molecule in the lattice and for cefazolin sodium, which is characterised by an extensive network of tunnel space which can accommodate water (Stephenson and Diseroad, 2000). The observed variation in hydration

levels for CTZNa may complicate its developability and manufacture, as more stringent environmental control may be needed.

An interesting behaviour of this sample was revealed by desorption/drying of the material in the DVS. The material dries slowly from 90% RH down to 10% RH, with a relatively constant drying rate between 60% RH and 10% RH. The sample recovered from the DVS instrument after desorption and equilibration at 10% RH showed a 12.9% mass loss by TGA corresponding to a DSC endotherm with an onset at 88 °C, peaking at 114.6 °C. Results obtained for the materials recovered during sorption at 60 and 90%RH in comparison to material recovered after desorption at 10%RH were the same regarding DSC pattern (Fig. 3.6d). The PXRD patterns of all four compared samples (Fig. 3.5. a-d) are the same and correlate well with simulation of PXRD pattern based on X-ray single crystal analysis (data not shown). Below 10% RH the crystal structure collapses and the hydration water is released quickly, until at 0% RH the sample becomes again the dehydrate.

3.2.5. Other physicochemical characteristics

Both CTZNa forms, the dihydrate and anhydrous, were subjected to elemental analysis. With respect to CTZNa dihydrate, the theoretically calculated contents of carbon, hydrogen and nitrogen were 23.77%, 2.56% and 11.88%, respectively, consistent with those obtained experimentally: 23.49±0.06%, 2.62±0.01% and 11.57±0.00%. CTZNa dihydrate was subjected to additional drying to obtain the anhydrous salt. Theoretical contributions of carbon, hydrogen and nitrogen for the anhydrous form were 26.46%, 1.59% and 13.23%, respectively, which are also consistent with the experimental values of 25.82±0.04%, 1.65±0.01% and 12.59±0.01%, respectively. If the molar ratio of sodium to chlorothiazide in the salt is 1:1, then the theoretical sodium content in the salt is 6.9%. The results for sodium content obtained from ICP-MS analysis indicate that the sodium content in the sample is 7.6±0.9%, consistent with a stoichiometric ratio of chlorothiazide to sodium of 1:1.

The content of organic solvents in the recrystallised CTZNa was assayed by GC-MS. The residual content of acetone was 0.005% w/w for the sample recrystallised from 1:1 acetone/water mixture and 0.001% w/w of ethanol was present in the sample obtained from ethanol.

The true density calculated from the single crystal X-ray analysis (at 150K) of CTZNa dihydrate was 1.836 g/cm^3, while that measured by helium pycnometry (room temperature) was 1.728±0.004 g/cm^3 and for the anhydrous form it was 1.883±0.001 g/cm^3.The true density of CTZ raw material measured by helium pycnometry was 1.798±0.001 g/cm^3, while the density calculated from the single crystal X-ray analysis was 1.861 g/cm^3.

FTIR spectrum of CTZNa systems, hydrated and anhydrous, reveals significant differences in FTIR pattern in the range of 2800-3600 cm^{-1}, where hydrogen bonds are expected (Fig. 3.11 c,

d). Strong, multiple bands of O-H stretching modes can be seen between 3400 and 3600 cm^{-1} confirming the presence of crystalline water in CTZNa (Fig. 3.11 c). FTIR pattern of CTZ recrystallised from acetone was consistent with that obtained for the raw material (Fig. 3.7 a, b).

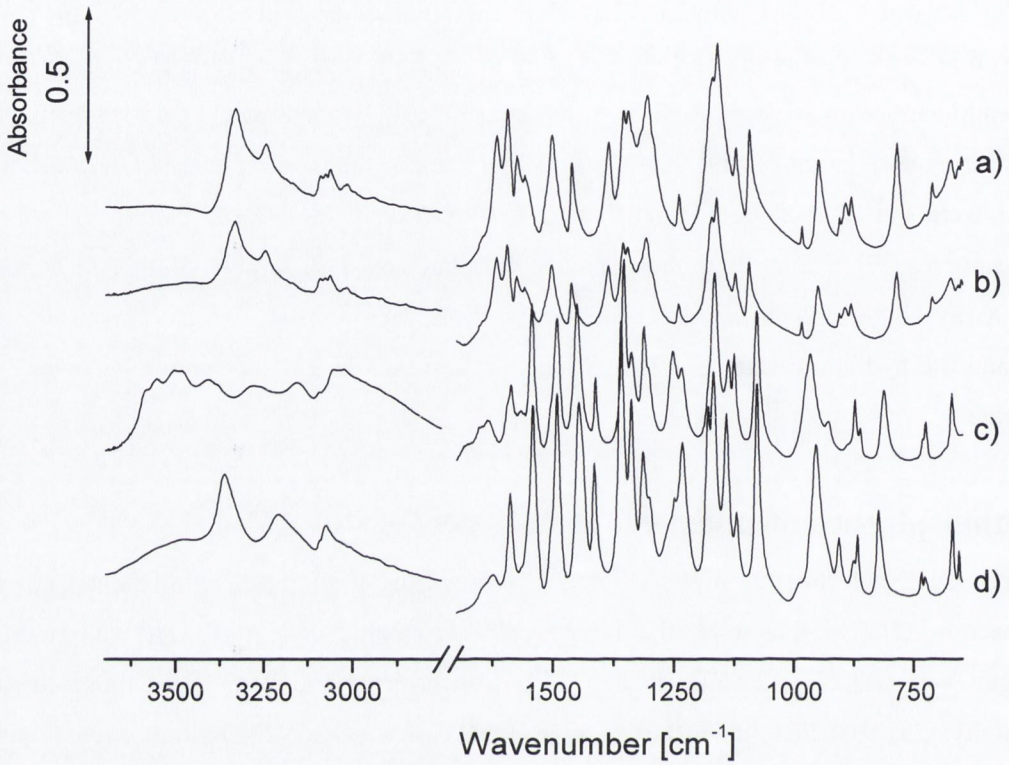

Fig. 3.7. FTIR spectra of: a) CTZ starting material, b) CTZ recrystallised from acetone, c) recrystallised CTZNa dihydrate and d) CTZNa anhydrous form.

The solubility of the dihydrate form of CTZNa, the stable form in aqueous solution, was determined to be 79.4±9.5 mg/ml (pH = 9.5±0.2), while the aqueous solubility of CTZ at 37 °C was determined to be 0.200 ± 0.004 mg/ml (pH = 4.8±0.1) which is in agreement with the value of 0.2 mg/ml reported previously by Charnicki and co-workers (1959). Therefore the solubility difference between CTZ and CTZNa is of the order of 400-fold.

3.3. Conclusions

This thesis reports, for the first time, the crystal structure of a dihydrate chlorothiazide sodium salt as an intramolecular self-assembly: $(CTZ)_3 \cdot (H_2O) \cdot Na(H_2O)_2Na \cdot (H_2O) \cdot (CTZ)_3$, which has a triclinic crystal structure and a space group P-1, regardless of whether water, a 1:1 water/acetone mixture or ethanol was employed for recrystallisation. Each of the sodium cations coordinates six oxygen atoms. Sodium cations are bridged through two molecules of water. Each of the sodium cations coordinates an additional not shared molecule of water and three chlorothiazide molecules through the oxygens of the sulphonyl groups.

It has been established by NMR and SC-XRD that the presence of the sodium cation induces a negative charge in the SO_2NH_2 group i.e. SO_2NH^- is formed. The sodium cation displaces the H of the secondary sulphonamide group of the heterocyclic ring. SC-XRD confirmed the presence of NH group in the heterocyclic ring at the nitrogen atom next to the SO_2 moiety. In CTZNa, the proton is likely to be attached to N(2) rather than N(3) as in CTZ. A crystalline anhydrous form of CTZNa was also identified and its PXRD pattern presented.

DVS analysis confirmed the existence of CTZNa dihydrate over a broad range of relative humidities, 10-90% RH, at 25 °C. For material subjected to relative humidities between 30% and 40%, slight changes in the PXRD pattern, with differences in the intensity of some Bragg peaks (at 16.64, 19.63 and 26.52 2θ) and the disappearance of others (at 17.72 and 26.52 2θ), suggests the formation of another hydrated form, possibly a monohydrate. The presence of the anhydrous form was evident close to 0% RH.

CTZ has one of the highest melting-decomposition points of all APIs, at around of 363 °C, which is consistent with the extensive hydrogen bond network. The melting/degradation point of the dehydrated CTZNa was at around of 289 °C, ~70 °C lower than that of CTZ. The solubility of CTZNa dihydrate was determined to be 79.4±9.5 mg/ml, around 400-fold higher than of CTZ. Therefore it can be concluded that favourable pharmaceutical properties of CTZNa result from a significantly reduced melting point and improved solubility by salt formation.

Chapter 4

Preparation and characterisation of novel chlorothiazide potassium solid-state salt forms: intermolecular self assembly suprastructures

4.1. Introduction

Approximately 40% of active pharmaceutical ingredients (API) are described as having poor aqueous solubility (Wu and Benet, 2005) and therefore are classified as classes II and IV of the Biopharmaceutics Classification System. There is great interest in the optimisation of the physicochemical properties of APIs, leading to an improved solubility of material and therefore improved bioavailability (Blagden et al., 2007). One of the main solubility enhancement approaches employed for ionisable drugs is salt formation (Stahl and Wermuth, 2008).

It is known that increasing hydrophilicity and decreasing melting point can result in the formation of a salt with increased aqueous solubility. Other desirable physicochemical properties include low hygroscopicity, physical stability of the crystal form under different storage conditions and chemical stability.

The salt formers (counterions) may be chosen from a few classes. The first class of salt-formers have unrestricted use for this purpose because they form physiologically ubiquitous ions (e.g. Cl^-, Na^+, K^+) or because they occur as intermediate metabolites in biochemical pathways (e.g. citrate, glucuronate). Nearly 90% of the reported pharmaceutical salts are with sodium, calcium, potassium, magnesium, meglumine or ammonia with more than 55% made with sodium cations (Stahl and Wermuth, 2008). Pharmaceutical salts of potassium are less frequent in comparison to sodium salts. However, there are reports outlining several advantages of potassium over sodium salts. Sodium forms hydrated salts more readily than the potassium cation and the latter are less deliquescent than the sodium counterparts (Remington, 2005), e.g. the potassium salt of penicillin G is preferred to the sodium salt because it is less hygroscopic (Swarbrick, 2007). Potassium salts may have better aqueous solubility than the corresponding sodium salts (Derry et al., 2009, Adams et al., 2000, Antoncic and Copar, 2009).

Chlorothiazide (CTZ) is a thiazide diuretic which is administered orally in the crystalline form as tablets or as an oral suspension (Brunton et al., 1996). CTZ has a particularly high melting point (~350 °C with degradation) (Chapter 3). It is very slightly soluble in water, but readily soluble in aqueous alkali solutions (European Pharmacopoeia, 2010), which is as a result of its acidic properties, allowing salt formation Due to its salt-forming properties and taking into account the drug's poor solubility, it is considered advantageous to prepare a more soluble form. CTZ is available as a sodium salt, marketed as Diuril Sodium®, however the solid-state properties of chlorothiazide sodium have only recently been presented (Chapter 3). Thiazides are considered to be effective antihypertensives, used as front-line drugs to treat hypertension (Appel, 2002). As with other thiazides, one limitation of the therapeutic use of CTZ is the risk of hypokalemia and the requirement for potassium supplementation (Ellison and Loffing, 2009). Thus the delivery of a potassium salt of CTZ may, first of all, have clinical advantages

and furthermore, an improved solubility leading to an enhanced dissolution and potentially bioavailability. Therefore the main aim of this project was to establish the conditions of preparation of a potassium salt of CTZ and characterise any salt products formed.

4.2. Results and discussion

4.2.1. Physicochemical analysis

Chlorothiazide potassium monohydrate, crystallised from water (form I), was a white crystalline powder. The DSC thermogram (Fig. 4.1e) of form I shows a small endotherm with an onset at around 58.0±2.0 °C which corresponds to a loss of around 1.0±0.4% of residual moisture by TGA (Fig. 4.1a), the second endotherm is related to the loss of hydrated water and has an onset at 160.6±0.5 °C.

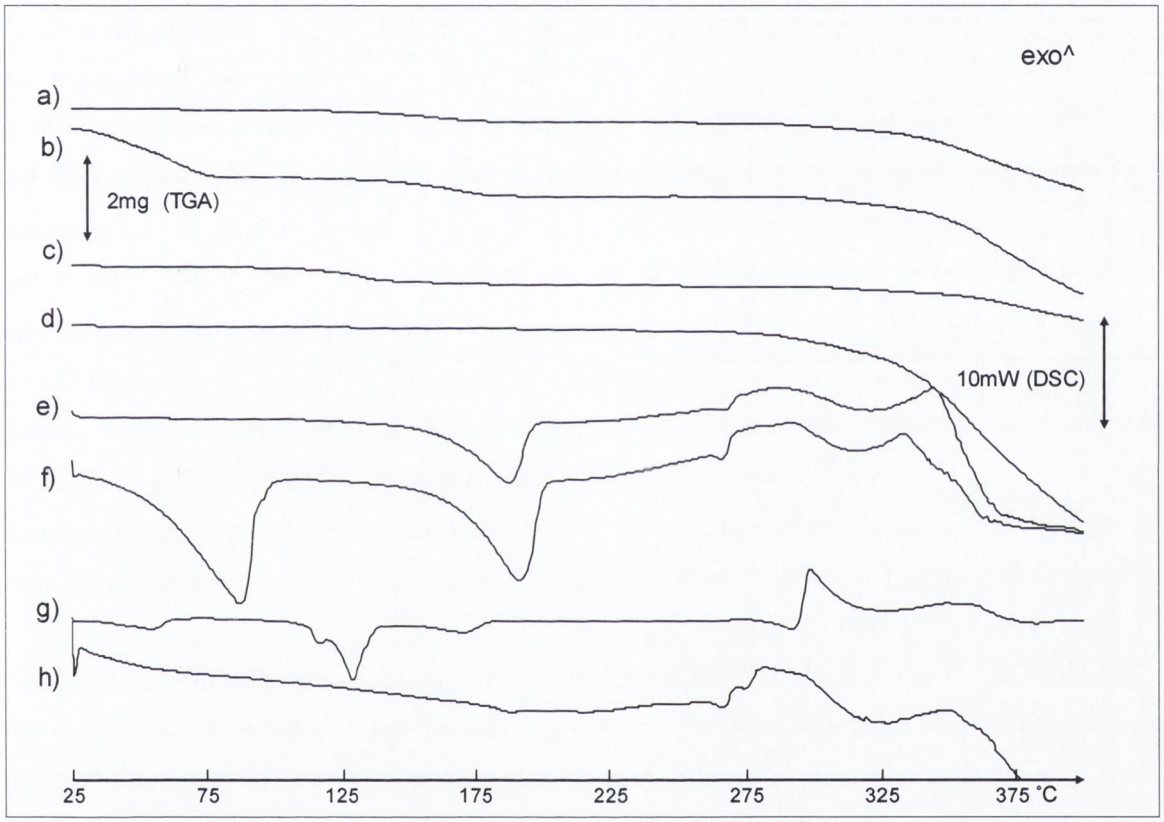

Fig. 4.1. Thermal analysis of CTZK: a) TGA scan of CTZK form I, b) TGA scan of CTZK form II, c) TGA scan of CTZK form IV, d) TGA scan of CTZK form III (anhydrous), e) DSC scan of CTZK form I, f) DSC scan of CTZK form II, g) DSC scan of CTZK form IV, h) DSC scan of CTZK form III (anhydrous).

The first event can be assigned to evaporation of loosely bound water and the second to liberation of water more tightly attached to the molecule of CTZK. The overall water loss corresponds to a 4.9±0.2% mass loss (TGA) which, when converted to the molar ratio, indicates that 1 mole of CTZK contains one mole of water; thus form I is CTZ monohydrate. The theoretical calculation of water content in CTZK monohydrate is 5.1% w/w. This result was consistent with Karl Fischer titration which determined the water content to be 5.3±0.6%. Results of elemental analysis

for CTZK form I were as follows: 23.58±0.1% of carbon 1.86±0.05% of hydrogen and 11.69±0.06% of nitrogen, consistent with theoretical calculations for the monohydrate of: 23.90% of carbon, 2.01% of hydrogen and 11.94% of nitrogen.

The results of DSC/TGA analysis of CTZK form II (Fig. 4.1 b and f) differ from the results obtained for form I, as well as those for CTZK form IV (Fig. 4.1: c and g). CTZK form II (Fig. 4.1: b and f) presents two strong endotherms in the DSC scan, the first one starting immediately at the beginning of the scan (at 25 °C), corresponding to a TGA mass loss of 6.6±0.4% detected between 25-100 °C and the second endotherm with an onset at 159.6±0.5 °C corresponding to a TGA mass loss of 4.6±0.2% (temperature range of 100-200 °C).

DSC and TGA analysis is consistent with CTZK form II being a dihydrate (theoretical water content of 9.7%), possibly containing interstitial/channel water molecule(s). For this sample the KF titrimetry indicated 13.4%±0.3% of water content. This was higher than the mass loss determined by TGA analysis (11.2±0.6% measured between 25 and 200 °C), which may be attributed to different sample handling conditions pertaining to the two techniques. Dehydration of this sample, occurring in two steps, was different to that of the sodium salt (CTZNa) dihydrate, which dehydrated in a single step (Chapter 1). Also, the onset of CTZNa dihydrate desolvation was 83.7 ± 0.5 °C, higher than that of the first endothermal event for CTZK form II indicating lower thermal stability of CTZK dihydrate. CTZK form II starts to melt at 263±0.5 °C and this is immediately followed by decomposition. The potassium content was determined to be 12.5±0.6% w/w, consistent with a 1:1 molar ratio of potassium to CTZ, where the theoretical content of potassium is 11.7%. The acetone content for the sample recrystallised from the acetone/water 1:1 (v/v) mixture was determined to be 3.0 ± 0.6 ppm.

The DSC scan of CTZ form IV (crystallised from ethanol) presents three endotherms with onsets at 35.4±1.5 °C, 120.3±1.2 °C (double endotherm) and 154.4±0.6 °C. TGA showed a two step mass loss, one being 2.1±0.2% (25-100 °C) and the other 11.3±1.0% (100-200 °C). The ethanol content in the sample was 6.1±0.2% as determined by GC-MS and consistent with the ethanol content of a monohydrate hemiethanolate of CTZ (i.e. CTZ:H_2O:ethanol of 1:1:0.5). The theoretical molar ratio corresponds to 6.1% w/w of ethanol and 4.8% w/w of water. This gives 10.9% total solvent content in the crystallised material, slightly lower than the total 13.4±2.0% mass loss observed between 25-200 °C by TGA. The melting point of CTZK form IV is 272.0±1.0 °C and the process of melting is followed by exothermic decomposition.

The PXRD pattern of CTZK form I and that of CTZK form IV (Fig. 4.2) are different in terms of peak positions indicating the different crystal form, which is not surprising considering the presence of ethanol in the latter material. Drying the crystals of CTZK form IV for 24 hours at 80 °C allowed the ethanol content to be reduced to 1.4±0.4 ppm indicating that the ethanol molecules could easily be removed. It was confirmed by PXRD that the pattern of the dried sample showed a major change indicating modifications of the original crystal lattice. The diffraction

peaks were reduced in intensity and the peak pattern was considered to be different to that of CTZK form IV (Fig. 4.2. a).

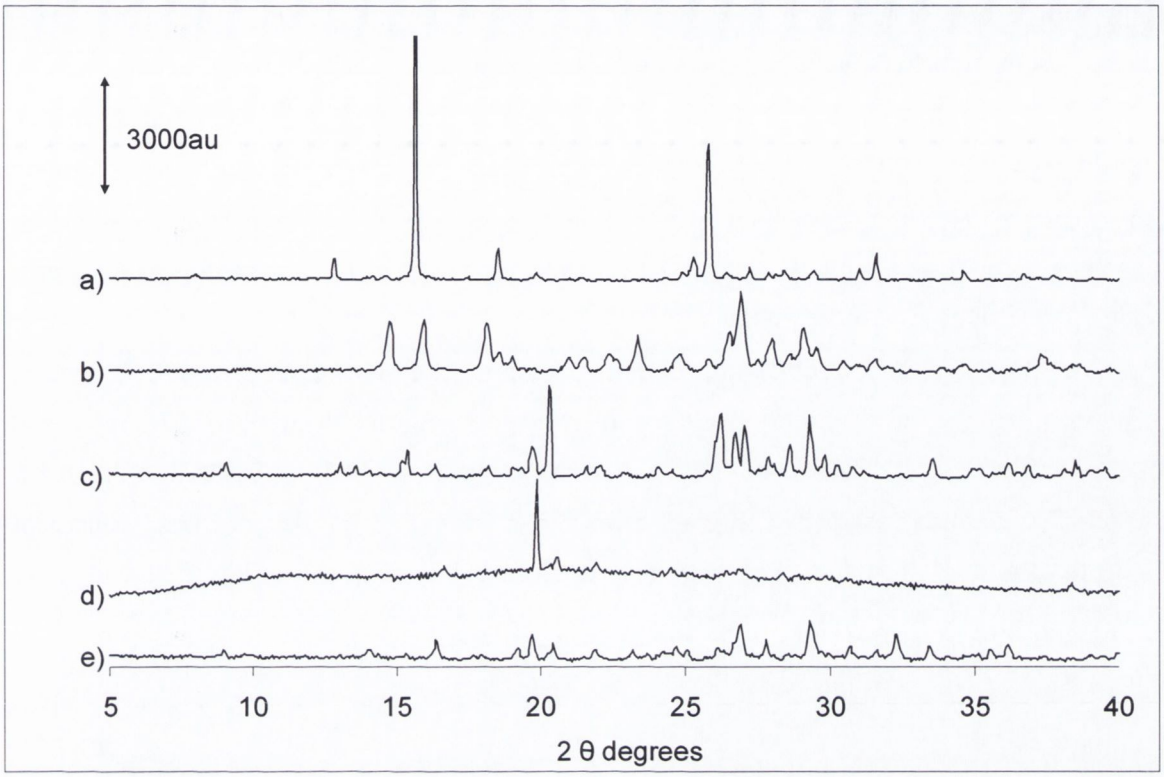

Fig. 4.2. PXRD pattern of CTZK: a) form IV (monohydrate hemiethanolate) , b) form I (monohydrate), c) form II (dihydrate), d) form III (anhydrous), e) form V (desolvated monohydrate hemiethanolate).

Morphologically a difference could be noticed as transparent colourless hard crystals became white, very fragile and formed a powder. Therefore the new form V is a desolvate originating from CTZK form IV and due to its distinctive X-ray powder pattern (Fig. 4.2 e), also different to that of the monohydrate form I (Fig. 4.2 b), it may be an alternative polymorphic form of the CTZK monohydrate. The diffraction pattern for CTZK form II (Fig. 4.2 c) was different to that of CTZK form I (Fig. 4.2 b).

Additional drying of form I converted the monohydrate to an anhydrous form III. The PXRD pattern of the anhydrate (Fig. 4.2 d) is characterised by peaks having very low intensities with only one prominent peak at 19.85 2θ suggesting major damage to the original crystal structure.

Investigations of the solid-state behaviour of CTZK imply that form II (dihydrate) is preferentially crystallised from an aqueous environment (water and water/acetone mixture studied). At ambient conditions over approximately 2-3 days, large crystals of this form were observed to loose their transparency and break apart from one another, converting to the form I (monohydrate), followed by the formation of the anhydrous form III when exposed to higher temperatures (over 160 °C). The latter is very sensitive to moisture and in humid conditions tends

to recrystallise towards a mono and dihydrated form. Form IV (hemiethanolate) is recrystallised from ethanol, however at ambient conditions ethanol is progressively liberated and, depending on the environmental humidity and temperature, the desolvated CTZK forms a dihydrate, monohydrate or the anhydrous form III at a higher temperature.

To specify more precisely the humidity conditions which stabilise or induce transformation of the hydrate forms, CTZK form I (monohydrate) was subjected to dynamic vapour sorption analysis. An isothermal experiment of sorption and desorption at 25 °C (Fig. 4.3) established that even ~ 0 %RH (0.5-0.7% RH actual %RH) transformation of the monohydrate (I) towards an anhydrous form was not observed.

A sample of form I equilibrated at 0% RH remained stable as the monohydrate, in contrast to CTZNa, where the same conditions resulted in an anhydrous form (Chapter 3). CTZK recovered from the DVS experiment (after equilibration at 0% target RH) was analysed by PXRD (Fig. 4.4 f, g), and by thermal methods (Fig. 4.5.1a, 2a). The PXRD pattern was consistent with the pattern of CTZK monohydrate raw material (form I) described above (Fig. 4.2 b).

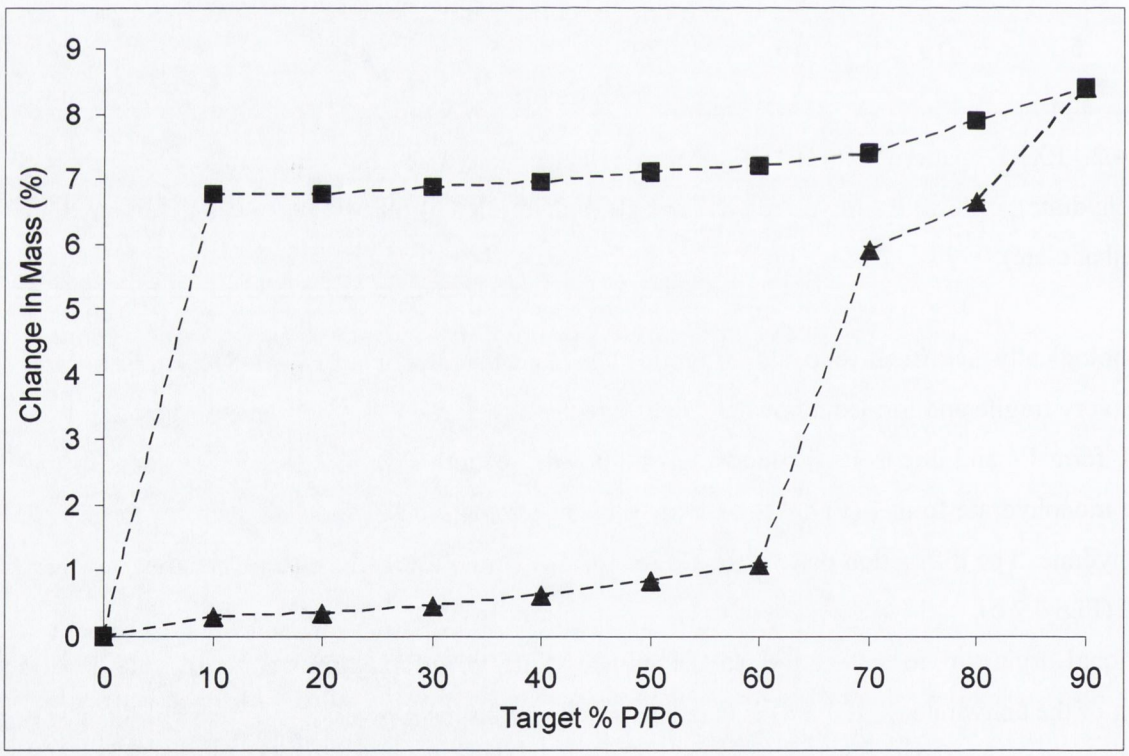

Fig. 4.3. Isothermal (25 °C) plot of sorption (triangle) and desorption (square) of water vapour for CTZK form I (monohydrate).

A sample of form I equilibrated up to 60% RH in 10% RH steps adsorbed less than 1% of water relative to the initial sample mass (CTZK monohydrate), indicating better moisture-related stability in comparison to CTZNa monohydrate, which was found to form *in situ* by DVS

at 30-40% RH, rapidly absorbed water above 40% RH and recrystallised to a dihydrate (Chapter 1). The sample of CTZK recovered from the DVS instrument and subjected to thermal analysis presented a two stage mass loss, by TGA (Fig. 4.5. 2 f), the first of 3.44% and second of 5.47%, which correlated with two respective endothermal events on the DSC with onsets at 57.7 °C and 142.5 °C (Fig. 4.5.1 f). PXRD analysis of the sample equilibrated during sorption at 60% RH (Fig. 4.4 e) had a Bragg peaks pattern which was very similar to that of the monohydrate form I but with the appearance of additional peaks, in particular at ~17.05 and ~20.20 2θ degrees, which were weak in intensity, and which can be assigned to the dihydrate form. The PXRD pattern of this sample may be described as a combination of the mono and dihydrate forms.

Between 60 and 70% RH the sample adsorbed nearly 6% of water relative to the initial mass of monohydrate. PXRD of the recovered and analysed material (Fig. 4.4 d) indicated the presence of a dihydrate, with the peak pattern corresponding with the material which was subjected to single crystal analysis (Chapter 4.2.2.) (Fig. 4.2 a). Overall TGA mass loss in the range from 25-200 °C was ~12%, divided into two steps of 7.4% and 4.9% (Fig. 4.5.2 e), corresponding with respective onsets of peaks on the DSC at 57.0 °C and 157.8 °C, due to the first and second stages of water evaporation (Fig. 4.5.1 e). Further conditioning of CTZK dihydrate form II, at 80 and 90% RH did not result in additional changes (Fig. 4.4 c) to the PXRD pattern, nor to DSC and TGA profiles of the dihydrated material (Fig. 4.5.1 d and 4.5.2 d). Comparison of water vapour intake by CTZK form II to that of CTZNa dihydrate suggests that the former is less hygroscopic than the latter at high humidities (70-90% RH).

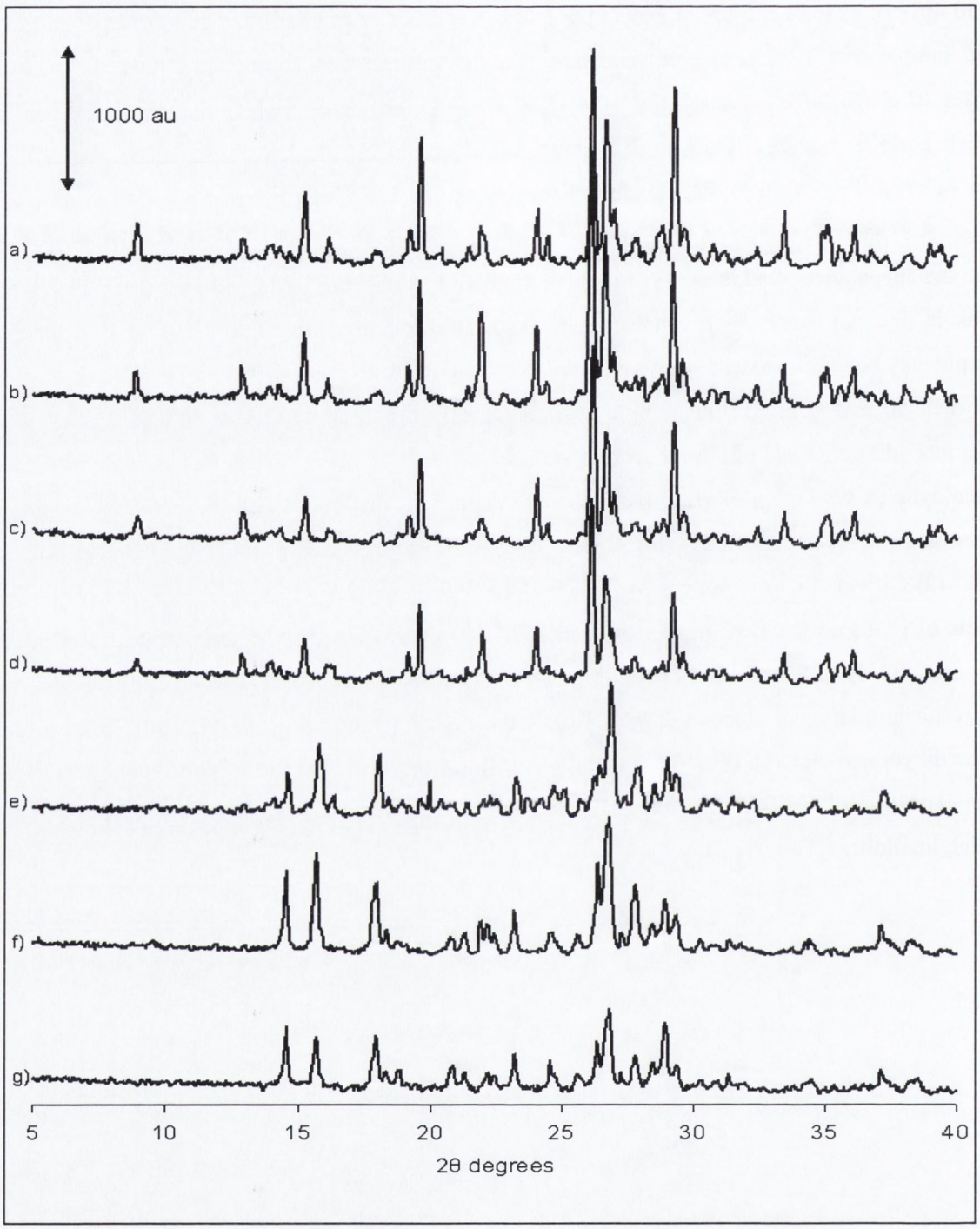

Fig. 4.4. PXRD results of CTZK: a) dihydrate raw material, b) dihydrate, equilibrated at 10%RH, c) dihydrate equilibrated at 90%RH, d) dihydrate equilibrated at 70%RH, e) monohydrate equilibrated at 60%RH, f) monohydrate equilibrated at 0%RH (starting material: monohydrate), g) monohydrate equilibrated at 0%RH (starting material: dihydrate).

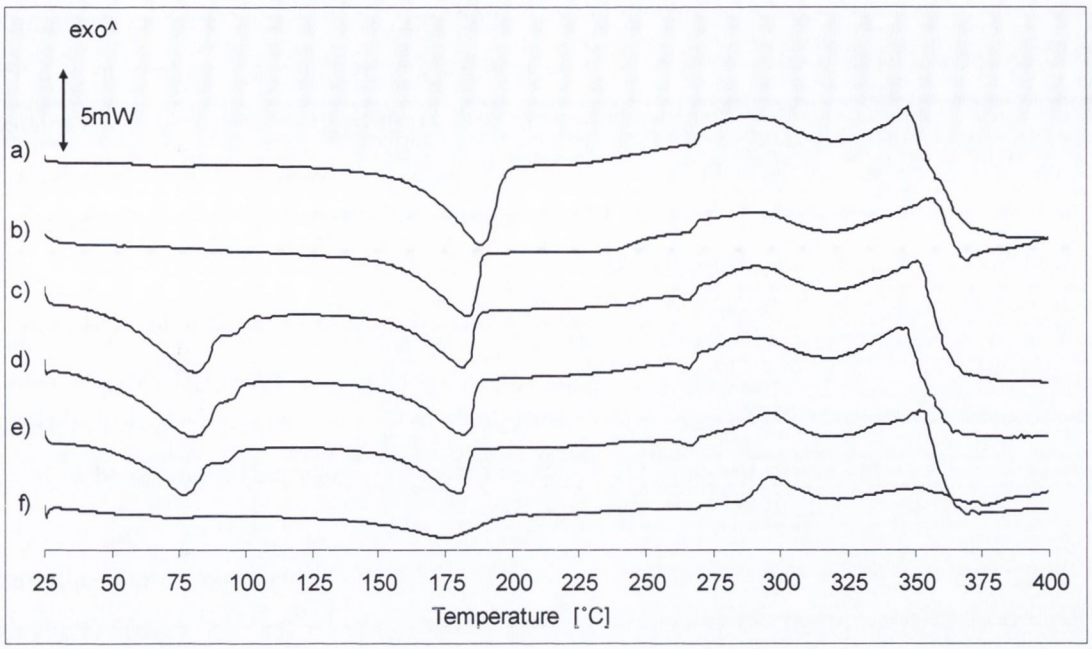

I

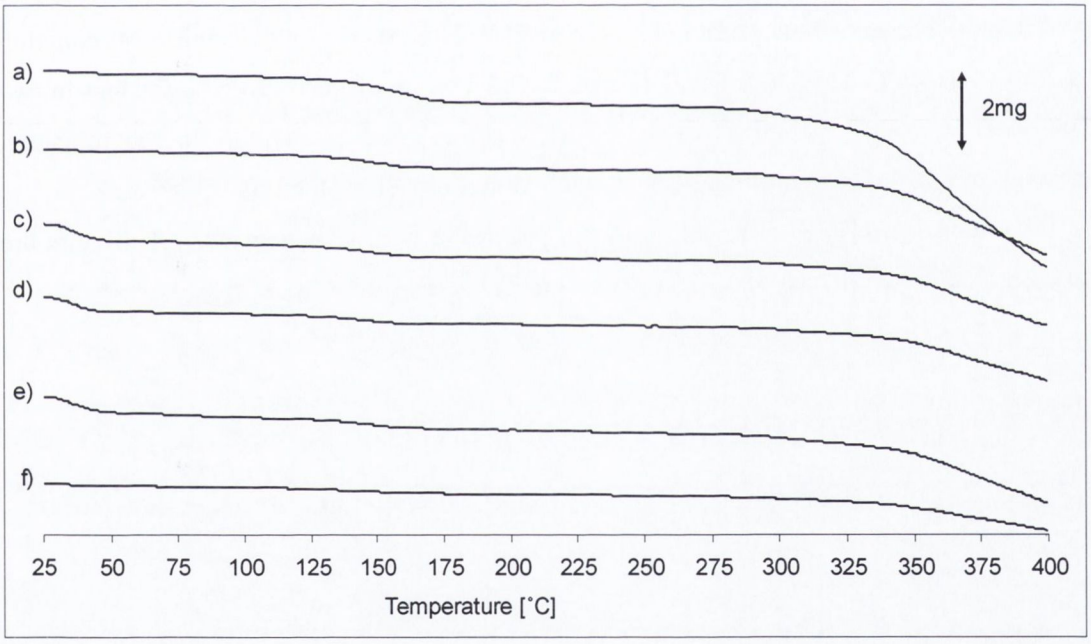

II

Fig. 4.5. DSC (I) and TGA (II) analysis of CTZK: a) monohydrate starting material equilibrated at 0% RH, b) monohydrate equilibrated at 0% RH after desorption, c) dihydrate equilibrated at 10% RH, d) dihydrate equilibrated at 90% RH, e) dihydrate equilibrated at 70% RH, f) monohydrate equilibrated at 60% RH.

After equilibration at 90% RH the sample of CTZK form II (dihydrate) was subjected to desorption. As shown in figure 4.3, the sample in the range from 90 to 10% RH lost just 1.6% mass relative to the starting mass. The pattern of mass loss of CTZK dihydrate on desorption shows two different stages of approximately linear mass loss: the first in the range from 90 to 70% RH

where the mass loss was ~1%, and the second in the range from 70% to 10% RH where the sample lost a further 0.6% of water, relative to the starting mass of the monohydrate, ending up at 6.8% total water uptake. We hypothesise that the water loss in the first range (90%-70% RH) is related to adsorbed surface moisture, the second mass loss (70%-10% RH) is related to the loss of what we have described as interstitial water in form II, however it is difficult to distinguish between surface-adsorbed and interstitially captured water.

Supporting analyses by PXRD, DSC and TGA confirmed that the sample equilibrated at 10% RH remained as a dihydrate. The PXRD pattern (Fig. 4.4 b) remained consistent with materials equilibrated at 70% and 90% RH respectively (Fig. 4.4 c, d) and with raw material of form II (Fig. 4.4 a). DSC and TGA scans are the same for all three materials conditioned at 70%, 90% and 10% RH (after desorption) (Fig. 4.5.1 c-e and 4.5.2 c-e).

Below 10% RH on the desorption curve (Fig. 4.3), the dihydrated form collapsed and transformed to the monohydrate (form I). The change was verified by PXRD analysis (Fig. 4.4 f, g) and the Bragg peaks pattern was consistent with the PXRD analysis of the monohydrated raw material, form I (Fig. 4.2 b). DSC analysis showed a significant reduction in the size of the starting endothermal peak (Fig. 4.5.1 b). TGA analysis recorded mass loss in two steps. The first detectable mass loss of 1.5% may be attributed to loss of surface moisture, and the second, of 5.2%, to dehydration of the monohydrate form (Fig. 4.5.2 b).

FTIR patterns of CTZK recrystallised from water and from acetone/water 1:1 mixture are similar to each other and represent the FTIR pattern of form I (Fig. 4.6).

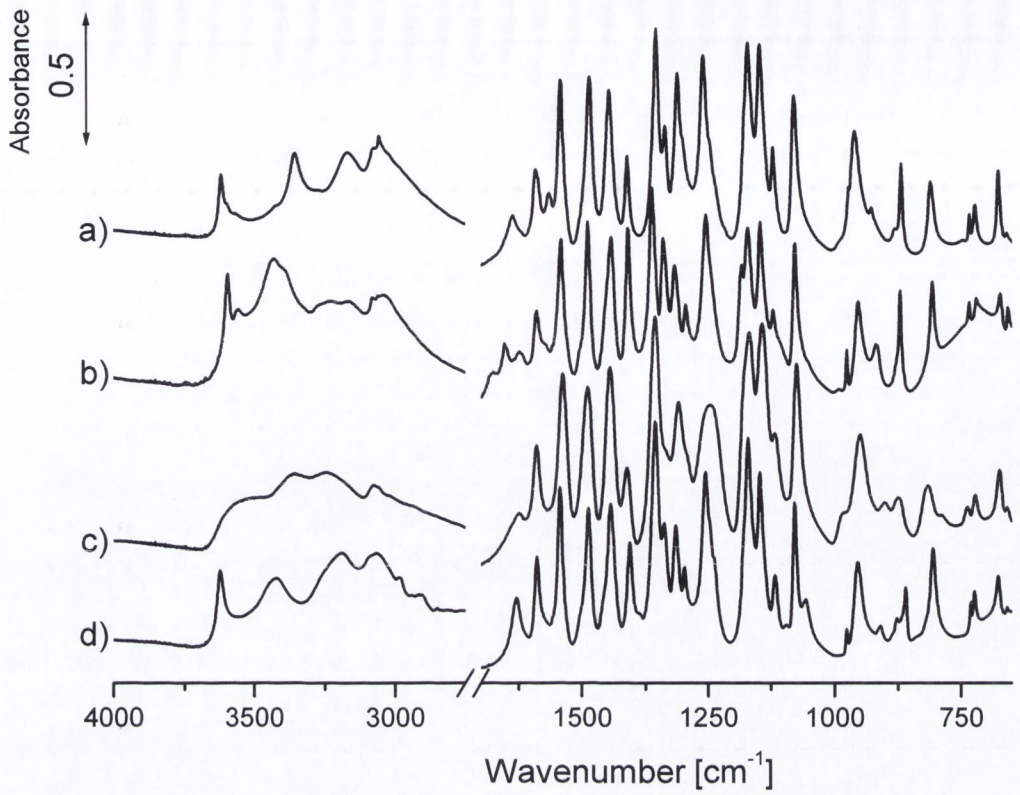

Fig. 4.6. FTIR analysis of CTZK: a) form I, b) form II, c) anhydrous form III, d) form IV.

The bands of $-CH_3$ and $-CH_2$ groups were clearly visible in the range of 3000 cm^{-1} to 2700 cm^{-1} of CTZK form IV in contrast to the other forms of CTZK. A sharp OH- stretching peak (crystalline water) was seen at around 3600 cm^{-1} for all the hydrated forms. Closer analysis of the water band revealed that this peak appeared at 3618 cm^{-1} for form I, 3595 cm^{-1} for form II and 3623 cm^{-1} for form IV indicating that this solvent was bonded most strongly in the dihydrate and most weakly in the ethanol-containing compound. A small, but clearly visible band at 3559 cm^{-1} was also noted for form II. The anhydrous form did not display the water band, but broadening of the peaks was seen, consistent with a decreased crystallinity of this form which was supported by the PXRD pattern shown above (Fig. 4.2 d). The N-H stretching vibrations for this form appeared at 3357 cm^{-1} and 3243 cm^{-1}. One of the N-H bands displayed a relatively steady position for all the three solvated forms.

It appeared at 3171, 3169 and 3191 cm^{-1} and for form I, II and IV, respectively. The other N-H peak was observed at 3354, 3428 (with a further vibration at 3359 cm^{-1}) and 3420 cm^{-1} for form I, II and IV, respectively showing greater shifts in peak positions, most likely depending on the bound solvent. This N-H peak was therefore ascribed as the N-H fragment attached

to the benzene ring as it is the only N-H group in the structure directly interacting with the solvent. FTIR spectrum of form IV also differed from the di- and mono-hydrates by the presence of an extra band at 1057 cm^{-1} due to the O-CH_2 stretch vibrations from ethanol.

The aqueous solubility of CTZK form II (dihydrate) was determined. This form was chosen due to the greatest expected stability in solution. The solubility was determined to be 78.71±1.82 mg/ml (pH 8.5±0.1) indicating that CTZK has an aqueous solubility ~400-fold higher compared to 0.2 mg/ml for CTZ reported previously by Charnicki et al. (1959).

Both, form II and IV, pseudopolymorphic structures of CTZK tend to crystallise as colourless and transparent prismoidal agglomerates (Fig. 4.7).

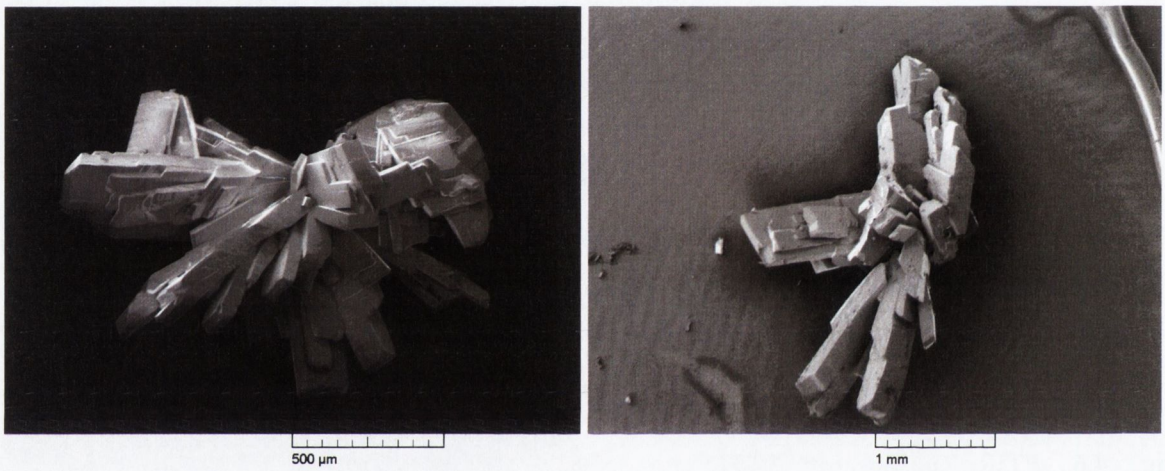

a) b)

Fig. 4.7. SEM images of CTZK: a) form II, b) form IV.

4.2.2. Crystal structure

Single crystal X-ray analysis resulted in the determination of the molecular structures of CTZK forms II and IV. Experimental data images are reported in Fig. 4.8.

Chlorothiazide potassium dihydrate, form II, can be classified as an intermolecular coordinate consisting of chlorothiazide molecules bonded together with potassium. Single crystal X-ray diffraction studies (Fig. 4.9) show that the structure obtained can be described as follows: $(CTZ)_3 \cdot K \cdot (H_2O)_2(CTZ)_2 \cdot (H_2O)_2 \cdot K \cdot (CTZ)_3$ (CTZK form II). The structure is of a supramolecular self-assembly type formed by several molecules of CTZ.

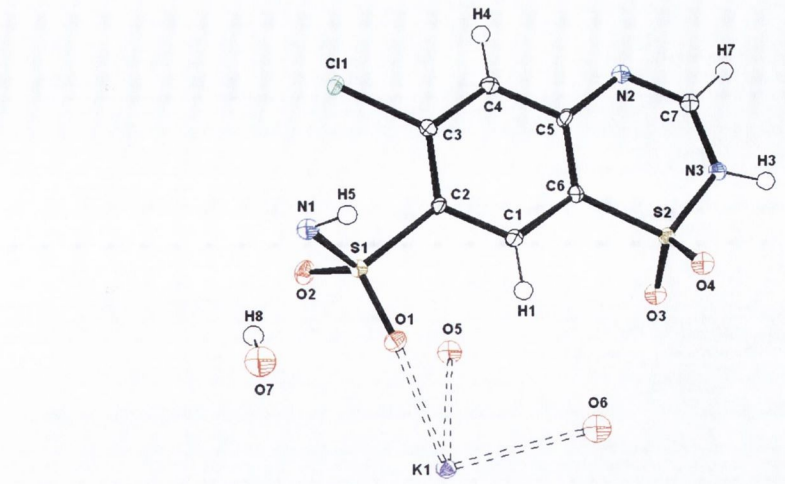

a)

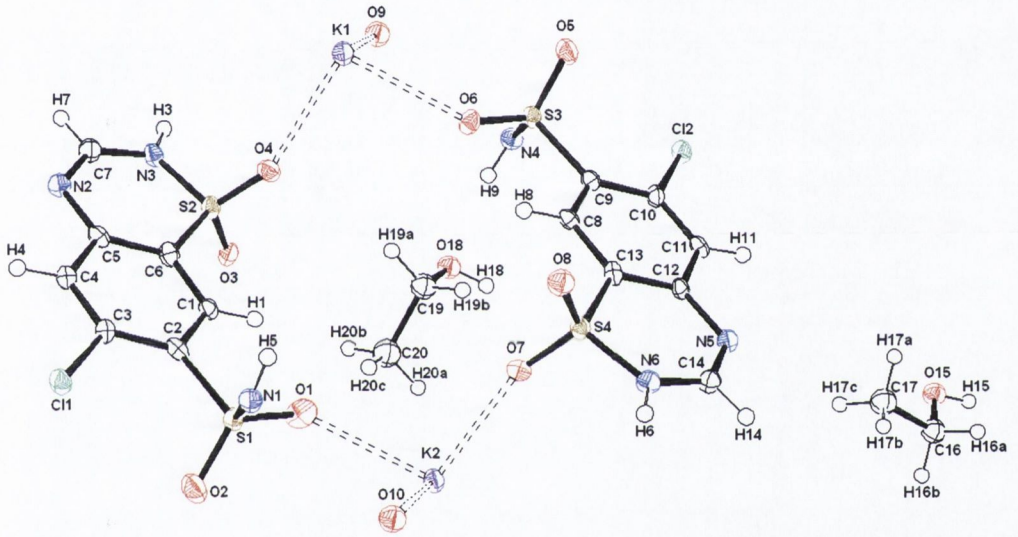

b)

Fig. 4.8. View of chlorothiazide potassium: a) dihydrate (CTZK form II), b) monohydrate hemiethanolate (CTZK form IV) by Ortep visualisation.

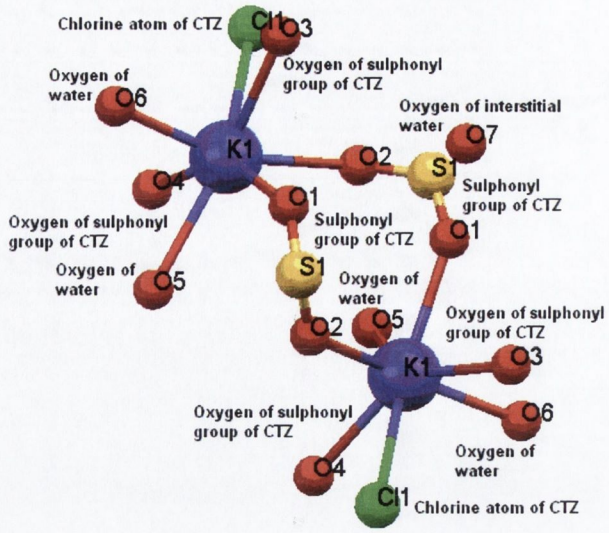

a)

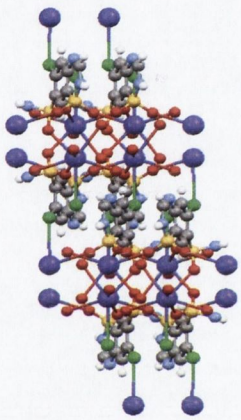

b)

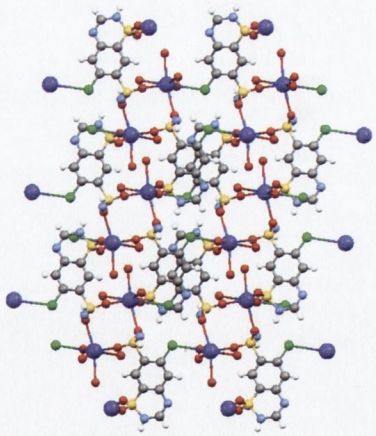

c)

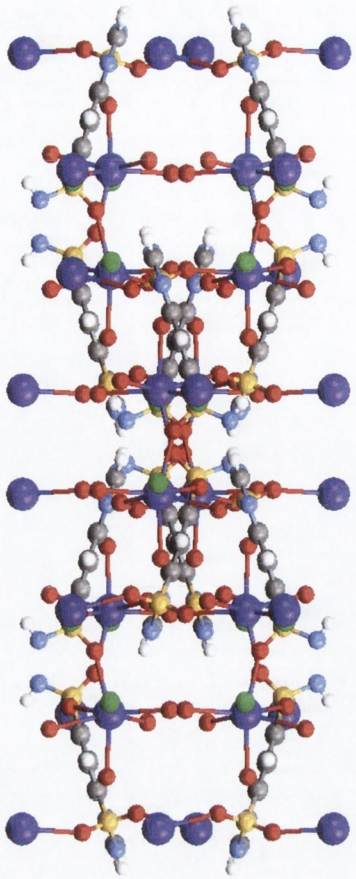

d)

Fig. 4.9. CTZK form II: a/ potassium ion coordinates, b/ cell unit packing view along "a" axis, c/ cell unit packing view along "b" axis, d/ cell unit packing view along "c" axis. Atom colours: carbon: grey, nitrogen: blue, hydrogen: white, oxygen: red, sulphur: yellow, chlorine: green, potassium: violet. Interstitial water molecules are removed for clarity.

CTZK form II intermolecular self-assembly consists of two cations of potassium bridged by the oxygens of the sulphonyl group (O(1) and O(2)) attached to the phenyl groups of CTZ (Fig. 4.9a). The bond length between the potassium and each of the oxygens is similar and is 2.67 Å and 2.75 Å for [K(1)-O(1)] and [K(1)-O(2)], respectively. Each of the potassium cations coordinates five molecules of chlorothiazide, four of them through the oxygens of the sulphonyl groups (O(1), O(2), O(3) and O(4)) and one through the chlorine atom (Cl(1)). Two of the coordinated chlorothiazide molecules are bridged to the potassium through the oxygen atoms of the SO_2 group (O(3) and O(4)) attached to the heterocyclic ring of CTZ. The bond distances between oxygen and potassium are: 2.71 Å for [K(1)-O(4)] and 2.79 Å for [K(1)-O(3)]. The unique feature of molecular coordination observed in CTZK form II is that the potassium cation is able to coordinate the chlorine atom ([Cl(1)-K(1)] distance of 3.33 Å). To our knowledge, no reports of [K-Cl] coordination in salts of APIs have been published to date.

Apart from interacting with CTZ, each of the potassium cations coordinates two molecules of water with the [K(1)-O(5)] and [K(1)-O(6)] distances of 2.86 Å and 2.65 Å, respectively. None of these water molecules is shared and/or bridged between the two cations of potassium. Additionally, a molecule of water, appearing as an interstitial/channel type, is also present in the neighbourhood of two of the potassium cations in CTZK form II. The oxygen of water is present at an equal distance of 5.39 Å from each of potassium atoms ([K(1)-O(7)-K(1)]) in the assembly. A summary of the key crystallographic information is given in Table 4.1.

CTZK recrystallised from ethanol (form IV) presents a different crystal structure compared to CTZK form II (Fig. 4.10). In CTZK form IV the two potassium cations are bridged by two oxygens of water and additionally by the oxygens of the sulphonyl group (O(1), O(2), O(5) and O(6)) attached to the phenyls of two molecules of chlorothiazide (Fig. 4.10a). The distances between the oxygens of water (O(9) and O(10)) and the potassium cations are 2.74 Å and 2.85 Å for [K(1)-O(9)] and [K(1)-O(10)], respectively and 2.88 Å and 2.71 Å for [K(2)-O(9)] and [K(2)-O(10)], respectively. The distances between the potassium cation and CTZ oxygens are of a similar range as those between K(1)/K(2) and O(9)/O(10) and are 2.80 Å and 2.76 Å for [K(1)-O(2)] and [K(1)-O(6)], respectively and 2.77 Å and 2.80 Å for [K(2)-O(1)] and [K(2)-O(5)], respectively.

Table 4.1. Crystal cell characteristics of CTZK recrystallised from water or acetone/water mixture (CTZ form II) and CTZK recrystallised from ethanol (CTZK form IV).

Analysis parameters	CTZK form II		CTZK form IV	
Identification code	CTZK form II		CTZK form IV	
Empirical formula	$C_{56}H_{40}Cl_8K_8N_{24}O_{52}S_{16}$		$C_{18}H_{20}Cl_2K_2N_7O_{11}S_4$	
Formula weight	2990.48		787.75	
Temperature	108(2) K		118(2) K	
Wavelength	0.71075 Å		0.71075 Å	
Crystal system	Monoclinic		Triclinic	
Space group	C2/c		P-1	
Unit cell dimensions	α= 90°	a = 18.328(4) Å	α = 87.522(13)°	a = 7.078(3) Å
	β= 99.729(3)°	b = 7.3662(16) Å	β= 84.064(14)°	b = 9.842(5) Å
	γ = 90°	c = 19.993(5) Å	γ= 78.822(12)°	c = 21.994(11) Å
Volume	2660.4(11) $Å^3$		1494.6(12) $Å^3$	
Z	1		2	
Density (calculated)	1.867 g/cm^3		1.750 g/cm^3	
Absorption coefficient	0.946 mm^{-1}		0.843 mm^{-1}	
Crystal size	0.50 x 0.30 x 0.30 mm^3		0.20 x 0.20 x 0.20 mm^3	
Reflections collected	6225		20149	
Completeness to theta = 25.00°	94.6 %		96.7 %	
Goodness-of-fit on F^2	1.106		1.149	
Final R indices [I>2sigma(I)]	R^1 = 0.0384, wR^2 = 0.1098		R^1 = 0.0605, wR^2 = 0.1814	
R indices (all data)	R^1 = 0.0399, wR^2 = 0.1113		R^1 = 0.0654, wR^2 = 0.1966	

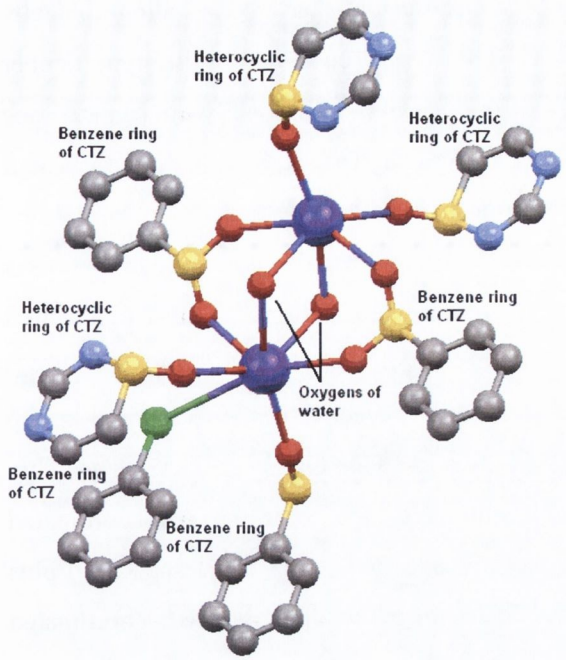

a)

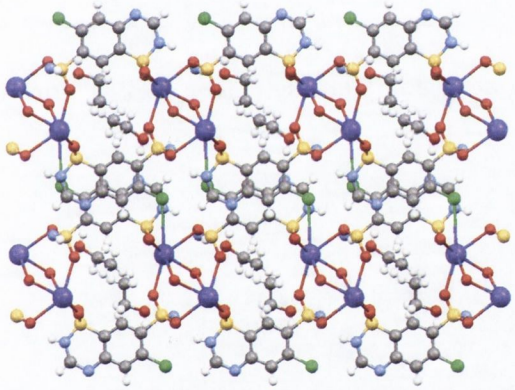

b)

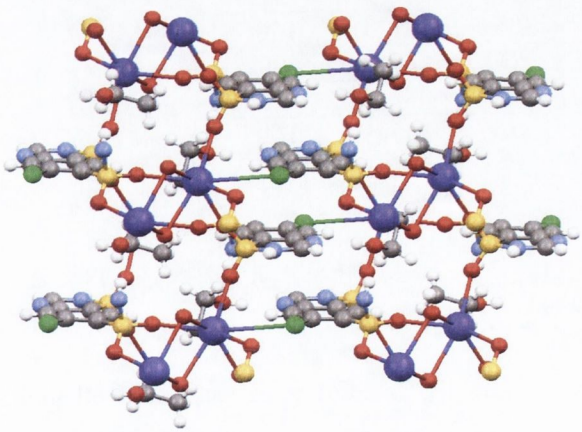

c)

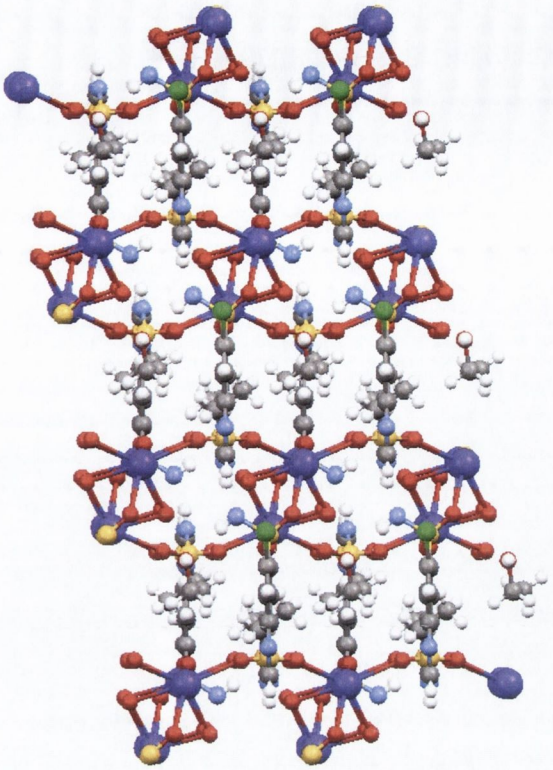

d)

Fig. 4.10. CTZK form IV: a/ potassium ion coordinates, b/ cell unit packing view along "a" axis, c/ cell unit packing view along "b" axis, d/ cell unit packing view along "c" axis. Atom colours: carbon: grey, nitrogen: blue, hydrogen: white, oxygen: red, sulphur: yellow, chlorine: green, potassium: violet.

CTZK form IV is composed of two types of CTZ molecules that are crystallographically independent (Fig. 4.8). The two potassium cations in CTZK form IV coordinate a different number of atoms each. They both coordinate six oxygens, but one of them additionally coordinates one chlorine atom of CTZ [Cl(2)-K(2)] with a distance of 3.57 Å. The distance between the potassium and chlorine in CTZK form II described above was shorter i.e. was 3.33 Å. In CTZK form IV one of potassium ions (K(1)) coordinates four molecules of chlorothiazide through oxygens of the sulphonyl groups: two from the phenyl ring mentioned before (O(6), O(4) shared with the second potassium cation) plus two from the heterocyclic ring of chlorothiazide (O(2) and O(1)). The distances between the potassium atom and oxygens of the sulphonyl group of the heterocyclic ring of CTZ are: [K(1)-O(3)]: 2.75 Å and [K(1)-O(4)]: 2.71 Å. The other potassium (K(2)) coordinates five molecules of chlorothiazide: four of them are coordinated by the oxygens of the sulphonyl group: three from the benzene ring (O(3), O(5) and O(7)) plus the fourth oxygen of the heterocyclic ring (O(30). The fifth chlorothiazide molecule is coordinated to the potassium ion through the chlorine atom of the CTZ molecule.

Extensive network of hydrogen bonds were determined in both of the pseudopolymorphic forms (II and IV) of CTZK and are presented in Table 4.2.

Table 4.2. Bond lengths and dihedral angles for hydrogen bonding interactions in CTZK form II and CTZK form IV.

Bond type D-H...A	**D-H [Å]**	**H..A [Å]**	**D...A [Å]**	**D-H...A [°]**
CTZK form II				
N(3)-H(3)...N(1)[(a)]	0.88	2.15	2.933(4)	148
N(1)-H(5)...N(2)[(b)]	0.82(5)	2.38(6)	3.027(3)	136(5)
O(7)-H(8)...N(1)	0.97(6)	2.29(6)	3.069(3)	138(5)
C(1)-H(1)...O(1)	0.95	2.41	2.824(4)	106
CTZK form IV				
N(3)-H(3)...N(1)[(c)]	0.88	2.22	2.998(5)	148
N(1)-H(5)...O(15)[(d)]	0.83(5)	2.09(5)	2.922(5)	173(4)
N(6)-H(6)...N(4)[(e)]	0.88	2.27	3.038(5)	146
N(4)-H(9)...O(18)	0.87(6)	2.01(6)	2.865(5)	169(5)
O(15)-H(15)...N(2)[(f)]	0.84	1.92	2.758(5)	173
O(18)-H(18)...N(5)[(d)]	0.84	1.90	2.733(5)	169
C(1)-H(1)...O(1)	0.95	2.36	2.791(5)	107
C(8)-H(8)...O(6)	0.95	2.36	2.799(5)	107

Symmetry codes: (a) -½+x, ½+y, z; (b) ½-x, ½-y, -z; (c) x, 1+y, z; (d) 1-x, 1-y, 1-z; (e) x, -1+y, z; (f) x, y, 1+z.

CTZK from IV occurs as a monohydrate additionally containing molecules of ethanol with the molar ratio of H_2O: ethanol: CTZ of 2:1:2 based on the single crystal X-ray analysis, in excellent agreement with the ratio determined by thermal analysis and GC-MS (Methods 2.2.13.) It has a different crystal unit cell than CTZK form II (Table 4.1). While CTZK form II is

monoclinic with a space group of C2/c, CTZK form IV has a triclinic crystal structure and a space group of P-1.

To date only a limited number of APIs containing similar coordinates formed by potassium cation have been described and reported, suggesting that crystal structures of pharmaceutically relevant potassium salts have not been widely investigated. Geddes et al. (1974) reported a crystal structure of nigericin potassium salt and compared it with a nigericin silver salt. In nigericin, the potassium cation coordinates seven oxygen atoms with distances between the oxygens and potassium between 2.58 Å and 3.09 Å. All the coordinated oxygens come from the same molecule of nigericin i.e. the structure of the complex is 1 molecule of K^+ to 1 molecule of nigericin. On the other hand, Tauvel et al. (2009) described crystal structures of a potassium salt of tenatoprazole. Depending on the solvent used, the mono-potassium salt of tenatoprazole presented the following forms: a monoclinic- diethanolate, a monoclinic-(x)methanolate,-(2-x)ethanolate, where ($0 \leq x < 1$), diethanolate and an orthorhombic structure of ethylenglycolate (EG). Similarly to CTZK, a hydrated form of potassium tenatoprazole recrystallised from ethanol. The authors observed 1D ribbon arrangements for the diethanolate and ethylenglycolate forms of the API, therefore showing that a supramolecular organisation for potassium salts is possible, however CTZK (especially form IV) exhibits a complex crystal structure compared to those previously described.

Bekdemir et al. (2002) published the crystal structure of potassium p-nitrobenzoxasulfamate monohydrate. This orthorhombic structure is based on two cations of potassium which, as in the CTZK form III structure, are crystallographically independent. One of the potassium cations coordinated six oxygens in the range 2.6538-3.0916 Å and one atom of nitrogen (2.9236 Å) while the second potassium cation coordinated seven atoms of oxygens in the range 2.7502-3.0468 Å and one nitrogen (2.7942 Å).

4.2.3. Hirshfeld surfaces

Hirshfeld surfaces analysis allowed for visualisation and comparison of reciprocal interactions among atoms in crystal lattices of CTZK form II and form IV. The visualisation is based on a 3-D surface surrounding a single molecule of CTZK. Parameters describing this surface are d_i and d_e, where d_i corresponds to the distance between the surface and atom placed the closest internally to the surface. d_e corresponds to the distance between the surface and atom placed the closest externally to the surface. Presented surfaces by d_{norm} are the sum of d_i and d_e where each of them is normalised to the van der Waals radius of the involved atom. 3-D images of surfaces of molecules are partially coloured and partially gray. The colour spectrum ranges from blue to white to red. If the surface is coloured blue, it means, that reciprocal interactions between two molecules placed internally and externally to the Hirshfeld surface are longer (weaker) on a relative scale than van der Waals forces. White planes are equal to van der Waals

distance, while red surfaces represent interactions stronger than van der Waals forces. The surfaces presented in Fig. 4.11 reveal the close contacts between the atoms highlighting hydrogen bond donors and acceptors and interactions of the potassium ions.

The 3-D surface (Fig. 4.11) surrounding the molecule can be depicted by a D-2 fingerprint plot (Fig. 4.12) where $d_e=f(d_i)$. The fingerprint plot is pseudo-mirrored along $d_e=d_i$ which reflects the reciprocated interactions between selected atoms. The fingerprint plot depicts the percentage of overall Hirshfeld surface covered by a particular type of bond. This is important as red strong interactions, so called hot-spots, can be crucial in the formation of a particular crystal structure, but will not cover a large percentage of the Hirshfeld surface, so the overall stabilising effect on the crystal structure can be weaker than the less intensive blue interaction, but which covers a larger percentage of the Hirshfeld surface.

Figures 4.12 and 4.13 illustrate decomposition of the fingerprint plots for CTZ II and IV. This detailed analysis allows one to discern that the largest contribution to the overall Hirshfeld surface in CTZK form II are O...H, O...O and O...K (Fig. 4.12) and in form III are H...H, O...H and O...O (Fig. 13) contacts, suggesting that weak but repulsive H...H contacts contribute to the stability of CTZK form IV.

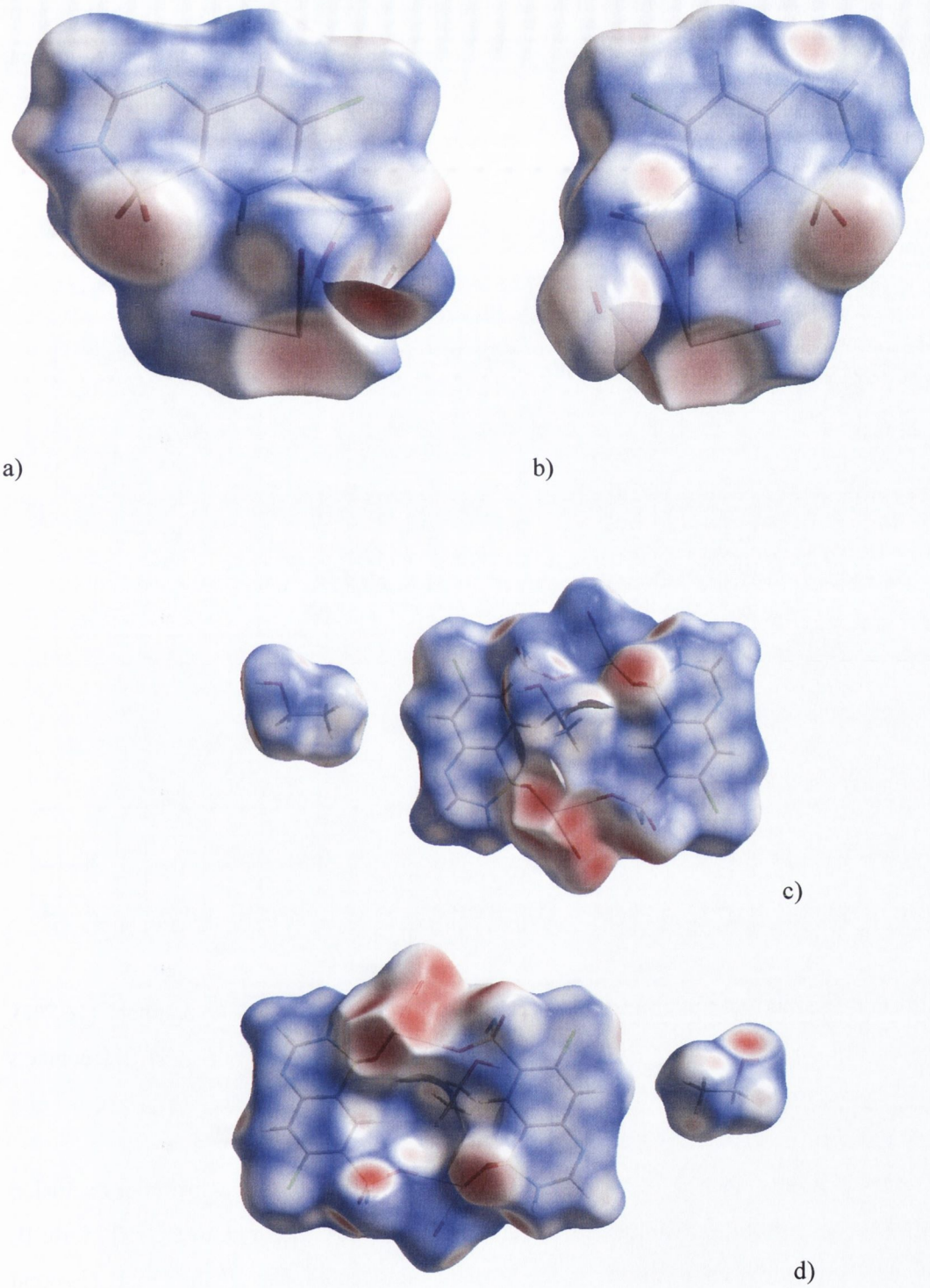

Fig. 4.11. (a) Front, (b) back view of d_{norm} mapped on the Hirshfeld surface of Form II, (c) front and (d) back view of d_{norm} mapped on the Hirshfeld surface of Form IV.

Both fingerprints presented the appearance of spikes characteristic of hydrogen bonds involving O...H and N...H contacts. The fingerprint plot of CTZK form II is quite asymmetric and this asymmetry is due to the presence of the channel water molecule. The fingerprint plots can also be considered in terms of hydrogen bond donors/acceptors, where $d_e > d_i$ contacts correspond to the hydrogen bond donors and $d_e < d_i$ contacts indicate the hydrogen bond acceptors.

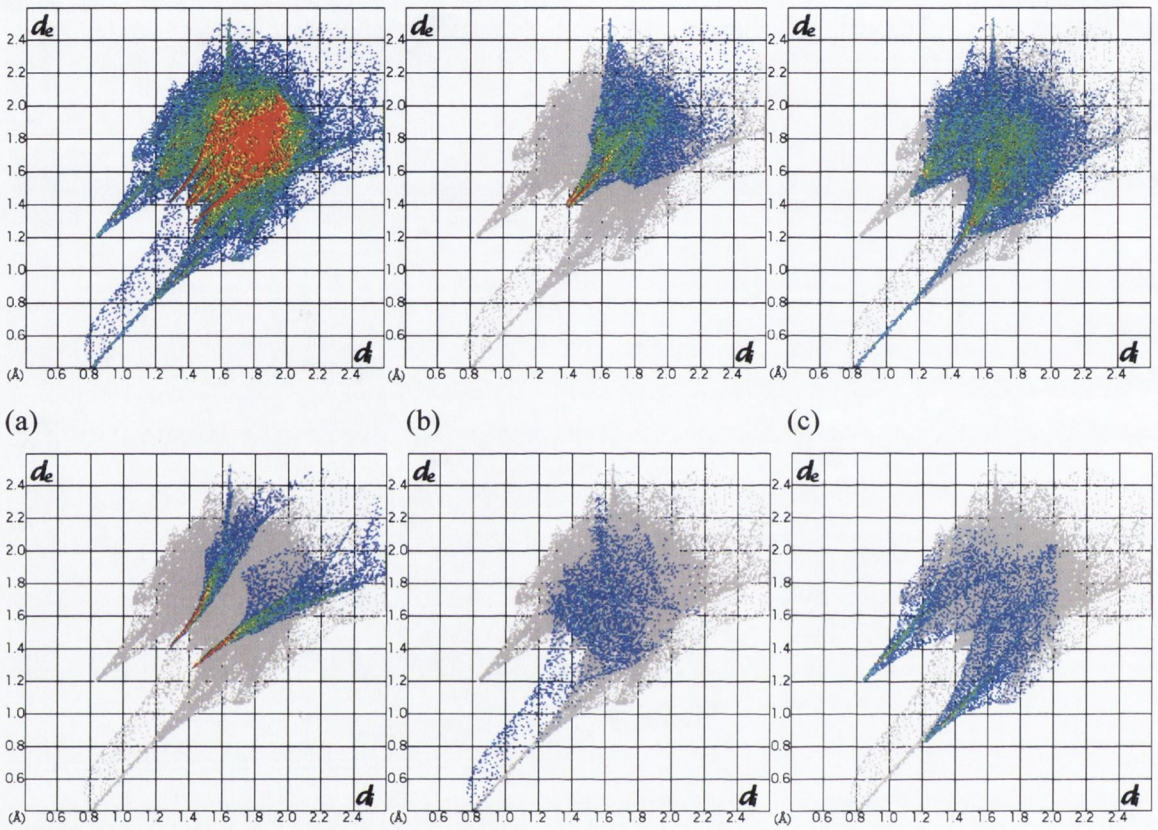

Fig. 12. Full (a) and partial fingerprint plots for CTZK form II: b) O...O contacts (16.7%), c) O...H reciprocal contacts (28.4%), d) O...K reciprocal contacts (12.5%), e) H...H contacts (5.2%), f) N...H reciprocal contacts (8.0%).

This examination indicates that the O...H contacts are more sensitive to the inclusion or exclusion of the solvated water molecules compared to contacts of other types. The hydrated CTZK form II, inclusive of the channel and coordinated by the K^+ water molecules, has 17.1% O...H (H-bond acceptors), 11.3% H...O (H-bond donors) as well as 5.4% O...K, 7.1% K...O and 16.7% O...O contacts contributing towards stability of the crystal structure of this form. Exclusion of the channel water only slightly changed these proportions to: 16.0% O...H, 9.6% H...O, 5.6% O...K, 7.7% K...O and 14.6% O...O interactions. Removal of all water molecules hydrating the CTZK altered the contributions of H...O and H...O contacts to 9.9% and 12.9%, respectively and changed the balance of H-bond donors and acceptors able to interact with the groups participating in such contacts.

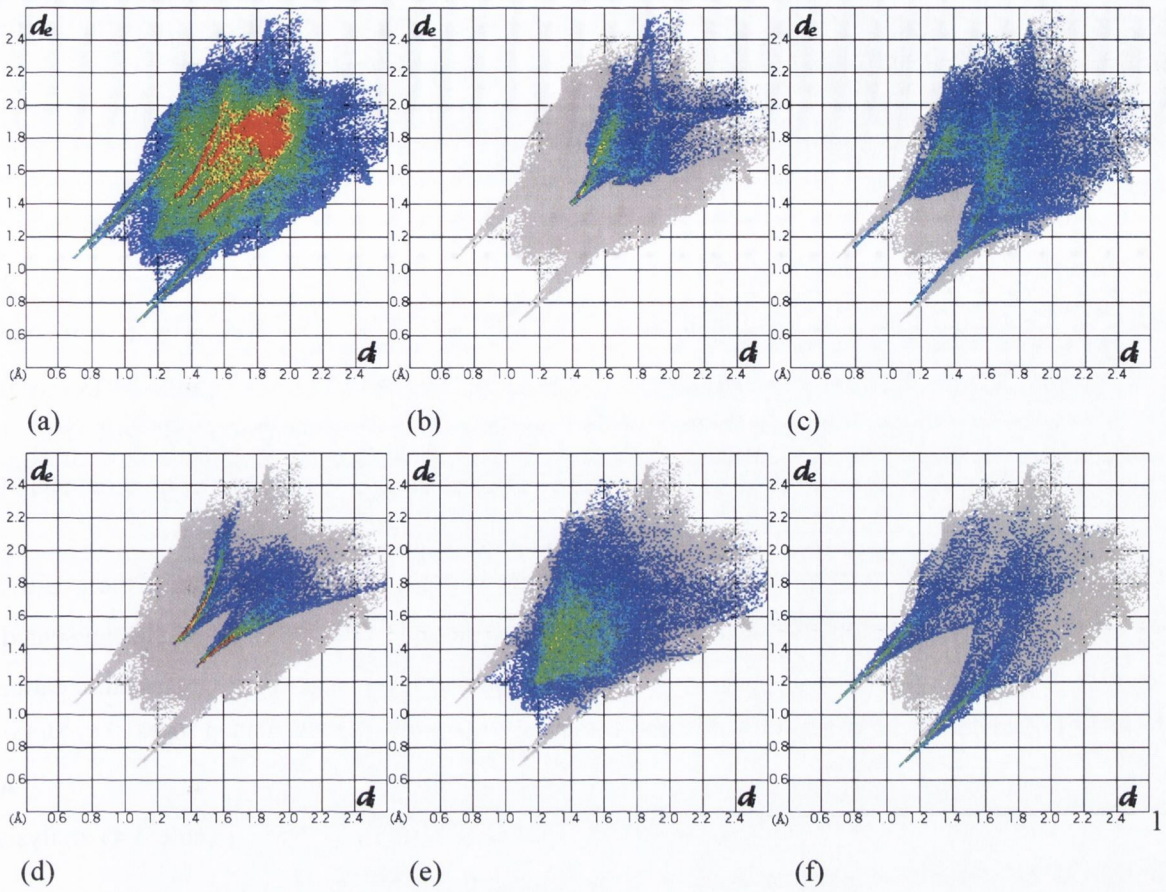

Fig. 4.13. Full (a) and partial fingerprint plots for CTZK form IV: b) O…O contacts (9.8%), c) O…H reciprocal contacts (19.7%), d) O…K reciprocal contacts (9.5%), e) H…H contacts (24.2%), f) N…H reciprocal contacts (8.1%).

This suggests that the water molecules bound by the potassium ions are essential for maintaining of the crystal lattice integrity of form II, whereas exclusion of the channel water impacts on the stability to a much lesser degree. The proportions of the O…K, K…O and O…O contacts in the fully water deprived structure are 5.9%, 12.7% and 9.6%, respectively.

In form IV, the mixed ethanolate/hydrate form, the O…H/H…O contributions change as follows: 10.9%/8.9%, 15.5%/5.8%, 9.1%/9.0% and 13.5%/6.5% for the fully solvated form IV, the structure with ethanol excluded but water molecules left in, the structure with water excluded but ethanol left in and the desolvated form (water and ethanol excluded), respectively. This, in contrast to form II, indicates that both of the solvents may be important in maintaining the integrity of form IV. Omission of water of solvation results in a change of the O…K and K...O contacts from approximately 5% and 6% to approximately 4% and 9%, respectively, not surprisingly as the water interacts with the potassium ions directly. Form II and form IV also display a significant difference in the contribution of H…H weak contacts, 5.2% and 24.2%,

respectively showing a greater contribution of these weak interactions arising from interaction of hydrogen atoms of the ethanol molecules with adjacent aromatic rings of CTZK.

4.2.4. NMR studies

^{1}HNMR analysis of CTZK form II (Table 4.3) confirms the presence of all expected CH groups. The scans suggest an undefined nature of the NH_2 moiety of SO_2NH_2 group, with some confirming deprotonation of the sulphonamide moiety and some showing it as an uncharged NH_2. 2D NH HSQC confirms though that the group is a primary sulphonamide group. ^{1}HNMR analysis of CTZK form IV (Table 1) confirms the chemical structure of the API molecule, as it detects all expected C(1,4,7)H(1,4,7) bonds and deprotonated N(1)H(5,6) of the NH_2SO_2 group.

It is hypothesised that the primary sulphonamide group is deprotonated to neutralise the positive charge of the potassium ion, which is consistent with the single crystal X-ray results presented. The distances from nitrogen of the deprotonated sulphonamide group to the potassium cation [K(1)-N(1)] for the form II are 4.33 Å and 5.08 Å, and for the form IV: 4.03 Å for [K(1)-N(1)], 4.45 Å for [K(1)-N(4)], 3.89 Å for [K(2)-N(4)[and 4.53 Å for [K(2)-N(1)]. ^{13}CNMR (Table 4.4) analysis confirmed the presence of all seven carbons in the chlorothiazide molecule.

Table 4.3. Results of ^{1}HNMR analysis of CTZK form II and IV.

Peak	**CTZK form II**	CTZ-CTZK form II Δ ν(F1) [ppm]	**CTZK form IV***	CTZ-CTZK form IV Δ ν(F1) [ppm]
	ν(F1) [ppm]		ν(F1) [ppm]	
C(4)-H(4)	8.15	+0.61	8.15	+0.61
C(1)-H(1)	7.43	-0.86	7.51	-0.78
C(7)-H(7)	7.22	-0.90	7.22	-0.90
N(2)-H(2)	-	-	-	-
N(1)H_2(5,6)/ N(1)H(5 or 6)*	7.51	-0.38	7.44	-0.45

Table 4.4. Results of ^{13}CNMR analysis of CTZK form II and IV.

Peak	CTZK form II	CTZ-CTZK form II Δ v(F1) [ppm]	CTZK form IV	CTZ-CTZK form IV Δ v(F1) [ppm]
	v(F1) [ppm]		v(F1) [ppm]	
C(4)-H(4)	124.85	+4.55	125.22	+4.93
C(1)-H(1)	126.47	+1.47	126.73	+1.73
C(7)-H(7)	155.45	+6.85	155.74	+7.14
C(5)	151.06	+12.16	150.70	+11.79
C(6)	134.01	-3.79	136.11	-1.69
C(2)	122.56	-11.84	122.91	-11.49
C(3)	131.26	+11.06	131.68	+11.48

Numerous shifts are observed in ^{13}C NMR spectra of CTZK form II and IV compared to CTZ. The largest shift between the two CTZ forms is observed for C(6) where the difference is 2.1 ppm. The largest downfield shift is observed for C(5) directly bonded to N(2) and the carbon (C(3)) to which the chlorine is attached (shifts of +12.2 and +11.06, respectively in comparison to CTZ). The most affected signal, compared with CTZ, was that of C(5) of the benzene ring and with the upfield shift of H(7) bonded to C(7) suggesting a change in protonation of N(2) and migration of H(2) to N(3). However, no signal from proton bonded to N(3) was directly detected (Table 4.3).

NMR analysis confirms the presence of ethanol captured in the crystal lattice of CTZK form IV. Peaks of the carbon and hydrogen nuclei of ethanol are visible in the spectrum as molecules of non-bonded solvent, indicating that ethanol is weakly bonded to CTZK.

4.3. Conclusions

Chlorothiazide formed a range of intermolecular self-assemblies (ISA) with potassium cations when crystallised from different liquid environment by solvent evaporation.

Potassium cations of CTZK can coordinate up to seven atoms (oxygens of water, oxygens of sulphonyl groups and the chlorine of CTZ molecule). The potassium cations are not bridged by water in CTZK recrystallised from water, whereas a more complex coordinate with two types of crystallographically independent CTZ molecules, is formed in CTZK ISA recrystallised from ethanol (form IV). In the latter, the potassium cations do not coordinate an equal number of atoms (K(1) coordinates seven and K(2) coordinates six). Potassium cations deprotonate the primary sulphonamide groups of CTZ and shift the proton of the secondary amine group in the heterocyclic ring

of CTZ, analogous to results reported for CTZNa (Chapter 3).

The different CTZK forms have different physical stabilities when temperature and/or humidity is changed. Drying form IV leads to evaporation of ethanol present in the crystal lattice, but not water, and transforms the original crystals to a desolvated material (CTZK form V) that has a different Bragg peak pattern compared to CTZK form I (monohydrate). The latter can be obtained by crystallisation from water but is also found to form by direct drying of CTZK form II. DVS analysis showed that CTZK form I had better moisture-related stability than CTZNa monohydrate and was stable up to 60% RH (at 25 °C). The dihydrate (form II) existed over a broad range of relative humidities, 10-90%RH, at 25 °C. Extensive drying of form I results in an anhydrous material (form III) which was seen to be exceptionally moisture sensitive and converted to form I even at a very low humidity of 0.5-0.7% RH in the DVS at 25 °C. This contrasted with the behaviour of CTZNa anhydrous form which was stable up to 20% RH (Chapter 3). The rich solvatomorphism of CTZK presented here is in contrast to some reports that the potassium cation forms hydrated salts less readily than the sodium cation (Remington, 2005). However, the solvates of CTZK seem to be less hygroscopic compared with the hydrated CTZNa, consistent with previously published data (Swarbrick, 2007).

The aqueous solubility of CTZK dihydrate was estimated to be 78.71±1.82 mg/ml, 400-fold higher than that of CTZ (Charnicki et al. 1959), thus indicating a biopharmaceutical advantage for the salt form.

Chapter 5

Impact of spray drying variables: solvent, feed concentration, inlet temperature and drying mode, on the physicochemical and micromeritic characteristics of chlorothiazide

5.1. Introduction

Spray drying is a one-step processing method resulting in the production of a dry powder product. Several available sizes of drying chambers, ranging in cubic capacity from a few to thousands of litres give this process large potential and ease in scaling up from laboratory to industrial scale outputs (Masters, 2002). Fast spray drying, in comparison to other production methods like slow crystallisation, has a potential to be conducted continuously without unnecessary disruptions, bringing high efficiency in terms of production time (Re, 1998). Spray drying gives flexibility in designing expected particle sizes varying in range from millimetres (Masters, 2002) to nano-scale particles (Ditte et al., 2010). Overall, spray drying excludes the necessity for further milling or sieving, therefore minimising possibilities of solid state transformation during those processes (Gonzalez et al., 2009).

Spray drying can result in amorphous (Corrigan et al., 1984) and crystalline products (Islam et al., 2010). Depending on the process conditions, spray drying has the potential to deliver high enough energy to prevent crystal lattice formation. On the other hand, spray drying may also yield conditions suitable for material crystallisation upon solvent drying.

Despite spray drying being well understood and widely investigated (Masters, 2002), some aspects of the process have not been researched to a large extent. One such element is the solvent choice. Many spray drying processes use organic solvents, primarily to improve the solubility of the components to be processed (Kristmundsdottir et al., 1996 and Di Martino et al., 2001). Selection of solvents gives flexibility in designing the production process, as a wide range of solvents or mixtures of solvents can be used. However, how the solvent or solvent mixture impacts on the physicochemical properties of the spray dried material remains poorly understood.

A few references have been published on the impact of feed composition on the production of spray dried polymeric composite microparticles containing active pharmaceutical ingredients: itraconazole (Janssens et al., 2009) and etanidazole (Wang and Wang, 2002). Even fewer reports can be found on the solid-state changes of spray dried single-component materials as a result of solvent change in spray drying feeds. Najafabadi et al., (2004) spray dried sodium cromoglycate from water as an 8% w/v solution and from absolute ethanol as an 8% w/v suspension. An amorphous solid and a crystalline material were obtained, respectively. The two batches differed in relation to particle size and density. The same authors (Gilani et al., 2005) expanded the above work by describing extra samples, based on ethanol/water mixtures, however, they also were suspensions. It was noted that increasing the amount of water from 12.5% to 50% v/v resulted in a decrease in crystallinity of the samples. It was reported that crystals of the active were not formed when a 1:1 ethanol/water mix was used for spray drying and that the presence of water facilitated the solubility of the drug and, overall, the formation of amorphous particles. Addition of ethanol reduced the solubility of the drug and resulted in the formation of crystals. Harjunen et al., (2002) investigated the impact of ethanol to water ratio in the feed solution

on the crystallinity of spray dried lactose and concluded that amorphous lactose was obtained by processing from pure water while 100% crystalline lactose monohydrate was collected after spray drying from pure ethanol.

No systematic and comprehensive studies on the effects of solvent and spray drying parameters on the solid-state nature of the spray dried material have been published to date. The present work aims to address this lack of knowledge and discuss the importance of the process conditions in attaining powders which differ in their solid-state. Chlorothiazide (CTZ) was chosen as a model substance as only one polymorphic form has been shown to exist at ambient conditions, with the other polymorph only being formed at 4.4 GPa (Oswald et al., 2010). This pressure is however too high and not encountered in pharmaceutical industry e.g. for tabletting. Earlier studies on spray drying of this compound from an ethanol/water mixture determined that no polymorphic transition occurred during the process (Corrigan et al., 1984). This compound also has a very high melting point suggesting a low likelihood of thermal decomposition.

This study therefore aims to investigate the impact of spray drying variables, including solvent composition, configuration of the spray dryer, inlet temperature and drug concentration on the solid state nature and morphological characteristics of the spray dried material.

5.2. Results and discussion

5.2.1. Solubility studies of CTZ

Initially, to establish the solubility profiles of CTZ, needed for spray drying studies, solubility studies using a few solvents commonly used for processing were undertaken. Water (as a first choice solvent for spray drying (Masters, 2002)), ethanol, an organic polar solvent, acceptable for use in the open spray drying mode as an alternative to water, and acetone (known to be a relatively good solvent for CTZ (Chapter 3) were selected as solvents for spray drying. CTZ belongs to class IV of the Biopharmaceutics Classification System (low solubility, low permeability) with an aqueous solubility of 0.02 mg/ml (at 37 °C) (Chapter 3). Solubility studies in pure ethanol indicated that CTZ solubility was only slightly higher (~0.07% w/v) compared to pure water (~0.02% w/v), while CTZ solubility in acetone was around 0.9% (w/v) (Table 5.1).

Table 5.1. Solubility studies of CTZ in various solvents.

content of organic solvent (volume %)	water/ethanol mixtures (mg/100 ml)	water/acetone mixtures (mg/100 ml)
0	20 ± 0.0	20±0.0
10	27.5 ± 3.5	32.5±3.5
30	45 ± 7.1	534±21.6
50	190 ± 0.0	120± 14.14
70	340 ± 14.1	1580 ± 254.6
80	325 ± 14.1	5340 ± 113.1
90	145 ± 21.2	5430 ± 240.4
100	67.5 ± 3.5	880 ± 28.3

The results of solubility studies of CTZ are presented in Table 5.1. The ethanolic systems exhibited a maximum solubility at 0.7 ethanol volume fraction of 0.34% (w/v) and the acetone mixtures gave a maximum solubility of CTZ of 5.4% (w/v) at 0.9 acetone volume fraction. The concentration of feed solutions in the different solvent systems was therefore varied depending on the actual solubility of CTZ in the liquid system. Obtained solubility results presented non-linear pattern of solubility of CTZ versus concentration of organic solvent in mixture with water (Fig. 5.1.).

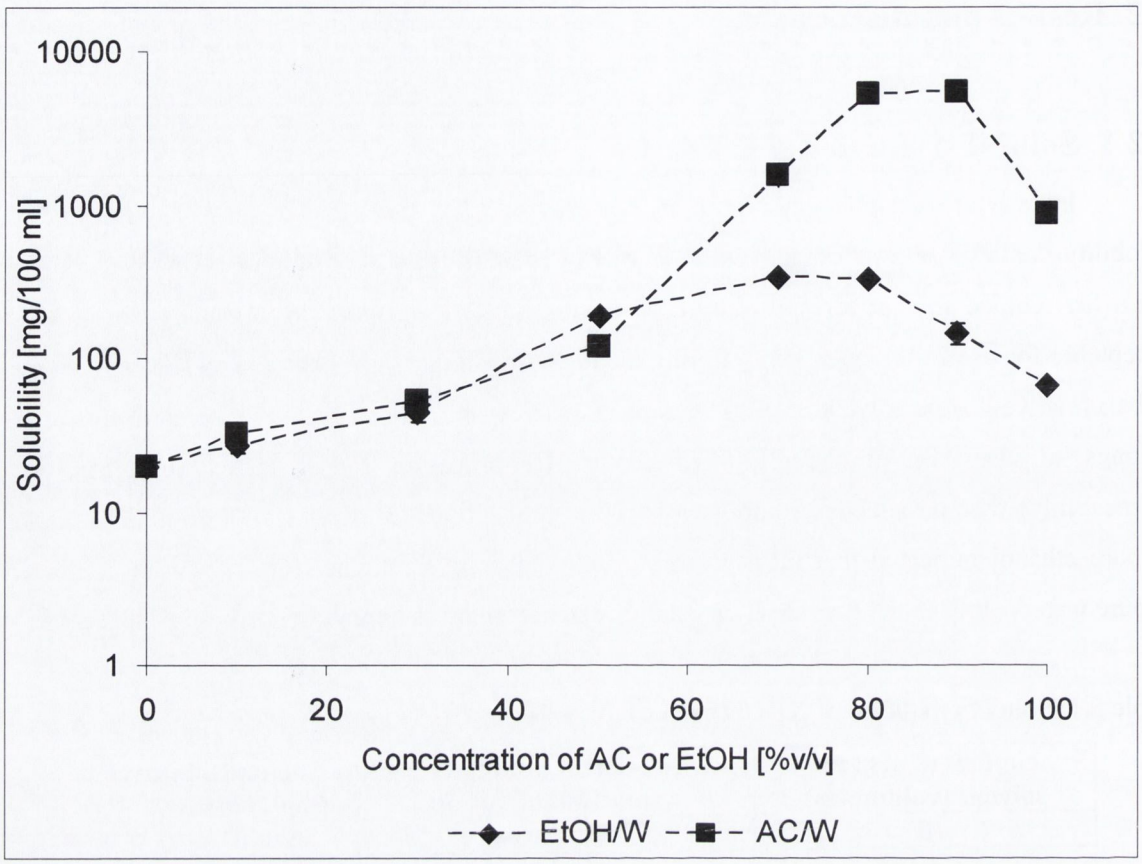

Fig. 5.1. Solubility of CTZ in acetone, ethanol and their mixtures with water.

5.2.2. Spray drying of CTZ

Spray drying was performed as described earlier in Methods (2.2.2.). The conditions of spray drying are listed in table 5.2.

Table 5.2. Spray drying conditions used for CTZ samples.

Sample No #	Solvent system	Feed conc. (% w/v)	Inlet temp (°C)	Outlet temp (°C)	Mode*
#5.1	Raw material	-	-	-	-
#5.2	AC	0.5	80	61	CM
#5.3	AC/W 9:1	0.5	80	53	CM
#5.4	AC/W 7:3	0.5	80	44	CM
#5.5	AC/W 1:1	0.5	80	38	CM
#5.6	AC/W 3:7	0.5	80	32	CM
#5.7	AC/W 9:1	0.5	80	45	OM-S
#5.8	AC/W 9:1	0.5	80	44	OM-B
#5.9	AC/W 9:1	5.0	80	54	CM
#5.10	AC/W 9:1	0.5	100	76	CM
#5.11	AC/W 9:1	2.0	120	99	OM-B
#5.12	EtOH	0.03	100	66	OM-S
#5.13	EtOH	0.03	80	56	CM
#5.14	EtOH/W 9:1	0.03	100	52	OM-S
#5.15	EtOH/W 1:1	0.03	100	46	OM-S
#5.16	EtOH/W 1:9	0.03	100	43	OM-S
#5.17	W	0.02	160	94	OM-S
#5.18	W (feed temp. ~98 °C)	0.1	160	98	OM-S

* OM-S – open, suction mode, OM-B – open, blowing mode, CM- closed mode.

5.2.2.1. Spray drying CTZ from acetone and acetone/water solutions

It was concluded from the solubility studies that acetone and acetone/water mixtures are the best solvent systems to be used in spray drying due to the greatest solubility of CTZ in acetone/water mixtures.

5.2.2.1.1. Impact of solvent composition and feed concentration

Due to the use of acetonic solutions of CTZ as the processing feed, the closed mode configuration was used, as recommended for safety reasons (Büchi 93001 en.). The concentration of CTZ in the liquid was set to 0.5% w/v and kept constant regardless of the acetone content in the mixture. This concentration of CTZ was the highest possible to be used in order to obtain a solution even at low ratios of acetone.

CTZ spray dried from pure acetone (#5.2) was PXRD crystalline. The Bragg peaks pattern was consistent with the starting "as supplied" material (#5.1) powder with only slight differences

in peak intensities (Fig. 5.2). The DSC trace was essentially identical to that of the unprocessed CTZ with one endothermic peak ascribed to melting with an onset at ~370 °C, which compares to an onset of ~363.5 °C for the starting CTZ sample (Fig. 5.3). No other thermal events indicating either residual solvent content or recrystallisation were detected by DSC (Fig. 5.3 b). The enthalpy of melting (fusion) could not be determined due to decomposition of CTZ on melting (36% mass loss by TGA evaluated between onset and endset of melting).

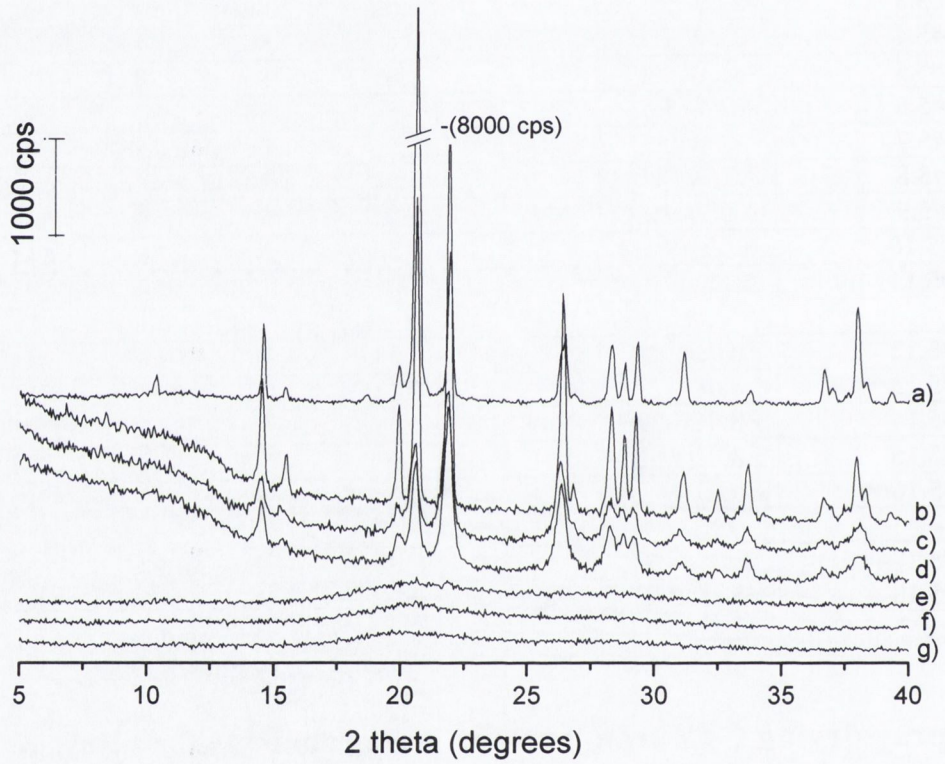

Fig. 5.2. XRD of a) CTZ recrystallised from acetone (#5.1*), b) CTZ starting material (#1), c) CTZ spray dried from 100% acetone in closed mode (#5.2), d) CTZ spray dried from 50% acetone/50% water in closed mode (#5.5), e) CTZ spray dried from 50% acetone/50% water in the open suction mode (#5.7), f) CTZ spray dried from 100% ethanol (#5.12) and g) CTZ spray dried from aqueous boiling solution (#5.18).

To compare the impact of acetone/water ratio on the thermal and solid-state properties of the processed powders, a set of CTZ solutions based on the acetone/water volume ratios of 9:1, 7:3, 5:5 and 3:7 was prepared and spray dried (#5.3-6). The spray dried samples were PXRD crystalline but the relative peak intensities varied depending on the acetone content in the feed. A PXRD pattern of CTZ spray dried from a 1:1 acetone/water mixture (#5.5) is presented in Fig. 5.2c. DSC showed that the melting endotherm of the CTZ samples occurred

sharply at around 370 ˚C and was followed by thermal decomposition of CTZ. The melting point was observed to be steady and did not vary by more than 2 °C for the powders processed from solutions containing 50% v/v and more of acetone. For the 30% acetonic sample (#5.6) the melting point shifted to ~360 °C (Fig. 5.3c, sample #5.5). TGA analysis indicated the residual solvent content for all acetone/water CTZ systems was in the range from 0.1 to 0.6%, and the higher the water proportion in the feed the greater mass loss on drying was noted.

Due to the solubility limits it was impractical to investigate the change of spray drying conditions for each of the solvent composition points. Therefore only the acetone/water 9:1 v/v mix, as the solvent mixture at which the greatest solubility of CTZ was measured, was chosen for further studies. This solvent mix was giving the largest flexibility regarding solid concentration in drying feed. The melting point of a sample spray dried from a 5% w/v solution (#5.9) was ~366 °C, which compares to ~369 °C measured for the 0.5% w/v. PXRD analysis (Fig. 5.2) of samples #5.3 and #5.9 recorded relatively high and comparable Bragg peaks intensities, indicating apparently high crystallinity of these two batches of CTZ.

Changing the inlet temperature of the process did not impact on the solid-state properties of CTZ. The sample spray dried from the acetone/water 9:1 v/v mix at an inlet temperature of 100 °C (#5.10), the same as that used for ethanolic feed solutions (#5.12, #5.14), was crystalline. The peak intensities were however different and the main peak at 22.4 2θ of the powder processed at 100 °C (#5.10) was twice as intense as that of the sample spray dried at 80 °C (#5.3).

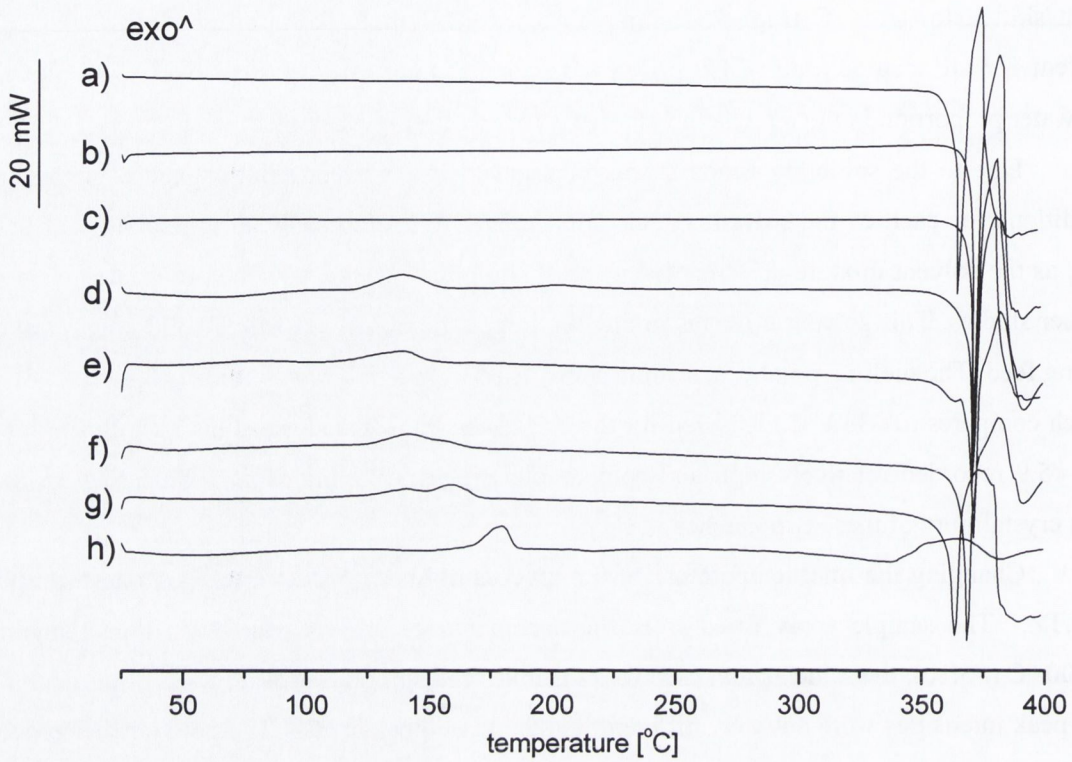

Fig. 5.3. DSC of a) CTZ starting material (#5.1), b) CTZ spray dried from 100% acetone in closed mode (#5.2), c) CTZ spray dried from 50% acetone/50% water in closed mode (#5.5), d) CTZ spray dried from 50% acetone/50% water in open mode (#5.7), e) CTZ spray dried from 100% ethanol (#5.12), f) CTZ spray dried from 50% ethanol/50% water (#5.15), g) CTZ spray dried from aqueous solution kept at room temperature (#5.17) and h) CTZ spray dried from aqueous boiling solution (#5.18).

The solid-state transformations of CTZ were easily identified by DSC and PXRD. All samples, regardless of the solvent and process parameters employed, exhibited a melting event in the DSC scan. This was the sole process visible in the DSC scan for X-ray crystalline CTZ, while all X-ray amorphous powders showed either a single or double exothermic peak. The two exotherms may be assigned to recrystallisation and a solid/solid transition or crystal rearrangement, respectively, similar to the thermal behaviour exhibited by amorphous sulfapyridine (Bottom, 1999).

FTIR presented no visible structural changes occurring in CTZ upon processing and all spectra of the samples spray dried from acetonic solutions (#5.2-11) were superimposable (Fig. 5.4).

The particles spray dried from the 0.5% w/v solutions were spherical in shape with rough, porous surfaces as observed by SEM (Fig. 5.5). Rarely agglomerates were visible and in general the powders were homogeneous with well isolated particles (Fig. 5.5 b-d). The largest pores were evident for the particles spray dried from pure acetone.

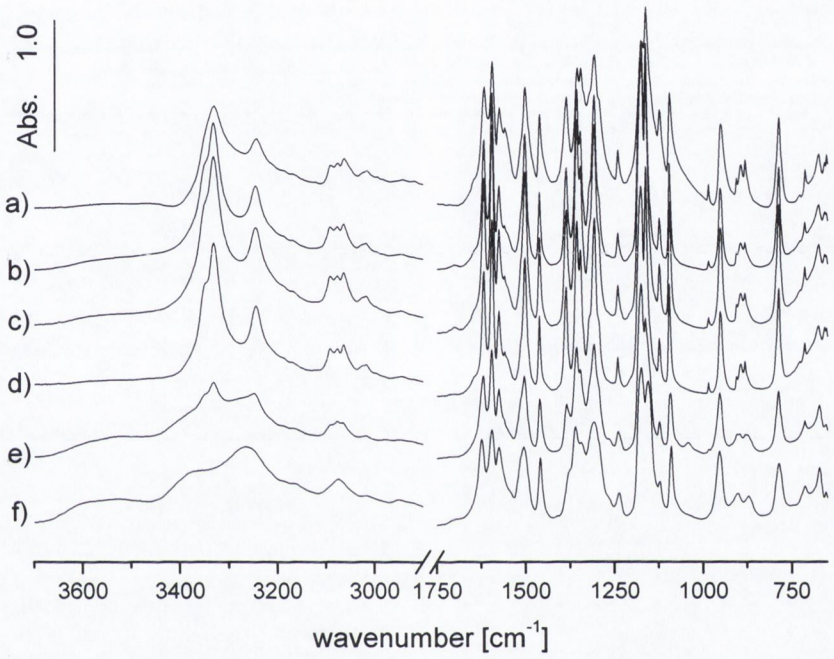

Fig. 5.4. FTIR of a) CTZ starting material (#5.1), b) CTZ spray dried from 100% acetone in closed mode (#5.2), c) CTZ spray dried from 50% acetone/50% water in closed mode (#5.5), d) CTZ spray dried from 50% acetone/50% water in open mode (#5.7), e) CTZ spray dried from 100% ethanol (#5.12) and f) CTZ spray dried from aqueous boiling solution (#5.18).

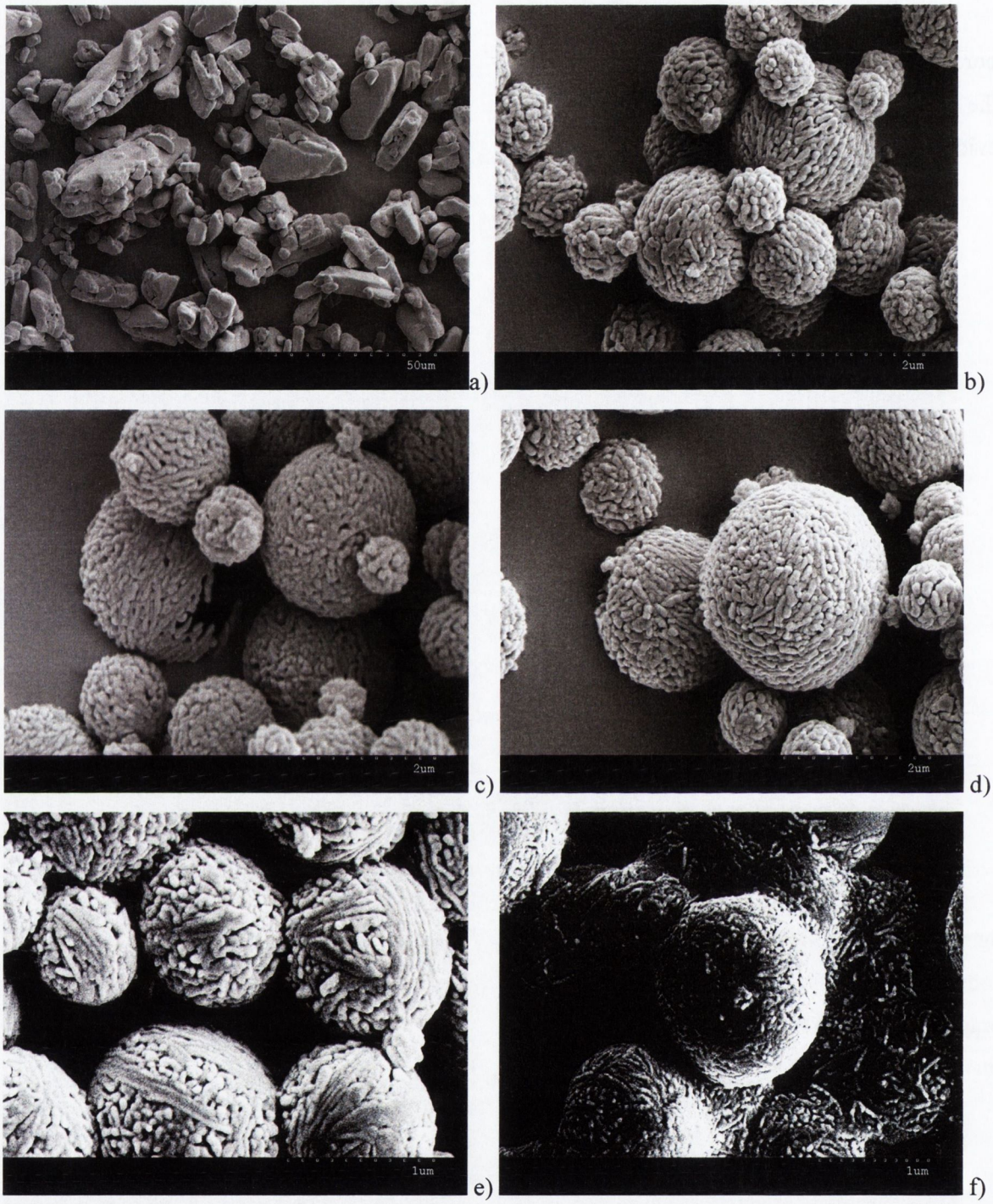

Fig. 5.5. SEM of a) CTZ starting material (#5.1), b) CTZ spray dried from 100% acetone in closed mode (#5.2), c) CTZ spray dried from 90% acetone/10% water in closed mode (#5.3), d) CTZ spray dried from 50% acetone/50% water in closed mode (#5.5), e) CTZ spray dried from 100% ethanol (#5.12) and f) CTZ spray dried from aqueous solution (#5.17).

Specific surface area (T_{BET}) values of CTZ spray dried from acetone/water and from pure acetone (Table 5.3) revealed that spray drying led to an increase in the specific surface area of about 7 (#5.6) to 10 (#5.2) times when compared with the starting CTZ powder (#5.1). Particle

size analysis showed that the solvent type, feed concentration and drying mode did not have a significant effect on the median particle size of spray dried CTZ. The median particle sizes (by laser diffraction) varied between 2.2 and 2.7 μm (Table 5.3). True density values obtained for the spray dried materials (#5.2-6) were significantly ($p<0.05$) lower than that of the unprocessed CTZ sample #5.1 (1.798±0.001 g/cm^3) and varied between 1.756±0.002 to 1.770±0.002 g/cm^3 of (Table 5.3).

Table 5.3. Specific surface area by BET (T_{BET}), by laser diffraction (T_{LD}), median particle size (d(50)) and surface weighted mean particle size (d[3,2]) and true density (d_0) results of CTZ spray dried from AC/W mixtures (abbreviations as Table 5.2).

Sample	T_{BET} [m^2/g]	T_{LD} [m^2/g]	d(50) [μm]	d[3,2] [μm]	d_0 [g/cm^3]
#5.1	0.50±0.00	0.38±0.01	12.6±0.1	8.9±0.2	1.798±0.001
#5.2	5.35±0.07	1.79±0.02	2.7±0.1	1.9±0.0	1.770±0.002
#5.3	4.55±0.07	1.77±0.14	2.6±0.1	1.9±0.2	1.762±0.003
#5.4	3.85±0.07	1.66±0.02	2.7±0.1	2±0.0	1.756±0.002
#5.5	3.50±0.00	1.63±0.01	2.5±0.1	2±0.0	1.753±0.001
#5.6	3.40±0.14	1.73±0.02	2.2±0.1	1.9±0.0	1.756±0.002

HLPC analysis carried out on the samples spray dried from acetonic solutions showed no evidence of chemical decomposition when compared to the starting CTZ material.

5.2.2.1.2. Impact of spray drying mode

A laboratory spray dryer Büchi B-290 can operate in three different modes, as described in Methods. Although the closed mode is recommended to be used when processing from organic solvents, it was of interest to study the effects of changing instrument configuration.

Open mode yielded (both suction and blowing configuration), surprisingly, samples (#5.7, #5.8) that were amorphous (a sample PXRD trace is presented in Fig. 5.2d). This was in contrast to the solid-state nature of CTZ spray dried in the closed mode setting. The halo patterns indicated the amorphous nature of the samples, however a very weak peak at 22.0 2θ could be distinguished for the powder spray dried in the open suction mode. This sample (#5.7) presented two recrystallisation exotherms with onsets at 110 °C (ΔH of 10.2 J/g) and 130 °C (ΔH of 12.5 J/g) and melting at 363 °C, different to that processed in the open blowing mode which presented only one, sharp exotherm with an onset at 110 °C (ΔH of 24.4 J/g) and melting at 368 °C. Also, no glass transition temperature events (Tgs) were observed.

Nonetheless, FTIR presented a spectrum overlapping with those of crystalline samples (both unprocessed CTZ and CTZ spray dried in the closed mode, Fig. 5.4) despite the fact that thermal analysis and PXRD suggested that the samples were predominantly amorphous in nature.

5.2.2.2. Spray drying CTZ from ethanol and ethanol/water and water solutions

Samples spray dried from ethanol (#5.12, #5.13) and ethanol/water mixtures (#5.14-16) (data not shown) were amorphous as determined by PXRD which showed only broad halo patterns as presented, for example on figure 5.2 f. Recrystallisation peaks, but no Tgs, were clearly visible in DSC thermograms (Fig. 5.3 e, f) in contrast to CTZ samples spray dried in the closed mode from acetone/water mixtures where no recrystallisation was observed (Fig. 5.3 b, c). The exotherms were located between around 110 °C and 127 °C (onset temperatures) and their shapes were different depending on the ethanol/water ratio. Some of them were presented as double exothermic events. Enthalpy of recrystallisation varied from ~42.4 J/g (for pure ethanol) to 63.8 J/g (for the 9:1 v/v ethanol/water mix #5.14). The melting points determined by DSC ranged from ~362 °C for the powder spray dried from the 1:9 v/v ethanol/water mixture (#5.16) to ~369 °C for the sample processed from the 9:1 v/v ethanol/water solution (#5.14). The shift of melting points towards lower temperatures may be due to incomplete recrystallisation of the material.

The impact of spray drying in the closed mode configuration was also investigated and the obtained powder (#5.13) was amorphous with a visible, single recrystallisation exotherm with an onset at ~119 °C and melting at ~365 °C.

FTIR spectrum of the sample spray dried from 100% ethanol (#5.12) was more diffuse compared to that of the starting material powder of CTZ (#5.1) and a very broad band between 3500 and 3700 cm^{-1} characteristic of a hydrogen bonding network appeared (Fig. 5.4e). Also, a weak peak at around 1050 cm^{-1} was visible and suggests that residual ethanol may have been left after the process. HPLC, again, revealed no significant chemical degradation of CTZ when spray dried from ethanol ($p>0.05$).

Particles of the CTZ powders formed upon spray drying in the open mode from ethanol (#5.12) had porous exteriors and appeared as having a more compact nature than the particles collected after processing from acetonic solutions in the closed mode (Fig. 4e).

Finally, for comparison purposes, spray drying of CTZ from water was investigated even though the solubility of CTZ in water is very low (0.02% w/v). Initially, a 0.02% w/v solution was prepared and spray dried (#5.17). The feed mixture was kept at room temperature (RT). The powder obtained was PXRD amorphous and the DSC pattern presented a broad, double exotherm with an onset at ~120 °C and peaks at 141 °C (ΔH of 33 J/g) and 159 °C (ΔH of 67 J/g) (Fig. 5.3 g). The onset of melting was at ~361 °C, which was considerably lower than that of the starting material powder. No Tg event was observed.

In order to increase the feed concentration of CTZ, spray drying from a boiling feed solution was investigated. This allowed the solubility of the CTZ in water to be increased to 0.1% w/v. The powder (#5.18), again, was PXRD amorphous (Fig. 5.2g) but with a different DSC trace

compared to that processed from an aqueous solution kept at RT. A clear Tg midpoint was recorded at ~135 °C. This was followed by a single exotherm with an onset at 168 °C (Fig. 5.3 h). StepScan analysis confirmed the location of Tg to be at 135.3±0.6 °C with a specific heat change (ΔCp) of 0.19±0.01 J/g °C. Due to the higher onset of the recrystallisation exotherm in the DSC for CTZ spray dried from hot water, it can be concluded that this sample is more thermally stable than that processed from a solution held at RT, for which the recrystallisation exotherm appeared to overlap with the Tg. The sample spray dried from a hot aqueous solution was also the sample with the highest onset of recrystallisation among all processed batches of CTZ (including the acetonic samples) however, crystalline peaks were detected after 8 hours of storage at RT and relative humidity of about 40% RH, suggesting that the overall physical stability of the sample was poor.

The shifts of absorption bands observed by FTIR for the sample spray dried from water (#5.17) were greater than those observed for the samples spray dried from ethanol (#5.12) and the N-H stretch peaks moved from 3331 and 3245 cm^{-1} to 3360 and 3264 cm^{-1}, respectively. Also, a broad band at 3500-3700 cm^{-1} was noticed, similar to that observed for the samples spray dried from ethanolic solutions, but of a greater intensity. The spectrum was also more diffuse compared to that of CTZ processed from 100% ethanol (Fig. 5.4 f).

CTZ spray dried from water resulted in a powder (#5.17) comprised of spherical and partially fused together particles with a porous morphology (Fig. 5.5 f).

The powder obtained on spray drying from the boiling solution was tested by HPLC for chemical degradation. Only around 90% of intact CTZ was recovered.

5.2.3. Crystallinity of spray dried CTZ

All samples spray dried from either pure ethanol, water or ethanol/water systems were amorphous in nature. Crystallinity of the acetonic CTZ samples was, however, dependent on the spray drier configuration, with the open mode yielding amorphous samples. The samples obtained by processing of CTZ from acetone/water solutions in the closed mode were all crystalline. It was of interest, observing the different peak intensities of CTZ powders spray dried in the closed mode, to evaluate the ability of PXRD analysis to differentiate between the samples and assess the degree of crystallinity with varying acetone/water ratio. The feed concentration was kept constant, therefore only samples processed from 0.5% w/v solutions were investigated.

CTZ recrystallised from acetone (Chapter 3) (henceforth referred to as #5.1*) was chosen as a reference of a fully crystalline sample to calculate the relative crystallinity of the commercial CTZ "as supplied" and CTZ spray dried from the different ratios of acetone and water. SEM of the commercial sample (#5.1) indicated that the material was micronised (Fig. 4a). The PXRD pattern was typical for a micronised sample, with peak positions the same as for sample #5.1*

(Fig. 5.2. a) but with lower intensities. As shown above, the spray dried powders were also crystalline with peak intensities decreased even further compared to the commercial sample. It was therefore apparent that the degree of crystallinity of the processed materials was lower and moreover, it was noted that the peaks broadened compared with the recrystallised CTZ indicating that the crystallite size had also changed (Torrado et al., 1998) as a result of spray drying or micronisation. The Scherrer equation (Eqn. 5.1) was employed to estimate the crystallite size (Torrado et al., 1998):

$$d_{XRD} = \frac{K\lambda}{\beta \cos\theta} \qquad \text{Eqn. 5.1.}$$

Where d_{XRD} is the crystallite size, β is the difference in the full width at half-maximum (FWHM) values of the peaks between broadened and standard maxima, K is a constant (0.89 (Wang et al., 2007)), λ is the wavelength (1.54056 Å) and θ is the diffraction angle. This equation reveals that larger values of FWHM indicate smaller crystallite sizes. However, since no correction for the particle shape was implemented the values obtained are relative rather than the absolute sizes (Torrado et al., 1998).

The percent of relative crystallinity (RC) (Eqn. 5.2) of the spray dried samples was calculated by summing the areas (A_p) of all the peaks of the PXRD pattern of the tested sample (S) and comparing to the commercial sample (Ahn et al., 2002).

$$RC = \frac{100 \cdot \sum_{i=1}^{n} \left(\overline{A}_{pi}\right)_S}{\sum_{i=1}^{n} \left(\overline{A}_{pi}\right)_{\mathrm{Re}f}} \qquad \text{Eqn. 5.2.}$$

In this comparison the commercial, "as supplied" sample was used as a reference rather than CTZ recrystallised from acetone due to the strong preferred orientation effects, as large variability of peak intensities, when compared the PXRD patterns of the recrystallised and commercial powder batches, was observed.

Since spray drying is a process of forming a solid from its solution, it was of interest to investigate if the degree of powder crystallinity is related to the size of crystallites forming particles. A crystallinity index (C_I) was calculated from the FWHM including the average broadening factor for all of the peaks in the PXRD pattern of the tested sample (S) and comparing an inverse of this to micronised CTZ as 100% C_I (Eqn. 5.3).

$$C_I = \frac{100 \cdot \sum_{i=1}^{n} \overline{FWHM}_{i\mathrm{Re}f}}{\sum_{i=1}^{n} \overline{FWHM}_{iS}} \qquad \text{Eqn. 5.3.}$$

The greatest reduction in RC was observed for the sample spray dried from 1:1 v/v AC/W (#5.5) but this system was comparable to that spray dried from pure AC (#5.2) and 7:3 v/v AC/W (#5.4) (Table 5.4). The most crystalline of the spray dried materials was #5.3, CTZ prepared from 9:1 v/v AC/W. The same sample also had the largest crystallite sizes and the greatest C_I. The RC and C_I correlated quite well except for the sample spray dried from 3:7 v/v AC/W- sample (#5.6). This relationship may be expected to be observed for spray dried materials as the crystals are formed *in situ* during the process from solutions, the bottom-up approach, in contrast to micronisation, for example, where larger structures are subjected to mechanical stress leading to breaking up of such particles. The size and number of crystallites formed depends on the process parameters and therefore may reflect the overall degree of crystallinity of such formed material.

It may also be concluded that the reduction in crystallinity observed for the samples was mainly due to crystal defect rather than amorphisation as no exotherm was seen in the DSC traces.

Table 5.4. Comparison of the full width at half-maximum (FWHM, [°]), crystallite size (nm), relative degree of crystallinity (RC), crystallinity index (C_I) and initial solution saturation (S_0) for CTZ recrystallised from acetone (#5.1*), raw material (#5.1) and spray dried CTZ (#5.2-6).

2θ [°] (lattice plane)	**FWHM [°] (crystallite size, [nm])**						
14.50 (010)	0.135	0.160(317)	0.350(47)	0.180(176)	0.260(63)	0.275(57)	0.280 (55)
15.50 (011)	0.165	0.175(783)	0.285(66)	0.210(176)	0.350(43)	0.315(53)	0.415(32)
20.01 (01-1)	0.155	0.155	0.180(319)	0.205(160)	0.195(199)	0.265(73)	0.295(57)
20.73 (002)	0.160	0.180(399)	0.325(67)	0.225(123)	0.290(61)	0.275(69)	0.375(37)
22.00 (111)	0.205	0.180	0.380(46)	0.220(534)	0.360(52)	0.36(52)	0.380(46)
31.21 (121)	0.215	0.275(136)	0.485(30)	0.295(102)	0.330(71)	0.385(48)	0.475(31)
33.80 (11-2)	0.230	0.235(1642)	0.325(91)	0.300(117)	0.605(22)	0.350(68)	0.325(86)
RC (%)	-	100	55	92	57	52	72
C_I FWHM (%)	-	100	58	83	57	61	53
S_0	-	-	0.57	0.09	0.32	0.42	0.94
Sample	**#5.1***	**#5.1**	**#5.2**	**#5.3**	**#5.4**	**#5.5**	**#5.6**

5.2.4. Investigations into the cause of the variable solid-state properties of spray dried CTZ

Having spray dried CTZ from a range of solvents and solvent mixtures, investigating the feed concentration and instrument configuration impact, it is obvious that CTZ can be rendered either amorphous or crystalline, depending on the choice of processing parameters. Spray drying is a process of a solid precipitation which combines two unit operations: crystallisation and drying with a high level of process parameters control. Thus an understanding of the process requires an understanding of conventional crystallisation processes and the very quick evaporation/drying step typical of spray drying.

Factors known to have an effect on crystallisation can be thermodynamic in nature. They include parameters such as boiling/melting points, solute activity (concentration), solute solubility, diffusivity, viscosity etc. (Rodriguez-Hornedo, 2006). In the present work as only one substance is investigated, the solid-state changes observed for different spray dried samples cannot be attributed to differences in the solute properties. The physicochemical characteristics of spray dried material will therefore be dictated by the solvent used and/or process conditions.

Leong (1981) stated that the process of particle formation in spray drying is considered to be a 2-phase process. Firstly, evaporation of the solvent occurs to the onset of crystallisation of the solute and the second phase is the growth of the crystal(s) to the complete evaporation of the solvent. Crystallisation in spray drying will initiate on the surface where the solute concentration is the highest and the concentration gradient is formed as a result of the low diffusivity of the solute. The solution supersaturates substantially before homogenous nucleation occurs. In the context of spray drying Vehring (2008) defined a so called "precipitation window" (τ_p), a time closely related to the time available for the solute to recrystallise. Vehring (2008) stated that for components that do not readily crystallise, the characteristic times associated with crystal nucleation are frequently longer than the τ_p and a partially or fully amorphous solid is formed. The τ_p is defined by Eqn. 5.4.

$$\tau_p = \tau_D - \tau_{sat} = \frac{4r_0^2}{\kappa} \cdot (S_0 E)^{\frac{2}{3}} \qquad \text{Eqn. 5.4}$$

where τ_D is the characteristic droplet drying time, τ_{sat} is the characteristic time to saturation, r_0 is the initial droplet radius, κ is the solvent evaporation rate, S_0 is the initial solution saturation (ratio of initial feed concentration to solubility of the solid) and E is surface enrichment in the solute. The E parameter is further defined as the ratio of the solute surface concentration to the average solute concentration in a droplet.

Equation 5.4 indicates that the larger the droplet size the longer will be τ_d (for a particular solvent composition and solution concentration) and thus the more likely it is that the solute will recovered from the spray drying process as a crystalline material. Since the nozzle used to spray

dry the samples was identical and the solute concentration was low (not exceeding 5% w/v), it is assumed that the droplet size is determined mainly by the surface tension of the solvent. The surface tension, at 20 °C, of water, ethanol and acetone is 72 mN/m, 22 mN/m and 23 mN/m, respectively (Muratov, 1980). Surface tension will decrease with an increase in temperature (e.g. surface tension of water at 150 °C is 48.2 and the surface tension of ethanol at 100 °C is 15.3 mN/m (Muratov, 1980). Based on these surface tension values, the largest initial droplet size (and thus the expected greatest crystallinity) should be for the aqueous CTZ solution. The sample spray dried from water was, however, amorphous in contrast to samples spray dried from acetonic solutions.

The time available to crystallisation can be increased if the rate of evaporation (κ), surface enrichment (E) and the solution saturation (S_o) are decreased. The rate of evaporation is dependent on the solvent or a solvent mix and can be decreased by reducing the effective inlet temperature of the process. The vapour pressure of acetone is 210.5 kPa at 80 °C and 363.6 kPa at 100 °C; the vapour pressure of ethanol is 225.7 kPa at 100 °C, while the vapour pressure of water is 47.4 kPa at 80 °C, 101.3 kPa at 100 °C and 617.7 kPa at 160 °C (Lides and Frederikse, 1995) Comparing the evaporative properties of the solvents at the same temperature (e.g. 80 °C) it can be noted that the rate of evaporation from water is the lowest of the three solvents. However, the rate of evaporation at the inlet temperature used (i.e. 160 °C for water) is greatest for water compared to the other solvents (spray dried at inlet temperatures of 80 °C or 100 °C). This is therefore consistent with the observation that the aqueous sample is amorphous. Following this reasoning, it would be expected that the sample spray dried from 90% acetonic solution at 100 °C would be less crystalline than that processed from the same solvent composition at 80 °C, however the experimental data shows the opposite effect. Surface area increases with an increase in the content of the organic solvent.

The configuration of the spray dryer has a profound effect on the solid-state properties of CTZ as all samples processed in the open mode, with exception of sample #5.11, were amorphous. All acetonic, but not the ethanolic samples were crystalline when dried in the closed loop mode. It is known that the evaporation kinetics in the closed-loop spray dryers is different due to the higher relative content of solvent in the drying gas (Dobry et al., 2009).

According to Eqn. 5.4, surface enrichment (E), defined as the ratio of the solute surface concentration to the average solute concentration in a droplet, and the solution saturation (S_o), described as the ratio of the feed concentration to the solubility of the solute in a given solvent, should be kept low to form samples which are crystalline in nature. The S_o for pure acetone (feed concentration of 0.5% w/v) is 0.57, while that for pure ethanol (feed concentration of 0.03% w/v) is 0.45 and for water (feed concentration of 0.02% w/v) is 1. When 90% acetone/10% water was used, the S_o changes to 0.09 (feed concentration of 0.5% w/v) and 0.9 (feed concentration of 5% w/v). No differences in crystallinity were observed for the latter case when the feed concentration

differed 10-fold, but the changes in S_0 seem to follow the trend of changing crystallinity when the impact of acetone content in the feed was investigated (Fig. 5.6) (Section 5.2.2.1.).

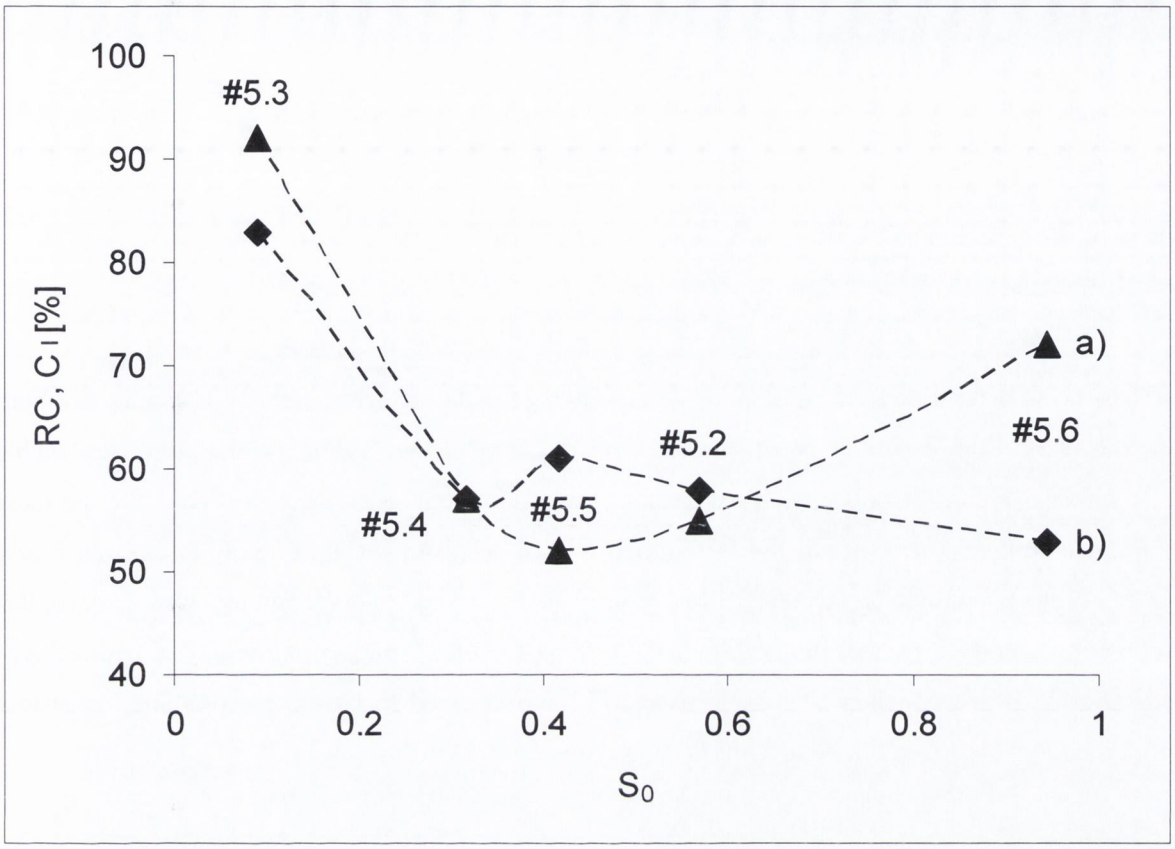

Fig. 5.6. Initial solution saturation (S_0) versus a) relative crystallinity (RC) (triangles) and b) crystallinity index (C_I) (diamonds).

The molecular recognition factors that also may affect the crystallinity of the spray dried product include specific interactions between the solute and solvent molecules and their abilities to form molecular networks (Rodriguez-Hornedo, 2006). A functional group (here from a solvent molecule) with a high affinity to a particular chemical group of the crystallising API ensures the anchoring of the molecule on a particular face and this protects the surface from coalescing with the next. The mechanism could be based on either electrostatic repulsion or steric hindrance and may lead to the inhibition of growth of a crystal face.

The solvents used in this work possess different properties as regards their polarity and H-bond donor/acceptor characteristics. Acetone can only be an H-acceptor (due to the C=O), ethanol has an –OH group that could be either an H-donor or H-acceptor and water is known to be a strong H-donor and acceptor. The dielectric constants (related to the polarity of the solvent molecules) and Hansen solubility parameters for the CTZ and solvents are summarised in Table 5.5.

Table 5.5. Hansen solubility parameters and dielectric constants of CTZ and solvents investigated. The solubility parameters (Hancock et al., 1997) of CTZ were calculated as specified earlier (Tajber et al., 2005).

Substance	Dielectric constant	Total solubility parameter (δ_t) [$MPa^{1/2}$]	Dispersion component (δ_d) [$MPa^{1/2}$]	Polarity component (δ_p) [$MPa^{1/2}$]	H-bond component (δ_h) [$MPa^{1/2}$]
CTZ	-	26.0	22.0	6.3	12.4
Acetone	20.5	19.2	15.5	10.4	7.0
Ethanol	24.9	26.2	15.8	8.8	19.4
Water	78.4	48.0	15.3	16.0	42.3

It has been determined earlier that CTZ has a crystal lattice very rich in H-bonds resulting in the very high melting point of this substance (Chapter 3). It is therefore reasonable to hypothesise that the solvent with a greater H-bond donor/acceptor capacity will have the most influence on the crystallinity of the spray dried CTZ. Therefore, if CTZ is spray dried from water, an amorphous sample is expected to be obtained due to interactions of water molecules with H-bond donor/acceptor moieties of CTZ, thus inhibiting nucleation and/or growth of API crystallites. However when acetone is used, CTZ is presumed to be more crystalline, consistent with the low H-bond component of the solubility parameter for this solvent.

5.3. Conclusions

Choice of solvent used for spray drying, apart from determining usable feed concentration, has a profound effect on the physicochemical and micromeritic properties of the spray dried powder. These properties may also be affected by the spray dryer setup (open or closed mode) and processing parameters such as the inlet temperature. PXRD analysis proved useful in the assessment of differences in relative crystallinity and the crystallinity index of chlorothiazide powders spray dried from different solvents and using different process parameters. All assessed parameters have an impact on the precipitation window. Solvent choice determines the initial concentration of the solute. The greater is the solute concentration the shorter is the precipitation window, promoting the production of the amorphous form of solid. The faster the evaporation rate of the solvent used, the smaller is the precipitation window, thus the open mode of drying without recirculation of traces of not-recovered solvent vapours together with higher inlet temperature promotes the recovery of an amorphous form of the solid. The production of the crystalline form of a given API in a spray drying process may be promoted or inhibited due to API/solvent interactions.

Chapter 6

Impact of spray drying variables on morphology of microparticles of chlorothiazide sodium and potassium salts

6.1. Introduction

Particles characterised by a porous morphology have been reported to have advantageous properties over non-porous materials when formulated in a variety of dosage forms. Hirst et al. (2002) described favourable pulmonary deposition of micron-sized porous particles produced by spray drying from emulsions (Pulmospheres^{TM}). The microparticles formed stable homodispersions in propellant systems when formulated as pressurised metered dose inhalers (pMDIs). Dellamary et al. (2000) reported a better physical stability of suspension pMDIs containing porous particles over conventionally micronised materials. Nolan at al. (2011) reported favourable aerodynamic properties of spherical nanoporous microparticles (NPMPs) of sodium cromoglicate formulated as a dry powder inhaler (DPI) over non-spherical NPMPs, nonporous spray dried microparticles and micronised (milled) drug. NPMPs were reported to present a large specific surface area. Materials with a large surface area usually present favourable compaction properties, facilitating dry roller compaction or/and direct compression in tabletting. Korhonen et al. (2002) reported that large specific surface area together with high moisture content was a favourable property of starch acetate used in direct compression, especially for small particles of irregular and rough surface morphology. Thus large surface area/porous materials may be considered to be useful as binders in tablet formulations. Materials with large specific surface areas and porosity may also be used as efficient carriers for liquids. Such a possibility was exploited by Carretero et al. (2009), who successfully incorporated both hydrophobic and hydrophilic emulsions into porous, solid matrix-carrier (hydroxyapatite). Takeuchi (2005) reported that rapidly dissolving tablets containing a solid dispersion of indomethacin and porous silica particles produced by co-spray drying presented favourable dissolution properties over tablets prepared from physical mixtures of indomethacin and porous silica. Additionally, the tensile the strength of tablets comprising the co-spray dried system was much higher than that of tablets containing the physical mix.

NPMPs are novel types of particles produced by spray drying. Production and characterisation of excipient-free NPMPs was first reported by Healy et al. (2008) who stated that NPMPs of hydrophobic bendroflumethiazide could be obtained by spray drying from mixed solvent solutions (methanol/water or ethanol/water) containing ammonium carbonate as a pore forming and process enhancing agent. The API feed concentration was 2% w/v and resulted in the production of an amorphous powder consisting of particles with visibly porous morphologies. Later, in 2009 Nolan et al. reported the production of budesonide NPMPs for pulmonary delivery. These NPMPs were spray dried from 1% w/v ethanolic solutions with and without ammonium carbonate using a Büchi-290 spray dryer in the open drying mode (where the drying gas passes once through the spray dryer and then is released to the atmosphere). Attempts to obtain budesonide NPMPs from methanol/water solutions by spray drying in the closed mode (where the drying gas is recirculated through the spray dryer) failed and resulted

in non-porous material. The failure was attributed to worse solvent evaporation conditions in the closed drying mode. The largest specific surface area was obtained for budesonide NPMPs spray dried from an ethanolic solution in the open mode and was 10.5 m^2/g. Ni Ógáin et al. (2011) described for the first time the preparation of NPMPs of hydrophilic materials, i.e. carriers of raffinose and trehalose. Due to the hydrophilic nature of these materials, the sugars were spray dried from methanol (MeOH)/butyl acetate (BA) solvent systems mixed at different proportions such as 1:1, 3:2, 7:3, 4:1 and 9:1 v/v MeOH:BA. The feed concentrations used were low and were 0.5% w/v for trehalose and 1% w/v for raffinose. Also, the drying process was carried out in the closed mode in contrast to the earlier ethanolic systems. The largest specific surface area measured for both sugars was approximately 44 m^2/g. The largest specific surface area of an NPMP system reported to date was for another hydrophilic material, sodium cromoglicate, and was 98 m^2/g (Nolan et al., 2011). In this case a very low active pharmaceutical ingredient (API) concentration of 0.3% w/v was used and the solvent system employed was a mix of MeOH and BA.

The above studies on NPMPs indicate that particles with porous morphology and large specific surface area can be obtained, especially when the solvent system is MeOH/BA. The impact of feed concentration has not been investigated to date, although studies on spray drying suggest that this factor may have an impact on the physicochemical properties of the particles formed (Vehring et al., 2007). The spray dryer configuration (open versus closed mode) was investigated by Nolan et al. (2009) for the ethanol/water combination, but this was not assessed for the MeOH/BA system, because of safety considerations.

The production and characterisation of chlorothiazide sodium (CTZNa) and potassium (CTZK) have extensively been presented in Chapters 3 and 4 and these two APIs were chosen as model hydrophilic compounds. Their good aqueous solubility and hydrophilic nature indicates, on the basis of previous studies (Ní Ógáin et al., 2011; Nolan et al., 2011), that NPMPs should be obtained by spray drying from MeOH/BA solvents system. The goals of this work were therefore to investigate if it was possible to obtain NPMPs of hydrophilic model compounds from a feed concentration higher than that reported to date (1% w/v) and to systematically assess the impact of the feed concentration, MeOH/BA solvent ratio and spray drying mode on morphology and other micromeritic properties including surface area of the NPMPs produced. Also, despite spray drying being a widely used technological process for the production of microparticles, no systematic classification of the morphology of sprays dried particles has been introduced to date. In the context of the present work we introduce a morphology classification system which may be applied to all spray dried microparticles.

6.2. Results and discussion

6.2.1. Spray drying

Spray drying conditions for CTZNa and CTZK are listed in table 6.1.

Table 6.1. Spray drying conditions for CTZNa and CTZK samples. Sample numbers in this table correspond to samples numeration in the text. C_{MeOH} is the concentration of MeOH in the MeOH/BA solvent mixture.

Sample (No #)	Solvent system	C_{MeOH} (%v/v)	Feed conc. (% w/v)	Inlet temp (°C)	Outlet temp (°C)	Mode*
#6.1. CTZNa	Water	-	2.0	160	99	OM-S
#6.2. CTZK	Water	-	2.0	160	101	OM-S
#6.3. CTZNa	MeOH/BA	30	0.5	120	87	CM
#6.4. CTZNa	MeOH/BA	40	0.5	120	92	CM
#6.5. CTZNa	MeOH/BA	50	0.5	120	97	CM
#6.6. CTZNa	MeOH/BA	60	0.5	120	98	CM
#6.7. CTZNa	MeOH/BA	70	0.5	120	98	CM
#6.8. CTZNa	MeOH/BA	80	0.5	120	98	CM
#6.9. CTZNa	MeOH/BA	90	0.5	120	99	CM
#6.10. CTZNa	MeOH	100	0.5	80,100	75,87	CM
#6.11. CTZK	MeOH/BA	60	0.5	120	97	CM
#6.12. CTZNa	MeOH/BA	30	2.0	120	98	CM
#6.13. CTZNa	MeOH/BA	40	2.0	120	98	CM
#6.14. CTZNa	MeOH/BA	50	2.0	120	98	CM
#6.15. CTZNa	MeOH/BA	60	2.0	120	99	CM
#6.16. CTZNa	MeOH/BA	70	2.0	120	100	CM
#6.17. CTZNa	MeOH/BA	80	2.0	120	101	CM
#6.18. CTZK	MeOH/BA	30	2.0	120	98	CM
#6.19. CTZNa	MeOH/BA	30	2.0	120	99	OM-B
#6.20. CTZK	MeOH/BA	30	2.0	120	99	OM-B

* OM-S – open, suction mode, OM-B – open, blowing mode, CM- closed mode.

6.2.2. Morphology and micromeritic properties of spray dried CTZNa and CTZK

Different morphologies of the spray dried particles were observed when spray drying conditions and solvent type were varied (Fig. 6.1). Therefore, to facilitate the description of the different appearances, a systematic and easy classification system describing the morphology was developed. It is referred to as a Morphology Classification System (MCS) for spray dried (SD) compounds (MCS-SD) (Table 6.2). Firstly, the MCS-SD describes the class of morphology, here it recognises 5 different classes from I to V. Secondly, the system introduces a code describing the shape of particles: 1 for generally spherical and 2 for irregular, non-spherical shape of particles. The third symbol indicates the surface description: A for smooth surface particle and B for crumpled particles. The last symbol describes the interior of the particles and it is possible to describe: S for solid/non-hollow, H for hollow and X for unknown.

Extensive characterisation of the sodium and potassium CTZ salts in their various solid-state forms was previously reported (Chapters 3 and 4). The dihydrated forms of CTZNa and CTZK were chosen in this study for spray drying from water due to ease of material preparation and their known physical stability at ambient temperature in the range of humidities from 10 to 90% RH (Chapters 3 and 4).

CTZNa (Fig. 6.1a) and CTZK (Fig. 6.1b) materials spray dried from water consisted of microparticles spherical in shape. CTZNa microparticles had smooth surfaces classified as I1AS (Table 6.2), while CTZK particles had a slightly crumpled morphology classified as I1BS (Table 6.2), as additional imaging of spray dried samples #6.1 and #6.2, after grinding in agate mortar revealed interiors of microparticles to be solid (Fig. 6.1 c, d). It is suspected that the crumpling in this case is not related to the saturation of the API in the solution feed, as hypothesised by Vehring et al. (2007), because the reported aqueous solubilities of both salts are very similar (Chapters 3 and 4). The difference in morphology may be attributed to a higher degree of plasticity of CTZK, reflected in the lower Tg of this material (CTZNa: ~192 °C, CTZK: ~160 °C). It has been reported that materials with lower Tgs have higher tendency to crumpling (Masters, 2002).

Table 6.2. Morphology Classification System of Spray Dried Particles (MCS-SD).

Morphology type	Description of morphology	Sample example #No
Porosity		
I	Non-porous	#6.1, #6.2, #6.9, #6.10, #6.17.
II	Porous with nano-sized pores	#6.3-5, #6.8
III	Porous pumice-like	#6.15, #6.16
IV	Porous sponge-like	#6.6, #6.7, #6.11.
V	Porous, conglomerates of nanoparticles	#6.12-14, #6.18-20.
Shape		
1	Spherical	#6.1-7, #6.10, #6.18-20
2	Non-spherical, irregular	#6.8, #6.9, #6.11-17
Surface		
A	Smooth	#6.1, #6.9, #6.17
B	Crumpled	#6.2-8, #6.10, #6.11-16
Interior		
S	Solid/non-hollow	#6.1, #6.2, #6.10, #6.19, #6.20, #6.3-5, #6.8, #6.9, #6.12-20
H	Hollow	N/A
X	Unknown	#6.6, #6.7, #6.11.

The true density of amorphous CTZNa microparticles (Table 6.3. #6.1) was 1.837±0.015 g/cm^3. The specific surface area by BET was 1.3±0.0 m^2/g and the median particle size (d(50)) by laser diffraction was 2.6±0.1 μm. The true density of amorphous CTZK microparticles (Table 6.3. #6.2) was 1.872±0.003 g/cm^3, significantly higher than that for CTZNa ($p<0.05$). The crumpled morphology of CTZK particles did not result in a change of specific surface area of the powder. It was measured to be 1.3±0.0 m^2/g, the same as for sample #6.1. The median particle size of CTZK of 3.1±0.1 μm was slightly larger than that of CTZNa.

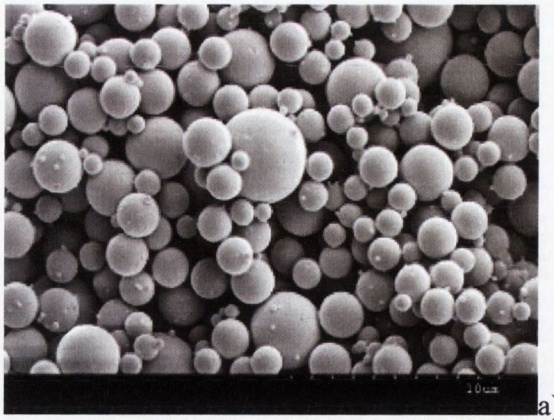

a)

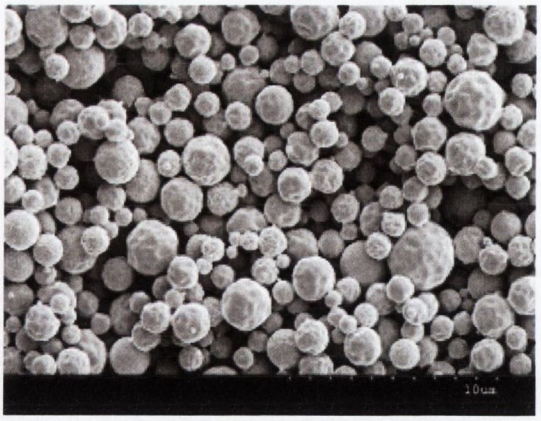

b)

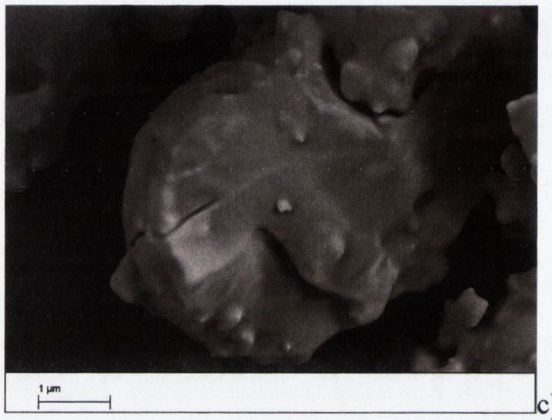

c)

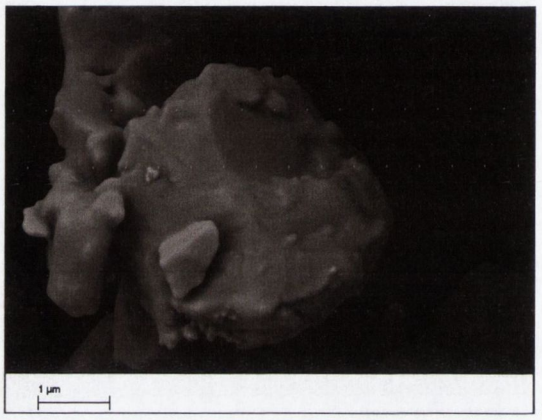

d)

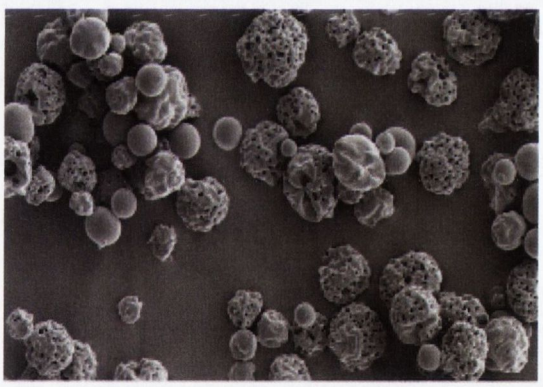

e)

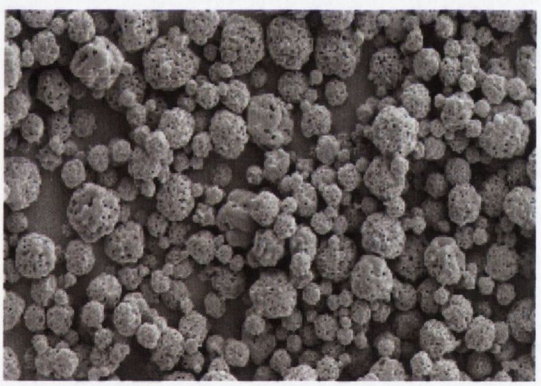

f)

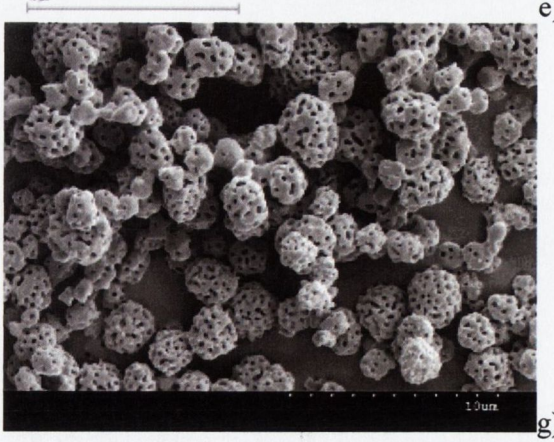

g)

h)

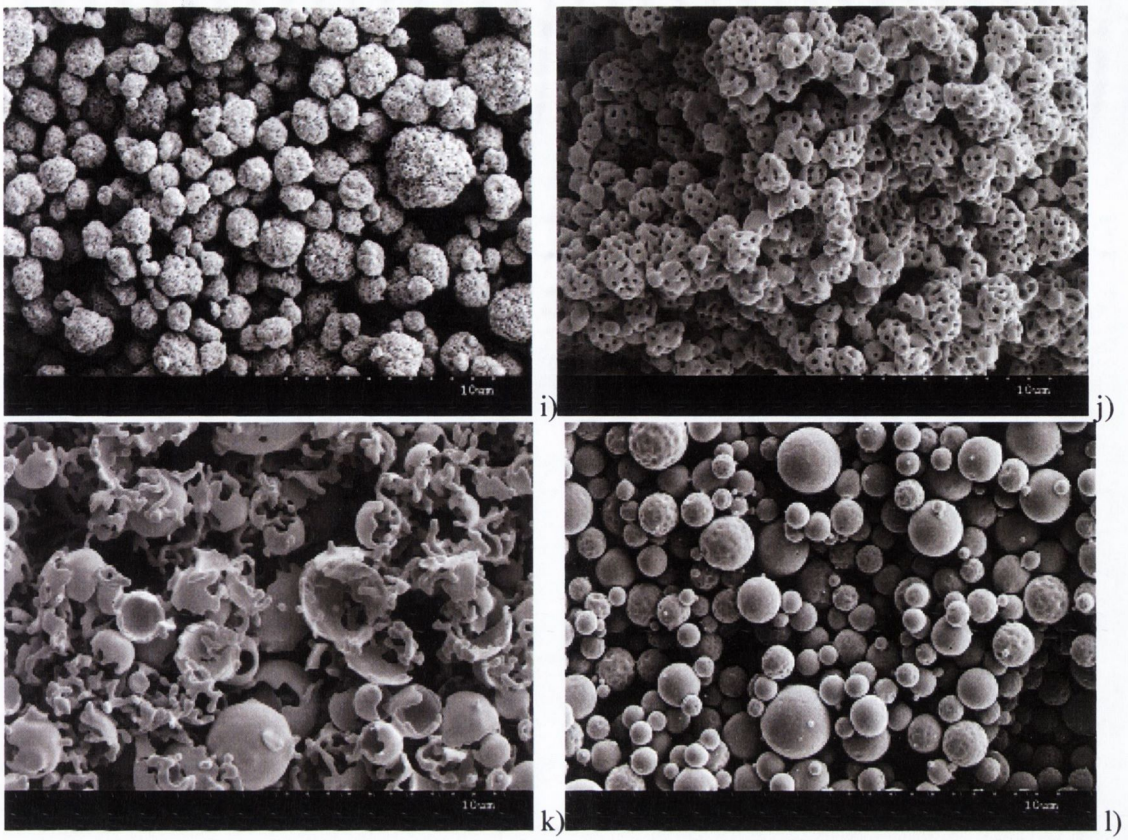

Fig. 6.1. SEM of CTZNa and CTZK spray dried samples: a) sample #6.1 (I1AS), b) sample #6.2 (I1BS), c) ground sample #6.1, d) ground sample #6.2 e) sample #6.3 (I1B+II1BS), f) sample #6.4 (II1BS), g) sample #6.5 (II1BS), h) sample #6.6 (IV1BX), i) sample #6.7 (IV1BX), j) sample #6.8 (II2BS), k) sample #6.9 (I2AS) and l) sample #6.10 (I1AH+I1BH).

To spray dry from MeOH/BA solvent mixtures, CTZNa and CTZK were used in the anhydrous forms, in order to prevent introducing another solvent (water) to the spray drying feed. It was previously reported (Ní Ógáin at al. 2011) that nanoporous microparticles (NPMPs) of a hydrophilic system can be formed by precipitation of the solid in a less volatile solvent (antisolvent, BA) when the more volatile solvent (MeOH) is evaporated.

Table 6.3. Specific surface area, particle size and true density results of CTZNa and CTZK spray dried from methanol/butyl acetate mixtures.

Sample	Specific surface area [m^2/g]	Median particle size [μm]	True density [g/cm^3]
#6.1. CTZNa	1.3±0.0	2.6±0.1	1.837±0.015
#6.2. CTZK	1.3±0.0	3.1±0.1	1.872±0.003
#6.3. CTZNa	33.2±0.2	1.8±0.0	1.744±0.002
#6.4. CTZNa	34.8±0.2	1.7±0.1	1.734±0.004
#6.5. CTZNa	36.7±0.1	1.7±0.0	1.722±0.003
#6.6. CTZNa	66.2±0.2	1.9±0.1	1.727±0.004
#6.7. CTZNa	65.1±0.4	2.0±0.1	1.757±0.003
#6.8. CTZNa	34.8±0.3	2.1±0.1	1.747±0.002
#6.9. CTZNa	26.9±0.4	3.4±0.0	1.719±0.027
#6.10. CTZNa	3.7±0.1	1.6±0.0	1.473±0.001
#6.11. CTZK	57.2±0.5	2.0±0.1	1.862±0.004

Different morphologies of the processed CTZNa with different degrees of porosity were observed with a change in solvent ratio (Fig. 6.1. samples #6.3.-#6.9.) and classified in Table 6.2. The change in morphology was reflected in the increased surface area of these powders (Table 6.3). Sample #6.10 spray dried from 100% methanol (I1AH+I1BH of MCS-SD) had the smallest specific surface area (of those samples spray dried from non-aqueous solvent) of about 3.65±0.07 m^2/g, as it did not form porous particles (Fig. 6.1. l sample #6.10). The specific surface area of sample #6.10 was three times larger than that of sample #6.1 spray dried from pure water, most likely due to slight crumpling and/or lower particle size (Table 6.3).

The porosity of particles did not impact on the measured particle size. For example, sample #6.10 spray dried from 100%MeOH and CTZNa spray dried from a MeOH/BA 1:1 v/v mixture (#6.5- II1BS of MCS-SD) had similar median particle sizes of 1.6 and 1.7 μm, respectively. Overall, the median particle sizes for the CTZNa powders varied between 1.7 and 3.4 μm (Table 6.3).

The specific surface area by BET of the processed samples #6.1-10 showed that the largest surface area was determined for sample #6.6 (dried from a 3:2 v/v MeOH/BA mix) followed by sample #6.7 spray dried from a 7:3 v/v MeOH/BA solutions with only a slightly, but significantly ($p<0.05$) lower surface area (Table 6.3). Samples #6.6 and #6.7 presented morphology type of IV1BX of MCS-SD. The smallest surface areas were measured for samples #6.9 and #6.10 spray dried from a 1:4 v/v MeOH/BA solvent mix and from pure methanol, respectively (Table 6.3). The particles of sample #6.9 were non-spherical, resembling shattered hollow and porous shells (Fig. 6.1k.) classified as I2AS, while sample #6.10 was made of spherical but crumpled (I1AH) and smooth (I1BH) particles. A content of at 20% v/v or less of BA was found to be critical for the formation of porous particles (Fig. 6.1j, #6.8- II2BS). True density of the sample spray dried

from methanol (#6.10) was significantly lower ($p<0.05$) than density of any CTZNa sample spray dried from mixed solvent systems (Table 6.3).

The feed composition which resulted in the largest surface area for CTZNa was also utilised with CTZK. Anhydrous CTZK at 0.5% w/v concentration was spray dried in the same conditions as those used for sample #6.6 from a 3:2 v/v MeOH/BA solvent system. The resulting CTZK sample was named #6.11. Particles of #6.11 were spherical and porous with similar morphologies to sample #6.6 classified as IV1BX of MCS-SD (Fig. 6.1h). BET analysis of the spray dried material determined a specific surface area of 57.2±0.5 m^2/g. The median particle size was 2.0±0.1μm while the measured true density was 1.862±0.004g/cm^3, slightly lower in comparison to sample #6.2 spray dried from water.

6.2.3. Effect of increasing feed concentration and spray dryer configuration on CTZNa and CTZK particle morphology

The production of NPMPs from a solution containing 0.5% w/v of solids resulted in only 50 to 60% of the recovered dry material (batch size approximately 1 g). An increase in the batch size to 10 g and higher required production yields greater than 60%. Low yield values would result in the loss of large amounts of processed material and clogging of the filter. One of the most important process parameters, impacting directly on the production yield is the feed concentration (Goula and Adamopoulos 2004). Therefore the feed concentration was increased, to the highest possible concentration not resulting in precipitation of the solid during feed preparation in ambient conditions. Experimentally this was established to be 2% w/v of anhydrous CTZNa or CTZK in MeOH. Addition of BA did not result in precipitation during processing (samples #6.12-#6.20). Production yield was thus increased to 75-80%. The change in feed concentration resulted in a decrease in T_{BET} of the spray dried CTZNa from 66.2±0.2 m^2/g (sample #6.6) to approximately 42.6±0.4 m^2/g (sample #6.15- III2BS) when spray dried from 2% w/v solutions (Table 6.4). Readjustment of the optimal MeOH/BA ratio was thus required. It was hypothesised that, in order to obtain the largest possible surface area, the proportion of the anti-solvent (BA) should be increased with an increased concentration of the solid in the solvent (MeOH). It is hypothesised, the solid dissolved in the solvent/antisolvent mixture, due to solvent evaporation starts to precipitate in the liquid environment of antisolvent (BA) (Fig. 6.2. 1a and 2 a). In each point of volume of the BA where spontaneous precipitation of solid occurred due to MeOH evaporation, occurs formation of nanoparticles suspended in BA (Fig. 6.2. 1b and 2b) and they grow until precipitation of solid and evaporation of MeOH is finished (Fig. 6.2. 1c). Finally due to secondary evaporation of BA, nanoparticles stick together forming microconglomerate described as morphology of type V (Fig. 6.2. 1d). If the volume of BA is insufficient, nanoparticles merge during growth (Fig. 6.2. 2c) prior to final precipitation of solid and final evaporation of MeOH, forming morphologies of types: IV, III or II (Fig. 6.2. 2d).

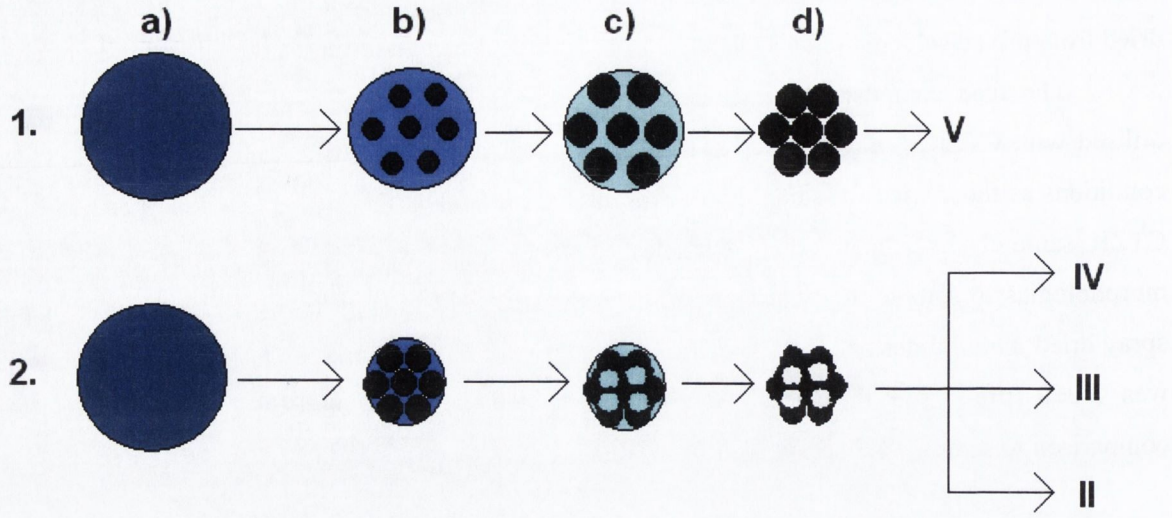

Fig. 6.2. Schematic formation of nanoporous microparticles. 1. Morphology of type V. 2. Morphology of types: IV, III and II. 1a, 2a- droplet stage, 1b, 2b- precipitation of solid phase (black), 1c- Suspension stage of nanoparticles in BA, 2c- Bridging stage (bridging of nanoparticles due to further solid precipitation) 1d- Microconglomeration stage- final evaporation of BA and consolidation of nanoparticles , 2d- Evaporation stage- final evaporation of BA. The brightening gradient of blue colour mimics reduction of concentration of solid in volume of solvent until final evaporation of solvent- white voids remaining.

Therefore, by changing only the proportion of the solvents, the greatest porosity and the specific surface area was obtained for the materials spray dried in the closed mode from 3:7 v/v MeOH/BA mixture - sample #6.12 (Table 6.4) classified as V2BS. For this sample, the change in concentration of the solid in the feed from 0.5% to 2.0% changed remarkably the class of morphology from I+II (#6.3) to class V.

In general, increasing the ratio of MeOH:BA resulted in a reduction of porosity (as assessed from SEM) and non-porous materials were obtained when the MeOH/BA ratio was 7:3 and 4:1 v/v (samples: #6.16- III2BS, #6.17- I2AS, Fig. 6.3). Exceptionally, the sample spray dried from the MeOH/BA 3:2 v/v mix (#6.15- III2BS) resulted in a larger surface area than that spray dried from MeOH/BA 1:1 v/v (#6.14- V1BS). An SEM image of #6.15 showed visually reduced porosity (class III of MCS-SD) in comparison to sample #6.14 (Fig. 6.3- class V). Most likely the difference in T_{BET} was related to the non-spherical shape of the particles (class B of MCS-SD) constituting system #6.15, while #6.14 remained spherical belonging to class A of MCS-SD.

Table 6.4. Micromeritic parameters of NPMPs spray dried from 2% v/v solid concentration and in open blowing mode

Sample	Specific surface area [m^2/g]	Median particle size [μm]
#6.12 CTZNa	52.6±0.5	2.2±0.1
#6.13 CTZNa	35.7±0.3	2.1±0.0
#6.14 CTZNa	31.5±0.3	2.1±0.1
#6.15 CTZNa	42.6±0.4	2.4±0.2
#6.16 CTZNa	40.4±0.4	2.9±0.2
#6.17 CTZNa	38.5±0.2	2.7±0.1
#6.18 CTZK	72.0±0.6	2.1±0.1
#6.19 CTZNa	72.3±0.7	2.9±0.0
#6.20 CTZK	90.2±0.9	3.1±0.1

The 3:7 v/v MeOH/BA solvent composition resulted in specific surface area values of 52.6±0.3 m^2/g and 72.0±0.6 m^2/g for CTZNa (sample #6.12- V1BS) and CTZK (sample #6.18- V1BS), respectively. Attempts to spray dry CTZK form I (monohydrate) (Chapter 4) from the 3:7 v/v MeOH/BA mixture resulted in achieving only a 1% w/v feed concentration being achieved and a decreased surface area (of 33.5±0.3 m^2/g) when compared to sample #6.18.

Further process modification included changing the mode of the spray dryer from the closed to the open, blowing system (as described in Methods 2.2.2.) to ascertain the feasibility of processing in a configuration similar to that used on an industrial scale (Masters 2002). This modification resulted in a further significant improvement in the production yields to 90-95% (samples #6.19 and #6.20, both classified as V1BS). An additional increase in specific surface area of the materials to 72.3±0.7 and 90.2±0.9 m^2/g for CTZNa (sample #6.19) and CTZK (sample #6.20), respectively, was also seen (Table 6.4, Fig. 6.4. I).

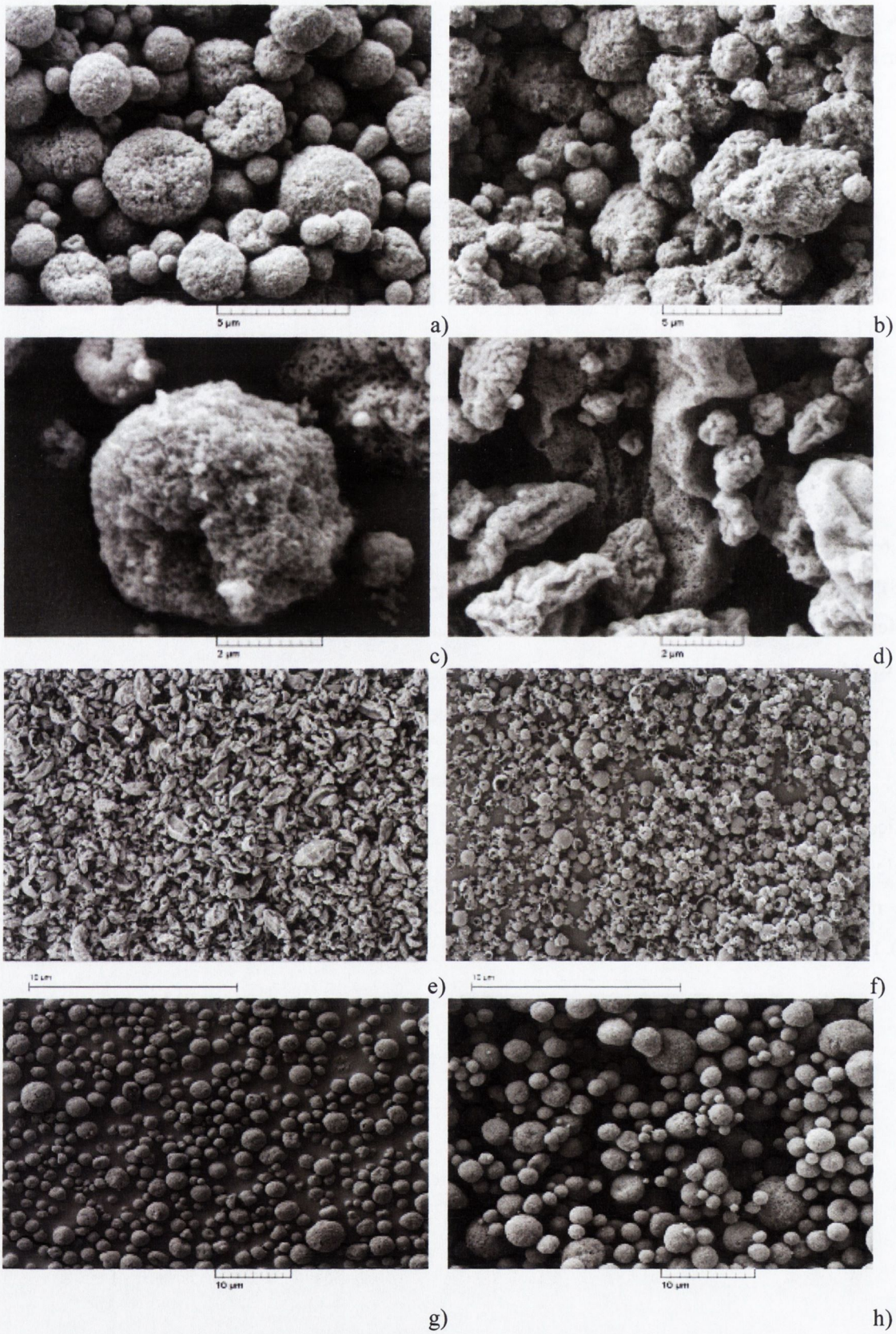

Fig. 6.3. SEM of CTZNa spray dried systems: a) sample #6.12 (V2BS), b) sample #6.13 (V2BS), c) sample #6.14 (V1BS), d) sample #6.15 (III2BS), e) sample #6.16 (III2BS) and f) sample #6.17 (I2AS), g) sample #6.19 and h) sample #6.20, both V1BS.

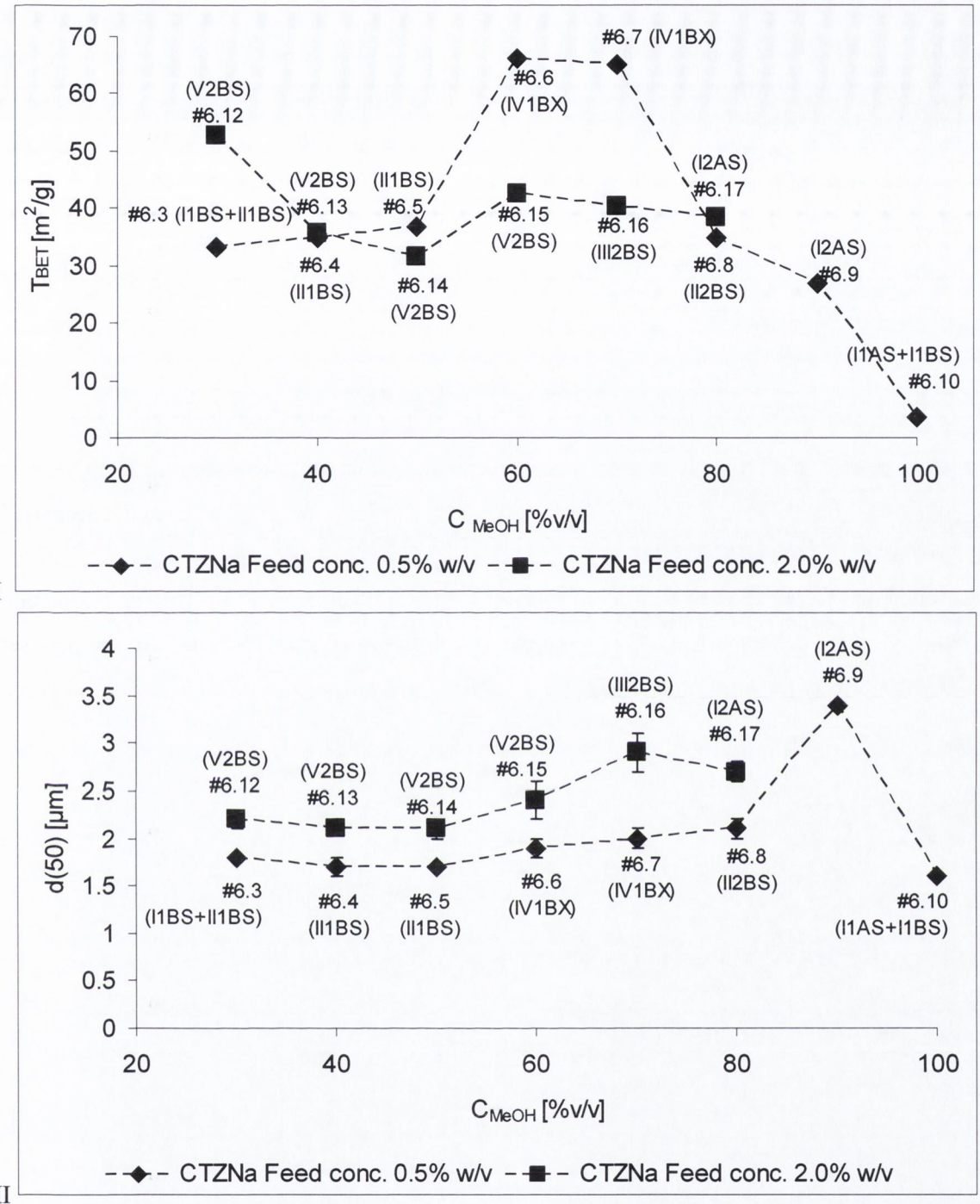

Fig. 6.4. I- Specific surface area T_{BET} and II- median particle size of CTZNa samples spray dried from different methanol concentrations.

Figure 6.4. II presents the relationship between d(50) diameter of the particles and changing concentration of methanol in MeOH/BA mixture for materials spray dried from two concentrations 0.5% w/v and 2.0% w/v. The diameters of the particles spray dried from the 2.0% w/v solutions are about 1.4 times larger than of those spray dried from 0.5% w/v concentration (a 4-fold difference in concentration). This 1.4-fold difference is close to the theoretical ratio of 1.66 for a 4-fold increase in the initial feed concentration assuming that the particles are solid.

It can be seen from figure 6.4 II that the d(50) diameter for sample #6.9 is significantly larger ($p<0.05$) compared with diameters of other samples spray dried from 0.5% w/v feed. For the samples (#6.12-#6.17) spray dried from the initial feed concentration of 2.0% w/v a difference in d(50) is statistically significant ($p<0.05$) comparing with the equivalent samples spray dried from 0.5% solutions (#6.3-#6.8) .

The diameter of a droplet (Φ_d) formed from the liquid feed in spray drying was calculated using equation 6.1 (Hickey et al., 1994).

$$\phi_d = 2 \cdot \sqrt[3]{\frac{((d[3,2]/2)^3 \cdot d_0)}{C_0}} \qquad \text{Eqn. 6.1.}$$

An upward trend of the droplet diameter versus methanol concentration was seen for the 0.5% w/v feed solutions with exception of the 100% methanol feed, where the droplet diameter decreased to approximately 10.6 μm (Fig. 6.5 I)

It was found that the Φ_d showed a linear correlation with d[3,2] values (Fig. 6.5 II). The correlation coefficient (R^2) for the set of values representing samples #6.3-10 was 0.998 and for the data set #6.12-17 it was 0.981.

Table 6.5. Summary of the results of average particle diameter by surface area by laser diffraction d[3,2], estimated particle diameter $\Phi(T_{BET})$ calculated from specific surface area (T_{BET}), estimated specific surface area by laser diffraction T_{LD}, and estimated droplet diameter (Φ_d) (Eqn. 6.1).

Sample (No #)	d[3,2] [µm]	T_{LD} [m^2/g]	$\Phi(T_{BET})$ [µm]		T_{BET} [m^2/g]	Φ_d [µm]
			LP	CP		
#6.1. CTZNa	1.9±0.0	1.8±0.0	2.423	3.418	1.3±0.0	8.39
#6.2. CTZK	2.2±0.0	1.6±0.0	2.423	3.418	1.3±0.0	9.77
#6.3. CTZNa	1.4±0.0	2.1±0.0	0.095	0.134	33.21±0.2	10.14
#6.4. CTZNa	1.3±0.0	2.0±0.1	0.090	0.128	34.83±0.2	9.53
#6.5. CTZNa	1.5±0.0	2.2±0.0	0.086	0.121	36.7±0.1	10.97
#6.6. CTZNa	1.5±0.0	2.1±0.0	0.048	0.067	66.2±0.2	10.66
#6.7. CTZNa	1.7±0.0	1.9±0.0	0.048	0.068	65.1±0.4	12.35
#6.8. CTZNa	1.9±0.0	1.7±0.1	0.091	0.128	34.8±0.3	13.70
#6.9. CTZNa	2.2±0.0	1.5±0.0	0.117	0.165	26.9±0.4	15.89
#6.10. CTZNa	1.5±0.0	2.3±0.0	0.851	1.201	3.7±0.1	10.56
#6.11. CTZK	1.6±0.0	2.1±0.0	0.055	0.078	57.2±0.5	11.28
#6.12. CTZNa	1.7±0.0	2.0±0.0	0.060	0.084	52.6±0.5	7.79
#6.13. CTZNa	1.6±0.0	2.1±0.0	0.088	0.124	35.7±0.3	7.39
#6.14. CTZNa	1.7±0.0	2.1±0.0	0.100	0.141	31.5±0.3	7.46
#6.15. CTZNa	1.9±0.0	2.0±0.0	0.074	0.104	42.6±0.4	8.48
#6.16. CTZNa	1.8±0.0	2.2±0.1	0.078	0.110	40.4±0.4	7.95
#6.17. CTZNa	2.1±0.0	2.2±0.0	0.082	0.115	38.5±0.2	9.48
#6.18. CTZK	1.7±0.0	2.1±0.1	0.044	0.062	72.0±0.6	7.56
#6.19. CTZNa	1.9±0.0	1.8±0.0	0.044	0.061	72.3±0.7	8.39
#6.20. CTZK	2.0±0.0	1.7±0.0	0.035	0.049	90.2±0.9	9.15
#6.19*. +AD	N/A	N/A	N/A		N/A	N/A
#6.20*. +AD	N/A	N/A	N/A		N/A	N/A

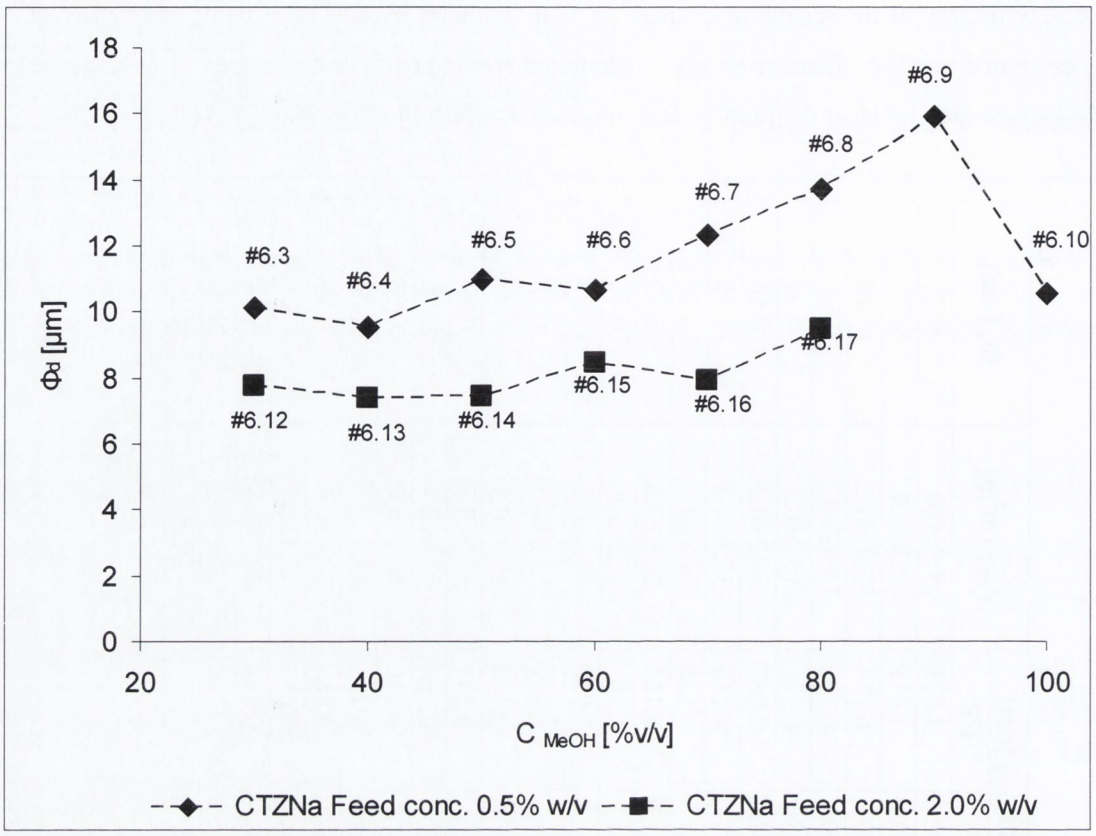

I

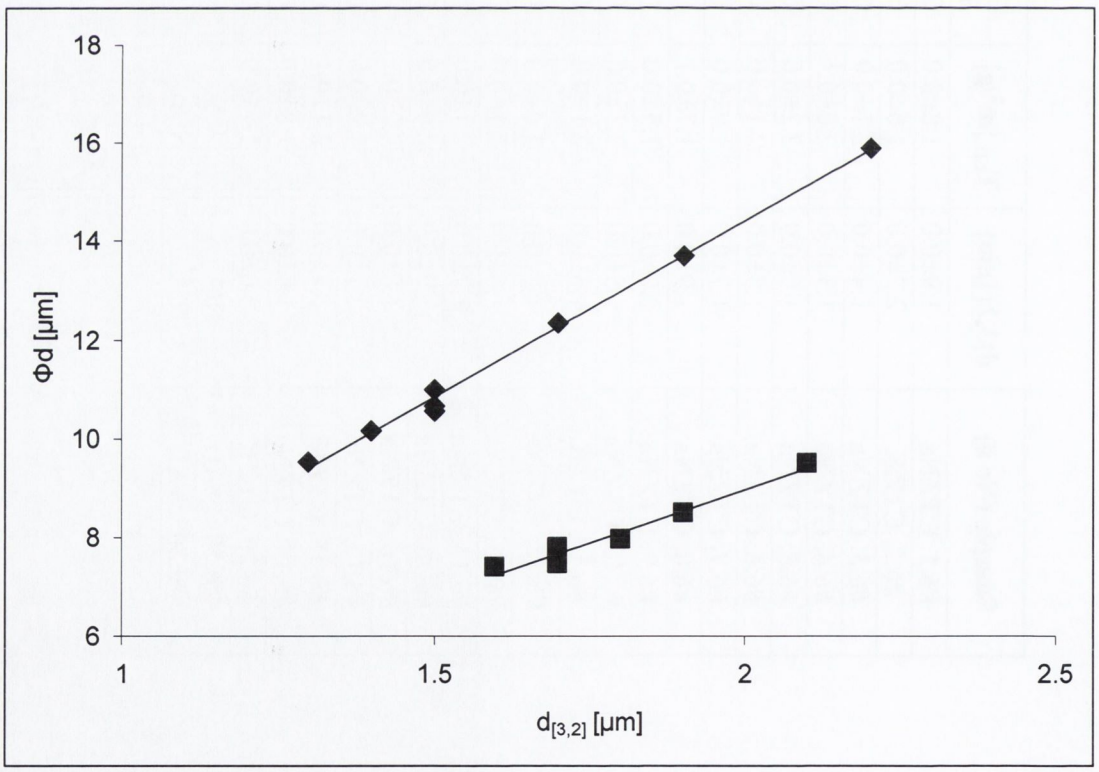

II

Fig. 6.5. I. Droplet diameter versus concentration of methanol. II. Droplet diameter in relation to particle diameter d[3,2].

Droplet diameters calculated from Eqn. 6.1 are comparable to those determined by Masters (2002) and those presented in the study of Elversson et al. 2003, where droplet diameters (d(50)) of 5 to 20 μm were measured depending on atomisation conditions and initial feed concentration. The linear correlation between Φ_d and d[3,2] observed in this work is consistent with observations of Elversson et al. (2003). Elverson et al. investigated the droplet and particle size relationship as well as shell thickness of inhalable lactose particles upon spray drying. Measured by laser diffraction particles diameters d(10), d(50) and d(90) correlated linearly with the respective values of measured droplet diameters.

To calculate the diameter of a particle with the same T_{BET} as that measured for the powder, but assuming the non-porous nature of that particle the following model was developed. A presumption was made that 1 cm^3 (10^{12} μm^3) is represented by a cube with an edge of 1 cm (10^4 μm). Assuming that a particle can be represented by a sphere with a radius r of 1 μm (diameter Φ of 2 μm), the loose packing (LP) of spheres in the model cube will result in 5000 spheres placed along the edge. Therefore 125,000,000,000 ($125 \cdot 10^9$) loosely packed spheres with 2 μm in diameter will be packed in the total volume of 10^{12} μm^3. Assuming close packing (CP) of spheres in the model cube (~74% of the total cube volume (Steinhaus, 1999), $176 \cdot 10^9$ spheres can now be inserted into the model cube. One model sphere (Φ of 2 μm) has an area of 12.6 μm^2. Assuming LP, the surface area of all spheres is equal to $1575 \cdot 10^9$ μm^2 (1.575 m^2). Assuming CP, the surface area of all spheres is equal to $2218 \cdot 10^9$ μm^2 (2.218 m^2). The surface area of the sphere is inversely proportional to the radius of the sphere. The calculated values for LP and CP are presented in table 6.5.

The calculated ΦT_{BET} values well corresponded to median particle sizes obtained from laser diffraction for nonporous samples (#6.1,6.2,6.10) and gave probable estimation of nanoparticles size in NPMP microaglomerates. The latter are in the range of tens of nanometres. The smallest ΦT_{BET} was estimated for sample #6.20, where the average diameter of nanoparticles forming the NPMP microconglomerate was in the range from 35.5 nm for loose packing of spheres up to 49 nm for close packing, this sample also had the greatest T_{BET}.

6.2.4. Physicochemical properties of spray dried samples

Both CTZNa (#6.1) and CTZK (#6.2) after spray drying from water were PXRD amorphous (Fig. 6.6) as were all the spray dried CTZNa and CTZK samples (#6.3-#6.20, data not shown). The amorphous materials were found to be unchanged by PXRD, DSC and HPLC for 6 months under the conditions of the stability studies (data not shown).

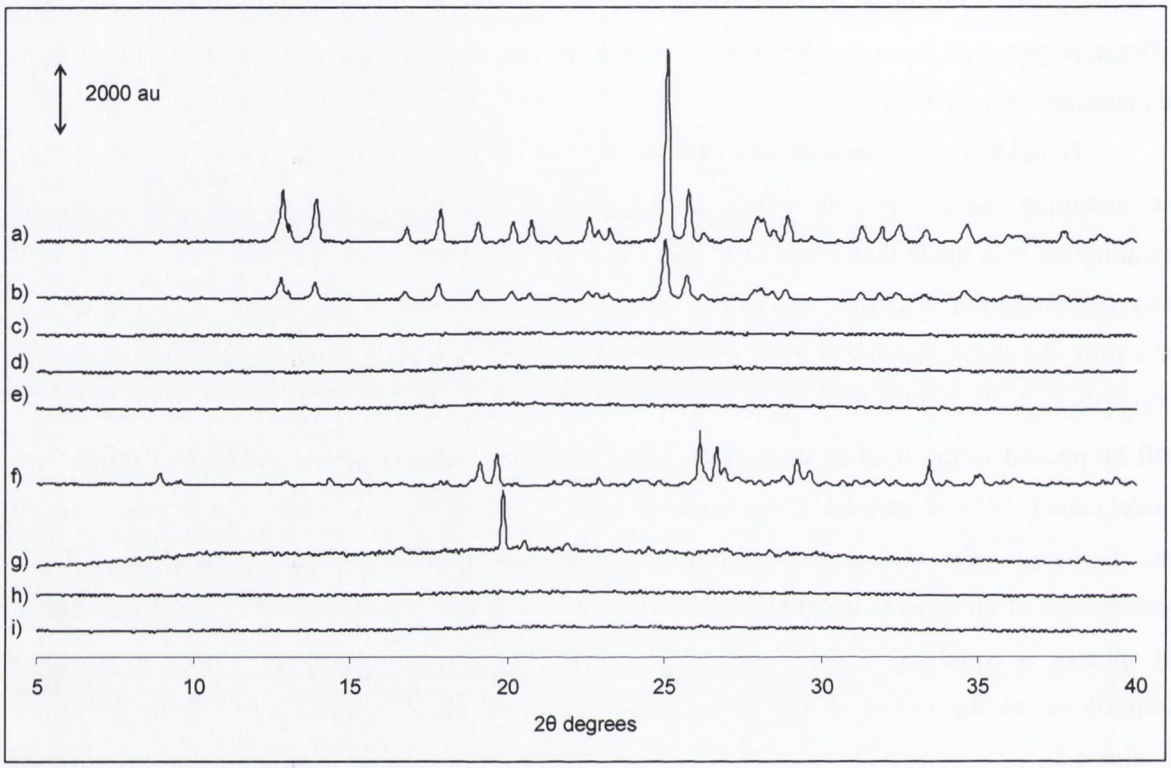

Fig. 6.6. PXRD results of: a) CTZNa dihydrate, b) CTZNa anhydrous, c) CTZNa spray dried from water (#6.1), d) CTZNa spray dried from MeOH/BA mixture (6:4 v/v solvent ratio) (#6.6), e) CTZNa spray dried from methanol (#6.10), f) CTZK dihydrate, g) CTZK anhydrous, h) CTZK spray dried from water (#6.2), i) CTZK spray dried from MeOH/BA mixture (6:4 solvent ratio) (#6.11).

Considering previous studies of crystal forms of CTZNa and CTZK (Chapters 3, 4), obtaining amorphous forms of CTZNa and CTZK salts on spray drying can be ascribed to two factors. The first aspect is related to the fast, highly-energetic process of solvent evaporation in spray drying. The evaporation is fast enough to prevent crystal nucleation after the concentration of solid in drying droplets reaches supersaturation. Spray drying was previously reported as an effective method for the production of amorphous APIs by Corrigan et al. (1984). The second aspect is related to the hydrated nature of both solids (Chapters 3 and 4). CTZNa and CTZK need molecules of a solvent (water or ethanol) in order to develop the crystal lattice. Due to the rapid solvent evaporation (or excluding water using organic solvents and anhydrous salt forms) during spray drying, the contact of water with precipitating API is strongly limited. Thus spray drying

prevents the crystal lattice formation due to the rapid isolation of the solid from a co-crystallising agent (water).

The DSC thermogram (Fig. 6.7e) of CTZNa spray dried from water (#6.1) begins with a broad endotherm of residual water evaporation followed by a wide Tg event at about 195 °C ending with an exotherm of decomposition (~240 °C). Melting was not observed. Thermal analysis confirmed that CTZNa spray dried from water was amorphous and did not recrystallise upon heating. StepScan™ analysis confirmed that the Tg of amorphous CTZNa was 191.8 ± 0.5 °C (change of the specific heat at the Tg (ΔCp) 0.21±0.04 J/g). Thermogravimetric analysis detected 5.6% residual moisture content (25-150 °C at 10 °C/min heating rate) (Fig. 6.8e).

DSC analysis of CTZK spray dried from water (#6.2) (Fig. 6.7i) indicated that the starting endotherm of residual water drying correlated with a 5.5% mass loss by TGA analysis (Fig. 6.8i), similarly to CTZNa (#6.1), Solvent evaporation was followed by a Tg event with its midpoint at approximately 160 °C. After the Tg event the sample decomposed. The Tg of amorphous CTZK was confirmed using the StepScan™ method to be at 159.0±0.4 °C (ΔCp 0.023±0.06 J/g).

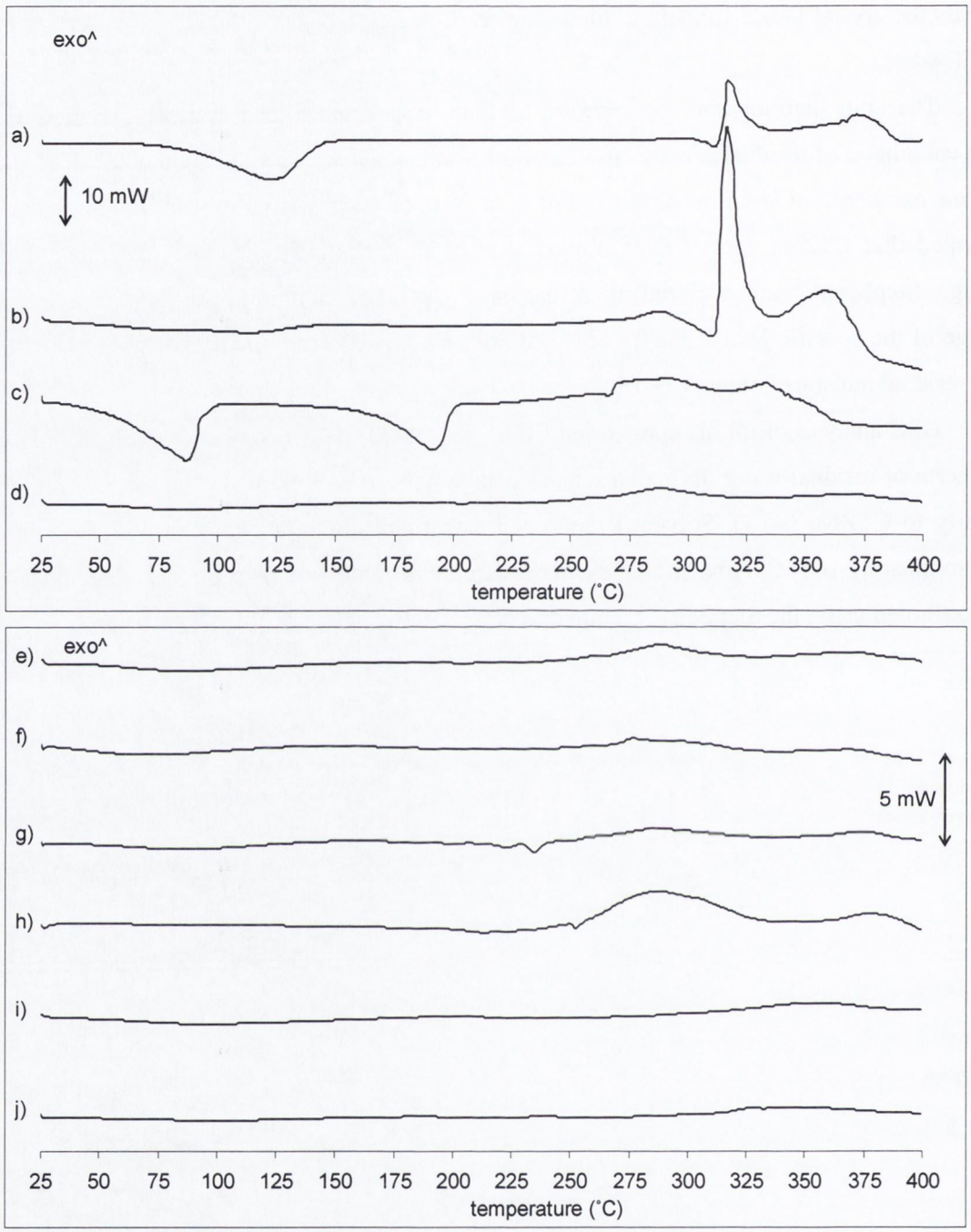

Fig. 6.7. DSC of: a) CTZNa dihydrate, b) CTZNa anhydrous, c) CTZK dihydrate, d) CTZK anhydrous, e) CTZNa (#6.1) spray dried from water, f) CTZNa (#6.6) spray dried (CM) from MeOH/BA (6:4 v/v solvent ratio), g) CTZNa spray dried from methanol (#6.10), h) CTZNa spray dried from methanol (#6.10) and dried (25 °C -250 °C -25 °C at 10 °C/min by TGA), i) CTZK spray dried from water (#6.2), j) CTZK spray dried (CM) from MeOH/BA (6:4 v/v solvent ratio) (#6.11).

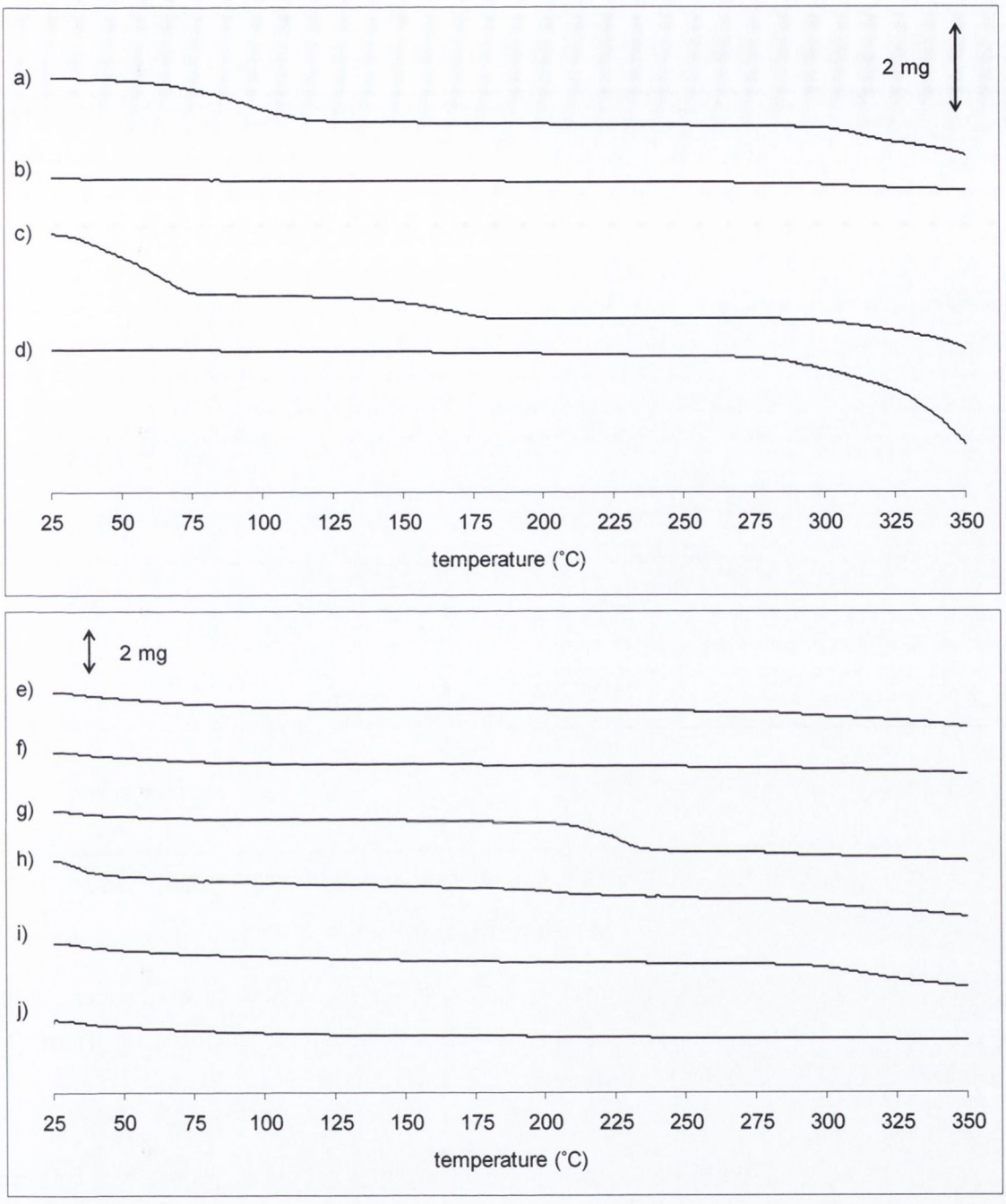

Fig. 6.8. TGA of: a) CTZNa dihydrate, b) CTZNa anhydrous, c) CTZK dihydrate, d) CTZK anhydrous, e) CTZNa (#6.1) spray dried from water, f) CTZNa (#6.6) spray dried from MeOH/BA (6:4 v/v solvent ratio), g) CTZNa (#6.10) spray dried from methanol, h) CTZNa (#6.10) spray dried from methanol, secondary dried (25 °C -250 °C -25 °C at 10 °C/min by TGA), i) CTZK (#6.2) spray dried from water, j) CTZK (#6.11) spray dried from MeOH/BA (6:4 v/v solvent ratio).

FTIR spectra of CTZNa dihydrate (Fig. 6.9a) CTZNa anhydrous (Fig. 6.9b) and the amorphous material spray dried from water (#6.1) did not show significant changes in the fingerprint region except for smoothing and slight broadening of peaks of the amorphous material. Similar changes were observed for the hydrated and anhydrous CTZK (Fig. 6.10a, b) and the amorphous material spray dried from water (#6.2).

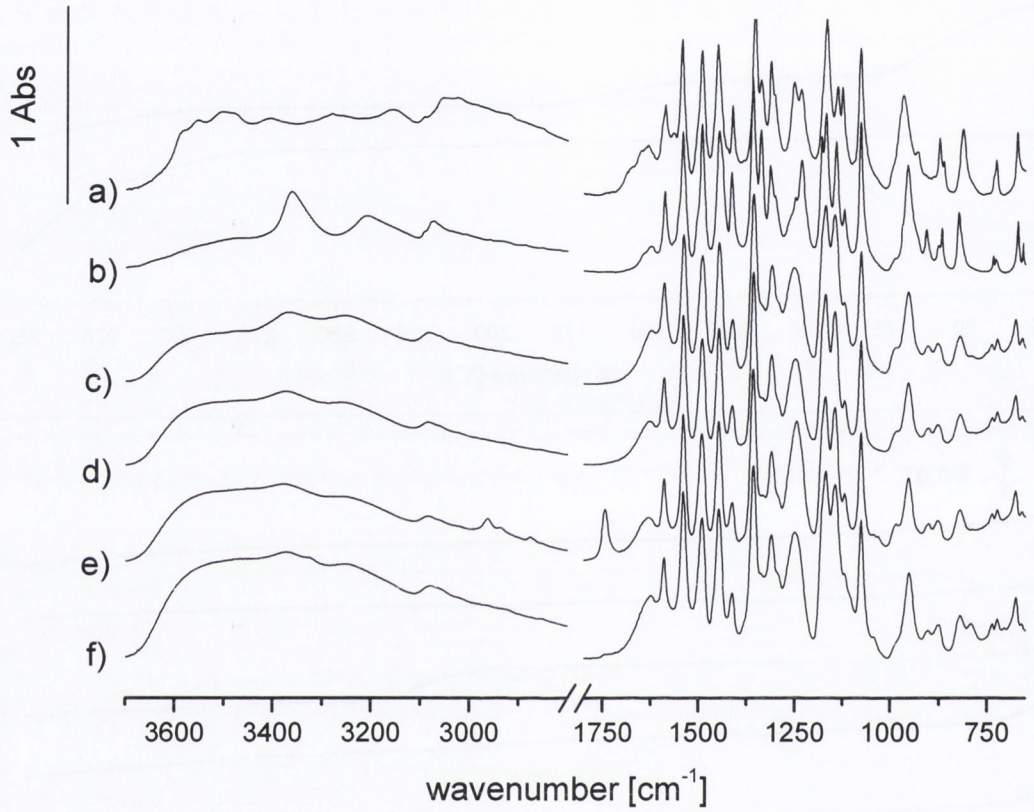

Fig. 6.9. FTIR spectra of CTZNA: a) dihydrate, b) anhydrous, c) spray dried from water (#6.1), d) spray dried from MeOH/BA (6:4 v/v) (#6.6), e) spray dried from methanol (#6.10), f) sample #6.10 after drying to 250 °C in the TG analyser.

A change in the hydrogen bond region due to the loss of water molecules was seen between 3000 and 3500 cm^{-1} in FTIR spectra of the processed materials (Fig. 6.9c, 6.10c). Disappearance of water peaks and noticeable smoothing was observed for the amorphous and anhydrous, crystalline CTZNa (Fig. 6.9b, 6.10b). This suggests that the network of hydrogen bonds in the amorphous matrix is similar to that present in the anhydrous forms.

The DSC scan (Fig. 6.7g) of sample #6.10 (spray dried from 100% MeOH in inlet temp. 100 °C) indicated three small endothermal events in the temperature range from 200 °C to 260 °C. The sample spray dried from pure methanol (#6.10) (Fig. 6.8g) displayed a two-stage mass loss by TGA of 6.63±0.21% and 22.21±0.34%. The DSC endotherms corresponded to the second mass loss recorded by TGA (Fig. 6.8g), most likely attributed to the solvent captured in the amorphous matrix.

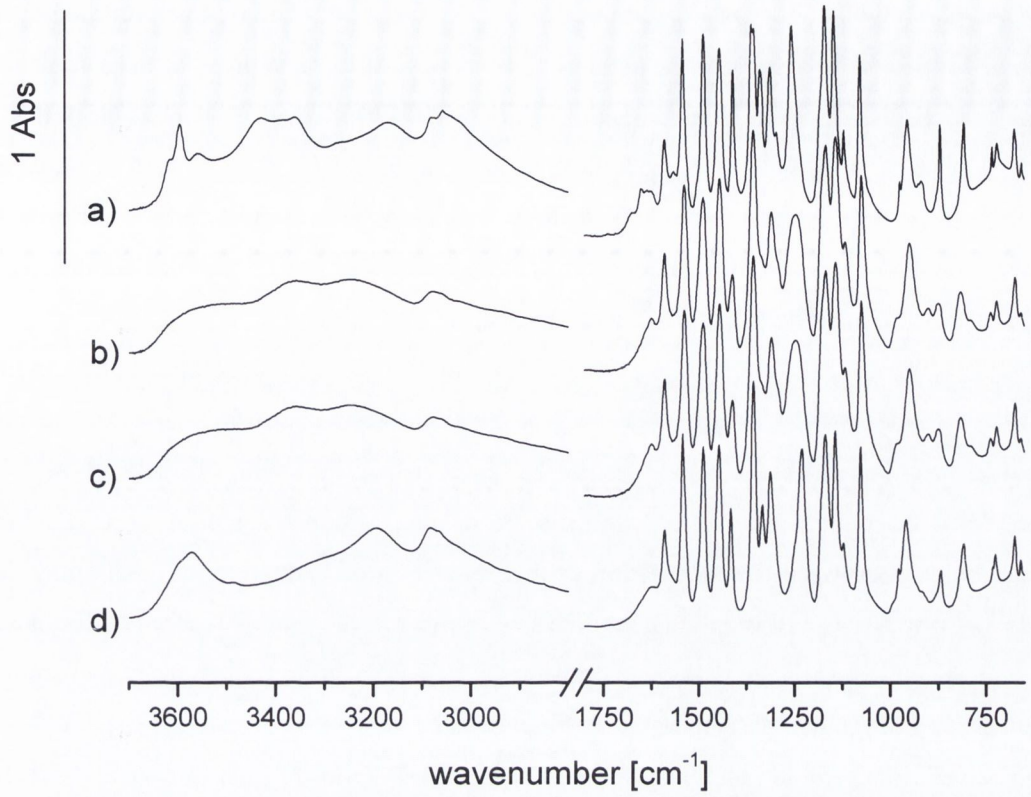

Fig. 6.10. FTIR spectra of CTZK: a) dihydrate, b) anhydrous, c) spray dried from water (#6.2), d) spray dried from MeOH/BA (3:2 v/v) (#6.9).

The material (#6.10) was PXRD amorphous (Fig. 6.6e). Additional drying of the material in the TGA instrument at 40 °C for 30 min did not result in a change in the DSC pattern of the material and the endotherms were still visible. However heating up to 250 °C removed the captured solvent and DSC analysis of this additionally dried material (Fig. 6.7h) did not record the previously visible endotherms. This suggests that the changes in CTZNa observed by DSC were caused by a volatile substance and high temperature was needed to remove this contaminant. FTIR spectrum of CTZNa freshly spray dried from MeOH clearly indicated the differences (Fig. 6.9e). A few absorption bands appeared at 2870-3000 cm^{-1} suggesting the presence of CH aliphatic groups. A sharp and intense peak emerged at around 1740 cm^{-1} indicative of a compound with a C=O group and a weak band at 1050-1100 cm^{-1} implying the existence of the methanol residues. FTIR of the methanolic sample dried at 250 °C presented the absence of the extra absorption peaks.

As the sample was processed from 100% methanol, it was hypothesised that the captured methanol was oxidised to methanal (formaldehyde) during spray drying and that this contaminant was captured in amorphous matrix of CTZNa. The support of this theory are weak FTIR peaks at 2850-2870 cm^{-1} that can be assigned to aldehydic C-H stretching modes. The aldehyde test with Purpald® reagent confirmed the presence of an aldehyde in sample #6.10, and its disappearance after additional drying in the TGA instrument. TGA analysis allowed the molar ratio of CTZNa

to formaldehyde in the adduct to be determined as 1:2. The 22.2±0.3% mass loss recorded by TGA corresponded well with the theoretical content of 21.6% w/w of formaldehyde in the sample #6.10. The exact mechanism of this phenomenon is not known, however it depends on the inlet temperature of process as the material obtained at the inlet of 80 °C was identical with that spray dried from water i.e. had no traces of captured formaldehyde. It was further observed that formaldehyde evaporated within 72 hours when the sample was left at ambient conditions, thus the nature of the CTZNa/aldehyde adduct was metastable.

Mollica et al. (1969 and 1971) describing hydrolysis of benzothiadiazines indicated a possibility of opening the heterocyclic ring of hydrochlorothiazide (HCTZ) with the release of formaldehyde, convertible to methanediol in aqueous environment. Revelle et al. (1997) indicated that one of the photolytic products of decomposition of HCTZ is CTZ. Further photodegradation comprised dehalogenation or methoxylation of CTZ. Even though spray drying of sample #6.10 was not performed in an aqueous environment, the sample was tested for chemical decomposition. HPLC showed that decomposition of CTZNa spray dried from methanol was insignificant ($p>0.05$) in comparison to the starting material.

Thermal analysis of samples #6.3-9 and #6.11-20 showed the presence of residual solvent(s) in all samples spray dried from mixtures of MeOH/BA, as evaporation endotherms were visible at the beginning of each DSC scan (Fig. 6.7f, sample #6.6), corresponding to various TGA mass loses (Fig. 6.8f, sample #6.6). The DSC and TGA scans corresponding to samples #6.6 and #6.11 show patterns similar to one another. In all samples of CTZNa spray dried from MeOH/BA (#6.3 - #6.9, #6.12 - #6.17 and #6.19) the DSC starting, evaporation endotherm was followed by a glass transition with the midpoint at 197-206 °C. TGA determined that the residual solvent(s) content was in the range of 8 to 11% (measured between 25-100 °C) (Fig. 6.8f, sample #6.6).

NPMP CTZNa powders spray dried from lower methanol concentrations (#6.3-#6.8) presented FTIR spectra patterns consistent with that recorded for the amorphous material spray dried from water (#6.1) (Fig. 6.9). The sample processed from 90% MeOH/10% v/v BA (#6.9) presented a few additional FTIR peaks at around 3530 and 3445 cm^{-1}, perhaps of OH stretching modes, and a band at 1425 cm^{-1}, probably of C-O-H from butyl acetate, indicating residues of spray drying solvents.

The DSC pattern of sample #6.11 (Fig. 6.7j) was consistent with that recorded previously for the CTZK material spray dried from water (#6.2). TGA analysis (Fig. 6.8j) of sample #6.11 recorded a mass loss of 10.4±0.3% indicating residual content of solvents in the amorphous matrix of dried powder.

6.2.5. DVS studies of amorphous CTZNa and CTZK

Due to the amorphous nature of the spray dried CTZ salts, dynamic vapour sorption studies (Fig. 6.11) were performed to assess the physical stability of amorphous solids in comparison to the stability of the previously reported crystalline forms (Chapters 3 and 4). Experiments enabled the critical relative humidity of recrystallisation ($RH_{cryst\,0}$) of the amorphous materials in isothermal conditions at 25 °C to be established. The $RH_{cryst\,0}$ describes the limit of the highest environmental humidity, below which an amorphous material will not recrystallise under storage or processing conditions (Burnett et al. 2004). The $RH_{cryst\,0}$ for CTZNa was determined to be 56.6% RH (R^2= 0.997) and for CTZK the value was established to be 58.2% RH (R^2= 0.999). The described and used method was time limited, which resulted in no time for sample mass equilibration at a particular humidity, which means that water uptake was incomplete in the given conditions as $\Delta m/\Delta t$ was greater than 0.002 mg/h at each measured time point. This is why the experiment was repeated under time independent conditions, waiting every 10% RH in the 0-90% RH range until sample mass reached mass equilibrium and water sorption was complete ($\Delta m/\Delta t \leq 0.002$ mg/h with the initial sample mass m_0 of 10 mg). This resulted in recrystallisation (represented as an inflection in the graph) of CTZNa in the range of 40-50% RH, earlier than determined by the time dependent method. For CTZK the inflection was not recorded, indicating that the water sorption event overlapped with recrystallisation. These results show that recrystallisation of an amorphous material is not only related to the rate of RH% changes over time but also to the time of equilibration of the material under given RH conditions.

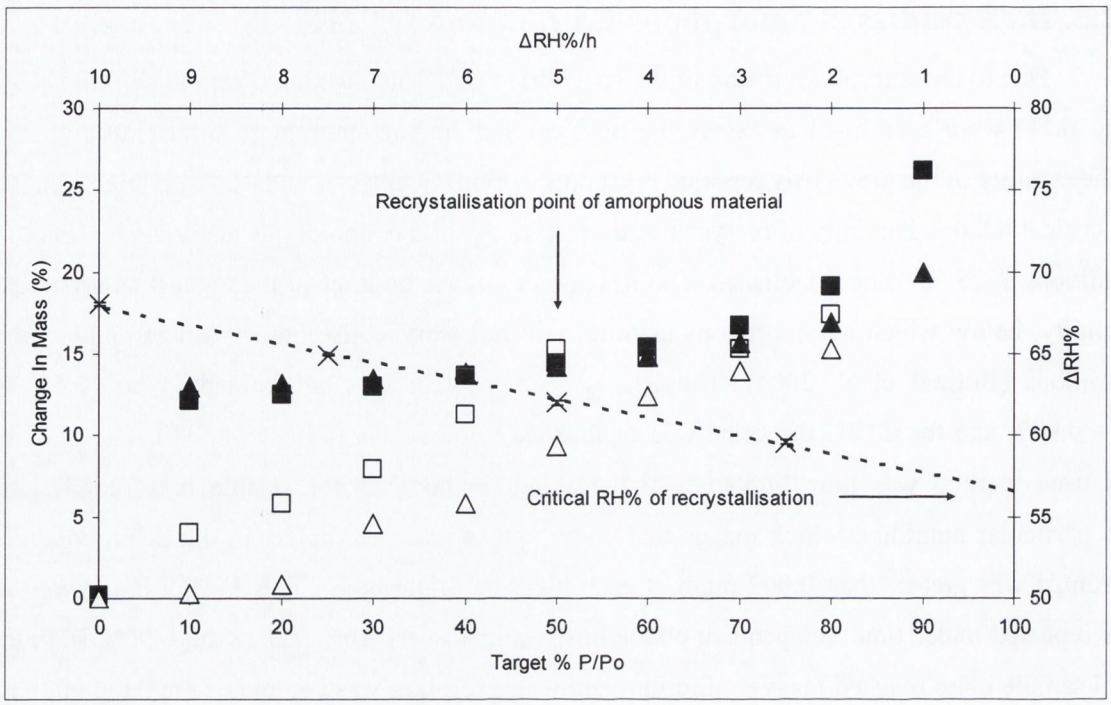

I

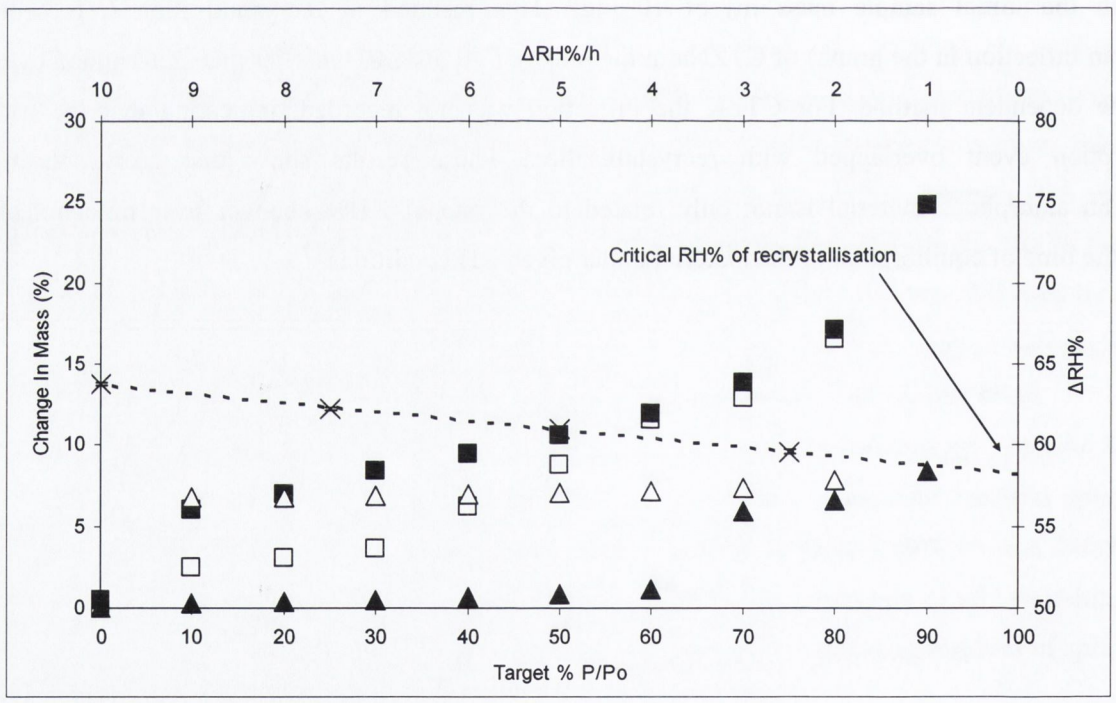

II

Fig. 6.11. DVS analysis of: I CTZNa, II CTZK, triangles - crystalline material (anhydrous CTZNa and monohydrate of CTZK), squares - amorphous material, white - sorption, black -desorption, dotted - f(ΔRH% of recrystallisation) ΔRH% /hour.

6.2.6. Residual solvent content

Assessment of the residual solvent content by GC-FID and KF showed that the CTZNa (#6.12) and CTZK (#6.18) powders collected after spray drying in the closed mode from 2% w/v solutions contained 1.27±0.05% MeOH and 4.98±0.81% BA and 0.85±0.08% MeOH and 4.55±0.55% BA, respectively. Spray drying of the equivalent systems (CTZNa #6.19, CTZK #6.20) in the open blowing mode reduced the level of MeOH in CTZNa and CTZK to a concentration below the detection level (for CTZNa: 0.19±0.02% and for CTZK: 0.19±0.01%) and of BA to 2.4±0.1% and 1.9±0.3%, respectively. A further reduction in the organic solvent content in the spray dried batches was obtained by additional drying (See Methods 2.2.2.1.). The final contents of the organic solvents were as follows: MeOH was below the limit of detection and BA was 9200±0 ppm and 10200±1500 ppm for CTZNa (#6.19*) and CTZK (#6.20*), respectively. The limits of detection for BA were for CTZNa: 1900±200 ppm and for CTZK: 1900±100 ppm.

The European Pharmacopeia lists permitted daily exposures (PDE) of the residual organic solvents and the limit is 30 mg/day (or 3000 ppm) for methanol and 50 mg/day (5000 ppm) for butyl acetate (European Pharmacopeia 2010). Maximal daily dose of chlorothiazide is 1500 mg which is equivalent to 1616.31 mg of anhydrous CTZNa or 1698.33 mg of anhydrous CTZK. Therefore maximal daily exposure to BA for CTZNa is ~15 mg/day and for CTZK is ~17 mg/day so for both salts approximately 3 times below PDE.

The experiments showed that the open blowing mode was more efficient in reducing residual BA content and resulted in a 2-fold decrease in BA content compared to the closed configuration. The combination of the open blowing mode and secondary fluid bed drying simulation appeared to be the most efficient and resulted in a 3-fold reduction of the residual BA content in comparison to the sample spray dried in the closed mode.

KF titrimetry of the spray dried samples indicated lower residual water content was attained by processing in the closed mode (#6.12 and #6.18) compared to the open mode configuration (#6.19 and #6.20). The highest levels of residual water were measured after fluid bed drying simulation (#6.19* and 6.20*) (Table 6.6). These results concur with the spray drying mode used as moisture levels are limited when operating in the closed mode due to the use of dehumidifier and dry nitrogen. Changing the configuration to the open mode increases the exposure to environmental humidity of air. This is even more marked when additional drying process as the incubator uses air with relative humidity of 30 - 50%. The hygroscopic nature of amorphous CTZNa and CTZK was presented earlier (Section 6.2.5).

Table 6.6. Assessment of the residual solvent content.

Sample	TGA mass loss	BA content by GC-FID [%]	MeOH content by GC-FID [%]	Water content by KF [%]
#6.12	8.6±0.4	4.98±0.81	1.27±0.05	2.81±0.18
#6.19	7.6±0.2	2.4±0.10	<0.19±0.02	4.00±0.19
#6.19* after AD	6.4±0.3	0.92±0.00	<0.19±0.02	5.15±0.11
#6.18	8.0±0.4	4.55±0.55	0.85±0.08	3.50±0.08
#6.20	7.1±0.2	1.9±0.30	<0.19±0.01	4.46±0.07
#6.20* after AD	6.5±0.3	1.02±0.15	<0.19±0.01	5.21±0.17

6.3. Conclusions

The work presented here shows that spray drying is an effective method of production of MPs and NPMPs of amorphous chlorothiazide sodium and potassium salts (CTZNa and CTZK). Morphology of MPs was determined to be dependent on the type (water versus MeOH and MeOH/BA) and the ratio of solvents (MeOH/BA) used, concentration of the solid in spray drying feed and the spray drying mode. The Morphology Classification System of spray dried particles (MCS-SD) developed was an efficient tool for morphology characterisation.

Samples spray dried from 0.5% w/v feed concentration comprised NPMPs with morphologies of class II to IV. The use of 2% w/v feed concentration resulted in NPMPs with morphologies of class III and V. The particles spray dried from water had morphologies of type I1AS and I1BS for CTZK and CTZNa, respectively. The development of the different morphologies (A and B) for the aqueous samples was attributed to the different Tgs of the amorphous compounds (CTZNa: ~192 °C, CTZK: ~160 °C). NPMPs with specific surface areas of 70 m^2/g and 90 m^2/g for CTZNa and CTZK, V1BS of MCS-SD respectively, were obtained with satisfactory yields (~90-95%) by spray drying from 2% w/v feed and a MeOH/BA (3:7 v/v) mixture. NPMPs with the largest specific surface areas presented morphology type V. Dynamic vapour sorption experiments determined time dependent critical relative humidity of recrystallisation of CTZNa and CTZK to be 57% RH and 58% RH, respectively.

This work highlighted a risk of solvent oxidation, here observed only when spray dried from pure methanol. The reaction was inlet temperature dependant and not observed when a lower inlet temperature (80 °C) was employed. The spray drying open blowing mode coupled with secondary drying appeared to be 3 times more effective in the reduction of residual BA in comparison to spray drying in closed mode.

Chapter 7

Assessment of compactibility performance of spray dried nanoporous microparticles of chlorothiazide, chlorothiazide sodium and potassium.

7.1. Introduction

One of the main requirements of a tablet as a porous specimen formed by compression is to remain intact upon production, handling, storage and administration conditions (Augsburger and Hoag, 2008). The tablet is expected to resist attrition and fracture and to possess the desired mechanical strength. At the same time the tablet is expected to fulfil disintegration and dissolution requirements. Disintegration and dissolution requirements are getting even more important, when final dosage form is considered as orally dissolving or orally disintegrating tablet (ODT). Current industrial requirements went ahead over pharmacopoeial requirements (European Pharmacopia, 2010), and at the moment the fastest disintegration or dissolution state quality of the ODTs. All of the above-mentioned requirements are dependent on the micro-structural properties of the tablet such as the size of powder particles, morphology of the powder and the type of contact between compressed particles (Augsburger and Hoag, 2008).

To date, several methods including pharmacopoeial, have been designed to analyse properties of the compacted tablets. The "compactibility" term was introduced by Leuenberger and Jetzer in 1982 and is equivalent to "tabletability", which is defined as the ability of powder bed to form a coherent tablet as a result of compression. Compressibility is defined as a propensity of powder enclosed in defined volume of space to reduce its volume upon load. Compressibility is described as a relationship between relative density (porosity-ε_t) of the tablet and the compression pressure and may be expressed using several equations (MacLeod, 1983).

A coherent tablet may be described as a tablet characterised by high fracture, crack and erosion resistance and no tendency to cap or laminate (Augsburger and Hoag, 2008). To evaluate the mechanical strength of tablets they can be subjected to mechanical stress by compression, bending or impaction. Among all of the methods for testing mechanical strength of tablets, two pharmacopoeial methods are the most popular: friability and fracture resistance tests (European Pharmacopeia, 2010 and United States Pharmacopia, 2010). Friability is restricted to final tablet formulations and reflects resistance of the tablets to attrition upon sliding, shaking or tumbling. Fracture resistance in the pharmaceutical industry is most often referred to as a resistance of the tablet to applied force along a given direction until the tablet fails. The tablet may fail by cracking, fracturing in two (tensile failure) or more pieces (double or triple cleft) or by crushing into several small pieces (Fell and Newton, 1970).

The force required to fracture the tablet is dependent on the dimensions of the tablet. Determination of tensile strength (σ_t) of the tablet allows for comparison of properties of tablets of different shapes and dimensions. Tensile strength of the tablet can be determined using the diametral compression method leading to tensile failure.

Due to the importance of powder compactibility or the impact of powder compactibility on compactibility of blends of powders (formulation), different aspects of compactibility of pure pharmaceutical compounds are often reported in the literature. Experiments of Sun (Sun and Grant

2001 and Sun 2004) investigated the impact of hydration on tabletability of L-lysine and hydroxybenzoic acid. Joiris et al. (1998) studied compression behaviour of orthorhombic paracetamol. Maggi et al. (1998) described the tabletability of amorphous α-cyclodextrin hydrates. The changes in relative tensile strength was reported by Berggren et al. (2004) where they compared the tablet-forming ability of spray dried amorphous two- and three-component composite particles. Particles of lactose alone, two-component particles of lactose and PVP and three-component particles of lactose, PVP and a small amount of polysorbate 80 were prepared by spray-drying and compressed under different compression pressures in the range from close to zero up to 250 MPa. A larger change of tensile strength versus compression pressure was determined for tablets made of composite particles containing only lactose and 25% PVP K90. According to a classification introduced by Sonnergaard in 2006, descriptors of powder compactibility can be divided into single-point values and σ_t-porosity relationships or σ_t-compaction pressure relationships. The single point values include mechanical strength of the tablet formed at a given compression force or at a given porosity and compaction pressure needed to form a tablet of desired mechanical strength.

Several factors controlling powder compactibility have been reported to date. They can be organised into three main groups: particle mechanics, particle dimensions and particle adhesiveness. The most commonly reported relationships include an increase in tablet strength following a decrease in powder particle size and greater tablet strength as a result of greater particle shape irregularity. Particle size distribution was reported by Fichtner et al., (2005) to have a limited but direct impact on tensile strength of tablets made of sodium chloride and sucrose. Wide, narrow and bimodal particle distributions of particles with median particle size of about 400 μm were investigated.

This chapter evaluates compactibility performance of amorphous, anhydrous nanoporous microparticles (NPMPs) of chlorothiazide, chlorothiazide sodium and potassium in comparison to:

- hydrated or anhydrous crystalline microparticulate forms of the same compounds,
- anhydrous, amorphous spray dried nonporous microparticles,
- and direct compacting sugar Dipac™.

Dipac™ direct compacting sugar was chosen in this experiment as a reference material to compare its tabletability performance with tested materials. Dipac™ is hydrophilic tablet filler, which is readily soluble in water and may be used as the main excipient in a tablet formulation. The material is not hygroscopic and can be stored at humidities not exceeding 70% RH. The tableting performance of tested powders was assessed without additives in order to observe the physical properties of the pure compounds upon compaction, therefore Dipac™ was a suitable reference.

Pure API tablets are subjected to pharmacopoeial dissolution test studies in order to evaluate advantages of the use of NPMPs in potential final formulations.

7.2. Results and discussion

7.2.1. Physicochemical characterisation of powders subjected to compaction

Materials used for tableting are listed in table 7.1.

Table 7.1. Description of materials used for tableting studies.

Abbreviation	Description of system
Dipac™	Direct compacting and tableting sugar: 96.5±1.5% sucrose, 3.0±0.75% maltodextrin
CTZ	Raw chlorothiazide-micronised, crystalline material
CTZ NPMPs (#5. 11)	Spray dried, crystalline nanoporous microparticles of chlorothiazide
CTZNa DH	Micronised particles of crystalline chlorothiazide sodium dihydrate
CTZNa ANH	Micronised particles of anhydrous, amorphous chlorothiazide sodium
CTZNa MPs (#6.1)	Spray dried nonporous microparticles of amorphous, anhydrous chlorothiazide sodium
CTZNa NPMPs (#6.19)	Spray dried nanoporous microparticles of amorphous, anhydrous chlorothiazide sodium
CTZK DH	Micronised particles of crystalline chlorothiazide potassium dihydrate
CTZK MH	Micronised particles of crystalline chlorothiazide potassium dihydrate
CTZK ANH	Micronised particles of anhydrous, amorphous chlorothiazide potassium
CTZK MPs (#6.2)	Spray dried nonporous microparticles of amorphous, anhydrous chlorothiazide potassium
CTZK NPMPs (#6.20)	Spray dried nanoporous microparticles of amorphous, anhydrous chlorothiazide potassium

The final micromeritic properties of powders subjected to compaction are listed in table 7.2.

Table. 7.2. Micromeritic properties of powders which were subjected to compaction (d_0, specific surface area by BET (T_{BET}), and specific surface area calculated by laser diffraction (T_{LD}) based on surface weighted mean (d[3,2]). Abbreviation as per table 7.1.

Material	True density d_0 [g/cm^3]	T_{BET} [m^2/g]	T_{LD} [m^2/g]
Dipac^{TM}	1.554±0.001	0.2±0.0	0.1±0.0
CTZ	1.798±0.001	0.5±0.0	0.4±0.0
CTZ NPMPs (#5.11)	1.762±0.003	3.9±0.1	1.8±0.0
CTZNa DH	1.728±0.004	2.7±0.0	1.4±0.0
CTZNa ANH	1.883±0.001	3.1±0.0	1.0±0.0
CTZNa MPs (#6.1)	1.837±0.015	1.3±0.0	1.8±0.0
CTZNa NPMPs (#6.19)	1.856±0.001	72.3±0.7	1.8±0.0
CTZK DH	1.887±0.003	0.6±0.0	0.7±0.0
CTZK MH	1.859±0.001	1.7±0.0	0.8±0.0
CTZK ANH	1.881±0.003	1.3±0.0	0.9±0.0
CTZK MPs (#6.2)	1.872±0.003	1.3±0.0	1.6±0.0
CTZK NPMPs (#6.20)	1.863±0.012	90.2±0.9	1.7±0.0

Dipac^{TM} is PXRD crystalline (data not shown). The DSC analysis indicated an onset of melting at 185.4 °C followed by decomposition. TGA analysis indicated a 0.45% mass loss up to 100 °C without a distinctive drying pattern, which may be attributed to residual surface moisture.

True density of the Dipac^{TM} (Table 7.2) was the lowest of all tested materials and was measured to be 1.554±0.001 g/cm^3. Dipac^{TM} had also the lowest measured specific surface area (T_{BET}) of 0.2±0.0 m^2/g, in agreement with the calculated result of specific surface area by laser diffraction (T_{LD}) analysis 0.1±0.0 m^2/g. The median particle size, d(50), of Dipac^{TM} by laser diffraction was 178.4±0.6 μm (Table 7.3).

Table 7.3. Detailed particle size distribution of tested powders.

Sample	d(10)	d(50)	d(90)	Span	Particle size distribution
Dipac™	27.3±0.3	178.4±0.6	398.5±1.2	2.1±0.1	Monomodal
CTZ	5.7±0.2	12.6±0.1	26.0±0.2	1.6±0.1	Bimodal
CTZ NPMP (#5.11)	1.1±0.1	2.7±0.1	5.3±0.1	1.6±0.3	Monomodal
CTZNa DH	0.9±0.0	5.4±0.1	53.1±0.1	9.6±0.2	Trimodal
CTZNa ANH	1.3±0.1	6.2±0.3	49.4±0.2	7.7±0.3	Trimodal
CTZNa MP (#6.1)	1.4±0.2	2.6±0.1	7.2±0.1	1.8±0.1	Monomodal
CTZNa NPMP (#6.19)	1.1±0.1	2.9±0.0	6.8±0.2	1.9±0.1	Monomodal
CTZK DH	1.3±0.1	8.7±0.1	58.4±0.2	6.6±0.2	Trimodal
CTZK MH	1.3±0.2	5.2±0.2	16.8±0.1	3.0±0.1	Bimodal
CTZK ANH	1.7±0.1	9.7±0.2	113.4±0.3	11.6±0.3	Bimodal
CTZK MP (#6.2)	1.2±0.1	3.1±0.1	6.6±0.2	1.8±0.2	Monomodal
CTZK NPMP (#6.20)	1.0±0.0	3.1±0.1	6.8±0.0	1.9±0.1	Monomodal

The modality of particle size distributions is exemplified in Fig. I.1., Appendix I.

Chlorothiazide raw material (CTZ) had a true density of 1.798±0.001 g/cm^3. The material was PXRD crystalline, as described in Chapter 3. The PXRD pattern was comparable with the theoretical pattern based on single crystal analysis of CTZ performed by Shankland et al. 1997. As was revealed by SEM analysis (Figure 7.1a), the CTZ material after crystallisation was micronised. The median particle size was found to be 12.6±0.1 μm.

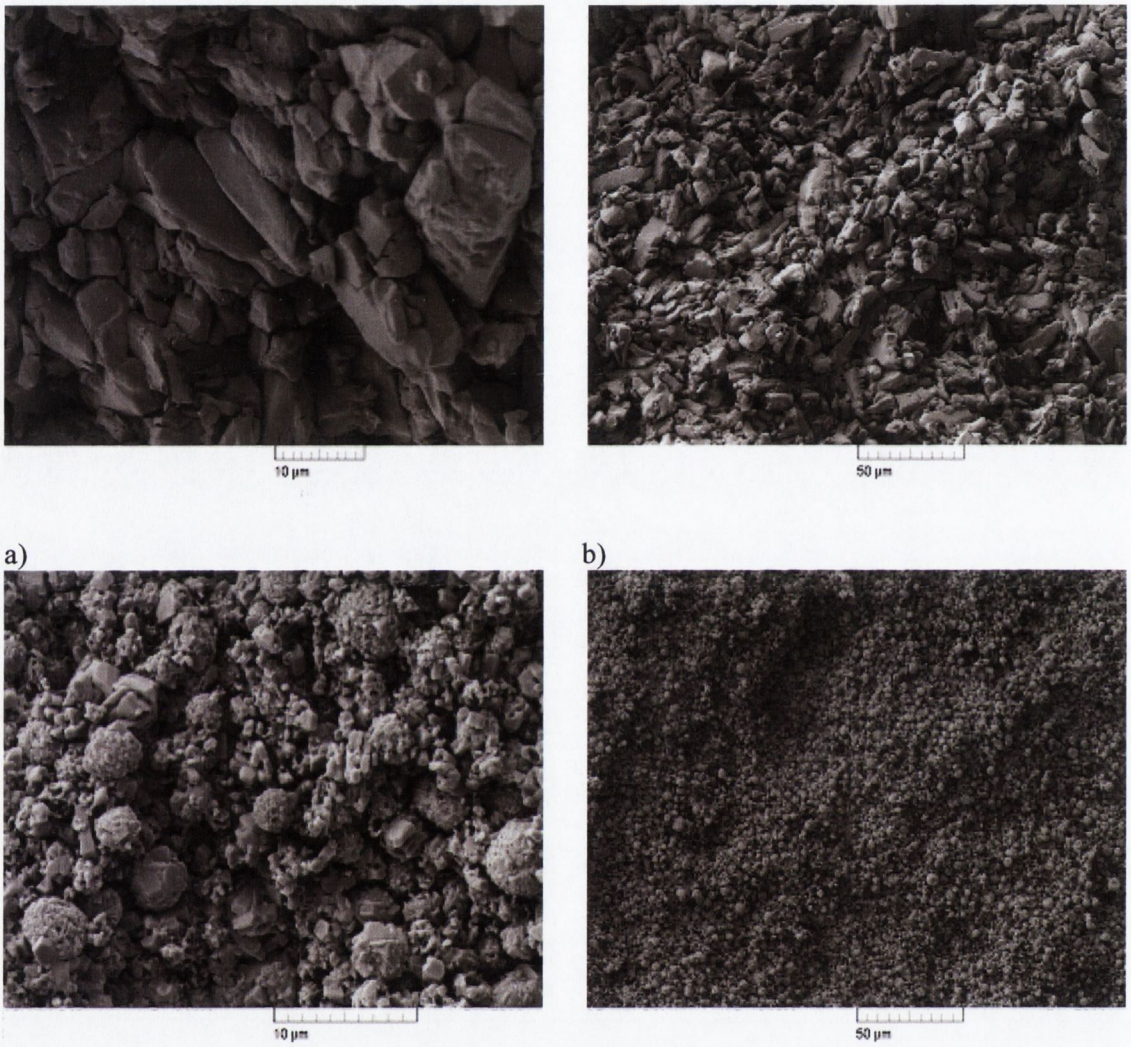

Fig. 7.1. SEM images of: a) morphology of CTZ, b) cross section of the tablet made of CTZ compressed at 6 kN, c) morphology of CTZ NPMPs, d) cross section of the tablet made of CTZ NPMPs compressed at 6 kN.

Surface area analysis of CTZ by BET was 0.5±0.0 m^2/g. This is close to the value estimated by LD of 0.4±0.0 m^2/g. The difference occurs because the crystal habit of CTZ is prismoidal (Chapter 1) if CTZ is recrystallised from acetone or ethanol, as was presented in Chapter 3. Despite micronisation, particles of CTZ, although blunted on edges, retained their oblong shape. This resulted in a difference between the values of specific surface area as estimated

by LD and that measured by BET. Thermal analysis, as described in Chapter 3, revealed the melting point of CTZ at 361 °C and a residual solvent content of 0.5%.

The CTZ spray dried NPMP material was PXRD crystalline as described in Chapter 5. Thermal analysis showed the residual solvent content was below 0.5%. SEM analysis (Figure 7.1c) showed spherical agglomerates of submicron sized crystals with a distinctive prismoidal crystal habit. The true density of spray dried CTZ was slightly lower than for the micronised material and was 1.762±0.003 g/cm^3. Particle size analysis by LD confirmed a median particle size of 2.7±0.1 μm. T_{BET} was measured to be 3.9±0.1 m^2/g and T_{LD} was estimated to be 1.8±0.0 m^2/g. The difference may again be related to the morphology of the particles, which porosity is not included in T_{LD} surface area estimation.

Preformulation characteristics of chlorothiazide sodium dihydrate (CTZNa DH) and anhydrous (CTZNa ANH) materials were comprehensively described in Chapter 3. CTZNa DH had a true density of 1.728±0.004 g/cm^3. The median particle size by LD was 5.4±0.1 μm. Surface area by BET was measured to be 2.7±0.0 m^2/g. T_{LD} was estimated to be 1.4±0.0 m^2/g. In comparison to CTZNa DH, CTZNa ANH micronised in a mortar had a higher true density d_0 of 1.883±0.001 g/cm^3 and a very similar morphology. The median particle size was 6.2±0.3 μm. The specific surface area of CTZNa ANH estimated by LD was 1.0±0.0 m^2/g but the measured T_{BET} was about 2 m^2/g larger and was 3.07±0.01 m^2/g. The CTZNa DH system showed that the difference in surface area resulting from shape irregularities (deviations from spherical shape) between T_{BET} (measured) and LD (estimated) specific surface area (Chapter 1) is about ~1 m^2/g (Table 7.2). In the case of CTZNa ANH the difference in surface area between T_{BET} and T_{LD} of ~ 2 m^2/g, may be due, not only to the shape of particles, but to the presence of empty voids in the crystal lattice of the material after water evaporation. These voids are not included in the LD specific surface area algorithm calculation but are large enough to be penetrated by nitrogen molecules during BET analysis, and as a consequence measured as additional surface area of the material.

Preformulation properties of spray dried systems of CTZNa amorphous, anhydrous and nonporous microparticles spray dried from water (CTZNa MPs) and amorphous anhydrous nanoporous microparticles spray dried from methanol (solvent) and butyl acetate (antisolvent) mixture (CTZNa NPMPs) are described in Chapter 6.

Both spray dried materials, CTZNa MPs and CTZNa NPMPs, were anhydrous and presented similar values of true density (Table 7.2) in comparison to CTZNa ANH: 1.837±0.015 g/cm^3 and 1.856±0.001 g/cm^3, respectively, for CTZNa MPs and CTZNa NPMPs. As both materials after spray drying are fully PXRD amorphous, as previously described in Chapter 6, a slight decrease in the true density values in comparison to CTZNa ANH (raw material with residual crystal lattice) was not surprising, as amorphisation induces a decrease of true density in comparison to the crystalline material (Saleki-Gerhardt et al. 1994). In both

systems LD analysis confirmed a monomodal particle size distribution with the median particle size for MPs and NPMPs of 2.6±0.1 μm and 2.9±0.0 μm, respectively. The estimated specific surface areas were the same for both systems and were 1.8±0.0 m^2/g, for MPs and CTZNa NPMPs. The T_{BET} of NPMPs confirmed an increase in surface area of the material, as expected due to the porosity of spray dried particles observed on SEM (Figure 7.2a), T_{BET} was 72.31±0.69 m^2/g.

Preformulation properties of chlorothiazide potassium dihydrate, monohydrate and anhydrous form were described in Chapter 4. The true density of CTZK DH material was 1.887±0.003 g/cm^3, close to the theoretical value calculated based on the single crystal data of 1.867 mg/cm^3.

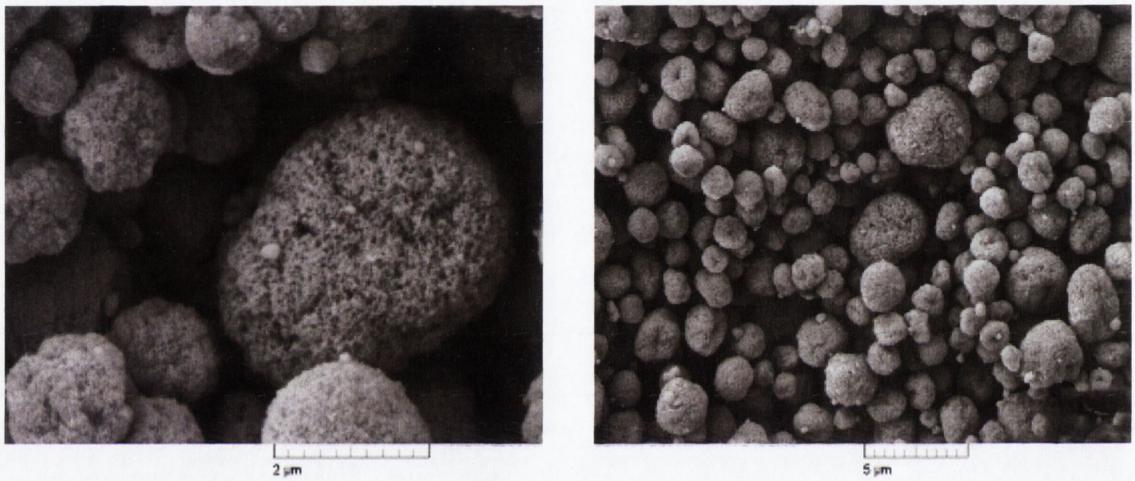

a)

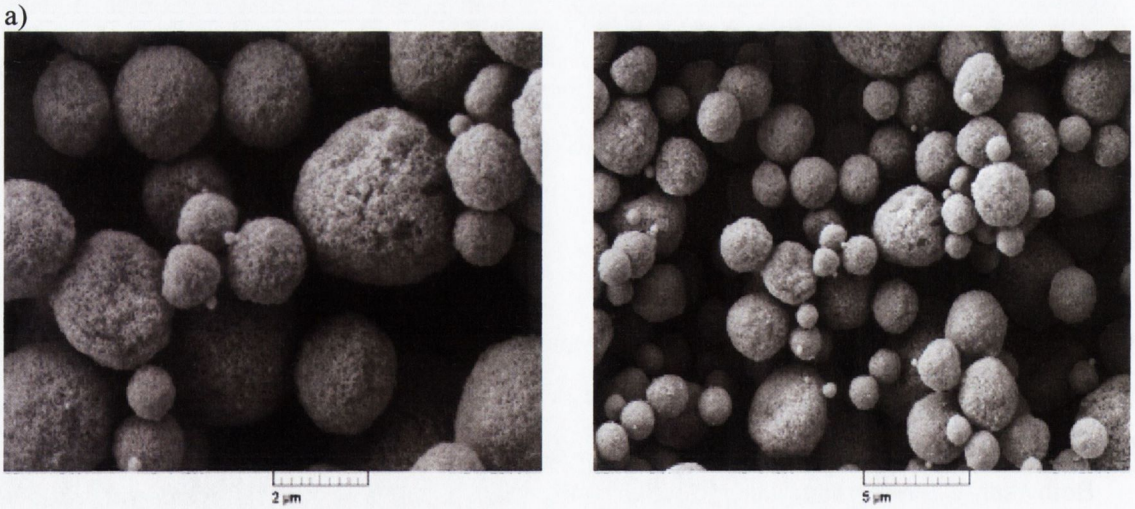

b)

Fig. 7.2. SEM images of NPMPs a) CTZNa, b) CTZK.

The median particle size of the CTZK DH micronised material was 8.7±0.1 μm. The estimated specific surface area by LD was calculated to be 0.7±0.0 m^2/g, close to the T_{BET}

surface area of 0.6±0.0 m^2/g. CTZK MH had a true density of 1.859±0.001 g/cm^3 and a median particle size of 2±0.15 μm. The T_{BET} of CTZK MH was measured to be 1.7±0.0 m^2/g and it was higher than the T_{LD} of 0.8±0.0 m^2/g. This difference may be attributed to irregularities of morphology and empty voids formed due to the loss of crystal water. The anhydrous material CTZK ANH of d_0 1.881±0.003 g/cm^3 had a median particle size d(50) of 9.7±0.2 μm. The T_{BET} specific surface area was 0.4 m^2/g higher (1.30±0.02 m^2/g) than that estimated by LD (0.9±0.0 m^2/g). The CTZK MPs sample presented a median particle size d(50) of 3.1±0.1 μm. The measured surface area T_{BET} of 1.3±0.0 m^2/g was close to 1.6±0.0 m^2/g as estimated by T_{LD}. Due to porosity of NPMPs material (Figure 7.2b) the specific surface area of this sample was measured to be 90.2±0.9 m^2/g. The estimated surface area (T_{LD}) was determined to be 1.7±0.0 m^2/g, as the porosity was not included in calculations. The median particle size was of CTZK NPMPs was 3.1±0.1 μm.

7.2.2. Geometrical characterisation of compressed tablets

All characterised powders were subsequently compressed under different compression forces. The geometric parameters of the tablets produced from the materials described are listed in tables I.1-3, Appendix I.

Analysis of geometrical parameters of the compressed materials revealed that diameter and height of the tablet slightly changed. Observed changes are material dependant and they are also dependant on the compression force used during compaction.

Analysing the behaviour of Dipac™ upon compression (Appendix I, Fig. I.2,3), it can be noticed that the tablet became flatter and slightly larger in diameter upon increasing compression force. CTZ (raw chlorothiazide material) does not follow the Dipac™ pattern of diameter change upon compression force. Regardless of applied compression pressure, the change of the diameter of the tablet was statistically insignificant ($p>0.05$) and only the height of the CTZ tablets was slightly reduced over the tested force range. A different pattern of change of diameter of tablets was recorded for CTZ NPMPs where an increased compression force resulted in a decrease in both geometrical parameters: the height of the tablet and the tablet diameter.

The diameter of tablets composed of CTZNa MPs, CTZNa ANH and CTZNa DH increased upon increasing compression force, while the height of the tablets was decreased (Appendix I, Fig. I.4,5). The system composed of CTZNa NPMPs, similarly to the previously described CTZ NPMPs, had the tendency of decreasing the tablet diameter and the largest tendency for tablet height reduction with increasing compression force.

The analysis of equivalent CTZK systems (Appendix I, Fig. I.6,7) revealed some differences in comparison to the CTZNa systems. The change of diameter of CTZK MPs material upon rising compaction pressure was not statistically significant ($p=0.523$) comparing tablets compressed at 128 and 214 MPa but differed significantly ($p<0.05$) when compared tablets

compressed at 128 and 278 MPa. The difference in the compaction behaviour may be assigned to the different particle morphology in comparison to CTZNa MPs, as described in Chapter 6, where, according to the morphology classification system, CTZNa MPs were classified as I1AS, while CTZK as I1BS. The largest reduction of tablet height was recorded for the system composed of CTZK NPMPs.

It is postulated here that mechanisms of changing (expanding or shrinking) of tablet diameter upon rising compression force may be related to micro-migration of compressed particles in the tablet bed or to a reversible expansion of elastic material along the vertical compression axis. The first postulated mechanism is based on the assumption that compressed powder during compression can move towards the outer side of the tablet bed expanding the final diameter of the tablet, or otherwise due to cohesion forces between powder particles upon compression, particles at the periphery are folded towards the interior part of the tablet. Sinka et al. (2004) reported maps of density distribution in convex tablets. Analysis of maps of density for tablets produced in a lubricated die (simulating low friction conditions), as was done in this work, reveals that the lowest density areas are located at the circumference of the tablet band. Moreover, analysing the cross section of the tablet, areas of the lowest density penetrate towards the interior of the tablet, suggesting that the pressure applied in this area of the tablet in the lubricated die was the lowest, and possibly was able to promote the internal "folding" of the tablet. On the other hand, analysis of maps of density of the material in tablet compressed in a non-lubricated die, simulating high friction conditions, revealed the highest densities at the circumference of the tablet. This could suggest the migration of the material towards the outer edges of the tablet and could help to explain increasing diameter of the tablet under increasing compression force.

The second postulated mechanism assumes that after releasing of mechanical stress applied to the elastic (more or less) material, the tablet relaxes along the axis of compression pulling inwards at the edge of the tablet reducing its circumference. The elastic relaxation of starch tablets during ejection was reported by Anuar and Briscoe in 2009. Reported relaxation correlated with variations in the tablet diameter during the emergence. The continuous variations of the tablet diameters indicated an initial expansion followed by contraction, which continued in a wave-like motion.

A comparison of geometrical parameters of the tablets under different compression forces, indicates that the most prone to height reduction are tablets composed of NPMPs. They do not tend to expand in diameter upon compression, rather a slight reduction of diameter is recorded. This suggests the largest production and tablet design flexibility as the height of the tablet can be modified and controlled in a relatively large range using different compression forces.

7.2.3. Compression force versus force to tensile failure and tensile strength – compactibility

Table I.4 (Appendix I) presents a compilation of all parameters of the tablets discussed below in relation to the tablet compression force (F). Listed are: force to tensile failure, hardness (P), tensile strength (σ_t), tablet porosity (ε_t) and specific surface area (T_{BET}).Assuming the powder bed forming the tablet has good compactibility performance, it is expected that the desired hardness of the tablet (here referred to as force to tensile failure) will be reached using relatively low compression force. Furthermore, hardness of the tablet will not vary significantly under fluctuations of the preset compression force during processing and the change of the tablet hardness will be responsive to the change of compression force.

In contrast to the P value, which is directly related to tablet shape and size, the tensile strength (σ_t) value may be compared for different tablet sizes, shapes and, which is most important, for different materials. The comparison may be based on a single point value of tensile strength in comparison to compression force expressed directly in Newtons (N) or compression force in relation to the surface area of the tablet, where the force was applied (N/m^2) and expressed as compression pressure in mega Pascals (MPa). As both units are discussed in the literature, dependent variable values in all charts presented in this chapter are expressed using two independent variables corresponding to compression pressure and compression force.

As an example of compactibility performance of a pure pharmaceutical compound designed for direct compression, Dipac™ tablets at compression force as low as 3kN presented a hardness of 23.7 N. The hardness increased linearly with compression force at the rate of 23.6 N per 1kN, (Fig. 7.3).

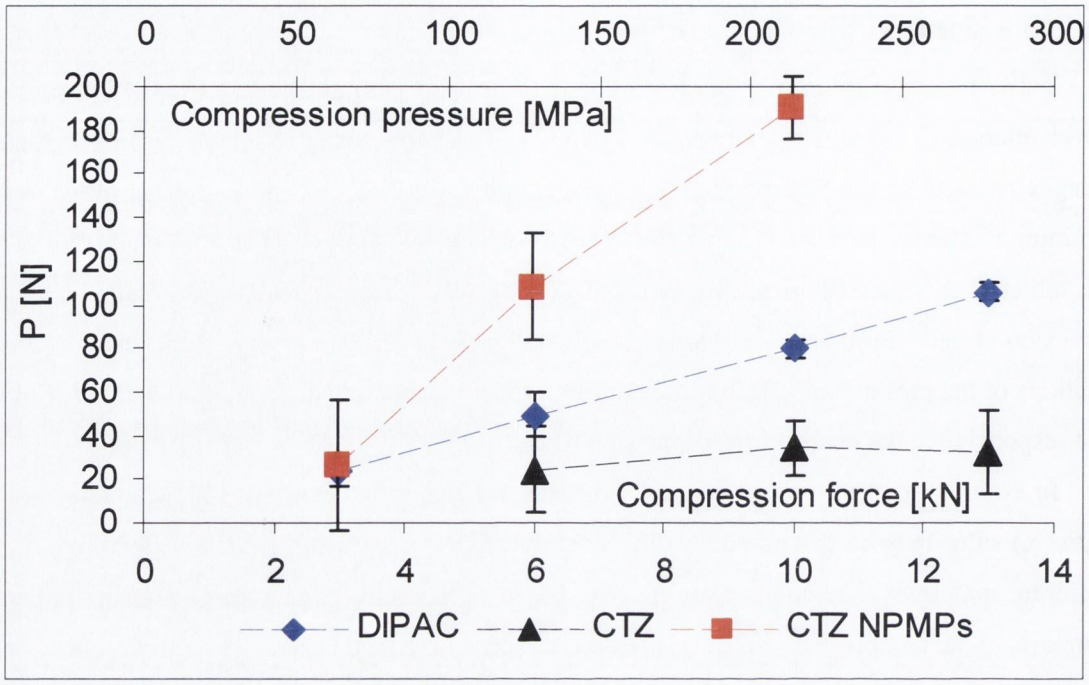

I

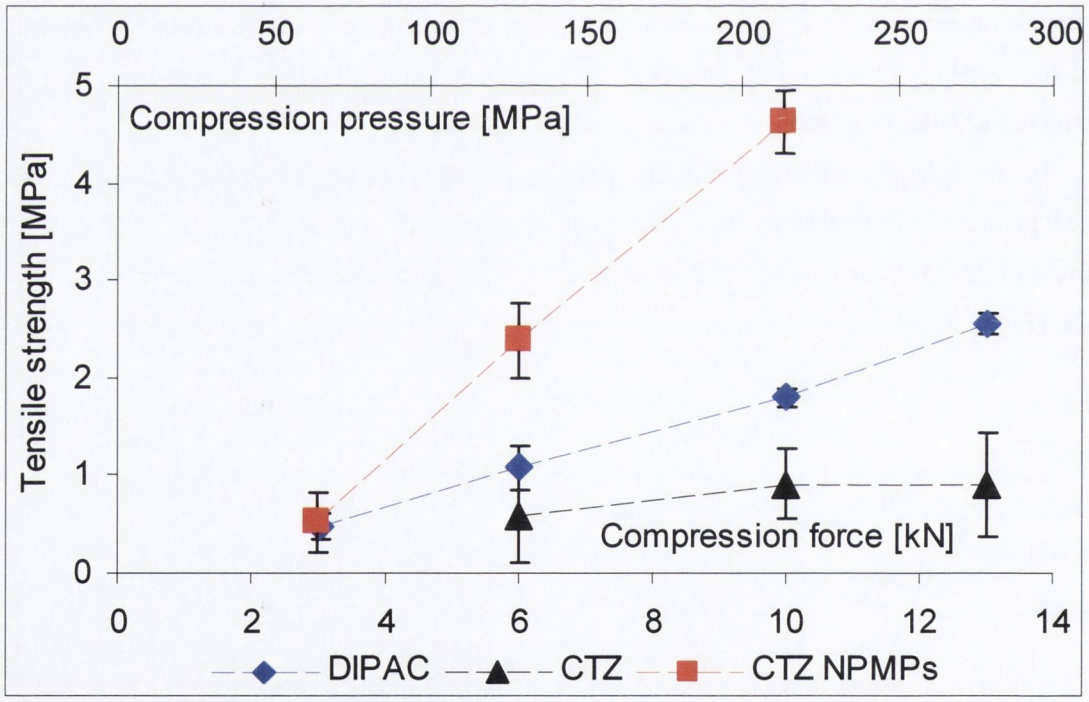

II

Fig. 7.3. (I) Force to tensile failure of the tablet (P) versus compression force (F) (II) tensile strength (σ_t) versus compression force (F) for: Dipac™, CTZ and CTZ NPMPs. Error bars express relative standard deviation (σ_r) for comparison purposes.

In comparison, CTZ material did not present a similar pattern of change of P versus compression force. The increase in P with increase in F started to fall off at higher values of F over 10 kN. The force to tensile failure comparable to Dipac™ material compressed at 3 kN was recorded only starting from F of 6 kN. It indicated that the response of CTZ material regarding change of force to tensile failure to changing compression force is lower than for Dipac™. Processing of CTZ into CTZ NPMPs improved the compactibility of CTZ. The tablet formed at 3 kN had a hardness of 26.5 N which was slightly higher than for Dipac™, but the response of change of P versus compression force of 8.1 N/kN was nearly 3 times lower than for Dipac™, indicating a lower dependence of the material on the compression force variations. The above findings are consistent with the result of studies of Di Martino et al. (2001), where spray drying of acetazolamide converted crystals into crystalline nonporous microparticles, improving the compression behaviour of the API.

Calculation of tensile strength values of tablets of CTZ and CTZ NPMPs materials allowed for direct comparison of change of tensile strength between the micronised and spray dried crystalline materials as was reported by Di Martino et al. (2001). The aim of that study was to improve the compactibility performance of crystalline acetazolamide. Microparticles prepared by spray drying acetazolamide from an ammonia aqueous solution had a mean particle size of 9.66 μm and were a mixture of type I and II crystals. Microparticles were round in shape with slightly rough surfaces. At a compression pressure of 224 MPa, comparable to 214 MPa used in this work, acetazolamide tablets had a tensile strength of about 1.61 MPa and 21% of porosity. The CTZ NPMPs material (Figure 7.3) at a lower compression pressure of 128 MPa had a much higher tensile strength of about 2.38 MPa at even higher porosity of the tablet, 26.5% (Appendix I, Table I.4). In the present study, the improvement in tensile strength in comparison to micronised CTZ was significant ($p<0.05$, comparing the values at two different compression pressures: 128 and 214 MPa), because tablets of CTZ micronised material compressed at an equivalent compression pressure (128MPa) had a tensile strength of only 0.6 MPa with a lower tablet porosity of 15.75%. The tensile strength at a given compression pressure for CTZ NPMPs was always higher than for Dipac™.

The best compactibility performance regarding tensile strength versus compression force among all the CTZNa systems was that of CTZNa NPMPs (Figure 7.4) and corresponded profile of change of force to tensile failure as presented in Appendix I (Fig. I.8).

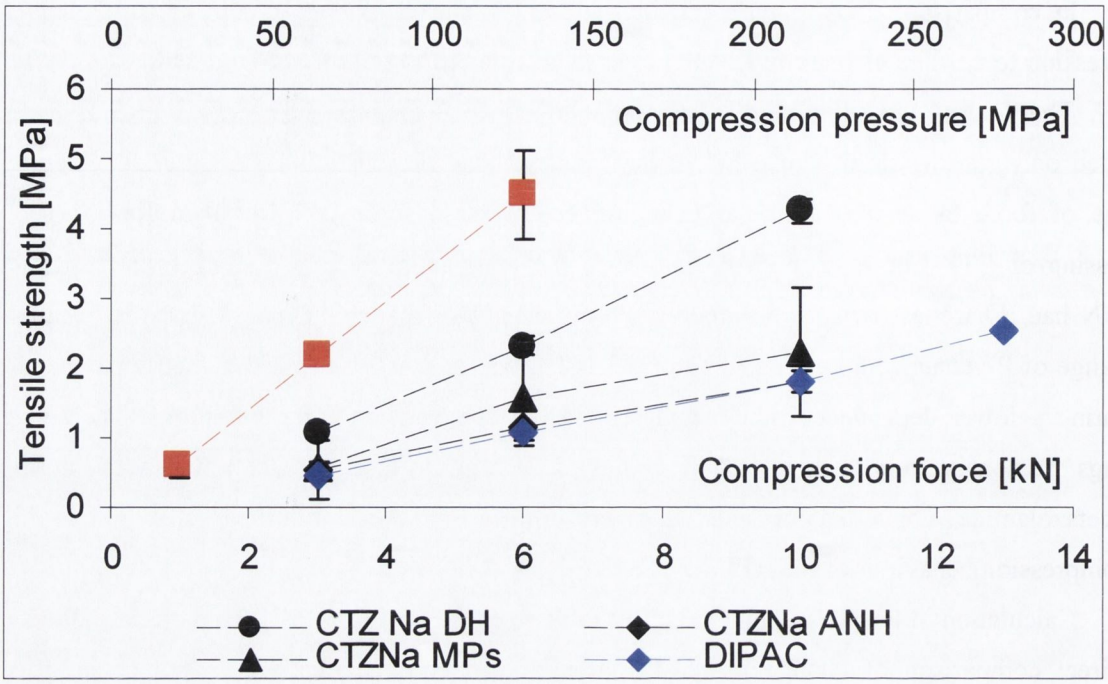

Fig.7.4 Tensile strength in relation to compression force (F) for: CTZNa DH, CTZNa ANH, CTZNa MPs, CTZNA NPMPs and Dipac™. Error bars express relative standard deviation (σ_r) for comparison purposes.

At a compression force of 1 kN CTZNa NPMPs formed tablets with a P of 60 N. The P value of the CTZNa NPMP material increased at rate of 30.2 N/kN, indicating the highest dependence of P on a change in compression force among all the CTZNa materials tested and it was about 7 N/kN greater than the increase in the rate of change of P with compression force recorded for Dipac™. Other CTZNa materials did not undergo compaction at 1 kN. The force to tensile failure recorded at F of 3 kN for CTZNa DH was 46.1 N and was significantly ($p<0.05$) higher than the equivalent values recorded for Dipac™, CTZNa ANH (22 N) and CTZNa MPs (29.4 N). Rates of increase of P versus F were respectively: 14.6 N/kN for CTZNa DH, 8.7 N/kN and 5.9 N/kN for CTZNa MPs and CTZNa ANH.

As was observed for CTZ, spray drying resulted in an improvement in compactibility over micronised material. The fact that the CTZNa DH showed better compactibility performance, than CTZNa ANH or CTZNa MPs may be ascribed to the presence of water molecules in the crystal lattice of CTZNa DH. A similar improvement was noticed by Sun (2004) when he investigated the impact of compaction pressure on the tensile strength of tablets of anhydrous and monohydrated hydroxybenzoic acid. It is hypothesised here that the water molecules coordinated in the crystal lattice may cause the microparticles of powder to stick together upon the application of compression force bringing an advantage in higher P value over the dehydrated material in which only plastic deformation, crushing, interlocking or thermal fusion of molecules can occur.

Figure 7.4 presents the relationship between tensile strength and compression pressure or compression force for CTZNa tablets. Anhydrous and amorphous CTZNa NPMPs had the greatest slopes indicating most dramatic change in tensile strength with increasing P. At 1 kN compaction force, corresponding to a compression pressure of 21 MPa, CTZNa NPMPs formed tablets which had a tensile strength of 0.62 MPa with tablet porosity of 64.5%. The same material at a compression pressure of only 128 MPa formed tablets with a tensile strength of 4.48 MPa and tablet porosity of 32%. At an equivalent compression pressure, the tablets made of micronised crystalline CTZNa DH had a tensile strength of 2.31 MPa, nearly two times lower than that for the CTZNa NPMP system and with an approximately two times lower tablet porosity of 17.6%. Worse compaction performance regarding tensile strength versus compression pressure (or compression force) was observed for CTZNa ANH and CTZNa MPs. It should be noted, that preparation by spray drying of equivalent anhydrous and amorphous systems results in compactibility improvement, since at 6kN compression force tablets formed from CTZNa MPs had a tensile strength of 1.59 MPa while the tablets made of micronised material had σ_t of only 1.17 MPa.

Analysis of figure 7.5, presenting profiles of tensile strength of CTZK materials, suggests similar conclusions to those made for the equivalent CTZNa systems, with the best compactibility performance regarding tensile strength being demonstrated for the spray dried materials, CTZK NPMPs and CTZK MPs. The profile of tensile strength versus compression pressure change for the CTZK systems corresponded to those showing force to tensile failure versus compression pressure and presented in Appendix I (Fig. I.9). Tablets made of CTZK NPMPs at 1 kN compression force had slightly better tensile strength than the equivalent CTZNa system (0.86 MPa). The tensile strength increased to 2.58 MPa and 5.11 MPa respectively at 64 MPa and 128 MPa compression pressures for CTZK NPMPs.

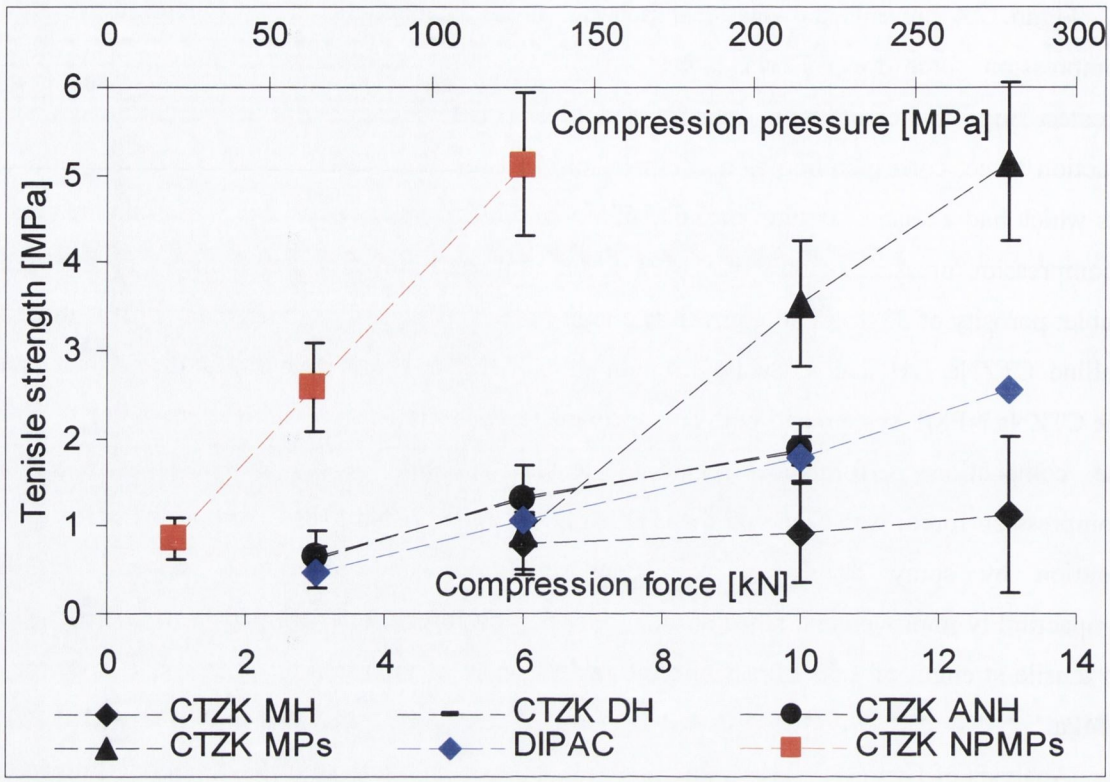

Fig. 7.5. Shows tensile strength (σ_t) in relation to compression force (F) for CTZK dihydrate, monohydrate and anhydrous microparticles, CTZK spray dried microparticles and CTZK nanoporous microparticles. Error bars express relative standard deviation (σ_r) for comparison purposes.

Tablets made of CTZK MPs, despite presenting a tensile strength value of 0.93 MPa at 128 MPa compression pressure, which was slightly lower than for micronised CTZK DH (1.34 MPa) and CTZK ANH (1.29 MPa), had the same rate of increase of tensile strength with P of ~0.4 MPa/kN as the CTZK NPMPs system. At compression force of 10kN, equivalent to 214 MPa compression pressure, CTZK MPs tablets had a tensile strength of 3.52 MPa, while the σ_t of CTZK ANH and CTZK DH systems were 1.87 MPa and 1.84 MPa respectively. The lowest response between σ_t and P was found for tablets made of CTZK MH. The tensile strength of this batch of tablets remained in the range from 0.81 MPa to 1.13 MPa at compression pressures up to 278 MPa.

7.2.4. Compression force versus tablet porosity- Compressibility

The porosity of the tablet is a relative measure of empty spaces in the volume of the tablet in relation to the true density of the compressed material. The compaction of the material is a result of several processes ongoing simultaneously in the compressed powder bed. The result of powder compression is the final reduction of the total volume of the tablet. The density of a completely compressed tablet with 0% porosity will be equal to the true density of the powder forming

the tablet. Porosity is one of the measures of compactibility performance of the material under applied compression pressure or compression force. Investigations of the change of porosity over a range of applied compression forces allow the responsiveness of the material to increasing compression pressure to be evaluated.

Figure 7.6 presents the tablet porosity versus compression force for Dipac™, micronised CTZ and spray dried CTZ NPMPs. Among these three systems the largest porosity, of 33.74%, was recorded for the CTZ NPMP system at a compression force of 64 MPa. Sebhatu and Alderborn (1999) compared the compressibility performance of particles of crystalline and amorphous lactose in order to investigate relationship between the effective interparticulate contact area and the tensile strength of tablets. For crystalline lactose tablets made of particles in the size range of 10 to 50 μm, compressed at 50 MPa, the recorded tablet porosity was ~30%, falling just below ~20% at a compression pressure of 125 MPa, where the recorded tensile strength was only ~1 MPa. The crystalline CTZ NPMP system performed much better since at a similar compression pressure of 128 MPa, the tablet exhibited higher porosity, of 26.45%, but also over two times greater tensile strength, of 2.38 MPa. At the compression force of 214 MPa, the porosity dropped to 20.26%, but still corresponded to a high tensile strength of 4.63 MPa.

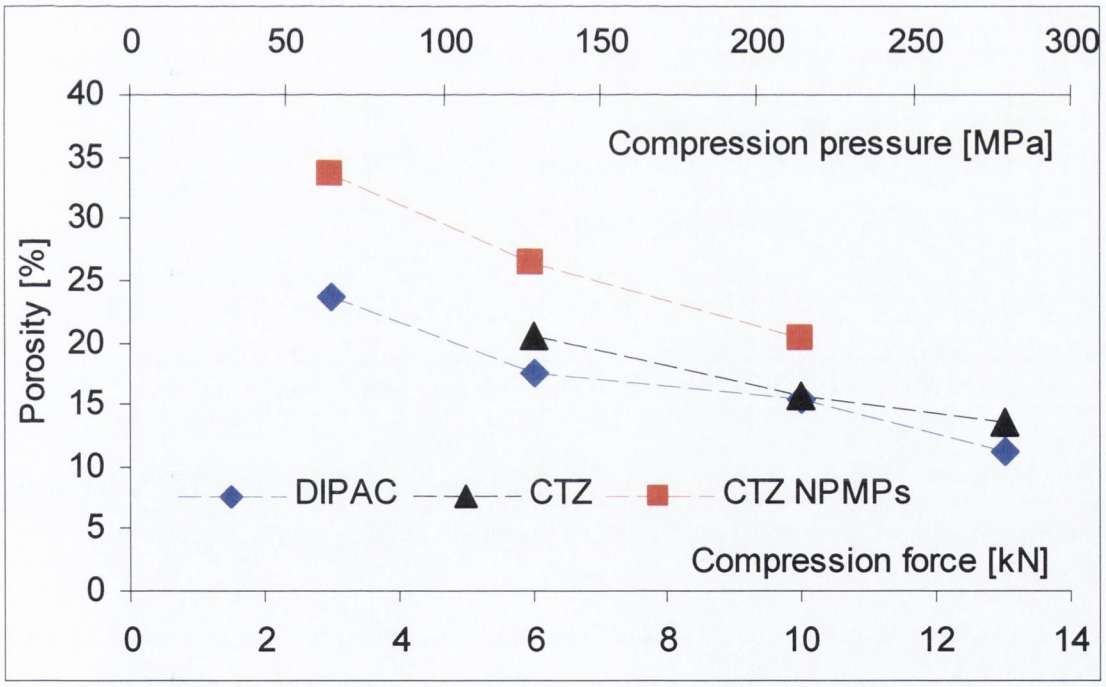

Fig. 7.6. Porosity of the tablet (ε_t) in relation to compression force (F) for: Dipac™, chlorothiazide raw material and nanoporous microparticles of spray dried chlorothiazide.

Analysing porosity and tensile strength data over a range of compression pressures, it can be noted that CTZ micronised material did not perform as well as the equivalent system made of NPMPs. Tablets formed from CTZ at 128 MPa had lower porosity of 20.5% and significantly ($p<0.05$) lower tensile strength of 0.6 MPa in comparison to the NPMP

system. Also the porosity of CTZ micronised system was higher than for Dipac™ at 6 kN compression force and Dipac™ presented a greater tensile strength of 1.08 MPa.

Over the range from 3 to 10 kN compression force equivalent to the range of 64-214 MPa compression pressure, the tablet porosity of Dipac™ decreased by about 8.38% while the tablet tensile strength increased by about 1.33 MPa. The porosity of tablets of CTZ made of spray dried crystalline anhydrous and nonhygroscopic (the same characteristics as for Dipac™) material decreased by about 13.48% and tablets tensile strength increased by 4.1 MPa. Poorer performance of Dipac™ in comparison to NPMP material was most likely due to the significantly ($p<0.05$) greater median particle size of the Dipac™ powder and lower specific surface area of the material.

Figure 7.7 presents the porosity of tablets made of CTZNa NPMPs material versus compression pressure.

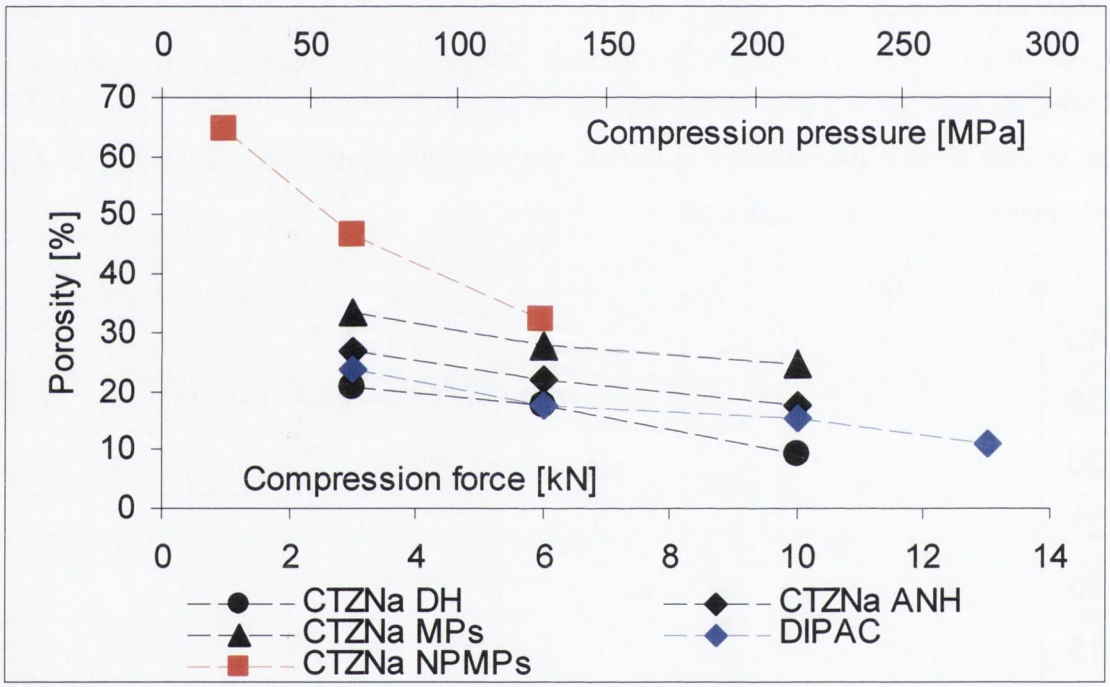

Fig. 7.7. Porosity of the tablet (ε_t) in relation to compression force (F) for: CTZNa dihydrate, anhydrous, CTZNa microparticles, CTZNA nanoporous microparticles and Dipac™.

The calculated porosity of the CTZNa NPMP tablets at a compression pressure of 21 MPa was 64.51 %; under a compression pressure of 64 MPa this dropped to 46.67% and reached 31.97% at 128 MPa. Over the range of compression forces analysed the porosity of the tablets reduced by about 32.54% gaining 3.86 MPa in the tablet tensile strength. The tablets made of nonporous materials tested over a range of compression pressure from 64 MPa to 214 MPa did not present such large variations in tablet porosity. Among the nonporous systems the largest porosity, of 33.5% at 64 MPa, was recorded for CTZNa MP spray dried material. The CTZNa ANH and CTZNa DH materials at 3 kN compression force had porosities of 26.67% and 20.63%, respectively. The analysis of the change of tablet porosity versus change of P indicated that CTZNa

DH, CTZNa ANH and CTZNa MP materials had similar responsiveness regarding increasing compression force, but the dihydrated material presented much better performance regarding the increase of tensile strength, similar to the NPMP system.

Figure 7.8 presents the relationship between CTZK tablet porosity and the change of compression force and pressure.

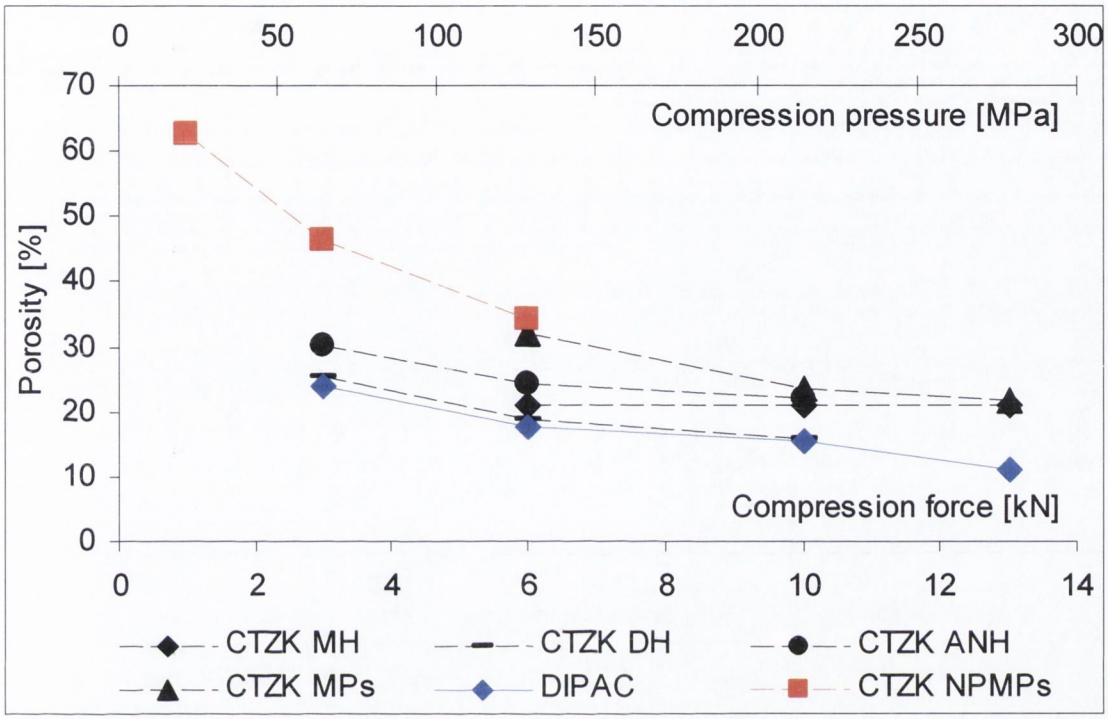

Fig. 7.8. Porosity of the tablet (ε_t) in relation to compression force (F) for: CTZK dihydrate, monohydrate and anhydrous microparticles, CTZK spray dried microparticles, CTZK nanoporous microparticles and Dipac™.

The largest change of ε_t versus rising compression pressure was recorded for CTZK NPMPs system. The change of ε_t was very similar to that of the equivalent CTZNa NPMPs system. The CTZK NPMP tablets compressed at 21 MPa compression pressure had a porosity of 62.79%. After the compression of the powder at 128 MPa the tablet porosity was reduced to 34.17%. In the tested range of compression force from 21 up to 128 MPa CTZK NPMPs tablets lost 28.62% of porosity, while the tensile strength increased by 4.25 MPa. Analysing tablets of other CTZK materials, at 128 MPa compression pressure the largest tablet porosity of 32.07% was recorded for nonporous spray dried material (CTZK MPs). The tablet porosity of micronised CTZK ANH, CTZK MH and CTZK DH had descending porosity according to higher degree of hydration, i.e.: 24.31%, 21.13% and 18.71%, respectively. The same order was maintained at 214 MPa compression pressure. A reduction of tablet porosity, by 0.07%, over the tested range of compression pressures from 128 to 278 MPa was recorded for CTZK MH micronised material. It corresponded to a very small, but statistically significant ($p<0.05$) change of tablet tensile strength,

by 0.32 MPa, indicating that this material among all tested presented the worst compactibility regarding reduction of tablet porosity and increase of tensile strength with change of compression force. This indicates that NPMP systems of API or other pharmaceutical compounds may play a role of super-bulking agents, not only by incorporation of additional substance in the tablet recipe but also due to the air, enclosed in the nanopores.

Compilation of obtained results of tablet porosity and corresponding tensile strength (Figure 7.9) confirms superior compactibility properties of anhydrous and amorphous CTZNa and CTZK NPMP systems.

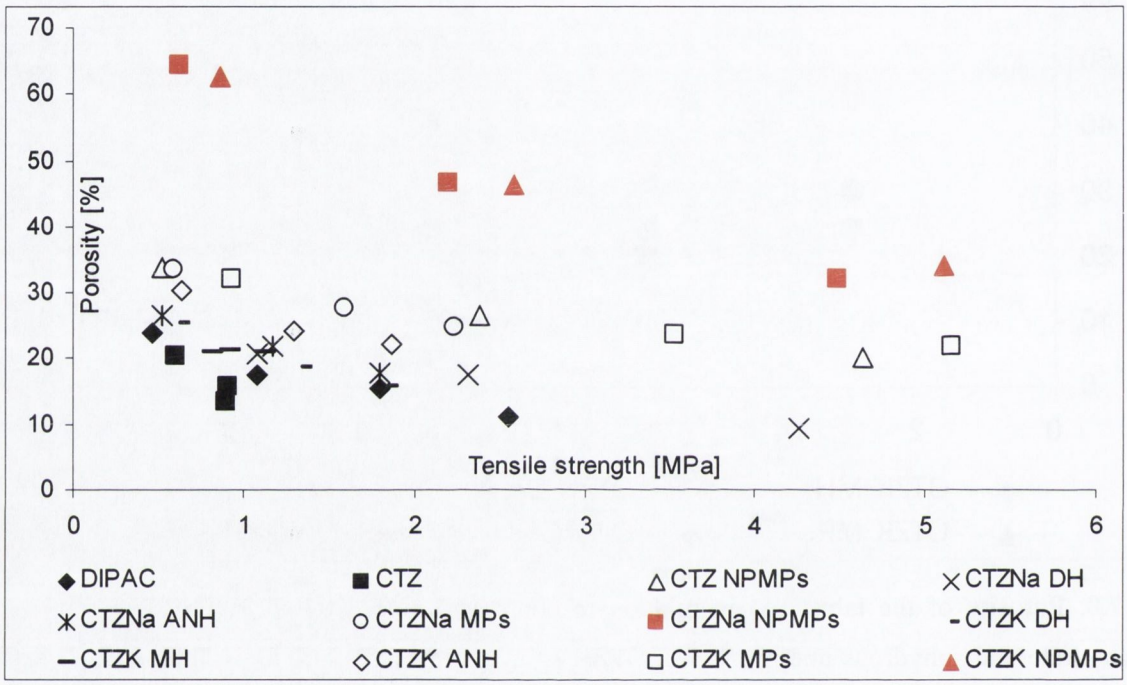

Fig. 7.9. Porosity of the tablet in relation to tensile strength, for all produced tablets.

At each data point corresponding to a certain compaction pressure or compaction force NPMP systems present higher tensile strength and higher porosity of the tablet when compared to the rest of the tested systems. Porosities of CTZK NPMPs and CTZNa NPMPs tablets (at a given compression pressure) are very similar; however CTZK NPMPs tend to have slightly higher tensile strengths.

7.2.5. Compression force versus tablet specific surface area

The porosity of NPMP tablets was seen to be reduced with increasing compression pressure and at 128 MPa was close to values of tablet porosities, made of conventionally processed materials, of about ~30%. Porosity of tablets may not reflect changes in the specific surface area of compressed materials. In order to evaluate changes of specific surface area of the compressed materials, tablets were subjected to BET analysis. It was hypothesised that particular compaction mechanisms can impact directly on the specific surface area of the material after compaction.

The mechanisms expected to enlarge specific surface area of the material are crushing and plastic deformation. The mechanisms reducing specific surface area are fusion of particles into larger agglomerates. Interlocking of particles or elastic deformation under compression are considered as compaction mechanisms which do not have an impact on the specific surface area of the tablets (Augsburger and Hoag 2008).

Analysis of changes of the specific surface area of Dipac™ (Fig. 7.10) indicated that the original T_{BET} of 0.2 m^2/g measured for loose powder started to increase when the same material was analysed as a compacted tablet at 3 and 6 kN compression force. The measured T_{BET} reached an inflection point at 10 kN and decreased at 13kN.

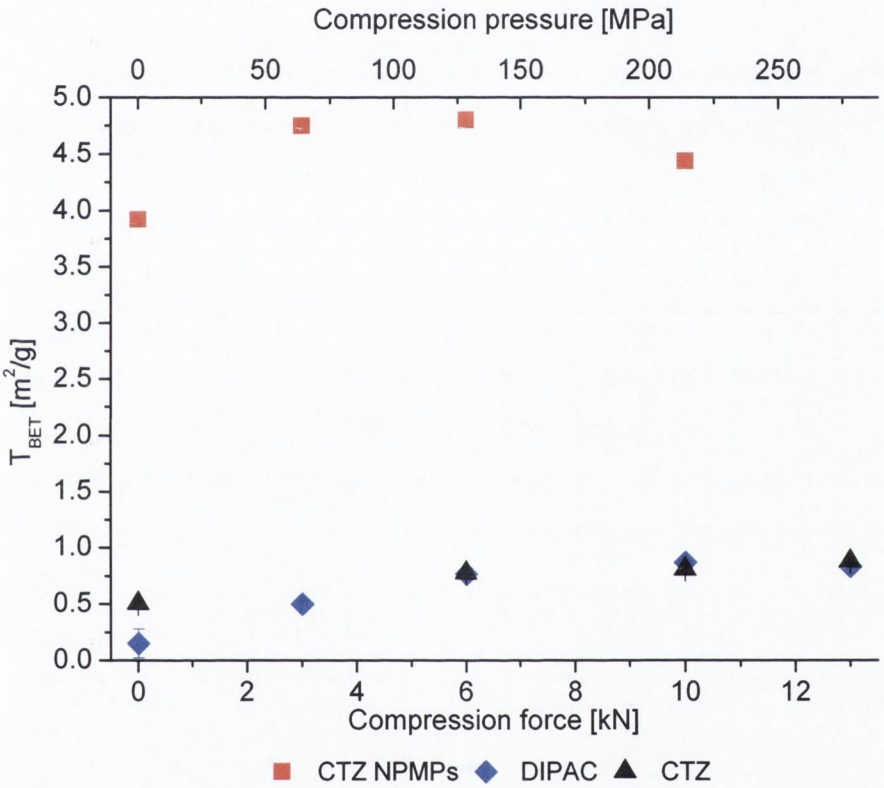

Fig. 7.10. Specific surface area of the tablet (T_{BET}) in relation to compression force (F) for: Dipac™, CTZ and CTZ NPMPs.

Under increasing compression force (pressure) the bed of powder placed in the die between upper and lower punches starts to compact firstly by migration of powder and interlocking (Augsburger and Hoag 2008). Secondly, elastic deformation can occur with increasing compression pressure; this elastic deformation may transfer into a permanent change of particle shape, i.e. plastic deformation. Further increase of compression load may result in particle cracking, crushing together with the same processes as those occurring at lower loads. Finally, under high compression pressure, smaller particles can merge (fuse) together into large particles.

Analysis of changes in T_{BET} for Dipac™ (Fig. 7.10.) suggests that under lower loads (compression pressure) particles undergo firstly plastic deformation and crushing and then, when a compression force of over 10 kN is applied, these processes cease and small particles fuse together, as shown by the decreased T_{BET} of compressed material.

In contrast to Dipac™, CTZ micronised material did not show a tendency for T_{BET} to decrease over the range of tested compression pressures from 128 to 278 MPa. The T_{BET} measured for the loose powder (0.51 m^2/g) was seen to increase in tablets. This indicated that CTZ micronised material compacted into tablets predominantly due to crushing and interlocking, however plastic deformation can not be excluded, but no fusion of particles can be determined, as a reduction in T_{BET} was not observed.

The CTZ NPMP system performed differently. The T_{BET} of loose powder was 3.92 m^2/g and increased slightly for the material compressed under 3 kN compression force to 4.75 m^2/g and under 6 kN to 4.8 m^2/g, only to drop to 4.44 m^2/g when a compression force of 10 kN was used. The pattern of change of T_{BET} of CTZ NPMPs indicated that processing of CTZ can result in a change in the mechanism of powder compaction. The pattern of change of T_{BET} presented by CTZ NPMPs was similar to that presented by Dipac™, although for Dipac™ the reduction in the T_{BET} occurred at a higher compression pressure than for CTZ NPMPs.

Figure 7.11 presents the behaviour of T_{BET} of CTZNa materials after compression into tablets. Analysis of the T_{BET} of micronised CTZNa ANH at the first compression pressure point revealed fusion of the material, as the T_{BET} decreased from 3.07 m^2/g (loose powder) to 2.61 m^2/g (tablet compressed at 3 kN compression force).

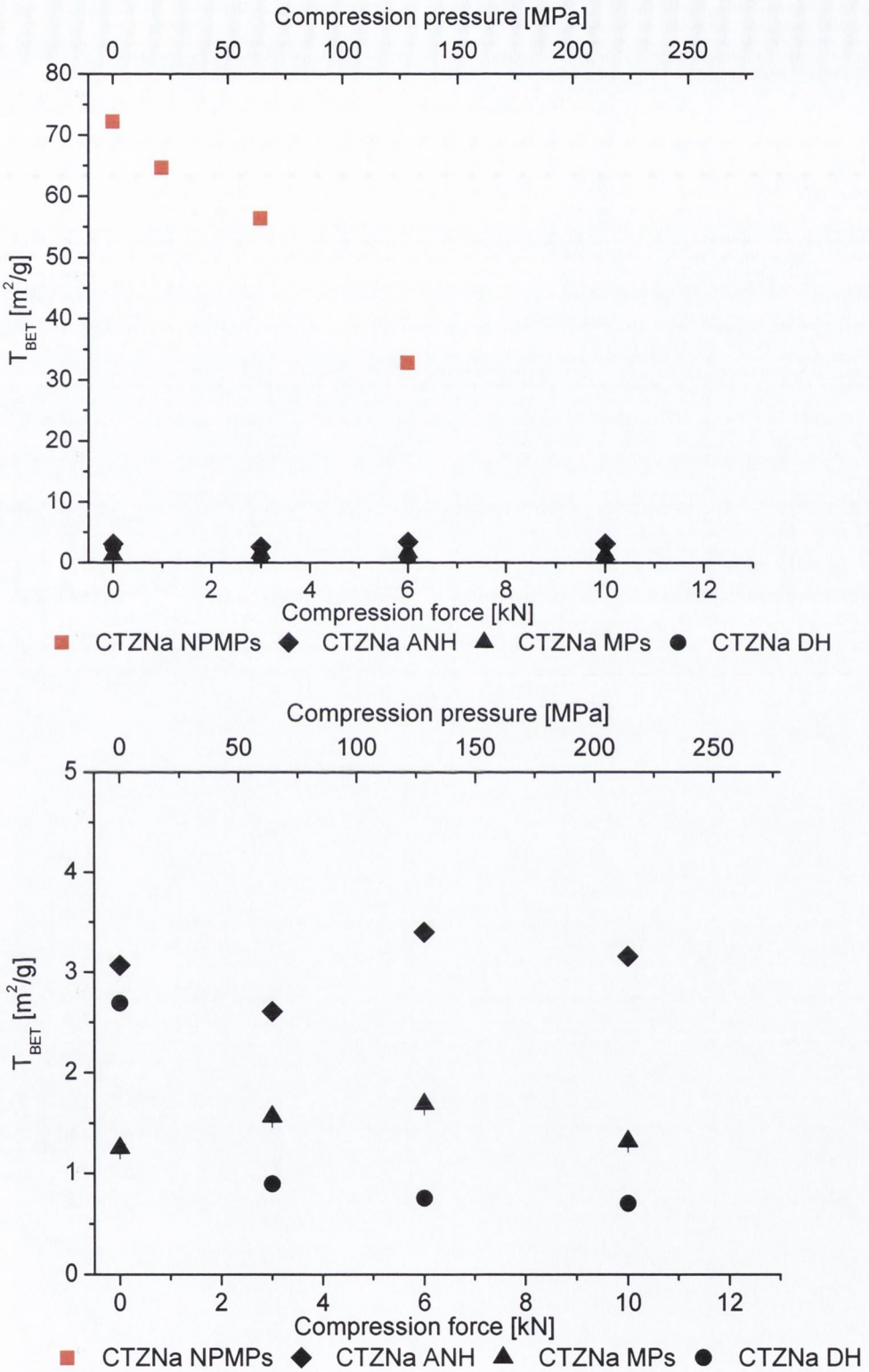

Fig. 7.11. Specific surface area of the tablet (T_{BET}) in relation to compression force (F) for: CTZNa DH, CTZNa ANH, CTZNa MPs and CTZNA NPMPs.

This untypical behaviour may be ascribed to the layered (foliated) structure of the microparticles of anhydrous CTZNa, recorded on SEM pictures (Figure 7.12c) (similar to slate rock). Foliating of particles of CTZNa DH form was not observed (Figure 7.12a). Foliation may be ascribed to evaporation of water molecules layered in the crystal structure, as presented in Chapter 3, looking at the packing of molecules of CTZNa in the crystal structure of CTZNa dihydrate along the a axis. There is a possibility that reduction of T_{BET} at the initial compression force of 3 kN may be assigned to compression of voids left after water in the crystal structure was evaporated. At 6 kN compression pressure T_{BET} increased over loose powder up to 3.4, indicating the possibility of cracking (Figure 7.12b) of particles, and slightly dropped to 3.16 m^2/g at compression pressure of 214 MPa, where possibly particles started to fuse.

In contrast to CTZNa ANH, CTZNa DH indicated a constant drop of T_{BET} from the value presented for the loose powder (2.69 m^2/g) to 0.89 m^2/g at the compression force of 3 kN, to 0.7 m^2/g at the compression force of 13 kN. This indicated that particles of this system fused together very easily even at low compression, possibly due to molecules of crystal water.

The behaviour of T_{BET} of tablets made of CTZNa MPs was similar to that for CTZ NPMPs, where firstly particles started to crack and break, increasing T_{BET} slightly, an equilibrium was reached between 3 and 6 kN and then the T_{BET} dropped at 10 kN compression force suggesting fusion of particles.

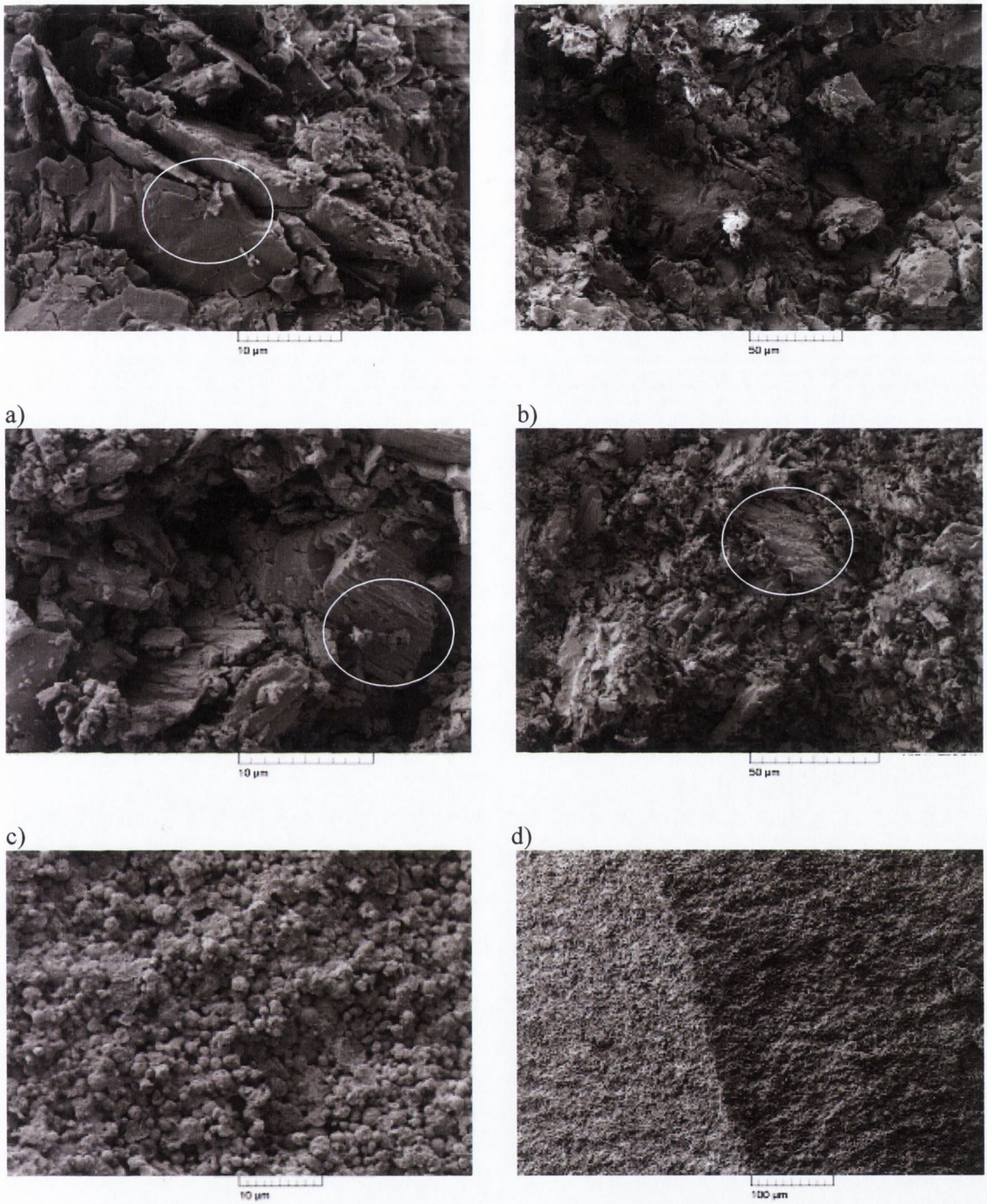

Fig. 7.12. SEM images of: a) morphology of CTZNa DH, b) cross section of the tablet made of CTZNa DH compressed at 6 kN, c) morphology of CTZNa ANH, d) cross section of the tablet made of CTZNa ANH compressed at 6 kN, e) cross section of the tablet made of CTZNa NPMPs compressed at 6 kN.

T_{BET} reduction under increasing compression pressure was also recorded for the CTZNa NPMPs system. This indicated that particles of this system compacted predominantly due to the fusion of particles, regardless of the compaction pressure.

Figure 7.13 shows the relationship between T_{BET} and compression force for all CTZK systems. The reduction in T_{BET} for the NPMPs tablets was approximately linear, similarly as for the CTZNa NPMPs in the range of 1 kN to 6 kN compression force. The change in T_{BET} for CTZK MH and CTZK MPs tablets on rising compression pressure was very low, indicating that these systems were compacted mainly due to elastic deformation and interlocking. Micronised CTZK ANH material behaved similarly to Dipac™, but differently to the equivalent CTZNa ANH system. CTZK ANH did not present a T_{BET} drop at the initial compression pressure, which may be ascribed to the different crystal structure of the hydrate, where, in contrast to CTZNa, chlorine atoms of CTZ are involved in direct coordination bond with potassium, as was presented in Chapter 4, which may prevent foliation as was described for CTZNa ANH.

Figure 7.14 compiles the T_{BET} with porosity data of the tablets for all tested systems. It indicates that the NPMPs systems of CTZK and CTZNa formed porous tablets made of materials with very large specific surface areas, which was not possible to achieve by compaction of conventionally produced materials. NPMP tablets, despite undergoing compression and reaching the porosities of tablets made of conventionally processed materials, still preserve large T_{BET} of pre-compressed material.

Figure 7.15 compiles the T_{BET} values versus tensile strength of the tablets for all tested materials. It indicates that the NPMPs systems of CTZK and CTZNa formed strong tablets made of materials with large specific surface areas. The tensile strength of NPMPs tablets was comparable or higher to the tensile strength of tablets made of conventionally produced materials.

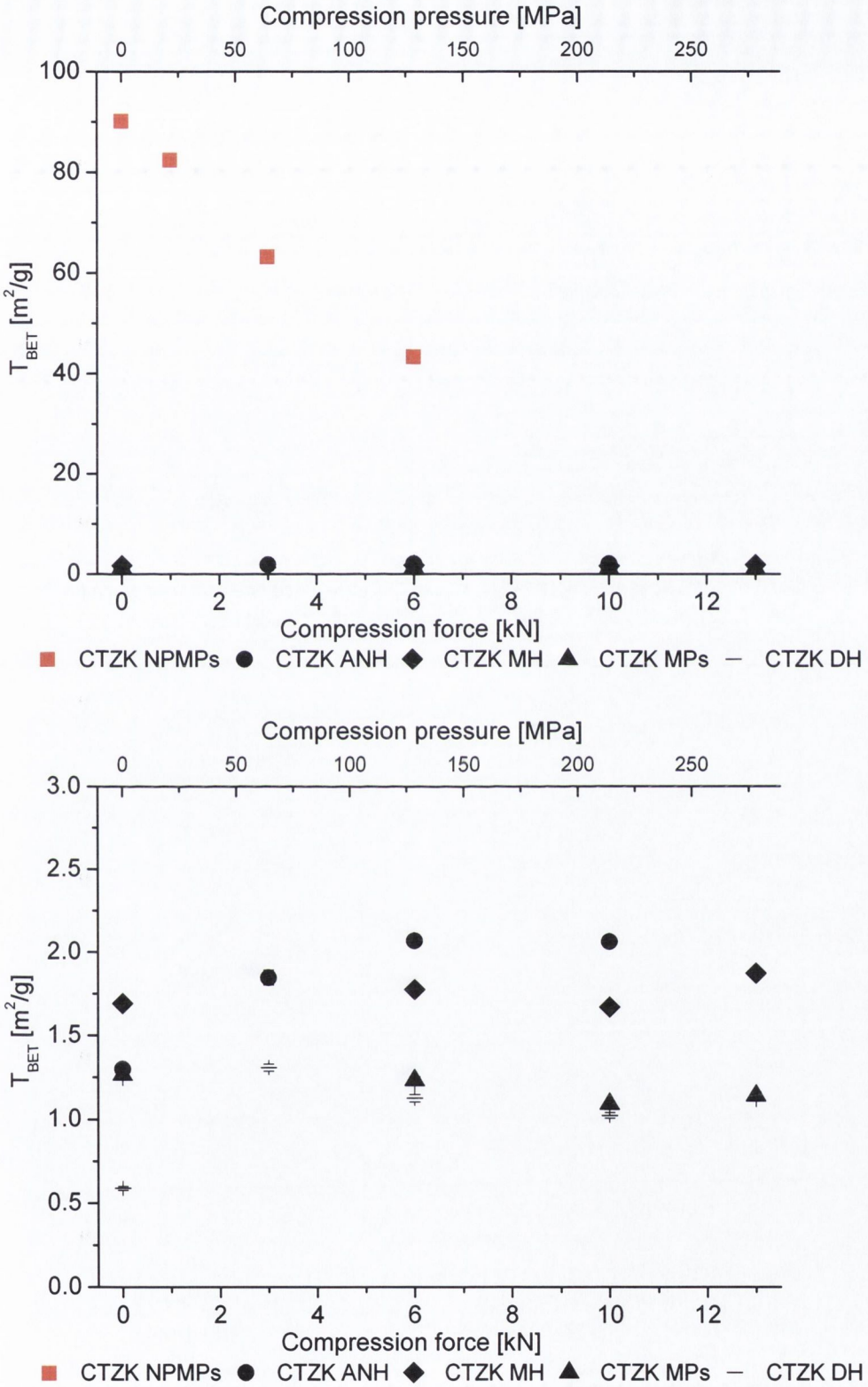

Fig. 7.13. Specific surface area of the tablet (T_{BET}) in relation to compression force (F) for: CTZK dihydrate, monohydrate and anhydrous microparticles, CTZK spray dried microparticles and CTZK nanoporous microparticles.

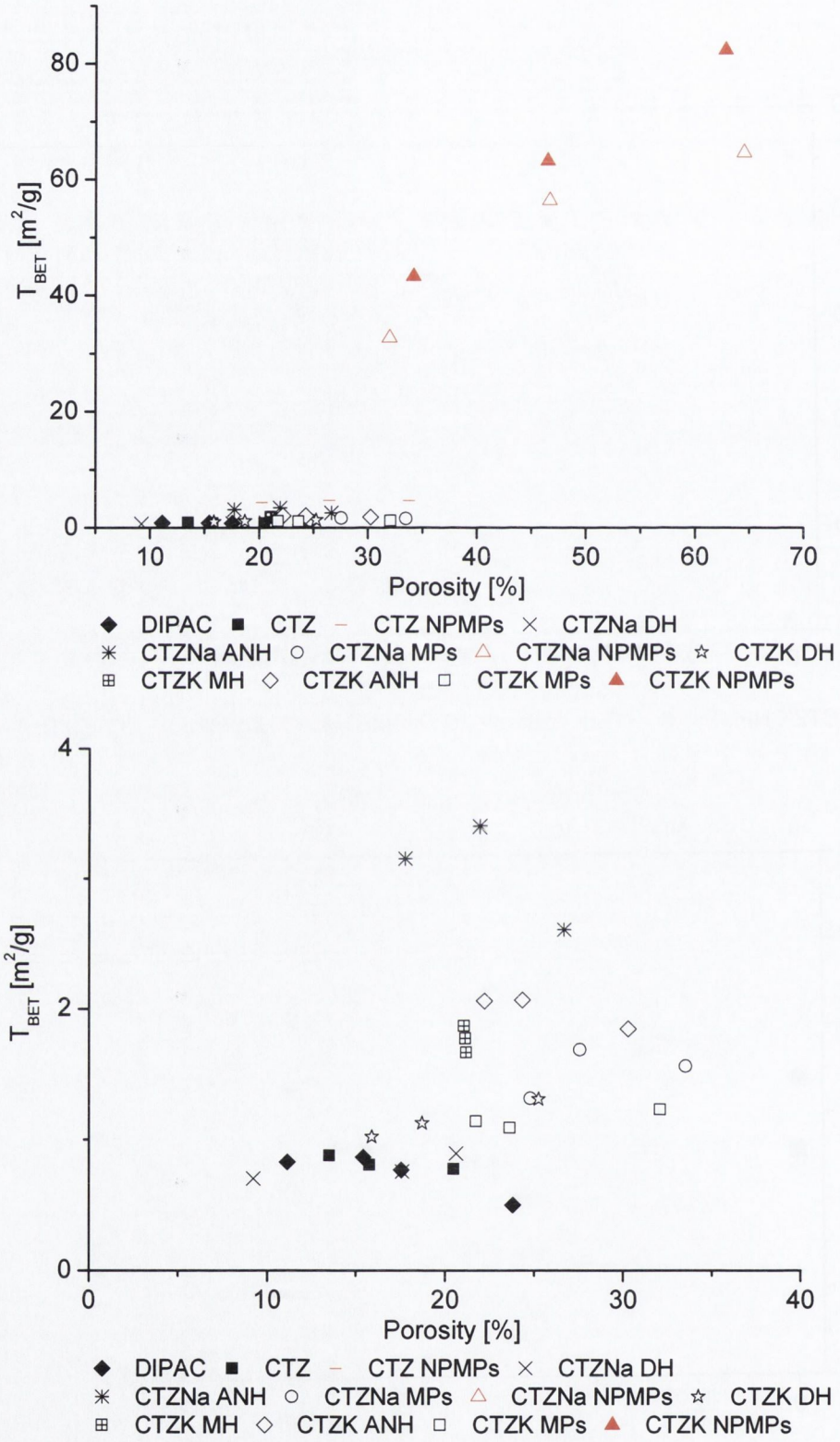

Fig. 7.14. Specific surface area of the tablet (T_{BET}) versus tablet porosity (ε_t).

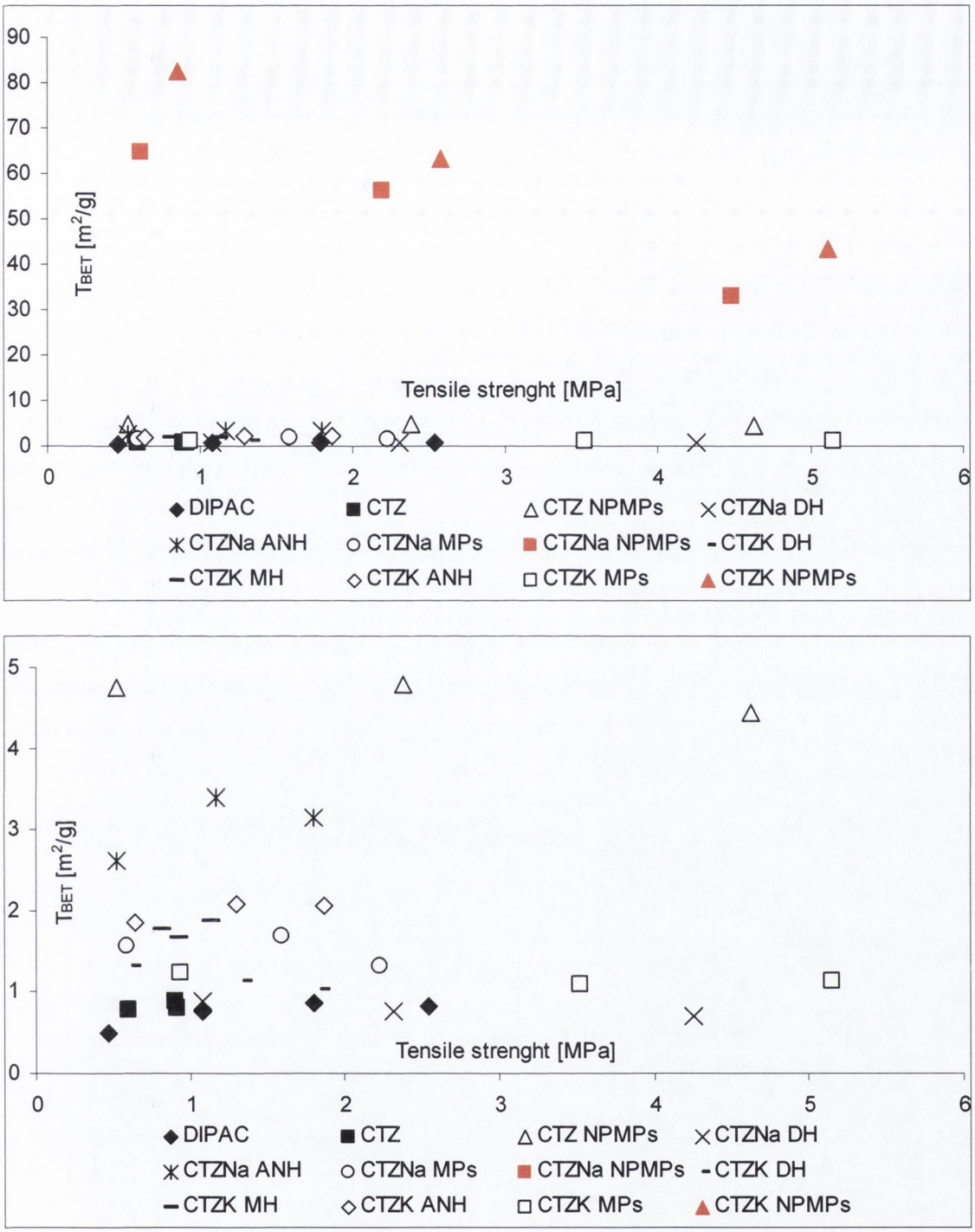

Fig. 7.15. Specific surface area (T_{BET}) of the tablet versus tablet tensile strength (σ_t).

7.2.6. Dissolution test results

It was hypothesised that the large T_{BET} of the NPMP powders preserved in formed tablets and the porosity of the tablets may promote faster dissolution of NPMP tablets over tablets made of conventional materials and present better dissolution characteristics. The tablets selected for dissolution studies were those compressed at the same compression pressure of 128 MPa corresponding to compression force of 6kN. Additionally, NPMPs tablets investigated were also compressed at 21MPa and 64 MPa.

Among all the tested systems of CTZNa materials (Figure 7.16) the fastest release of API was recorded for tablets made of NPMPs compressed at a compression force of 21 MPa. The tensile strength of these tablets was 0.62 MPa at the tablet porosity of 64.5% which corresponded to 64.7m^2/g of specific surface area of compacted CTZNa. Dissolution of tested tablets was very fast, as 100% of the 250 mg dose was released (at a paddle rotation speed of 50 rpm) between the third and fourth minute of the experiment. Tablets made of the same material compressed at 64 MPa performed nearly as well, though the difference in the performance among the tested tablets was slightly increased, resulting in slightly larger standard deviations. The pattern of increasing standard deviations was confirmed by testing tablets compressed at 128 MPa. These tablets had a very high average tensile strength of 4.48 MPa and this perhaps resulted in the large standard deviations.

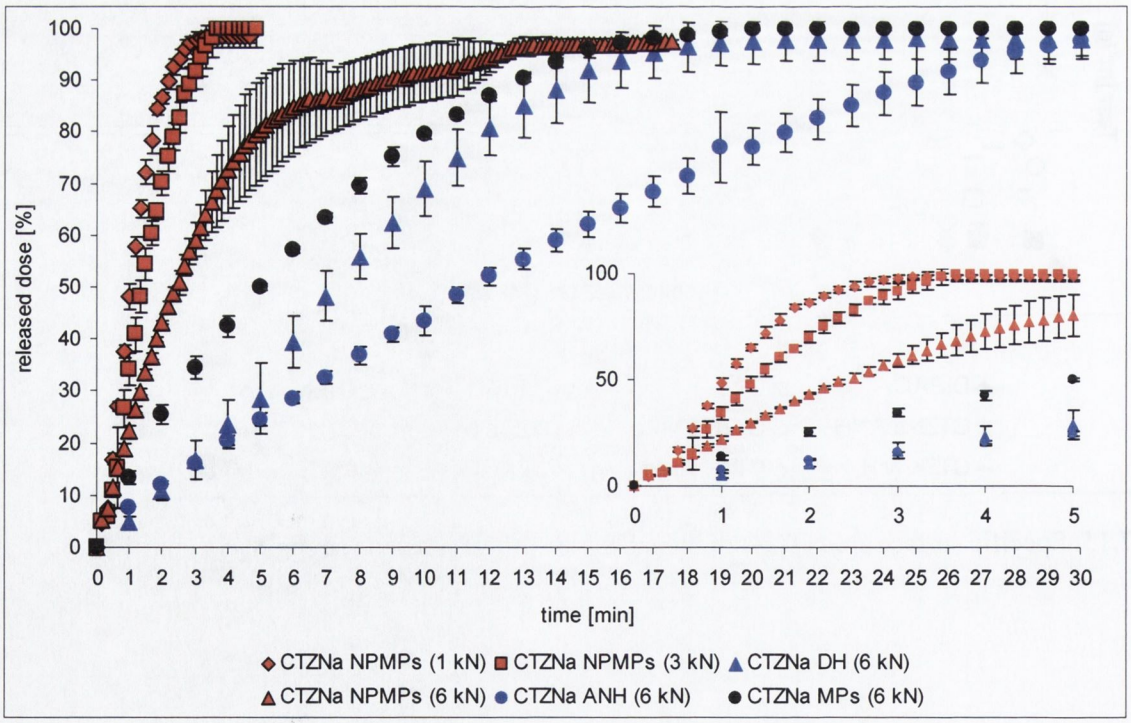

Fig. 7.16. Dissolution profiles of chlorothiazide sodium tablets. Compression force used is given in brackets.

Tablets made of NPMPs compressed at the highest tested compression pressure of 128 MPa released 100% of the API dose after 12 minutes. This was only slightly better than the dissolution performance of tablets made of CTZNa MPs compressed at 6 kN. The CTZNa MP tablets released 100% of the API after 19 minutes which was similar to the performance of tablets made of micronised CTZNa DH. What is interesting is that CTZNa DH tablets performed better than those made of CTZNA ANH even though the latter had larger T_{BET} and tablet porosity and lower tensile strength (Appendix I, Table I.4) in comparison to CTZNa DH tablets. Thus, it was expected that the CTZNa ANH tablets would exhibit faster dissolution than those formed from CTZNa DH. The cause of the lower dissolution rate of CTZNa ANH may be associated with hydration of CTZNa ANH to CTZNa DH during dissolution. Similarly, lower dissolution rates, in comparison to tablets made of hydrated theophylline, were observed for anhydrous theophylline tablets (Debnath and Suryanarayanan, 2004). This was ascribed to hydration of theophylline upon dissolution study. In the case of CTZNa ANH, 100% API was dissolved only after 30 minutes.

Considering the dissolution profiles of CTZK materials (Figure 7.17), the best dissolution performance was observed for tablets made of CTZK NPMPs.

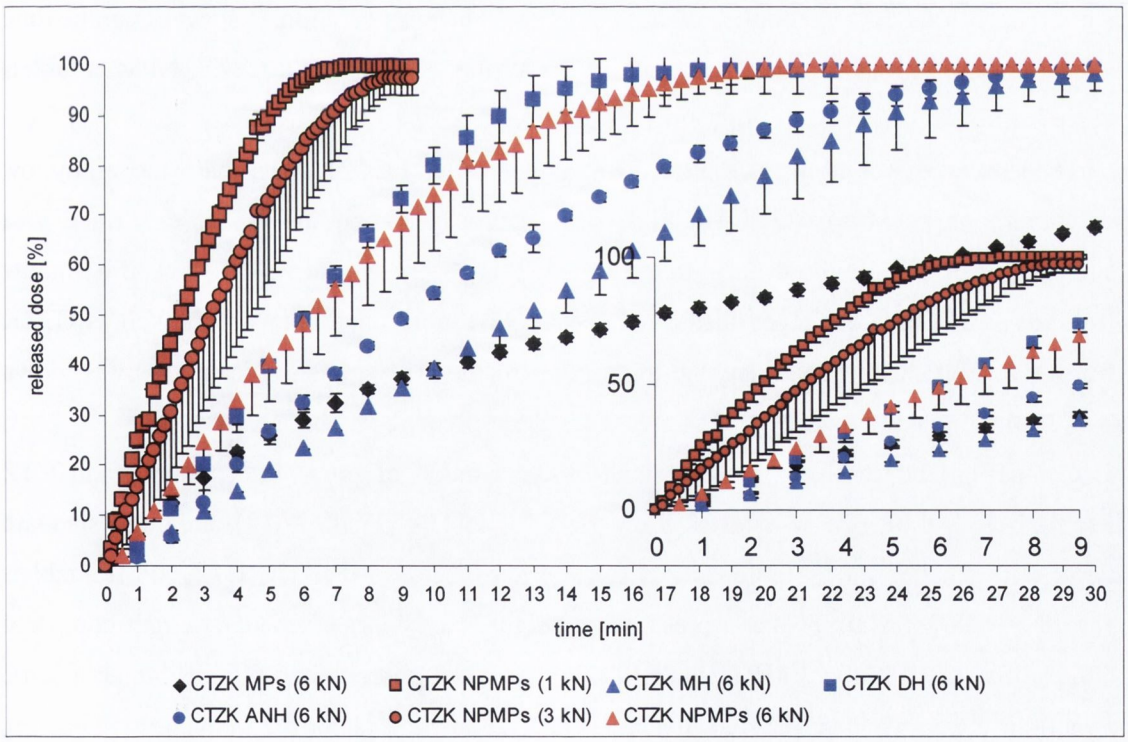

Fig. 7.17. Dissolution profiles of chlorothiazide potassium tablets. Compression force used is given in brackets. Only negative error bars are presented for some curves for clarity purposes.

With increasing compression pressure used to prepare NPMPs CTZK tablets, larger standard deviations were observed for the dissolution profiles. The best CTZK tablets in terms of time taken to release 100% of the API were those compressed from CTZK NMPS at 1 kN,

however it took 2 minutes longer, in comparison to the equivalent CTZNa NPMPs tablets, to release the whole API content (6 minutes). The time to release 100% of the dose from tablets made of NPMPs compressed at 3 kN was about 9 minutes and for the tablets compressed at 6 kN was about 19 minutes. The release profile of CTZK NPMPs tablets compressed at 6 kN was characterised by the greatest standard deviation.

In comparison to the tablets of CTZK NPMPs compressed at 6 kN, the dissolution profile for tablets of CTZK DH compressed at 6 kN had smaller standard deviations of the dissolution profile, but the tensile strength of these tablets was 3.77 MPa lower. The dissolution profiles these 2 systems did not vary as indicated by the overlapping standard deviation bars. CTZK ANH tablets were found to release the drug slower than CTZK DH, in accordance to the previous observations of the equivalent CTZNa tablets. But the release of the drug from the CTZK ANH tablets was faster than from the tablets made of CTZK MH, which may suggest that hydration of CTZNa ANH to DH during dissolution is faster than that of CTZK MH to DH.

CTZK ANH tablets had larger tensile strength than CTZK MH tablets and nearly 10% lower tablet porosity, but compressed CTZK ANH had two-times larger specific surface area (2.07 m^2/g) than CTZK MH (1.23 m^2/g). Despite the differences, CTZK ANH and CTZK MH tablets released 100% of the API dose within 30 minutes. This was 10 minutes slower than the time required to release 100% of dose for the tablets made of CTZK DH and CTZK NPMPs tablets compressed at 6 kN.

The slowest dissolution was recorded for tablets made of CTZK MPs characterised by low tensile strength (0.93 MPa), relatively high tablet porosity (32%) and specific surface area of compacted material of about 1.23 m^2/g. It may be observed that, up to the fifth minute of dissolution this system dissolved faster than CTZK MH tablets and comparably well as CTZK ANH, however after the fifth minute the dissolution of the API was significantly slowed down and up to 30-th minute only about 50% of the API had dissolved.

Comparing the two compressed tablet systems made of pure CTZ material and CTZ NPMPs, the API dissolution was faster from the CTZ tablets (Figure 7.18), although standard deviations were smaller for tablets made of spray dried CTZ NPMPs. The CTZ NPMPs tablets compressed at 128 MPa compression pressure had significantly larger tensile strength compared with CTZ tablets (2.38 vs. 0.92 MPa), over 10% higher tablet porosity and 6 times larger specific surface area of the compacted material. For the CTZ systems, the factor predominantly impacting (improving) dissolution profile is low tensile strength of the tablet over its porosity and T_{BET} of compressed material.

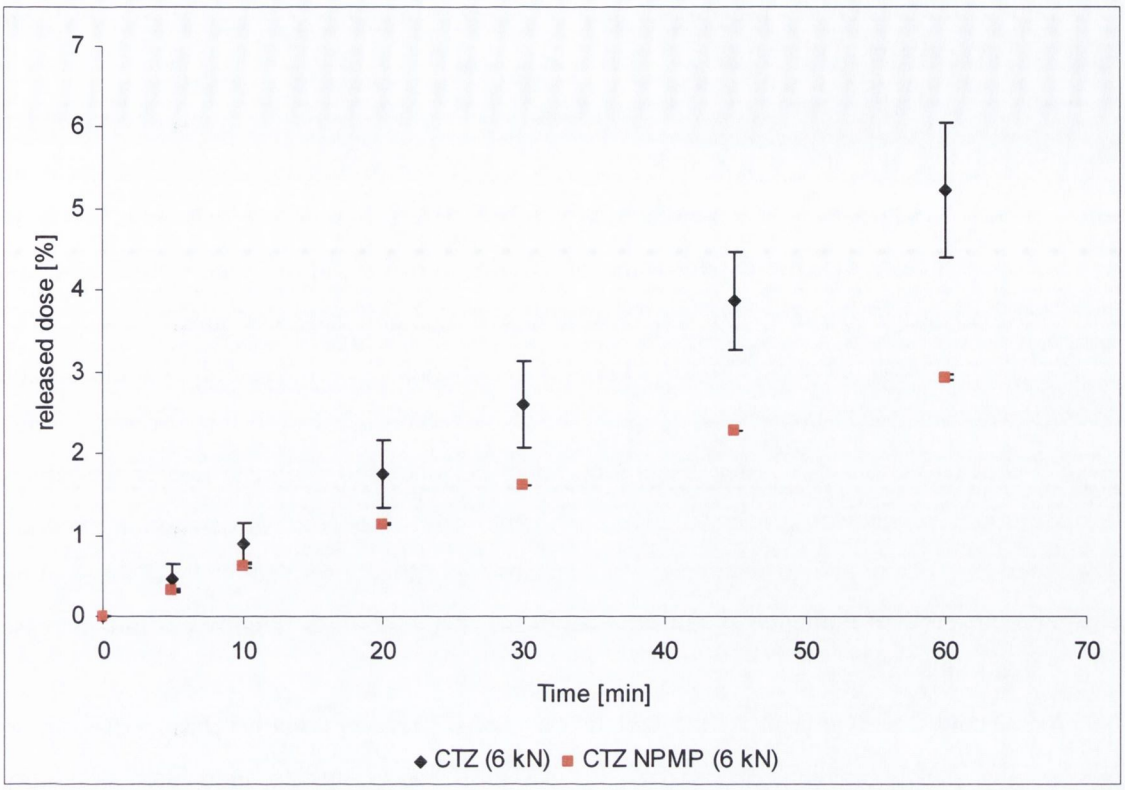

Fig. 7.18. Dissolution profiles of chlorothiazide tablets. Compression force used is given in brackets.

The tablets were observed to change the surface area during dissolution; therefore the Hixson Crowell model (Eq. 1.15) was selected to describe the experimental dissolution profiles. To calculate the $K_{1/3\ calc.}$ parameter (Eq. 1.16) ,aqueous solubility values for CTZ, CTZNa DH (Chapter 3) and CTZK DH (Chapter 4) were used. The diffusion coefficient (D) value was estimated based on that for benzoic acid (Healy et al., 2002) correcting for the molecular weight of the drugs using the Einstein-Stokes equation (Eqn. 7.1).

$$D = \frac{k_B T}{6 \prod \eta r} \qquad \text{Eqn. 7.1.}$$

Where T is the temperature of medium, η is the local viscosity of medium, r is the radius of molecular sphere and k_B -Boltzmann constant is equal to $k_B = \frac{R}{N_A}$ where R is the ideal gas constant (8.3145 J/mol K) and N_A is the Avogadro's number ($6.0221 \cdot 10^{23}$ 1/mol). Eqn. 7.1 suggests that the diffusion coefficient is inversely proportional to the cube root of its molecular weight assuming that the molecules are approximately spherical and have similar densities Jackson (2006). The diffusion layer thickness value, characterised by the hydrodynamic conditions of dissolution experiment, was adopted from the same study (Healy et al., 2002). The calculated, theoretical $K_{1/3\ calc.}$ values are listed in table 7.4. The Hixson Crowell equation was fitted to each

of the experimental dissolution profiles to obtain the experimental $K_{1/3\ fitted}$ values which are presented in table 7.5.

The $K_{1/3\ fitted}$ values did not agree with the $K_{1/3\ calc.}$ values (Table 7.5), with the exception of tablets made of CTZK MPs. Values of $K_{1/3\ fitted}$ of a 1.7-to 18-fold greater were observed, with the tablets made of CTZNa NPMPs compressed at 21 and 64 MPa showing the greatest differences. It was therefore apparent that the experimental dissolution profiles did not match the theoretical dissolution profiles described by the Hixson Crowell model as exemplified in figure 7.19.

The discrepancy between the model and experimental data suggested that dissolution of the tablets occurs much faster than it could be expected from the Hixson Crowell model. Therefore it is possible that this faster dissolution could be related to disintegration of the tablets during dissolution, which would affect the linear change of surface area of dissolving material. Disintegration may occur due to water penetrating into the tablet, resulting in its disintegration and erosion. The eroded elements of tablets floating in the dissolution medium could increase the surface area of the material subjected to dissolution.

Erosion and disintegration of the tablets was not observed (visually) during dissolution studies. For the tablets made of CTZ salts it was most likely due to their high solubility and for the CTZ tablets it was due to the low dissolution rate and perhaps much slower erosion of tablets. Therefore, to visualise any potential erosion and disintegration of the tablets, they were immersed in saturated solutions of the corresponding tablet material. As pictured in figure I.10 (Appendix I), the difference between not eroded tablet and tablet recovered after an hour is easily discernible. The recovered tablet had rough surfaces that may have been formed due to fragmentation/disintegration of the compact. Figure I.11 (Appendix I) presents clouding of the CTZ saturated medium due to tablet erosion and fragments of the tablet floating in the liquid. Similar study was performed on a CTZNa tablet. Figure I.12 (Appendix I) presents considerable visual erosion and disintegration of the tablet. The tablet recovered from the dissolution medium (presented in figure I.13) (Appendix I) was covered with a thick film of loose undissolved material. Consequently, these experiments provided an evidence of the disintegrating nature of the tablets investigated and explained why the Hixson Crowell model reproduced the dissolution profiles poorly.

Table 7.4. Calculated theoretical $K_{1/3\ calc}$ for the Hixson and Crowell model (Eqn.1.16).

Material	$K_{1/3\ calc.}$ [$s \cdot mg^{(-1/3)}$]
CTZ	$3.24 \cdot 10^{-6}$
CTZNa	0.00123
CTZK	0.00119

Table 7.5. Parameters of the experimental dissolution profiles fitted to the Hixson and Crowell model.

Tablet system	R^2	$K_{1/3\ fitted}$ [$s \cdot mg^{(-1/3)}$]	$K_{1/3\ fitted}$/ $K_{1/3\ calc.}$
CTZ (128 MPa)	0.9998	$3.08E\text{-}5 \pm 1.16 \cdot 10^{-7}$	9.52
CTZ NPMPs (128 MPa)	0.9926	$1.79E\text{-}5 \pm 3.88 \cdot 10^{-7}$	5.53
CTZNa NPMPs (21 MPa)	0.9740	$0.0229 \pm 8.43 \cdot 10^{-4}$	18.62
CTZNa NPMPs (64 MPa)	0.9660	$0.0171 \pm 6.33 \cdot 10^{-4}$	13.90
CTZNa NPMPs (128 MPa)	0.9628	$0.00801 \pm 1.389 \cdot 10^{-4}$	6.51
CTZNa DH (128 MPa)	0.9760	$0.00334 \pm 1.086 \cdot 10^{-4}$	2.72
CTZNa ANH (128 MPa)	0.9910	$0.00206 \pm 2.95 \cdot 10^{-5}$	1.67
CTZNa MPs (128 MPa)	0.9991	$0.00350 \pm 1.741 \cdot 10^{-4}$	2.85
CTZK NPMPs (21 MPa)	0.9927	$0.0102 \pm 1.2 \cdot 10^{-4}$	8.55
CTZK NPMPs (64 MPa)	0.9857	$0.00730 \pm 1.041 \cdot 10^{-4}$	6.12
CTZK NPMPs (128 Mpa)	0.9923	$0.00374 \pm 4.599 \cdot 10^{-5}$	3.13
CTZK DH (128 MPa)	0.9691	$0.00399 \pm 1.531 \cdot 10^{-4}$	3.34
CTZK MH (128 MPa)	0.9709	$0.00199 \pm 5.25 \cdot 10^{-5}$	1.67
CTZK ANH (128 MPa)	0.9912	$0.00246 \pm 3.71 \cdot 10^{-5}$	2.06
CTZK MPs (128 MPa)	0.9602	$0.00113 \pm 1.96 \cdot 10^{-5}$	0.95

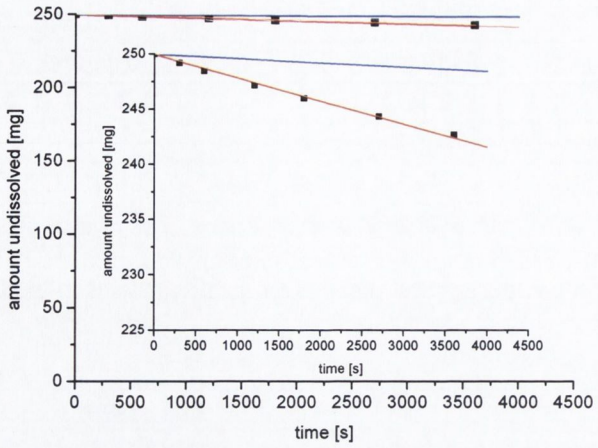

a)

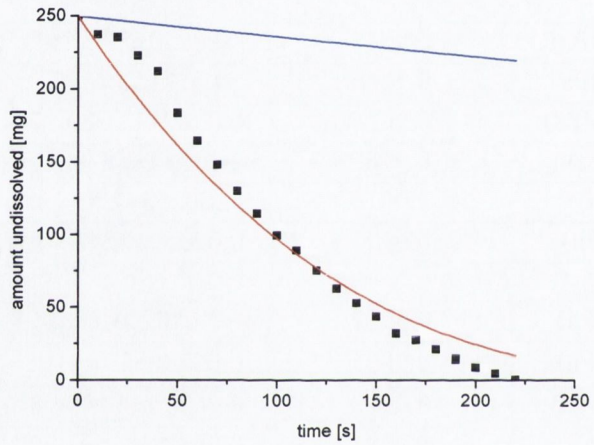

b)

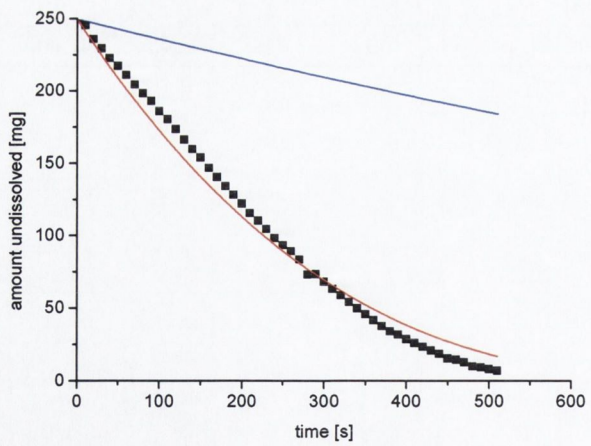

c)

Fig. 7.19. Experimental and calculated dissolution profiles of a) CTZ NPMPs (128 MPa), b) CTZNa NPMPs (64 MPa) and c) CTZK NPMPs (64 MPa). Experimental data are presented as filled squares are, the red line is the best fit to the Hixson Crowell model (R^2 and $K_{1/3}$ as per Table 7.5.) and the blue line is a calculated dissolution profile based on the theoretical $K_{1/3\ calc.}$ (Table 7.4).

7.3. Conclusions

NPMPs produced by spray drying had better tabletability performance, as seen from single point measures of force to tensile failure, tensile strength and tablet porosity versus compression pressure (compression force) used to compact material in comparison to tablets made of conventionally processed materials. The tablets made of NPMPs presented higher tensile strength and higher tablet porosity than those made of crystalline, micronised and non-porous spray dried material or material designed for direct compaction (Dipac™). Moreover, NPMPs compacts maintained large specific surface area, at the same time presenting large tablet porosity and satisfactory tensile strength. Salt (CTZNa and CTZK) NPMP tablets presented very good dissolution test performance, presenting the shortest times for dissolution of 100% of the API. NPMPs may be considered as suitable for direct compaction and for inclusion in tablets formulations as bulking agents, APIs, carriers or binders due to their good compactibility performance.

Chapter 8

Solid state characterisation of novel active pharmaceutical ingredients: co-crystal of a salbutamol hemiadipate salt with adipic acid (2:1:1) and salbutamol hemisuccinate salt

8.1. Introduction

Salbutamol is a β2-mimetic used as a bronchodilator which is presented as the (±) racemic mixture in pharmaceutical inhalers (propellant-based and dry powder), nebules, injections, syrups and tablets, including controlled-release forms (BMJ, British National Formulary). The hemisulfate salt (commonly referred to as salbutamol sulfate) is the most common form of salbutamol used in pharmaceutical products however the (*R*)-salbutamol hydrochloride form is also available on the market as an inhalation solution (Xopenex™, manufactured by Sepracor Inc.). Although some other salbutamol salts have been reported in the literature, e.g. ethanolated salbutamol adipate and salbutamol stearate (Jashnani et al., 1993), to date only two crystal structures are reported in the Cambridge Structural Database: salbutamol base (SB) (Beale and Grainger, 1972) and salbutamol sulfate (SS) (Leger et al., 1978). The information about the solid state nature of other forms of salbutamol is sparse.

From a pharmaceutical point of view, different solid-state characteristics of salt forms can result in different *in vitro* solubility and dissolution properties, which in turn can result in an alteration of the *in vivo* activity of the active pharmaceutical ingredient (API). In particular, for pulmonary delivery, possibilities for modification of the dissolution profile of the API from a formulation point of view are limited and may result in additional costs and regulatory obstacles associated with the development of a new drug product. This may be avoided by the direct production of alternative crystalline forms of the API with the desired solubility and dissolution profiles. The marketed solid dosage forms contain only SS, which is freely soluble in water (European Pharmacopoeia, 2010). The advantage of prolonged release tablets containing SS was reported in clinical studies (Vyse and Cochrane, 1989). New prolonged release oral dosage forms containing SS include hard capsules VentMax™ and tablet forms: Volmax CR™, Vospire ER™ (Murthy and Shobharani, 2004). Both, prolonged release capsules and tablets containing SS have monographs in the British Pharmacopeia. A transdermal delivery patch of SS was also developed (British Pharmacopeia 2010).

This study investigated the impact of replacing the sulfate anion in the SS salt structure by an organic dicarboxylic acid, either the four-carbon chain, succinic (butanedioic) acid or the six-carbon chain, adipic (hexanedioic) acid, on the physicochemical characteristics of the API. These two organic acids were chosen in order to investigate the impact of small changes in the chemical structure of the co-former on the physicochemical properties of the resulting salbutamol forms. A reasonable correlation between the melting points of organic co-formers and melting points of the resulting salts was previously reported for diclofenac (O'Connor and Corrigan, 2001). The authors also observed a trend between the salt melting point and the logarithm of the solubility. The reported melting points of adipic and succinic acids are ~151-154 °C and ~185-187 °C, respectively (Stahl and Wermuth, 2008), hence it may be hypothesized that the succinate would have a lower solubility than that of the adipate. On the other

hand, increasing the hydrophilicity of the counterion as a means of increasing the water solubility of the resultant salt has been proposed and investigated for a series of erythromycin (Anderson and Conradi, 1985). The calculated logPs of adipic and succinic acid are 0.356 and -0.655 respectively (Veber et al., 2002), indicating that a salt of adipic acid may be less soluble than that of succinic acid. The study performed by Li at al. (2006) successfully investigated the possibility of forming ionic (salts) or neutral (co-crystals) complexes of a heterocyclic base (an ErbB2 inhibitor for the treatment of cancer) with dicarboxylic acids comprising succinate, malonate and maleate co-formers. The acids (adipic and succinic) used in the current study have similar pKa values. The pKa1 and pKa2 for succinic acid are 4.21 and 5.64 (Stahl and Wermuth, 2008) and for adipic acid these are 4.44 and 5.44 (Stahl and Wermuth, 2008). As pKas of salbutamol are 9.1 and 10.4 (Imboden and Imanidis, 1999), it was expected that the new forms of the API would be novel 1:1 salts of salbutamol.

Both acids are classified by the U.S. Food and Drug Administration (FDA) as Generally Recognised As Safe (GRAS) and listed in the European Pharmacopeia (European Pharmacopoeia, 2010). Adipic acid is currently used to produce salts of piperazine (Entacyl™) and spiramycine (Rovamycine™ injectable form) (Stahl and Wermuth, 2008). Succinic acid is used to form salts of e.g. benfurodil, bamethan, chloramphenicol, cibenzoline, deanol, doxylamine, ergotamine, loxepine, metoprolol, oxaflumazine, sumatriptan and iron (FeII) (Stahl and Wermuth, 2008).

8.2. Results and discussion

8.2.1. Single crystal X-ray analysis

Single crystal analysis of salbutamol adipate (SA) and salbutamol succinate tertmethanolate (SSU.MeOH) was undertaken, of which details are shown in Table 8.1. Crystals of SA are centrosymmetric, with both enantiomers present in the lattice. Figure 8.1a presents the atomic labelling in the unit-cell of the adipate system, which has a 1:1 ratio of salbutamol base to adipic acid. The adipate exists in the lattice in both protonated O(5) and ionized (O(6), O(7) forms, as shown by the C-O distances: 1.322(2) Å for the protonated form, and C(17)-O(6): 1.265(1) Å and C(17)-O(7): 1.261(2) Å for the ionized form. In addition, there is some disorder in the hydroxyl group on the stereogenic centre, C(8). Further views of the crystal packing are depicted in Figure 8.2 a, b.

Table 8.1. Crystallographic data for SA and SSU.MeOH.

Analysis parameters	SA	SSU.MeOH
Crystal system	triclinic	monoclinic
Space group	$P\bar{1}$	$P\ 2_1/n$
Z	2	4
Unit cell dimensions	a = 9.733(3)Å α = 66.354(5)° b = 10.700(3)Å β = 86.080(6)° c = 10.926(3)Å γ = 67.906(5)°	a = 10.3934(5)Å b = 20.2011(10)Å β =114.5300(10)° c = 10.3962(5)Å
Volume, $Å^3$	961.2(4)	1985.76(17)
R^1 [I>2σ(I)], wR^2 (all data)	0.038, 0.090	0.039, 0.104

Crystals of SSU.MeOH (Figure 8.1b) are also centrosymmetric and were determined to be solvated with methanol molecules (Figure 8.2c and 8.2d). This was subsequently confirmed by DSC, TGA, elemental analysis and ^1H NMR spectroscopy. The succinate was found in its ionized form, with C-O bond distances of 1.274(1) Å and 1.253(2) Å. The SSU.MeOH stoichiometry was 2:1:4.

8.2.2. Analysis of hydrogen bond network

Analysis of the hydrogen bonds in SA (Table 8.2) reveals that the vast majority of these bonds occur between the hydroxyl groups on the salbutamol and the ionized adipic carboxylate. This carboxylate is also hydrogen bonded to the secondary amine group of salbutamol. The protonated adipic acid does not play a crucial role in the creation of the hydrogen bond network, with only one hydrogen bond to a hydroxyl group of the salbutamol molecule

Table 8.2. Hydrogen bonding in SA.

D-H...A	D-H [Å]	H...A [Å]	D...A [Å]	D-H...A [°]
N(1)-H(1)A...O(7)	0.951(19)	1.845(19)	2.7945(18)	175.6(14)
N(1)-H(1)B...O(1)B	0.96(2)	2.404(18)	2.808(5)	105.0(12)
N(1)-H(1)B...O(6)[a)]	0.96(2)	1.88(2)	2.8353(18)	172.2(16)
O(1)A-H(1)C...O(7)[a)]	0.84	1.93	2.7619(19)	169
O(1)B-H(1)D...O(6)[a)]	0.84	2.46	2.816(5)	106
O(1)B-H(1)D...O(7)[a)]	0.84	1.79	2.609(5)	166
O(2)-H(2)A...O(6)[b)]	0.84	1.81	2.6327(17)	165
O(3)-H(3)A...O(4)[a)]	0.84	1.92	2.7437(18)	167
O(5)-H(5)...O(3)[d)]	0.88(3)	1.76(3)	2.6314(18)	172(2)
C(6)-H(6)...O(3)	0.95	2.50	2.8470(19)	101
C(8)-H(8)B...O(2)[c)]	0.99	2.54	3.457(2)	154
C(16)-H(16)A...O(1)B[a)]	0.99	2.29	3.148(5)	144

Symmetry codes: (a)1-x, -y, 1-z; (b) 1-x, -y, 2-z; (c) –x, -y, 2-z; (d) 1+x, 1+y, -1+z;

Interestingly, analysis of the hydrogen bonds in methanolated salbutamol succinate (Table 8.3) reveals the crucial role of the methanol in the formation of the lattice and no significant interaction with the ionized succinate. Two molecules of methanol are hydrogen bonded together. There is an O-H...O interaction with the hydroxyl group of salbutamol, as well as O-H...O hydrogen bonding between the methanol hydroxyl group and salbutamol. In addition, the carboxylate of the succinate interacts with the secondary amine and a hydroxyl group of salbutamol.

Table 8.3. Hydrogen bonding in SSU.MeOH.

D-H...A	D-H [Å]	H...A [Å]	D...A [Å]	D-H...A [°]
O(1)-H(1)...O(5)[b)]	0.84	1.79	2.6297(14)	173
N(1)-H(1)A...O(4)[b)]	0.929(18)	1.852(19)	2.7786(15)	175.0(13)
N(1)-H(1)B...O(1)[c)]	0.912(16)	1.924(17)	2.7953(13)	159.1(17)
O(2)-H(2)A...O(7)[d)]	0.84	1.80	2.6312(16)	171
O(3)-H(3)A...O(4)[e)]	0.84	1.85	2.6721(13)	165
O(6)-H(6)A...O(3)[g)]	0.84	1.84	2.6754(13)	174
O(7)-H(29)...O(6)[h)]	0.84	1.81	2.6523(15)	176
C(2)-H(2)...O(5)[a)]	0.95	2.53	3.4744(14)	177
C(6)-H(6)...O(3)	0.95	2.56	2.8788(14)	100
C(8)-H(8)A...O(2)[e)]	0.99	2.38	3.3068(15)	155
C(11)-H(11)B...O(2)[f)]	0.98	2.57	3.5145(15)	162

Symmetry codes: (a) 1-x, 2-y, 2-z; (b) 1+x, y, z; (c) 2-x, 2-y, 2-z; (d) x, 1+y, z; (e) 1-x, 2-y, 1-z; (f) 3/2-x, -1/2+y, 3/2-z; (g) x, -1+y, z; (h) -1/2+x, 1/2-y, 1/2+z

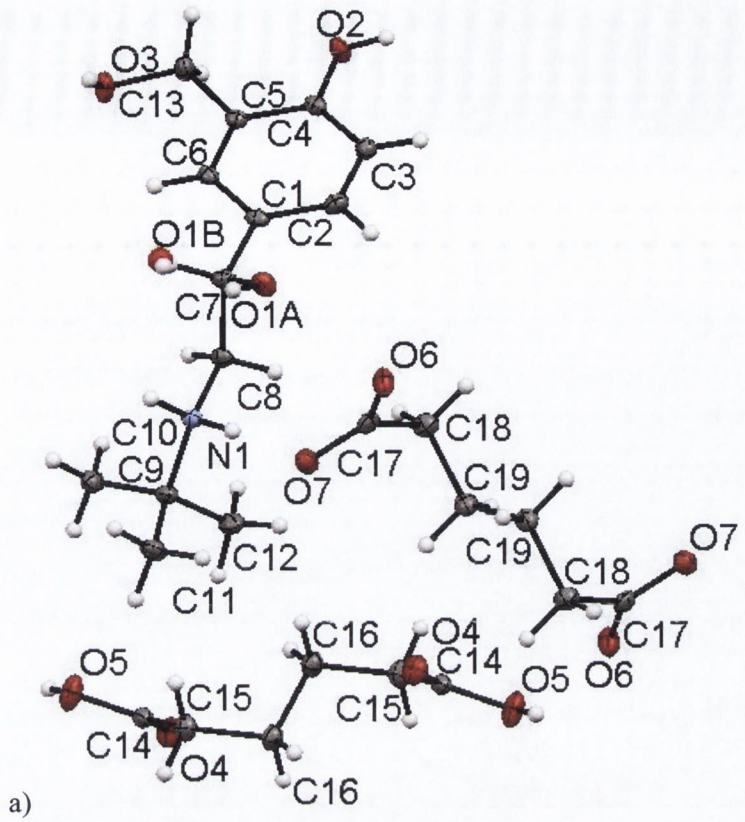

a)

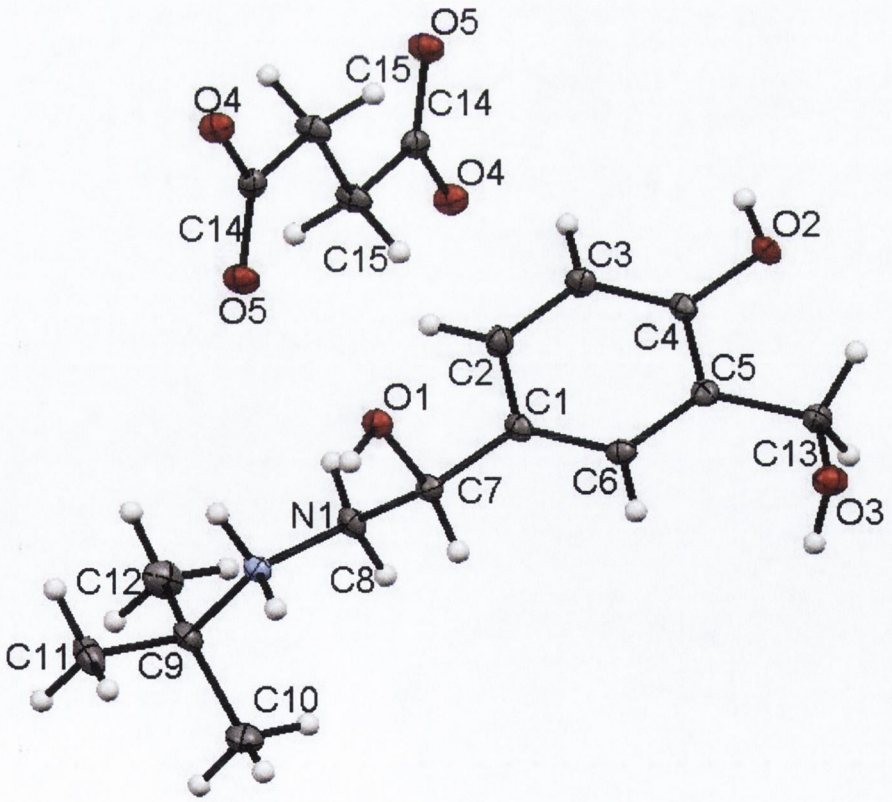

b)

Fig. 8.1. a) SA and b) SSU.MeOH showing the atomic labeling. The solvent molecules in SSU.MeOH are omitted for clarity. Probability ellipsoids are shown at the 50% level.

A comparison of the crystal packing of SSA (Fig. 8.2a,b) with SSU.MeOH (Fig. 8.2c,d) indicates why SSA contains an "additional" protonated molecule of adipic acid. It can be seen that SSA molecules packing along the c axis (Fig. 8.2b) consists of channels made of salbutamol molecules. These channels are placed centrally around the molecules of adipic acid. The adipic acid molecules are placed one below the other, alternating ionized with protonated molecules in each layer. The ionized carboxylic groups of adipic acid face towards the secondary amine moieties of salbutamol molecules, while protonated groups are placed in close proximity to methoxyls of the benzene ring of salbutamol molecules. This indicates that the ionized acid stabilizes more polar parts of the salbutamol molecule, where partial polarizability of R-NH-Me-MeOH molecule fragment was calculated to be α: 15.68±0.5 $Å^3$ while the protonated molecule is responsible for interaction with less polar parts of salbutamol, where partial polarizability of HOMe-Ar part was calculated to be: α 12.96±0.5 $Å^3$. The interaction is promoted by the close proximity of carboxylic acid groups to the channels formed by salbutamol molecules.

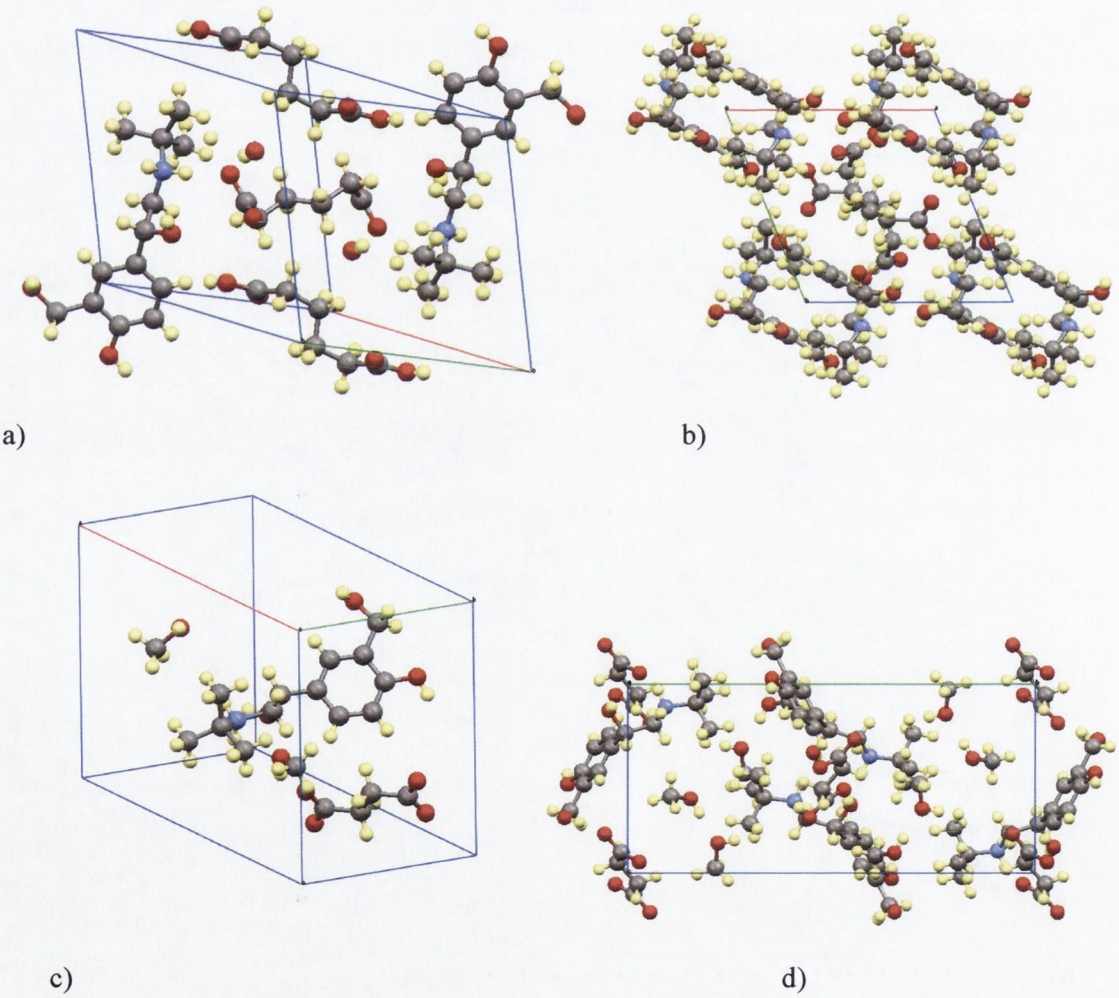

Fig. 8.2. a) unit cell of SA, b) extended packing diagram of SA along c axis, c) unit cell of SSU.MeOH, d) extended packing diagram of SSU.MeOH along b axis. Carbons-grey, hydrogens-yellow, nitrogens- blue, oxygens- red.

This is due to the similar length of adipic acid to the length of the between-salbutamol channel, i.e. approximately 8 Å -O(5)-O(5) distance.

Succinic acid is much shorter than adipic acid, the O(5)-O(4) distance is approximately 5 Å, and forms a different arrangement to SSA along the c axis. Despite the fact that the pKa(s)1,2 of succinic acid (4.21 and 5.64 at 25 °C) (Stahl and Wermuth, 2008) and adipic acid (4.44 and 5.44 at 25 °C) (Stahl and Wermuth, 2008) are only slightly different, this difference seems to be large enough to allow ionized succinic acid to stabilize the amine group and neighboring hydroxyl of salbutamol simultaneously. In SSU.MeOH each salbutamol molecule is stabilized, as described, by a succinic acid from the one side and a second molecule of salbutamol, in that the amine group of SB(A) interacts with the hydroxyl next to the amine group of SB(B). The solvated nature of SSU.MeOH arises from the interaction of H-bond dimers (as later described in hydrogen bond network analysis) of methanol with hydroxyls of salbutamol.

Haynes and co-workers presented a review reporting the occurrence of pharmaceutically acceptable anions and cations in the Cambridge Structural Database (CSD) (Haynes et al., 2005). No examples of a co-crystal of a salt of adipic acid were reported and only 23 co-crystalline forms of adipic acid were found. The same report indicated the occurrence of only 9 salts of succinic acid indicating that both forms of salbutamol presented here are rare in terms of their solid state structures. The SA reported in the current work should be classified as a co-crystal of the salbutamol hemiadipate salt with adipic acid in contrast to the previously reported ethanolated salt of salbutamol hemiadipate (Jashnani et al., 1993).

Previously, a co-crystal of the salt of the API with an unionized counterion was reported for the anticonvulsant drug valproic acid, where the API comprised co-crystalline form of sodium valproate salt with valproic acid (Petrusevski, et al. 2008). The use of co-crystals in a similar manner to salts in order to alter the physicochemical properties of API has been comprehensively investigated (Bailey et al., 2003, McNamara et al., 2006, Variankaval et al., 2006, Zegarac, 2007, Shan and Zaworotko, 2008, Dova et al., 2008, Cheney et al., 2010), though only one paper published so far reports on the co-existence of dianions and an unionized form of the acid in the same crystal lattice, similarly to what we have determined for SA, it was a hydrated crystal of escitalopram oxalate with oxalic acid (Harrison et al., 2007).

8.2.3. Hirshfeld surfaces analysis

Hirshfeld surfaces analysis (Fig. 8.3) allowed for visualization and comparison of reciprocal interactions among atoms in crystal lattices of salbutamol base and salbutamol sulfate compared to salbutamol adipate and succinate. The visualization is based on a 3-D surface surrounding a single molecule of salbutamol.

Noticeably, the same chemical structure of salbutamol may present different intensity of reciprocal interactions externally and internally to the Hirshfeld surface. Red places named "hot spots", indicate areas of salbutamol molecules where the interactions are the strongest and the distance between attracting atoms is shorter than in the case of attraction caused by Van der Waals forces (corresponding to white colour on Hirshfeld surface). In all of the derivatives of salbutamol, the most involved areas in the formation of hot spots include hydroxyl groups, where hydrogens and oxygens generate separate, independent crystallographically hot spots and the secondary amine group. Hirshfeld surface analysis also confirmed that hydrogens of methyl groups of the butyl moiety, secondary methyl group and hydrogens of the benzene ring are able to form weak hot spot interactions. It is evident that the molecule of salbutamol in the crystal structure of SB forms an intensive hot spot interactions close to O(1)–H(1), the same as in co-crystalline form of SA, while this interaction is visibly weaker for salbutamol molecules forming crystal structures of salt forms SS and SSU.MeOH. The intensity of hot spot interaction also differs in the case of the methoxyl group O(3)–H(3) attached to the benzene ring of salbutamol. Involvement in the strongest (the most intense red color) interaction was for O(3) of SB, a slightly weaker interaction was demonstrated by H(3) in crystal structures of SA and SSU.MeOH, while O(3) contact lost its intensity. The SS structure presented two weak hot spots, one from the oxygen and the other from hydrogen atom. The weakest intensity and distribution on Hirshfeld surface of hot spot interactions was for salbutamol base and its co-crystalline form. The hot spot interactions identified corresponded well with detected H-bond interactions for SA and SSU listed in tables 8.3 and 8.4.

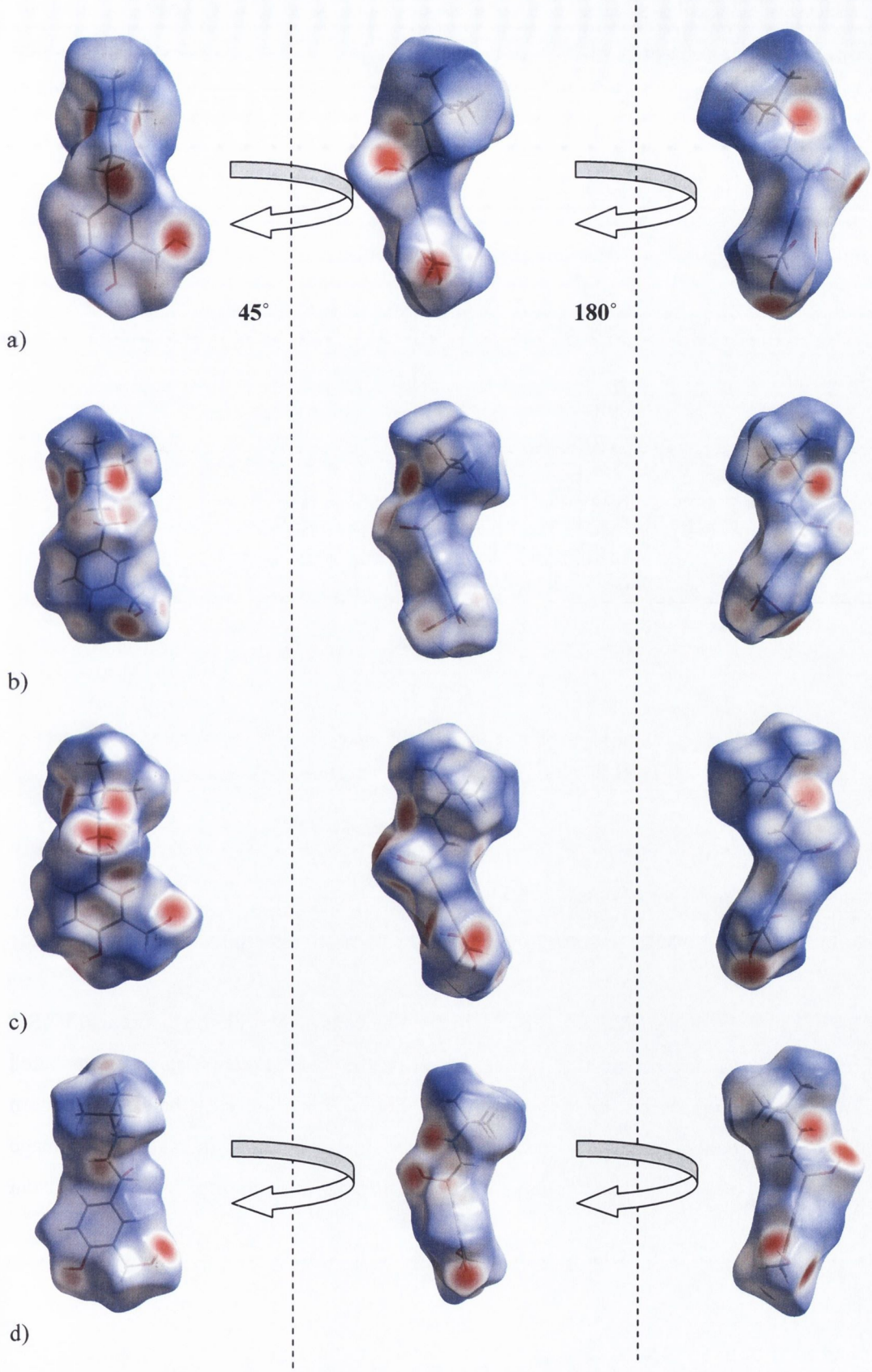

Fig. 8.3. Hirshfeld surfaces of: a) SB, b) SS, c) SA and d) SSU.

8.2.4. Results of PXRD analysis

The theoretical powder pattern of SA generated from the single crystal X-ray analysis at 100 K (Figure 8.4 a) is consistent with the powder XRD pattern of the bulk material determined at ambient conditions (Figure 8.4 b). There are small differences between the two patterns, which most likely can be attributed to thermal anisotropic expansion of the lattice.

The bulk material consisted of colorless, transparent, rhomboidal, thin, plate-like crystals.

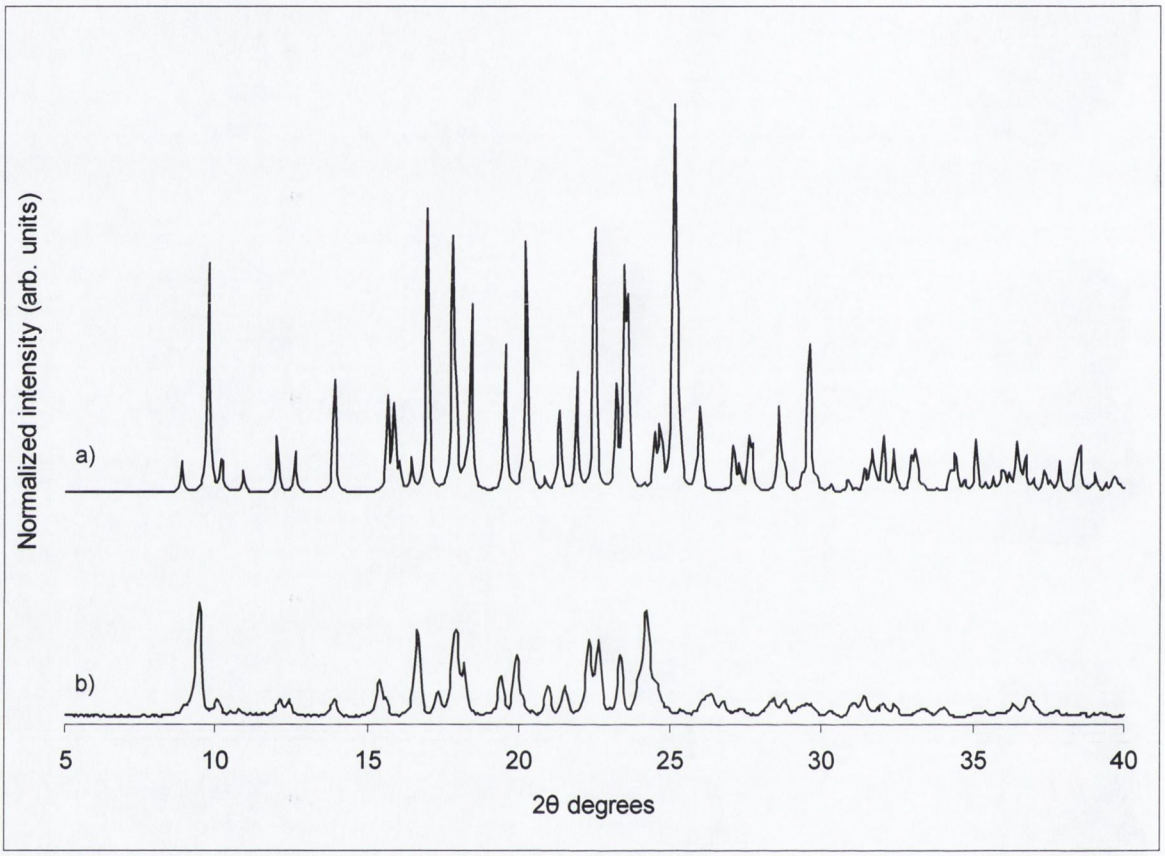

Fig. 8.4. Comparison of SA PXRD patterns: a) theoretical pattern, b) experimental diffractogram.

Results of PXRD analysis of SSU.MeOH (Fig. 8.5 b) are also consistent with the theoretical PXRD pattern (Fig. 8.5 a). Again, small differences between the two patterns can be attributed to the different temperatures used for the experiments. Figure 8.8 c presents the PXRD pattern of desolvated SSU. Broadening and lower intensity of the Bragg peaks is indicative of damage to the crystal lattice due to methanol evaporation, confirming the importance of the solvent in crystal lattice formation.

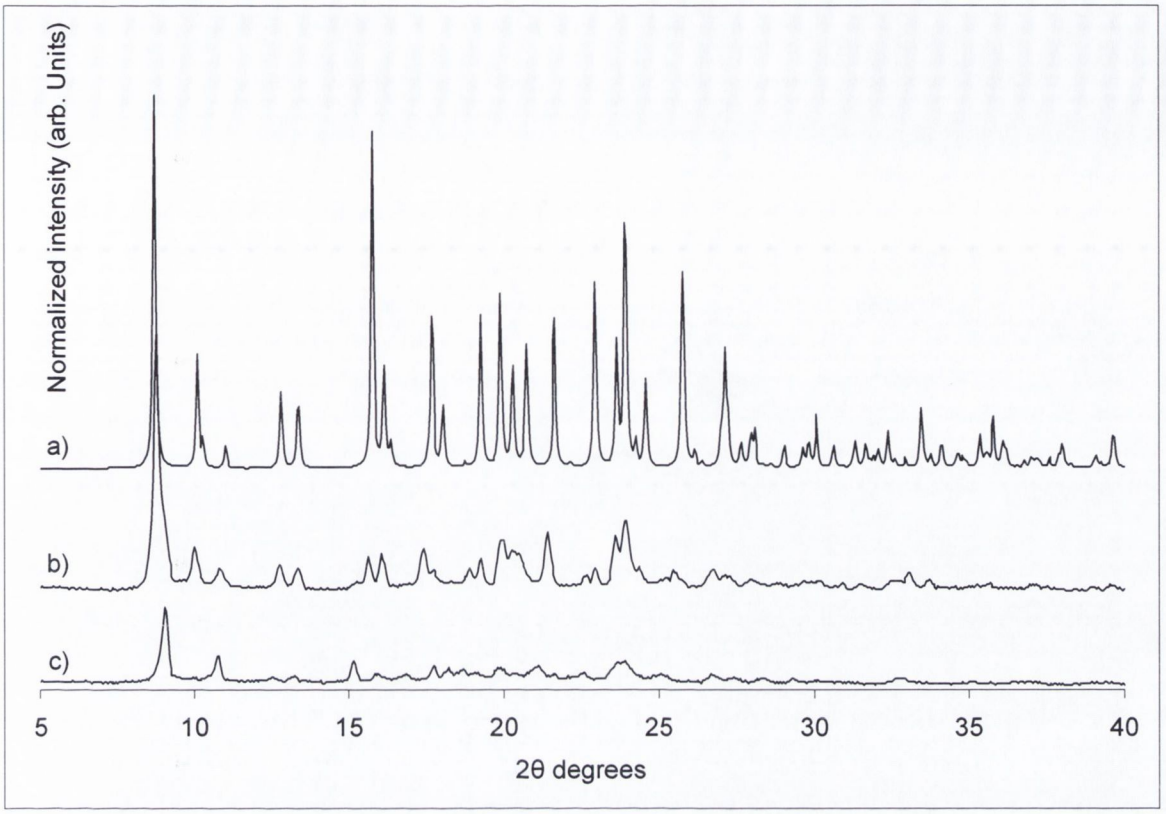

Fig. 8.5. Comparison of PXRD patterns: a) SSU.MeOH theoretical pattern, b) SSU.MeOH experimental diffractogram and c) SSU experimental diffractogram.

8.2.5. NMR results

Table 8.4 compares ^{1}H NMR data recorded for SB and the following salts: SS, SA, SSU.MeOH and SSU. Results obtained for SB are consistent with data previously reported by Regla at al. (1997). ^{1}H NMR confirmed the presence of methanol in the crystal structure due to the methyl group (3.18 ppm), which was absent in the desolvated form. Slight shifts in peak positions between SB and salbutamol salt forms may be ascribed to interactions of molecules of dissolved APIs with DMSO.

Results of ^{13}C NMR analysis are listed in Table 8.5. The number and position of the carbon peaks correlate well with data reported by Regla at al. (1997) for SB. The carbons of adipic acid appeared as three peaks corresponding to 6 symmetrical carbons and the carbons of succinic acid showed as two peaks corresponding to 4 symmetrical carbons. The ^{13}C NMR also detected the carbons (17,16) of methanol in the solvated form of SSU.MeOH and their absence in the desolvated form (SSU).

Table 8.4. ^{1}H NMR analysis of SB and SS, SA, SSU.MeOH and SSU.

Peak	SB		SB (Regla at al. 1997)	SS	SA	SSU.MeOH	SSU
	v(F1) [ppm]	Integral	v(F1) [ppm]	v(F1) [ppm]	v(F1) [ppm]	v(F1) [ppm]	v(F1) [ppm]
C(10,11,12) H(10,11,12)	1.02	9.08	1.02	1.22	1.21	1.16	1.16
C(8)H(8AB)	2.54	2.79	2.55	2.78	2.84	2.74	2.71
C(7)H(7)	4.40	1.09	4.42	4.69	4.70	4.61	4.59
C(13)H(13AB)	4.48	1.99	4.47	4.50	4.48	4.59	4.49
C(2)H(2)	6.69	1.00	6.69	6.75	6.74	6.755	6.75
C(3)H(3)	6.99	1.02	6.99	7.08	7.07	7.04	7.04
C(6)H(6)	7.27	1.04	7.27	7.34	7.32	7.31	7.31
C(15,18) H(15,18/AB) C(15) H(15/AB)	-	-	-	-	2.11	2.28	2.28
C(16,19)	-	-	-	-	1.49	-	-
C(16) H(16/ABC) C(17) H(29-31)	-	-	-	-	-	3.18	-

Table 8.5. ^{13}C NMR analysis of SB and SS, SA, SSU.MeOH and SSU.

Peak	SB	SB (Regla at al. 1997)	SS	SA	SSU.MeOH	SSU
	ν(F1) [ppm]	ν(F1) [ppm]	ν(F1) [ppm]	ν(F1) [ppm]	ν(F1) [ppm]	ν(F1) [ppm]
C(10,11,12) H(10-12/ABC)	28.9	28.74	26.7	26.4	27.4	27.4
C(9)	49.6	49.8	49.7	49.1	50.1	50.2
C(8)H(8AB)	50.8	50.7	49.6	49.6	49.98	50.0
C(13)H(13AB)	58.3	58.3	58.7	58.8	58.73	58.8
C(7)H(7)	72.4	72.3	70.3	69.9	71.11	71.1
C(2)H(2)	114.0	114.0	114.6	114.7	114.60	114.6
C(3)H(3)	124.8	124.9	125.5	125.3	125.40	125.4
C(6)H(6)	125.0	125.1	125.6	125.5	125.54	125.5
C(1,4,5)	127.9	127.9	128.6	128.6	128.61	128.6
C(1,4,5)	134.6	134.5	133.4	133.3	133.79	133.8
C(1,4,5)	153.1	153.1	153.9	154.0	153.90	153.9
C(14,17)	-	-	-	176.7	176.18	176.2
C(15,18)	-	-	-	35.9	32.92	32.9
C(16,19)	-	-	-	25.6	-	-
C(17,16)	-	-	-	-	49.06	-

8.2.6. Stoichiometry and elemental analysis

Elemental analysis confirms the molar ratio of salbutamol and adipic acid in SA is 1:1 (Table 8.6).

Table 8.6. Comparison of theoretical values and experimental results of elemental analysis of carbon, nitrogen and hydrogen contents in salbutamol salts.

Content (%w/w)		C %	H %	N %
SA	Theory 1:1	59.20	8.11	3.63
	Experimental	59.00±0.01	8.20±0.08	3.68±0.07
SSU.MeOH	Theory	56.34	8.90	3.86
	Experimental	56.53±0.37	8.19±0.18	3.59±0.53
SSU	Theory 2:1	60.38	8.11	4.69
	Experimental	60.275±0.05	8.01±0.07	4.61±0.01

Elemental analysis of SSU.MeOH correlates well with single crystal X-ray analysis data suggesting a ratio of two molecules of salbutamol to one molecule of succinic acid to four molecules of methanol, the presence of which in the crystallized material was confirmed by NMR analysis. Results for the solvated material have greater variation due to solvate instability at ambient conditions and methanol evaporation. Results of elemental analysis confirm that the molar ratio of salbutamol to succinic acid in SSU is 2:1.

8.2.7. Thermal analysis

Thermal analysis (TGA) of SA did not indicate a significant mass loss on drying at the beginning of the scan. Overall mass loss recorded during the TGA scan (Fig. 8.6 a) up to 100 °C was 0.94±0.03% of initial mass of the sample. DSC analysis of the material showed a single strong endothermal event (Fig. 8.6 d) related to melting with decomposition at 181.00±0.04 °C, correlating with the beginning of significant further mass loss in the TGA. The melting point of adipic was measured to be at 150.93±0.10 °C.

DSC analysis of SSU.MeOH (Fig. 8.6 e) indicated a large broad endotherm with an onset at 69.97±0.30 °C and enthalpy of 139.43 J/g. These endothermal events correlated well with the sample mass loss due to liberation of methanol (Fig. 8.6 b) of 17.26±1.20 %. The theoretical content of solvated methanol was calculated to be 17.68%.

The onset of thermal decomposition after desolvation was recorded to be 179.23±0.10 °C and corresponded with further significant mass loss. In contrast, succinic acid melted at 185.90±0.21 °C. There was a 0.80±0.02 % overall mass loss up to 100 °C in the TGA determined for SSU (Fig. 8.6 c, f) indicating very slight drying. Onset of thermal decomposition was recorded at 182.83±0.15 °C.

The onsets of thermal decomposition of the new salbutamol forms were consistent with the onset of decomposition of about 180 °C (Larhrib et al., 2003) for SS. Thus it can be concluded that the new forms and SS have similar thermal stability.

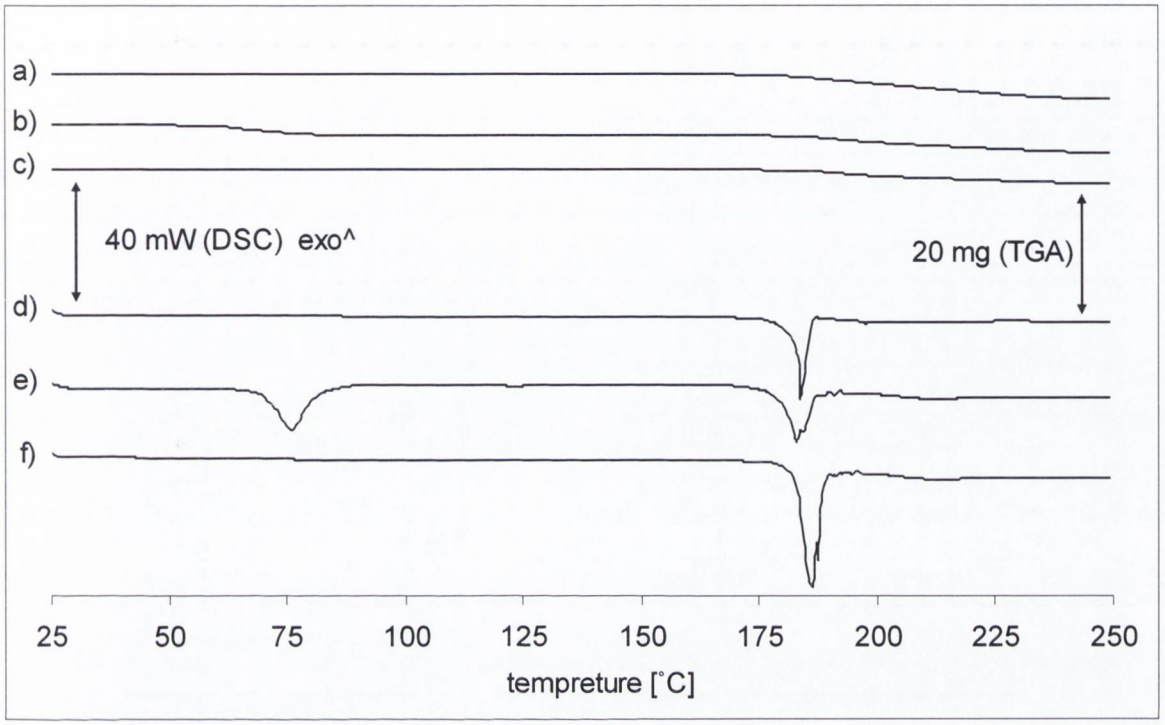

Fig. 8.6. Thermal analysis: a) TGA scan of SA, b) TGA scan of SSU.MeOH, c) TGA scan of SSU, d) DSC of SA, e) DSC scan of SSU.MeOH, f) DSC scan of SSU.

8.2.8. FT-IR analysis

The FTIR patterns of SA (Fig. 8.7 c) and SSU (Fig. 8.7 b) differ in comparison to spectra of the parent compounds (Fig. 8.7 a, d, e). The main difference between SSA, SSU and SB is the strong suppression of conjugated C=C stretching vibrations of benzene ring of salbutamol just above 1600 cm^{-1} and changes in the intensity of the carboxylic acid C=O stretch peaks. The stretching vibration of N-H band of salbutamol (Fig. 8.7 a) recorded at 3300 cm^{-1} for SB was nearly completely suppressed and slightly shifted towards longer wavelengths in SSU (Fig. 8.7 b) indicating a complete ionization of the secondary amine group. In contrast, the N-H stretching vibration of the secondary amine group in SA (Fig. 8.7 c) is relatively noticeable with a strong shift to 3450 cm^{-1}. These observations agree with the single crystal X-ray data suggesting a co-crystal form of SA, where one out of two adipic acid molecules per two molecules of salbutamol base remains unionized, but strongly H-bonded to the secondary amine group of salbutamol. The co-crystal versus salt forms of salbutamol are clearly distinguishable by FTIR, where the broad stretching vibration of C=O of the acid in SSU has been completely suppressed, while the acidic

carbonyl group vibration in SA remained highly visible with a slight shift towards longer wavelengths.

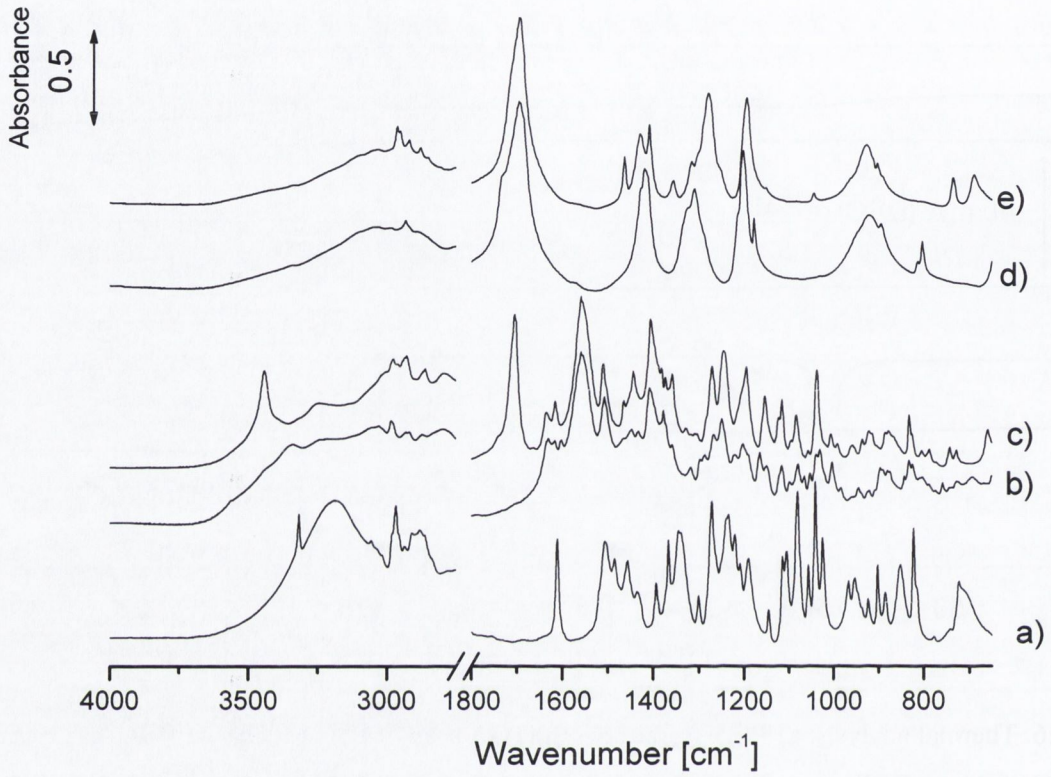

Fig. 8.7. FTIR spectra of: a) SB, b) SSU, c) SA, d) succinic acid, e) adipic acid.

8.2.9. Dynamic Vapor Sorption (DVS)

Both SSU and SA do not adsorb more than 2% of moisture and under the conditions of dynamic vapor sorption analysis do not tend to form hydrates (Fig. 8.8). Results of equilibration of SSU at any given RH%, regardless of whether assessed in the sorption or desorption stage, are similar to SS, and in both cases the amount of adsorbed liquid does not exceed 0.3% of initial sample mass at 90% RH. In the case of SA sample less than 1.6% of initial mass was adsorbed at 90% RH.

Since the moisture sorption behavior may be attributed to the powder surface area, the samples subjected to the DVS analysis were also characterized in terms of their specific surface area and particle size. The specific surface area (T_{BET}) of SS was measured to be 1.53±0.02 m^2/g, that of SA was 1.81±0.02 m^2/g and T_{BET} of SSU was 2.26±0.06 m^2/g. The median particle size determined was 8.09±0.18, 19.26±0.07 and 8.73±0.09 μm for SS, SA and SSU, respectively. It is possible, therefore, that the higher propensity of SA to sorb moisture may be due to the different particle

size, but cannot be explained by the difference in the surface area. It is likely that other surface properties, such as surface energy, contribute to this effect and will be the subject of further studies.

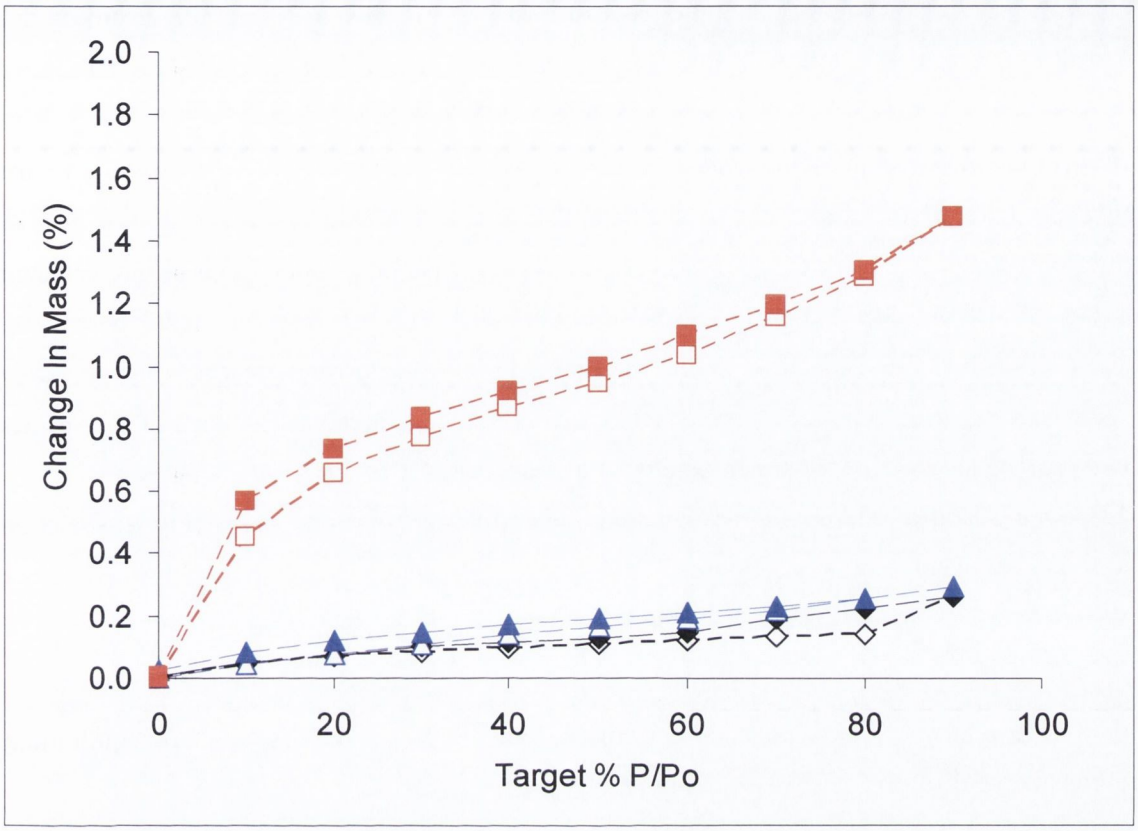

Fig. 8.8. Dynamic Vapor Sorption of: SA (squares), b) SSU (triangles), c) SS (diamonds).

8.2.10. Solubility and dissolution studies

The estimated aqueous solubilities of SA, SSU and SB were found to be 82±2 mg/ml (equivalent to 0.231±0.001 M of salbutamol) at pH 4.5±0.1, 334±13 mg/ml (equivalent to 1.183±0.045 M of salbutamol) at pH 6.6±0.1 and 2.63±0.09 mg/ml (equivalent to 0.0110±0.0004 M of salbutamol) at pH 10.0±0.1, respectively. Thus the improvement in solubility, compared to SB, was 21- and 108-fold for the drug presented as SA and SSU, respectively, indicating that SSU has a 5-fold greater solubility than SA.

As the new forms of salbutamol are composed of the drug and co-former that are able to ionize in solution, it is expected that the pH of the saturated medium may have a profound effect on the solubility of the compounds (Stahl and Wermuth, 2008). This was investigated for SA, as it was easier to change the pH for this compound due to the lower solubility in comparison to SSU. When the pH of medium was adjusted to 5.3, the solubility of SA was measured to be 60±1 mg/ml.

Equations describing the solubility of gabapentin/3-hydroxybenzoic acid cocrystal, (Sreenivas et al. 2009) and carbamazepine and itraconazole cocrystals have been reported (Bethune et al., 2009).

These models allow relationships between the pH and co-crystal solubility to be predicted knowing only the solubility product constant (K_{sp}) and acid dissociation constants of the co-crystal constituents (pK_as). Although the theoretically-derived models neglect nonidealities due to complexation and other specific interactions, very good agreements between the calculated and experimental values were observed (Sreenivas et al. 2009 and Bethune et al., 2009). This approach was employed in this work as the authors suggest that co-crystal solubility and its pH relationship may be estimated from a single measurement (Bethune et al., 2009). Similar mathematical equations were therefore developed for the new salbutamol forms to predict their solubility-pH dependence and estimate the solubility difference in relation to the pure drug. The co-formers and the drug have acidic and amphoteric characteristics, respectively, therefore the previously reported equations were adapted, taking into consideration that each of the species has two pKa values and that the stoichiometry of the succinate form is 2:1.

SA has a molar ratio 1:1, hence the equation for equilibrium reaction describing dissociation of the co-crystal in solution is as follows:

$$S - H_2A \leftrightarrow S_{solution} + H_2A_{solution} \qquad \text{Eqn. 8.1.}$$

where S-H_2A is the co-crystal/salt in the solid phase, $S_{solution}$ and $H_2A_{solution}$ are equilibrium solubilities of the drug and acid, respectively, thus

$K_{sp} = \frac{[S][H_2A]}{[S - H_2A]}$, and with S-$H_2A$ in the solid phase the soluble product constant (K_{sp}) can be presented as:

$$K_{sp} = [S][H_2A] \Rightarrow [H_2A] = \frac{K_{sp}}{[S]} \qquad \text{Eqn. 8.2.}$$

Equilibrium reactions for adipic acid and salbutamol are presented in Eqns. 8.3 and 8.4 (for the acid) and Eqs. 8.5 and 8.6 (for the drug).

$$H_2A \leftrightarrow HA^- + H^+ \qquad K_{a1,H_2A} = \frac{[H^+][HA^-]}{[H_2A]} \qquad \text{Eqn. 8.3.}$$

$$HA^- \leftrightarrow A^{2-} + H^+ \qquad K_{a2,H_2A} = \frac{[H^+][A^{2-}]}{[HA^-]} \qquad \text{Eqn. 8.4.}$$

$$SH^+ \leftrightarrow S + H^+ \qquad K_{a1,S} = \frac{[S][H^+]}{[SH^+]} \qquad \text{Eqn. 8.5.}$$

$$S \leftrightarrow S^- + H^+ \qquad K_{a2,S} = \frac{[S^-][H^+]}{[S]} \qquad \text{Eqn. 8.6.}$$

where $[HA^-]$, $[A^{2-}]$ are concentrations of the monodissociated and fully dissociated acid species and $[SH^+]$, $[S^-]$ are concentrations of protonated and monobasic salbutamol species.

Combining the total acid and drug concentrations, the solubility of salbutamol adipate can be expressed as (Eqn. 8.7):

$$S_{cocrystal} = \sqrt{K_{sp} \cdot (1 + \frac{K_{a1,H_2A}}{[H^+]} + \frac{K_{a2,H_2A} \cdot K_{a1,H_2A}}{[H^+]^2}) \cdot (1 + \frac{[H^+]}{K_{a1,S}} + \frac{K_{a2,S}}{[H^+]})} \qquad \text{Eqn. 8.7.}$$

where $S_{cocrystal}$ is co-crystal solubility, $K_{a1,H2A}$ and $K_{a2,H2A}$ are the first and second dissociation constants for the acid and $K_{a1,S}$ and $K_{a2,S}$ are the first and second dissociation constants for the drug.

Using a similar approach, the equation for salbutamol succinate, considering the 2:1 stoichiometry, is as follows (Eqn. 8.8):

$$S_{salt} = \sqrt[3]{\frac{K_{sp}}{4}(1 + \frac{K_{a1,H_2A}}{[H^+]} + \frac{K_{a2,H_2A} \cdot K_{a1,H_2A}}{[H^+]^2}) \cdot (1 + \frac{[H^+]}{K_{a1,S}} + \frac{K_{a2,S}}{[H^+]})^2} \qquad \text{Eqn. 8.8.}$$

The pK_{sp} constants for salbutamol adipate and succinate, calculated using the aqueous solubility values, were 6.3 and 8.6, respectively. Substituting in pKa values as follows: pK_{a1}=4.44, pK_{a2}=5.44 for adipic acid (Stahl and Wermuth, 2008), pK_{a1}=4.21, pK_{a2}=5.64 for succinic acid (Stahl and Wermuth, 2008) and pK_{a1}=9.1, pK_{a2}=10.4 for salbutamol (Yazan et al., 1995), the pH-solubility profiles derived from Eqs. 8.7 and 8.8 are presented in Fig. 8.9. The theoretical models suggest that a minimum SA solubility occurs at pH around 5 and that of SSU at pH 7.

The comparison of intrinsic dissolution rates (IDRs) of salbutamol from SA (4.18 mg/cm^2/min, R^2 of 0.999) and SSU (14.94 mg/cm^2/min, R^2 of 0.997) with that of salbutamol sulfate (15.47 mg/cm^2/min, R^2 of 0.999) (Fig. 8.10) reveals that the rate of salbutamol release from SA is lower than that from SS or SSU. The IDR of salbutamol from SA is ~4 times lower than that of the other salt forms, consistent with the ~5-fold difference in salbutamol solubility. There was no significant difference in the IDRs of salbutamol in SS and SSU. Our results for the co-crystal of the salbutamol hemiadipate salt with adipic acid (SA) contrasts with that of Jashnani et al. (1993) who obtained a salbutamol hemiadipate diethanolate which had an IDR equivalent to SS.

Interestingly, the difference in the IDR values obtained reflect the different acid solubilities i.e. the saturated solubility of succinic acid at 20 °C is reported to be 7.7% w/v and that of adipic acid to be 1.8% w/v (Stahl and Wermuth, 2008), therefore it may be expected that the solubility of salbutamol adipate is lower than that of salbutamol succinate.

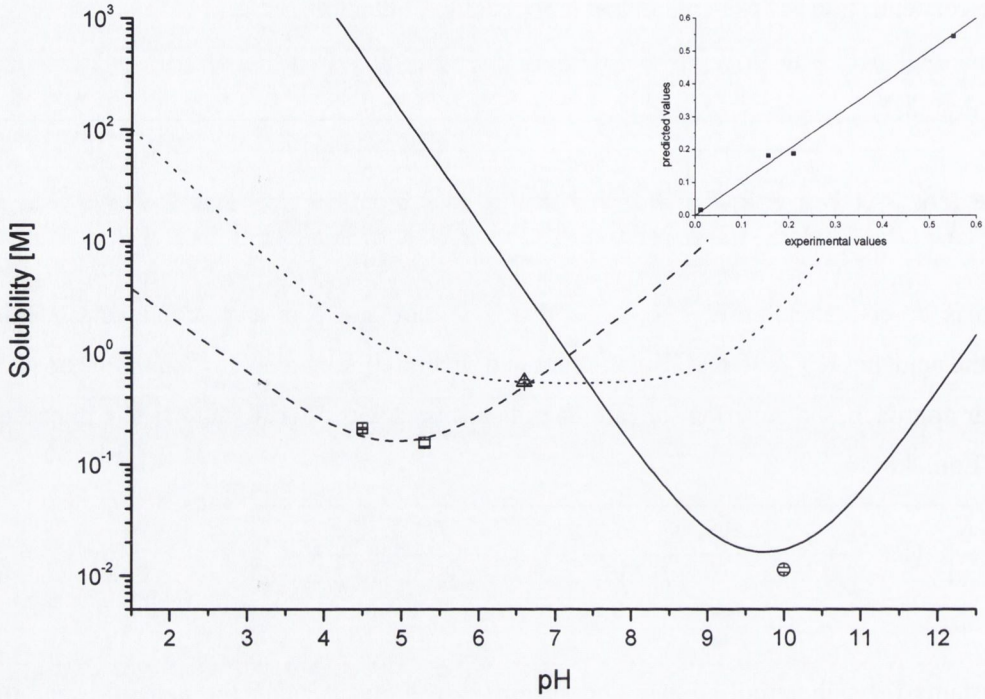

Fig. 8.9. Theoretical profiles describing pH-solubility dependence for SA (dashed line), SSU (dotted line) and SB (solid line). Empty squares indicate experimental solubility values for SA, the triangle for SSU and the circle shows the experimental solubility of SB. The inset shows a correlation (y=x) between the experimental and predicted data points.

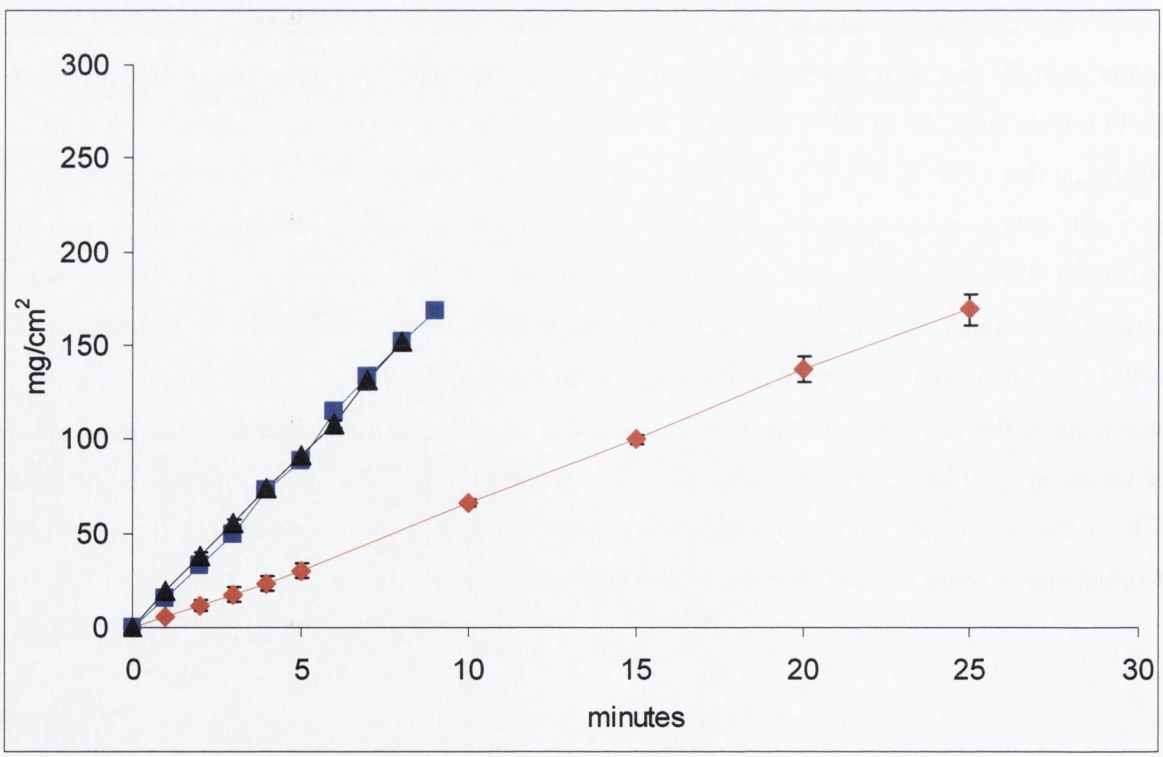

Fig. 8.10. Intrinsic dissolution profiles of SA, SSU and SS.

8.3. Conclusions

Despite the chemical similarity of succinic and adipic acids, the solid state properties of their salbutamol salts when made by the same methods are significantly different. For the first time we reported the involvement of adipic acid molecule in the formation of a co-crystal of a salt. Salbutamol succinate is a rare example of the succinate constituting a solvated salt form with API molecule. The intrinsic dissolution rate of salbutamol in SSU was around 4-fold greater than that of SA, consistent with the ~5-fold difference in aqueous solubility of salbutamol in SA and SSU, thus the difference in the intrinsic dissolution rates was comparable to the solubility trend. Both materials presented similar thermal stability and did not undergo hydration under increasing humidity. The effectiveness of anion choice as a modification of *in vivo* bioavailability of salbutamol needs further investigations, as the concept of retarding dissolution of an API by the formation of an appropriate salt/co-crystal is a promising approach, which may alleviate some issues associated with formulation of extended release dosage forms such as component compatibility and regulatory approval for the use of excipients.

Results described here show that salt and/or co-crystal formation remains largely unpredictable and requires predominantly empirical screening. The arrangement of molecules in the crystal lattice is dependent on the geometry of the molecules involved and their potential for forming chemical interactions. Even the careful choice of similar counter ions can have a profound effect on the observed crystalline lattice and further work in this area is required.

Chapter 9

General Discussion

9.1. Introduction

Preformulation refers to the phase of drug development, where potential advantages or disadvantages of active molecules and excipients should be comprehensively investigated. The result of preformulation studies should be the full physicochemical characteristics of the API that allows an optimal formulation to be manufactured. The final dosage form should be considered, as the API may be used in a solid and/or liquid formulation. Furthermore, the manufacturing process may affect the properties of the API/excipient(s), so the desired physicochemical and micromeritic properties of the formulation components should be defined in preformulation studies.

The scope and results of preformulation studies depend on the initial requirements set for the final formulation. The programme of studies should include all suitable characterisation methods that will allow for the determination of the required properties of the API. The requirements for preformulation may be restricted or defined by the physicochemical properties of the API, an optimal solubility or dissolution profile of the API (affecting biopharmaceutical properties of the API), physical and chemical stability, the required delivery site, pharmaceutical processing, the drug form, regulatory issues, the cost of production or a combination of these.

This thesis is concerned with preformulation studies of APIs only.

9.2. Characterisation and processing of chlorothiazide (CTZ)

CTZ was chosen as a model API due to its low aqueous solubility of 0.2 mg/ml and very high (as for a pharmaceutical compound) melting point of 365 °C. Experiments on CTZ started with characterisation of this API upon processing. Processing of the API was restricted to spray drying. Spray drying of many APIs results in the formation of amorphous materials due to rapid evaporation of the solvent, thus resulting in a very narrow precipitation window that does not allow sufficient nucleation and growth of crystals.

The background to spray drying of CTZ was set by the studies of Corrigan et al. (1984), who spray dried CTZ from an ethanol/water mixture and obtained a crystalline powder. It was therefore of interest to study why this API remains crystalline on spray drying and the goal was to see if alterations of the process conditions could result in amorphisation of CTZ.

This work shows that it is possible to produce amorphous CTZ using either water or ethanol to prepare the spray drying feed. Also, the choice of spray dryer configuration (open versus closed mode) impacted on the solid state nature of CTZ with the open mode of drying favouring the production of amorphous CTZ. Extensive solubility studies of CTZ in organic solvents: acetone, ethanol and their mixtures with water were carried out and resulted

in an improvement of processing in terms of increasing the API concentration in spray drying feed, therefore an increase in production yields was observed.

HPLC studies on the powders spray dried from the different solvents and their mixes revealed limited chemical stability of CTZ processed from ethanolic solutions and from an aqueous solution where the feed had a temperature of 98 °C. The amorphous form produced and characterised by a Tg at 135 °C, was physically unstable and recrystallised over 8h. Spray drying from acetone and acetone/water mixtures showed that spray drying was an efficient process of modification of relative crystallinity, morphology and micromeritic properties of CTZ. The largest reduction of relative crystallinity (RC) to 52% was obtained by spray drying from the 1:1 v/v acetone/water solvent ratio. The largest apparent, visual porosity, as assessed by SEM, was determined for the sample spray dried from acetone. The largest apparent porosity was in agreement with the largest specific surface area of this material (~5 m^2/g), although the T_{BET} of the sample spray dried from 100% acetone was two times lower than the T_{BET} (~10 m^2/g) of nanoporous microparticles (NPMPs) of budesonide (poorly soluble in water API, similarly to CTZ) spray dried from EtOH/W solution reported by Nolan et al. (2009) (Table 9.1).

The production of NPMPs was described for the first time for bendroflumethiazide by Healy et al. (2008). Further studies on the properties and mechanism of formation of NPMPs were carried out by Nolan et al. (2009), Nolan et al. (2011) and Ni Ógáin et al. (2011) for budesonide, sodium cromoglycate, trehalose and raffinose, respectively. On the basis of these studies, the ability to form NPMPs by spray drying CTZ would appear to be limited by the hydrophobicity of molecule coupled with poor ethanolic solubility.

It was previously reported (Charnicki et al., 1959) that the poor aqueous solubility of CTZ can be improved by increasing pH of solutions by adding an alkali. The CTZ formulated in injectable form was claimed to form a sodium salt (Charnicki et al., 1959), however its crystal structure up to date remained unknown.

9.3. Solid state studies

9.3.1. Solid state nature and physicochemical properties of chlorothiazide salts

The conclusions made from the first stage of the studies on physicochemical properties of CTZ led to the second part of the thesis, which was focused on the production of CTZ salt forms with possibly improved solubility in alcoholic solutions, thus making CTZ more suitable to form highly porous NPMPs upon spray drying. The approach taken was to prepare salts of CTZ with the sodium and potassium counterions chosen to investigate the impact of counterion choice on the physicochemical properties of CTZ.

The study resulted in the successful production, determination of crystal structures and a comprehensive physicochemical characterisation of new salt forms of CTZ: chlorothiazide sodium (CTZNa) as a dihydrate (DH) and an anhydrous (ANH) form and chlorothiazide potassium (CTZK) as a DH, a monohydrate (MH), an ANH and a monohydrate hemiethanolate form.

Crystal structures of the dihydrates of CTZNa and CTZK were different to each other (Fig. 9.1). The sodium and potassium cations, despite chemical similarity including the same valency, differed in the size of Van de Waals radii being 2.27 Å and 2.75 Å for Na and K, respectively and were shown to have different abilities to form coordination bonds between cations, molecules of water and the host molecule, CTZ. The sodium ion coordinated six atoms while the potassium ion coordinated seven atoms including the chlorine atom of CTZ. The type of hydrates formed was complex. Single crystal X-ray analysis revealed that water molecules n the crystal structures of both hydrates are coordinated, constituting the stoichiometric fraction of water in hydrates, similar to the reported sodium salt of naproxen (Kim et al., 1990). Additionally, experiments revealed that the water molecules that were hosted in the interstitial voids of the crystal lattices were in a non-stoichiometric proportion to the CTZ and counterions. The presence of non-stoichiometric interstitial water was also reported for the crystal structure of cefazolin sodium (Stephenson and Diseroad, 2000). Dynamic vapour sorption and PXRD studies performed in the present work showed that those interstitial molecules of water had no impact on the PXRD patterns of hydrates. The presence of interstitial water in the crystal structures of the CTZ salts had an effect, as discussed later, in the compactibility properties of the dihydrates in comparison to CTZK MH or anhydrous forms of CTZNa and CTZK.

The CTZK dihydrate had better thermal physical stability in comparison to CTZNa DH. The DSC analysis showed dehydration of two coordinated molecules of water of CTZNa as a one-step process, while the CTZK monohydrate form was thermally stable up to 170 °C, suggesting difficulties in the production of anhydrous CTZK. The production of an anhydrous form of CTZNa was much easier and did not require drying at as high temperature (80 °C) as that needed

to dehydrate CTZK (170 °C). Spray drying resulted in amorphisation of the CTZNa and CTZK salts and combined with additional drying of solvent residues was shown to be a more effective method of dehydration of CTZK DH compared to conventional single step drying of crystalline CTZK.

The measured Tgs of CTZNa and CTZK were ~192 °C and ~160 °C, respectively, and followed the trend reported by Tong et al., (2002), who investigated the influence of alkali metal counterions on the glass transition (Tg) temperature of amorphous indomethacin (IMC) salts. A comparison of the Tg values of the salts showed Tg values in the order of $Li^+ > Na^+ > K^+ > Rb^+ > Cs^+$, consistent with an order of decreasing ionic radius. The differences in Tg were attributed to an increased charge density and increased electrostatic interaction energy between the carboxylate ion and the alkali metal cation.

The sodium and potassium salt of CTZ had very good aqueous solubilities of approximately 79 mg/ml for CTZNa and CTZK. Dihydrated forms were stable when subjected to a broad range of relative humidities between 10 and 90% RH.

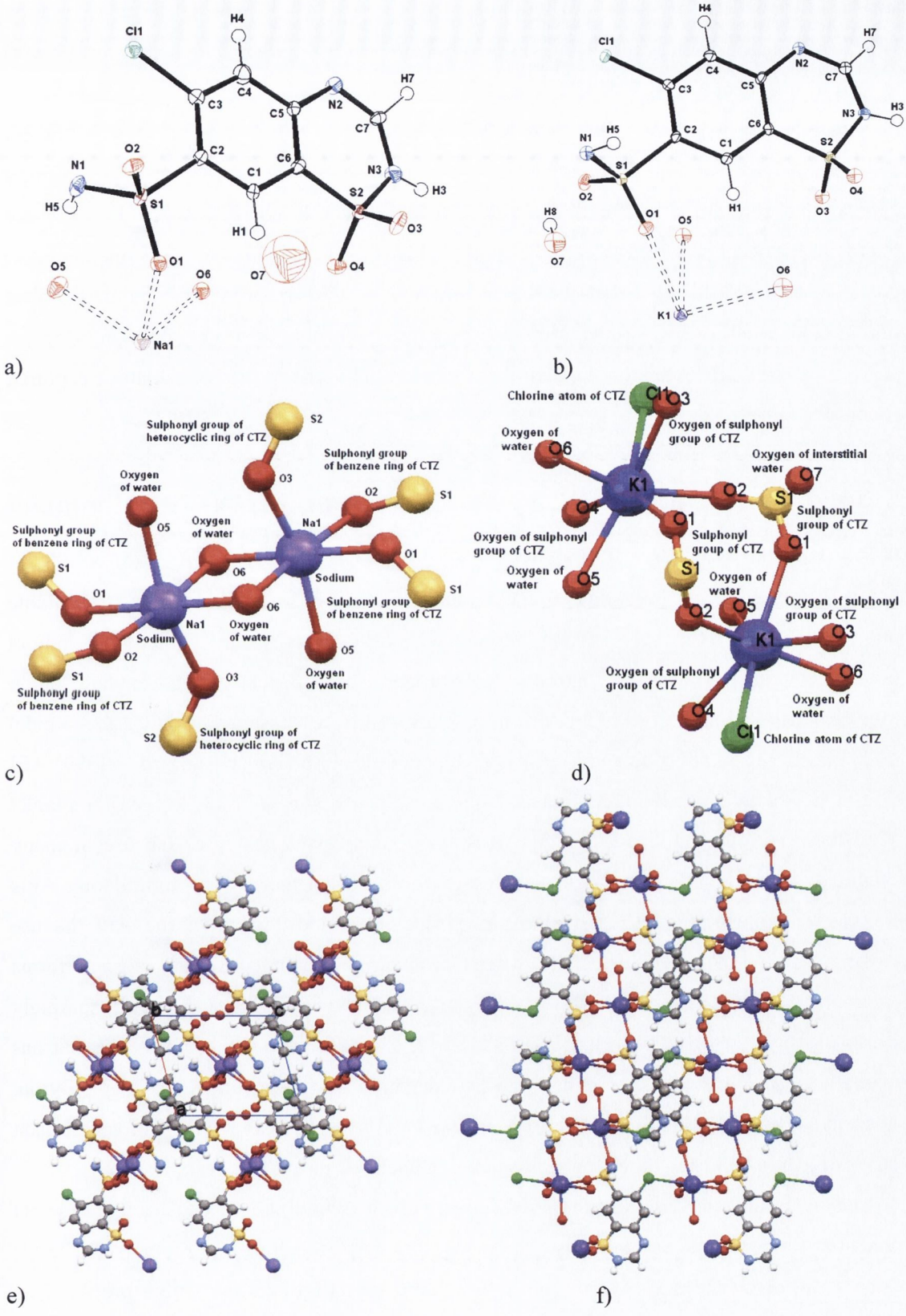

Fig. 9.1. Crystal structures of chlorothiazide sodium (a) and potassium (b) dihydrates: c) coordinates of the sodium cations, d) coordinates of the potassium cations, e) crystal cell structure of CTZNa DH (packing along "b" axis), f) CTZK DH cell unit packing view along "b" axis.

Anhydrous forms of the CTZ salts had much better solubilities in methanolic solutions in comparison to the salt hydrates, for example, it was possible to increase the concentration of CTZK in the spray drying feed (C_0) 2-fold by replacing CTZK monohydrate (C_0 of 1%w/v) with the anhydrous form (C_0 of 2% w/v).

Attempts to crystallise anhydrous CTZNa or CTZK from organic solvents failed. The crystal structure of CTZK monohydrate hemiethanolate showed a high affinity of the potassium cation for hydrophilic moieties (water) and the competitive nature of water and ethanol molecules in the formation of the crystal lattice of CTZK monohydrate hemiethanolate. Though it should be noted that in the metastable CTZK monohydrate hemiethanolate the coordination bonds were formed only between the molecules of water, potassium cation and CTZ molecules while ethanol remained only in interstitial voids of the crystal lattice captured by H- bonds.

9.3.2. Solid state nature and physicochemical properties of salbutamol adipate and salbutamol succinate

Previous experiments resulted in the production and characterisation of water soluble alternative salt forms of CTZ. These were formed with cationic inorganic counterparts, sodium and potassium ions. It was of interest to evaluate the impact of an organic anion on the physicochemical properties of an API, in contrast to the previous studies on CTZ. A model substance was chosen to be salbutamol, as it is an amphoteric (Imboden and Imanidis, 1999) API able to form salts with acids. Salbutamol as salbutamol sulphate is used in inhalers and in a tablet form. The delivery route of interest in this work was pulmonary delivery as the use of many excipients, e.g. those used frequently in oral dosage forms, is restricted when formulating APIs for pulmonary administration. Thus by the physicochemical modification of the API the use of excipients can be avoided, especially when formulating prolonged release dosage forms of salbutamol. Salbutamol base is characterised by a low aqueous solubility (~3 mg/ml, sparingly soluble in water by European Pharmacopoeia (2010) in comparison to the sulphate salt, but has been reported to be more adhesive to dry powder inhalation device materials (Jashnani, Byron, 1996) than the sulphate salt and has much poorer chemical and physical stability, in comparison to the sulphate salt, when formulated in metered dose inhalers (Tzou et al., 1997).

As an alternative, to achieve prolonged delivery of salbutamol, it may be desirable to select appropriate co-formers and co-crystallise them together with the host molecule (salbutamol) to produce a salt or co-crystalline form with the required solubility and dissolution profile. This study resulted in the production of a co-crystal of salbutamol hemiadipate with adipic acid and salbutamol hemisuccinate tertmethanolate which could be converted to a desolvated salbutamol hemisuccinate form. Salbutamol adipate presented a 4-fold decreased intrinsic dissolution rate

in comparison to the sulphate and succinate salts. Therefore salbutamol adipate may be considered as an API form for prolonged release of salbutamol in oral or pulmonary drug delivery forms.

An example of an alternative salt form of an API designed to achieve a prolonged release characteristic is a pamoate salt of olanzapine. This antipsychotic API is used in the treatment of schizophrenia and it is marketed as film coated tablets and orodispersible tablets (lyophilised formulation VeloTab™ known in the U.S. as Zydis™), but to maintain the treatment of stable schizophrenia a depot, an injectable form was developed containing olanzapine pamoate monohydrate. A dihydrated form of olanzapine pamoate is described in Allen et al. (2007) patent. It is interesting to note that this disolvated structure had nearly a twice slower release profile in comparison to the monosolvated pamoic salt.

9.4. Processing of chlorothiazide salts, morphology studies

CTZNa ANH and CTZK ANH were subjected to spray drying from water and a methanol/butyl acetate (MeOH/BA) mix. The latter solvent system was reported before by Nolan et al. (2011) to be effective in the production of NPMPs from hydrophilic APIs. The NPMPs were characterised by a large specific surface area (T_{BET}).

Initially, as experiments involving the production of NPMPs from CTZ were limited only to the 0.5% w/v feed concentration, the same concentration was used to prepare feeds containing CTZ salts in order to assess their ability to form NPMPs.

The assumption was that greater porosity of the material should result in an increased T_{BET}. Also, the relative change of the porosity of NPMPs powders observed by SEM was assumed to correspond to a change in the value of specific surface area of spray dried materials. The greatest T_{BET} measured for CTZ NPMPs, which were spray dried from pure acetone, was ~5 m^2/g, approximately 10-fold greater than that of the raw micronised material. The spray dried sample remained PXRD crystalline. In 2009 Nolan et al. reported NPMPs of budesonide, an API which is similar to chlorothiazide in terms of its poor solubility in water. The budesonide, as for CTZ, was spray dried using water as the antisolvent. The T_{BET} increase relative to the raw material, observed in present study for CTZ, was 3.5 times higher than that measured for budesonide sample BUD-NPMP3 (~10 m^2/g), produced and characterised by Nolan et al. (2009) and compared to micronised budesonide. This batch of budesonide was processed from the EtOH/W 1:4 v/v solvent ratio. The total concentration of solids in the mix of solvents was 1% w/v, where budesonide was in concentration of 0.85% w/v with the addition of 0.15% w/v of ammonium carbonate (AMC) as a pore enhancer. The BUD-NPMP3 sample, in contrast to CTZ sample #5.2, was spray dried in the open mode and after processing was PXRD amorphous.

The variety of morphologies of spray dried particles published resulted in the necessity to introduce a classification system of morphologies of spray dried particles, named Morphology

Classification System MCS (Chapter 6 p.120) in order to ease the description of materials produced.

Comparing morphologies of samples BUD-NPMP3 and CTZ #5.2 (Table 9.1), the difference is in the type of porosity as BUD-NPMP3 is in class V while CTZ sample #5.2 required to be classified in a new class VI, describing porous microaglomerates formed by anisometric nanoparticles. Both samples may be further classified as 1A (1 means spherical and A relates to the smooth morphology). Regarding the particles interior the CTZ sample #5.2 was hollow (H) while the interior of BUD-NPMP3 remained unknown (X). This comparison is consistent with one of the general conclusions of chapter 6 that morphology of type V (for the same material and equivalent solid concentration) is usually related to higher surface area than the other types of classified porous morphologies II-IV and VI.

Table 9.1. Selected morphology types of produced up to date porous microparticles with corresponding T_{BET}.

Sample (Ref.)	**SEM**	**T_{BET} [m^2/g]**	**Class of MCS**
BFMT/AMC 85:15 w/w 2.5% w/v (EtOH/W 4:1 v/v) (Healy et al., 2008)		N/A	V1BX
BFMT/AMC 85:15 w/w was 2.5% w/v (MeOH/W 4:1 v/v) (Healy et al., 2008)		N/A	V1BX

Table 9.1. Selected morphology types of produced up to date porous microparticles with corresponding T_{BET} - continuation.

Sample (Ref.)	SEM	T_{BET} [m^2/g]	Class of MCS
Budesonide (BUD-NPMP3) EtOH/W 1:4 v/v BUD 0.85% w/v AC_1 0.15% w/v 1% w/v, (Nolan et al., 2009)		10	V1AX
Chlorothiazide (#5.2) 0.5 w/v Pure AC (Chapter 5)	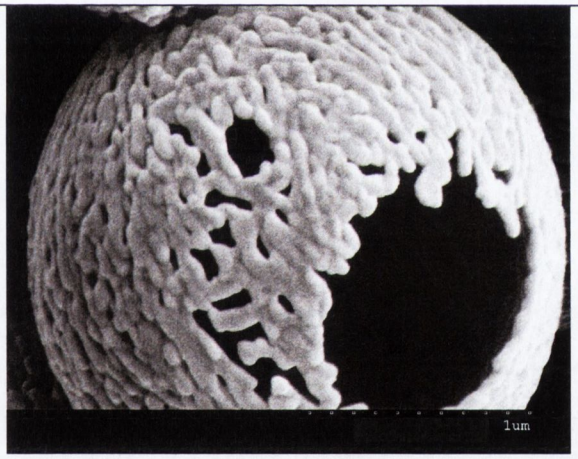	5	VI1AH
Chlorothiazide (#5.11) 2.0 w/v AC/W 9:1 v/v (Chapter 5)	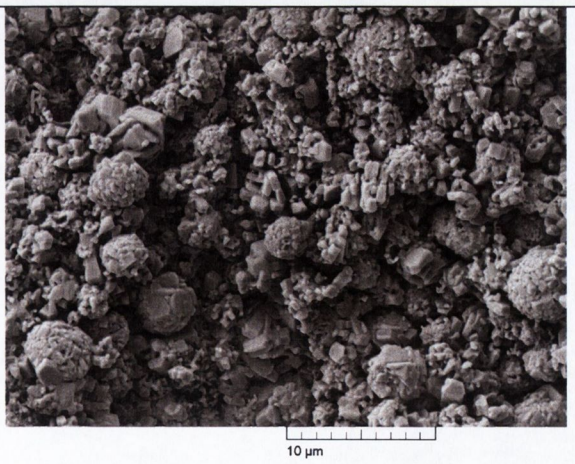	4	V2BS

Table 9.1. Selected morphology types of produced up to date porous microparticles with corresponding T_{BET} - continuation.

Sample (Ref.)	SEM	T_{BET} [m^2/g]	Class of MCS
Chlorothiazide potassium (#6.11) 0.5% w/v MeOH/BA 3:2 v/v (Chapter 6)	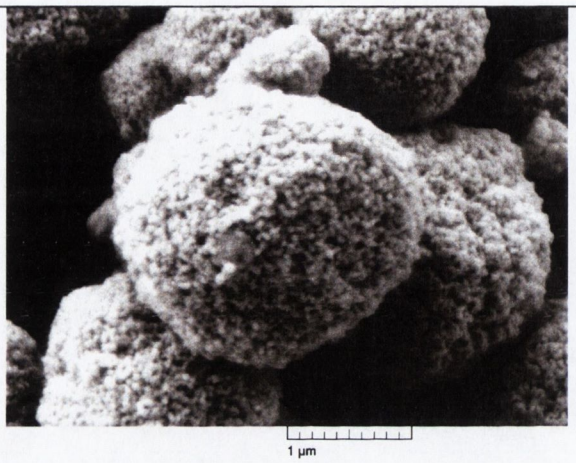	57	IV2BX
Chlorothiazide potassium (#6.20) 2.0% w/v MeOH/BA 3:7 v/v (Chapter 6)		90	V1BS
Chlorothiazide sodium (#6.6) 0.5% w/v MeOH/BA 3:2 v/v (Chapter 6)		66	IV1BX

Table 9.1. Selected morphology types of produced up to date porous microparticles with corresponding T_{BET} - continuation.

Sample (Ref.)	SEM	T_{BET} [m^2/g]	Class of MCS
Chlorothiazide sodium (#6.19) 2.0% w/v MeOH/BA 3:7 v/v (Chapter 6)		72	V1BS
Cromoglycate sodium 0.3 %w/v W/MeOH/BA 1:15:15 v/v (Nolan et al., 2011)	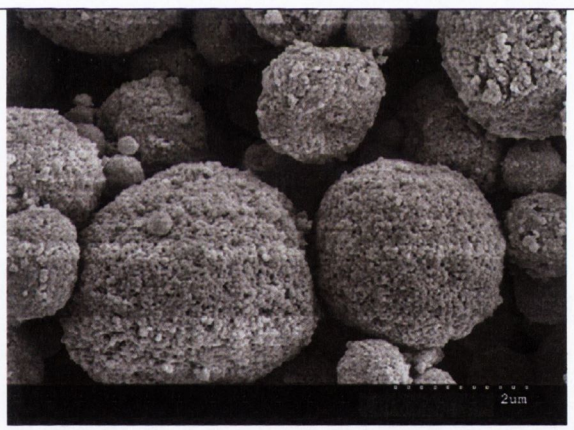	98	V1AX
Raffinose pentahydrate and lysozyme (4:1 w/w) 1%w/v MeOH/BA 8:2 v/v (Ni Ógáin et al., 2011)		44	IV1AX

Table 9.1. Selected morphology types of produced up to date porous microparticles with corresponding T_{BET} - continuation.

Sample (Ref.)	SEM	T_{BET} [m^2/g]	Class of MCS
Trehalose dihydrate 0.5%w/v MeOH/BA 8:2 v/v (Ni Ógáin et al., 2011)		44	IV1AX

The NPMPs of bendroflumethiazide (BMFT) which were the first NPMPs described by Healy et al., (2008) had morphology of V1BX type (Table 9.1). In comparison, the CTZ salt samples spray dried from 0.5% w/v solid concentration (#6.6 and #6.11) presented surface areas of 66 m^2/g, 57 m^2/g and morphologies types: IV1BX and IV2BX for CTZNa and CTZK, respectively (Table 9.1).

The surface area of these samples is comparable to those determined for the samples produced and described by Ni Ógáin et al. (2011). Trehalose dihydrate and raffinose pentahydrate were spray dried from 0.5% and 1% w/v feed concentration, respectively. The feed which resulted in the greatest apparent porosity comprised MeOH/BA in the 8:2 v/v ratio in contrast to samples #6.6 (CTZNa) and #6.11 (CTZK), where the largest surface area recorded was for the 3:2 v/v MeOH/BA ratio. The difference may be related to water introduced into the feeds of raffinose and trehalose formed after dissolving of raw material hydrates in organic solvents, while the CTZ salts were used in their anhydrous forms. The T_{BET} of both spray dried sugars was about 44 m^2/g. The morphology ascribed to them, IV1AX, was similar to CTZNa #6.6 and CTZK #6.11. The morphology of NPMPs made of raffinose did not change on incorporation of 20% w/w lysozyme (Ni Ógáin et al., 2011) (Table 9.1).

The largest specific surface area of 98 m^2/g measured for NPMPs and published to date was obtained by spray drying of sodium cromoglycate (CRGNa) from 0.3 % w/v feed concentration using a solvent system of W/MeOH/BA 1:15:15 v/v (Nolan et al. 2011). The particle morphology type was V1AX, similar to the morphology of the systems with the largest surface areas produced and described in this work, namely samples #6.19 (CTZNa) and #6.20 (CTZK)

with surface areas 72 and 90 m^2/g respectively and morphologies of V1BS (Table 9.1). Other CRGNa systems reported by (Nolan et al., 2011) spray dried without the addition of water presented a similar type of porosity but they differed in shape and morphology. CRGNa spray dried from the 19:1 MeOH/BA ratio presented morphology of V2BX. Crumpling was not observed when the solvent ratio changed to 9:1 MeOH/BA, particles remained spherical and the morphology type assigned was V1AX. A further increase in BA content in the solvent mixture appeared to impact on the class of porosity of spray dried materials as the morphology of the CRGNa spray dried from the 4:1 v/v MeOH/BA solvent ratio may still be classified as a type V1AX while the sample spray dried from 7:3 v/v MeOH/BA solvent ratio may be classified as a type IV of the porosity 1AX.

It can be concluded from this work and the studies of Healy et al., (2008), Nolan et al., (2009 and 2011) and Ni Ógáin et al., (2011) that a given type of the porosity, taking as an example the morphology of type V may be obtained by spray drying both, a hydrophobic and a hydrophilic material. The modification of type of morphology for classes II to V can be obtained by the adjustment of a solvent/antisolvent ratio as was reported by Nolan et al. 2011 and discussed previously in Chapter 6. Higher feed concentrations promote formation of NPMPs with morphology type V, the type of morphology giving the greatest likelihood of production of particles with the highest specific surface areas.

Achieving the maximum specific surface area of a powder was one of the goals of Chapter 6, as it was hypothesised that the materials with large T_{BET} will present favourable compactibility and compressability properties, as presented in Chapter 7.

9.5. Tabletability of solid state forms of chlorothiazide

Further evaluation of NPMPs presenting morphology type V (CTZNa sample #6.19 and CTZK sample #6.20), as those with the largest T_{BET} obtained in this work (Table 9.1), was carried to assess compactibility performance of NPMPs. The study comprised analysis of compactibility of the various solid state forms of CTZNa and CTZK. These included crystalline dihydrates (Chapters 3 and 4) and CTZK monohydrate (Chapter 4), dehydrated forms (Chapters 3 and 4), amorphous forms of CTZNa and CTZK (morphology types of I1AS and I1BS) and finally amorphous, anhydrous NPMPs with morphology type V1BS (Chapter 6). CTZ crystalline forms (micronised raw material and spray dried porous crystalline particles) were also included. The reference material was Dipac, co-spray dried crystalline mixture of sugars (96.5±1.5% sucrose, 3.0±0.75% maltodextrin), intended for direct compression.

The main results discussed in Chapter 7 were consistent with the previous findings reported by Pande and Shangraw (1995) and Sun and Grant (2004). Sun and Grant reported that water of crystallisation improves tableting properties of p-hydroxybenzoic acid, while Pande and Shangraw (1995) reported a reduced compactibility performance of β-cyclodextrin due to dehydration. In this work, it was observed that, on average, the tensile strength of tablets made

of CTZNa dihydrate compressed at the same compression pressure was greater than the tensile strength of tablets made of CTZNa anhydrous.

It was therefore of interest to investigate if the crystal water is released from the crystal lattice of CTZNa dihydrate and causes surface wetting to improve binding of the particles. Combining the results of crystallographic studies and observing that the PXRD pattern of compressed CTZNa dihydrate did not change in comparison to the starting material suggested that not the coordinated molecules of water, but the interstitial water may be responsible for the better compactibility of CTZNa DH over the anhydrous form. This is supported by extensive studies involving dynamic vapour sorption of water and impact of absorbed water on the PXRD pattern of CTZNa DH was described in Chapter 3.

Conclusions from the compactibility studies involving the different solid state forms of CTZK are more complicated, as no improvement in the tensile strength of compacts made of CTZK DH in comparison to those made of the anhydrous form was seen.

Trasi et al. (2011) reported that drying, and in consequence dehydration, of glucose in higher temperatures promoted the formation of amorphous phases, responsible for better compacting properties of processed glucose. These conditions are similar to the conditions of dehydration of CTZK, where the temperature of drying was higher (170 °C) than the Tg of CTZK (162 °C) and could result in a partial amorphisation of CTZK.

The lowest change of tensile strength in relation to compression pressure applied was observed for CTZK monohydrate tablets and this may be related to two aspects. The first is the lack of interstitial molecules of water, the presence of which was related to the good tensile strength of CTZNa and CTZK dihydrate tablets. The other factor is related to the reduced possibility of amorphisation of CTZK as the drying temperature of dihydrate resulting in the monohydrate form is approximately 80 °C below the Tg of amorphous form of CTZK, as described in Methods (2.2.1.2.).

Besides the physicochemical properties, processing of materials can impact on the tabletability. In 2001 Di Martino et al., presented a method to improve tabletability of crystalline acetazolamide by spray drying. The crystalline material spray dried from an ammonia aqueous solution was reported to be a mixture of polymers I and II. The microparticles had morphology of type I1BX and higher tensile strength than the crystallised pure polymorph I (precipitated by cooling of water solution) or II (precipitated by neutralisation of ammonia solution). Spray dried CTZ gave tablets with a greater tensile strength/compression pressure rate compared to CTZ micronised material. The morphology of the spray dried CTZ sample, in contrast to I1BX morphology type of spray dried acetazolamide, comprised prismoidal in crystal habit nanocrystals forming larger microparticulate conglomerates (Chapter 7).

Tablets made of NPMPs were characterised by best compactibility. These tablets presented the highest tensile strength at low compaction pressures compared to other tablets. The highest

tensile strength corresponded with the highest tablet porosity and the highest specific surface area of the material forming tablet after compression. The tablets made of NPMPs presented the fastest dissolution profiles.

In 1999 Sebhatu and Alderborn published a study on relationships between the effective interparticulate contact area and the tensile strength of tablets made of amorphous (milled) and crystalline lactose of varying particle size. The porosity of the tablets made of amorphous material was similar to those made of crystalline lactose and was approximately 30% at a compression pressure of 75 MPa. At a compression pressure of 125 MPa the porosity decreased to approximately 20%. For the amorphous systems it corresponded with an increase of the tensile strength from 0.5 MPa to approximately 3 MPa, while the tensile strength of tablets made of crystalline lactose was increasing in the range from 0.2 up to nearly 1 MPa.

A comparable range of compression forces was used in this work and it was in the range from 64 MPa to 128 MPa. The porosity of the tablets made of amorphous CTZNa and CTZK NPMPs varied in this compression pressure range from ~47% to ~32%. These higher values of tablet porosity in comparison to the reported lactose tablets corresponded with a greater change and range of tensile strengths from 2.2 MPa to 5.1 MPa (Fig. 9.2). Furthermore, the NPMPs tablets preserved the large specific surface area of the pre-compressed material, ranging from 33 m^2/g to 65 m^2/g and 43 m^2/g to 83 m^2/g for CTZNa and CTZK tablets, respectively.

The CTZNa MPs changed tensile strength from 0.59 to 1.59 MPa, while CTZK MPs changed from 0.93 to 3.52 MPa, when compressed at 64 and 128 MPa compression force, respectively. (Fig. 9.1). The change in tensile strength for CTZNa MPs was lower than for amorphous lactose (Sebhatu and Alderborn, 1999), while the values for CTZK MPs were very similar to those of amorphous lactose. The difference in the change of tensile strength may be attributed to the difference in Tg between amorphous CTZNa (~192 °C) and CTZK (~160 °C), indicating that lower Tg, as exemplified by lactose (Tg of ~ 105 °C) (Haque et al., 2006), may result in better compactibility of the powder.

Crystalline lactose compacted below 128 MPa as reported by Sebhatu and Alderborn (1999), while the micronised CTZ raw material did not (Fig. 9.2). Spray drying of CTZ improved its compactibility properties. Crystalline CTZ NPMPs were compactable at 64 MPa and in the range from 64 up to 128 MPa differed in tensile strength of tablets from 0.53 up to 2.38 MPa (Fig. 9.2). The change in tensile strength of crystalline CTZ NPMPs on changing compression pressure was higher than that of crystalline lactose reported by Sebhatu and Alderborn (1999). These observations suggest that the change of the solid state form of the material from crystalline to amorphous may not be predominant in terms of improving compactibility of the material.

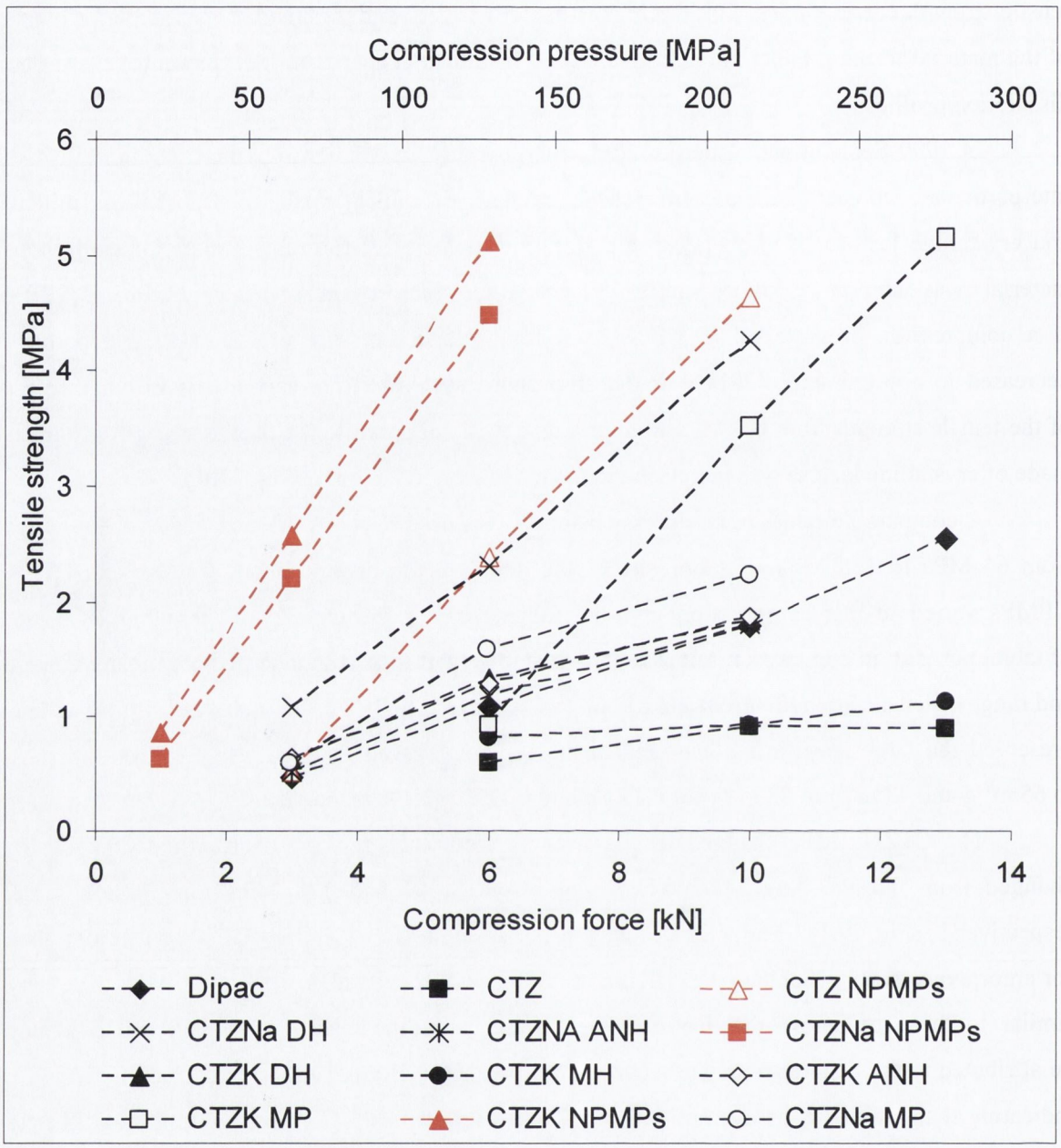

Fig. 9.2. Compactibility of powders tested in chapter 7. Abbreviations as for table 7.1.

The various tablet parameters may be compared to those reported in the study of Westermarck et al., (1998), who investigated the pore structure and surface area of mannitol powder, granules and tablets. In this study Westermarck et al. compared compactibility of tablets prepared by direct compression of mannitol powder and tablets made of granulate. The granulate was prepared by high shear mixing of mannitol powder and addition of 20% aqueous solution of PVP K25, so 75 ml of the PVP solution was added per 1 kg of mannitol. The tablets were compressed at compression pressures from 72 up to 196 MPa. Tablet hardness, porosity, pores volume and specific surface area of tablets were analysed. The tablets made of the mannitol powder had a porosity decreasing from 21% to 14% when the compression pressure was increased. These values corresponded with a slight growth of specific surface area of the tablet from 0.58 to 0.61

m^2/g in comparison to the initial surface area of the powder of 0.34 m^2/g. The increase of specific surface area for mannitol tablets was similar to that observed in this thesis for tablets made of anhydrous CTZK and it was ascribed to the mechanism of brittle fraction of microparticles upon rising compression pressure.

In comparison, the tablets made of the mannitol granulate had a porosity ranging from 26% to 17%, but the reduction of porosity, in contrast to tablets made of the mannitol powder, corresponded to the reduction of the specific surface area of the material. The specific surface area decreased from 1.55 to 1.26 m^2/g in comparison to the initial specific surface area of the granulate of 1.60 m^2/g. A similar reduction of specific surface area, corresponding to the reduction of tablet porosity, under rising compression force was described in this work for tablets made of NPMPs powders or the CTZNa dihydrate micronised powder and ascribed to the mechanism of fusion of micro- or nanoparticles upon rising compression pressure (Fig.9.3).

The results and conclusions of experiments conducted by Busignies et al. (2011) are consistent with the work published by Westermarck et al., (1998) and Sebhatu and Alderborn, (1999). Busignies et al. (2011) investigated changes in the specific surface area of tablets made of microcrystalline cellulose, lactose and anhydrous calcium phosphate in the range of compression pressures from 40 MPa to 280 MPa. The relationship of the change of specific surface area versus compression pressure was different for the three tested batches of tablets. The specific surface area of microcrystalline cellulose reduced upon increasing compression pressure from approximately 1.1 m^2/g, for the uncompressed powder, to 0.4 m^2/g for the tablets made at a compression force of 280 MPa. The reduction of the initial specific surface area was 0.23 %/MPa, two-fold lower in comparison to that of 0.43%/MPa for the CTZNa NPMP tablets and 0.41%/MPa for the CTZK NPMP tablets.

The specific surface area of lactose first increased from 0.2 m^2/g to 0.7 m^2/g when compression pressures up to 160 MPa were used. At a compression pressure of 160 MPa the specific surface area started to decline and fell down to 0.55 m^2/g at a compression pressure of 280 MPa. A similar behaviour of the specific surface area versus compression pressure was observed in this work for CTZ NPMPs, CTZNa MPs and CTZNa ANH tablets indicating that the initial mechanism of compaction is plastic deformation and/or ductile fraction and later the predominant mechanism of compaction is fusion of particles.

Furthermore, for tablets made of NPMPs of CTZ, CTZNa and CTZK, it is observed that the reduction of T_{BET} corresponds to the increase of density of the tablet (d_t) (Fig. 9.4. and Tables I.1-3. in the Appendix I). The mechanism of compaction of NPMPs was discussed in details in Chapter 7, where it was concluded that the fusion of nanoparticles is the predominant mechanism of NPMPs tablet formation. Figure 9.4 presents that the fusion of nanoparticles has a direct impact on the reduction of overall volume of the tablet (Tables I.1-3. in the Appendix I) resulting in an increase of d_t.

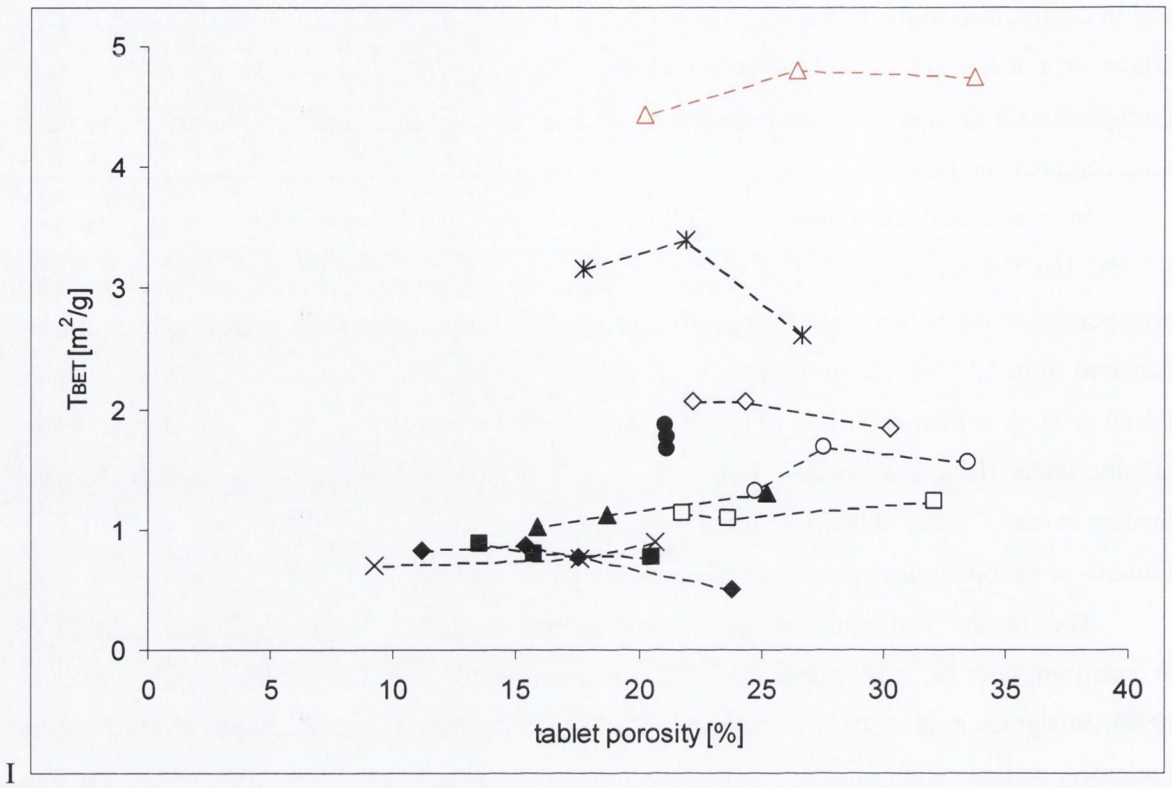

I

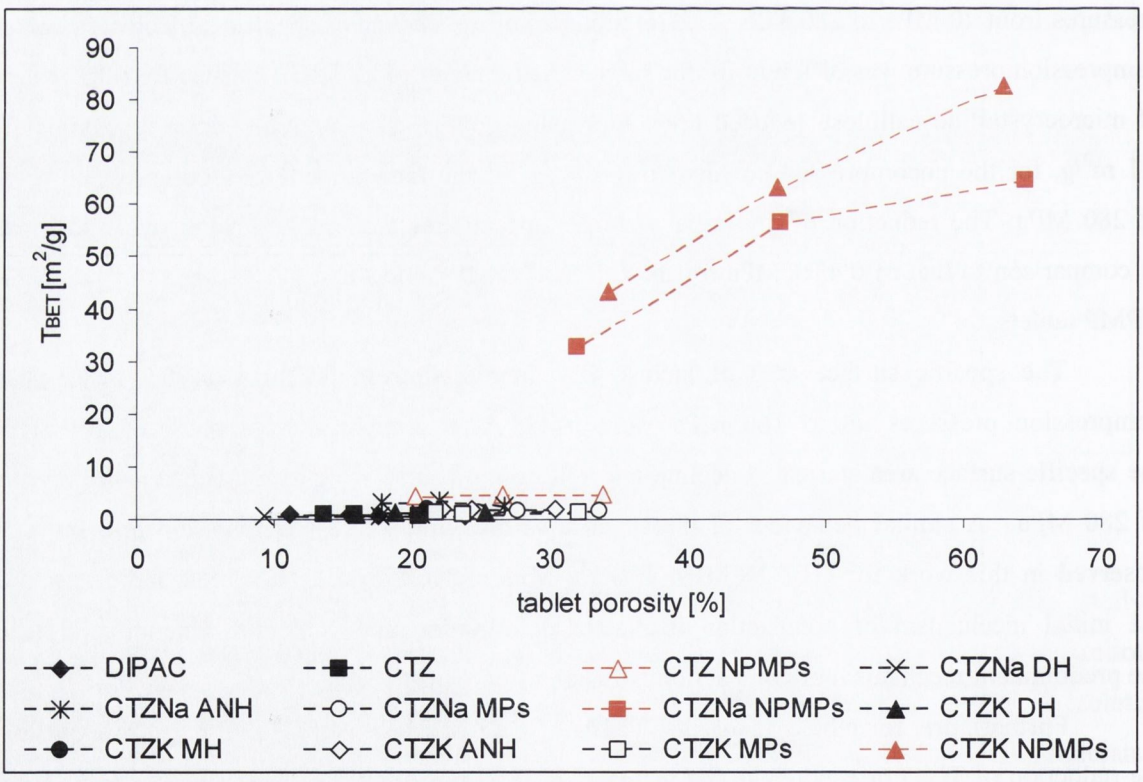

II

Fig. 9.3. Specific surface area (T_{BET}) of the tested tablets versus porosity of tablets (ε_t). Abbreviations as for table 7.1. I. Tablets with exception of tablets made of CTZNa and CTZK NPMPs. II. All tablets.

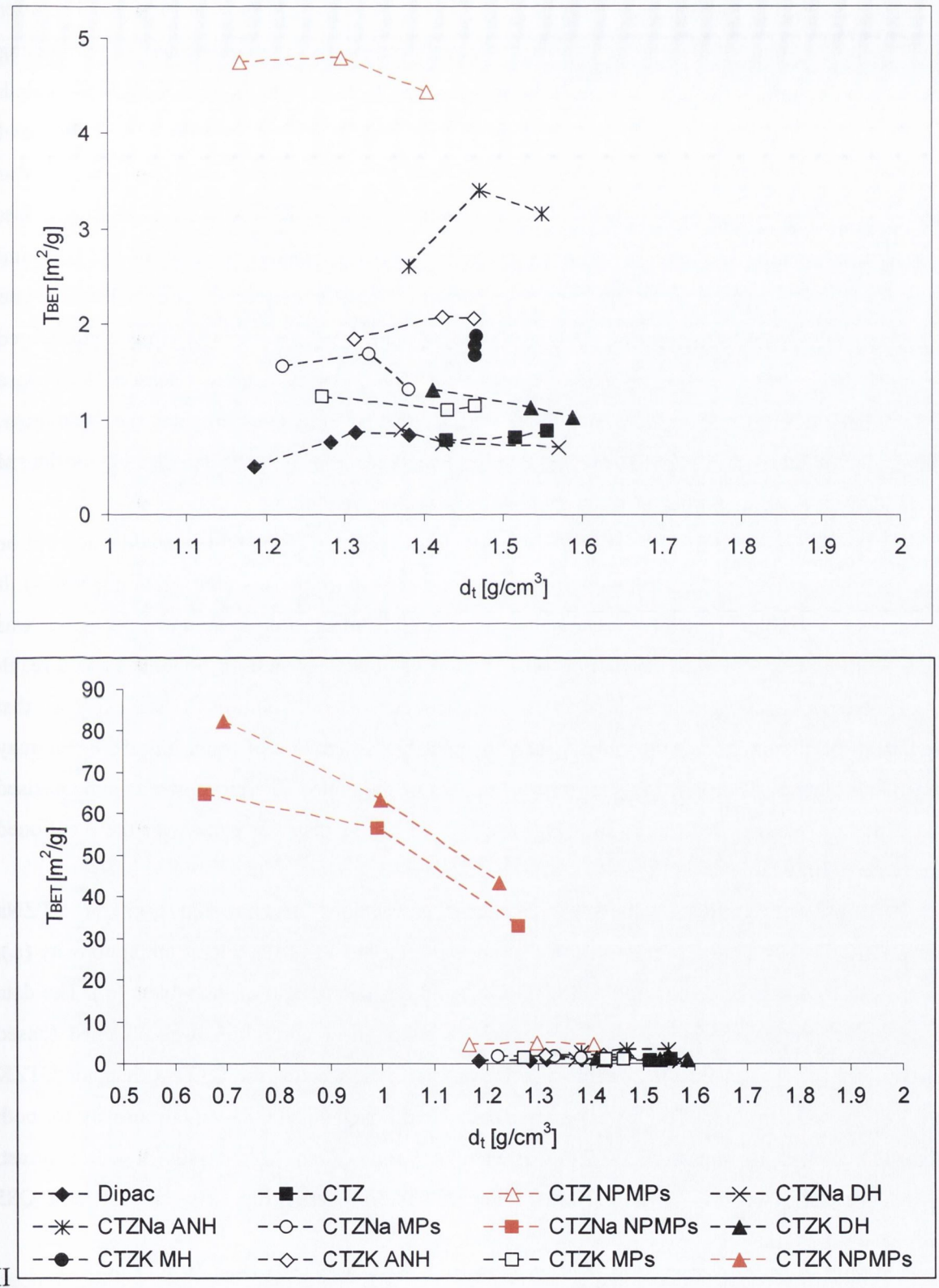

Fig. 9.4. Specific surface area (T_{BET}) of the tested tablets versus density of tablets (d_t) (Appendix I Tables I.1-3). Abbreviations as for table 7.1. I. Tablets with exception of tablets made of CTZNa and CTZK NPMPs. II. All tablets.

Tablets presenting the largest specific surface area in this work had the fastest dissolution rates. The 100% of dose released for CTZNa NPMPs and CTZK NPMPs tablets was reached after the 3rd and 6th minute of dissolution experiment, respectively. This can be deemed as a promising result considering that the tablets comprised of processed API only and no excipients were added. Jaleel et al., (2010) formulated orally dispersible tablets containing loratadine using its solid dispersion with PVP K30 (1:3 w/w ratio, loratadine dose of 10 mg). The formulation (200 mg) also contained other excipients such as Polyplasdone XL-10™ (30 mg, crosspovidone, a superdisintegrant), sodium saccharin (4 mg), talc (4 mg), magnesium stearate (2 mg) and mannitol as a diluent used up to 200 mg. Dissolution studies were performed using 0.1 N HCl and a higher rate of paddle rotation of 100 rpm than that used in this work. The tablets, considered as orally dispersible (ODTs) formulations, containing the superdisintegrant released 100% dose of loratadine after the 3rd minute and those without the superdisintegrant after the 5th minute. The results of Jaleel et al., (2010) suggest that the tablets made of NPMPs can also be considered as an ODT type and might perform comparably to Jaleel's formulations.

It was presented in Chapter 7 that the dissolution profiles of the tablets made could not be described by the Hixson Crowell equation (describing release from non-disintegration systems). It was shown that tablets may have undergone erosion and disintegration, despite this behaviour was not visually observed during dissolution. The erosion and disintegration of the tablets could result in an increase of the surface area of the material subjected to dissolution. It was expected that erosion and disintegration of the tablet, caused by possible penetration of water into the tablet, may depend on the tablet porosity, T_{BET} or tensile strength of the tablet. Therefore, it was hypothesised that times to release 50% (Q50) and (Q85) of the API dose may correlate with the mentioned parameters of the tablets.

Table 9.2 compiles parameters of linear correlations of Q50 and Q85 for CTZNa and CTZK NPMPs tablets compressed in the range from 21 to 128 MPa versus tablet porosity (ε_t), specific surface area of compacted material (T_{BET}) and tensile strength of the tablets (σ_t). The data is presented graphically in Fig. 9.5. In general, a good linear correlation was obtained (based on comparison of R^2 values). In each case the R^2 value was better for CTZNa than for CTZK and for Q50 than for Q85. The lowest R^2 was calculated for Q50 and Q85 versus porosity for both salts. The greatest R^2 in case of CTZNa was calculated for Q50 and Q85 versus T_{BET}. In contrast, in the greatest R^2 value for CTZK was calculated for a relationship between Q50 and Q85 and tensile strength.

The differences between the R^2 values are not large. To explain the observed differences, it may be hypothesised that the difference between the R^2 values for Q50 and Q85 may be related to the degree of erosion and disintegration of the tablet.

The initial tablet porosity (ε_t), specific surface area of compacted material (T_{BET}) and tensile strength of the tablets (σ_t) may not be constant over the time of dissolution, this is why

better linear correlation coefficients are observed at the initial phase of dissolution until Q50 is released. The difference between R^2 values, being greater for CTZNa than for CTZK tablets, may be ascribed to the discussed in the previous chapters (3, 4 and 6) different propensity of these materials to hydration. CTZK tends to hydrate faster and bonding of water is stronger than for CTZNa. It may be hypothesised that hydration of the CTZK material progresses faster than erosion and dissolution of the tablet resulting in, as discussed in Chapter 7, slowing down of dissolution. As hydration of CTZK NPMPs should additionally affect the T_{BET} and ε_t the greatest R^2 value was recorded for tensile strength of the CTZK NPMPs tablets suggesting that erosion limited by hardness of the tablet is the main driving force of dissolution of the CTZK material.

Table 9.2. Parameters of linear correlations of Q50 and Q85 for CTZNa and CTZK NPMPs tablets versus tablet porosity (ε_t), specific surface area of compacted material and tensile strength of the tablets (σ_t).

System		slope	Y-intracept	R^2
Q50 and Q 85 vs. tablet porosity (ε_t)				
CTZNa NPMPs	Q50	-2.6923	229.23	0.9423
	Q85	-7.4176	566.04	0.8583
CTZK NPMPs	Q50	-7.7419	599.03	0.8848
	Q85	-16.876	1267.8	0.8719
Q50 and Q 85 vs. T_{BET}				
CTZNa NPMPs	Q50	-2.7723	242.31	0.9967
	Q85	-7.9865	619.98	0.9926
CTZK NPMPs	Q50	-5.6661	585.07	0.9181
	Q85	-12.366	1238.3	0.9069
Q50 and Q 85 vs. tensile strength (σ_t)				
CTZNa NPMPs	Q50	23.526	42.831	0.9932
	Q85	66.413	48.617	0.9497
CTZK NPMPs	Q50	52.918	79.184	0.9623
	Q85	115.73	133.52	0.9544

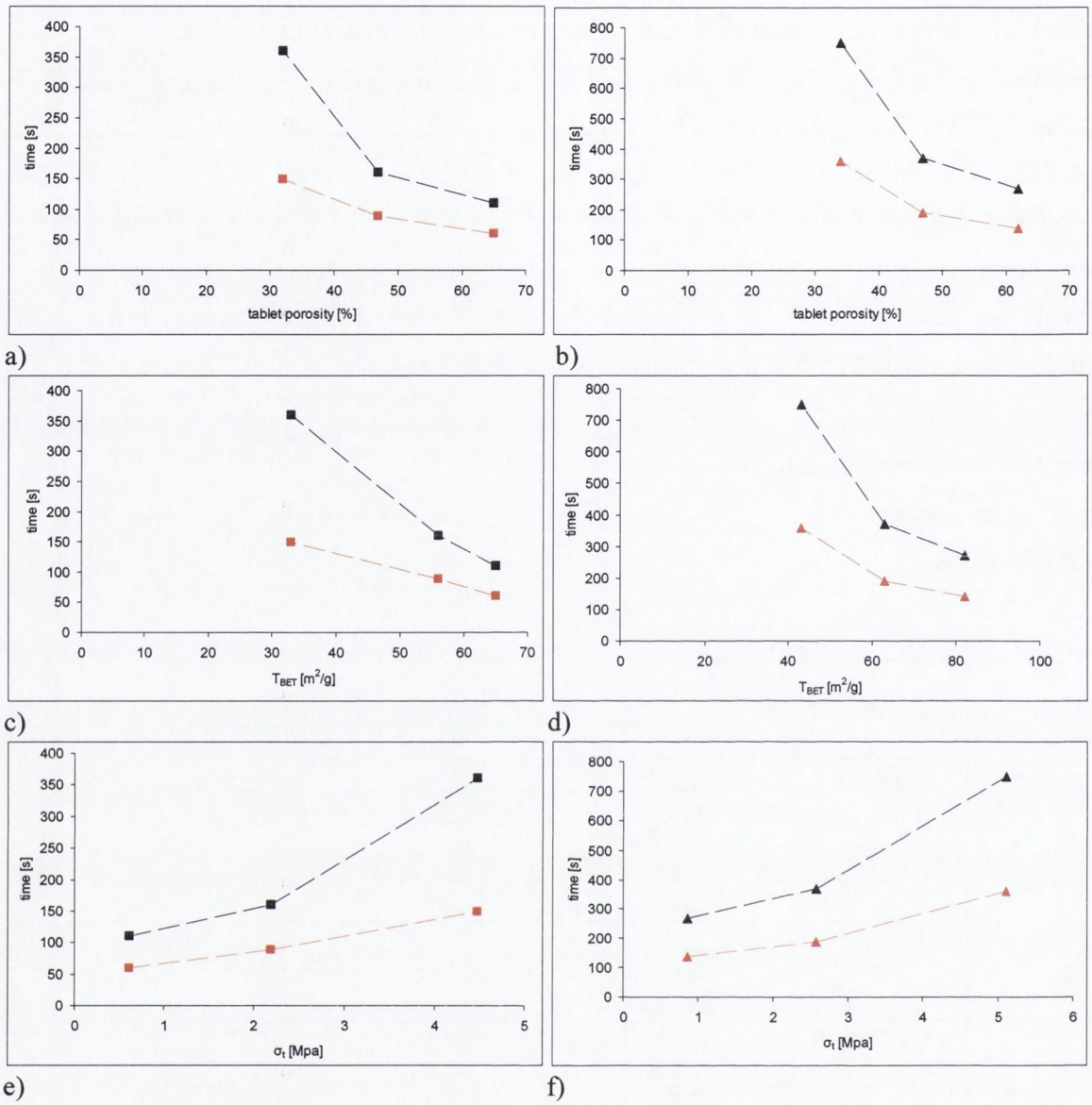

Fig. 9.5. Relationship of time to release 50% of dose- Q50 (red) and 85% of dose- Q85 (black) for CTZNa NPMPs (squares) and CTZK NPMPs (triangles) versus: a), b) porosity of the tablets (ε_0), c), d) specific surface area of the tablets (T_{BET}) and e), f) tensile strength (σ_t).

Main findings

- CTZ can form salts with sodium (CTZNa) and potassium (CTZK) counterions; these salts can present different solid state forms.
- CTZNa can be obtained as a dihydrate (CTZNa DH), anhydrous and amorphous form (Tg at 192 °C).
- CTZK can be obtained as a dihydrate, monohydrate, monohydrate hemiethanolate, anhydrous and amorphous form (Tg at 160 °C).
- CTZNa DH formed an intramolecular self-assembly (ISA) when crystallised from water or water/acetone (1:1 v/v) mixture.
- CTZ formed a range of ISAs with potassium cations when crystallised from water and ethanol.
- Anhydrous CTZNa and CTZK had the following melting/decomposition points: ~289 °C and ~263 °C, respectively.
- The solubilities of CTZNa DH and CTZK DH were determined to be ~80 mg/ml.
- Spray drying of CTZ resulted in its amorphous form with Tg at 135 °C.
- Spray drying was an effective method of production of MPs and NPMPs of amorphous CTZNa and CTZK.
- The Morphology Classification System of spray dried particles (MCS-SD) developed was an useful tool for characterisation of morphology of spray dried powders.
- NPMPs with specific surface areas of 70 m^2/g and 90 m^2/g for CTZNa and CTZK, respectively, and morphology types of V1BS of MCS-SD were obtained with satisfactory yields (~90-95%) by spray drying from 2% w/v feed and a MeOH/BA (3:7 v/v) mixture.
- NPMPs of CTZNa and CTZK produced by spray drying had better compactibility and compressability in comparison to crystalline and non-porous spray dried (MPs) salts.
- NPMPs compacts maintained large specific surface area, at the same time presenting large tablet porosity and satisfactory tensile strength.
- CTZNa and CTZK NPMPs tablets presented very good dissolution performance presenting the shortest times of a complete release of the API dose loaded.
- For the first time it was reported that salbutamol can form a co-crystal.
- For the first time the involvement of adipic acid molecule in the formation of a co-crystal of a salt was reported.
- Produced salbutamol succinate tertmethanolate (SSU.MeOH) was a rare example of the succinate constituting a solvated salt form.
- The intrinsic dissolution rate of SSU was around 4-fold greater than that of salbutamol adipate (SA), consistent with the ~5-fold difference in aqueous solubility of salbutamol in SA and SSU.

Future work

- Chlorothiazide may be used as a model host molecule in further crystallisation studies using organic bases, to investigate the modification of H-bonds in the crystal lattice of chlorothiazide and their impact on aqueous solubility of chlorothiazide. The novel compounds can be compared to CTZNa and CTZK salts formulated in this work.

- Chlorothiazide as a diuretic agent may be co-spray dried with chosen glucocorticoids to assess superiority of the combined pulmonary delivery therapy in cystic fibrosis in comparison to conventional treatment methods.

- Morphology classification system of spray dried particles can be expanded to describe all reported types of morphology including types of morphologies of non-porous spray dried particles.

- The approach to tableting of NPMPs requires investigation of flowability of NPMP powders and the impact of particle size on the T_{BET} and flowability of powder.

- Tabletability of NPMPs may be expanded by investigations of tabletability performance of hydrophobic and hydrophilic pharmaceutical excipients formulated into NPMPs.

- Co-crystalline salbutamol adipate and succinate may be compared by subjecting them to biopharmaceutic studies in a form of a tablet and/or as a DPI. They may also be spray dried or co-spray dried with a carrier into NPMPs.

- The solubility behaviour of salbutamol succinate and salbutamol adipate co-crystal with adipic acid may be investigated using ternary phase diagrams.

- Salbutamol as a host molecule may be co-crystallised with a broader range of acidic co-formers including e.g. pamoic acid to further decrease the dissolution rate, in a similar manner as was applied to olanzapine.

References

Adams, M.E., Subhash, D., Aziz, K., Kalidas, P., Douglas, J.S., Zold, D.J., 2000. Potassium, sodium and tris oxaprozin salt pharmaceutical formulations, US Patent 6030643.

Ahn, S.H., Cho, C.B., Lee, K.Y., 2002. The Kinetics of Shear-Induced Crystallization in Poly(Ethylene Terephthalate). J. Reinf. Plast. Comp., 21, 617-628.

Allen, D.J., Dekemper, K.D., Ferguson, T.H., Garvin, S.J., Murray, L.C., Brooks, N.D., Bunnell, C.A., Mascarenhas, S.S., Shinkle, S.L., Hendriksen, B.A., Tupper, D.E. Sanchez-Felix, M.V. 2007. 2-methyl-thieno-benzodiazepine formulation. WO/2006/073886.

Allen, T., 1992. Particle Size Measurement, 4th edition, Chapman and Hall

Allesø, M., Chieng, N., Rehder, S., Rantanen, J., Rades, T., Aaltonen, J., 2009. Enhanced dissolution rate and synchronized release of drugs in binary systems through formulation: Amorphous naproxen–cimetidine mixtures prepared by mechanical activation. J. Control. Release, 136(1), 45-53.

Altria K.D., 1993. Determination of salbutamol-related impurities by capillary electrophoresis. J. of Chromatography, 634(2), 323-328.

Amidon, G.L., Lennernas, H., Shah, V.P., Crison, J.R., 1995. A theoretical basis for a biopharmaceutic drug classification - the correlation of in-vitro drug product dissolution and in-vivo bioavailability. Pharm. Res., 12, 413-420.

Anderson, B.D., Conradi, R.A., 1985. Predictive relationships in the water solubility of salts of a nonsteroidal anti-inflammatory drug. J. Pharm. Sci., 74(8), 815–820.

Anderson, B.D., Flora, K.P.,1996. Preparation of water-soluble compounds through salt formation. The Practice of Medicinal Chemistry, Academic Press, London, pp. 739–754.

Antoncic, L., Copar, A., 2009. Preparation of telmisartan salts with improved solubility. US Patent Application: 20090012140.

Anuar, M.S., Briscoe, B.J., 2009. The elastic relaxation of starch tablets during ejection. P. Tech., 195, 96–104.

Appel, L.J., 2002. The verdict from ALLHAT-thiazide diuretics are the preferred initial therapy for hypertension. JAMA, 18, 3039-3042.

Augsburger, L.L., Hoag, S.W., 2008. Pharmaceutical dosage forms: Tablets, Third edition, Vol. 2 Rational design and formulation, Informa Healthcare USA Inc.

Bailey, R.D., Wals, M.W., Bradner, S., Fleischman, L., Morales, A., Moulton, B., Rodríguez-Hornedo, N., Zaworotko, M.J., 2003. Crystal engineering of the composition of pharmaceutical phases, Chem. Commun., 186–187.

Barbosa, J., Barron, D., Berges, R., Buti, S., Sanz-Nebot, V., 1998. Evaluation of the effect of organic modifier on pK values of diuretics in mobile phases used in LC. Int. J. Pharm., 160, 173-185.

Beale, J.P., Grainger, C.T. 1972. DL-N-t-Butyl-2(4-hydroxy-3-hydroxymethylphenyl)2-hydroxyethylamine, (salbutamol, Ah. 3365), $C_{13}H_{21}NO_3$. Cryst. Struct. Comm., 67(1): 71-74.

Bekdemir, Y., Kutuk, H., Celik, S., Yilmaz, V.T., Thoene, C., 2002. Trans-Tetraaquabis (p-nitrobenzoxasulfamato)cobalt(II), J. Mol. Struct., 604, 239-244.

Berge, S.M., Bighley, L.D., Monkhouse, D.C., 1977. Pharmaceutical salts. J. Pharm. Sci. 66, 1-19.

Berggren, J., Frenning, G., Alderborn, G., 2004, Compression behaviour and tablet-forming ability of spray-dried amorphous composite particles. Eur. J. Pharm. Sci., 22, 191–200.

Bethune, S.J., Huang, N., Jayasankar, A., Rodriguez-Hornedo, N., 2009. Understanding and Predicting the Effect of Cocrystal Components and pH on Cocrystal Solubility. Cryst. Growth Des., 9(9), 3976–3988.

Beyer, K.H., 1982. Chlorothiazide. Br. J. Pharmacol., 13, 15-24.

Blagden, N., de Matas, M.P.T., York, G.P., 2007, Crystal engineering of active pharmaceutical ingredients to improve solubility and dissolution rates, Adv. Drug Deliver. Rev., 59, 617-630.

Blake, A.J., Clegg, W., Cole, J.M., Evans, J.S.O., Main, P., Parsons, S., Watkin, D.J., 2009. Crystal Structure Analysis Principles and Practice, Second Edition, by Clegg, W., IUCR. Crystall. Symp., Oxford Science Publications.

Blessing, R.H., 1995. An empirical correction for absorption anisotropy. Acta Cryst. A51, 33-38.

BMJ Publishing, British National Formulary, Current Ed. Accessed online: 29.10.2010.

Bottom, R., 1999. The role of modulated temperature differential scanning calorimetry in the characterisation of a drug molecule exhibiting polymorphic and glass forming tendencies. Int. J. Pharm. 192, 47-53.

Bragg, W.L., 1913. The diffraction of short electromagnetic waves by a crystal. P. Camb. Philos. Soc., 17, 43–57.

British pharmacopoeia, 2010. Electronic resource., Publisher British Pharmacopoeia, [current], Accessed online, 29.11.2010.

Brittain, H.G., 2009. Polymorphism and solvatomorphism 2007. J. Pharm. Sci., 98(5), 1617-42.

Brunauer, S., Emmett, P.H., Teller, E., 1938. Adsorption of gases in multimolecular layers. J. Am. Chem. Soc., 60, 309-319.

Bruner, E., 1904. Reaktionsgeschwindigkeit in heterogenen systemen. Zeitschrift für Physikalische Chemie, 47, 56-102.

Brunton, L.L., Lazo, J.S., Parker, K.L., (Eds.), 1996. Goodman and Gilman's. The Pharmacological Basis of Therapeutics. The McGraw-Hill, New York.

Büchi 93001 en Operation manual Mini Spray Dryer B-290.

Burnett, D.J., Thielmann, F., Booth, J., 2004. Determining the critical relative humidity for moisture-induced phase transitions. Int. J. Pharm. 287, 123–133.

Busignies, V., Leclerc, B., Truchon, S., Tchoreloff, P., 2011. Changes in the specific surface area of tablets composed of pharmaceutical materials with various deformation behaviors. Drug. Dev. Ind. Pharm. 37(2), 225-33.

Carretero, M.I., Pozo, M., 2009. Clay and non-clay minerals in the pharmaceutical industry Part I. Excipients and medical applications Appl. Clay Sci., 46, 73–80.

Carstensen, J.T., Franchini, M., Pudapeddi, M., Morris, T., 1993. Reaction orders of decomposition of anhydrous amorphates, Drug Dev.Ind. Pharm., 19(15), 1811-1820.

Charnicki, W.F., Bacher, F.A., Freeman, S.A., Decesare, D.H., 1959. The pharmacy of chlorothiazide (6-chloro-7-sulfamyl-1,2,4-benzothiadiazine-1,1-dioxide) - a new orally effective diuretic agent. J. Am. Pharm. Assoc., 48, 656-659.

Cheney, M.L., Shan, N., Healey, E.R., Mazen, H., Wojtas, Ł., Zaworotko, M.J., Sava, V., Song, S., Sanchez-Ramos, J.R., 2010. Effects of Crystal Form on Solubility and Pharmacokinetics: A Crystal Engineering Case Study of Lamotrigine. Cryst., Growth Des., 10(1), 394–405.

Chow, A.H.L., Tong, H.H.Y., Chattopadhyay, P., Shekunov, B.Y., 2007. Particle Engineering for Pulmonary Drug Delivery. Pharm. Res., 24(3) 411-437.

Chu, K.A., Yalkowsky, S.H., 2009. An interesting relationship between drug absorption and melting point. Int. J. Pharm., 373, 24-40.

Cobby, J., Mayersohn, M., Walker, G.C., 1974. Influence of shape factors on kinetics of drug release from matrix tablets II: Experimental. J. Pharm. Sci., 63(5), 732 – 737.

Connors, K.A., Amidon, G.L., Stella, V.J., 1986. Chemical stability of pharmaceuticals. A handbook for pharmacists. Second Ed. John Willey and Sons, Inc., USA

Corrigan, D.O., Corrigan, O.I., Healy, A.M., 2004. Predicting the physical state of spray dried composites: salbutamol sulphate/lactose and salbutamol sulphate/polyethylene glycol co-spray dried systems. Int. J. Pharm., 273, 171–182.

Corrigan, D.O., Corrigan, O.I., Healy, A.M., 2006a. Physicochemical and in vitro deposition properties of salbutamol sulphate/ipratropium bromide and salbutamol sulphate/excipient spray dried mixtures for use in dry powder inhalers. Int. J. Pharm. 322, 22–30.

Corrigan, D.O., Healy, A.M., Corrigan, O.I., 2006b. Preparation and release of salbutamol from chitosan and chitozan co-spray dried compacts and multiparticulates. Eur. J. Pharm. Biopharm., 62, 295–305.

Corrigan, O.I., Holohan, E.M., Reilly, M.R., 1985. Physicochemical properties of indomethacin and related compounds co-spray dried with polyvinyl-pyrrolidone. Drug Dev. Ind. Pharm., 11(2-3), 677-695.

Corrigan, O.I., Holohan, E.M., Sabra, K., 1984. Amorphous forms of diuretics prepared by spray drying. Int. J. Pharm., 18, 195–200.

Corrigan, O.I., O'Driscoll, K.M., 1980. The effect of dosage on the bioavailability of chlorothiazide administered in solution. J. Pharm. Pharmacol., 32, 547-549.

Corrigan, O.I., Sabra, K., Holohan, E.M., 1983. Physicochemical properties of spray dried drugs: phenobarbitone and hydroflumethiazide. Drug Dev. Ind. Pharm., 9(1-2), 1-20.

Corveleyn, S., Remon, J.P., 1998. Bioavailability of hydrochlorothiazide: conventional versus freeze-dried tablets. Int. J. Pharm., 173, 149–155.

Costa, P., Sousa Lobo, J.M., 2001. Modelling and comparison of dissolution profiles. Eur. J. Pharm. Sci., 13, 123–133.

De Jong, W.F., 1959. General Crystallography A Brief Compendium, San Francisco, Freeman, W.H. and Company.

Debnath, S., Suryanarayanan, R., 2004. Influence of process-induced phase transformation on dissolution of theophylline tablets. AAPS PharmSciTech 5, 8.

Dellamary, L.A., Tarara, T.E., Smith, D.J., Woelk, C.H., Adractas, A., Costello, M.L., Gill, H., Weers, J.G., 2000. Hollow porous particles in metered dose inhalers. Pharm. Res., 17(2), 168-74.

Derry, P., Derry, S., Moore, R.A., McQuay, H.J., 2009. Single dose oral diclofenac for acute postoperative pain in adults, Cochrane Database, Syst. Rev., 2, CD004768.

Di Martino, P., Scoppa, M., Joiris, E., Palmieri, G.F., Andres, C., Pourcelot, Y., Martelli, S., 2001. The spray drying of acetazolamide as method to modify crystal properties and to improve compression behaviour. Int. J. Pharm., 213, 209–221.

Ditte, M., Krohn, J., Dongmei, C., Maltesen, M.J., Frokjaer, S., Nielsen, H.M., Foged, C., 2010. Spray drying of siRNA-containing PLGA nanoparticles intended for inhalation. J. Cont. Rel., 142(1), 138-145.

Dobry, D.E., Settell, D.M., Baumann, J.M., Ray, R.J., Graham L.J., Beyerinck, R.A., 2009. A model-based methodology for spray-drying process development. J. Pharm. Innov., 4, 133-142.

Dova, E., Mazurek, J.M., Anker, J., 2008. Tenofovir Disoproxil Hemi-Fumaric Acid Co-Crystal WO/2008/143500.

Dupont, L., Dideberg, O., 1970. Etude radiocristallographique préliminaire de quelques thiazides. Acta Crystallogr. B Struct. Crystallogr. Cryst. Chem., B26, 1884-1885.

Ellison, D.H., Loffing, J., 2009. Thiazide effect and adverse effects: Insights from molecular genetics. Hypertension, 54, 196-202.

Elversson, J., Millqvist-Fureby, A., Alderborn, G., Elofsson, U., 2003. Droplet and particle size relationship and shell thickness of inhalable lactose particles during spray drying. J. Pharm. Sci., 92(4), 900–910.

Es-Saheb, M.H.H., 1996. Tensile fracture characteristics of double convex-faced cylindrical powder compacts. J. Mat. Sci., 31(1), 214-223.

European Pharmacopoeia. 6th ed., 2010. Council of Europe, Strasbourg.

Fadda, H.M., Sousa, T., Carlsson, A.S., Abrahamsson, B., Williams, J.G., Kumar, D., Basit, A.W., 2010. Drug Solubility in Luminal Fluids from Different Regions of the Small and Large Intestine of Humans. Mol. Pharm., 7(5), 1527–1532.

Farrugia, L.J., 1997. ORTEP-3 for Windows - a version of ORTEP-III with a Graphical User Interface (GUI). J. Appl. Crystallogr., 30, 565.

Fell, J.T., Newton, J.M., 1970. Determination of tablet strength by the diametral-compression test J. Pharm. Sci., 59(5), 688–691.

Fichtner, F., Rasmuson, A., Alderborn, G., 2005. Particle size distribution and evolution in tablet structure during and after compaction, Int. J. Pharm., 292, 211–225.

Flick, E.W., 1998. Industrial solvents handbook, 5th Edition, Noyes Data Corporation, USA.

Ford, J.L., Mitchell, K., Rowe, P., Armstrong, D.J., Elliott, P.N.C., Rostron, C., Hogan, J.E., 1991. Mathematical modelling of drug release from hydroxypropylmethylcellulose matrices: Effect of temperature, Int. J. Pharm., 71(1-2), 95-104.

Gad, E., Mahmoud, A., Khairou, K.S., 2008. QSPR for HLB of Nonionic Surfactants Based on Polyoxyethylene Group. J. Disper. Sc. Technol., 29(7), 940 – 947.

Gans, E.H., Higuchi, T., 1957. The solubility and complexing properties of oxytetracycline and tetracycline I. Interaction in aqueous solution. J. Am. Pharm. Assoc., 46(8), 458–466.

Garcia-Raso, A., Fiol, J.J., Rigo, S., Lopez-Lopez, A., Molins, E., Espinosa, E., Borras, E., Alzuet, G., Borras, J., Castineiras, A., 2000. Coordination behaviour of sulfanilamide derivatives. Crystal structures of [Hg(sulfamethoxypyridazinato)(2)], [Cd(sulfadimidinato)(2)(H2O)] center dot 2H(2)O and [Zn(sulfamethoxazolato)(2)-(pyridine)(2)(H2O)(2)]. Polyhedron, 19, 991-1004.

Geddes, A.J., Sheldrick, B., Stevenson, W.T.J., Steinrauf, L.K., 1974. The crystal structure of the potassium salt of nigericin, Biochem. Biophys. Res Commun., 60, 1245-1251.

Gibson M (ed.), Pharmaceutical preformulation and formulation: a practical guide from candidate drug selection to commercial dosage form, 1st edition, Informa Healthcare, 2001

Gilani, K., Najafabadi, A.R., Barghi, M., Rafiee-Tehrani, M., 2005. The effect of water to ethanol feed ratio on physical properties and aerosolization behavior of spray dried cromolyn sodium particles. J. Pharm. Sci., 94(5), 1048-1059.

Gonzalez, G., Sagarzazu, A., Bonyuet, D., D'Angelo, L., Villalba, R., 2009. Solid state amorphisation in binary systems prepared by mechanical alloying. J. All. Comp., 483(1-2), 289-297.

Goula, A.M., Adamopoulos, K.G., 2004. Spray Drying of Tomato Pulp: Effect of Feed Concentration. Dry. Tech., 22(10), 2309-2330.

Gupta, M.K., Vanwert, A., Bogner, R.H., 2003. Formation of physically stable amorphous drugs by milling with neusilin. J. Pharm. Sci., 92(3), 536-51.

Hakes, L.B., Meakin, B.J., Winterborn, I.K., 1980. the effect of sugars on the stability of salbutamol sulphate solutions. J. Pharm. Pharmacol. 32(S1) 49

Haleblian, J., McCrone, W.C., 1969. Pharmaceutical applications of polymorphism. J. Pharm. Sci., 58, 911-929.

Hall, S.R., Allen, F.H. Brown, I.D., 1991. The Crystallographic Information File (CIF): a new standard archive file for crystallography. Acta Cryst., A47, 655-685.

Hancock, B.C., York, P., Rowe, R.C., 1997. The use of solubility parameters in pharmaceutical dosage form design. Int. J. Pharm., 148(1), 1-21.

Hankins, J., Lonsway, R.A., Hedrick, C., Perdue, M., (Eds.), 2001. Infusion therapy in clinical practice. Intravenous Nurses Society, Saunders, Philadelphia.

Haque, K., Kawai, K., Suzuki, T., 2006. Glass transition and enthalpy relaxation of amorphous lactose glass. Carbohyd. Res., 341(11), 1884-1889.

Harjunen, P., Lehto, V.P., Välisaari, J., Lankinen, T., Paronen, P., Järvinen, K., 2002. Effects of ethanol to water ratio in feed solution on the crystallinity of spray-dried lactose. Drug Dev. Ind. Pharm., 28(8), 949-55.

Harrison, W.T.A., Yathirajan, H.S., Bindya, S., Anilkumar, H.G., Devaraju, 2007. Escitalopram oxalate: co-existence of oxalate dianions and oxalic acid molecules in the same crystal. Acta Cryst., C63, 129-131.

Haynes, D.A., Jones, W., Motherwell, W.D.S., 2005. Occurrence of pharmaceutically acceptable anions and cations in the Cambridge structural database. J. Pharm. Sci., 94, 2111-2120.

Healy, A.M., Corrigan, O.I., 1996. The influence of excipient particle size, solubility and acid strength on the dissolution of an acidic drug from two-component compacts. Int. J. Pharm., 143(2), 211-221.

Healy, A.M., McCarthy, L.G., Gallagher, K.M., Corrigan, O.I., 2002. Sensitivity of dissolution rate to location in the paddle dissolution apparatus. J. Pharm. Pharmacol., 54(3), 441–444.

Healy, A.M., McDonald, B.F., Tajber, L., Corrigan, O.I., 2008. Characterisation of excipient-free nanoporous microparticles (NPMPs) of bendroflumethiazide. Eur. J. Pharm. Biopharm., 69(3), 1182-6.

Herting, M.G., Kleinebudde, P., 2007. Roll compaction/dry granulation: Effect of raw material particle size on granule and tablet properties. Int. J. Pharm., 338, 110–118.

Hickey, A.J., Kuchel, K., Masinde, L.E., 1994. Comparative efficiency of solution and suspension output from jet nebulisers. Respirat. Drug Deliv., 4, 259–263.

Hickey, M.B., Peterson, M.L., Manas, E.S., Alvarez, J., Haeffner,F., Almarsson, O., 2007.

Hirshfeld, F.L., 1977. Bonded-atom fragments for describing molecular charge-densities. Theor. Chim. Acta, 44, 129-138.

Hirst, P.H., Pitcairn, G.R., Weers, J.G., Tarara, T.E., Clark, A.R., Dellamary, L.A., Hall, G., Shorr, J., Newman, S.P., 2002. In vivo lung deposition of hollow porous particles from a pressurized metered dose inhaler. Pharm. Res. 19(3), 258-264.

Hixson, A.W., Crowell, J.H., 1931. Dependence of reaction velocity upon surface and agitation. Ind. Eng. Chem. Res., 23, 923-31.

Höhne, G., Hemminger, W. Flammersheimer, H.J., 1996. Differential Scanning Calorimety- An Introduction for Practioners, Springer-Verlag, Berlin, Heidelberg, New York.

Holubová, J., Ernošek, Z., Ernošková, E., 2005. The study of the glass transition by the Step Scan DSC technique. J. Optoelectr. Adv. Mat. 7(5), 2671 – 2676.

Howell, G., Edwards, M., Lawson, E., de Matas, M., Shields L., York, P., 1997. Metamorphosis of caffeine hydrate and anhydrous caffeine. J. Chem. Soc., Perkin Trans. 2, 1985-1990.

Hull, A.W., 1919. A New Method of Chemical Analysis, J. Am. Chem. Soc., 41(8), 1168–1175.

Hussain, M.A., Bruce, J., Aungst, M., Maurin, B., Wu, L.S., 1991. Injectable suspensions for prolonged release nalbuphine. Drug Dev. Ind. Pharm., 17(1), 67-76.

Hydrates and solid-state reactivity: a survey of beta-lactam antibiotics. J. Pharm. Sci. 96, 1090-9.

Imboden, R., Imanidis, G., 1999. Effect of the amphoteric properties of salbutamol on its release rate through a propylene control membrane, Eur. J. Pharm. Biopharm., 47, 161-167.

Islam, M.I.U., Langrish, T.A.G., Chiou, D., 2010. Particle crystallization during spray drying in humid air. J. Food Eng., 99(1), 55-62.

Jackson, M.B., 2006. Molecular and cellular biophysics, Cambridge University Press, New York. USA.

Jain, N., Yalkowsky, S.E., 2001. Estimation of the aqueous solubility. I. Application to organic nonelectrolytes. J. Pharm. Sci., 90, 234-252.

Jakobsen, P., Treppendahl, S., 1979. Structure of 1,2,4-benzothiadiazine-1,1-dioxides. Tetrahedron, 35, 2151-2153.

Jaleel, A., Omar, W., Abdulrasool, Alaa, A., Ghareeb, Mowafaq, M., 2010. Preparation and Characterization of Orally Disintegrating Loratadine Tablets from PVP Solid Dispersions Int. J. Pharm. Sci., 2(3), 759-770.

Janssens, S., Anné, M., Rombaut, P., Van den Mooter, G., 2009. Spray drying from complex solvent systems broadens the applicability of Kollicoat IR as a carrier in the formulation of solid dispersions. Eur. J. Pharm. Sci., 37, 241–248.

Jashnani, R.J., Byron, P.R., 1996. Dry powder aerosol generation in different environments: Performance comparisons of albuterol, albuterol sulfate, albuterol adipate and albuterol stearate. Int. J. Pharm., 130(1), 13-24.

Jashnani, R.N., Byron, P.R., Dalby, R.N., 1993. Preparation, characterization, and dissolution kinetics of two novel albuterol salts., J. Pharm. Sci. 82(6): 613- 616.

Johnston, A., Florence, A.J., Fernandes, P., Kennedy, A.R., 2007b. Chlorothiazide N,N-dimethylacetamidedisolvate. Acta Crystallogr., Sect. E: Struct. Rep. Online 63, O2422.

Johnston, A., Florence, A.J., Fernandes, P., Kennedy, A.R., 2007c. Chlorothiazide dimethyl sulfoxide solvate. Acta Crystallogr., Sect. E: Struct. Rep. Online 63, O2423.

Johnston, A., Florence, A.J., Kennedy, A.R., 2007a. Chlorothiazide formic acid solvate (1/2). Acta Crystallogr., Sect. E: Struct. Rep. Online 63, O4021.

Johnston, A., Florence, A.J., Kennedy, A.R., 2008. Chlorothiazide-pyridine (1/3). Acta Crystallogr., Sect. E: Struct. Rep. Online 64, O1105.

Joiris, E., Martino, P.D., Berneron, C., Guyot-Hermann, A.M., Guyot, J.C., 1998. Compression behavior of orthorhombic paracetamol. Pharm. Res., 15, 1122–1130.

Jørgensen, A.C., Airaksinen, S., Karjalainen, M., Luukkonen, P., Rantanen, J., Yliruusia, J., 2004. Role of excipients in hydrate formation kinetics of theophylline in wet masses studied by near-infrared spectroscopy. Eur. J. Pharm. Sci., 23(1), 99-104.

Kim, Y.B., Park, I.Y., Lah, W.R., 1990. The crystal structure of naproxen sodium, (C14H13O3Na), a non-steroidal antiinflammatory agent. Arch. Pharmacol. Res. 13, 166-173.

Kippax, P., 2005. Appraisal of the Laser Diffraction Particle Sizing Technique. Pharm. Tech., 3, 88-96.

Kordis-Krapez, M., Abram, V., Kac, M., Ferjancic, S., 2001. Determination of Organic Acids in White Wines by RP-HPLC. Food Technol. Biotechnol., 39, 93-99.

Korhonen, O., Pohja, S., Peltonen, S., Suihko, E., Vidgren, M., Paronen, P., Ketolainen, J., 2002. Effects of Physical Properties for Starch Acetate Powders on Tableting. AAPS Pharm. Sci. Tech. 3(4), 1-9.

Kristmundsdottir, T., Gudmundsson, O.S., Ingvarsdottir, K., 1996. Release of diltiazem from Eudragit microparticles prepared by spray-drying. Int. J. Pharm., 137, 159-165.

Kuhnert-Brandstätter M., Gasser, P., 1971. Solvates and polymorphic modifications of steroid hormones. I. Microchem. J., 16(3), 419-428.

Langmuir, I., 1916. The constitution and fundamental properties of solids and liquids. Part I. Solids., J. Am. Chem. Soc., 38, 2221-95.

Larhrib, H., Martin, G.P., Marriott, C., Prime, D. 2003. The influence of carrier and drug morphology on drug delivery from dry powder formulations. Int. J. Pharm., 257, 283–296.

Ledwidge, M.T., Corrigan, O.I., 1997. Effects of environmental factors on the dehydration of diclofenac HEP dihydrate and theophylline monohydrate. Int. J. Pharm., 147, 41–49.

Leech, C.K., Fabbiani, F.P.A., Shankland, K., David, W.I.F., Ibberson, R.M., 2008. Accurate molecular structures of chlorothiazide and hydrochlorothiazide by joint refinement against powder neutron and X-ray diffraction data. Acta Crystallogr., Sect. B: Struct. Sci., 64, 101-107.

Leger, J.M., Goursolle, M., Gadret, E.M. 1978. Structure Cristalline du Sulfate de Salbutamol [tert-Butylamino-2 (Hydroxy-4 hydroxymethyl-3 phenyl)- 1 Ethanol. ½ H_2SO_4]. Acta Cryst., B34, 1203-1208.

Leong, K.H., 1981. Morphology Of Aerosol-Particles Generated From The Evaporation Of Solution Drops. J. Aer. Sci., 12(5), 417-435.

Leuenberger, H., Jetzer, W., 1982. The compactibility of powder systems - a novel approach. Int. J. Pharm., 12, 41-55.

Li, Z.J., Abramov, Y., Bordner, J., Leonard, J., Medek, A., Trask, A.V., 2006. Solid-State Acid-Base Interactions in Complexes of Heterocyclic Bases with Dicarboxylic Acids: Crystallography, Hydrogen Bond Analysis, and ^{15}N NMR Spectroscopy. J. Am. Chem. Soc., 128, 8199-8210.

Liedes, D.R., Frederikse, H.P.R., 1995. CRC Handbook of Chemistry and Physics, Eds. Leides, D.R., Frederikse, H.P.R., Boca Raton, New York, London, Tokyo, CRC Press.

Mackenzie, R.C., 1969. Nomenclature in thermal analysis. Talanta, 16, 1227–30.

MacLeod, H.M., 1983. Compaction of ceramics. In: N.G. Stanley-Wood, Editor, Enlargement and Compaction of Particulate Solids, Butterworths, London, 259–260.

Macrae, C.F., Bruno, I.J., Chisholm, J.A., Edgington, P.R., McCabe, P., Pidcock, E., Rodriguez-Monge, L., Taylor, R., van de Streek, J., Wood, P.A., 2008. J. Appl. Cryst., 41, 466-470.

Maggi, L., Conte, U., Bettinetti, G.P., 1998. Technological properties of crystalline and amorphous a-cyclodextrin hydrates. Int. J. Pharm., 172, 211–217.

Malcolmson R.J, Embleton, J.K., 1998. Dry powder formulations for pulmonary delivery. PSTT 1, 394-398.

Mälkki, L., Tammilehto, S., 1990. Decomposition of salbutamol in aqueous solutions. I. The effect of pH, temperature and drug concentration. Int. J. Pharm., 63(1), 17-22.

Mälkki-Laine, L., Bruins, A.P., 1994. Structural characterisation of the decomposition products of salbutamol by liquid chromatography-ion spray mass spectrometry. J. Pharm. Biomed. Anal. 12, 543–550.

Mälkki-Laine, L., Purra, K., Kähkönen, K., Tammilehto, S., 1995. Decomposition of salbutamol in aqueous solutions. II. The effect of buffer species, pH, buffer concentration and antioxidants. Int. J. Pharm. 117(2), 189-195.

Malvern Instruments Ltd., 1998. Scirocco 2000 user manual, United Kingdom.

Maschke, A., Bang, F., Meyer-Böhm, K., Kolter, K., 2008. Effect of Crosspovidone Particle Size

Masters, K., 2002. Spray drying in Practice, 2002, SprayDryConsult International ApS.

McCrone, W.C., 1965. Physics and Chemistry of the Organic Solid State, Edited by Fox, D., Labes, M.M., Weissberger, A., Wiley-Interscience, New York, 2, 725-767.

McGregor, C., Saunders, M.H., Buckton, G., Saklatvala, R.D., 2004. The use of high-speed differential scanning calorimetry (Hyper-DSC(TM)) to study the thermal properties of carbamazepine polymorphs. Thermochim. Acta, 417(2), 231-237.

McKinnon, J.J., Jayatilaka, D., Spackman, M.A., 2007. Towards quantitative analysis of intermolecular interactions with Hirshfeld surfaces. Chem. Commun., 3814-3816.

McKinnon, J.J., Spackman, M.A., Mitchell, A.S., 2004. Novel tools for visualizing and exploring intermolecular interactions in molecular crystals, Acta Cryst., B, 60, 627-668.

McNamara, D.P., Childs, S.L., Giordano, J., Iarriccio, A., Cassidy, J., Shet, M.S., Mannion, R., O'Donnell, E., Park, A., 2006. Use of a glutaric acid co-crystal to improve oral bioavailability of a low solubility API. Pharm. Res., 23(8), 1888-1897.

Micromedex® Healthcare Series (intranet database). Version 5.1. Greenwood Village, Thomson Reuters (Healthcare) Inc. Accessed online: 20.09.2010.

Mizuno, H., Fujiwara, T., Tomita, K.I., 1969. Crystal and molecular structure of sodium salt of xanthine. Bull. Chem. Soc. Jpn., 42, 3099-3105.

Mollica, J.A., Rehm, C.R., Smith, J.B. 1969, Hydrolysis of hydrochlorothiazide. J. Pharm. Sci., 58, 635–636.

Mollica, J.A., Rehm, C.R., Smith, J.B., Govan, H.K. 1971. Hydrolysis of benzothiadiazines.J. Pharm. Sci., 60(9), 1380–1384.

Muratov, G.N., 1980. Surface-tension of benzene and ethyl-alcohol. Zh. Fiz. Khim., 54(8), 2088-2089.

Murthy, S.N., Shobharani, H.R., 2004. Clinical pharmacokinetic and pharmacodynamic evaluation of transdermal drug delivery systems of salbutamol sulfate. Int. J. Pharm., 287, 47–53.

Najafabadi, A.R., Gilani, K., Barghi, M., Rafiee-Tehrani, M., 2004. The effect of vehicle on physical properties and aerosolisation behaviors of disodium cromoglycate microparticles spray dried alone or with L-leucine. Int. J. Pharm., 285, 97-108.

Nernst, W., 1904. Theorie der reaktionsgeschwindigkeit in heterogenen systemen. Zeitschrift für Physikalische Chemie, 47, 52-55.

Ní Ógáin, O., Li, J., Tajber, L., Corrigan, O.I., Healy, A.M., 2011. Particle engineering of materials for oral inhalation by dry powder inhalers. I - Particles of sugar excipients (trehalose and raffinose) for protein delivery. Int. J. Pharm., 405, 23–35.

Niebergall, P.J., Milosovich, G., Goyan, J.E., 1963. Dissolution rate studies. II. Dissolution of particles under conditions of rapid agitation. biphasic polymer hydrogels. J. Pharm. Sci., 52, 236–241.

Nocent, M., Bertocchi, L., Espitalier, F., Baron, M., Couarraze, G., 2001. Defnition of a Solvent System for Spherical Crystallization of Salbutamol Sulfate by Quasi-Emulsion Solvent Diffusion (QESD) Method. J. Pharm. Sci., 90(10), 1620-7.

Nolan, L.M., Li, J., Tajber, L., Corrigan, O.I., Healy, A.M., 2011. Particle engineering of materials for oral inhalation by dry powder inhalers. II - sodium cromoglycate. Int. J. Pharm., 405, 36–46.

Nolan, L.M., Tajber, L., McDonald, B.F., Barham, A.S., Corrigan, O.I. Healy A.M., 2009. Excipient-free nanoporous microparticles of budesonide for pulmonary delivery. Eur. J. Pharm. Sci., 37(5), 593-602.

Noyes, A.A., Whitney, W.R., 1897. The rate of solution of solid substances in their own solutions. J. Am. Chem. Soc., 19, 930-934.

O'Connor, K.M., Corrigan, O.I., 2001. Preparation and characterisation of a range of diclofenac. Int. J. Pharm., 226, 163–179.

Operation manual Mini Spray Dryer B-290. Büchi 93001 en

Oswald, I.D.H., Lennie, A.R., Pulham, C.R., Shankland, K., 2010. High-pressure structural studies of the pharmaceutical, chlorothiazide. Cryst. Eng. Comm., 12, 2533-2540.

Otsuka, M., (1993) Drug Dev. lnd. Pharm. 9, 541.

Pande, G.S., Shangraw, R.F., 1995. Characterization of β-cyclodextrin for direct compression tableting: II. The role of moisture in the compactibility of β-cyclodextrin Int. J. Pharm., 124(2,3), 231-239.

Patel, U.H., 1995. The crystal-structure of Na-sulfadimidine. Cryst. Res. Technol., 30, 381-387.

Petrusevski, G., Naumov, P., Jovanovski, G., Bogoeva-Gaceva, G., Weng, N.G.S., 2008. Solid-State Forms of Sodium Valproate, Active Component of the Anticonvulsant Drug Epilim. Chem. Med. Chem., 3, 1377 – 1386.

Pitt, K.G., Newton, J.M., Richardson, R., Stanley, P., 1989. The material tensile strength of convex-faced aspirin tablets. J. Pharm. Pharmacol., 41(5), 289-92.

Prista, L.N., Alves, A.C., Morgado, R.M., 1995. In: 5th Edition. Tecnica Farmaceutica e Farmacia Galenica,Vol. I. Fundacao Calouste Gulbenkian, Lisboa, 453–454.

Qiu, Y., Chen, Y., Zhang, G.G.Z., 2009. Developing solid oral dosage forms. Pharmaceutical theory and practice. Edited by Liu, L., Porter, W.R., Copyright Elsevier Inc., New York, U.S.A.

Quesenberry, M.S., Lee, Y.C., 1996. A rapid formaldehyde assay using Purpald™ reagent: application under periodation conditions. Analytical Biochem., 234(1), 50-55.

Rė, M.I., 1998. Microencapsulation by spray drying. Dry. Tech. 16(6), 1195-1236.

Regla, I., Reyes, A., Körber, C., Demare, P., Estrada, O., Juaristi, E., 1997. Novel Applications of Raney Nickel/Isopropanol: Efficient System for the Reduction of Organic Compounds. Synthetic Commun., 27(5), 817-823.

Remington: the science and practice of pharmacy, 2005. 21st Edition, Lippincott Williams & Wilkins.

Revelle, L.K., Musser, S.M., Rowe, B.J., Feldman, I.C. 1997. Identification of chlorothiazide and hydrochlorothiazide UV-A photolytic decomposition products. J. Pharm. Sci., 86(5), 631-4.

Robens, E., Unger, K.K., 2005. Thermogravimetric Apparatus, ICTAC News, 35(1), 43-51.

Rodriguez-Hornedo, N., Kelly, R.C., Sinclair, B., Miller, J., 2006. Crystallization: General Principles and Significance on Product Development. Encyclopaedia of Pharmaceutical Technology. Boylan, J.C., Swarbrick, J., Eds. Marcel Dekker Inc., New York, 2006.44.

Saleki-Gerhardt, A., Ahlneck, C., Zografi, G., 1994. Assessment of disorder in crystalline solids, Int. J. Pharm., 101(3), 237-247.

Scholz, E., 1987. Reagents for Karl Fischer Titration. Riedel-de Haën Aktiengesellschaft

Sebhatu, T., Alderborn, G., 1999. Relationships between the effective interparticulate contact area and the tensile strength of tablets of amorphous and crystalline lactose of varying particle size. Eur. J. Pharm. Sci., 8, 235-242.

Shan, N., Zaworotko, M.J., 2008. The role of cocrystals in pharmaceutical science. Drug Discov. Today, 13(9-10), 440-446.

Shankland, K., David, W.I.F., Sivia, D.S., 1997. Routine ab initio structure determination of chlorothiazide by X-ray powder diffraction using optimised data collection and analysis strategies. J. Mater. Chem., 7, 569-572.

Sheldrick, G.M., 2008. A short history of SHELX. Acta Cryst., A 64, 112-122.

Sherif, I., Badawy, F., Hussain, M.A., 2004. Effect of starting material particle size on its agglomeration behaviour in high shear wet granulation, AAPS PharmSciTech., 5(3), 1-7.

Sheth, A.R., Bates, S., Muller, F.X., Grant, D.J.W., 2005. Local structure in amorphous phases of piroxicam from powder X-ray diffractometry, Cryst. Growth Des., 5(2), 571-578.

Sinka, J.C., Cunningham, J.C., Zavaliangos, A., 2004. Analysis of Tablet Compaction. II. Finite Element Analysis of Density Distributions in Convex Tablets. J. Pharm. Sci., 93(8), 2040–2053.

Sonnergaard, J.M., 2006. Quantification of the compactibility of pharmaceutical powders. Eur. J. Pharm. Biopham. 63, 270–79.

Spek, A.L., 2003. Single-crystal structure validation with the program PLATON. J. Appl. Crystallogr. 36, 7-13.

Sreenivas, R.L., Bethune, S.J., Kampf, J.W., Rodriguez Hornedo, N., 2009. Cocrystals and Salts of Gabapentin: pH Dependent Cocrystal Stability and Solubility. Cryst. Growth Des., 9(1), 378-385.

Stahl, P.H., Wermuth, C.G., 2008. Handbook of Pharmaceutical Salts Properties, Selection and use, ISBN 3-906390-26-8.

Stahly, G.P., 2007. Diversity in single- and multiple-component crystals. The search for and prevalence of polymorphs and cocrystals. Cryst. Growth Des., 7, 1007-1026.

Steinhaus, H.. 1999. Mathematical Snapshots, 3rd ed. New York: Dover, pp. 202-203.

Stephenson, G.A., Diseroad, B.A., 2000. Structural relationship and desolvation behaviour of cromolyn, cefazolin and fenoprofen sodium hydrates. Int. J. Pharm., 198, 167-177.

Sun, C.C., 2004. A novel method for deriving true density of pharmaceutical solids including hydrates and water-containing powders. J. Pharm. Sci., 93, 646–653.

Sun, C.C., Grant, D.J.W., 2001. Influence of crystal shape on the tableting performance of L-lysine monohydrochloride dihydrate. J. Pharm. Sci., 90(5), 569–579.

Swarbrick, J., 2007, Encyclopaedia of pharmaceutical technology, Informa Healthcare USA, Inc.

Tajber, L., Corrigan, D.O., Corrigan, O.I., Healy, A.M., 2009. Spray drying of budesonide, formoterol fumarate and their composites. I. Physicochemical characterisation. Int. J. Pharm., 367, 79-85.

Tajber, L., Corrigan, O.I., Healy, A.M., 2005. Physicochemical evaluation of PVP-thiazide diuretic interactions in co-spray-dried composites - analysis of glass transition composition relationships. Eur. J. Pharm. Sci., 24, 553-563.

Takeuchi, H., 2005. Tableting of solid dispersion particles consisting of indomethacin and porous silica particles. Chem. Pharm. B. 53(5), 487-491.

Taub, M.E., Kristensen, L., Frokjaer, S., 2002. Optimized conditions for MDCK permeability and turbidimetric solubility studies using compounds representative of BCS classes I-IV. Eur. J. Pharm. Sci. 15, 331-340.

Tauvel, G., Sanselme, M., Coste-Leconte, S., Petit, S., Coquerel, G., 2009, Structural studies of several solvated potassium salts of tenatoprazole crystallizing as conglomerates, J. Mol. Struct. 936, 60-66.

Teunou, E., Fitzpatrick, J.J., Synnott, E.C., 1999. Characterisation of food powder flowability. J. Food Eng., 39, 31-37.

Tian, F., Qu, H., Louhi-Kultanen, M., Rantanen, J., 2010. Insight into Crystallization Mechanisms of Polymorphic Hydrate Systems, Chem. Eng. Technol., 33(5), 833–838.

Tong, P., Taylor, L.S., Zografi, G., 2002. Influence of Alkali Metal Counterions on the Glass Transition Temperature of Amorphous Indomethacin Salts. Pharm. Res., 19(5), 649-654.

Torrado, G., Fraile, S., Torrado, S., Torrado, S., 1998. Process-induced crystallite size and dissolution changes elucidated by a variety of analytical methods., Int. J. Pharm. 166, 55.

Trasi, N.S., Boerrigter, S.X.M., Byrn, S.R., Carvajal, T.M., 2011. Investigating the effect of dehydration conditions on the compactability of glucose. Int. J. Pharm., 406, 55–61.

Tzou, T-Z., Pachuta, R.R., Coy, R.B., Schultz, R.K., 1997. Drug from selection in albuterol containing metered dose inhaler formulations and its impact on chemical and physical stability. J. Pharm. Sci., 86(12), 1352–1357.

Ulvi, V., Keski-Hynnilä, H., 1994. First-derivative UV spectrophotometric and high-performance liquid chromatographic analysis of some thiazide diuretics in the presence of their photodecomposition products. J. Pharm. Biomed. Anal., 12(7), 917-22.

United States of America Food and Drug Administration (FDA), Database of Select Committee on GRAS Substances (SCOGS) Reviews, Succinic acid,
http://www.accessdata.fda.gov/scripts/fcn/fcnDetailNavigation.cfm?rpt=scogsListing&id=339, Accessed online: 29.10.2010.

United States of America Food and Drug Administration (FDA), Database of Select Committee on GRAS Substances (SCOGS) Reviews, Adipic acid,
http://www.accessdata.fda.gov/scriptshttp://www.accessdata.fda.gov/scripts/fcn/fcnDetailNavigation.cfm?rpt=scogsListing&id=9/fcn/fcnDetailNavigation.cfm?rpt=scogsListing&id=9, Accessed online: 29.10.2010.

United States Pharmacopeia USP 33–NF 28 2010 The United States Pharmacopoeial Convention

Variankaval, N., Wenslow, R., Murry, J., Hartman, R., Helmy, R., Kwong, E., Clas, S.D., Dalton, C., Santos, I., 2006. Preparation and solid-state characterization of nonstoichiometric co-crystals of a phosphodiesterase- IV inhibitor and l-tartaric acid. Cryst. Growth Des., 6, 690–700.

Veber, D.F., Johnson, S.R., Cheng, H.Y., Smith, B.R., Ward, K.W., Kopple, K.D., 2002. Molecular properties that influence the oral bioavailability of drug candidates. J. Med. Chem., 45, 2615-2623.

Vehring, R., 2008. Pharmaceutical Particle Engineering via Spray Drying. Pharm. Res., 25(5), 999-1022.

Vehring, R., Foss, W.R., Lechuga-Ballesteros, D., 2007. Particle formation in spray drying Aerosol Science. 38, 728 – 746.

Vyse, T., Cochrane, G.M., 1989. Controlled release salbutamol tablets versus sustained release theophylline tablets in the control of reversible obstructive airways disease. J. Int. Med. Res., 17(1), 93-8.

Wang, F.J., Wang, C.W., 2002. Sustained release of etanidazole from spray dried microspheres prepared by non-halogenated solvents, J. Cont. Rel., 81, 263–280.

Wang, L., Han, G., Zhang, Y., 2007. Comparative study of composition, structure and properties of Apocynum venetum fibers under different pretreatments. Carb. Pol., 69, 391-397.

Westermarck, S., Juppo, A.M., Kervinen, L., Yliruusi, Y., 1998. Pore structure and surface area of mannitol powder, granules and tablets determined with mercury porosimetry and nitrogen adsorption. Eur. J. Pharm. Biopharm., 46(1), 61-68.

Whitesides, G.M., Mathias, J.P., Seto, C.T., 1991. Molecular self-assembly and nanochemistry - a chemical strategy for the synthesis of nanostructures. Science, 254, 1312-1319.

World Intellectual Property Organisation.
http://www.wipo.int/pctdb/en/wo.jsp?WO=2006073886&IA=US2005046752&DISPLAY=DOCS. Accessed online: 31.01.2011.

Wu, C.Y., Benet, L.Z., 2005, Predicting drug disposition via application of BCS: transport/absorption/ elimination interplay and development of a biopharmaceutics drug disposition classification system. Pharm. Res., 22, 11-23.

Yazan, Y., Demirel, M., Güler, E., 1995. Preparation and in vitro dissolution of salbutamol sulfate microcapsules and tabletted microcapsules. J. Microencapsul., 12, 601-607.

York, P., 1983. Solid-state properties of powders in the formulation and processing of solid dosage forms, Int. J. Pharm., 14(1), 1-28.

Young, P.M., Chiou, H., Tee, T., Traini, D., Chan, H.K., Thielmann, F., Burnett, D., 2007. The Use of Organic Vapor Sorption to Determine Low Levels of Amorphous Content in Processed Pharmaceutical Powders. Drug Dev. Ind. Pharm., 33(1), 91 – 97.

Zegarac, M., 2007. Pharmaceutically acceptable co crystalline forms of sildenafil. WO080362 A1.

Zhang, M., Efremov, M.Y., Olson, E.A., Zhang, Z.S., Allen, L.H., 2002. Real-time heat capacity measurement during thin-film deposition by scanning nanocalorimetry. Appl. Phys. Lett., 81, 3801.

Zhu, H.J., Padden, B.E., Munson, E.J., Grant, D.J.W., 1997. Physicochemical characterization of nedocromil bivalent metal salt hydrates.2. Nedocromil zinc. J. Pharm. Sci., 86, 418-429.

Ziegler, T.K., 1998. Simultaneous quantification of released succinic acid and a weakly basic drug compound in dissolution media. Eur. J. PharmBiopharm. 46, 183–190.

Zografi, G., Kontny, M.J., 1995. Sorption of water by solids. Physical characterization of pharmaceutical solids, edited by Brittain, H.G., Marcel Dekker, New York, NY, 385-418.

Appendix I

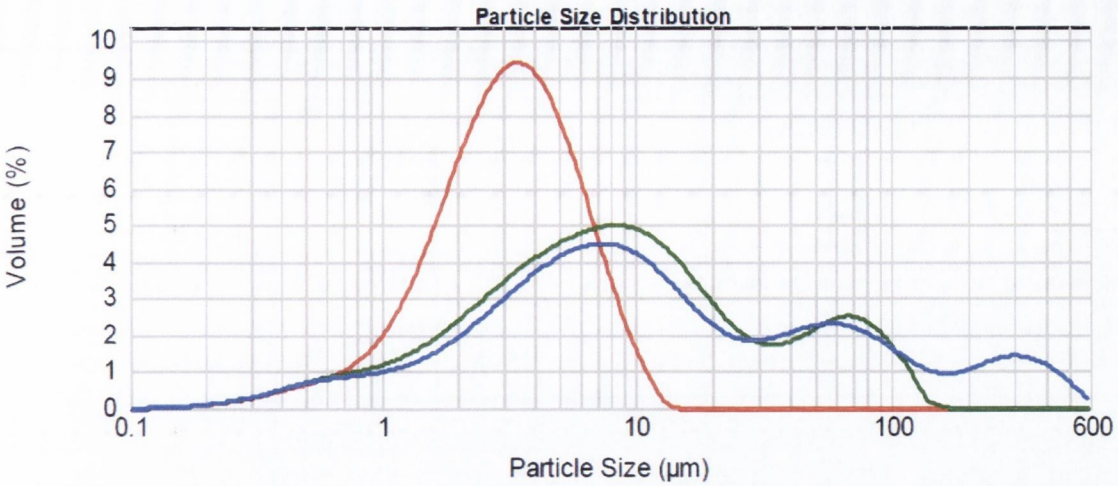

Fig. I.1. An example of modality of particle size distribution. Red- monomodal. Green- bimodal. Blue- trimodal.

Table I.1. Geometrical parameters of prepared tablets.

System	F [kN]	$2r_1$ [mm]	H [mm]	m [g]	h_2 [mm]	A [mm^2]	V_t [mm^3]	d_t [g/cm^3]	T_t [$m^2/g \cdot 10^{-5}$]
Dipac™	3	8.987±0.002	4.172±0.002	0.251±0.000	2.500±0.035	162.250	212.187	1.184	64.6
	6	9.010±0.002	3.932±0.002	0.252±0.000	2.210±0.011	160.571	196.435	1.282	63.8
	10	9.015±0.001	3.781±0.004	0.251±0.001	2.183±0.013	145.870	190.842	1.314	58.2
	13	9.018±0.000	3.707±0.001	0.251±0.000	1.965±0.021	156.199	181.833	1.381	62.2
CTZ	6	9.020±0.009	3.507±0.001	0.251±0.000	1.966±0.043	133.824	175.308	1.429	53.4
	10	9.016±0.004	3.387±0.001	0.251±0.001	1.790±0.011	134.655	165.761	1.515	53.6
	13	9.019±0.004	3.297±0.004	0.251±0.000	1.737±0.008	129.306	161.265	1.555	51.6
CTZ NPMPs	3	9.035±0.001	4.299±0.020	0.251±0.001	2.383±0.025	190.614	215.123	1.167	75.9
	6	9.026±0.000	3.809±0.001	0.251±0.000	2.239±0.025	144.681	193.982	1.296	57.6
	10	9.019±0.001	3.596±0.001	0.251±0.000	1.990±0.107	141.386	178.977	1.405	56.2

Table I.2. Geometrical parameters of prepared tablets.

System	F [kN]	$2r_1$ [mm]	H [mm]	m [g]	h_2 [mm]	A [mm^2]	V_t [mm^3]	d_t [g/cm^3]	T_t [$m^2/g \cdot 10^{-5}$]
CTZNa DH	3	8.989±0.009	3.729±0.002	0.252±0.001	2.053±0.035	150.179	184.033	1.371	59.5
	6	9.008±0.003	3.513±0.014	0.251±0.000	1.999±0.015	131.661	176.064	1.424	52.5
	10	9.015±0.001	3.390±0.010	0.251±0.001	1.600±0.073	151.590	159.974	1.569	60.4
CTZNa ANH	3	8.984±0.011	3.704±0.010	0.251±0.000	2.008±0.054	151.080	181.664	1.381	60.2
	6	9.019±0.001	3.517±0.004	0.251±0.000	1.814±0.068	147.285	170.919	1.470	58.6
	10	9.028±0.003	3.412±0.007	0.251±0.000	1.624±0.042	152.337	161.919	1.549	60.7
CTZNa MPs	3	8.989±0.006	3.923±0.001	0.251±0.000	2.548±0.631	133.350	205.672	1.222	53.1
	6	9.050±0.002	3.833±0.007	0.251±0.001	2.013±0.042	168.000	188.777	1.331	66.9
	10	9.064±0.002	3.651±0.030	0.250±0.000	1.944±0.081	152.686	181.141	1.382	61
CTZNa NPMPs	1	8.993±0.004	6.885±0.016	0.251±0.001	5.089±0.051	250.244	381.027	0.659	99.7
	3	8.834±0.209	4.966±0.024	0.251±0.000	3.275±0.036	181.776	253.173	0.990	72.5
	6	8.980±0.001	3.879±0.040	0.252±0.000	2.406±0.056	138.471	199.433	1.263	55

Table I.3. Geometrical parameters of prepared tablets.

System	F [kN]	$2r_1$ [mm]	H [mm]	m [g]	h_2 [mm]	A [mm^2]	V_t [mm^3]	d_t [g/cm^3]	T_t [$m^2/g \cdot 10^{-5}$]
CTZK DH	3	8.984±0.000	3.607±0.030	0.251±0.000	1.989±0.061	141.752	177.907	1.411	56.5
	6	9.009±0.000	3.412±0.004	0.251±0.000	1.703±0.033	144.683	163.665	1.534	57.6
	10	9.013±0.001	3.312±0.014	0.252±0.000	1.640±0.015	138.673	158.552	1.587	55.1
CTZK MH	6	9.023±0.008	3.535±0.007	0.251±0.000	1.807±0.008	150.222	171.433	1.466	59.8
	10	9.042±0.000	3.507±0.000	0.251±0.000	1.812±0.037	146.898	171.394	1.465	58.5
	13	9.046±0.001	3.499±0.002	0.251±0.001	1.810±0.010	146.247	171.217	1.467	58.2
CTZK ANH	3	8.999±0.003	3.771±0.034	0.251±0.000	2.224±0.078	141.180	191.119	1.312	56.3
	6	9.023±0.000	3.601±0.019	0.251±0.000	1.893±0.056	150.257	176.272	1.424	59.9
	10	9.039±0.005	3.480±0.023	0.251±0.000	1.840±0.037	141.374	171.251	1.463	56.4
CTZK MPs	6	9.056±0.005	3.840±0.017	0.252±0.000	2.291±0.089	144.703	197.918	1.272	57.5
	10	9.050±0.001	3.580±0.007	0.251±0.000	1.852±0.035	152.181	175.353	1.430	60.7
	13	9.037±0.007	3.489±0.019	0.251±0.000	1.840±0.026	142.335	171.460	1.465	56.7
CTZK NPMPs	1	8.982±0.001	6.543±0.035	0.251±0.000	4.872±0.046	229.044	362.241	0.693	91.2
	3	8.983±0.004	4.785±0.008	0.251±0.000	3.142±0.039	177.045	251.717	0.997	70.6
	6	8.984±0.002	4.058±0.005	0.251±0.000	2.389±0.042	158.737	204.896	1.226	63.2

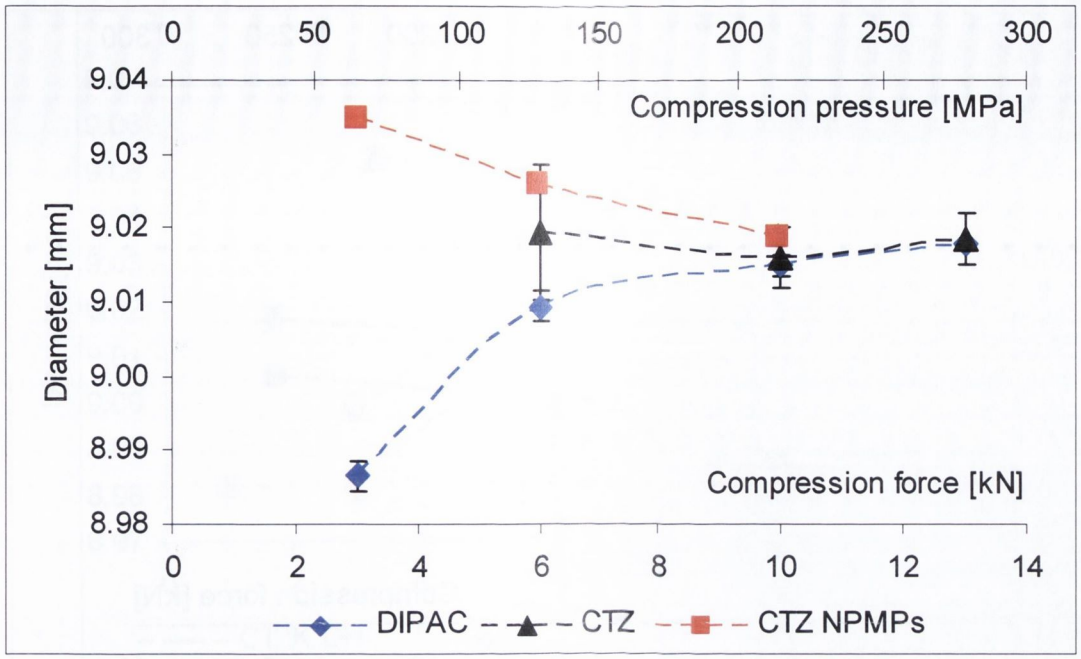

Fig. I.2. Relationship between the diameter of the tablet and compression force for: Dipac™, CTZ and CTZ NPMPs. Abbreviations as per Table 7.1.

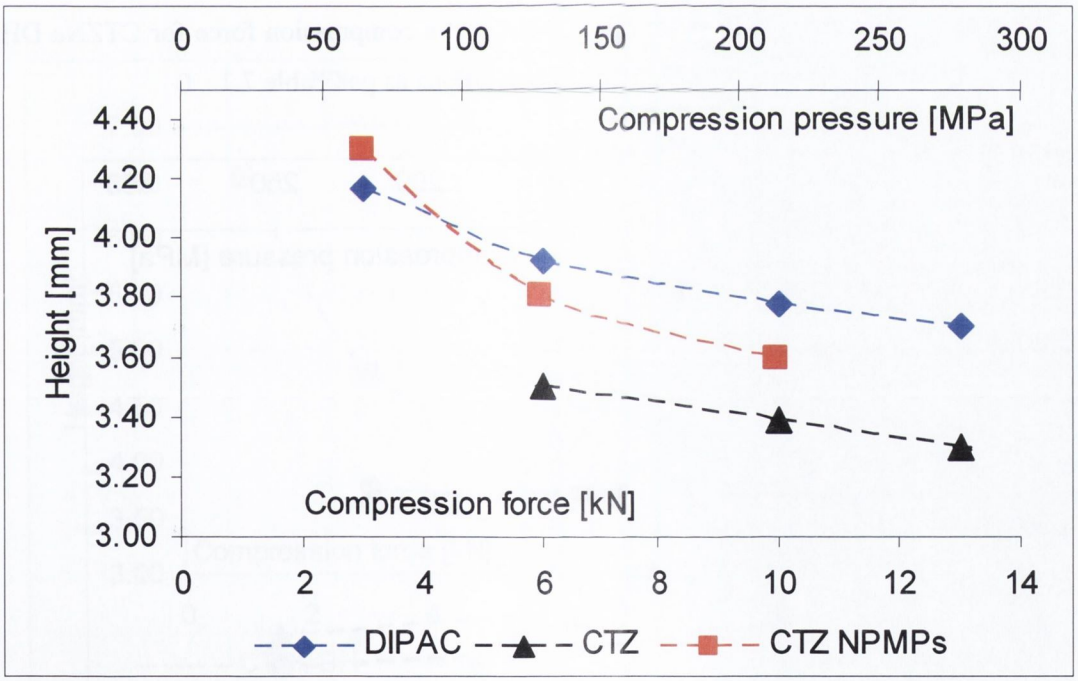

Fig. I.3. Relationship between the height of the tablet and compression force for: Dipac™, CTZ and CTZ NPMPs. Abbreviations as per Table 7.1.

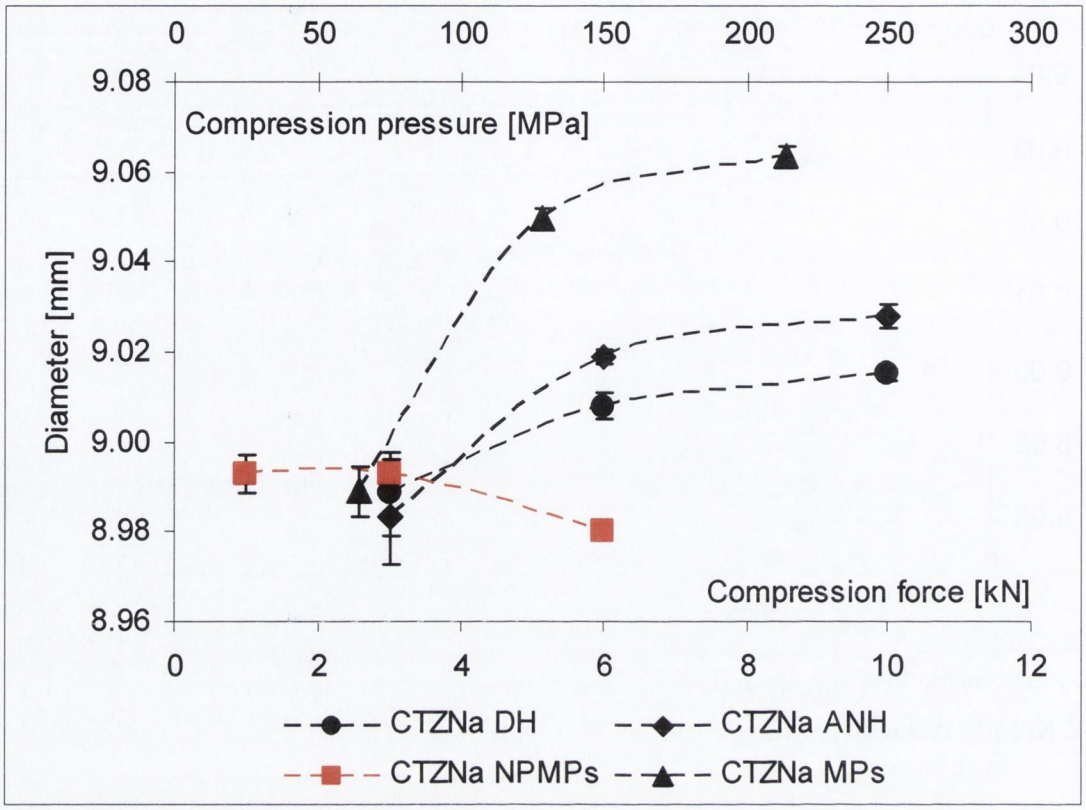

Fig. I.4. Relationship between the diameter of the tablet and a compression force for CTZNa DH, CTZNa ANH, CTZNa NPMPs and CTZNa MPs. Abbreviations as per Table 7.1.

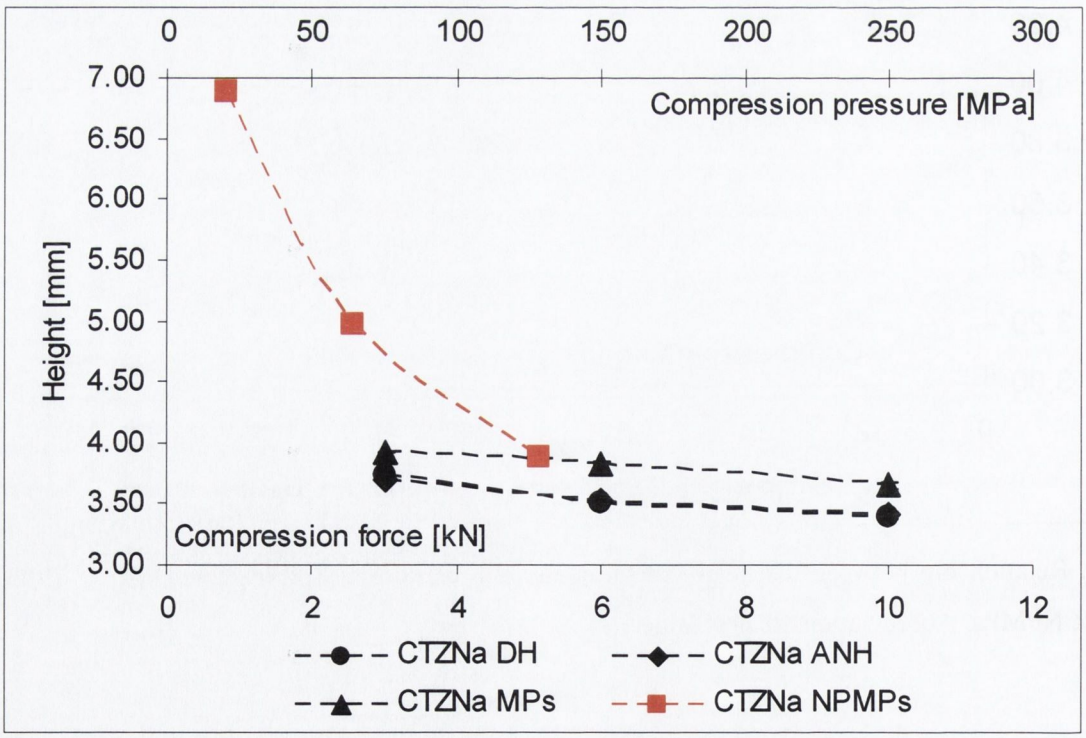

Fig. I.5. Relationship between the height of the tablet and a compression force for CTZNa DH, CTZNa ANH, CTZNa NPMPs and CTZNa MPs. Abbreviations as per Table 7.1.

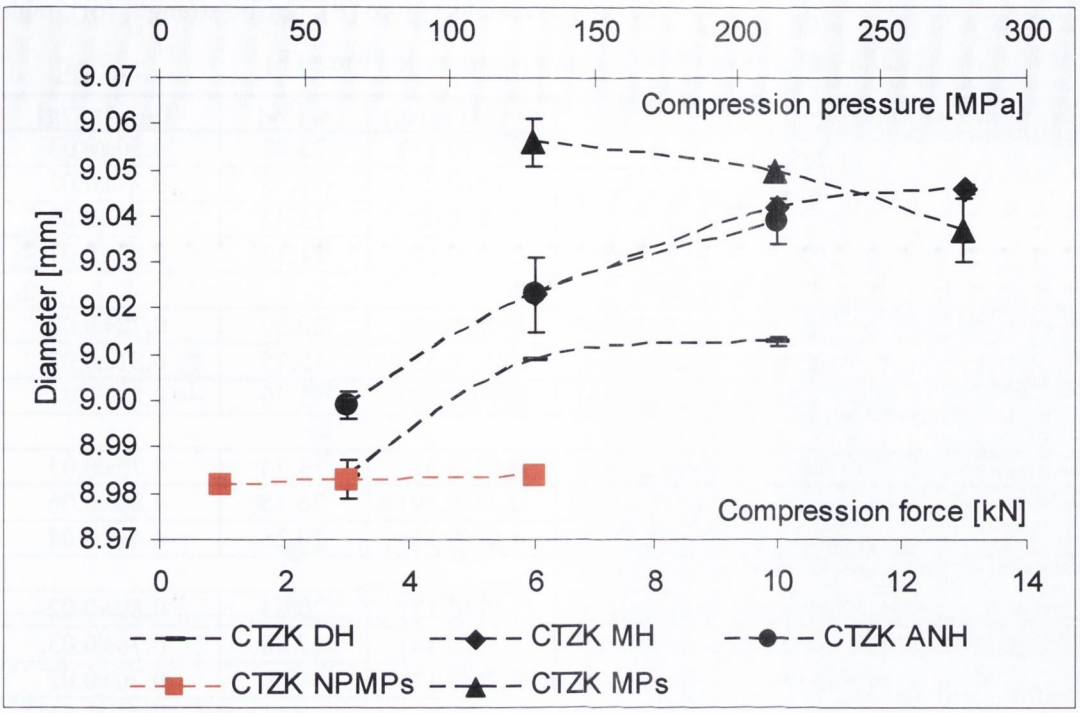

Fig. I.6. Relationship between the diameter of the tablet and a compression force for CTZK DH, CTZK MH, CTZK ANH, CTZK NPMPs and CTZK MPs. Abbreviations as per table 7.1.

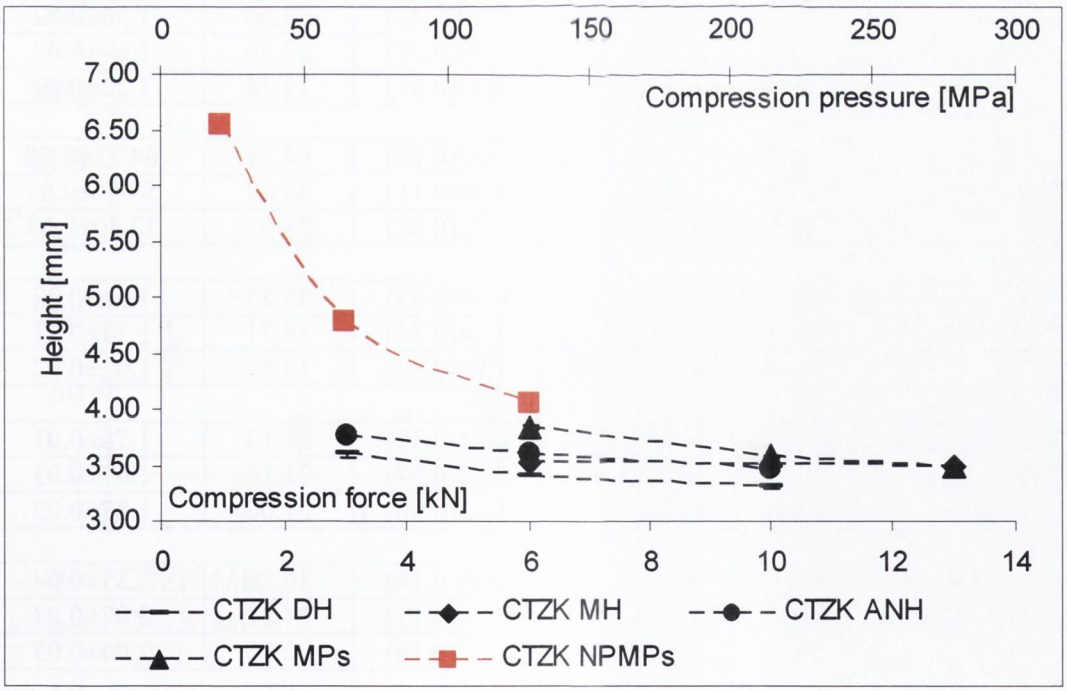

Fig. I.7. Relationship between the height of the tablet and compression force for CTZK DH, CTZK MH, CTZK ANH, CTZK NPMPs and CTZK MPs. Abbreviations as per table 7.1.

Table I.4. Compilation of tablet parameters: force to tensile failure (P), tensile strength (σt), tablet porosity (Tp), and specific surface area (T_{BET}) against compression force (F).

Formulation	F [kN]	P [N](σ_r)	σt [MPa](σ_r)	ε_t [%]	T_{BET} [m^2/g]
Dipac™	3.00	23.70(6.62)	0.47(0.13)	23.80	0.50±0.03
	6.00	49.50(10.27)	1.08(0.22)	17.53	0.77±0.02
	10.00	80.00(3.95)	1.80(0.09)	15.42	0.87±0.03
	13.00	105.80(4.34)	2.55(0.10)	11.14	0.83±0.01
CTZ RAW	6.00	24.10(19.80)	0.60(0.49)	20.50	0.78±0.02
	10.00	34.20(12.99)	0.92(0.35)	15.75	0.81±0.02
	13.00	32.56(19.43)	0.90(0.54)	13.50	0.88±0.01
CTZ NPMPs	3.00	26.50(23.85)	0.53(0.31)	33.74	4.75±0.05
	6.00	108.30(30.71)	2.38(0.39)	26.45	4.80±0.06
	10.00	190.40(37.58)	4.63(0.31)	20.26	4.44±0.04
CTZNa DH	3.00	46.10(5.16)	1.08(0.12)	20.63	0.89±0.02
	6.00	94.00(5.58)	2.31(0.14)	17.58	0.76±0.03
	10.00	148.80(6.48)	4.26(0.19)	9.22	0.70±0.02
CTZNa ANH	3.00	22.00(5.67)	0.53(0.14)	26.67	2.61±0.04
	6.00	45.10(7.50)	1.17(0.19)	21.93	3.40±0.04
	10.00	63.90(5.03)	1.80(0.14)	17.74	3.16±0.04
CTZNa MPs	3.00	29.40(23.85)	0.59(0.49)	33.50	1.56±0.02
	6.00	68.40(30.71)	1.59(0.71)	27.56	1.69±0.02
	10.00	91.60(37.58)	2.23(0.91)	24.78	1.32±0.03
CTZNa NPMPs	1.00	60.20(18.99)	0.62(0.20)	64.51	64.73±0.06
	3.00	139.00(6.98)	2.19(0.11)	46.67	56.44±0.07
	6.00	213.20(29.59)	4.48(0.62)	31.97	32.80±0.03
CTZK DH	3.00	25.60(13.68)	0.62(0.33)	25.25	1.31±0.02
	6.00	48.80(12.48)	1.34(0.34)	18.71	1.13±0.02
	10.00	64.40(11.20)	1.84(0.32)	15.89	1.02±0.02
CTZK MH	6.00	31.40(12.40)	0.81(0.32)	21.13	1.78±0.01
	10.00	35.60(22.09)	0.92(0.57)	21.18	1.67±0.03
	13.00	43.40(34.57)	1.13(0.90)	21.06	1.87±0.02
CTZK ANH	3.00	28.80(6.51)	0.64(0.14)	30.26	1.85±0.04
	6.00	51.80(5.05)	1.29(0.13)	24.31	2.07±0.03
	10.00	72.20(6.36)	1.87(0.16)	22.20	2.06±0.03
CTZK MPs	6.00	43.30(32.61)	0.93(0.70)	32.07	1.23±0.02
	10.00	139.10(10.68)	3.52(0.27)	23.63	1.09±0.01
	13.00	199.40(10.67)	5.15(0.27)	21.74	1.14±0.02
CTZK NPMPs	1.00	79.30(21.91)	0.86(0.24)	62.79	82.47±0.86
	3.00	159.30(31.49)	2.58(0.51)	46.50	63.28±0.61
	6.00	248.40(39.59)	5.11(0.81)	34.17	43.39±0.41

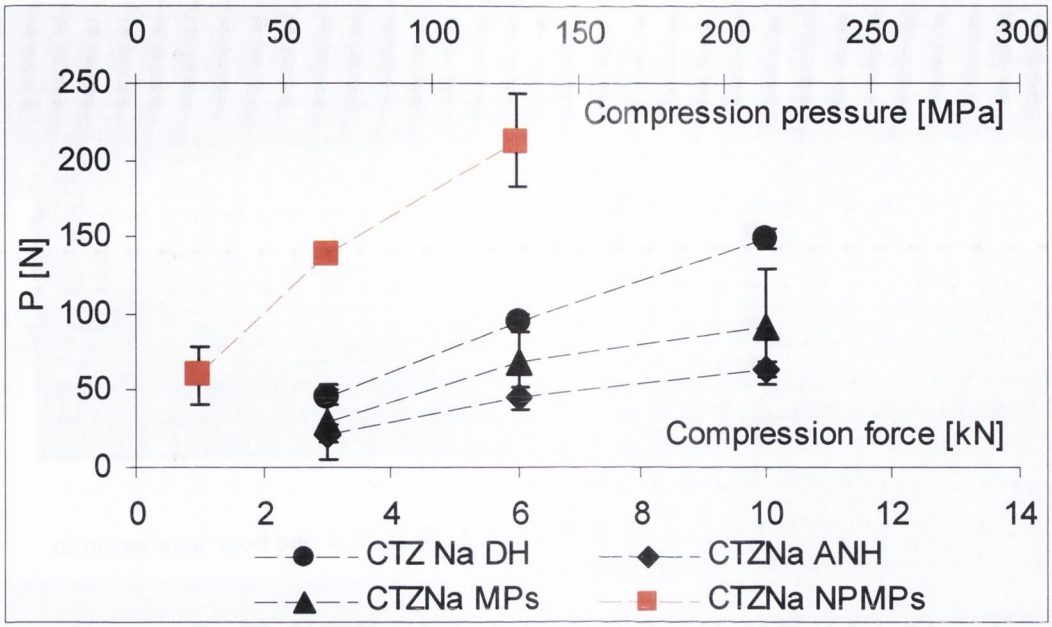

Fig. I.8. Force to tensile failure of the tablet (P) for: CTZNa DH, CTZNa ANH, CTZNa MPs and CTZNA NPMPs. Error bars express relative standard deviation (σ_r) for comparison purposes.

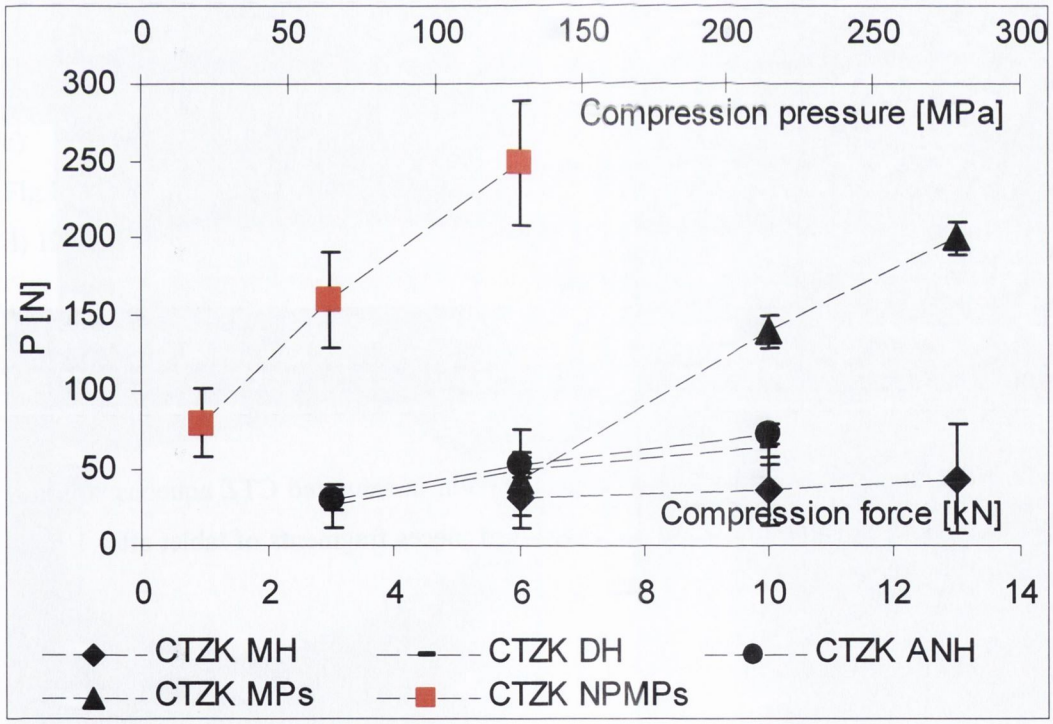

Figure I.9. Force to tensile failure of the tablet (P) for CTZK dihydrate, monohydrate and anhydrous microparticles, CTZK spray dried microparticles and CTZK nanoporous microparticles. Error bars express relative standard deviation (σ_r) for comparison purposes.

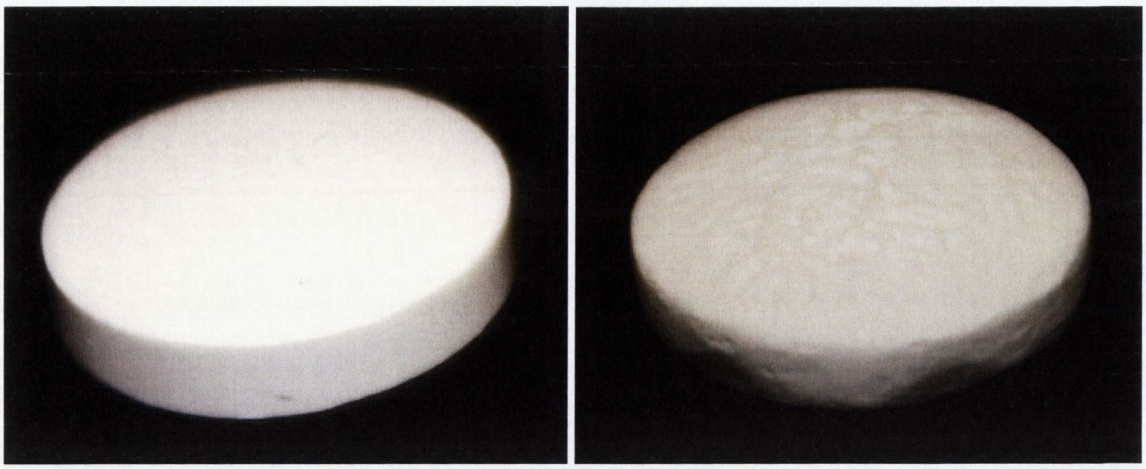

a) b)

Fig. I.10. CTZ NPMPs tablet. a) after compaction, b) eroded tablet after one hour incubation in saturated CTZ aqueous solution.

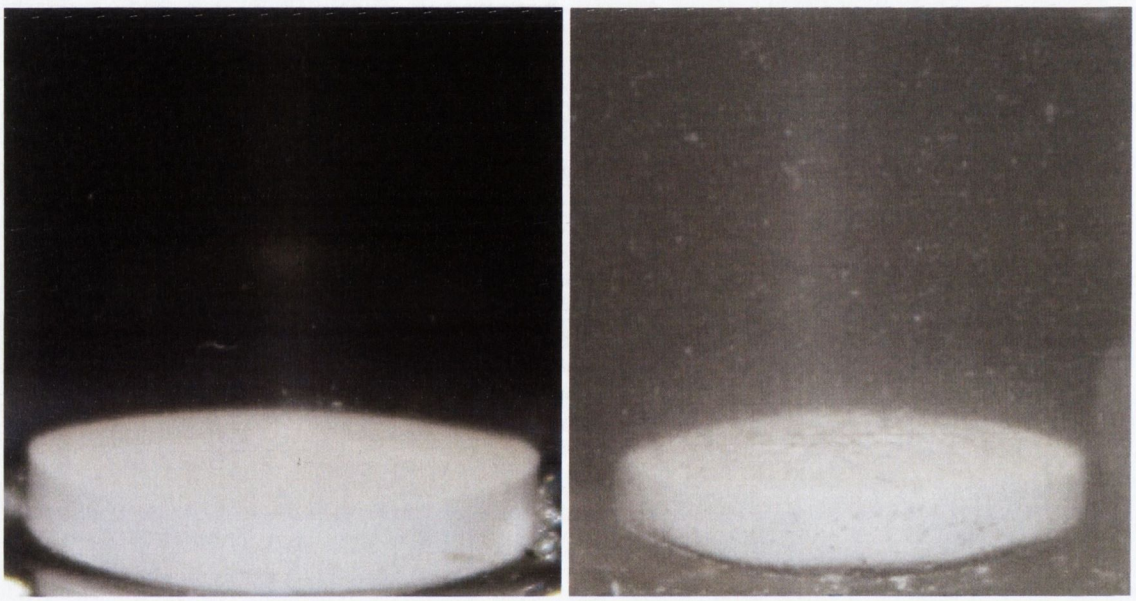

a) b)

Fig. I.11. CTZ NPMPs tablet. a) immediately after immersion in saturated CTZ aqueous solution and b) visible erosion of tablet and flotation of undissolved pieces fragments of tablet after 1 hour incubation.

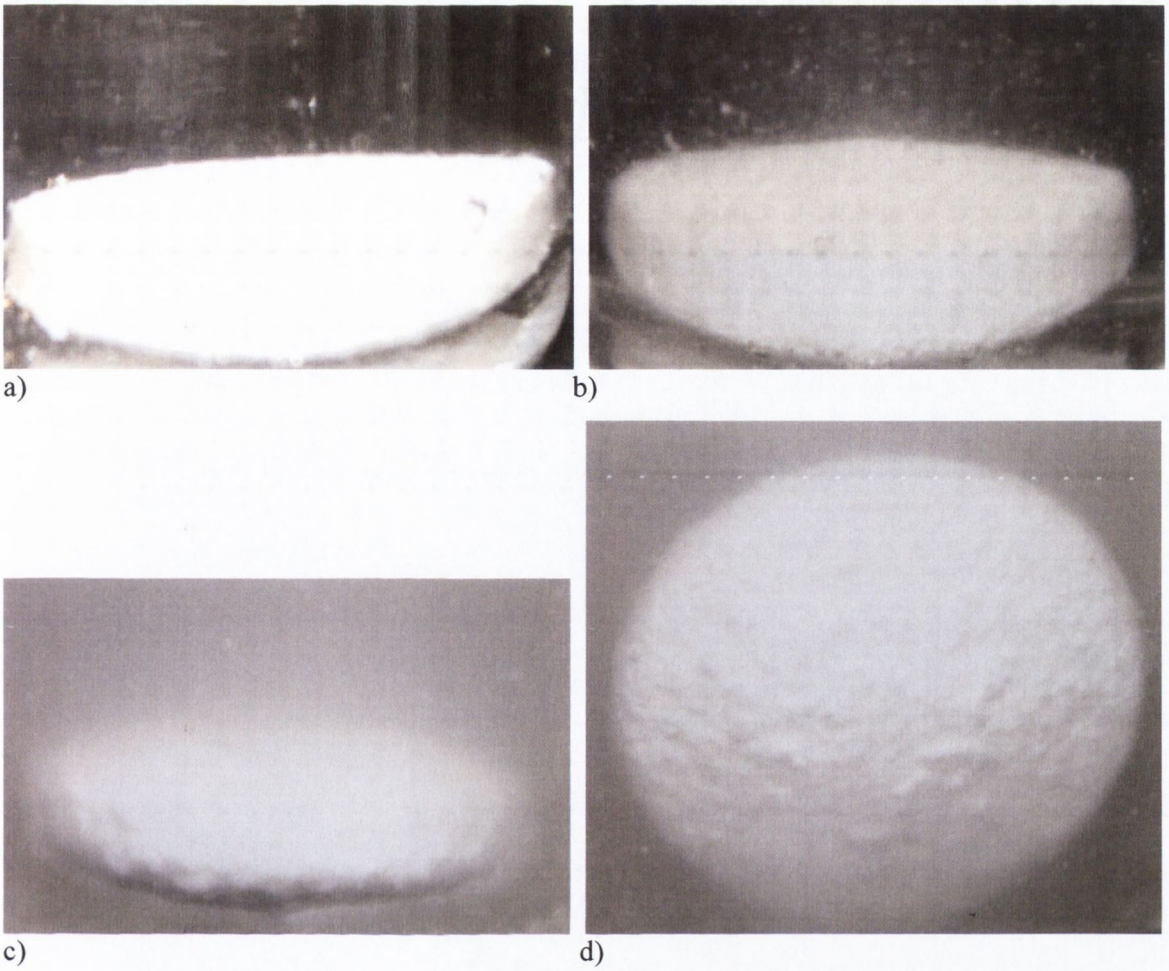

a) b)

c) d)

Fig.I.12. CTZNa ANH tablet immersed in saturated CTZNa solution. a) after 30 s, b) 60 s, c) 90 s, d) 120 s.

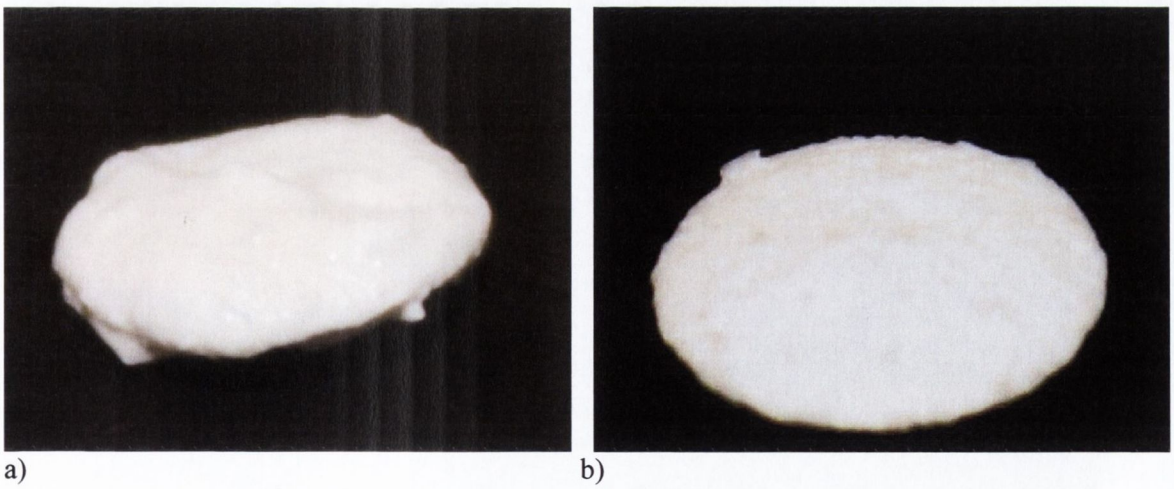

a) b)

Fig. I.13. CTZNa ANH tablet after immersion in saturated CTZNa solution for 2.5 minutes. a) visible film of loose undissolved material covering b) undissolved solid core of the tablet.

Appendix II

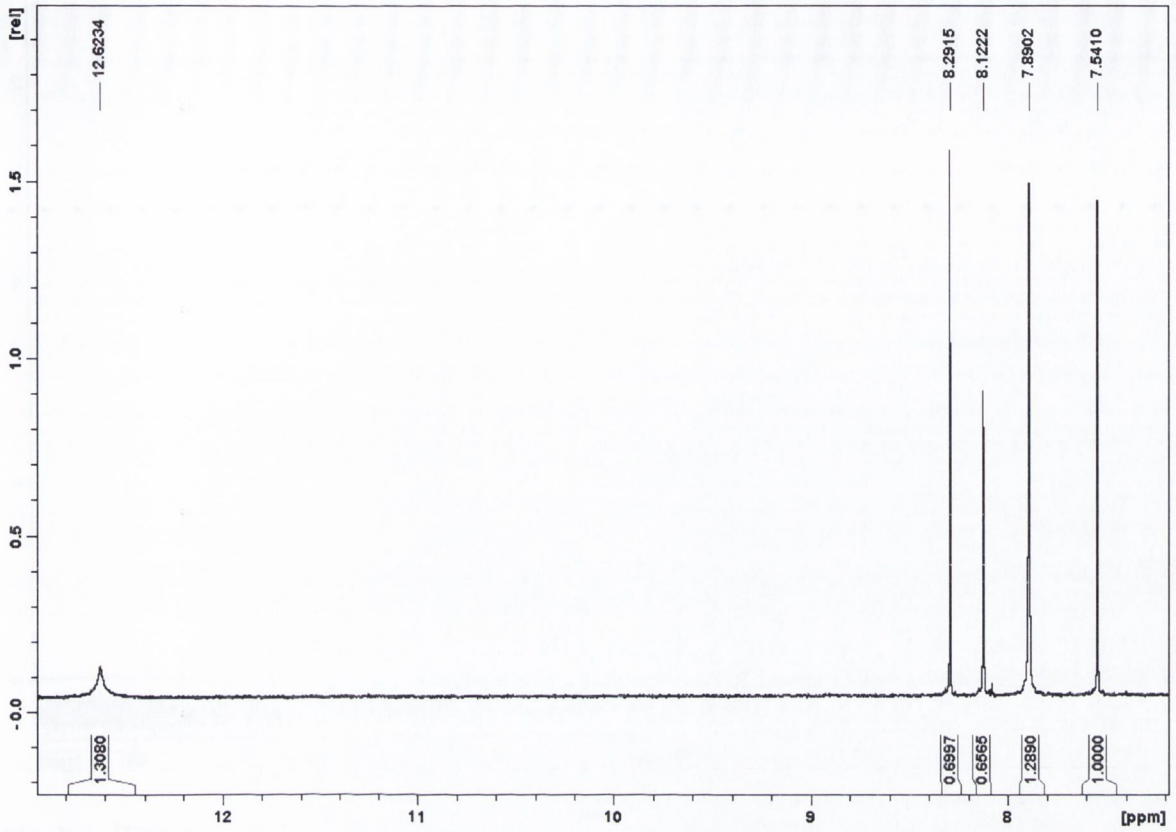

Fig. II.1 ^{1}HNMR results of chlorothiazide.

Table II.1. ^{1}HNMR results of chlorothiazide.

Peak	ν(F1) [ppm] (Jakobsen and Treppendahl, 1979)	ν(F1) [ppm]	Intensity [abs]	Split	Integral [rel]
C(4)H(4)	7.51	7.54	386678.57	s	1.0000
N(1)H_2(5,6)	-	7.89	498425.04	s	1.2890
C(7)H(7)	8.10	8.12	253838.92	s	0.6565
C(1)H(1)	8.26	8.29	270559.58	s	0.6997
N(2)H(2)	11-13	12.62	505784.93	s	1.3080

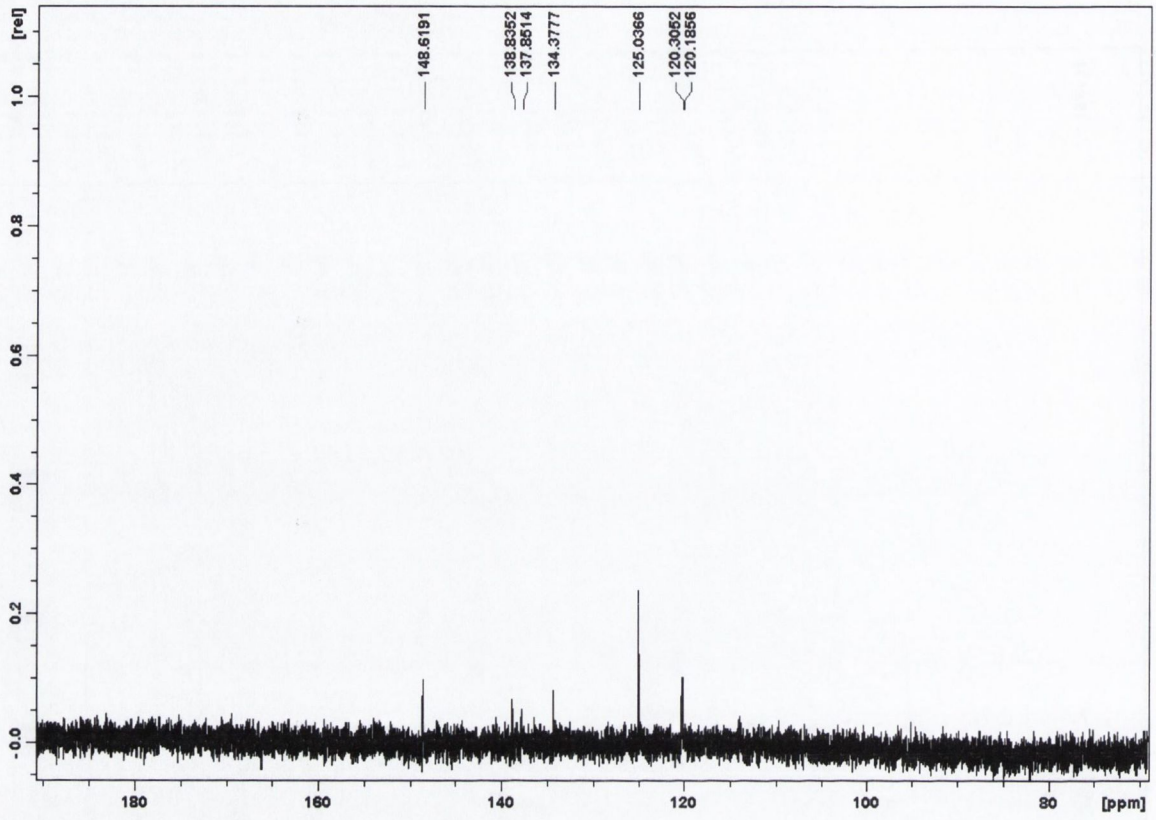

Fig. II.2. ^{13}CNMR of chlorothiazide.

Table II.2. Summary ^{13}CNMR data for chlorothiazide.

Peak	ν(F1) [ppm] (Jakobsen and Treppendahl, 1979)	ν(F1) [ppm]
C(7)H(7)	149.7	148.6
C(5)	135.6	134.4
C(2)	139.9	138.8
C(1)H(1)	126.2	125.0
C(4)H(4)	121.5	120.3
C(6)	121.4	120.2
C(3)	139.0	137.9

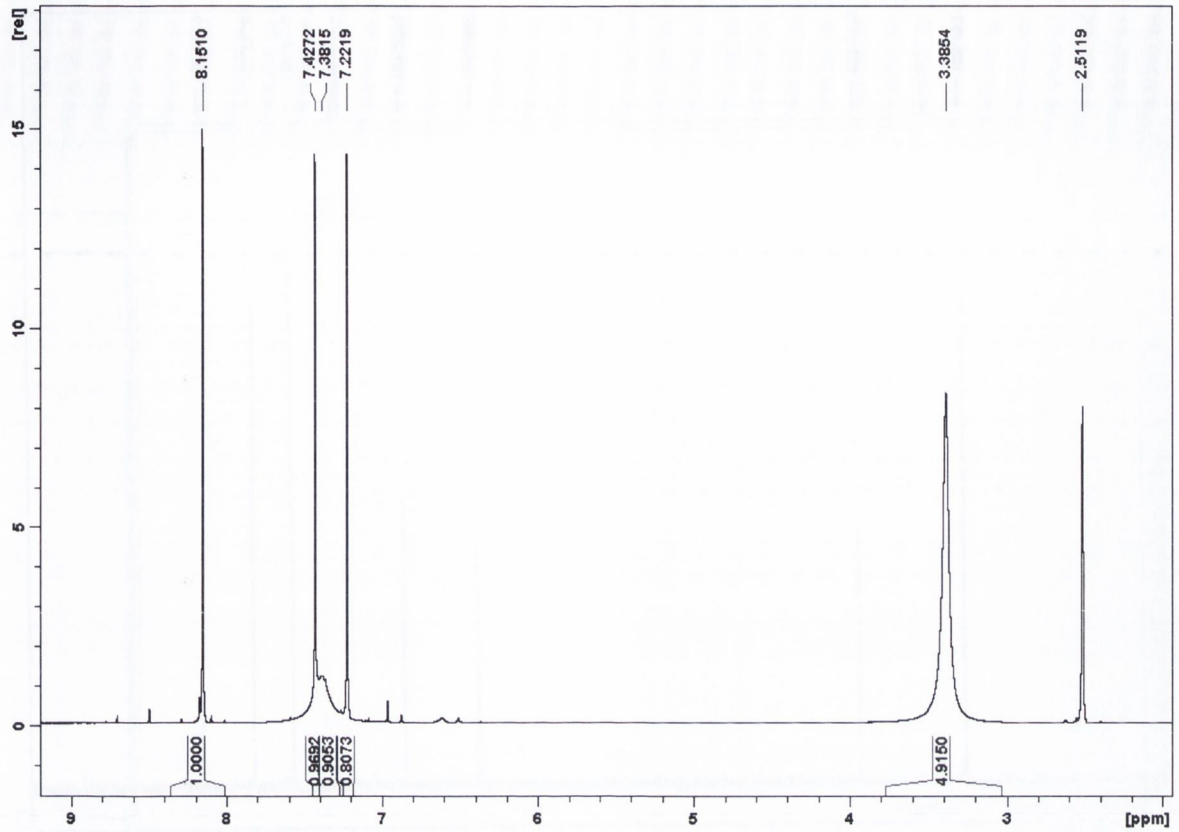

Fig. II.3. ^{1}HNMR analysis results of chlorothiazide sodium dihydrate.

Table II.3. Summary ^{1}HNMR data for chlorothiazide sodium dihydrate.

Peak	ν(F1) [ppm]	Intensity [abs]	Split	Integral [rel]
C(7)H(7)	7.22	10261581.08	s	0.8073
C(1)H(1)	7.38	11507461.95	br s	0.9053
N(1)H(5)	7.43	12318922.91	s	0.9692
C(4)H(4)	8.15	12710782.11	s	1.0000

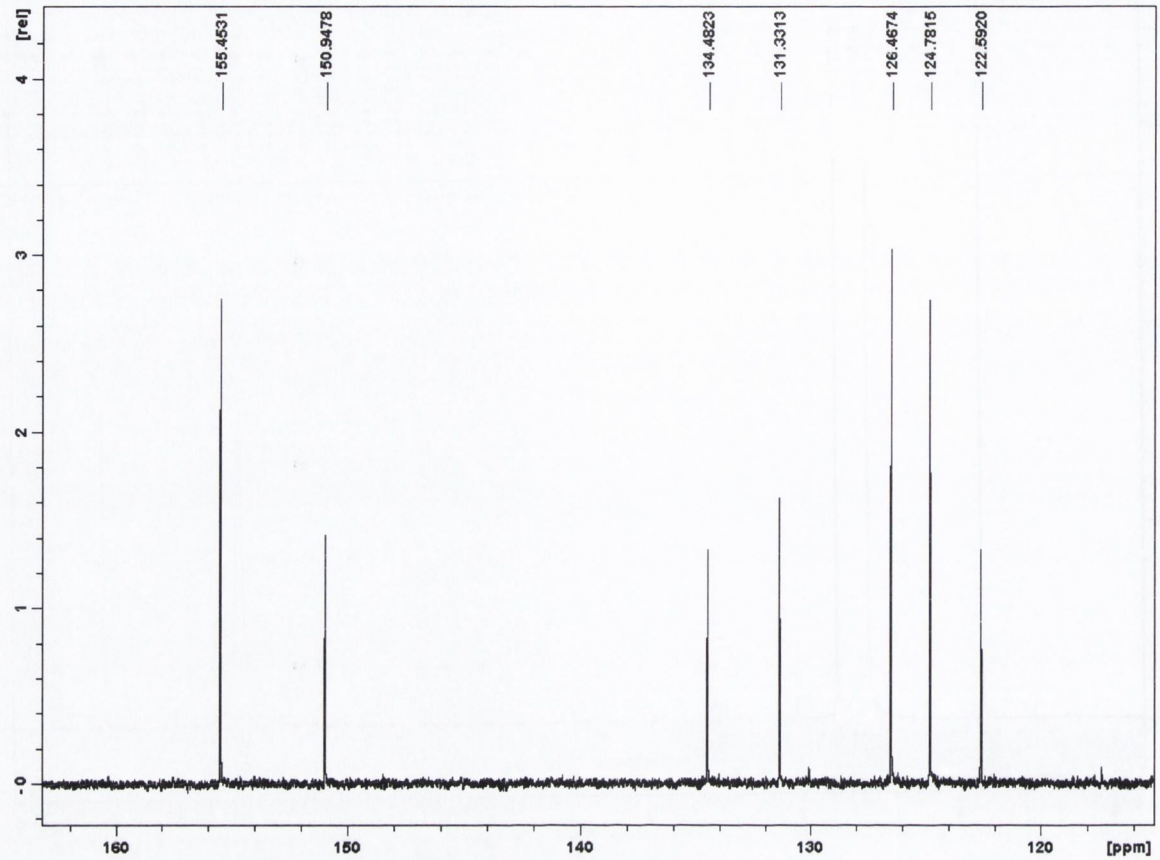

Fig. II.4. ^{13}CNMR results of chlorothiazide sodium dihydrate.

Table II.4. Summary ^{13}CNMR data for chlorothiazide sodium dihydrate.

Peak	ν(F1) [ppm]
C(7)H(7)	155.5
C(5)	150.9
C(3)	134.5
C(6)	131.3
C(1)H(1)	126.5
C(4)H(4)	124.8
C(2)	122.6

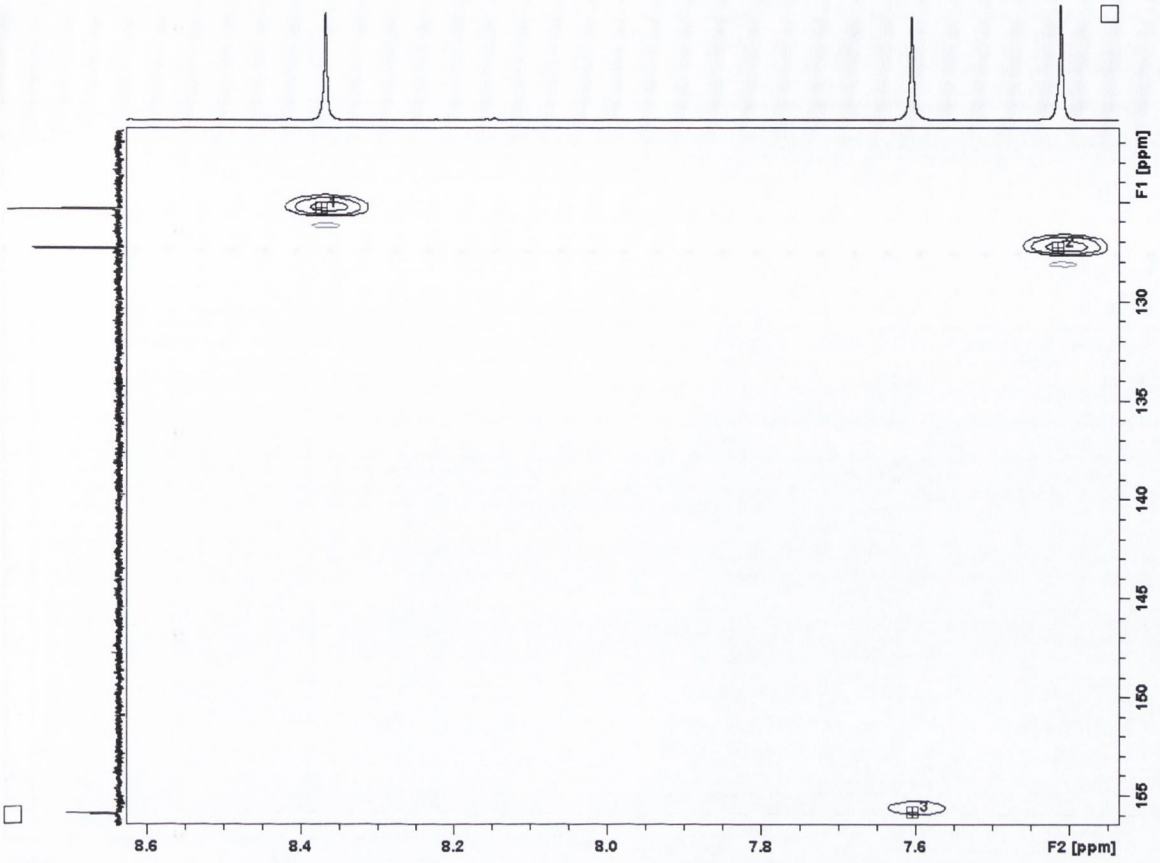

Fig. II.5. ^{1}HNMR and ^{13}CNMR 2D HSQC correlation analysis of chlorothiazide sodium dihydrate.

Table II.5. Summary ^{1}HNMR and ^{13}CNMR 2D HSQC correlation analysis data for chlorothiazide sodium dihydrate.

Peak	ν(F2) [ppm]	ν(F1) [ppm]	Intensity [abs]
C(4)H(4)	8.37	125.3	487126.15
C(1)H(1)	7.41	127.2	512641.60
C(7)H(7)	7.60	155.8	182063.44

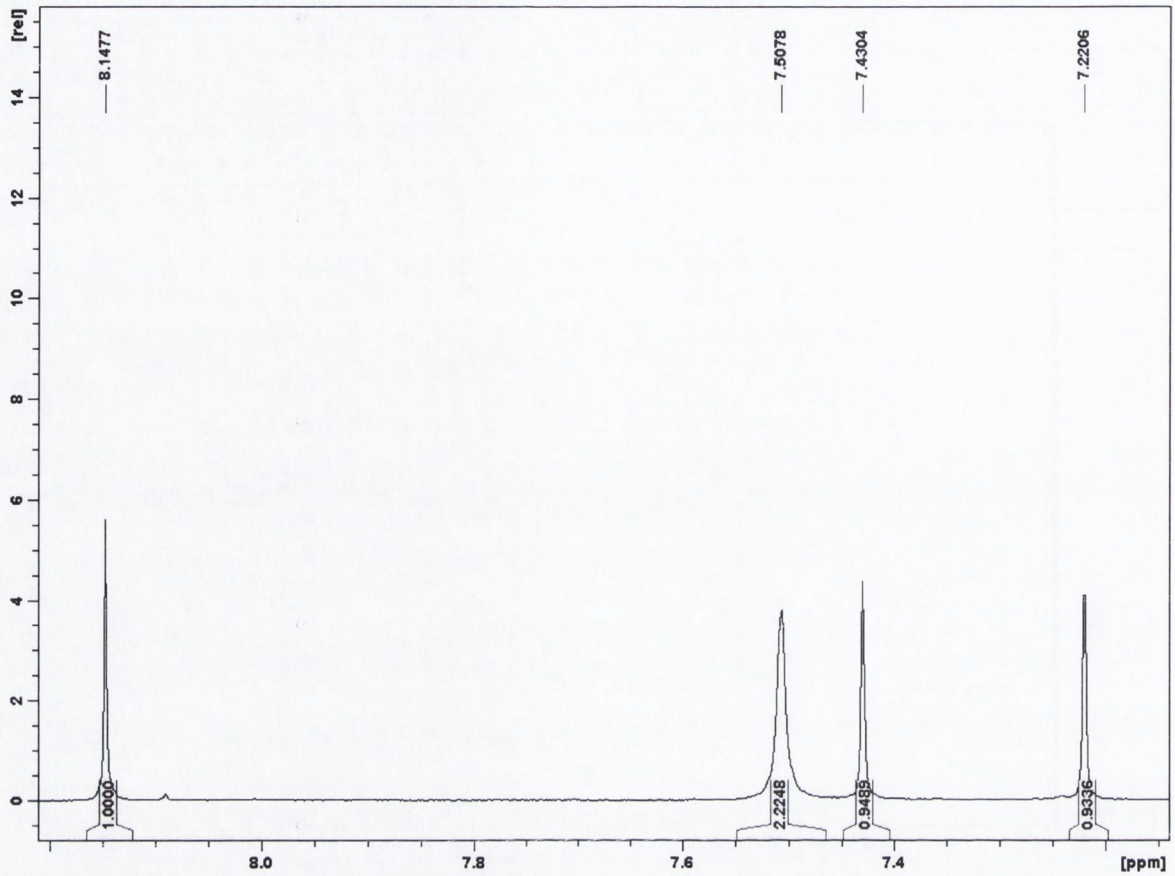

Fig. II.6. ^{1}HNMR of chlorothiazide potassium dihydrate.

Table II.6. Summary ^{1}HNMR data for chlorothiazide potassium dihydrate.

Peak	ν(F1) [ppm]	Intensity [abs]	Split	Integral [rel]
C(4)-H(4)	8.15	203718.71	s	1.0000
N(1)H_2(5,6)	7.51	138006.88	s	2.2248
C(1)-H(1)	7.43	115556.64	s	0.9489
C(7)-H(7)	7.22	149114.31	s	0.9336

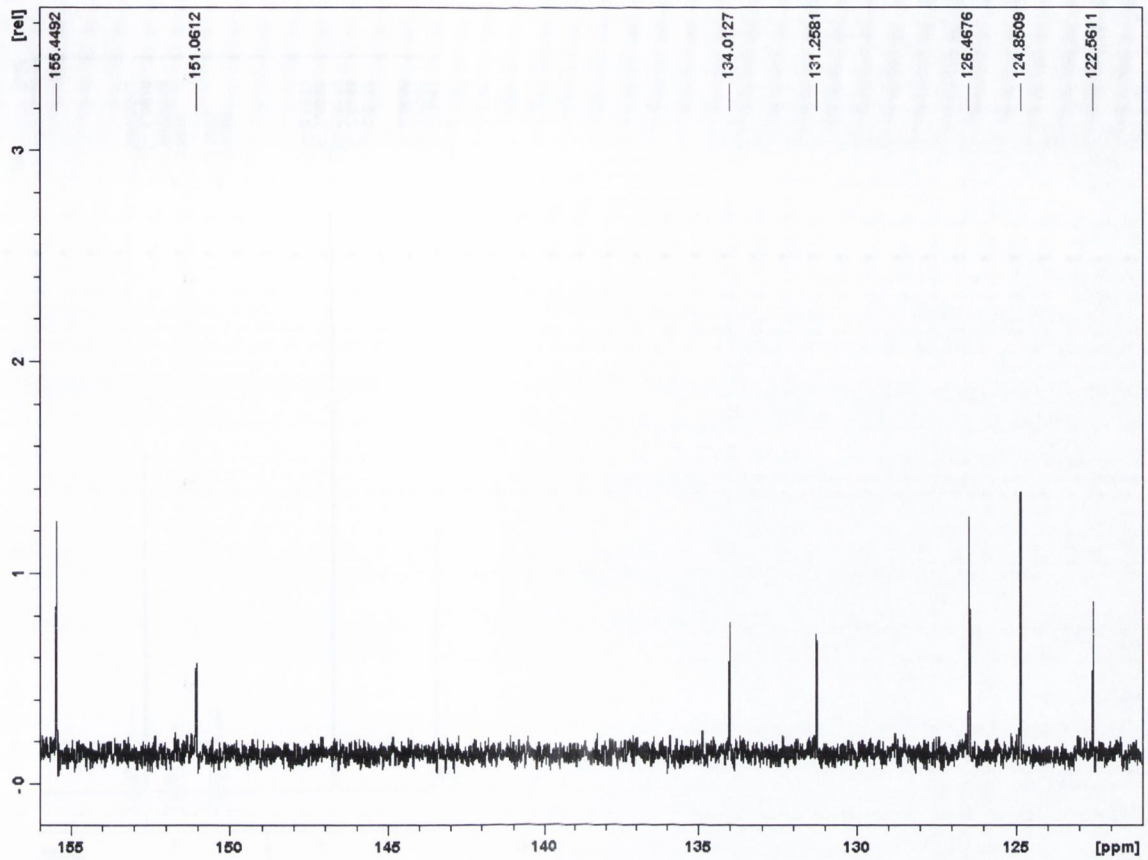

Fig. II.7. ^{13}CNMR of chlorothiazide potassium dihydrate

Table II.7. Summary ^{13}CNMR data for chlorothiazide potassium dihydrate

Peak	ν(F1) [ppm]
C(7)-H(7)	155.4
C(5)	151.1
C(3)	134.0
C(6)	131.3
C(1)-H(1)	126.5
C(4)-H(4)	124.9
C(2)	122.6

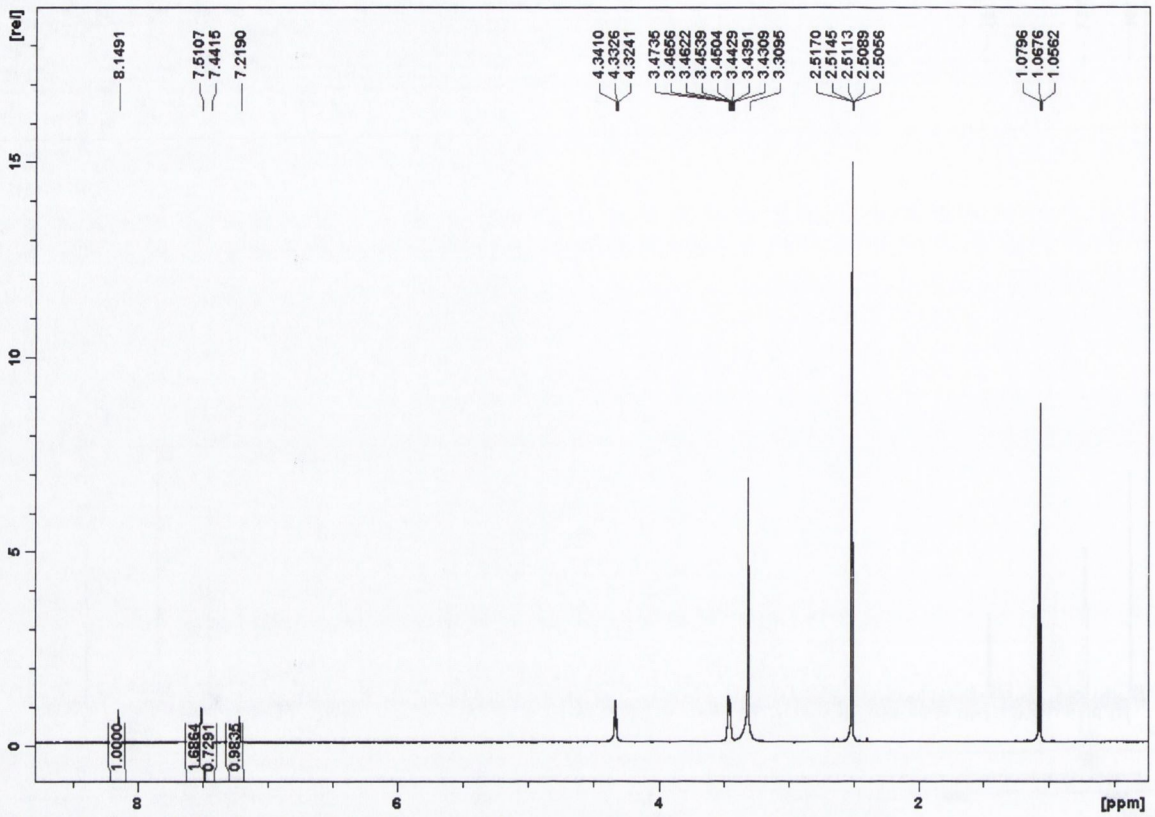

Fig. II.8. ^{1}HNMR of chlorothiazide potassium monohydrate hemiethanolate

Table II.8. Summary ^{1}HNMR data for chlorothiazide potassium monohydrate hemiethanolate.

Peak	ν(F1) [ppm]	Intensity [abs]	Split	Integral [rel]
C(4)-H(4)	8.15	14067.55	s	1.0000
C(1)-H(1)	7.51	15331.89	s	1.6864
N(1)H(5 or 6)	7.44	6815.83	s	0.7291
C(7)-H(7)	7.22	11831.90	s	0.9835

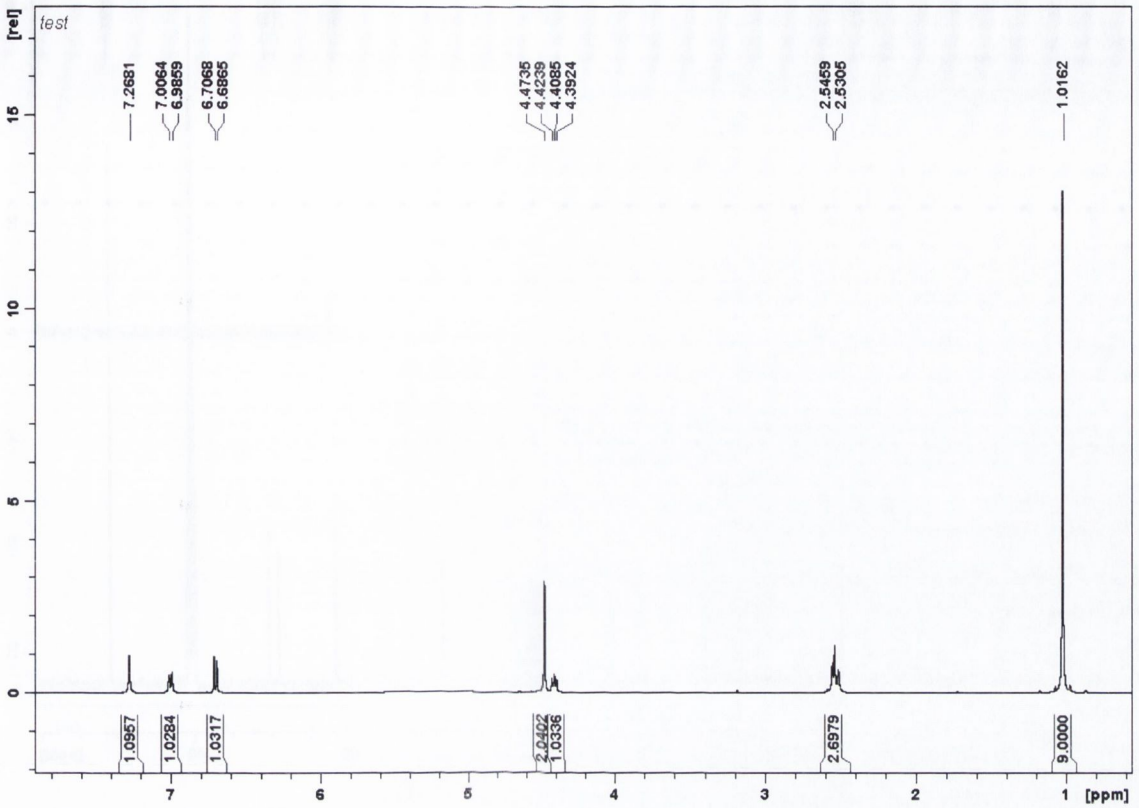

Fig. II.9. ^{1}HNMR of salbutamol.

Table II.9. Summary ^{1}HNMR data for salbutamol.

Peak	ν(F1) [ppm]	Intensity [abs]	Split	Integral [rel]
C(10,11,12) H(10,11,12)	1.01	505428467.75	s	9.0000
C(8)H(8AB)	2.53	151509310.75	d	2.6979
C(7)H(7)	4.39	58046259.50	t	1.0336
C(13)H(13AB)	4.49	114572573.50	s	2.0402
C(2)H(2)	6.70	57936546.50	d	1.0317
C(3)H(3)	7.00	57753391.00	d	1.0284
C(6)H(6)	7.26	61532817.50	d	1.0957

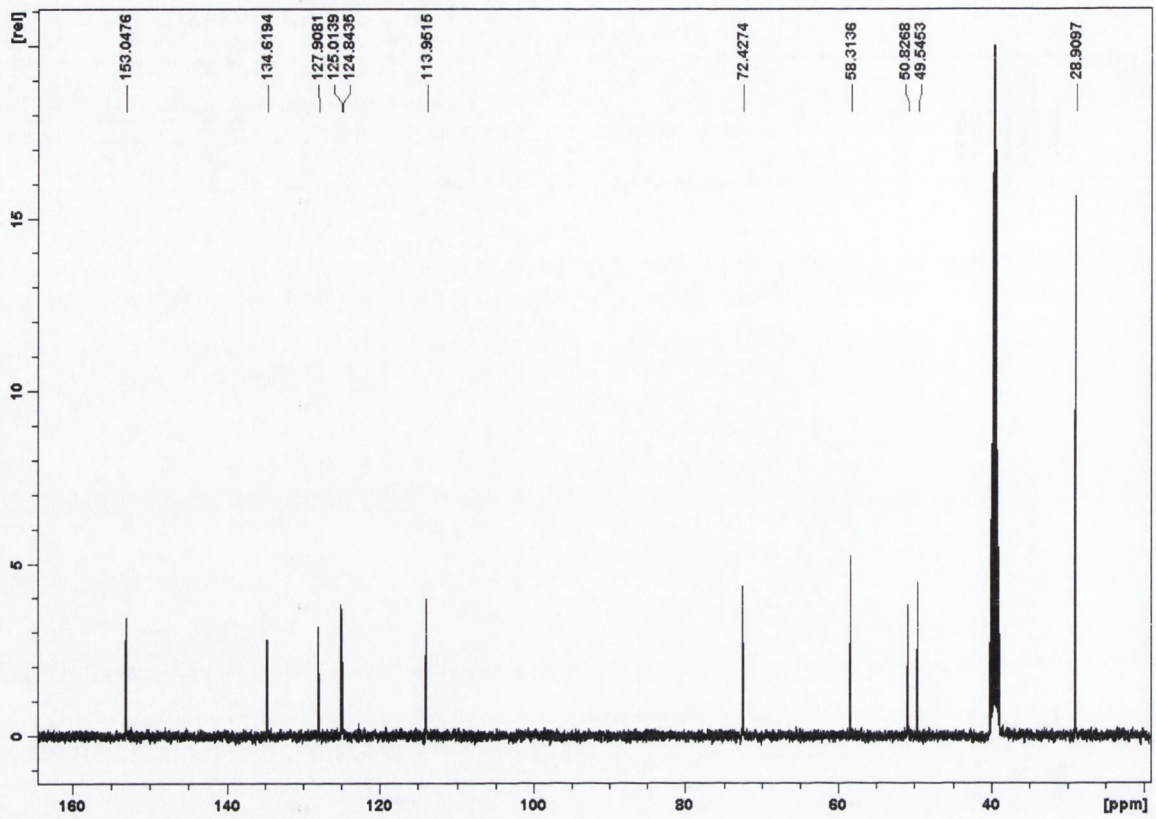

Fig. II.10. ^{13}CNMR of salbutamol.

Table II.10. Summary ^{13}CNMR data for salbutamol.

Peak	ν(F1) [ppm]
C(10,11,12) H(10-12/ABC)	28.9
C(9)	49.5
C(8)H(8AB)	50.8
C(13)H(13AB)	58.3
C(7)H(7)	72.4
C(2)H(2)	114.0
C(3)H(3)	124.8
C(6)H(6)	125.0
C(1,4,5)	127.9
C(1,4,5)	134.6
C(1,4,5)	153.0

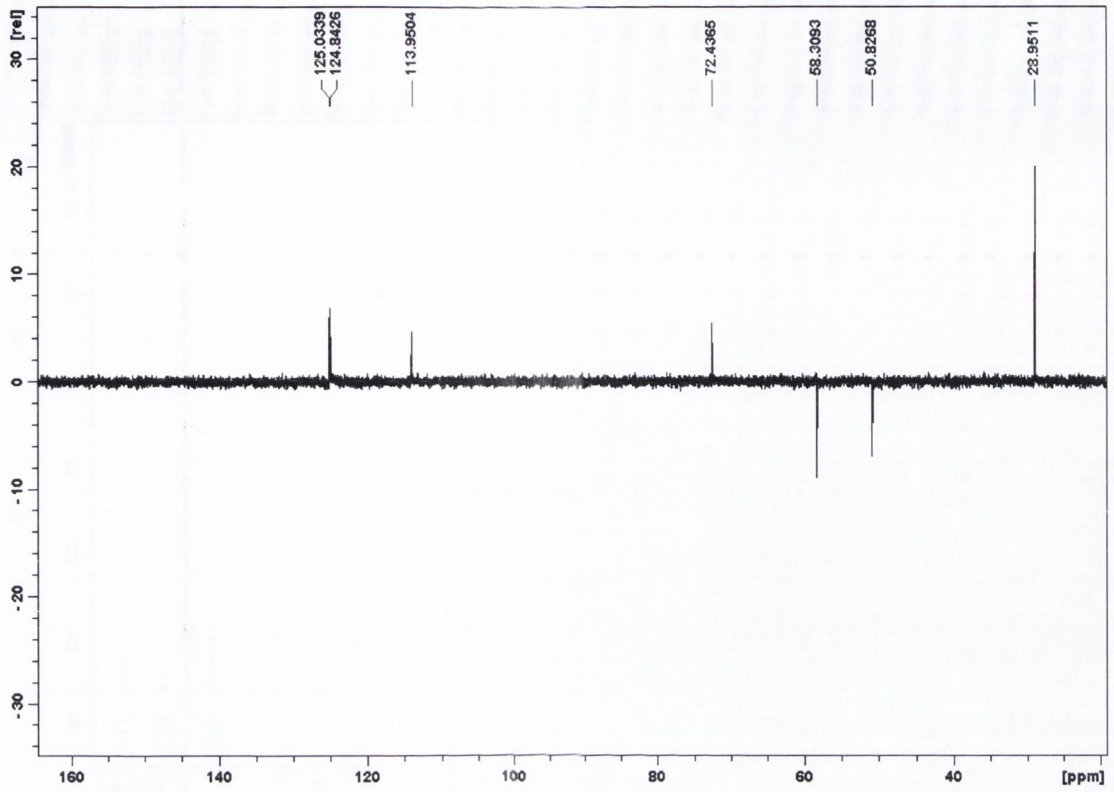

Fig. II.11. DEPT 135° ^{13}CNMR of salbutamol.

Table II.11. Summary DEPT 135° ^{13}CNMR data for salbutamol.

Peak	ν(F1) [ppm]
C(10,11,12) H(10-12/ABC)	29.0
C(8)H(8AB)	50.8
C(13)H(13AB)	58.3
C(7)H(7)	72.4
C(2)H(2)	114.0
C(3)H(3)	124.8
C(6)H(6)	125.0

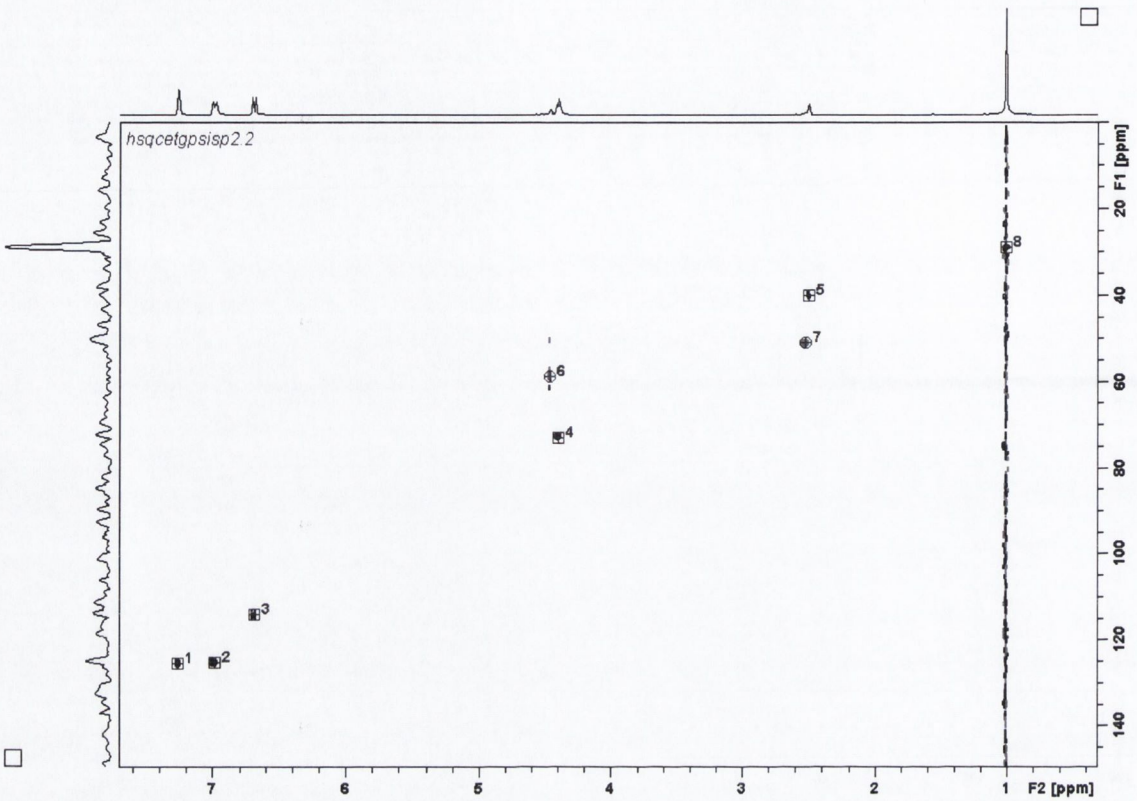

Fig. II.12. HSQC 2D ^{1}HNMR ^{13}CNMR of salbutamol.

Table II.12. Summary HSQC 2D ^{1}HNMR ^{13}CNMR data for salbutamol.

Peak	ν(F2) [ppm]	ν(F1) [ppm]	Intensity [abs]
C(10,11,12) H(10-12/ABC)	29.0	1.01	64491476.50
C(8)H(8AB)	51.0	2.53	-9641084.47
C(13)H(13AB)	58.8	4.47	-3756689.97
C(7)H(7)	72.9	4.40	4743591.50
C(2)H(2)	114.1	6.69	2066931.50
C(3)H(3)	125.2	6.98	5468044.50
C(6)H(6)	125.4	7.27	9562782.50

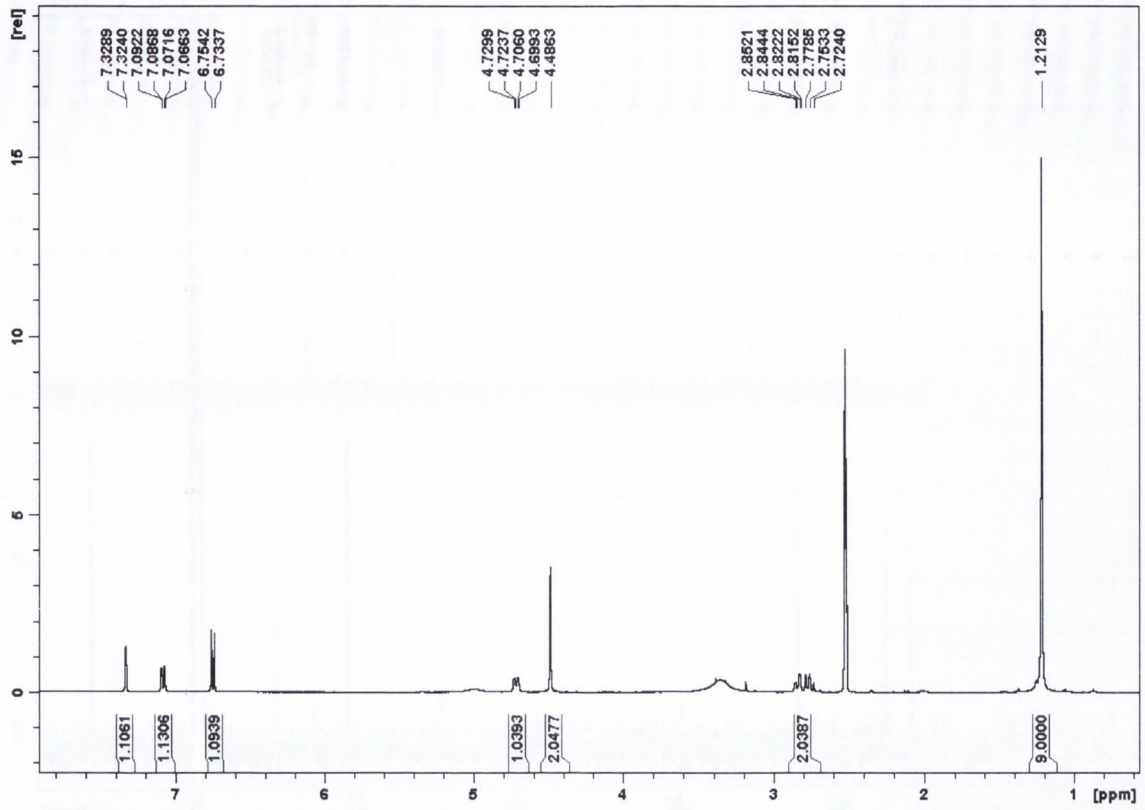

Fig. II.13. ^{1}HNMR of salbutamol sulphate.

Table II.13. Summary ^{1}HNMR data for salbutamol sulphate.

Peak	ν(F1) [ppm]	Intensity [abs]	Split	Integral [rel]
C(10,11,12) H(10,11,12)	1.21	234945975.50	s	9.0000
C(8)H(8AB)	2.79	53221101.41	m	2.0387
C(7)H(7)	4.46	53454144.59	s	2.0477
C(13)H(13AB)	4.70	27130031.00	d	1.0393
C(2)H(2)	6.73	28555797.25	d	1.0939
C(3)H(3)	7.07	29514581.59	d	1.1306
C(6)H(6)	7.33	28874527.25	s	1.1061

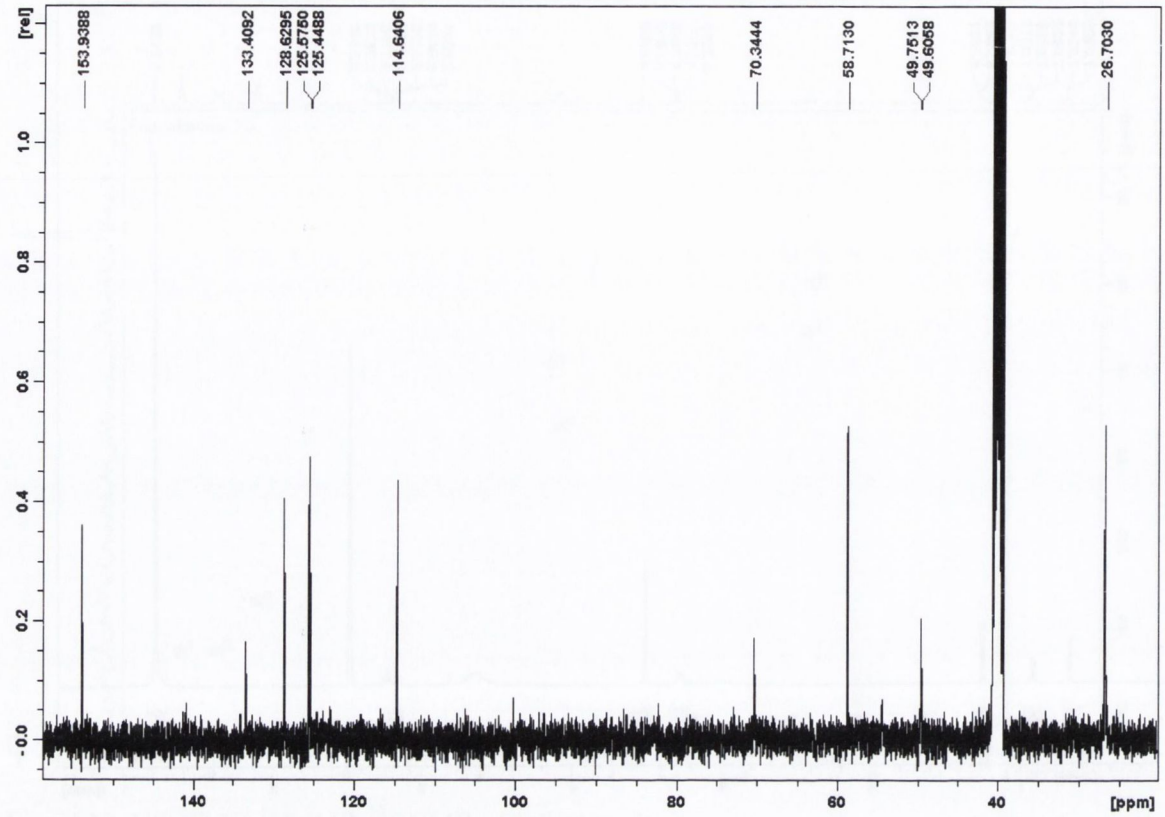

Fig. II.14. ^{13}CNMR of salbutamol sulphate.

Table II.14. Summary ^{13}CNMR data for salbutamol sulphate.

Peak	ν(F1) [ppm]
C(10,11,12) H(10-12/ABC)	26.7
C(9)	49.8
C(8)H(8AB)	49.6
C(13)H(13AB)	58.7
C(7)H(7)	70.3
C(2)H(2)	114.6
C(3)H(3)	125.4
C(6)H(6)	125.6
C(1,4,5)	128.6
C(1,4,5)	133.4
C(1,4,5)	153.9

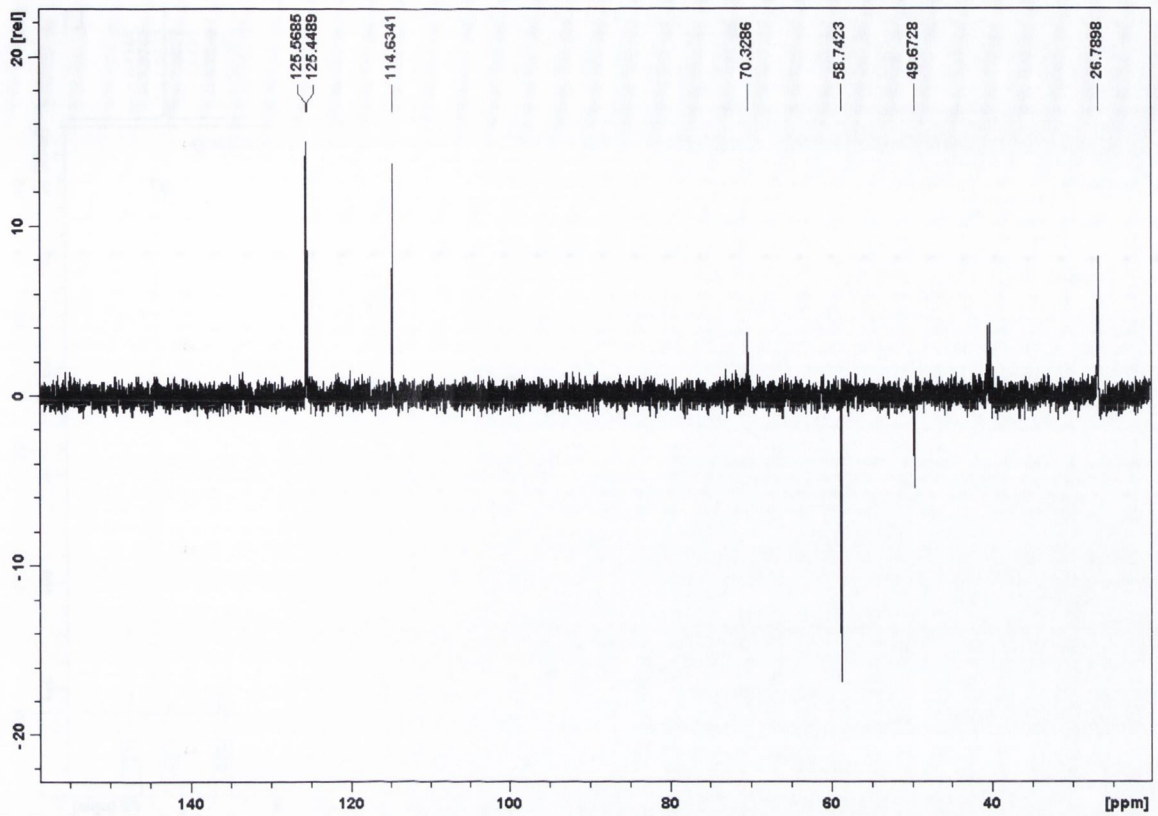

Fig. II.15. DEPT 135° ^{13}CNMR of salbutamol sulphate.

Table II.15. Summary DEPT 135° ^{13}CNMR data for salbutamol sulphate.

Peak	ν(F1) [ppm]
C(10,11,12) H(10-12/ABC)	26.8
C(8)H(8AB)	49.7
C(13)H(13AB)	58.7
C(7)H(7)	70.3
C(2)H(2)	114.6
C(3)H(3)	125.4
C(6)H(6)	125.6

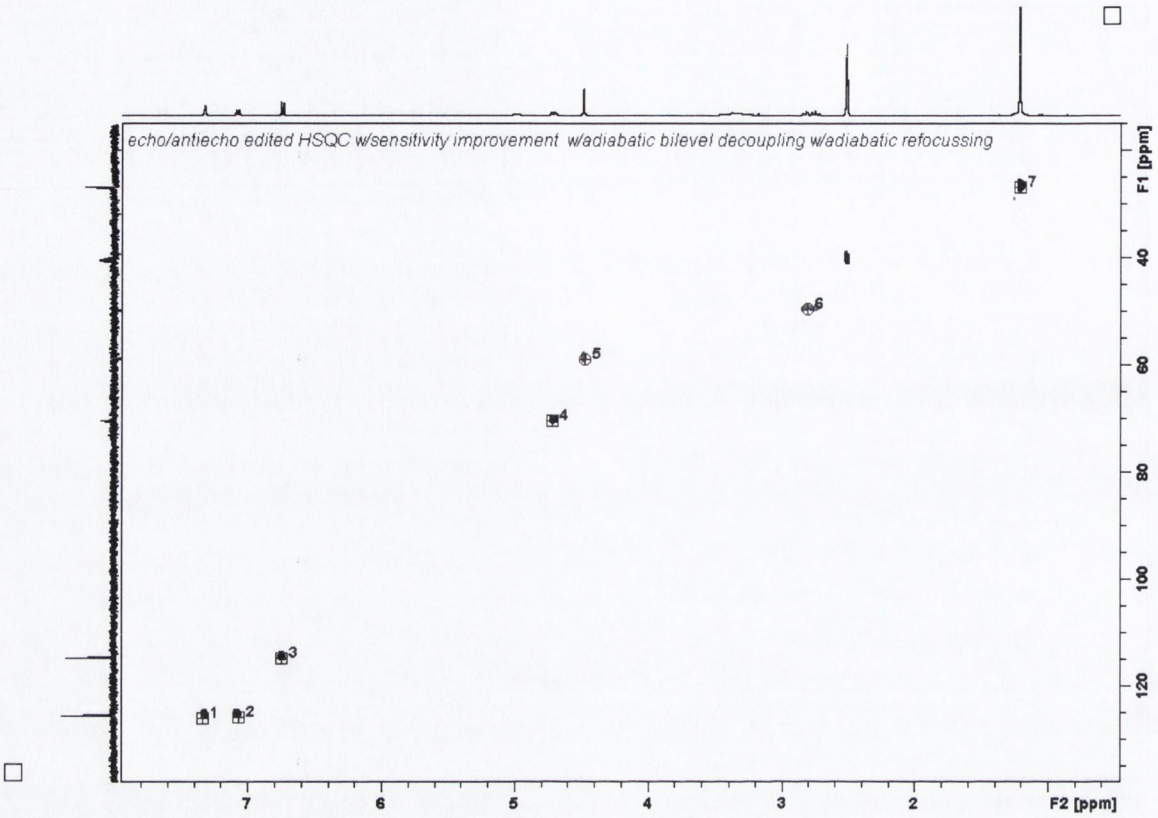

Fig. II.16. HSQC 2D ^{1}HNMR ^{13}CNMR of salbutamol sulphate.

Table II.16. Summary HSQC 2D ^{1}HNMR ^{13}CNMR data for salbutamol sulphate.

Peak	ν(F2) [ppm]	ν(F1) [ppm]	Intensity [abs]
C(10,11,12) H(10-12/ABC)	1.22	26.9	847942.14
C(8)H(8AB)	2.81	49.7	-78334.69
C(13)H(13AB)	4.48	59.0	-237256.16
C(7)H(7)	4.72	70.4	96694.64
C(2)H(2)	6.75	114.9	86622.50
C(3)H(3)	7.07	125.9	54687.30
C(6)H(6)	7.34	126.1	20259.36

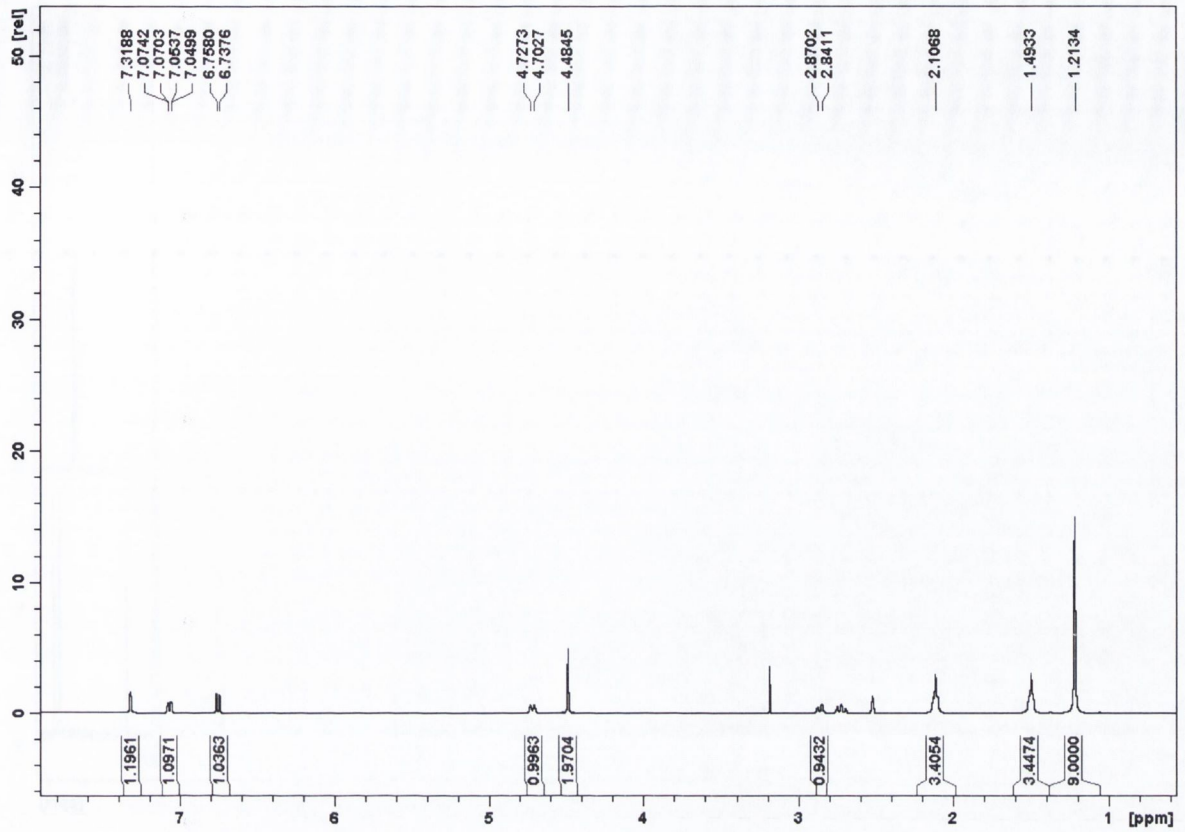

Fig. II.17. ^{1}HNMR of salbutamol adipate.

Table II.17. Summary ^{1}HNMR data for salbutamol adipate.

Peak	ν(F1) [ppm]	Intensity [abs]	Split	Integral [rel]
C(10,11,12) H(10,11,12)	1.22	326163592.91	s	9.0000
C(8)H(8AB)	2.85	34182310.56	d	0.9432
C(7)H(7)	4.70	36106776.28	s	0.9963
C(13)H(13AB)	4.48	71407490.62	d	1.9704
C(2)H(2)	6.74	37556368.34	d	1.0363
C(3)H(3)	7.06	39760960.09	d	1.0971
C(6)H(6)	7.31	43345757.69	s	1.1961
C(15,18) H(15,18/AB) C(15) H(15/AB)	2.11	123414541.75	s	3.4054
C(16,19)	1.50	124935807.22	s	3.4474

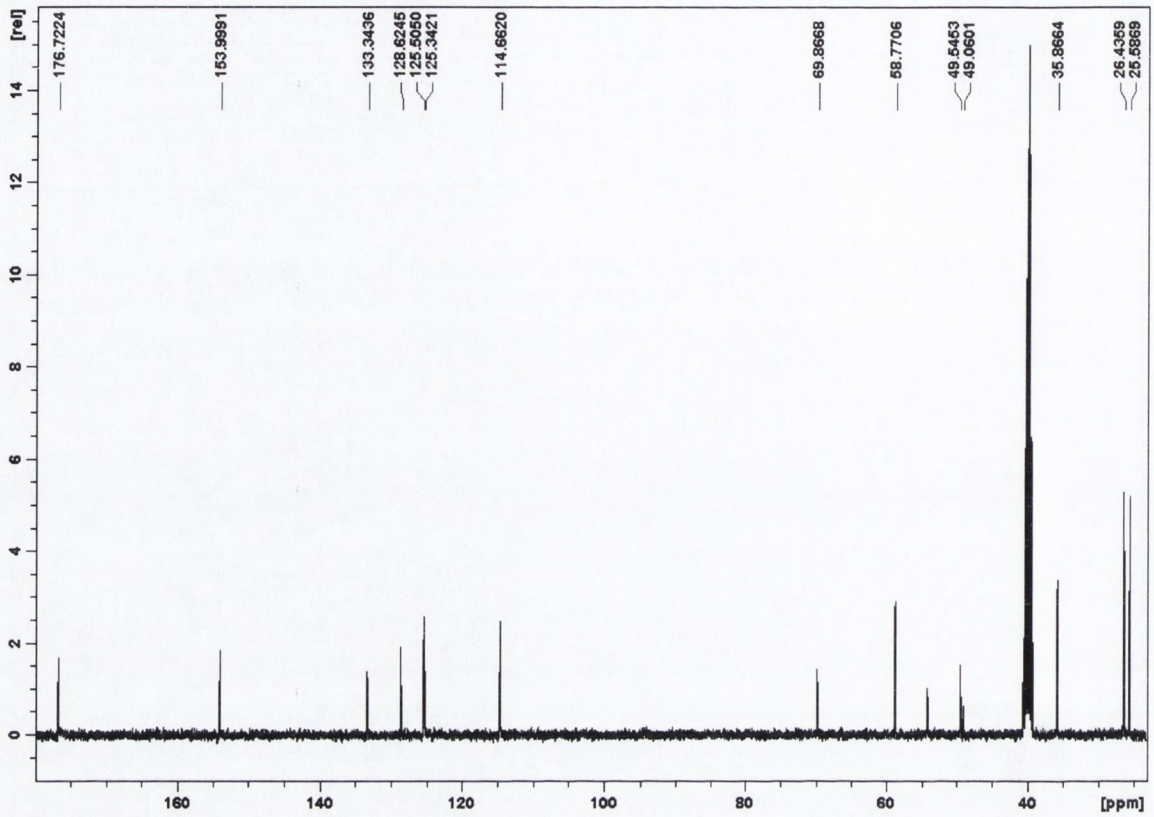

Fig. II.18. ^{13}CNMR of salbutamol adipate.

Table II.18. Summary ^{13}CNMR data for salbutamol adipate.

Peak	ν(F1) [ppm]
C(10,11,12) H(10-12/ABC)	26.4
C(9)	49.1
C(8)H(8AB)	49.5
C(13)H(13AB)	58.8
C(7)H(7)	69.9
C(2)H(2)	114.7
C(3)H(3)	125.3
C(6)H(6)	125.5
C(1,4,5)	128.6
C(1,4,5)	133.3
C(1,4,5)	154.0
C(14,17)	176.7
C(15,18)	35.9
C(16,19)	25.6

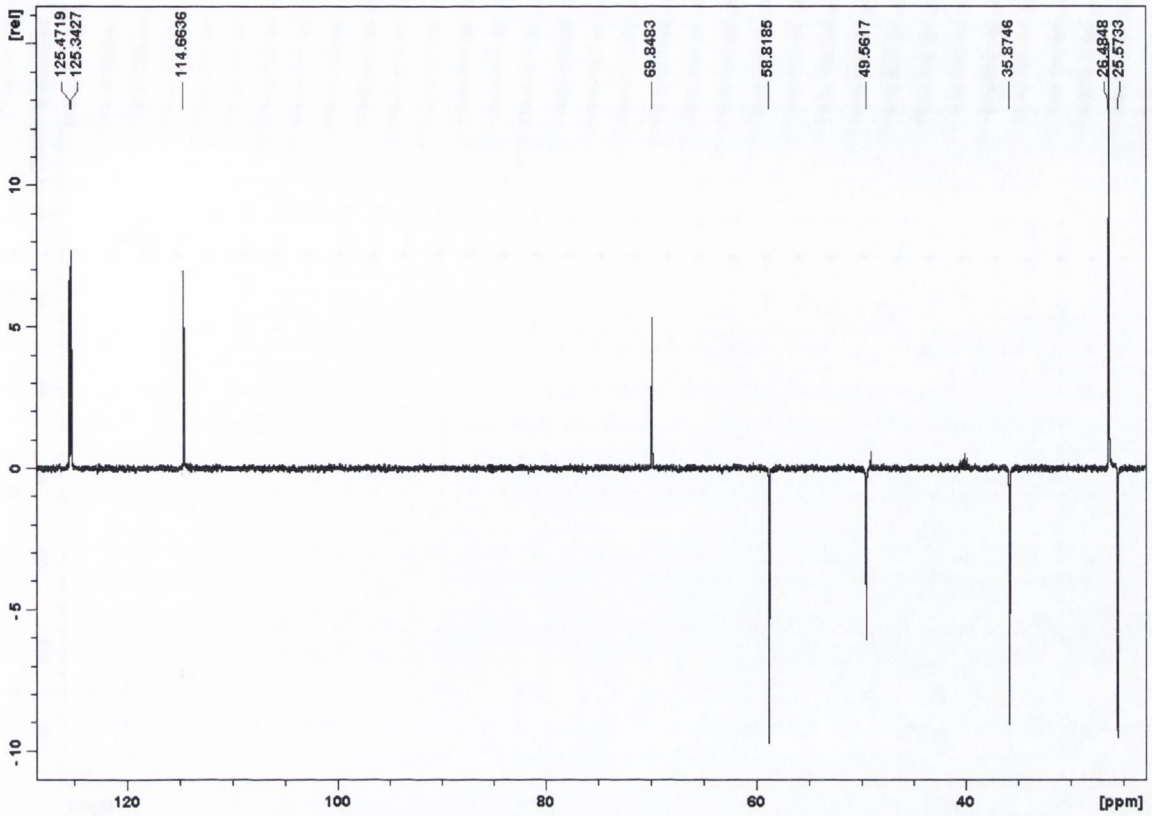

Fig. II.19. DEPT 135° ^{13}CNMR of salbutamol adipate.

Table II.19. Summary DEPT 135° ^{13}CNMR data for salbutamol adipate.

Peak	ν(F1) [ppm]
C(10,11,12) H(10-12/ABC)	26.5
C(8)H(8AB)	49.6
C(13)H(13AB)	58.8
C(7)H(7)	69.8
C(2)H(2)	114.7
C(3)H(3)	125.5
C(6)H(6)	125.3
C(15,18)	35.9
C(16,19)	25.6

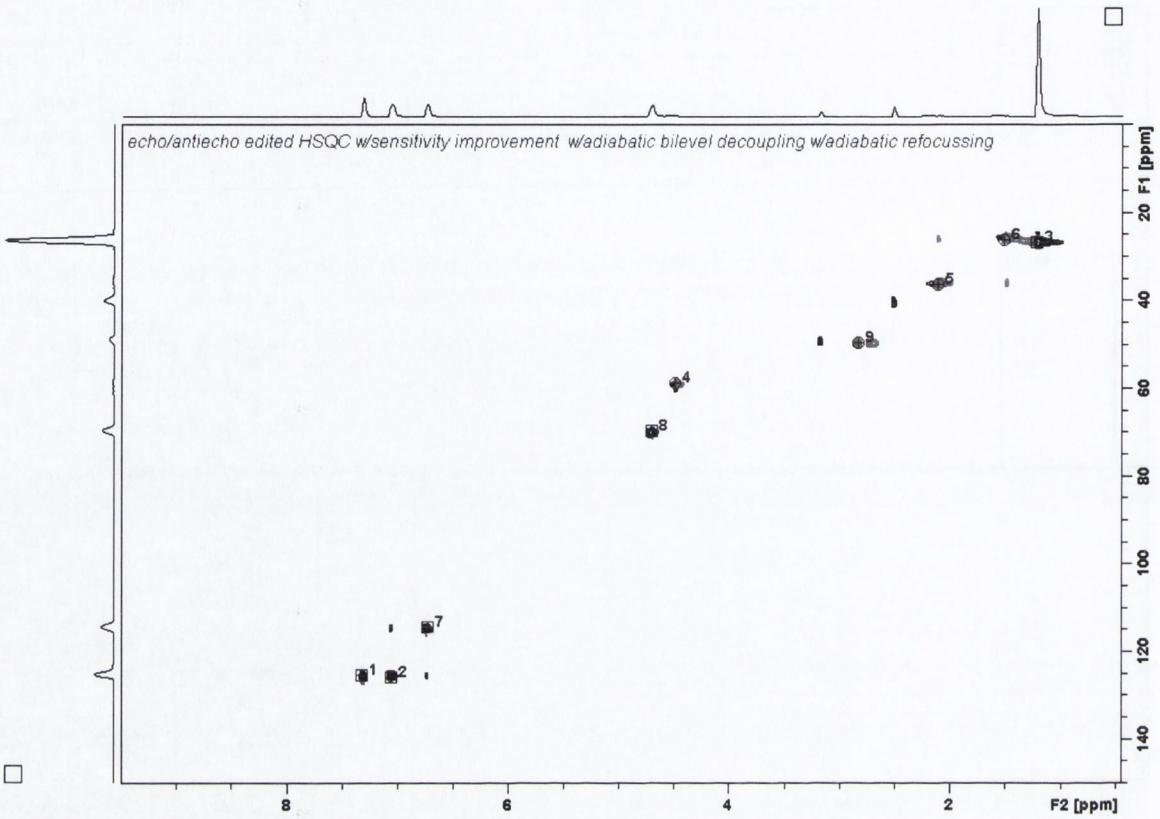

Fig. II.20. HSQC 2D ^{1}HNMR ^{13}CNMR of salbutamol adipate.

Table II.20. Summary HSQC 2D ^{1}HNMR ^{13}CNMR data for salbutamol adipate.

Peak	ν(F2) [ppm]	ν(F1) [ppm]	Intensity [abs]
C(10,11,12) H(10-12/ABC)	1.22	26.6	2323969.97
C(8)H(8AB)	2.83	49.5	-905940.91
C(13)H(13AB)	4.49	58.8	-3180529.18
C(7)H(7)	4.71	69.7	1152695.78
C(2)H(2)	6.74	114.5	1389190.88
C(3)H(3)	7.06	125.9	351255.34
C(6)H(6)	7.33	125.4	1096846.03
C(15,18)	2.12	36.4	-1264155.27
C(16,19)	1.51	26.1	-893910.31

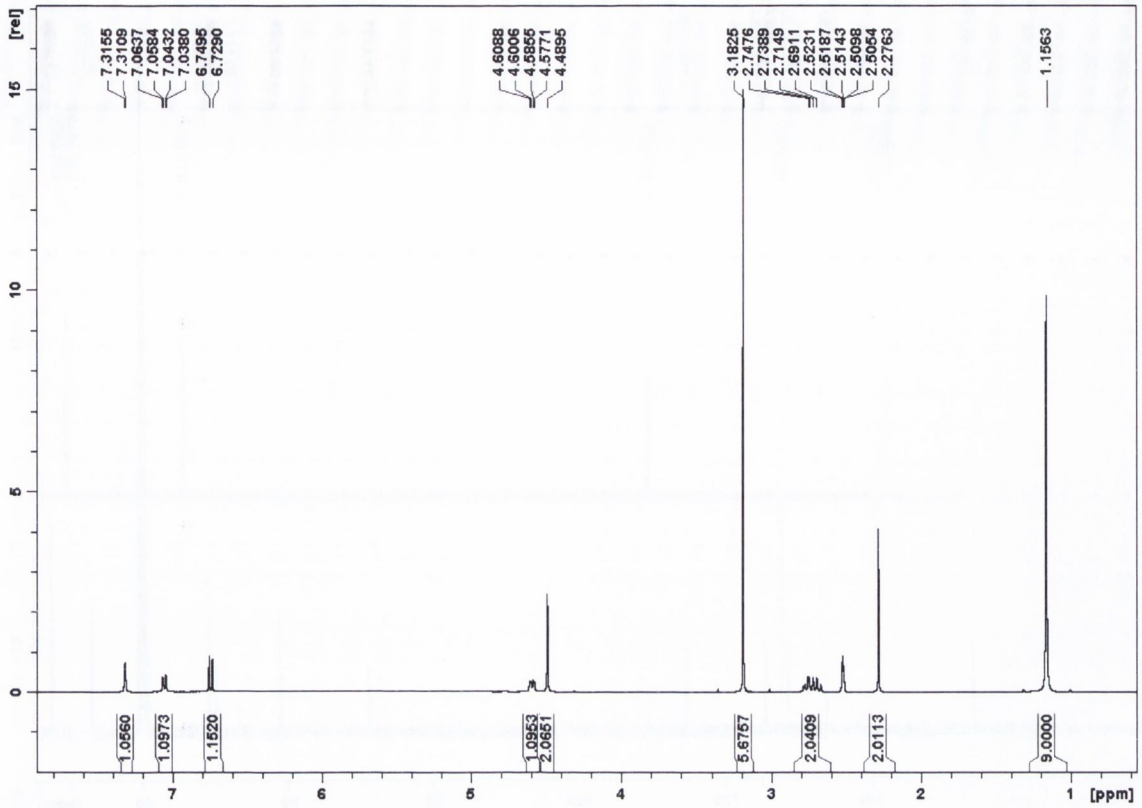

Fig. II.21. ^{1}HNMR of salbutamol succinate tetramethanolate.

Table II.21. Summary ^{1}HNMR data for salbutamol succinate tetramethanolate.

Peak	ν(F1) [ppm]	Intensity [abs]	Split	Integral [rel]
C(10,11,12) H(10,11,12)	1.15	455673768.00	s	9.0000
C(8)H(8AB)	2.73	103333803.50	m	2.0409
C(7)H(7)	4.50	104556943.38	s	2.0651
C(13)H(13AB)	4.60	55455395.00	d	1.0953
C(2)H(2)	6.73	58328186.25	s	1.1520
C(3)H(3)	7.05	55555742.62	d	1.0973
C(6)H(6)	7.31	53465776.88	d	1.0560
C(15,18) H(15,18/AB) C(15) H(15/AB)	2.28	101835421.38	s	2.0113
C(16) H(16/ABC) C(17) H(29-31)	3.18	287365001.12	s	5.6757

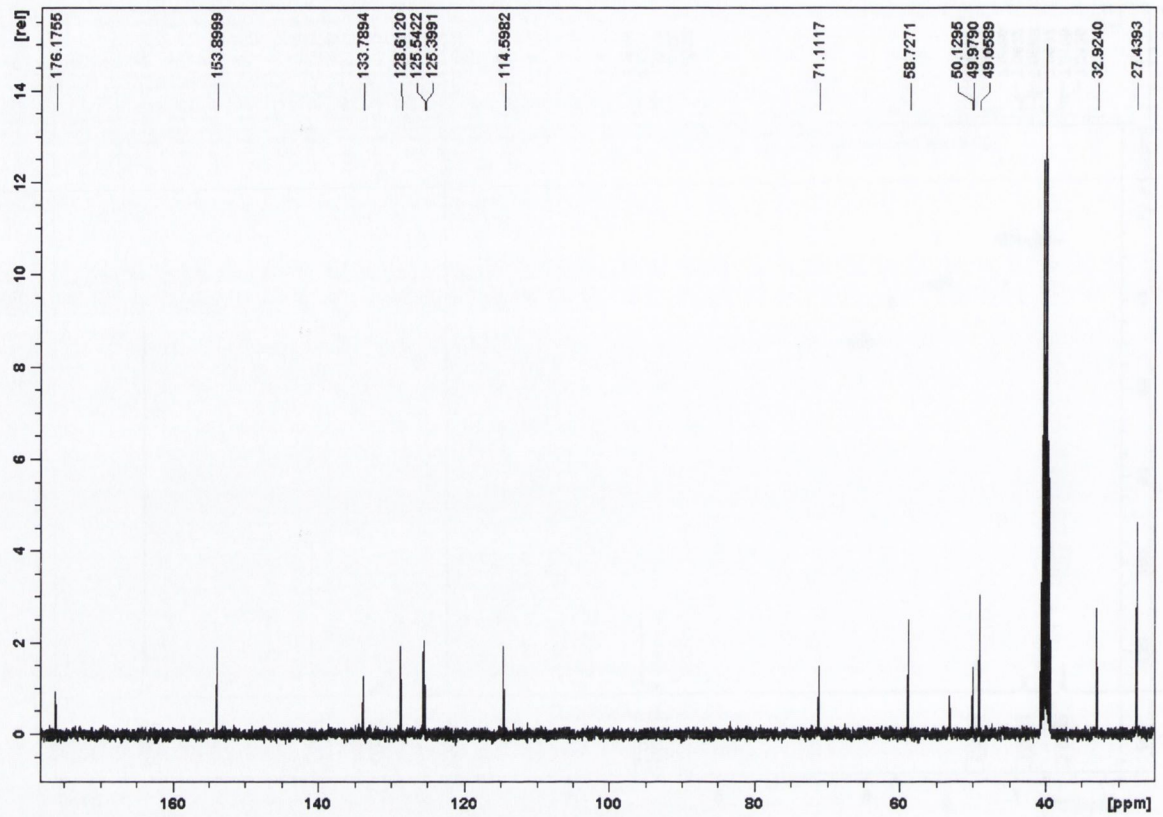

Fig. II.22. ^{13}CNMR of salbutamol succinate tetramethanolate.

Table II.22. Summary ^{13}CNMR data for salbutamol succinate tetramethanolate.

Peak	ν(F1) [ppm]
C(10,11,12) H(10-12/ABC)	27.4
C(9)	50.1
C(8)H(8AB)	45.0
C(13)H(13AB)	58.7
C(7)H(7)	71.1
C(2)H(2)	114.6
C(3)H(3)	125.4
C(6)H(6)	125.5
C(1,4,5)	128.6
C(1,4,5)	133.8
C(1,4,5)	153.9
C(14,17)	176.2
C(15,18)	32.9
C(17,16)	49.1

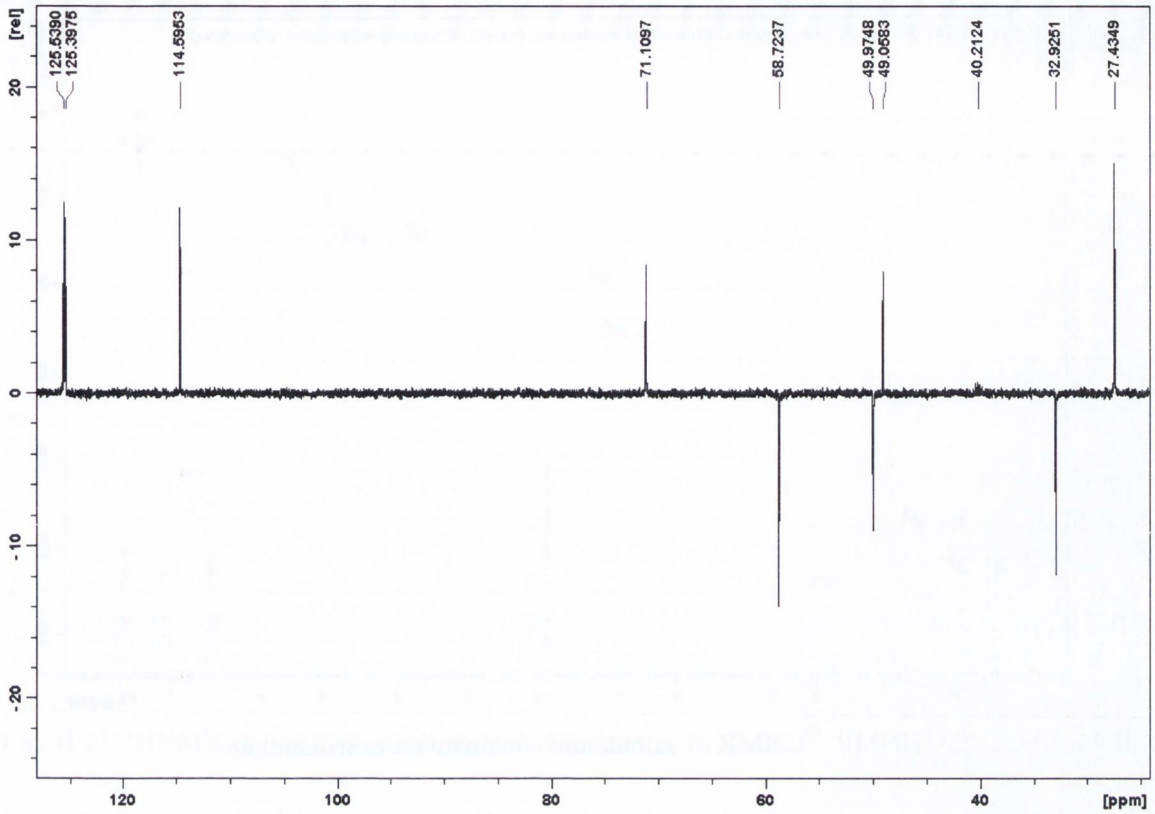

Fig. II.23. DEPT 135° ^{13}CNMR of salbutamol succinate tetramethanolate.

Table II.23. Summary DEPT 135° ^{13}CNMR data for salbutamol succinate tetramethanolate.

Peak	ν(F1) [ppm]
C(10,11,12) H(10-12/ABC)	27.4
C(8)H(8AB)	50.0
C(13)H(13AB)	58.7
C(7)H(7)	71.1
C(2)H(2)	114.6
C(3)H(3)	125.5
C(6)H(6)	125.4
C(15,18)	32.9
C(17,16)	49.1

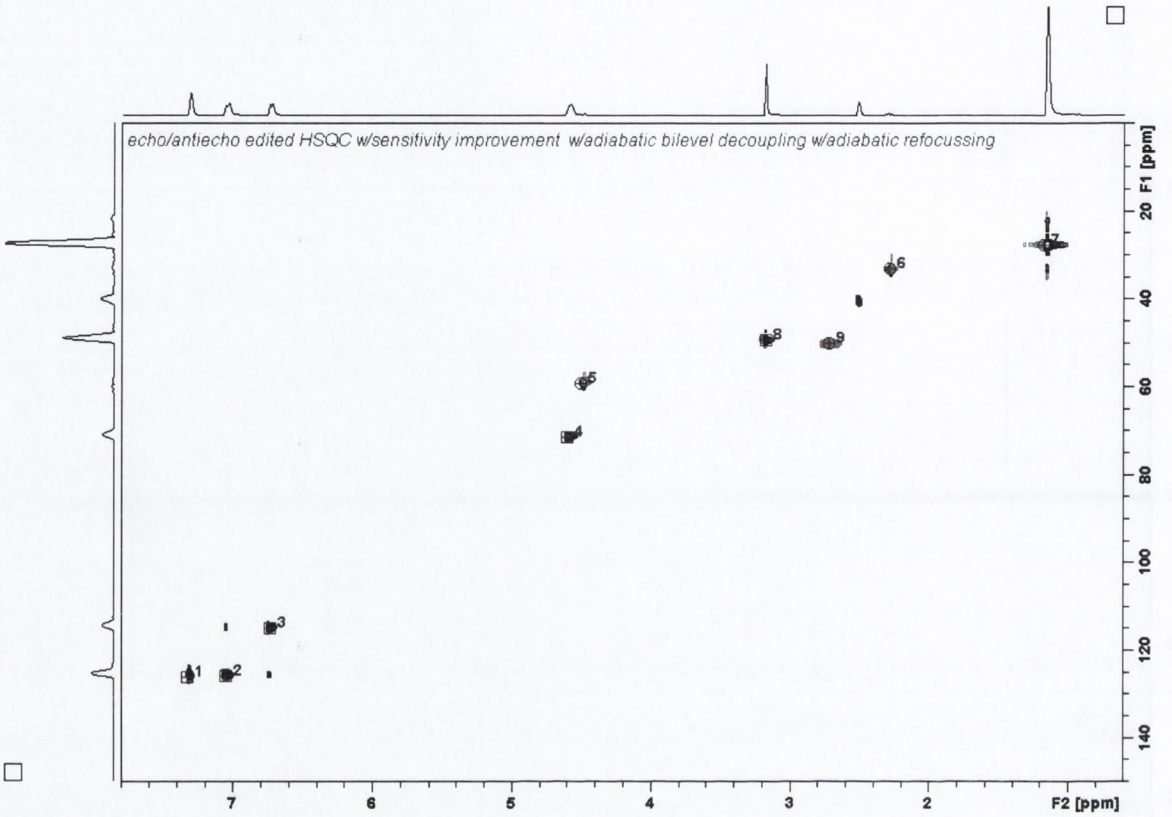

Fig. II.24. HSQC 2D ^{1}HNMR ^{13}CNMR of salbutamol succinate tetramethanolate.

Table II.24. Summary HSQC 2D ^{1}HNMR ^{13}CNMR data for salbutamol succinate tetramethanolate.

Peak	ν(F2) [ppm]	ν(F1) [ppm]	Intensity [abs]
C(10,11,12) H(10-12/ABC)	1.18	27.8	-50167.69
C(8)H(8AB)	2.72	50.1	-202404.25
C(13)H(13AB)	4.50	59.4	-37838.13
C(7)H(7)	4.60	71.5	322711.27
C(2)H(2)	6.74	114.9	217337.11
C(3)H(3)	7.05	125.8	207308.20
C(6)H(6)	7.33	126.0	17340.70
C(15,18)	2.28	33.1	-199595.55
C(17,16)	3.17	49.3	1228090.75

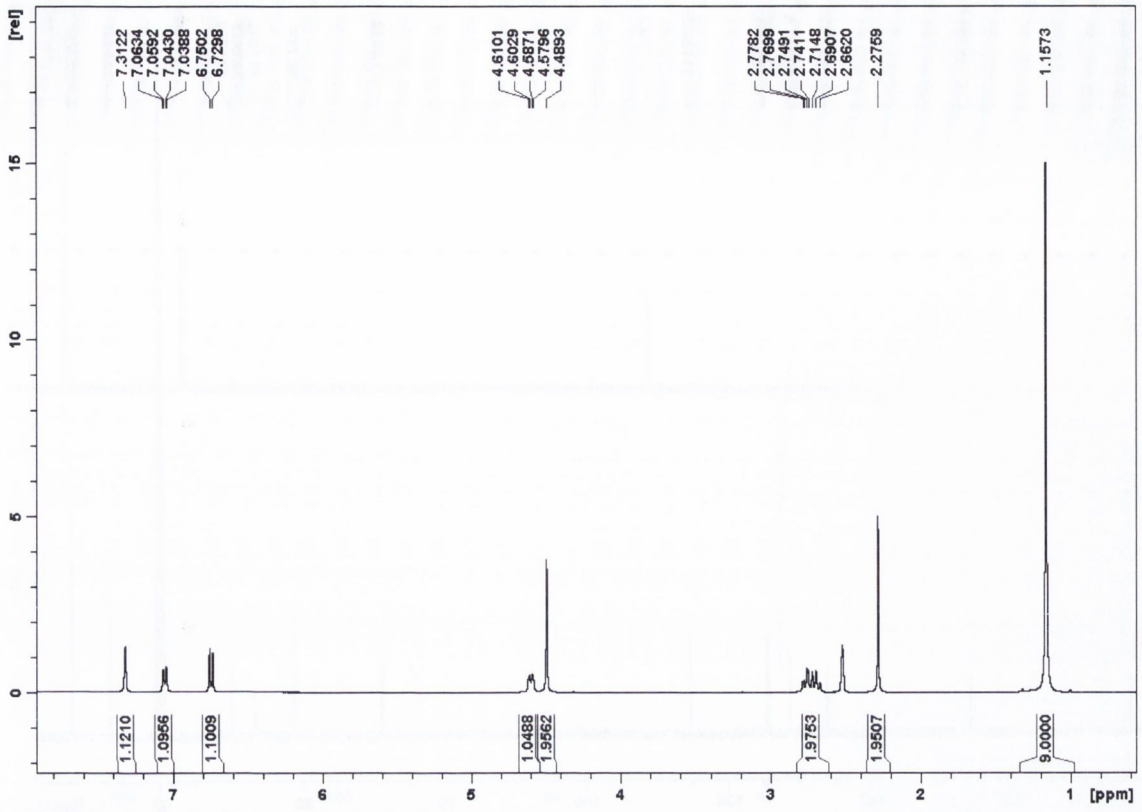

Fig. II.25. ^{1}HNMR of desolvated salbutamol succinate.

Table II.25. Summary ^{1}HNMR data for desolvated salbutamol succinate.

Peak	ν(F1) [ppm]	Intensity [abs]	Split	Integral [rel]
C(10,11,12) H(10,11,12)	1.1581	506963508.56	s	9.0000
C(8)H(8AB)	2.7224	111265820.25	m	1.9753
C(7)H(7)	4.4862	110189867.25	s	1.9562
C(13)H(13AB)	4.6109	59079315.62	d	1.0488
C(2)H(2)	6.7382	62011262.25	s	1.1009
C(3)H(3)	7.0554	61714562.69	d	1.0956
C(6)H(6)	7.3084	63144963.00	d	1.1210
C(15,18) H(15,18/AB) C(15) H(15/AB)	2.2805	109882078.69	s	1.9507

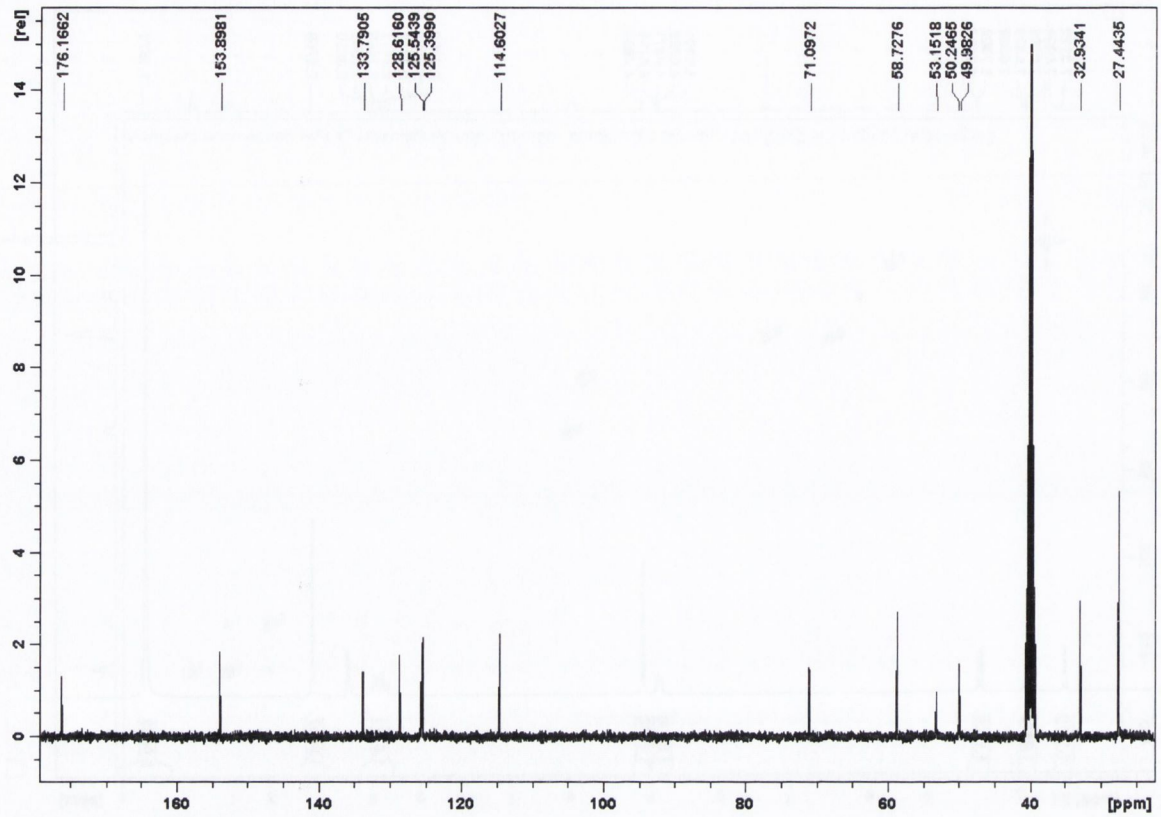

Fig. II.26. ^{13}CNMR of desolvated salbutamol succinate.

Table II.26. Summary ^{13}CNMR data for desolvated salbutamol succinate.

Peak	ν(F1) [ppm]
C(10,11,12) H(10-12/ABC)	27.4
C(9)	50.2
C(8)H(8AB)	50.0
C(13)H(13AB)	58.7
C(7)H(7)	71.1
C(2)H(2)	114.6
C(3)H(3)	125.4
C(6)H(6)	125.5
C(1,4,5)	128.6
C(1,4,5)	133.8
C(1,4,5)	153.9
C(14,17)	176.2
C(15,18)	32.9

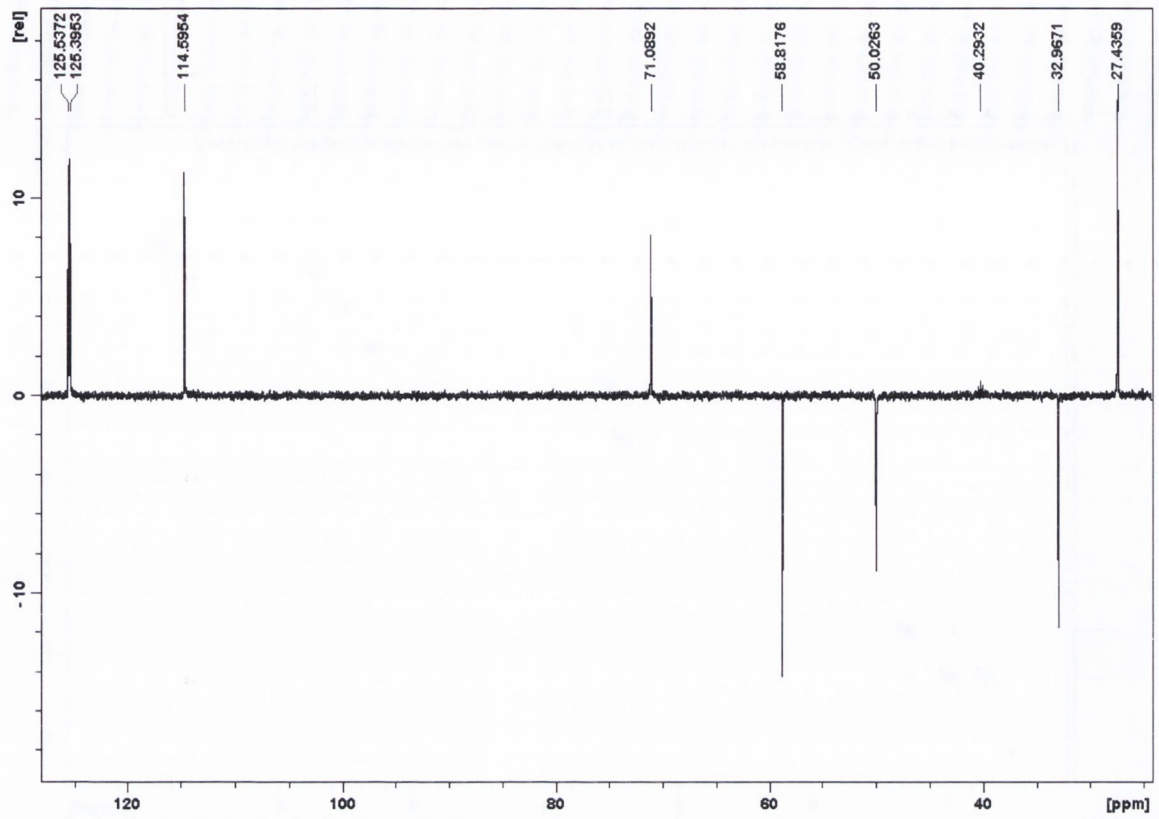

Fig. II.27. DEPT 135° ^{13}CNMR of desolvated salbutamol succinate.

Table II.27. Summary DEPT 135° ^{13}CNMR data for desolvated salbutamol succinate.

Peak	ν(F1) [ppm]
C(10,11,12) H(10-12/ABC)	27.4
C(8)H(8AB)	50.0
C(13)H(13AB)	58.8
C(7)H(7)	71.1
C(2)H(2)	114.6
C(3)H(3)	125.4
C(6)H(6)	125.5
C(15,18)	33.0

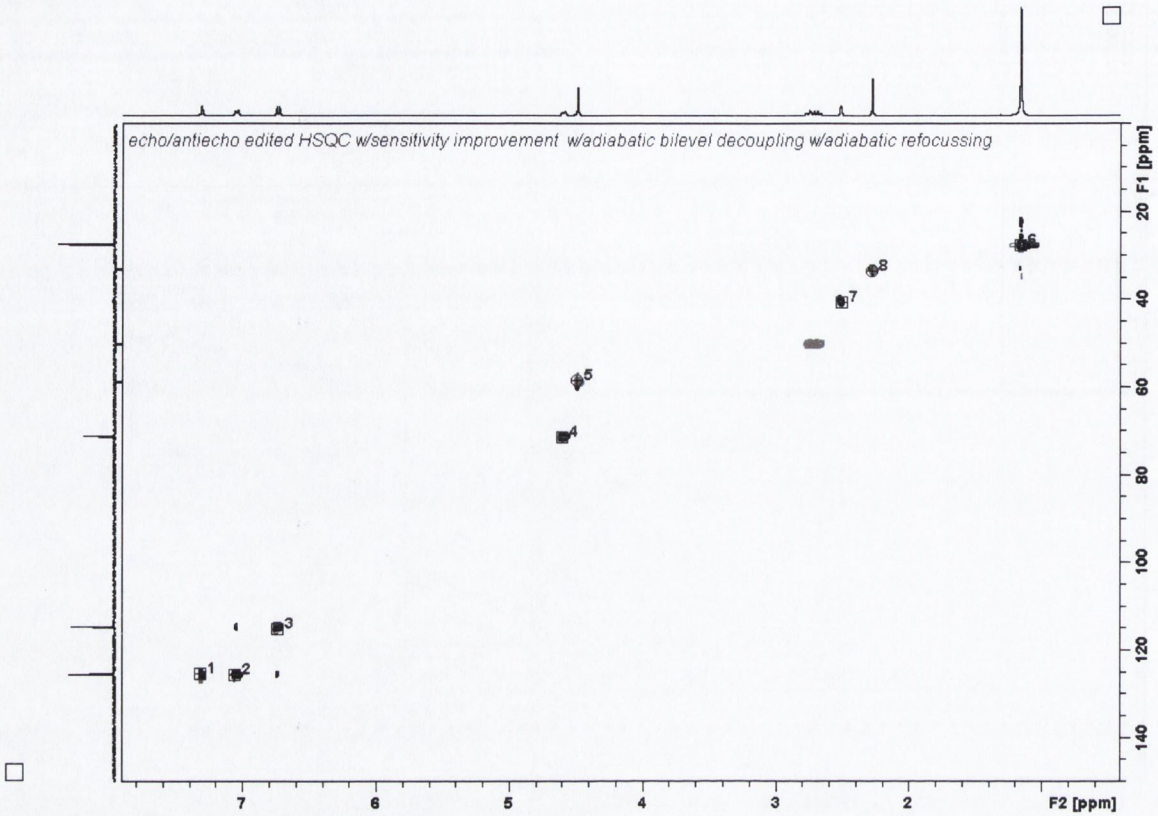

Fig. II.28. HSQC 2D ^{1}HNMR ^{13}CNMR of desolvated salbutamol succinate.

Table II.28. Summary HSQC 2D ^{1}HNMR ^{13}CNMR data for desolvated salbutamol succinate.

Peak	ν(F2) [ppm]	ν(F1) [ppm]	Intensity [abs]
C(10,11,12) H(10-12/ABC)	1.16	27.7	5044325.70
C(8)H(8AB)	2.73	50.1	-339711.76
C(13)H(13AB)	4.49	58.5	-2221419.78
C(7)H(7)	4.60	71.4	508582.94
C(2)H(2)	6.74	115.2	126481.80
C(3)H(3)	7.32	125.4	305727.63
C(6)H(6)	7.06	125.6	439433.84
C(15,18)	2.28	33.6	-626604.50